Physics of Atomic Nuclei, Vol. 63, No. 5, 2000, pp. 705–714. Translated from Yadernaya Fizika, Vol. 63, No. 5, 2000, pp. 773–782.

NUCLEI
Experiment

Rotational Bands in the ^{170}Er Nucleus

E. P. Grigoriev* and I. A. Gladkova

Institute of Physics (Petrodvorets Branch), St. Petersburg State University, Ul'yanovskaya ul. 1, Petrodvorets, 198904 Russia

Received June 8, 1998; in final form, March 30, 1999

Abstract—A critical analysis of the entire body of available experimental data on the excited states of the deformed even–even nucleus ^{170}Er is performed. By contrasting the spectrum of gamma rays from the relevant $(n, n'\gamma)$ reaction against data from other processes, it is possible to reveal new $K^\pi = 0^-$ and 2^- bands and to establish new levels, including rotational levels of known bands, with allowance for the moments of inertia. The structure of the excited states of ^{170}Er is investigated on the basis of the Nilsson scheme and of the quasiparticle–phonon model. © *2000 MAIK "Nauka/Interperiodica".*

1. INTRODUCTION

By and large, modern theoretical models describe well the properties of deformed even–even nuclei, although some excited states show as-yet-unexplained features that engage the attention of researchers. Obviously, reliable experimental data are required to consider these features in greater detail. A vast body of information has been obtained for the erbium isotopes ^{168}Er [1–3] and ^{166}Er [4, 5]. In particular, more than two tens of rotational bands are known for the former. There is much less information about ^{170}Er, the heaviest stable isotope of erbium [it is precisely because of this property of ^{170}Er that the access to its excited states is complicated in heavy-ion reactions; nor was it studied in the informative reaction (n, γ), since the initial nucleus for this reaction, ^{167}Er, is unstable].

2. EXPERIMENTAL DATA AND SCHEME OF EXCITED LEVELS OF ^{170}Er

Experimental data obtained before 1995 were included in the compilation of Baglin [6], who presented, among other things, information about the beta decay of two isomers of ^{170}Ho; about electron capture in ^{170}Tm; about Coulomb excitation; and about the relevant (d, d'), $(n, n'\gamma)$, and (γ, γ') reactions. New (γ, γ') data were presented in [7].

A global consideration of the entire body of experimental data makes it possible to extend considerably the scheme of excited levels of ^{170}Er. Here, a special role is played by the relevant $(n, n'\gamma)$ reaction. That levels are populated statistically in this reaction, irrespective of their nature, enables us to decide whether a specific level is present (or absent) and provides information about its spin.

* e-mail: epgrig@snoopy.phys.spbu.ru

2.1. Reaction $(n, n'\gamma)$

The first results on the relevant $(n, n'\gamma)$ reaction were reported between 1981 and 1983 [8, 9]. These data made it possible to extend considerably the level scheme for ^{170}Er [10]. Two subsequent studies performed in 1992 [11] provided a more detailed and more precise spectrum of gamma rays and contributed to refining the level scheme from [10]. Having the entire body of available information about ^{170}Er at our disposal and using the intensities of gamma rays from [11], we plotted the occupation probabilities P for ^{170}Eu levels versus their energies E (Fig. 1). For a given level, the quantity P was defined as the difference of the total intensity of gamma transitions occurring from this level and the total intensity of gamma transitions terminating at it. On the basis of the data in Fig. 1, we can estimate the energy of the level and its spin J; these data give virtually no way, however, to deduce information about the parity of the relevant wave function. It turned out that the $J = 1$, 2, and 3 levels are characterized by the highest values of P. The dependence $P(E)$ in Fig. 1 enabled us to draw some new conclusions about the excited levels of ^{170}Er; to find some new bands; to supplement known bands with new rotational levels; to introduce some new levels; to verify the existence of many states; and to eliminate, from the scheme of ^{170}Er levels, about a dozen states that were not confirmed in studying the reaction $(n, n'\gamma)$.

2.2. Beta Decay of the Ground State of ^{170}Ho ($J^\pi = 6^+$, $T = 2.76$ min)

In the article of Tuurnava *et al.* [12], who studied beta radiation from ^{170}Ho isomers, it was found that the high-spin state with lifetime $T = 2.76$ min appears to be the ground state. We tested here the level scheme from [13] by using the spectrum for the $(n, n'\gamma)$ reaction and revealed overall agreement.

1063-7788/00/6305-0705$20.00 © 2000 MAIK "Nauka/Interperiodica"

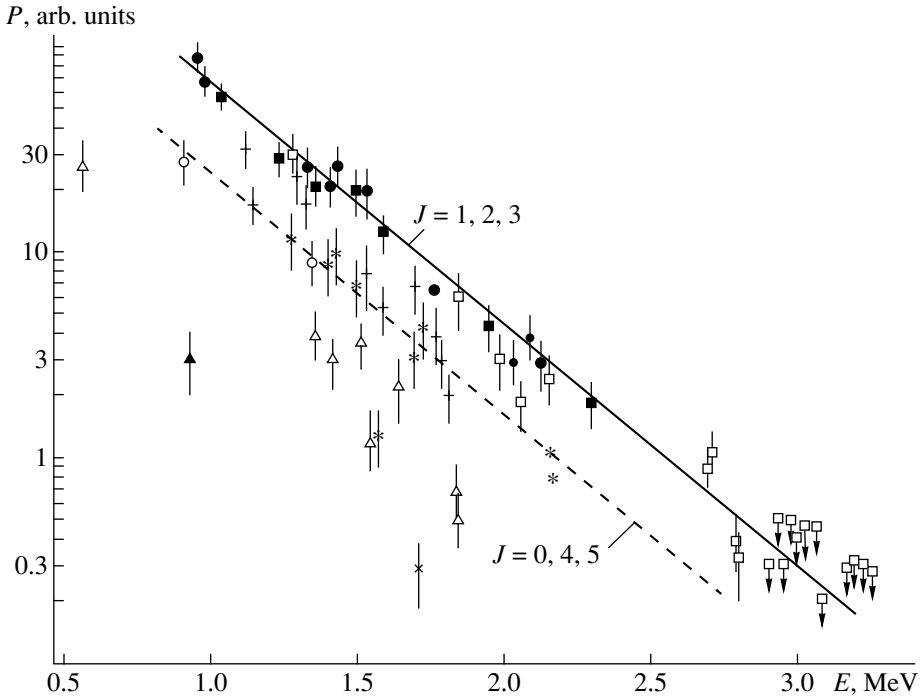

Fig. 1. Occupation probabilities P for the ^{170}Er nuclei in the (n, $n'\gamma$) reaction versus the energy and spin of the levels: (○) 0^+, (□) 1, (●) 2, (■) 3, (+) 4, (∗) 5, (△) 6, (×) 7, (▲) 8, and (•) 1 or 2. The values of P are presented in units normalized to the corresponding values for ^{56}Fe [8].

A 1226-keV transition participates in the deexcitation of the 4^+3_1 level at 1304.55 keV. The spectrum for the (n, $n'\gamma$) reaction features a 1226-keV doublet, whose weak component, with an intensity of $I_\gamma = 4.1$ arb. units versus the total intensity of 29 arb. units, is involved in the deexcitation of the 1304.55-keV level.

The occupation probability for the 2158.97-keV level in beta decay corresponds to an allowed unhindered (au) transition. There is only one possibility for an au transition from ^{170}Ho: $n523\downarrow \longrightarrow p523\uparrow$; this leads to unambiguous quantum-number assignments for the ground state of ^{170}Ho (6^+, $p523\uparrow + n512\uparrow$) and for the 2158.97-keV level of ^{170}Er (5^+, $n523\downarrow + n512\uparrow$). Beta decay to the 1590.74-keV level ($\log ft = 6.4$) has the character of a first-forbidden unhindered beta transition. Here, there is also the only possibility of interpreting it: $n633\uparrow \longrightarrow p523\uparrow$. The level at 1590.74 keV has the 6^-, $n633\uparrow + n512\uparrow$ structure.

2.3. Beta Decay of the ^{170m}Ho isomer ($J^\pi = 1^+$, $T = 43$ s)

The richest set of information about the gamma-ray spectrum of ^{170m}Ho can be found in [14]. Its decay energy was refined in [12] (3970 keV), and the value of $I_\gamma = 40(10)$ arb. units was presented there for the intensity of the 79-keV transition instead of 170 arb. units in [14]. Half of the observed gamma transitions were arranged in the scheme of the ^{170}Er levels [6, 14]. By using data on the spectrum for the (n, $n'\gamma$) reaction and the analysis of these data from [10], we were able to place all these transitions in the level scheme and correct the errors made in [6, 14]. For the sake of comparison, Table 1 presents the energies and intensities of the gamma transitions in question.

For the first time, we arranged transitions from 1267-, 1305-, 1324-, 2070-, 2133-, 2701-, and 2790-keV levels in the level scheme. Levels that were observed in resonance gamma-ray scattering on a ^{170}Er target [6, 7] are included in Table 1. Taking into account the dependence $P(E)$ (see Fig. 1), we introduced levels at 1741.86 and 2019.1 keV. We were unable to confirm the $J \le 4$ level at 1500.9 keV, which was introduced in [14] on the basis of the deexciting 540.9-keV transition alone, because this transition is not observed in the (n, $n'\gamma$) reaction.

For the beta decay of the isomer, we estimated the branching fraction for the decay to each level and $\log ft$ values. The estimate $\Delta \log ft \sim 0.2$ was obtained by taking into account the incompleteness of the spectrum. Only one very fast au beta transition to the 3606.5-keV level ($\log ft = 4.8$) is observed. It corresponds to the $n523\downarrow \longrightarrow p523\uparrow$ transformation and determines the structure of the ^{170m}Ho isomer ($p523\uparrow - n512\uparrow$). The position of the 1^+ and 6^+ doublet levels corresponds to the Gallagher–Moszkovski rule at a normal spacing between the components (about 100 keV).

Table 1. Deexcitation of ^{170}Er levels in the beta decay of ^{170}Ho ($J^\pi = 1^+$, 43 s)

$J^\pi K_i$	E_{level}, keV [1]	^{170}Ho			$(n, n'\gamma)$	
		E_γ, keV	I_γ, arb. units	logft	E_γ, keV	I_γ, arb. units
0^+0_1	0	–	–	6.0	–	–
2^+0_1	78.59(2)	78.7(2)	40(10)	6.3	78.63(3)	131(15)
4^+0_1	260.13(2)	181.6(2)	9.6(10)	–	181.57(2)	276(31)
0^+0_2	890.88(4)	812.3(2)	100.0(31)	7.1	812.29(3)	27(4)
2^+0_2	959.98(3)	959.4(5)	12.4(12)	7.4	959.96(6)	19(4)
		881.2(2)	19.7(8)		881.38(2)	28(4)
		699.8(3)	12.9(6)		699.87(2)	20(3)
1^-1_1	1266.64(3)	1187.5(3)	25.5(10)	7.3	1188.04(2)	28(4)
2^-1_1	1305.23(7)	1226.3(7)	13.4(13)	7.6	1226.64(6)	25(4) m ?
0^+0_3	1324.28(5)	1245.2(4)	2.6(5)	8.3	1245.69(4)	7.8(11)
		–	–		390.11(10)	1.3(2)
2^+2_2	1416.25(4)	1415.6(3)	5.0(5)	7.5	1416.23(7)	6.7(10) m
		1337.4(3)	5.8(6)		1337.64(3)	5.9(8)
1, 2	1741.86(8)	1663.8(8)	1.4(5)	8.0	1663.27(6)	3.7(5)
$1^{(+)}\gamma\gamma'$	1973.03(8)	1972.6(3)	36.5(13)	6.4	1973.1(3)	1.39(20)
		1894.0(3)	45.2(15)		1894.43(8)	1.65(24)
$2^+(1^-)$	2019.1	1940.1(3)	10.5(5)	7.2	1940.41(20)	2.8(5)
					1059.2(3)	0.23(5)
$1\gamma\gamma'$	2039.3(2)	2039.3(4)	2.9(3)	7.5	2039.3(3)	0.91(14) c
		1960.7(4)	2.7(3)		1960.7(6)	0.85(13) m
1^-, 2^+	2071.3(3)	–	–	7.5	2071.0(5)	0.81(13)
		1992.5(5)	4.8(4)		1992.8(3)	3.9(6)
$1\ \gamma\gamma'$	2132.9(2)	2132.8(6)	1.2(3)	7.8	2132.9(4)	1.24(18) m
		–	–		2054.37(15)	0.5(1) c
$1, 2\gamma\gamma'$	2684.8(3)	2684.8(4)	4.5(3)	6.6	2683.6(5)	0.15(2) c
		2606.1(4)	4.3(4)		2606.0(8)	0.14(6)
$1\ \gamma\gamma'$	2700.8(2)	–	–	7.3	2700.7(3)	0.75(12)
		2621.4(6)	0.8(3)		2622.4(4)	0.4(1) c
$1^+\ \gamma\gamma'$	2790.3(4)	2789.2(15)	1.2(3)	7.2	2790.3(4)	0.30(5)
		–	–		2711.2(12)	0.13(6)
(2^+)	3606.5(4)	2715.1(8)	2.5(3)	4.8	(2716.1(4))	(0.39(7))
		2646.5(4)	3.8(3)		–	–

Note: Here and in Tables 3, 5, and 6, the letter "c" labels the calculated values; the letter "m" means that a given level belongs to a multiplet.

2.4. Coulomb Excitation

Levels that belong to the rotational band built on the ground state and which are characterized by spin–parity values up to 12^+ manifest themselves in Coulomb excitation processes [6]. In addition, 2^+ 934-keV and 4^+ 1101-keV levels of the gamma band and 2^+ 960-keV and 4^+ 1124-keV levels of the $K^\pi = 0^+$ band were observed. Each of these was confirmed by gamma transitions in the $(n, n'\gamma)$ reaction. In Coulomb excitation processes, however, the 2^+ state at 1332 keV manifested itself through the 398- and 1332-keV gamma transitions. Although it is expected that the occupation probability will be high for the 2^+ level (P = 30 arb. units) and that the 398- and 1332-keV transitions will manifest themselves as strong peaks (with $I_\gamma \sim 15$ arb. units), neither of these two transitions has been seen in the spectrum for the $(n, n'\gamma)$ reaction. From the experimental spectrum, it follows that $I_\gamma(398) \le 1$ arb. units and $I_\gamma(1332) < 0.2$ arb. units. Accordingly, we can unambiguously conclude that there is no level at 1332 keV.

In Coulomb excitation processes, the 3^- level at 1371 was observed in the 1292-keV transition. There is

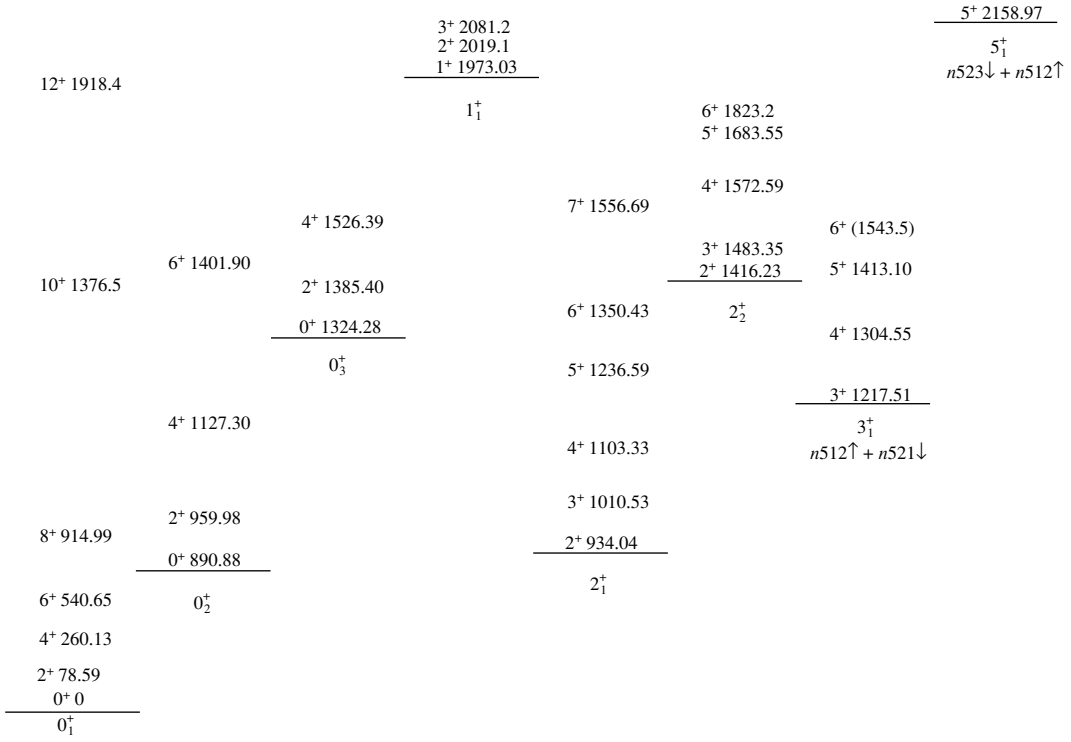

Fig. 2. Positive-parity rotational bands in ^{170}Er (the energies of the levels are given in keV).

no this transition in the $(n, n'\gamma)$ reaction. The estimate $I_\gamma(1292) < 0.2$ arb. units is much less than the expected occupation probability for the level in question, $P = 20$ arb. units, whence it follows that this level was erroneously included in the scheme of the ^{170}Er levels. It should be noted that the 5^-4_1 level at 1372.07 keV, which cannot be populated via Coulomb excitation processes and which is not deexcited through the 1292-keV transition, has a close energy.

3. ROTATIONAL BANDS IN ^{170}Er

3.1. Ground-State Band

In Coulomb excitation processes, the band built on the ground state of ^{170}Er (see Fig. 2) was observed up to the $J^\pi = 12^+$ level. In accord with [6, 8, 10], the 374.27(4)-keV gamma transition was taken to occur between the 8^+ and 6^+ levels. In [11], however, the $8^+ \longrightarrow 6^+$ rotational transition was associated with the 370.99(17)-keV gamma transition. In Coulomb excitation, the transition energy is 374.0(5) keV. It was established that the energies of the lowest levels of the corresponding bands in the neighboring nuclei ^{170}Er and ^{172}Yb are astonishingly close.

3.2. Close Collective Bands of $K_i^\pi = 0_2^+$ and 2_1^+ Vibrational States

The lowest collective nonrotational states at 890.88 (0^+) and 934.04 (2^+) keV were observed experimentally in [6]; they were predicted by Soloviev in [15] to occur at 0.9 and 1.0 MeV. Either band was supplemented with new levels, refined, and analyzed. The positions of the rotational levels in the 0_2^+ band are in accord with data presented in [6, 10, 11]. Considerable modifications were introduced in the gamma-vibrational band. The level at 1413 keV proved to be singlet; this level is not associated with the gamma band, but it has the quantum-number values of 5^+3_1. By using the inertial parameters, we estimated the position of the 6^+2_1 level; from data on three gamma transitions, we determined its energy to be 1350.43(7) keV.

The 7^+2_1 level at 1556.69(9) keV, which was proposed previously on the basis of data on the 1016.04-keV transition ($I_\gamma = 1.3$ arb. units) [10], was also associated with the 641.71-keV transition ($I_\gamma = 0.91$ arb. units) proceeding to the 8^+0_1 level at 914.92 keV. Table 2 contains data on the energies of rotational levels, the differences of these levels, and their inertial parameters. Here, we can reveal two special features.

(i) In the sequence of the rotational levels of the $K = 0$ band, the inertial parameter A increases with increasing angular momentum J, a dependence that is rarely observed experimentally in such cases.

(ii) In the $K = 2$ band, there is a considerable signature splitting.

In view of this, the parameters A calculated separately for even-spin and odd-spin levels are also pre-

Table 2. Rotational parameters (in keV) of the $K_i^\pi = 0_2^+$ and 2_1^+ bands

J	$K_i^\pi = 0_2^+$			$K_i^\pi = 2_1^+$						
	E_{level}	ΔE	A	E_{level}	ΔE	A	ΔE_{even}	A_{even}	ΔE_{odd}	A_{odd}
0	890.88	–	–	–	–	–	–	–	–	–
2	959.98	69.10	11.52	934.04	–	–	–	–	–	–
3	–	–	–	1010.53	76.49	12.75	–	–	–	–
4	1127.30	167.32	11.95	1103.33	92.80	11.60	169.29	12.09	–	–
5	–	–	–	1236.59	133.26	13.33	–	–	226.06	12.56
6	1401.90	274.60	12.48	1350.63	114.04	9.50	247.30	11.24	–	–
7	–	–	–	1556.69	206.05	14.72	–	–	320.09	12.31

sented in Table 2. They decrease with increasing J, as is observed in the neighboring nuclei.

A $6^+ \longrightarrow 4^+$ intraband transition was observed in either of the two bands. In each case, it proved to be enhanced in relation to transitions proceeding to the 6^+0_1 levels: $B(E2; 6^+0_2 \longrightarrow 4^+0_2)/B(E2; 6^+0_2 \longrightarrow 6^+0_1) = 26$ and $B(E2; 6^+2_1 \longrightarrow 4^+2_1)/B(E2; 6^+2_1 \longrightarrow 6^+0_1) = 38$. The presence of the $M1$ component in the $6^+2_1 \longrightarrow 6^+0_1$ transition only increases the above ratios, which are consistent with the systematics of intra- and interband transitions.

3.3. $K_i^\pi = 0_3^+$ Band Built on the 0^+0_3 Level at 1324.28 keV Involving a Two-Phonon Component

Three levels of this band are known. Table 3 lists the energies of the levels and the inertial parameters. A feature peculiar to the deexcitation of the levels of the band is that the reduced probability of deexcitation to the gamma band is much greater than that for the deexcitation to the ground-state band.

3.4. $K_i^\pi = 2_2^+$ Band Built on the 2^+2_2 Level at 1416.23 keV Involving a Two-Phonon Component

A band built on the 2_2^+ level at 1416.23 keV is indicated in [6, 10] for ^{170}Er. We modified the energy of the 5^+ level, added the 6^+ level, and associated other rotational levels with new transitions. Table 3 quotes the energies of the levels and the inertial parameters, while Table 4 illustrates the deexcitation of the levels of the band and presents the reduced probabilities for $E2$ transitions. It can be seen that the reduced probabilities $B(E2)$ for transitions to the 2_1^+ and 0_2^+ bands exceed considerably the reduced probabilities $B(E2)$ for transitions to the ground-state band. In just the same way as in the case of the 0_3^+ band, this may suggest the presence of a significant $0_2^+ \otimes 2_1^+$ two-phonon component in the 2_2^+ band. The lifetimes of the levels belonging to the band in question have yet to be established.

An intraband 250.8-keV transition proceeds from the 6^+2_2 level at 1832 keV. Its reduced probability is greater than $B(E2; 6^+2_2 \longrightarrow 4^+2_1)$ by a factor of 172. This value characterizes the role of the two-phonon component in the band.

3.5. $K_i^\pi = 3_1^+$ Band Built on the 3^+3_1 Level at 1217.51 keV

According to Soloviev's calculations based on the quasiparticle–phonon model [15], a 3^+, $n521\downarrow + n512\uparrow$ two-particle neutron level is expected to occur at 1.3 MeV. This level and the 4^+ and 5^+ levels of the rotational band are populated in the beta decay of ^{170}Ho and in the $(n, n'\gamma)$ reaction. In the present study, the above levels were supplemented with the 6^+3_1 level at 1543.5(2) keV, whose existence was suggested by the following two transitions from the spectrum in the $(n, n'\gamma)$ reaction: the 1002.63(17)-keV $6^+3_1 \longrightarrow 6^+0_1$ transition (0.94 arb. units) and the 1283.61(20)-keV $6^+3_1 \longrightarrow 4^+0_1$ transition (0.43 arb. units). From the data listed in Table 5, we can see that the values of the inertial

Table 3. Rotational parameters (in keV) of the $K_i^\pi = 0_3^+$ and 2_2^+ bands

J	$K_i^\pi = 0_3^+$			$K_i^\pi = 2_2^+$		
	E_{level}	ΔE	A	E_{level}	ΔE	A
0	1324.28	–	–	–	–	–
2	1385.40	61.12	10.19	1416.23	–	–
3	–	–	–	1483.35	67.12	11.19
4	1526.39	140.99	10.07	1572.59	89.24	11.16
5	–	–	–	1683.55	110.96	11.10
6	1746 c	220 c	10 c	1823.2	139.7	11.64

Table 4. Deexcitation of levels belonging to the $K_i^\pi = 2_2^+$ band

$(J_k^\pi)_f$	E_f, keV	E_γ, keV	I_γ, arb. units	E_{level}, keV	$B(E2)$, arb. units
2^+ level at 1416.23 keV					
0^+0_1	0	1416.23(7)	≤6.7 d	1416.23	–
2^+0_1	78.59	1337.64(3)	5.9	1416.23	1.0
2^+2_1	934.04	482.20(2)	13.3	1416.24	370
2^+0_2	959.98	456.53(12)	1.13	1416.51	41
3^+2_1	1010.53	405.71(9)	3.4	1416.24	255
3^+ level at 1483.35 keV					
2^+0_1	78.59	1404.73(4)	5.7	1483.32	1.0
4^+0_1	260.13	1223.55(9)	<4 d ?	1483.68	–
2^+2_1	934.04	549.31(8)	≤3.3 d ?	1483.35	<63
3^+2_1	1010.53	472.84(4)	5.4	1483.37	219
4^+2_1	1103.33	379.99(7)	≤1.67	1483.32	<190
4^+0_2	1127.30	356.27(14)	<0.5 d	1483.57	<80
4^+ level at 1572.59 keV					
4^+0_1	260.13	1312.51(11)	2.6	1572.64	1.0
2^+2_1	934.04	638.0(3)	0.25	1572.0	3.5
3^+2_1	1010.53	562.30(12)	1.0	1572.83	27
4^+2_1	1103.33	469.29(16)	0.52	1572.62	34
4^+0_2	1127.30	445.29(15)	0.63	1572.59	54
5^+2_1	1236.59	336.05(10)	<1.2 d	1572.64	<400
5^+ level at 1683.55 keV					
4^+0_1	260.13	1423.4(3)	<1.21 d	1683.5	<1.0
6^+0_1	540.65	1142.78(9)	1.16	1683.43	2.7
4^+2_1	1103.33	580.33(9)	1.23	1683.66	86
5^+2_1	1236.59	447.2(3)	0.26	1683.8	67
6^+ level at 1823.2 keV					
6^+0_1	540.65	1282.3(4)	0.23	1823.0	5.2
4^+2_1	1103.33	720.6(10)	0.25 d	1823.9	100
4^+0_2	1127.30	695.92(5)	<2.3 d	1823.21	–
5^+2_1	1236.59	586.67(14)	<2.0 d	1823.26	–
4^+2_2	1572.59	250.8(3)	0.22	1823.4	17200

Note: The letter "d" means that a given level appear to be a doublet, whose intensity is actually presented.

parameter A are close for three pairs of neighboring levels. The next level having the quantum-number values of 7^+3_1 is expected to occur at 1705 keV, but it is populated less intensively in the $(n, n'\gamma)$ reaction, so that it did not manifest itself.

Bands of the same structure are known in the neighboring isotope ^{168}Er and in the ^{172}Yb and ^{174}Hf isotopes. The inertial parameters A are also close in absolute value and in changes they suffer with increasing spin.

Two intraband transitions, $5^+3_1 \longrightarrow 3^+$, $E2$ and $5^+ \longrightarrow 4^+$, $E2 + M1$, were found to proceed from the 5^+3_1 level at 1413.10 keV. Assuming that the intrinsic quadrupole moment of the band, $Q_0 = 6.8(8)\ e$ b, is equal to the quadrupole moment of the ground state and using the intensity-ratio value of $I_\gamma(195.58, E2)/I_\gamma(108.32, E2 + M1) = 0.59(13)$, we have determined the gyromagnetic ratio to be $(g_K - g_R)^2 = 0.15(8)$ and the bandhead magnetic moment to be $\mu_1 = 0.0(4)$ or $\mu_2 = 1.8(4)$ nuclear magnetons. The first of these is in good agreement with one of the two values calculated for the configuration being considered by using the Nilsson functions, $\mu_1^T = 0.015$ or $\mu_2^T = -0.96$ nuclear magnetons.

Table 5. Rotational parameters (in keV) of the $K_i^\pi = 3_1^+$ bands in ^{170}Er, ^{168}Er, ^{172}Yb, and ^{174}Hf

J	$^{170}_{68}Er_{102}$			$^{168}_{68}Er_{100}$ [1]	$^{172}_{70}Yb_{102}$ [16]	$^{174}_{72}Hf_{102}$ [17]
	E_{level}	ΔE	A	A		
3	1117.51	–	–	–	–	–
4	1304.55	87.04	10.88	10.39	11.33	11.40
5	1413.10	108.57	10.86	10.27	11.28	11.36
6	1543.5	130.43	10.87	10.17	11.20	11.15
7	1705 c	151 c	10.8 c	9.93	11.14	11.15
8	–	–	–	–	10.98	–

3.6. 5^+5_1 Level at 2158.97(7) keV

The ground state of ^{170}Ho decays predominantly to the 2158.97-keV level with $\log ft = 5.2$. The structure of the ground state of ^{170}Ho is 6^+, $p523\uparrow + n512\uparrow$, while the structure of the 5^+ level at 2158.97 keV is $n523\downarrow + n512\uparrow$ (see Subsection 2.2). In accordance with the Gallagher–Moszkovski rule, the 6^+ level is the lowest one in the doublet, while the 1^+, $p523\uparrow - n512\uparrow$ level occurs higher. Experimental data confirm this arrangement of the levels in ^{170}Ho and lead to the splitting energy of 100 ± 60 keV [14].

3.7. $K_i^\pi = 1_1^-$ Band Built on the 1^- Octupole Level at 1266.64 keV

According to Soloviev's model from [15], the lowest collective level of negative parity (1^-) must occur at 1.2 MeV. The known levels include the 1^- level at 1266.64 keV and rotational levels characterized by the J values of up to 5 [6, 10]. In the present study, the band in question was supplemented with $J = 6$ and 7 levels (see Fig. 3). The 6^-1_1 state at 1631.2(4) keV is determined by two transitions:

6^+0_1, 1090.6(4) + 540.65 = 1631.2, $I_\gamma = 1.6$ arb. units;

6^+2_1, 280.52(2) + 1350.6 = 1631.1, $I_\gamma < 45$ arb. units.

The 7^-1_1 level at 1704.8 keV is determined by the 1164.16(18)-keV $7^-1_1 \longrightarrow 6^+0_1$ transition, its intensity being 0.27 arb. units.

For ^{170}Er and for its isotone ^{172}Yb, Table 6 presents the energies of the levels belonging to the $K_i^\pi = 1_1^-$ band, the differences of these energies, and the inertial parameters calculated separately for even-spin and for odd-spin levels. The following features are peculiar to both nuclei:

(i) The parameters A_{even} and A_{odd} differ significantly.

(ii) With increasing J, A_{odd} grows. This rare effect can be qualitatively explained by the "repulsion" of odd-spin levels in the $K = 0$ and 1 bands. However, two $K^\pi = 1^-$ bands are known in the ^{168}Er nucleus. The $K^\pi = 0$ band occurs in between these two. In contrast to expectations, however, the parameter A_{odd} behaves similarly in the two bands, this behavior being identical to that in ^{170}Er and ^{172}Yb. This may be due to the effect of higher $K^\pi = 0^-$ bands.

(iii) The greater signature splitting in ^{172}Yb is caused by a smaller spacing between the $K = 0$ and 1 bands in this nucleus than in ^{170}Er.

(iv) If the above repulsion is due to the interaction of two bands, this interaction is strong.

3.8. New $K_i^\pi = 0_1^-$ Band Built on the 1824.60-keV Level

The octupole 1^-0_1 level is expected at 1.6 MeV [15]. It is observed in the relevant (γ, γ') and $(n, n'\gamma)$ reactions, occurring at 1824.60 keV. The rotational 3^-0_1 level at 1935.44 keV manifested itself in the (d, d') and $(n, n'\gamma)$ reactions. Here, a new level in the 5^-0_1 band at $E = 2150.9(3)$ keV has been proposed on the basis of data

Table 6. Energies of the levels and inertial parameters (in keV) of the $K^\pi = 1^-$ bands in $^{170}_{68}Er_{102}$ and $^{172}_{70}Yb_{102}$

J	^{170}Er, $E(1^-0_1) = 1824$ keV				^{172}Yb, $E(1^-0_1) = 1600$ keV			
	E_{level}	ΔE	A_{even}	A_{odd}	E_{level}	ΔE	A_{even}	A_{odd}
1	1266.64	–	–	–	1154.94	–	–	–
2	1305.23	38.59	–	–	1198.47	43.53	–	–
3	1340.20	34.97	–	7.36	1221.72	23.25	–	6.68
4	1432.95	92.75	9.12	–	1330.69	108.97	9.44	–
5	1483.72	50.77	–	7.97	1352.95	22.26	–	7.29
6	1631.2	147.5	9.01	–	1540.61	187.66	9.54	–
7	1704.8	73.2	–	8.52	1557.58	16.97	–	7.87
8	1899 c	194 c	8.90 c	–	1828.71	271.13	9.61	–

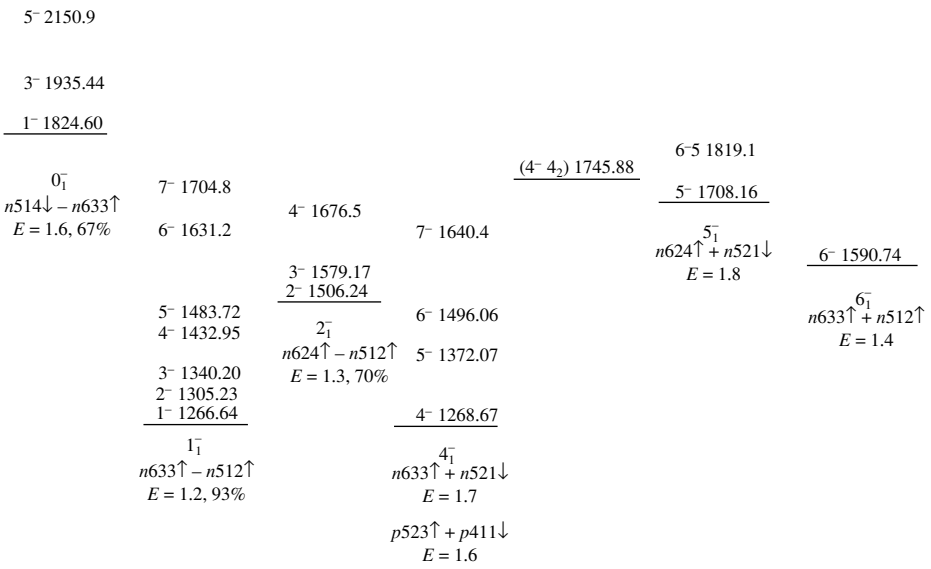

Fig. 3. Negative-parity rotational bands in ^{170}Er (the energies of the levels are given in keV).

on two transitions:

4^+0_1, 1890.8(3) + 260.1 = 2150.9, 0.74 arb. units,

6^+0_1, 1610.2(7) + 540.6 = 2150.8, 0.40 arb. units.

The inertial parameters A(3–1) = 11.08 keV and A(5–3) = 11.97 keV comply with the relevant systematics. For example, we have A(3–1) = 11.06 keV in ^{172}Yb. The occupation probabilities for all three levels in the (n, $n'\gamma$) reaction are consistent with the predictions of the statistical model.

3.9. New $K_i^\pi = 2_1^-$ Band Built on the 1506.24-keV Level

The 2^- 1.3-MeV collective octupole level predicted by Soloviev in [15] actually has the energy of 1506.24 keV. Previously, it was assigned the spin–parity of 4^+ [6, 10, 11], but the occupation probability in the (n, $n'\gamma$) reaction proves to be overly high, P = 20 arb. units, for a J = 4 level. The 2^- level is deexcited by the transitions to the 2^+ and 3^+ levels of the 3^+3_1 gamma band (see [6]) and by the 1427.40-keV transition (0.84 arb. units) to the 2^+0_1 level.

The rotational 3^-2_1 level at 1579.17(11) keV is deexcited by the following transitions:

4^+0_1, 1319.1(3) + 260.13 = 1579.2, 1.38 arb. units;

2^+2_1, 645.23(3) + 934.04 = 1579.27, 4.1 arb. units;

3^+2_1, 568.65(9) + 1010.53 = 1579.18, 4.5 arb. units;

4^+2_1, 475.47(7) + 1103.33 = 1578.80, 1.0 arb. units;

4^+0_2, 451.72(6) + 1127.29 = 1579.01, 2.2 arb. units;

4^+3_1, 274.43(21) + 1304.55 = 1579.98, <0.27 arb. units.

It should be noted that, because of selection rules in K, the gamma transition to the 4^+0_1 level is severely hindered. At the same time, selection rules in K do not manifest themselves in the transition to the 4^+0_2 level. This is due to the mixing of the wave functions of the 4^+2_1 and 4^+0_2 states.

The next rotational level (4^-2_1) at 1676.5(1) keV is introduced on the basis of the inertial parameters A(3–2) = 12.14 keV and A(4–3) = 12.17 keV:

4^+0_1, 1416.23(7) + 260.13 = 1676.33, <6.7 arb. units;

3^+2_1, 665.84(5) + 1010.53 = 1676.37, 2.9 arb. units;

4^+2_1, 572.22(5) + 1103.33 = 1676.55, <14 arb. units;

4^+0_2, 549.31(8) + 1127.30 = 1676.61, 3.3 arb. units;

3^+3_1, 459.5(2) + 1217.51 = 1677.0, 0.5 arb. units;

5^+2_1, 439.50(5) + 1236.59 = 1676.22, 3.4 arb. units;

2^-1_1, 370.99(17) + 1305.23 = 1676.22, <0.8 arb. units.

Selection rules in K in the transition to the 4^+0_1 level and the mixing of the 4^+2_1 and 4^+0_2 states also manifest themselves here.

The rotational 5^-2_1 level is expected at 1798 keV. No definitive conclusions can be drawn on this level since it is populated only slightly in the (n, $n'\gamma$) reaction and since it can be deexcited via several transitions, in just the same way as the 3^-2_1 level at 1579.07 keV.

3.10. $K^\pi = 4^-$ Band Built on the 1268.67-keV Level

The 4^-, 5^-, and 6^- levels of the $K^\pi = 4^-$ band are excited in the beta decay of ^{170}Ho and in the (n, $n'\gamma$) reaction (see Fig. 3). The band was supplemented with

the 7^-4_1 level at 1640.4(1) keV:

6^+0_1, 1099.99(11) + 540.65 = 1640.64, 2.2 arb. units;

8^+0_1, 725.29(8) + 914.99 = 1640.28, 1.7 arb. units.

The parameter values in the expression describing the order of the rotational levels are $A(5–4) = 10.34$ keV, $A(6–5) = 10.33$ keV, and $A(7–6) = 10.31$ keV.

The 6^- level at 1496.06 keV is deexcited by two intraband gamma transitions. These are the $M1 + E2$ 123.90-keV $6^- \longrightarrow 5^-$ and $E2$ 227.41-keV $6^- \longrightarrow 4^-$ transitions. According to beta-decay data, these transitions have identical intensities. By using the adiabatic model and the quadrupole-moment value of $Q_0 = 6.8(8)\ e$ b for the ground-state band, we have found the gyromagnetic ratio of $(g_K - g_R) = \pm 0.22(7)$ nuclear magnetons. Assuming that the gyromagnetic ratio takes the same value for all levels of the band, we have found the bandhead magnetic moment of $\mu_1(4^-) = 1.9$ nuclear magnetons or $\mu_2(4^-) = 0.5$ nuclear magnetons. By comparing them with the values calculated on the basis of the Nilsson functions, $\mu(pp) = 4.13$ or 3.51 nuclear magnetons and $\mu(nn) = 1.45$ or 0.40 nuclear magnetons, we arrived at the conclusion that the band has a two-quasiparticle neutron structure or a mixed structure.

3.11. 4^-4_2 Level at 1745.88 keV

The 413-keV gamma transition proceeding from the 5^+ 2158.97-keV level to the 1745.88-keV level, which is deexcited by the 477.4-keV transition, was observed in the beta decay of ^{170}Ho. The 477.21-keV transition was observed in the $(n, n'\gamma)$ reaction. Conceivably, a part of the intensity of the 374.27-keV doublet is associated with the transition between the 1746- and the 1372-keV level. In accordance with the occupation probability of $P = 4$ arb. units, the level at 1745.88 keV must be assigned a spin value of $J = 4$. We believe that the quantum numbers of the level are 4^-4_2. This conjecture was based on the following observations:

(i) Only one reliable transition of energy 477.21 keV was found to proceed to the 4^-4_1 level at 1268.67 keV. There is no deexcitation to the $K^\pi = 2^+$ and 3^+ bands. This suggests that the wave functions of the two $K = 4$ levels are close.

(ii) The 2158.97-keV level is deexcited to the 1268.67- and 1745.88-keV levels with close values of $B(E1)$. Their ratio is equal to 1.5, which is indicative of the similarity of the two levels.

(iii) According to the calculations from [15], the 4^-, $p523\uparrow + p411\downarrow$ and 4^-, $n633\uparrow + n521\downarrow$ levels occur at energies of 1.6 and 1.7 MeV, respectively, but, in fact, one of these has the energy of 1268.67 keV (see Subsection 3.10). The magnetic-moment value calculated here for it gives grounds to interpret the structure of this level as a mixture of configurations with close weights of the two-proton and two-neutron components. If we assume that the 4^- state at 1745.88 keV has a similar structure, the existing experimental data can be explained. However, we cannot rule out other interpretations of the 1745.88-keV level.

Searches for the 5^-4_2 rotational level in the range 1830–1860 keV did not lead to any positive result.

3.12. 5^-5_1 Level at 1708.16(2) keV and 6^-5_1 Level at 1819.1(2) keV

A level at 1709 keV was observed in the relevant (d, d') reaction, and it was tentatively assigned a spin–parity of $J^\pi = 5^-$. This level manifested itself in the $(n, n'\gamma)$ reaction through the 439.50- and 336.05-keV transitions to, respectively, the 4^-4_1 and the 5^-4_1 level (see [6]), but it did not show up in the beta decay of ^{170}Ho. This gives ground to treat its structure, according to the model predictions from [15], as $n624\uparrow + n521\downarrow$, the expected energy of the level being 1.8 MeV.

In accordance with the predictions of the rotational model, we propose a possible 6^-5_1 level at 1819.1(2) keV:

6^+0_1, 1278.32(23) + 540.65 = 1818.97, $I_\gamma = 0.20$ arb. units;

5^-4_1, 447.2(3) + 1372.07 = 1819.3, $I_\gamma = 0.26$ arb. units.

The occupation probability for either level in the $(n, n'\gamma)$ reaction is in accord with the known systematics.

3.13. 6^-6_1 Level at 1590.74(8) keV

The 6^-6_1 level at 1590.74(8) keV revealed itself through a very fast ($\log ft = 6.4$) beta transition from the ground (6^+) state of the ^{170}Ho nucleus. This beta transition satisfies the selection rules in the asymptotic quantum numbers for a first-forbidden unhindered (1u) transition. In accordance with the scheme of single-particle levels, this is the $n633\uparrow \longrightarrow p523\uparrow$ transition, and the 1590.74-keV level has the 6^-6_1, $n633\uparrow + n512\uparrow$ structure. The deexcitation of the level via 94.67- and 218.69-keV gamma transitions to the 6^-4_1 and 5^-4_1 levels was established in studying the beta decay of the ^{170}Ho nucleus. These transitions are naturally explained within the scheme of single-particle levels as $n633\uparrow + n512\uparrow \longrightarrow n633\uparrow + n521\downarrow$.

The spectrum for the $(n, n'\gamma)$ reaction shows a 218.66-keV transition. Possibly, this is a doublet, and a part of its intensity is associated with the deexcitation of the 6^-6_1 level.

4. DISCUSSION OF THE RESULTS

The above analysis of the properties of the excited states of the ^{170}Er nucleus has resulted in establishing

their structure. The most comprehensive theoretical predictions were made by Soloviev in [15]. They were confirmed for collective levels. The energies of seven states comply with the model predictions. Yet three other predicted levels can manifest themselves in an analysis of data for the $(n, n'\gamma)$ reaction. The bands that were established here are displayed in Fig. 2 and 3.

An important conclusion was drawn here for the second excited levels with spin–parities $K^\pi = 0^+$ and 2^+. From the enhanced deexcitation to the lowest excited bands with $K^\pi = 0^+$ and 2^+, it follows that these initial states involve a two-phonon component each.

For five levels, we have established a two-quasiparticle neutron structure. This identification was based on fast beta decay to the 5^+, $n512^\uparrow + n523^\downarrow$ level at 2158.97 keV and the 6^-, $n633^\uparrow + n512^\uparrow$ level at 1590.9 keV (see Subsection 2.2).

The gamma decay of the 2158.97-keV level occurs to the $K^\pi = 3^+$, $n512^\uparrow + n521^\downarrow$ band; this corresponds to the allowed $E2$ $n512^\uparrow \longrightarrow n521^\downarrow$ gamma transition. It is rather difficult to explain $E1$ transitions to the $K^\pi = 4^-$ $(n633^\uparrow + n521^\downarrow) + (p523^\uparrow + p411^\downarrow)$ band, because these transitions change states of two particles. The transitions in question can be understood if we assume that, in the 5^+ state at 2158.97 keV, there is an admixture of the wave function of the 5^+4, $n514^\downarrow + n521^\downarrow$ state and that the $E1$ transition corresponds to the $n514^\downarrow \longrightarrow n633^\uparrow$ transformation. Another admixed configuration corresponds to the 5^+3, $n523^\downarrow + n521^\downarrow$ state, and there occurs the $n523^\downarrow \longrightarrow n633^\uparrow$ gamma transition. Both $E1$ transitions are forbidden by the selection rules in the asymptotic quantum numbers, and the deexcitation of the level calls for a theoretical explanation.

The deexcitation of the 6^-6_1, $n633^\uparrow + n512^\uparrow$ level at 1590.77 keV to the 4^-, $n633^\uparrow + n521^\downarrow$ band via the $n512^\uparrow \longrightarrow n521^\downarrow$ transition is understandable. Here, the $M1$ transitions are singly hindered in the quantum number Λ, but a spin flip occurs. The $M1$ deexcitation of the 5^-, $n624^\uparrow + n521^\downarrow$ level at 1708.17 keV to the same $K^\pi = 4^-$ band via the $n624^\uparrow \longrightarrow n633^\uparrow$ transition is of a similar character.

An analysis of gamma transitions associated with collective levels requires knowing transition probabilities, on one hand, and performing quantitative calculations within one model of deformed nuclei or another, on the other hand.

5. CONCLUSION

The scheme of excited levels of the deformed nucleus ^{170}Er has been extended and refined on the basis of a comparison of data obtained in various nuclear processes. New $K^\pi = 0^-$ and 2^- bands have been found, and some bands have been supplemented with new rotational levels. The inertial parameters of the bands have been presented and discussed. Some levels have been introduced, while about a dozen levels whose existence was conjectured previously have been disproved. The structure of more than a dozen bandheads, including vibrational states featuring two-phonon components, has been identified. The applicability of the quasiparticle–phonon model of the nucleus has been confirmed.

REFERENCES

1. V. S. Shirley, Nucl. Data Sheets **71**, 261 (1994).
2. R. L. Gill *et al.*, Phys. Rev. C **54**, 2276 (1996).
3. S. A. Berendakov *et al.*, Yad. Fiz. **61**, 389 (1998) [Phys. At. Nucl. **61**, 329 (1998)].
4. E. N. Shurshikov and N. V. Timofeeva, Nucl. Data Sheets **67**, 45 (1992).
5. E. P. Grigor'ev, Yad. Fiz. **57**, 590 (1994) [Phys. At. Nucl. **57**, 556 (1994)].
6. C. M. Baglin, Nucl. Data Sheets **77**, 125 (1996).
7. H. Maser *et al.*, Phys. Rev. C **53**, 2749 (1996).
8. V. A. Bondarenko, E. P. Grigor'ev, and P. T. Prokof'ev, Izv. Akad. Nauk SSSR, Ser. Fiz. **45**, 2142 (1981); **46**, 2080 (1982).
9. V. A. Bondarenko and E. P. Grigor'ev, Izv. Akad. Nauk SSSR, Ser. Fiz. **47**, 2261 (1983).
10. V. M. Belen'kiĭ and E. P. Grigor'ev, *Structure of Even Nuclei* (Énergoatomizdat, Moscow, 1987).
11. S. A. Berendakov and A. M. Demidov, Izv. Akad. Nauk SSSR, Ser. Fiz. **56** (1), 23 (1992); **56** (11), 28 (1992).
12. T. Tuurnava *et al.*, Phys. Scr. **78**, 31 (1978).
13. R. Katajanheimo *et al.*, Z. Phys. A **286**, 57 (1978).
14. K. Kawade *et al.*, J. Phys. Soc. Jpn. **36**, 1221 (1974).
15. E. P. Grigor'ev and V. G. Soloviev, *Structure of Even Deformed Nuclei* (Nauka, Moscow, 1974).
16. B. Singh, Nucl. Data Sheets **75**, 199 (1995).
17. E. Browne, Nucl. Data Sheets **62**, 1 (1991).

Translated by A. Isaakyan

Physics of Atomic Nuclei, Vol. 63, No. 5, 2000, pp. 715–717. Translated from Yadernaya Fizika, Vol. 63, No. 5, 2000, pp. 783–786.

NUCLEI
Experiment

Elastic Scattering of 800-MeV Protons by ^{20}Ne Nuclei

Yu. A. Berezhnoy* and V. P. Mikhaĭlyuk[1)]

Kharkov State University, Kharkov, 310077 Ukraine

Received February 15, 1999; in final form, May 11, 1999

Abstract—The differential cross section and polarization observables are calculated for the elastic scattering of 800-MeV protons by ^{20}Ne nuclei. The assumption that the ^{20}Ne nucleus has an alpha-cluster structure is shown to lead to results that agree with the measured values of observables of the above scattering process.

At present, the structure of light nuclei has yet to be understood completely. Nonetheless, many properties of light nuclei can be explained on the basis of cluster models, including the alpha-cluster model, which stands out among this class of models. The effects of clustering clearly manifest themselves in scattering of intermediate-energy particles (by intermediate-energy particles, we mean those with energies of $E \geq 100$ MeV per projectile nucleon) by light nuclei.

A dispersive alpha-cluster model for the ^{12}C and ^{16}O nuclei was developed in [1–3]. In this model, it is assumed that the carbon and the oxygen nucleus consist of, respectively, three and four alpha-particle clusters occurring at the vertices of an equilateral triangle in the former case and at the vertices of a tetrahedron in the latter case. These alpha-particle clusters can execute vibrations about the most probable positions of their centers of mass at the vertices of the aforementioned geometric bodies.

For the elastic and inelastic scattering of protons, antiprotons, deuterons, and other particles by ^{12}C and ^{16}O nuclei at intermediate energies, various observables were computed in [3–5] on the basis of the dispersive alpha-cluster model and the theory of multiple diffractive scattering. The results of these calculations proved to be in accord with experimental data. In [3], it was shown that the inclusion of four-nucleon correlations of the alpha-cluster type and correlations between the alpha-particle clusters in the computational scheme makes it possible to obtain a better description of measured observables than that in the model of independent nucleons; as to the specific example of the spin-rotation function, it behaves differently within these two different frameworks.

The results obtained previously give sufficient ground to hope that the approach in question can be successfully applied to heavier nuclei that show an alpha-cluster structure. In the following, the dispersive alpha-cluster model is generalized to the case of the ^{20}Ne nucleus.

In contrast to what we have for the ^{12}C and ^{16}O nuclei, various equilibrium configurations of "crystal" type, including a quadrangular pyramid, a double triangular pyramid, and a tetrahedron featuring an alpha-particle cluster at the center, are possible for the ^{20}Ne nucleus [6]. None of these configurations, however, makes it possible to obtain an analytic expression for the amplitude of the elastic scattering of intermediate-energy particles by ^{20}Ne nuclei on the basis of the dispersive alpha-cluster model. In this study, the ^{20}Ne nucleus is treated as that which consists of a core (^{16}O nucleus) and an extra alpha-particle cluster. We note that a similar approach was applied in a number of studies (see, for example, [7–9] and references therein), but no account was taken there of the internal structure of the core.

The multiparticle density of the ^{20}Ne nucleus will be represented here in the form

$$\rho^{(\mathrm{Ne})}(\boldsymbol{\xi}, \boldsymbol{\eta}, \boldsymbol{\zeta}, \boldsymbol{\chi}) = \rho_{\Delta}^{(\mathrm{O})}(\boldsymbol{\xi}, \boldsymbol{\eta}, \boldsymbol{\zeta})\rho_{\alpha}(\boldsymbol{\chi}), \qquad (1)$$

where $\rho_{\Delta}^{(\mathrm{O})}(\boldsymbol{\xi}, \boldsymbol{\eta}, \boldsymbol{\zeta})$ is the density of the core (^{16}O nucleus); $\rho_{\alpha}(\boldsymbol{\chi})$ is the density of the extra alpha-particle cluster; $\boldsymbol{\xi}$, $\boldsymbol{\eta}$, and $\boldsymbol{\zeta}$ are the Jacobi coordinates of the alpha-particle clusters forming the core; and $\boldsymbol{\chi}$ is the coordinate of the extra alpha-particle cluster. Expression (1) for the density of the neon nucleus is not symmetrized; that is, it is not invariant under the interchange of the extra alpha-particle cluster with any alpha-particle cluster from the core. This circumstance, however, has virtually no effect on the behavior of observables in the scattering of particles with energies $E \geq 100$ MeV per projectile nucleon by nuclei.

The density of the ^{16}O nucleus, $\rho_{\Delta}^{(\mathrm{O})}(\boldsymbol{\xi}, \boldsymbol{\eta}, \boldsymbol{\zeta})$, is given by (see [3])

$$\rho_{\Delta}^{(\mathrm{O})}(\boldsymbol{\xi}, \boldsymbol{\eta}, \boldsymbol{\zeta}) = \int d^3\xi' d^3\eta' d^3\zeta' \rho_0^{(\mathrm{O})}(\boldsymbol{\xi}', \boldsymbol{\eta}', \boldsymbol{\zeta}') \times \Phi_{\Delta}^{(\mathrm{O})}(\boldsymbol{\xi} - \boldsymbol{\xi}', \boldsymbol{\eta} - \boldsymbol{\eta}', \boldsymbol{\zeta} - \boldsymbol{\zeta}'), \qquad (2)$$

* e-mail: berezhnoy@pem.kharkov.ua

[1)] National Center Institute for Nuclear Research, National Academy of Sciences of Ukraine, pr. Nauki 47, Kiev, 252028 Ukraine.

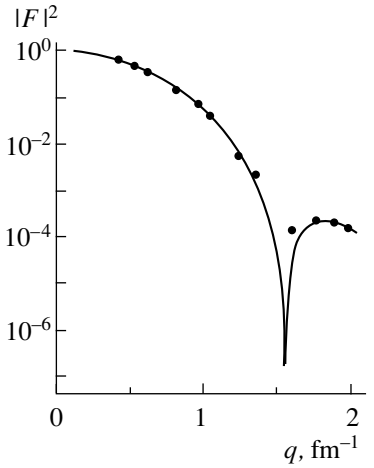

Fig. 1. Charge form factor for the ^{20}Ne nucleus as a function of momentum transfer. Experimental data were borrowed from [10].

where

$$\rho_0^{(O)}(\boldsymbol{\xi}, \boldsymbol{\eta}, \boldsymbol{\zeta}) = \frac{1}{(4\pi)^2}\delta(\xi - d)\delta\left(\eta - \frac{\sqrt{3}}{2}d\right) \times \delta\left(\zeta - \sqrt{\frac{2}{3}}d\right)\delta(\boldsymbol{\xi}\cdot\boldsymbol{\eta})\delta(\boldsymbol{\xi}\cdot\boldsymbol{\zeta})\delta(\boldsymbol{\eta}\cdot\boldsymbol{\zeta}), \quad (3)$$

$$\Phi_\Delta^{(O)}(\xi, \eta, \zeta) = \frac{1}{8(\pi\Delta^2)^9} \times \exp\left(-\frac{\xi^2 + 4/3\times\eta^2 + 3/2\times\zeta^2}{2\Delta^2}\right). \quad (4)$$

If the wave function of the extra alpha-particle cluster is chosen in the form

$$\Psi(\chi) = \frac{1}{(\lambda\sqrt{\pi})^{3/2}}\exp\left(-\frac{\chi^2}{2\lambda^2}\right), \quad (5)$$

its density $\rho_\alpha(\chi)$ appears to be

$$\rho_\alpha(\chi) = \frac{1}{(\lambda\sqrt{\pi})^3}\exp\left(-\frac{\chi^2}{\lambda^2}\right). \quad (6)$$

In the proposed approach, it is assumed that the most probable position of the extra alpha-particle cluster coincides with the core center of mass, the cluster itself executing vibrations about this point within the core. The parameter λ characterizes the root-mean-square deviation of the extra alpha-particle cluster from the core center of mass.

The form factor for the elastic scattering of a ^{20}Ne nucleus can be represented in the form

$$F(\mathbf{q}) = \exp\left(-\frac{1}{6}q^2\langle r^2\rangle_\alpha\right) \times \left[\frac{1}{5}\sum_{i=1}^{5}\int d^3r_i e^{i\mathbf{q}\cdot\mathbf{r}_i}\rho^{(Ne)}(\boldsymbol{\xi}, \boldsymbol{\eta}, \boldsymbol{\zeta}, \boldsymbol{\chi})\right], \quad (7)$$

where the coordinates r_i of the alpha-particle clusters entering into the composition of the core of the ^{20}Ne nucleus are reckoned from the core center of mass, while $\mathbf{q}$ is the momentum transfer. Performing integration on the right-hand side of (7), we arrive at

$$F(\mathbf{q}) = \exp\left(-\frac{1}{6}q^2\langle r^2\rangle_\alpha\right) \times \left[\frac{4}{5}\exp\left(-\frac{3}{16}q^2\Delta^2\right)j_0\left(\sqrt{\frac{3}{8}}qd\right) + \frac{1}{5}\exp\left(-\frac{q^2\lambda^2}{4}\right)\right], \quad (8)$$

where $j_0(x)$ is a spherical Bessel function; d and Δ are parameters that characterize, respectively, the mean spacing between the alpha-particle clusters of the core and their deviations from the corresponding equilibrium positions at the vertices of a regular tetrahedron [3]; and $\langle r^2\rangle_\alpha^{1/2}$ is the root-mean-square radius of the alpha-particle cluster.

Figure 1 shows the calculated form factor for the ^{20}Ne nucleus. For momentum-transfer values of $q \le 2$ fm^{-1}, these results comply with available experimental data on elastic electron scattering [10].

We note that the core of the ^{20}Ne nucleus differs from the ^{16}O nucleus because of core interaction with the extra alpha-particle cluster. The parameters of the density of the ^{20}Ne nucleus that were found from a comparison of the calculated and the measured form factor for this nucleus proved to be d = 3.595 fm, Δ = 0.998 fm, and λ = 0.345 fm.

In the case being considered, the root-mean-square radius of the ^{20}Ne nucleus is given by

$$\langle r^2\rangle_{Ne} = \langle r^2\rangle_\alpha + \frac{3}{10}d^2 + \frac{9}{10}\Delta^2 + \frac{3}{10}\lambda^2. \quad (9)$$

The values presented above for the parameters d, Δ, and λ of the ^{20}Ne nucleus lead to $\langle r^2\rangle_{Ne}^{1/2}$ = 2.72 fm, which is less than the experimental value of $\langle r^2\rangle_{Ne}^{1/2}$ = 3 fm [11]. We note that the ^{20}Ne nucleus is heavier than the ^{16}O nucleus; therefore, its root-mean-square radius is somewhat greater than that of the oxygen nucleus ($\langle r^2\rangle_O^{1/2}$ = 2.73 fm [12]).

The amplitude of proton scattering by ^{20}Ne nucleus has the form

$$F^{(Ne)}(\mathbf{q}) = \frac{ik}{2\pi} \times \int d^2b\, d^3\xi\, d^3\eta\, d^3\zeta\, d^3\chi\, e^{i\mathbf{q}\cdot\mathbf{b}}\rho^{(Ne)}(\boldsymbol{\xi}, \boldsymbol{\eta}, \boldsymbol{\zeta}, \boldsymbol{\chi})\Omega(\mathbf{b}, \mathbf{r}_j), \quad (10)$$

where k is the wave vector of the incident particle, $\mathbf{b}$ is the impact-parameter vector, $\mathbf{r}_j$ stands for the coordi-

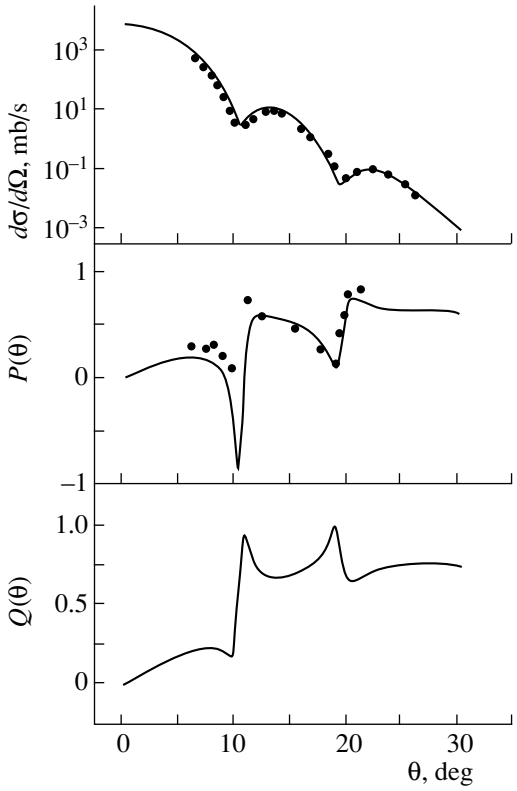

Fig. 2. Differential cross section $d\sigma/d\Omega$ (mb/sr), polarization $P(\theta)$, and spin-rotation function $Q(\theta)$ for the elastic scattering of 800-MeV protons by ^{20}Ne nuclei versus the scattering angle θ. Experimental data were borrowed from [13].

nates of the alpha-particle clusters in the ^{20}Ne nucleus, and

$$\Omega(\mathbf{b}, \mathbf{r}_j) = 1 - \prod_{j=1}^{5}\left[1 - \frac{1}{2\pi ik}\int d^2q e^{-i\mathbf{q}\cdot(\mathbf{b}-\mathbf{r}_j)} f_{p\alpha}(\mathbf{q})\right]. \quad (11)$$

Here, $f_{p\alpha}(\mathbf{q})$ is the amplitude of $p\alpha$ scattering.

The elementary amplitude $f_{p\alpha}(\mathbf{q})$ can be chosen in the form

$$f_{p\alpha}(\mathbf{q}) = f_c(\mathbf{q}) + f_s(\mathbf{q})\boldsymbol{\sigma}\cdot\mathbf{n}, \quad (12)$$

where $\boldsymbol{\sigma}$ is the operator of the incident-proton spin, while $\mathbf{n}$ is a unit vector defined as $\mathbf{n} = [\mathbf{k}\times\mathbf{k}']/|[\mathbf{k}\times\mathbf{k}']|$, $\mathbf{k}$ and $\mathbf{k}'$ being the wave vectors of, respectively, the incident and the scattered proton.

The central component of the amplitude, $f_c(\mathbf{q})$, has the form

$$f_c(\mathbf{q}) = k\sum_{i=1}^{2} G_{ci}\exp(-\beta_{ci}q^2). \quad (13)$$

The parameters of the central component of the amplitude in (13) were found in [3] by fitting the measured observables for elastic $p\alpha$ scattering. This yielded $G_{c1} = -0.330 + i1.258$ and $\beta_{c1} = 0.424 - i0.025$. According to [3], we have

$$G_{c2} = \frac{3iG_{c1}^2}{32\beta_{c1}}, \quad \beta_{c2} = \frac{1}{2}\beta_{c1}. \quad (14)$$

The spin–orbit component of the amplitude, $f_s(\mathbf{q})$, can be represented in a form similar to (13); that is,

$$f_s(\mathbf{q}) = kq\sum_{i=1}^{2} G_{si}\exp(-\beta_{si}q^2), \quad (15)$$

where $G_{s1} = 0.177 + i0.295$ and $\beta_{s1} = 0.490 + i0.052$. According to [3], we have

$$G_{s2} = \frac{3iG_{c1}G_{s1}\beta_{c1}}{8(\beta_{c1}+\beta_{s1})^2}, \quad \beta_{s2} = \frac{\beta_{c1}\beta_{s1}}{\beta_{c1}+\beta_{s1}}. \quad (16)$$

On the basis of the proposed approach, we have calculated the differential cross section $d\sigma/d\Omega$ (in mb/sr), the polarization $P(\theta)$, and the spin-rotation function $Q(\theta)$ for the elastic scattering of 800-MeV protons by ^{20}Ne nuclei. The results of these calculations, along with experimental data from [13], are displayed in Fig. 2, which shows that the calculated observables for elastic p^{20}Ne scattering at 800 MeV comply well with existing experimental data. It should be emphasized that the above observables for elastic p^{20}Ne scattering were computed without invoking any adjustable parameters. These calculations indicate that data on the elastic scattering of 800-MeV protons by ^{20}Ne nuclei can be successfully described under the assumption that this nuclear species has an alpha-cluster structure.

REFERENCES

1. Yu. A. Berezhnoy, V. V. Pilipenko, and G. A. Khomenko, Izv. Akad. Nauk SSSR, Ser. Fiz. **44**, 1950 (1980).
2. Yu. A. Berezhnoy, V. V. Pilipenko, and G. A. Khomenko, J. Phys. G **10**, 63 (1984).
3. Yu. A. Berezhnoy, V. P. Mikhailyuk, and V. V. Pilipenko, J. Phys. G **18**, 85 (1992).
4. V. P. Mikhailyuk, Mod. Phys. Lett. A **10**, 2915 (1995).
5. Yu. A. Berezhnoy and V. P. Mikhailyuk, Z. Phys. A **355**, 31 (1996).
6. P. S. Hauge, S. A. Williams, and G. H. Duffey, Phys. Rev. C **4**, 1044 (1971).
7. T. Wada and H. Horiuchi, Phys. Rev. Lett. **58**, 2190 (1987).
8. B. Buck, C. B. Dover, and J. P. Vary, Phys. Rev. C **11**, 1803 (1975).
9. R. K. Sheline and K. Wildermuth, Nucl. Phys. **21**, 196 (1960).
10. Y. Fukushima, M. Kamimura, and T. Matsuse, Prog. Theor. Phys. **55**, 1310 (1976).
11. G. Fey, H. Frank, W. Schutz, and H. Theissen, Z. Phys. A **265**, 401 (1973).
12. I. Sick and J. S. McCarthy, Nucl. Phys. A **150**, 631 (1970).
13. G. S. Blanpied, G. A. Balchin, G. E. Langston, *et al.*, Phys. Rev. C **30**, 1233 (1984).

Translated by A. Isaakyan

Physics of Atomic Nuclei, Vol. 63, No. 5, 2000, pp. 718–723. Translated from Yadernaya Fizika, Vol. 63, No. 5, 2000, pp. 787–792.

NUCLEI
Experiment

Measurement of the Light-Nuclide Yield from the Photon-Induced Fission of ^{232}Th

S. A. Karamian, J. Adam, A. G. Belov, Yu. V. Norseev, V. I. Stegaĭlov, and P. Chaloun

Joint Institute for Nuclear Research, Dubna, Moscow oblast, 141980 Russia

Received September 18, 1998; in final form, May 7, 1999

Abstract—The yield of ^{24}Na and ^{28}Mg radionuclides was determined by their gamma activity with the aid of radiochemistry. The corresponding measurements were performed upon the activation of purified Th targets with bremsstrahlung photons having endpoint energies of 12, 16.5, and 24 MeV. Possible background sources are carefully analyzed, and it is concluded that the yield of the above light nuclei is about 10^{-6} per event of ^{232}Th fission. *© 2000 MAIK "Nauka/Interperiodica".*

1. INTRODUCTION

Fission accompanied by the emission of a third fragment heavier than the alpha particle has been widely discussed in the literature (see, for example, [1]). However, the emission of medium-mass products ($A > 20$) has received less study because of a low probability of the process. The yield (Y) of ^{24}Na and ^{28}Mg nuclei from ^{238}U fission induced by alpha particles was measured in [2] by Geiger counters after a radiochemical separation of the reaction products. A strong energy dependence $Y(E^*)$ was revealed there—in particular, the yield fell below the experimental sensitivity threshold (less than 10^{-8} per fission event) at excitation energies of $E^* <$ 20 MeV. This result was confirmed indirectly by Gönenwein [3], whose experiments employed a kinematical separator for products originating from the thermal-neutron-induced fission of target nuclei from ^{229}Th to ^{249}Cf. An upper limit of 10^{-9} on the yield Y of masses between 20 and 30 was obtained in those experiments for ^{229}Th and ^{233}U targets; for ^{241}Am and ^{249}Cf, the result was $Y > 10^{-8}$, which may be associated with a sharp increase in the nuclear excitation energy at the scission point with increasing charge number.

Generally, a strong excitation-energy dependence of the cross section for a nuclear reaction corresponds to a subbarrier process. For example, it is natural for the cascade fission of highly excited nuclei into three fragments of comparable masses, which was observed in [4] in ^{238}U fission induced by heavy ions. The secondary fission of the heavy fragment is suppressed by a high fission barrier (B_f) typical of nuclei from the range between rare-earth elements and Au. The subbarrier emission of a light cluster from a heavy nucleus represents another case where we can expect a strong energy dependence of the cross section. However, ternary fission involving particle emission from the prescission configuration is not a subbarrier process, because the fissile system is severely deformed, which leads to a considerable reduction of the Coulomb barrier for particle emission. This was established in experiments that studied ternary fission accompanied by alpha-particle emission. In this case, it was found that the yield was surprisingly stable to variations in E^* [5] and that it changed slightly with increasing charge number of the nucleus undergoing fission [3]. The latter resulted in the growth of E^* at the scission point.

If the Coulomb barrier does not confine particles, their emission is determined exclusively by the particle-formation and particle-separation probabilities, which are not expected to depend strongly on E^*. It is therefore reasonable to assume that the ^{24}Na and ^{28}Mg yields determined in [2] are associated with subbarrier cluster emission from the compound nucleus. The same process must then be observed for nonfissile nuclei as well, but the measurements that were reported in [6] and which were performed for ^{181}Ta excited by bremsstrahlung photons with an endpoint energy of 24 MeV yielded a negative result.

Quite a small upper limit on the yield ($\leq 10^{-10}$–10^{-11}) was obtained there not only for ^{24}Na and ^{28}Mg but also for the decay process $^{181}\text{Ta}^* \longrightarrow {}^{48}\text{Ca} + {}^{133}\text{I}$ resulting in the emission of the doubly magic nucleus ^{48}Ca and the nearly magic nucleus ^{133}I. It worth noting that the favored emission of magic products is typical of spontaneous cluster decays [7].

We can conclude that the yield of ^{24}Na and ^{28}Mg nuclei and its energy dependence should be measured anew—especially for ^{232}Th, whose fission possesses a number of special features.

2. DESCRIPTION OF THE EXPERIMENT

2.1. Experimental Procedure

Thorium chloride $ThCl_4$, specially prepared and purified of light elements like Na, Mg, and Al, which could be a source of ^{24}Na background in reactions induced by bremsstrahlung photons and neutrons, was

used as a target material. In the form of a 1-g pellet coated with a copper foil, $ThCl_4$ to be irradiated with bremsstrahlung photons was brought into close proximity to a W-converter installed in an electron beam from the MT-25 microtron of the Laboratory for Nuclear Reactions at the Joint Institute for Nuclear Research (JINR, Dubna). The exposures were performed at three electron-energy values of 12, 16.5, and 24 MeV for a time of about 7 h, the beam current being about 15 μA. Immediately following the exposure, the activity of short-lived nuclear fission fragments was rather high, so that chemical operations could be begun only after a lapse of 3 h. It took about 2 h to extract chemically the fractions of alkaline and alkaline-earth elements. In order to measure gamma spectra, the source obtained in this way was then placed in a position immediately adjacent to a germanium HP detector equipped with thick Pb (+Cd+Cu) filters. Since the source activity was still high, we did not aim at isolating pure Na or Mg. The extracted fraction contained Sr, Ba, and Ra radionuclides, as well as other elements. The ^{91}Sr and ^{140}Ba yields were used as a reference for calibration of the yield of ^{24}Na and ^{28}Mg radionuclides per fission event. Special radiochemical procedures were carried out to purify the source of radioactive Pd and Te fragments, in order to eliminate undesirable background from these fragments in searches for ^{24}Na and ^{28}Mg (see below).

The germanium HP detector used (Canberra) ensures a high degree of differentiation between radionuclides and possesses a resolution of about 1.8 keV for ^{60}Co lines. Owing to this, the majority of the lines in the gamma spectrum could be resolved and identified individually despite complexity of the spectrum and the high absolute activity of the source. An excessive counting rate in the detector was suppressed with the aid of the aforementioned Pb absorbers of thickness 10–20 mm. While absorbing soft gamma radiation completely, the absorber had a moderately high transmission factor (60–30%) for the 2753.9- and 1778.8-keV lines of ^{24}Na and ^{28}Mg, respectively. The counting rate in the spectrometer reached 2×10^4 pulses per second, the dead time being below 20% of the real time of the measurements; neither a resolution degradation nor a shift of the gamma lines was observed. We relied on the method of internal energy calibration using the gamma lines of ^{140}Ba, ^{228}Ra, and their daughter products. The energy dependence of the detector efficiency was measured with the calibration sources under the same geometric conditions, and the results proved to be coincident with those of the relative measurements for the case of internal calibration. Information storage and spectra processing were performed with the aid of a modern ADC and a PC (Pentium). In order to decompose the spectra and to calculate the areas under the individual lines, the Maestro and Deimos codes were used in the automatic mode for seeking the lines in question and for processing them or in the dialog mode for fitting specific sections of the spectrum.

2.2. Analysis of Background Sources

The production of ^{24}Na in reactions on light target nuclei Na, Mg, and Al can be induced by bremsstrahlung photons, as well as by fast neutrons generated in the converter and by slow scattered neutrons. A low upper limit on the Na admixture in the target was established on the basis of the fact that the ^{22}Na line ($T_{1/2}$ = 2.6 y) does not appear in the spectra measured after a lapse of 2 months from the exposure. That typical photonuclear-reaction products like ^{51}Cr, ^{54}Mn, ^{58}Co, and ^{65}Zn were not found either confirmed a high general purity of the target material. Among reactions induced by photons or neutrons, the only one that produces ^{28}Mg is ^{30}Si(γ, 2*p*), but the threshold for this reaction is higher than the endpoint energy of the spectrum of bremsstrahlung used in the present study. Thus, ^{28}Mg can originate here only from ^{232}Th fission, and its observation is evidence for the ^{24}Na yield from this process, although it was difficult to disprove or prove directly the presence of Mg and Al admixtures in the target.

As was discussed in [6], the contribution to the background may also come from weak gamma lines appearing in the decays $^{132}\text{Te} \longrightarrow {}^{132}\text{I} \longrightarrow {}^{132}\text{Xe}$ (γ1778.6) and $^{112}\text{Pd} \longrightarrow {}^{112}\text{Ag} \longrightarrow {}^{112}\text{Cd}$ (γ2752.8) and mimicking ^{28}Mg (γ1778.8) and ^{24}Na (γ2753.9) lines, respectively. In either chain, the decay of the parent nucleus determines a sufficiently large half-life (78 and 21 h in the former and the latter chain, respectively), the radiation of the corresponding gamma line being emitted by the daughter nucleus. Taking into account the production of A = 112 and A = 132 isobars and the quantum yield I_γ of the background gamma lines in question, we can straightforwardly conclude that the above radionuclides, appearing as fission fragments, generate a background at a hazardous level of $Y \approx 10^{-5}$ per fission event to the observation of the ^{24}Na and ^{28}Mg yield. Therefore, it is necessary that, in searches for ^{24}Na and ^{28}Mg, the fraction of alkaline and alkaline-earth elements be chemically purified of Pd and Te, and this was indeed done in the present study. On the basis of the most intense lines of ^{112}Pd and ^{132}Te, the degree of chemical purification of these elements was found to be as high as 50–100. Nevertheless, their contribution to the ^{24}Na and ^{28}Mg lines was quantified and subtracted from the peak areas at energies of 2754 and 1779 keV, respectively.

The background from ^{112}Pd and ^{132}Te was not discussed in [2, 8], possibly for want of detailed information about the schemes of nuclear decays. A kinematical selection is not always efficient for light nuclei. For example, the mean range of nuclei identified as ^{24}Na in the measurements reported in [8] coincides with the range of the fragment ^{112}Pd. All the above leads to the conclusion that ^{24}Na and ^{28}Mg radionuclides could be identified reliably neither by combining chemical extraction with Geiger counter measurements [2] nor

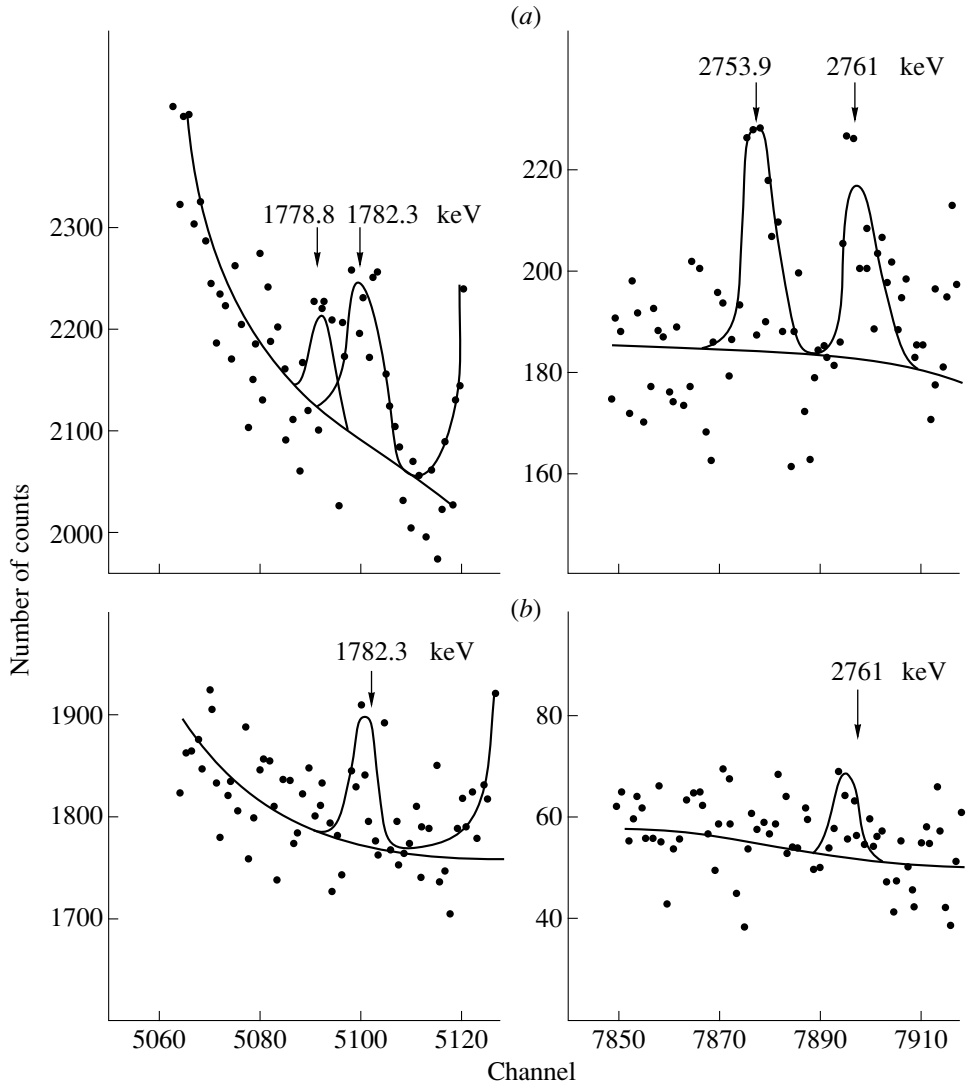

Fig. 1. Gamma-spectrum sections of the fraction of the alkaline and alkaline-earth elements according to the measurements performed (*a*) 7.5 and (*b*) 41.5 h after the completion of the exposure at the endpoint bremsstrahlung energy of 16.5 MeV. The corresponding fits, including the revealed gamma lines and the Compton background, are represented by the solid curves. The peak positions are indicated by the arrows, and the corresponding energies are indicated.

by using a Ge(Li) detector with the mean parameters in [8] alone.

Table 1 lists the gamma lines that we determined for some radionuclides studied in the present experiment. We also sought ^{7}Be, ^{38}S, and ^{59}Fe nuclei. The sensitivity as high as that for ^{24}Na and ^{28}Mg could not be achieved for ^{7}Be and ^{38}S, because their decay properties were less convenient for this; as to the yield of ^{59}Fe, it did not exceed 10^{-7} per fission event. The other nuclides from Table 1 were of auxiliary importance, as is obvious from the text.

2.3. Results of Measurements

Figure 1 shows the sections of the gamma spectra around the sought lines according to the measurements performed (*a*) 7.5 h and (*b*) 41.5 h after the completion of the exposure at the endpoint energy of 16.5 MeV. As might have been expected on the basis of the tabular values of $T_{1/2}$ for ^{24}Na and ^{28}Mg, the gamma lines corresponding to these radionuclides are seen in the spectrum in Fig 1*a*, but they are absent from the spectrum in Fig. 1*b*. Figure 1 also shows the neighboring lines: the 1782-keV gamma line is associated with a natural radioactive background, corresponding to the one-step-emission peak for the ^{222}Rn line (^{238}U family), while the 2761-keV gamma line has yet to be identified. In all probability, the latter represents the peak that is due to a summation of cascade transitions in one of the radionuclides. The source was placed close to the detector; therefore, the cascade energies could sum up despite the thick Pb absorber. The statistics were poor for the

spectrum in Fig. 1, but the number of events was sufficient for revealing the 2753.9- and 1778.8-keV lines of ^{24}Na and ^{28}Mg, respectively. The peak areas were determined by means of computer-based, computer-aided, and computer-free data processing. The last method is more reliable in the case of limited statistics. The final result takes into account all kinds of data processing. In order to smooth out the scatter, the count numbers from the neighboring channels were summed in pairs. The resolution was retrograded about 2.5 keV, and the 1778.8- and 1782-keV lines manifested themselves as an incompletely resolved doublet. The area of each line can be determined easily. Usually, the accuracy was at a level of ±30% of significant peak-area values. On this basis, we have found the number of ^{24}Na and ^{28}Mg nuclei in the source and their yield per fission event by a comparison with the number of ^{91}Sr and ^{140}Ba nuclei whose yields from Th photofission are known from [9, 10] and whose chemical-extraction efficiency was identical to that for ^{24}Na and ^{28}Mg. We took into account the quantum yields of gamma lines, the efficiency factors, and the kinetics of decay-event accumulation.

The statistical accuracy of ^{24}Na and ^{28}Mg determination is higher at the endpoint bremsstrahlung energy of 24 MeV than at 16.5 MeV. In Fig. 2, the corresponding spectrum in the form that it was transferred to the printer is shown along with the approximation obtained for the observed lines on the basis of the Deimos computer code. The ^{24}Na and ^{28}Mg lines are quite distinct, and their fit resulted in reasonable χ^2 values. At the endpoint bremsstrahlung energy of 12 MeV, we were able to set only an upper limit on the relevant yield, because the total number of fission events decreased with decreasing the electron-beam energy due largely to the attenuation of the bremsstrahlung intensity and also to a reduction of the endpoint energy of the spectrum.

Table 1. List of gamma lines used to determine radionuclide yields

Nuclide	$T_{1/2}$	E_γ, keV	I_γ, %
^{7}Be	53.3 day	477.6	10.4
^{24}Na	15.0 h	1368.5	100
		2753.9	100
^{28}Mg → ^{28}Al	20.9 h → 2.2 min	1342.2	54.0
		1778.8	100
^{38}S → ^{38}Cl	2.84 h → 37 min	1941.9	84.0
		2167.6	42.4
^{59}Fe	44.5 day	1099.3	56.5
		1291.6	43.2
^{91}Sr → ^{91}Y^{m}	9.5 h → 49 min	555.6	61.3
^{112}Pd → ^{112}Ag	21.1 h → 3.1 h	617.4	50
		2752.8	0.11
^{132}Te → ^{132}I	76.3 h → 2.3 h	667.7	100
		1778.6	0.08
^{140}Ba → ^{140}La	12.75 day → 40.3 h	537.3	24.4
		1596.5	95.4

3. DISCUSSION OF THE RESULTS

Table 2 summarizes the yields of light nuclei per event of ^{232}Th photofission at the three values of the endpoint energy of the bremsstrahlung spectrum. The ^{24}Na and ^{28}Mg yield is about 10^{-6}. Other values are represented by upper limits on the yield; this was dictated by experimental conditions.

Since the majority of the previous studies [1–3, 8] relied on a kinematical selection of fission products, thin targets from fissile matter were used there. In view of this, the resulting yield values at a level of 10^{-7} and below had a rather low statistical confidence. Yet another distinction between the methods used previ-

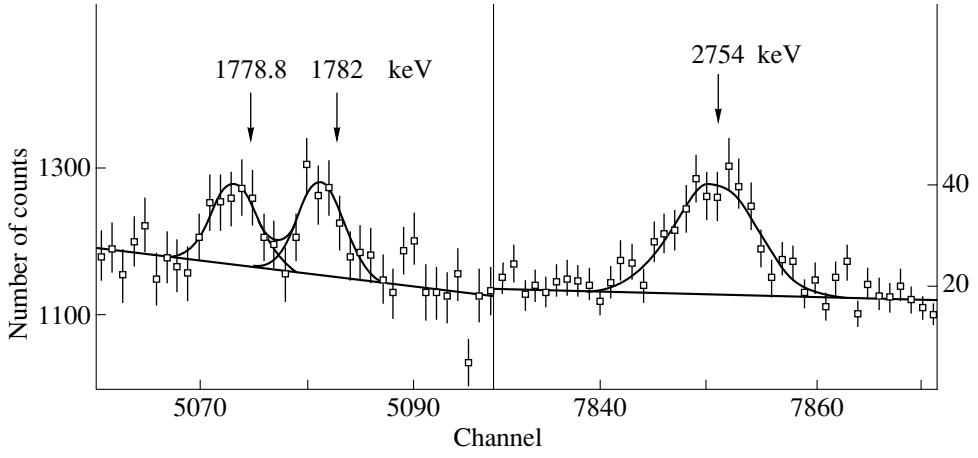

Fig. 2. As in Fig. 1, but at the endpoint bremsstrahlung energy of 24 MeV. The cooling time was 27 h.

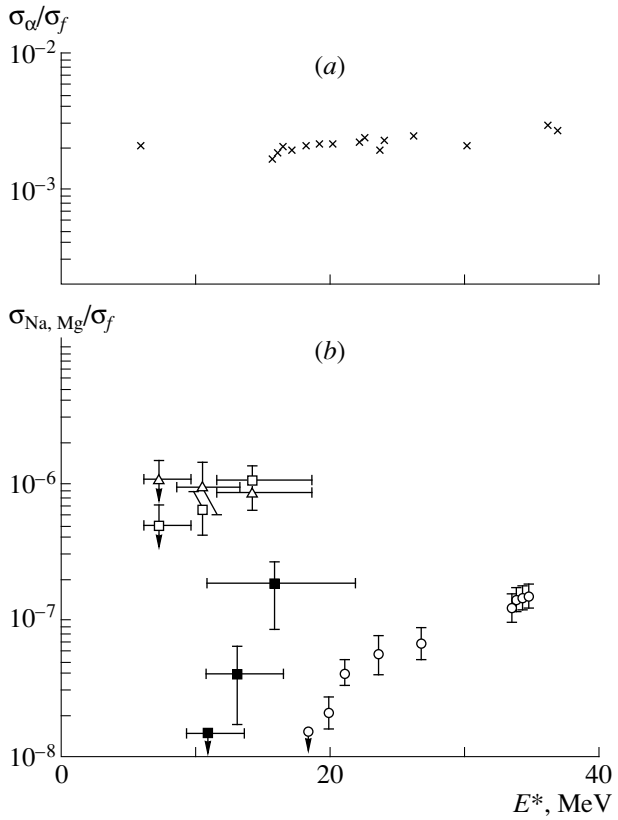

Fig. 3. Yield from ternary fission (with respect to that for binary fission) accompanied (*a*) by alpha-particle emission (according to data from [5]) or (*b*) by the emission of ^{24}Na and ^{28}Mg nuclei: (open circles and closed boxes) data on ^{24}Na from [2] and [8], respectively; (open boxes) our results for ^{24}Na; and (open triangles) our results for ^{28}Mg.

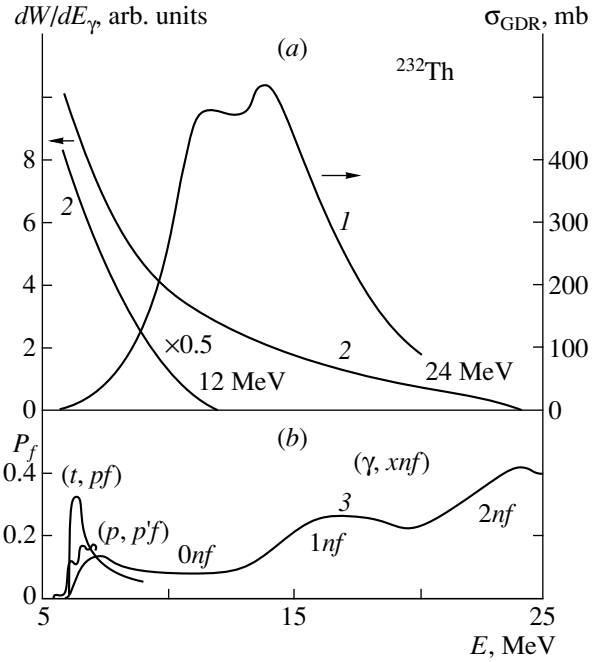

Fig. 4. Giant resonance in the photoabsorption cross section for ^{232}Th from [12] (curve *1*), bremsstrahlung spectrum (curve *2*), and fission probability P_f from [13–16] (*3*).

ously and in the present study is worthy of note: the yield of individual nuclides was measured with the aid of kinematical separators in [1, 3], and the cumulative yield of $A = 24$ and 28 isobars was determined by our method. Figure 3 displays our results along with data from [2, 8]. We cannot say that they are in good agreement, but the results of our measurements are preferable for the following reasons: (i) A high absolute sensitivity is ensured in our experiment. (ii) Alien activities are removed. (iii) Gamma-spectroscopic equipment of the latest generation is used. In the experiments reported in [2, 8], the backgrounds due to gamma radiation from fission fragments were not eliminated, as was discussed above.

Table 2. Light-nucleus yield per event of ^{232}Th photofission at three values of the endpoint energy of the bremsstrahlung spectrum

Reaction product	Yield		
	24 MeV	16.5 MeV	12 MeV
^{7}Be	$\leq 1.1 \times 10^{-4}$	–	$\leq 1.0 \times 10^{-4}$
^{24}Na	$(1.0 \pm 0.2) \times 10^{-6}$	$(0.65 \pm 0.20) \times 10^{-6}$	$\leq 0.5 \times 10^{-6}$
^{28}Mg	$(0.85 \pm 0.15) \times 10^{-6}$	$(0.93 \pm 0.30) \times 10^{-6}$	$\leq 1.2 \times 10^{-6}$
^{38}S	$\leq 2.5 \times 10^{-5}$	–	$\leq 1.0 \times 10^{-5}$
^{59}Fe	$\leq 1.0 \times 10^{-7}$	–	$\leq 2.6 \times 10^{-6}$

An unusual mechanism of ternary fission was proposed by Solyakin and Kravtsov [11], who assumed that the third fragment does not receive appreciable kinetic energy because the forces of its Coulomb repulsion from the other two fragments are balanced. In our experiment, all the radioactive products are included in the measured yield, irrespective of their kinetic energy. This can explain why the light-nucleus yields measured by our procedure are higher than those measured by the methods from [1, 3]. In order to clarify the role of the mechanism proposed in [11], comparative experiments are necessary in which the two methods are applied to the same reaction.

The results presented in Table 2 and in Fig. 3 make it possible to express the yield as a function of E^*. The mean excitation energy of the fissile nucleus ^{232}Th was determined by using the data taken from the literature and shown in Fig. 4. The calculated bremsstrahlung spectrum and the giant dipole resonance in the photoabsorption cross sections for ^{232}Th [12] are displayed in Fig. 4*a*, while the fission probability P_f is shown in Fig. 4*b*. The probability of the relevant (γ, *xnf*) process in a wide range of E^* was obtained by rescaling data on (*n*, *ynf*) from [13]. The probability P_f of the chance *x* in the former reaction was assumed to be equal to that of

the next chance $y = x + 1$ in the latter reaction. The data on photofission [14] and those on the (t, pf) and (p, $p'f$) reactions [15, 16] were taken into account in the near-barrier region. The product of the functions labeled with the figures 1, 2, and 3 in Fig. 4 yields the E^* distribution of fissile nuclei. On this basis, we have calculated the mean excitation energy $\bar{E}^*$ of the fissile compound nucleus. By way of example, we indicate that, at the endpoint bremsstrahlung energy of 12 MeV, $\bar{E}^*$ is about 8 MeV, which is slightly above the fission barrier in ^{232}Th, $B_f = 6.0$ MeV.

The relative yields from ternary fission accompanied either (a) by alpha-particle emission or (b) by the emission of $A > 20$ nuclei are displayed in Fig. 3 versus the mean excitation energy E^* of the fissile nucleus being studied. The results from [8] are also rescaled to the mean values of $\bar{E}^*$. The continuous spectrum of incident photons gives no way to fix E^* more precisely. The half-width of the energy distribution is represented by horizontal bars in Fig. 3*b*. The data in Fig. 3*b* have considerable standard deviations both along the x and along the y axis; nevertheless, there is no agreement for the whole host of the data within the errors.

4. CONCLUSION

Using a highly sensitive method, we have determined the yield of light nuclei ^{24}Na and ^{28}Mg from ^{232}Th photofission and validated the mechanism that may be responsible for ternary fission accompanied by the emission of light nuclei with $A > 20$ and which was studied thoroughly for long-range alpha particles.

REFERENCES

1. A. A. Vorobiev *et al.*, Phys. Lett. B **40**, 102 (1972).
2. R. H. Iyer and J. W. Cobble, Phys. Rev. **172**, 1186 (1968).
3. F. Gönenwein, in *Proceedings of the Second International Conference on Dynamical Aspects of Nuclear Fission, Smolenice, 1993* (Preprint No. E7-94-19, JINR, 1994), p. 47.
4. S. A. Karamian *et al.*, Yad. Fiz. **5**, 959 (1966) [Sov. J. Nucl. Phys. **5**, 684 (1967)].
5. V. M. Gorbachev, Yu. S. Zamyatnin, and A. A. Lbov, *Interaction of Radiations with Nuclei of Heavy Elements and Nuclear Fission: Handbook* (Atomizdat, Moscow, 1976).
6. S. A. Karamian *et al*., Izv. Akad. Nauk, Ser. Fiz. **61**, 2233 (1997).
7. D. N. Poenaru *et al.*, At. Data Nucl. Data Tables **48**, 231 (1991).
8. Yu. P. Gangrskiĭ *et al.*, Yad. Fiz. **44**, 294 (1986) [Sov. J. Nucl. Phys. **44**, 184 (1986)].
9. M. Piessens *et al.*, Nucl. Phys. A **556**, 88 (1993).
10. S. A. Karamian *et al.*, in *Proceedings of the International Workshop on Research with Fission Fragments* (World Sci., Singapore, 1997), p. 199.
11. G. F. Solyakin and A. V. Kravtsov, Phys. Rev. C **54**, 1798 (1996).
12. S. S. Dietrich and B. L. Berman, At. Data Nucl. Data Tables **38**, 199 (1988).
13. V. McLane *et al*., *Neutron Cross Sections: Handbook* (Academic, New York, 1988), Vol. 2.
14. G. N. Smirenkin and A. S. Soldatov, Yad. Fiz. **59**, 203 (1996) [Phys. At. Nucl. **59**, 185 (1996)].
15. J. D. Cramer and H. C. Britt, Nucl. Sci. Eng. **41**, 177 (1970).
16. H. Jansen *et al.*, in *Dynamics of Nuclear Fission and Related Collective Phenomena* (Springer-Verlag, Berlin, 1981), p. 95.

Translated by E. Kozlovskiĭ

Physics of Atomic Nuclei, Vol. 63, No. 5, 2000, pp. 724–728. Translated from Yadernaya Fizika, Vol. 63, No. 5, 2000, pp. 793–798.

NUCLEI
Theory

Parity-Nonconservation Effect in the Helicities of Conversion Electrons Accompanying the $(5/2)^- \longrightarrow (5/2)^+$ Nuclear Transition in the ^{229}Pa Nucleus

D. P. Grechukhin† and A. V. Lomonosov*

Russian Research Centre Kurchatov Institute, pl. Kurchatova 1, Moscow, 123182 Russia

Received May 28, 1999

Abstract—The ground state of the ^{229}Pa nucleus is a $5/2^{\pm}$ doublet with a splitting energy of 220 ± 50 eV. Such levels are peculiar to nuclei in the mass region around $A = 225$ that are characterized by octupole deformations. A direct observation of *P*-odd effects in this system is of great interest because this can furnish information about the parity-nonconserving nucleon–nucleon potential. The transition between the two doublet states of opposite parities proceeds predominantly through internal conversion; therefore, *P*-odd mixing can be explored by studying the helicities of the conversion electron. It is shown that the helicities of the $6s_{1/2}$, $6p_{1/2}$, and $6p_{3/2}$ conversion electrons are about 1%, which makes it possible to perform experiments aimed at determining the parameters of the effective parity-nonconserving nuclear potential. © *2000 MAIK "Nauka/Interperiodica".*

1. INTRODUCTION

This article reports on a continuation of investigations devoted to parity-nonconservation effect in the $(5/2)^- \longrightarrow (5/2)^+$ conversion transition in the ^{229}Pa nucleus. It was predicted in [1]—and this prediction was confirmed experimentally in [2]—that the ground state of this nucleus actually appears to be a system of two closely lying $I = 5/2$ states of opposite parities (±)—that is, it represents a doublet of the states, which are separated by 220 ± 50 eV. The parity-mixed ($E1 + M1$) nuclear transition proceeds almost entirely through conversion (the internal-conversion ratio is about 10^4). Therefore, the parity-nonconservation effect in the doublet can be explored in the conversion ($E1 + M1$) channel of the nuclear transition. The helicities of the $6s_{1/2}$, $6p_{1/2}$, and $6p_{3/2}$ conversion electrons are one of the effects accessible to observation in nuclear ($E1 + M1$) transitions. In [3], we estimated the deviation of the ratios of the intensities of the $6s_{1/2}$, $6p_{1/2}$, and $6p_{3/2}$ conversion lines from values that correspond to the pure $E1$ multipole and the half-life of the upper doublet state. The internal-conversion ratios for the ^{229}Pa atom were computed in [4, 5].

On the basis of the generalized model of the nucleus, the matrix element of the effective single-nucleon weak-interaction potential, which determines the weight of the opposite-parity admixture in the doublet components, was estimated in [6] within the single-particle approximation. In addition, the reduced probabilities of the $E1$ and $M1$ nuclear transitions between the doublet states were calculated there on the basis of various models of a deformed nuclear potential.

2. HELICITIES OF THE CONVERSION ELECTRONS IN THE PARITY-MIXED ($E1 + M1$) TRANSITION BETWEEN THE COMPONENTS OF THE $(5/2)^{\pm}$ DOUBLET IN THE ^{229}Pa NUCLEUS

We treat the doublet states in the $^{229}Pa_{91}$ nucleus as the $[523]\frac{5}{2}, -, \frac{5}{2}$ and $[642]\frac{5}{2}, +, \frac{5}{2}$ single-particle proton orbitals (in accordance with Nilsson's classification [7], the orbitals are denoted as $[Nn_Z\Lambda]\Omega$, Π, I) spaced by $\Delta E = 220 \pm 50$ eV. The parity-nonconserving weak-interaction potential $\hat{V}^N_{\rm pnc}$ mixes these states, leading to the formation of the new states

$$\begin{aligned}\left|\widetilde{\frac{5}{2}^-}\right\rangle &= \left|[523]\frac{5}{2}, -, \frac{5}{2}\right\rangle + ib\left|[642]\frac{5}{2}, +, \frac{5}{2}\right\rangle,\\ \left|\widetilde{\frac{5}{2}^+}\right\rangle &= \left|[642]\frac{5}{2}, +, \frac{5}{2}\right\rangle + ib\left|[523]\frac{5}{2}, -, \frac{5}{2}\right\rangle,\end{aligned} \quad (1)$$

where b is the coefficient that specifies the opposite-parity admixture and which is given by

$$ib = \frac{\left\langle [642]\frac{5}{2}, +, \frac{5}{2}\middle|\hat{V}^N_{\rm pnc}\middle|[523]\frac{5}{2}, -, \frac{5}{2}\right\rangle}{\Delta E}. \quad (2)$$

The phases of the wave functions are chosen in such a way that the matrix elements are pure imaginary; that is,

† Deceased.

* e-mail: lomon@cerber.mbslab.kiae.ru

$$\left\langle [523]\frac{5}{2}, -, \frac{5}{2}\middle|\hat{V}^N_{\rm pnc}\middle|[642]\frac{5}{2}, +, \frac{5}{2}\right\rangle^* = -\left\langle [523]\frac{5}{2}, -, \frac{5}{2}\middle|\hat{V}^N_{\rm PNC}\middle|[642]\frac{5}{2}, +, \frac{5}{2}\right\rangle. \quad (3)$$

The Hermitian operator of the parity-nonconserving effective potential acting on an intranuclear nucleon (proton) has the form [8]

$$\hat{V}^N_{\rm pnc}(\mathbf{r}, \hat{\mathbf{p}}, \hat{\boldsymbol{\sigma}}) = \frac{G}{2m_p c}\alpha(N, Z) \times \{(\hat{\boldsymbol{\sigma}}\cdot\hat{\mathbf{p}})\rho(\mathbf{r}) + \rho(\mathbf{r})(\hat{\boldsymbol{\sigma}}\cdot\hat{\mathbf{p}})\}, \quad (4)$$

where $G = 10^{-5}\hbar^3/m_p^2 c$ is the weak-interaction coupling constant, m_p is the proton mass, $\mathbf{p}$ is the nucleon-momentum operator, $\boldsymbol{\sigma}$ is the nucleon-spin operator, $\rho(\mathbf{r})$ is the volume nucleon-density distribution in the deformed nucleus, and $\alpha(N, Z)$ is a coefficient depending on the form of single-particle potentials used in averaging relevant quantities over intranuclear nucleons [$\alpha(N, Z) \sim 1$]. Data on parity-nonconservation effects in resonance-neutron interactions with heavy nuclei can be treated so that this coefficient is enhanced by one to two orders of magnitude, in which case observable effects are enhanced accordingly (see, for example, [9]). Nevertheless, we set $\alpha(N, Z) = 1$ in the ensuing calculations.

Nuclear conversion proceeds through a ($E1 + M1$) transition, where $\hbar\omega = E_1 - E_2$; this is accompanied by the transition of an electron from the $|\varepsilon_1 n_1 l_1 j_1\rangle$ state, where ε_1 is the energy, n_1 is the principal quantum number, l_1 is the orbital angular momentum, and j_1 is the total angular momentum, to a continuum state with energy ε_2. We assume that the nucleus is unpolarized in the initial state, because the half-life is sufficiently large for initial polarizations generated in the populating cascade to disappear.

The relativistic wave function of the initial electron state $|\varepsilon_1 n_1 l_1 j_1\rangle$—a solution to the Dirac equation in the spherically symmetric field—can be represented in the bispinor form [10]

$$\Psi_{j_1 l_1 m_1}(\mathbf{r}) = \begin{cases} g_{l_1 j_1}(r)\Omega_{j_1 l_1 m_1}(\mathbf{r}/r) \\ i f_{l'_1 j_1}(r)\Omega_{j_1 l'_1 m_1}(\mathbf{r}/r), \end{cases} \quad (5)$$

where

$$\Omega_{j_1 l_1 m_1}(\mathbf{r}/r) = \sum_{\mu_1 \nu_1} C^{j_1 m_1}_{l_1 \mu_1 s \nu_1} Y_{l_1 \mu_1}(\mathbf{r}/r)\chi_{\nu_1} \quad (6)$$

is a spherical spinor, while $g_{l_1 j_1}(r)$ and $f_{l'_1 j_1}(r)$ are radial functions satisfying the normalization condition

$$\int_0^\infty dx\left[g^2_{l_1 j_1}(x) + f^2_{l'_1 j_1}(x)\right] = 1. \quad (7)$$

At infinity, the asymptotic expression for the relativistic wave function of the final electron state $|\varepsilon_2, \nu_2\rangle$ (ν_2 is the electron polarization) has the form of a sum featuring a plane wave and a diverging spherical wave, whereas the function itself can be represented as [10]

$$\Psi_{\varepsilon_2 \nu_2}(\mathbf{r}) = \frac{4\pi}{p_2}\sqrt{\frac{\varepsilon_2 + mc^2}{2\varepsilon_2}} \times \sum_{j_2 l_2 m_2} (\Omega^+_{j_2 l_2 m_2}(\mathbf{p}_2/p_2)\chi_{\nu_2}) i^{l_2}\exp(-i\delta_{l_2 j_2}) \times \begin{cases} G_{l_2 j_2}(r)\Omega_{j_2 l_2 m_2}(\mathbf{r}/r) \\ iF_{l'_2 j_2}(r)\Omega_{j_2 l'_2 m_2}(\mathbf{r}/r), \end{cases} \quad (8)$$

where

$$\chi_{+1/2} = \begin{pmatrix} 1 \\ 0 \end{pmatrix}, \quad \chi_{-1/2} = \begin{pmatrix} 0 \\ 1 \end{pmatrix}.$$

The wave functions of continuum electron states are normalized in such a way that they satisfy the following asymptotic conditions for $r \longrightarrow \infty$:

$$G_{l_2 j_2}(r) \longrightarrow \sin\left(p_2 r - l_2\frac{\pi}{2} + \delta_{l_2 j_2}\right), \quad (9)$$

$$F_{l'_2 j_2}(r) \longrightarrow i^{l'_2 + 1 - l_2}\sqrt{\frac{\varepsilon_2 - mc^2}{\varepsilon_2 + mc^2}} \times \sin\left(p_2 r - l'_2\frac{\pi}{2} + \delta_{l_2 j_2}\right). \quad (10)$$

For the above case of the unpolarized initial nucleus and the unpolarized atomic shell, we take the coordinate frame comoving with the conversion electron and having the z axis aligned with its observed momentum $\mathbf{p}_2 = (0, 0, p_2)$. In this frame, the electron-spin projection ν_2 onto the quantization axis is the projection of the spin $\mathbf{s}_2$ onto the momentum $\mathbf{p}_2$. Experimentally, the detector used must record the momentum $\mathbf{p}_2$ within the solid angle $dO_{\mathbf{p}_2}$ (in the laboratory frame) and the projection of the spin $\mathbf{s}_2$ onto the momentum $\mathbf{p}_2$. In this way, the events $N_{\nu_2 = +1/2}$ and $N_{\nu_2 = -1/2}$ in which the electron is emitted with polarizations $\nu_2 = +1/2$ and $\nu_2 = -1/2$, respectively, are detected independently. In this case, the electron helicity is determined as the ratio

$$2\langle\nu_2\rangle = \left\langle\frac{(\boldsymbol{\sigma}\cdot\mathbf{p}_2)}{p_2}\right\rangle = \frac{N_{\nu_2 = +1/2} - N_{\nu_2 = -1/2}}{N_{\nu_2 = +1/2} + N_{\nu_2 = -1/2}}, \quad (11)$$

where $\mathbf{s}_2 = \frac{1}{2}\boldsymbol{\sigma}$ and where averaging is performed over the conversion-electron states.

It follows from (11) that

$$\langle \nu_2 \rangle = \frac{\sum_{\nu_2 = \pm 1/2} \nu_2 dW(I_1 \longrightarrow I_2; [\varepsilon_1 n_1 l_1 j_1 m_1]^1 \longrightarrow \mathbf{p}_2 \nu_2)}{\sum_{\nu_2 = \pm 1/2} dW(I_1 \longrightarrow I_2; [\varepsilon_1 n_1 l_1 j_1 m_1]^1 \longrightarrow \mathbf{p}_2 \nu_2)}, \quad (12)$$

where $dW(I_1 \longrightarrow I_2; [\varepsilon_1 n_1 l_1 j_1 m_1]^1 \longrightarrow \mathbf{p}_2 \nu_2)$ is the quantity obtained by summing the differential probability of electron ejection from the atomic state $|\varepsilon_1 n_1 l_1 j_1 m_1\rangle$ into the continuum state $|\mathbf{p}_2 \nu_2\rangle$ per electron in the filled shell over the unobservable projection M_2 of the nuclear spin I_2.

In calculating the differential probability of the conversion process, we used a decomposition into the $E1$ and $M1$ multipoles as in [10, 11] (for details, see [12]). For $6s_{1/2}$, $6p_{1/2}$, and $6s_{3/2}$ conversion in the protactinium atom, the $M1$-to-$E1$ ratio of the transition probabilities does not exceed a few percent (see, [3]). In the denominator of expression (12) for the helicity, we can therefore neglect the contribution from the $M1$ conversion nuclear transition. For the conversion-electron helicity (12), we then eventually obtain

$$\begin{aligned}
\langle \nu_2 \rangle &= \frac{\sqrt{s(s+1)} \left\langle \widetilde{\frac{5}{2}^+} \| M1 \| \widetilde{\frac{5}{2}^-} \right\rangle}{\left\langle \frac{5}{2}^+ \| E1 \| \frac{5}{2}^- \right\rangle \sum_{l_2 j_2} |\{l_2 j_2 [E1] n_1 l_1 j_1\}|^2 [j_2 l_2, 1, j_1, l_1]^2} \\
&\times \sum_{j_2 l_2 \tilde{l}_2} C^{\tilde{l}_2 0}_{l_2 0\, 10} u(\tilde{l}_2 j_2 1 s; s l_2) [j_2 l_2, 1, j_1, l_1] \\
&\times [j_2 \tilde{l}_2, 1, j_1, l_1'] (-i \{l_2 j_2 [E1] n_1 l_1 j_1\}^* \\
&\times \{\tilde{l}_2 j_2 [M1] n_1 l_1 j_1\} [i^{l_2} \exp(-i\delta_{l_2 j_2})] \\
&\times [i^{\tilde{l}_2} \exp(-i\delta_{\tilde{l}_2 j_2})]^* \\
&+ i \{l_2 j_2 [E1] n_1 l_1 j_1\} \{\tilde{l}_2 j_2 [M1] n_1 l_1 j_1\}^* \\
&\times [i^{l_2} \exp(-i\delta_{l_2 j_2})]^* [i^{\tilde{l}_2} \exp(-i\delta_{\tilde{l}_2 j_2})]).
\end{aligned} \quad (13)$$

The system of the radial integrals of the relativistic wave functions of the initial- and final-state electrons is given by

$$\begin{aligned}
\{l_2 j_2 [E\Lambda] n_1 l_1 j_1\} &= \int_0^\infty dx h^{(1)}_\Lambda (k a_0 x) \\
&\times \left[G_{l_2 j_2}(x) g_{l_1 j_1}(x) + F_{l_2' j_2}(x) f_{l_1' j_1}(x) \right] \\
&+ \int_0^\infty dx h^{(1)}_{\Lambda - 1}(k a_0 x) \\
&\times \left[G_{l_2 j_2}(x) f_{l_1' j_1}(x) - F_{l_2' j_2}(x) g_{l_1 j_1}(x) \right]
\end{aligned} \quad (14)$$

$$\begin{aligned}
\{l_2 j_2 [M\Lambda] n_1 l_1 j_1\} &= \frac{j_2(j_2+1) - l_2(l_2+1) - j_1(j_1+1) + l_1'(l_1'+1)}{\sqrt{\Lambda(\Lambda+1)}} \\
&\times \int_0^\infty dx h^{(1)}_\Lambda (k a_0 x) \\
&\times [G_{l_2 j_2}(x) f_{l_1' j_1}(x) + F_{l_2' j_2}(x) g_{l_1 j_1}(x)],
\end{aligned} \quad (15)$$

$$\begin{aligned}
&+ \frac{1}{\Lambda} [j_2(j_2+1) - l_2(l_2+1) \\
&- j_1(j_1+1) + l_1(l_1+1)] \int_0^\infty dx h^{(1)}_{\Lambda - 1}(k a_0 x) \\
&\times \left[G_{l_2 j_2}(x) f_{l_1' j_1}(x) + F_{l_2' j_2}(x) g_{l_1 j_1}(x) \right],
\end{aligned}$$

where $x = r/a_0$, a_0 being the Bohr radius.

In (13), we have used the notation

$$[j_2 l_2, \Lambda, j_1 l_1] = \sqrt{\frac{2j_2+1}{2j_1+1}} C^{l_1 0}_{l_2 0\, \Lambda 0} u(j_2 s \Lambda l_1; l_2 j_1), \quad (16)$$

where $u(abcd; ef) = \sqrt{(2e+1)(2f+1)}\, w(abcd; ef)$ is a normalized Racah coefficient.

The reduced nuclear matrix elements $\langle I_2 \| E(M)\Lambda \| I_1 \rangle$ used in our calculations are related to the conventional reduced probabilities $B(E(M)\Lambda; I_1 \longrightarrow I_2)$ of the $I_1 \longrightarrow I_2$ multipole nuclear transition [13] by the equations

$$e^2 R_N^{2\Lambda} \frac{2I_2+1}{2I_1+1} |\langle I_2 \| E\Lambda \| I_1 \rangle|^2 = B(E\Lambda; I_1 \longrightarrow I_2), \quad (17)$$

$$\begin{aligned}
&\frac{\Lambda}{\Lambda+1} e^2 R_N^{2\Lambda} \frac{2I_2+1}{2I_1+1} |\langle I_2 \| M\Lambda \| I_1 \rangle|^2 \\
&= B(M\Lambda; I_1 \longrightarrow I_2),
\end{aligned} \quad (18)$$

where R_N is the nuclear radius.

In the present calculation, we employed the results obtained in [6], where the severely deformed nucleus ^{229}Pa was described on the basis of the collective model [13]. The nucleon wave functions were obtained in the Woods–Saxon potential for a deformed nucleus; in order to test our results, we also used the deformed nuclear oscillator potential [7]. In [6], we calculated the reduced probabilities $B\left(E1; \frac{5}{2}^- \longrightarrow \frac{5}{2}^+\right)$ and $B\left(M1; \widetilde{\frac{5}{2}^-} \longrightarrow \widetilde{\frac{5}{2}^+}\right)$ of the electric dipole and magnetic dipole transitions, respectively, between the [523]5/2, –, 5/2 and

Table 1. Ratio of the reduced matrix element $\langle \frac{\widetilde{5}^+}{2} \| M1 \| \frac{\widetilde{5}^-}{2} \rangle$ for the magnetic dipole transition to the reduced matrix element $\langle \frac{5^+}{2} \| E1 \| \frac{5^-}{2} \rangle$ for the electric dipole transition

β_{20}	$\left\lvert \frac{\langle \frac{\widetilde{5}^+}{2} \| M1 \| \frac{\widetilde{5}^-}{2} \rangle}{\langle \frac{5^+}{2} \| E1 \| \frac{5^-}{2} \rangle} \right\rvert$
0.20	$\frac{2.95}{\Delta E}$
0.23	$\frac{2.52}{\Delta E}$
0.25	$\frac{2.31}{\Delta E}$
Expt.	$\frac{0.84}{\Delta E}$

Note: The values in the first three rows were calculated by using the Woods–Saxon potential with quoted values of the quadrupole deformation β_{20} at $\beta_{40} = 0.08$, while the value in the fourth row was obtained from the measured isomer lifetime τ_{expt} for $\beta_{20} = 0.23$ (ΔE is measured in eV).

Table 2. Helicities of the $6s_{1/2}$, $6p_{1/2}$, and $6p_{3/2}$ conversion electrons of the protactinium atom (the Hatree–Fock–Slater potential with the Latter correction is used for a conversion electron)

ΔE, eV	$\lvert\nu_2\rvert$, %					
	I			II		
	$6s_{1/2}$	$6p_{1/2}$	$6p_{3/2}$	$6s_{1/2}$	$6p_{1/2}$	$6p_{3/2}$
170	3.41	1.67	0.74	1.33	0.57	0.25
180	3.31	1.60	0.71	1.28	0.55	0.24
190	3.23	1.54	0.68	1.24	0.53	0.23
200	3.14	1.49	0.66	1.20	0.51	0.22
210	3.06	1.44	0.64	1.16	0.49	0.22
220	2.98	1.39	0.63	1.12	0.47	0.21
230	2.90	1.35	0.61	1.08	0.46	0.21
240	2.82	1.31	0.60	1.05	0.44	0.20
250	2.74	1.27	0.58	1.02	0.43	0.20
260	2.67	1.23	0.57	0.98	0.42	0.19
270	2.59	1.20	0.56	0.95	0.41	0.19

Note: In this table and in Tables 3 and 4, columns I and II quote the $B(E1;\ 5/2^- \longrightarrow 5/2^+)$ values as calculated by using the deformed Woods–Saxon potential and as obtained from the measured isomer lifetime τ_{expt}.

[642]5/2, +, 5/2 states (with allowance for their mixing) of the severely deformed nucleus ^{229}Pa. Expression (13) for calculating the conversion-electron helicity involves the ratio of the reduced nuclear matrix elements for the $E1$ and $M1$ transitions. Taking into account relations (17) and (18), we can express this ratio in terms of the reduced probabilities as

$$\left\lvert \frac{\left\langle \frac{\widetilde{5}^+}{2} \| M1 \| \frac{\widetilde{5}^-}{2} \right\rangle}{\left\langle \frac{5^+}{2} \| E1 \| \frac{5^-}{2} \right\rangle} \right\rvert = \sqrt{\frac{2B\left(M1; \frac{\widetilde{5}^-}{2} \longrightarrow \frac{\widetilde{5}^+}{2}\right)}{B\left(E1; \frac{5^-}{2} \longrightarrow \frac{5^+}{2}\right)}}. \qquad (19)$$

The values of this ratio, which are presented in Table 1, were borrowed from [6]. In what follows, we will calculate only the absolute value of the effect.

3. NUMERICAL CALCULATIONS

The electron-shell states of the protactinium atom were described by the relativistic Hartree–Fock–Slater (HFS) method [14]. In order to estimate the stability of the expected effect to uncertainties in the input parameters, the calculations were performed for 13 possible configurations $(5f_{5/2})^x(6d_{3/2})^y(7s_{1/2})^z$ $(x + y + z = 5)$ of the valence band of the atom in the interval $\hbar\omega = 170$–270 eV. For the standard configuration $(5f_{5/2})^2(6d_{3/2})^1(7s_{1/2})^2$ of the valence band, the potential acting on the conversion electron in the continuous spectrum was taken in the form of (i) the HFS potential with the Latter correction, (ii) the potential of the neutral protactinium atom, and (iii) the potential of the atom involving a hole in the nlj subshell where conversion occurs.

Table 3. Helicities of the $6s_{1/2}$, $6p_{1/2}$, and $6p_{3/2}$ conversion electrons of the protactinium atom (the potential of the neutral atom is used for the conversion electron)

ΔE, eV	$\lvert\nu_2\rvert$, %					
	I			II		
	$6s_{1/2}$	$6p_{1/2}$	$6p_{3/2}$	$6s_{1/2}$	$6p_{1/2}$	$6p_{3/2}$
170	8.78	2.93	0.76	3.29	1.00	0.26
180	8.34	2.75	0.73	3.10	0.94	0.25
190	7.95	2.59	0.70	2.93	0.88	0.24
200	7.59	2.45	0.67	2.78	0.83	0.23
210	7.26	2.32	0.65	2.65	0.79	0.22
220	6.95	2.21	0.63	2.53	0.75	0.21
230	6.67	2.11	0.61	2.41	0.71	0.20
240	6.41	2.01	0.59	2.31	0.68	0.20
250	6.17	1.93	0.57	2.22	0.65	0.19
260	5.95	1.85	0.56	2.13	0.63	0.19
270	5.74	1.78	0.54	2.05	0.60	0.18

Table 4. Helicities of $6s_{1/2}$, $6p_{1/2}$, and $6p_{3/2}$ conversion electrons of the protactinium atom (the potential of the atom involving a hole in the *nlj* subshell where conversion occurs is used for the conversion electron)

ΔE, eV	$\lvert\nu_2\rvert$, %					
	I			II		
	$6s_{1/2}$	$6p_{1/2}$	$6p_{3/2}$	$6s_{1/2}$	$6p_{1/2}$	$6p_{3/2}$
170	3.78	1.66	0.66	1.43	0.57	0.22
180	3.67	1.58	0.63	1.38	0.54	0.21
190	3.57	1.51	0.60	1.33	0.51	0.20
200	3.46	1.44	0.58	1.28	0.49	0.19
210	3.36	1.38	0.56	1.24	0.47	0.19
220	3.26	1.33	0.54	1.19	0.45	0.18
230	3.17	1.28	0.52	1.15	0.43	0.18
240	3.08	1.23	0.51	1.12	0.42	0.17
250	3.00	1.18	0.50	1.08	0.40	0.17
260	2.92	1.14	0.48	1.05	0.39	0.16
270	2.84	1.11	0.47	1.02	0.37	0.16

The results of the calculations are presented in Tables 2–4. It is interesting to note that the helicity values calculated by using the HFS potential with the Latter correction are close to those calculated by using the potential of the atom involving a hole in the *nlj* subshell.

4. CONCLUSION

We have calculated the helicity ν_2 for the $6s_{1/2}$, $6p_{1/2}$, and $6p_{3/2}$ conversion electrons of the protactinium atom, a quantity that is linear in the coupling constant of weak neutral interaction, and estimated the stability of expected ν_2 values to uncertainties in the parameters entering into the calculations such as the scatter of ΔE, variations in the form of the mean atomic field, and variations in the matrix elements for the nuclear transition from one model used to another. The parity-nonconservation effect is enhanced because the dominant nuclear $E1$ transition is suppressed in relation to the admixed $M1$ transition. Moreover, the smallness of the doublet-mixing amplitude is compensated, to a considerable extent, by the fact that, in the conversion channel, the $M1$ transition for the $6s_{1/2}$, $6p_{1/2}$, and $6p_{3/2}$ electron orbits is enhanced by the factor of about 10^2–10^3. For this reason, the helicity of a conversion electron having a kinetic energy in the range 100–200 eV is about 1%, which is a value measurable in experiments aimed at determining the parameters of the parity-nonconserving effective nuclear potential.

ACKNOWLEDGMENTS

We are grateful to A.L. Barabanov and B.V. Danilin for stimulating discussions on some problems considered in this study and for enlightening comments.

This work was supported by the Russian Foundation for Basic Research (project no. 96-15-96548).

REFERENCES

1. R. R. Chasman, Phys. Lett. B **96**, 7 (1980).
2. I. Ahmad, J. E. Gindler, R. R. Betts, *et al.*, Phys. Rev. Lett. **49**, 1758 (1982).
3. D. P. Grechukhin and A. V. Lomonosov, Preprint No. 6124/2 (Russian Research Centre Kurchatov Institute, Moscow, 1999); Yad. Fiz. **62**, 2288 (1999) [Phys. At. Nucl. **62**, 2106 (1999)].
4. I. M. Band, M. A. Listengarten, and M. B. Trzhaskovskaya, Izv. Akad. Nauk, Ser. Fiz. **56** (11), 110 (1992).
5. O. Dragoun, M. Rysavy, and C. Günther, Phys. Rev. C **47**, 870 (1993).
6. D. P. Grechukhin and A. V. Lomonosov, Preprint No. 6117/2 (Russian Research Centre Kurchatov Institute, Moscow, 1998); Yad. Fiz. **63**, 431 (2000) [Phys. At. Nucl. **63**, 365 (2000)].
7. S. G. Nilsson, Mat. Fys. Medd. K. Dansk. Vidensk. Selsk. **29** (16), 1 (1955).
8. R. J. Blin-Stoyle, *Fundamental Interactions and the Nucleus* (Elsevier, Amsterdam, 1973; Mir, Moscow, 1976).
9. J. J. Szymanski, J. D. Bowman, M. Leuschner, *et al.*, Phys. Rev. C **49**, 3297 (1994).
10. A. I. Akhiezer and V. B. Berestetskiĭ, *Quantum Electrodynamics* (Wiley, New York, 1965; Russ. original, 3rd. ed., Nauka, Moscow, 1969).
11. V. B. Berestetskiĭ, A. Z. Dolginov, and K. A. Ter-Martirosyan, Zh. Éksp. Teor. Fiz. **20**, 527 (1950).
12. D. P. Grechukhin and A. V. Lomonosov, Preprint No. 6125/2 (Russian Research Centre Kurchatov Institute, Moscow, 1999).
13. A. Bohr and B. R. Mottelson, *Nuclear Structure*, Vol. 1: *Single Particle Motion* (Benjamin, Reading, 1969; Mir, Moscow, 1971); Vol. 2: *Nuclear Deformations* (Benjamin, Reading, 1975; Mir, Moscow, 1977).
14. J. C. Slater, *The Self-Consistent Field for Molecules and Solids: Quantum Theory of Molecules and Solids* (McGraw-Hill, New York, 1974; Mir, Moscow, 1978).

Translated by R. Tyapaev

Physics of Atomic Nuclei, Vol. 63, No. 5, 2000, pp. 729–733. From *Yadernaya Fizika*, Vol. 63, No. 5, 2000, pp. 799–803.

NUCLEI
Theory

Born–Oppenheimer Expansion: From Muon Distribution to Dissipation in Fission*

F. F. Karpeshin[1), 2)]
Universidade de Coimbra, P-3000 Coimbra, Portugal
Received March 3, 1999; in final form, June 25, 1999

Abstract—It is shown that a consistent treatment of momentum translation by a muon in the problem of the distribution of muons among prompt-fission fragments modifies the nonadiabatic transition operator in the Born–Oppenheimer expansion and removes difficulties indicated in earlier calculations. The muon distribution for very asymmetric prompt fission proves to be highly sensitive to the velocity of the primary fragments at the scission point. The mean collective energy dissipated during saddle-to-scission descent due to the one-body mechanism is calculated within the same approach. © *2000 MAIK "Nauka/Interperiodica".*

1. INTRODUCTION

Since 1927, when the Born–Oppenheimer expansion was proposed for atomic collisions, it has found a vast application in this and also in other fields (for example, in solid-state physics) to describing atomic clusters. In nuclear physics, the Born–Oppenheimer expansion was frequently used to calculate the probability W_l of muon attachment to light fragments of the prompt fission of the muonic atoms of actinide elements. One of our present purposes is to show how it can be used to solve one of the most topical problems in the modern theory of fission—namely, the problem of microscopically calculating the dissipation of collective energy and its application to a comparison with experimental data.

Wheeler's proposition in 1948 [1] that the muonic atom of uranium can undergo prompt fission as the result of the $2s \longrightarrow 1s$ radiationless transition opened the way for using an exotic particle as a probe for fission dynamics. Although it was shown in subsequent publications that transitions of various multipolarities ($E1$, $E2$, $E3$) make approximately equal contributions to the radiationless excitation of actinide atoms [2–4], the problem remains very topical now in connection with studies on fission dynamics—specifically, on the time scale for fission.

In prompt fission, the muon is usually attached to the heavy fragment, forming a muonic atom. This gives rise to various processes and effects, which are being investigated. These include the muonic conversion of gamma rays from the fragment, muon capture by the fragment, muonic x radiation from the fragment, an increase in the fission barrier due to the presence of the muon, and many others (see, for example, [5–7] and references therein). Of these topics, the problem of muon attachment to the light fragment—the corresponding probability is denoted by W_l—was considered in a number of studies (see, for example, [5–16] and references therein). Lattice calculations show that W_l is expected to be sensitive to the amount of dissipated energy and, moreover, that the probability of a transition to muonic excited states is also significant and sensitive to energy dissipation [9, 16]. In contrast, more traditional calculations in an adiabatic basis usually do not reproduce this result [5–8, 12, 14, 15]. It should be noted in this respect that the behavior of the muon during the separation of the fragments is very complicated, especially in the vicinity of the pseudocrossing point. It is not clear whether lattice calculations are sufficiently subtle for adequately reproducing the resulting probability of muon attachment to the light fragment. Answering this question remains a challenging task. In addition, a calculation of the transition probability in the four-state basis [13] encountered the problem that nonadiabatic matrix elements between the $1s$ and $2p$ states of the same fragment do not vanish at large internuclear distances. As a result, the population amplitudes for these states continue oscillating in the asymptotic region of large internuclear distances R, where no interaction between the states survives. Moreover, these spurious transitions violate the Galilean invariance of the theory. It is worth noting the analogy between this problem and that encountered in describing one-body dissipation, where a modification to the original theory of one-body dissipation is introduced to rule out a spurious internal excitation of a uniformly moving fragment [17]. The present investigation was undertaken in order to obtain deeper insight into all these peculiarities, to refine the theory, and to apply it to the problem of energy dissipation in fission.

* This article was submitted by the author in English.

[1)] Università degli Studi di Milano, Dipartamento di Fisica, I-20133 Milano, Italy.
[2)] Institute of Physics (Petrodvorets Branch), St. Petersburg State University, Ul'yanovskaya ul. 1, Petrodvorets, 198904 Russia.

1063-7788/00/6305-0729$20.00

2. EQUATIONS OF MOTION

The separation of the fragments occurs with the large Massey adiabaticity parameter with respect to the motion of the bound muon. In the majority of cases, the muon therefore remains in the 1*s* state of the heavy fragment. The probabilities of transitions to higher states and to states of the lighter fragment are expected to be small. In order to determine these probabilities quantitatively, we modify the Born–Oppenheimer expansion, representing the wave function as the series

$$\Psi(\mathbf{r}; R(t)) = \sum_n C_n \Phi_n(\mathbf{r}; R(t)) e^{i(\mathbf{p}_n \cdot \mathbf{r})} e^{-\int^t E_n'(t')dt'}, \quad (1)$$

where the functions Φ_n form a complete set of quasimolecular wave functions. When the internuclear distance R tends to infinity, each of the functions Φ_n correlates with a certain μ-atomic state n of the corresponding fragment.

The momentum-translation exponents (MTE) are introduced in (1), where $\mathbf{p}_n = \mu\mathbf{v}_n$, with μ being the muon mass and $\mathbf{v}_n$ being a constant equal to the velocity of the fragment in the asymptotic region. The orthogonality of the basis functions is thus lost in this description. The great advantage is, however, that, in the asymptotic region, our basic product functions $\Phi_n(\mathbf{r}; R)e^{i(\mathbf{p}_n \cdot \mathbf{r})}$ satisfy the Schrödinger equation

$$(H - E_n')\Phi_n(\mathbf{r}; R)e^{i(\mathbf{p}_n \cdot \mathbf{r})} = 0, \quad (2)$$

where $E_n' = E_n + p_n^2/2\mu$ and where H is the two-center Hamiltonian of the form

$$H = -\frac{\Delta}{2\mu} + V_1(|\mathbf{r} - \mathbf{R}_1|) + V_2(|\mathbf{r} - \mathbf{R}_2|). \quad (3)$$

Substituting expansion (1) into the time-dependent Schrödinger equation, we arrive at the set of coupled equations

$$\frac{dC_i}{dR} = -\sum_k F_{ik} C_k, \quad (4)$$

$$F_{ik} = \mathcal{M}_{ik} e^{-i\int^R (E_k' - E_i'(R'))/V(R')]dR'}, \quad (5)$$

$$\mathcal{M}_{ik} = \left\langle \Phi_i \left| \frac{\partial}{\partial R} - \frac{\mathbf{v}_i + \mathbf{v}_k}{2V(R)} \nabla \right| \Phi_k e^{i(\mathbf{p}_k - \mathbf{p}_i) \cdot \mathbf{r}} \right\rangle, \quad (6)$$

where the differential operators act only on the wave functions Φ_i or Φ_k.

The introduction of the MTE is reflected in the initial condition for the set of coupled equations (4)–(6). The natural initial condition is that the muon is in the lowest $1s\sigma$ state at the saddle, in which case it is described by the wave function Φ_1. In going over to another basis, we therefore have to reexpand this wave function in terms of the new basis set. The expansion coefficients $C_i^{(0)} = \langle \Phi_1 | \Phi_i \exp(ipz) \rangle$, $i = 1, 2, 3, 4$ in our case, are to be used as the new initial condition. Because of the smallness of the parameter that can be estimated as $p_i z \lesssim 0.03$, the resulting amplitudes for $i > 1$ prove to be of about 0.003 or less, which is an order of magnitude less than final transition amplitudes. In the long-wave approximation, we can therefore use the usual initial condition

$$C_i(R = R_s) = \delta_{i,1}, \quad (7)$$

where R_s is the saddle point. The condition in (7) means that the muon is in the lowest $1s\sigma$ state at the saddle. The probability of a transition to a state n is

$$W_l = \lim_{R \to \infty} |C_n(R)|^2. \quad (8)$$

At large R, where the interaction between the atoms can be neglected and where the centers move uniformly, the operator $\partial/\partial R$ is proportional to $\partial/\partial z$. If the states i and k belong to the same center and if they are connected by an electric dipole transition, the matrix element of $\partial/\partial R$ therefore does not vanish. This poses the problem formulated above. In this case, however, the second term in (6), which arises from the MTE incorporated in (1), exactly cancels the contribution from $\partial/\partial R$, thereby resolving the problem and restoring the Galilean invariance of the theory. Furthermore, taking this term into account modifies the nonadiabatic matrix element in the range where the formation of the final attachment probabilities occurs.

From equation (6), it follows that, for the $1s\sigma \longrightarrow 2p\sigma$ transition, the transition operator $\partial/\partial R$ becomes $\partial/\partial R + \frac{v_1 - v_2}{2V(R)}\frac{\partial}{\partial z}$ upon taking the momentum transfer into account. The second term in the last expression can be treated as that which is due to the motion of the geometric center of the line segment between the fragments. Its contribution will be small, along with the difference $v_1 - v_2$, always, with the exception of the case of very asymmetric fission. The exponential factors in the matrix element in (6) can also be neglected in the long-wave approximation, and we arrive at essentially the old expression for this nonadiabatic matrix element. The latter vanishes, along with the overlap integral $\langle 2|1 \rangle$, for $R \longrightarrow \infty$. Thus, the inclusion of the momentum transfer does not have dramatic consequences if the quasimolecular states refer to the different fragments.

Let us examine the effect of introducing the MTE in the probability of a transition to an excited muon state $2s\sigma$, which goes over to the $2p$ state of the heavy fragment. For the two lowest states, $1s\sigma$ and $2p\sigma$, the energies, the wave functions, and the nonadiabatic matrix

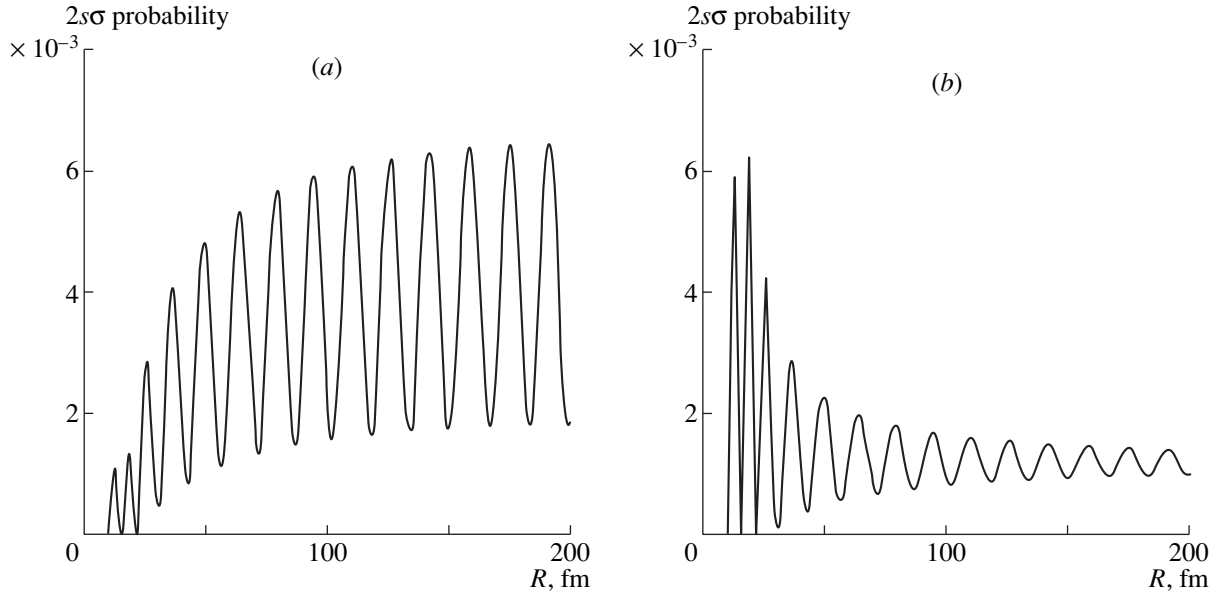

Fig. 1. Population probabilities calculated for the $2s\sigma$ level (correlating with the $2p$ state of the heavy fragment) as a function of the internuclear distance R for a representative pair of fragments with charge numbers $Z_1 = 52$ and $Z_2 = 40$ (*a*) without and (*b*) with allowing for the momentum-translation exponent.

elements were calculated in [14] with allowance for a finite nuclear size by solving numerically the two-dimensional Schrödinger equation by the method of finite elements. On the other hand, the LCAO method is appropriate for obtaining the energies and wave functions of the next relevant states, $2s\sigma$ and $3p\sigma$, which correlate with the $2p$ states of the heavy and the light fragment, respectively. For these states, the Schrödinger Coulomb wave functions can be used, since the effect of the finite nuclear size on these states is insignificant.

For the four aforementioned states, the population probabilities have been obtained by solving numerically the set of simultaneous equations (4)–(6) with the initial condition (7). In Fig. 1, we present the population probability for the $2s\sigma$ level as a function of the internuclear distance R for a representative pair of fragments with atomic numbers $Z_1 = 52$ and $Z_2 = 40$. These results were obtained for two cases, without (Fig. 1*a*) and with (Fig. 1*b*) allowance for the MTE. It can clearly be seen that taking account of the MTE diminishes the final attachment probability for this state by a factor of about 4, allowing one, in addition, to eliminate the oscillations in the attachment probability, which ultimately vanish for $R \longrightarrow \infty$. As might have been expected, the population of higher levels proves to have a relatively small effect on the final muon fate.

3. SENSITIVITY TO FISSION DYNAMICS

In order to study this aspect, we have calculated the final muon-attachment probabilities for various positions of the scission point R_{sc} using the results obtained in the preceding section. The relative velocity of the fragments was assumed to be determined by the Coulomb repulsion of the fragments for $R \geq R_{sc}$ and to be a constant for $R < R_{sc}$, with $V(R < R_{sc}) = V(R_{sc})$. Therefore, different values of R_{sc} correspond to different velocities of descent from the saddle to the scission point and, consequently, to different velocities of the primary fragments at the scission point. The calculations have been performed for various values of the total kinetic energy (TKE) of the fragments. The results of the calculation are listed in Tables 1 and 2 for representative fission fragments with a typical charge splitting, $Z = 52 + 40$, and with a relatively large asymmetry, $Z = 57 + 35$.

We can see that a more asymmetric fission mode is more sensitive to dynamics, as might have been expected. In this case, the pseudocrossing point of the muonic terms approaches the scission point [7, 14]. This is in contrast to the case of more symmetric fis-

Table 1. Calculated probabilities of attachment to light fragments, W_l (%), for fragments with charge numbers $Z_1 = 57$ and $Z_2 = 35$

TKE, MeV	R_{sc}, fm			
	20	22	24	26
140	0.21	0.23	0.026	0.033
150	0.37	0.14	0.12	0.038
160	0.33	0.29	0.10	0.020
170	0.56	0.24	0.064	0.053
180	0.49	0.17	0.10	0.18
190	0.38	0.20	0.23	0.40
200	0.39	0.34	0.47	0.71

Table 2. Calculated probabilities of attachment to light fragments, W_l (%), for fragments with charge numbers $Z_1 = 52$ and $Z_2 = 40$

TKE, MeV	R_{sc}, fm			
	20	22	24	26
140	2.38	2.38	1.65	1.51
150	2.77	2.73	2.43	2.13
160	3.82	3.56	3.00	2.69
170	4.84	4.07	3.52	3.37
180	5.35	4.52	4.18	4.20
190	5.35	4.52	4.18	4.20

sion, where the avoided crossing of the levels occurs after the rupture at a rather large distance between the fragments. It is worth noting that, although the theoretical results for the average value of W_l agree well with experimental data, the theoretical attachment probabilities are significantly lower than the experimental values in this region of charge sharing. Possible reasons for the discrepancy were considered in the literature (see, for example, [7, 18] and references therein); it is conceivable that this is a manifestation of dynamical effects. A very significant variation in the resulting values of W_l for the fragments with $Z_1 = 57$ and $Z_2 = 35$ at TKE = 170 MeV should be noted.

4. MODEL FOR STRONGLY INTERACTING PARTICLES AND DISSIPATION

In this section, we extend the results obtained previously to the case of strongly interacting particles—Λ hyperons and nucleons—in a fissile nucleus.

Let us consider the two-center harmonic-oscillator model for a Λ hyperon in a fissile hypernucleus [19]. Let the potential produced by a fragment J be

$$V_J(|\mathbf{r}-\mathbf{R}_J|) = \frac{1}{2}\omega_J^2|\mathbf{r}-\mathbf{R}_J|^2. \quad (9)$$

An analysis of the matrix elements of the commutator $[H, \partial/\partial R]$ leads to the useful relation

$$\left\langle \Phi_i\left|\frac{\partial}{\partial Q}\right|\Phi_j\right\rangle \approx \frac{1}{\Delta E_{ij}}\left\langle \Phi_i\left|\left(\frac{\partial V}{\partial Q}\right)\right|\Phi_j\right\rangle, \quad (10)$$

where Q stands for R or r, and ΔE_{ij} is the energy difference between the states. For a finite potential of constant depth, the presence of $\partial V/\partial Q$ in (10) gives rise to an interaction at the nuclear surface; qualitatively, this interaction corresponds to a semiclassical description [17].

Taking into account the dependence of the oscillator parameter $\hbar\omega$ on R [19] and using equations (5) and (9), we obtain the nonadiabatic matrix element in the form

$$\mathcal{M}_{ik} = \frac{1}{\Delta E_{ik}}\left\langle \Phi_i\left|\sum_J \omega_J\left(\frac{d\omega_J}{dR}\right)|\mathbf{r}-\mathbf{R}_J|^2\right|\Phi_k\right\rangle. \quad (11)$$

The nonadiabatic matrix element in (11) can be treated as that which consists of two parts for each fragment. The corresponding interaction potential for each fragment appears to be of a monopole character. Neglecting boundary effects in the region where the two potential wells intersect, we can see that interaction (11) then nearly cancels the electric dipole transitions for each fragment like $1s \longrightarrow 2p$ or electric quadrupole transitions like $1s \longrightarrow 3d$ if the fragment is not strongly deformed, whilst giving rise to monopole transitions like $1s \longrightarrow 2s$. Detailed calculations of the resulting Λ-attachment probabilities will be given elsewhere. However, the experimental cross section for Λ–nucleon collisions indicates [19, 20] that such collisions seem more important in determining the final Λ-attachment probabilities than the nonadiabatic quasimolecular effects considered previously.

Equation (11) can also be used to calculate the probability of nucleon promotion in a fissile nucleus. In this case, nucleons undergo transitions to excited orbitals, receiving energy from the collective motion of nascent fragments, whereby the intrinsic excitation of the fragments arises at the expense of the energy of their relative motion. The last effect corresponds to the conventional one-body dissipation of collective motion. Therefore, equation (11) can be used to define the microscopic Hamiltonian responsible for one-body dissipation in fission by invoking the adiabatic basis of the quasimolecular nuclear states.

In order to estimate the numerical magnitude of the effect, we consider the near-barrier ^{238}U fission, which can be induced, for example, by muonic radiationless transitions. The shape of a fissile nucleus can be parametrized in terms of two intersecting spheres of corresponding radii, with R being the distance between the centers of the spheres. We make use of the fact that $\hbar\omega \approx 41A^{-1/3}$ and, accordingly, $\partial\omega/\partial R$ are functions that change slowly in the fission process and approximate ΔE_{ik} by the energy of the giant monopole resonance, $\Delta E \approx 65A^{-1/3}$ MeV. In the leading order of perturbation theory, we then find from (4) and (11) that the amplitude of a nuclear transition from the ground state i to an excited state k satisfies the differential equation

$$\dot{C}_k(R) = \mathcal{M}_{ki}\exp\left(-i\int_{R_0}^{R}\frac{\Delta E}{V}dr\right), \quad (12)$$

with V being the velocity of fragments between the saddle point R_{sp} and the scission point R_{sc}. With allowance for the sum rule for the giant monopole resonance, the solution to equation (12) can be represented as

$$W = \sum_k |C_k(R_{sc})|^2 = \left(\frac{2V\omega}{\Delta E^2}\frac{d\omega}{dR}\right)^2\frac{A\langle R_0^2\rangle}{\Delta E}\sin^2\left[\frac{\Delta E}{2V}(R_{sc}-R_{sp})\right]. \quad (13)$$

Using the values of $d\omega/dR \sim 0.075$ and 0.12 MeV/fm for the heavy and light fragments, respectively, together with $\Delta E \sim 10$ MeV, $R_{sp} \approx 10$ fm, $R_{sc} \approx 20$ fm, and $V \approx 0.03$, and replacing $\sin^2\left[\frac{\Delta E}{2V}(R_{sc} - R_{sp})\right]$ in (13) by its mean value of about 1/2, we obtain $W \approx 1/6$. This means that the mean dissipated energy is about 2 MeV, which corresponds to a motion characterized by a relatively low damping. It is expected that this energy will be greater for the light fragment than for the heavy fragment by a factor of about 2.5 owing to the higher values of $d\omega/dR$ and V in the former case.

In the case of a deformed fragment, the main consequence of the deformation is expected to be the splitting of the giant monopole resonance and its interaction with the giant quadrupole resonance, with the sum rule in (13) being essentially unaffected.

5. CONCLUSIONS

The basic results of the present study can be summarized as follows:

(i) The probability of muon attachment to light fragments is a highly sensitive probe of the velocity of the saddle-to-scission descent, especially in the case of strongly asymmetric fission.

(ii) From the theoretical viewpoint, the present calculation is of great interest in view of applications to constructing the microscopic Hamiltonian and developing the quantitative theory of one-body dissipation. I would like to note that, historically, the study of the Λ-attachment probability was an important intermediate step toward introducing the MTE, as was done above.

(iii) The above consideration allows one to draw an important qualitative conclusion about one-body dissipation—namely, the conclusion that this dissipation is due to the excitation of the giant monopole resonance—and, in the case of deformed fragments, the quadrupole resonance. Numerical estimates of the amount of dissipated energy on the basis of this mechanism of dissipation leads to a saddle-to-scission descent characterized by a relatively weak damping.

ACKNOWLEDGMENTS

I am grateful to V.N. Ostrovsky for stimulating discussions on the problem. I would also like to thank J.R. Nix for his enlightening comments. I am also thankful to M.R. Harston for constructive discussions. I gratefully acknowledge the attention of Prof. J. da Providencia, Prof. I. Iori, and Dr. A. Moroni to this study and thank E. Alessandro for her help in preparing the manuscript.

This work was performed within the scholarship from the Program of PRAXIS–XXI.

REFERENCES

1. J. A. Wheeler, Phys. Rev. **73**, 1252 (1948).
2. D. F. Zaretsky and V. M. Novikov, Nucl. Phys. **14**, 540 (1959); **28**, 177 (1961).
3. E. Teller and M. S. Weiss, Trans. N.Y. Acad. Sci. **40**, 222 (1980).
4. F. F. Karpeshin and V. O. Nesterenko, J. Phys. G **17**, 705 (1991).
5. P. David, Ch. Rösel, F. F. Karpeshin, *et al.*, in *Proceedings of the Workshop on Muonic Atoms and Molecules, Monte Verita, Ascona, 1992.*
6. F. F. Karpeshin, J. Phys. G **16**, 1195 (1990).
7. F. F. Karpeshin, Nucl. Phys. A **617**, 211 (1997).
8. Yu. N. Demkov, D. F. Zaretsky, F. F. Karpeshin, *et al.*, Pis'ma Zh. Éksp. Teor. Fiz. **28**, 287 (1978) [JETP Lett. **28**, 263 (1978)]; D. F. Zaretsky, F. F. Karpeshin, *et al.*, Yad. Fiz. **31**, 47 (1980) [Sov. J. Nucl. Phys. **31**, 24 (1980)].
9. J. A. Maruhn, V. E. Oberacker, and V. Maruhn-Rezwany, Phys. Rev. Lett. **44**, 1576 (1980).
10. P. Leander, S. G. Nilsson, and P. Möller, Phys. Lett. B **90**, 193 (1980).
11. Z. Y. Ma, X. Z. Wu, G. S. Zhang, *et al.*, Nucl. Phys. A **348**, 446 (1980).
12. F. F. Karpeshin and V. N. Ostrovsky, J. Phys. B **14**, 4513 (1981).
13. Z. Y. Ma, X. Z. Wu, G. S. Zhang, *et al.*, Phys. Lett. B **106**, 159 (1981).
14. F. F. Karpeshin, M. Kaschiev, and V. A. Kaschieva, Yad. Fiz. **45**, 1556 (1987) [Sov. J. Nucl. Phys. **45**, 965 (1987)].
15. L. Bracci and G. Fiorentini, Nucl. Phys. A **423**, 429 (1984).
16. V. E. Oberacker *et al.*, Phys. Lett. B **293**, 270 (1992).
17. J. W. Negele, S. E. Koonin, P. Möller, *et al.*, Phys. Rev. C **17**, 1098 (1978).
18. F. F. Karpeshin, Yad. Fiz. **55**, 29 (1992) [Sov. J. Nucl. Phys. **55**, 18 (1992].
19. F. F. Karpeshin, C. G. Koutroulos, and M. E. Grypeos, Nucl. Phys. A **595**, 209 (1995).
20. F. F. Karpeshin, Yad. Fiz. **57**, 631 (1994) [Phys. At. Nucl. **57**, 594 (1994)].

Physics of Atomic Nuclei, Vol. 63, No. 5, 2000, pp. 734–738. Translated from Yadernaya Fizika, Vol. 63, No. 5, 2000, pp. 804–808.

NUCLEI
Theory

Deuteron Form Factors for the Nijmegen Potentials

S. B. Dubovichenko*

Kazakh State University, ul. Timiryazeva 46, Almaty, 480121 Republic of Kazakhstan,
and Institute for Physics and Technology, Kazakh Academy of Sciences, Almaty, Republic of Kazakhstan

Received June 11, 1998; in final form, March 10, 1999

Abstract—The deuteron form factors and tensor polarizations in elastic *ed* scattering are considered for four versions of the Nijmegen nucleon–nucleon potentials. The numerical deuteron wave functions in these potentials are approximated by a series of Gaussian functions with the result that it can be used in any computations of integrated characteristics. The quality of this approximation of the wave function is exemplified by comparing the results that it produces for the momentum distributions, the quadrupole moment, the *D*-state probability, and the deuteron radius with the results of the corresponding precise calculations. © *2000 MAIK "Nauka/Interperiodica".*

Not very long ago, a few new versions of phenomenological nucleon–nucleon potentials featuring a repulsive core were proposed in [1]. The parameters of these potentials were determined on the basis of the partial-wave analysis performed by the Nijmegen group [2]. At present, the Nijm-1, Nijm-2, and Reid-93 versions seem to be the best of those proposed thus far, because they yield the χ^2 value per point as low as 1.03 in the energy region extending up to 350 MeV. For example, the classical Reid potential [3] (1968) or the Paris potential [4] (1980) lead to χ^2 values of about 2 to 3 in the energy range 0–300 MeV. The fourth version of the Nijmegen potential, Nijm-93, yields the close value of $\chi^2 = 1.9$ for energies up to 350 MeV [1, 5]. It was shown [5] that only the Argonne potential [6] leads to a comparatively small value of $\chi^2 = 3.3$ at energies up to 350 MeV. Other potentials, such as Hamada–Johnston-62, Reid-68, Urbana-81, and Bonn-89, result in much greater values of χ^2, because the parameters of these potentials were derived from analyses performed over a narrower energy range.

The partial-wave analysis in [2] covered the energy range 0–350 MeV, but, by and large, its results comply quite well with the results from [7] and [8], where the partial-wave analyses were performed over the much broader energy ranges 0–1600 MeV and 0–2500 MeV, respectively. On the basis of the partial-wave analysis reported in [2], the Nijmegen group refined some features of the deuteron (binding energy, charge radius, quadrupole moment) and some characteristics of *np* scattering (scattering length, effective range) [9].

It should be noted that the value of 0.074 used for the πNN coupling constant f^2 in parametrizing all versions of the above potentials is considerably smaller than the values reported in [10] and [11] [0.0776(9) and 0.0803(14), respectively]; it is closer to the values of 0.0760(8) and 0.0760(2) reported in [12] and [13], respectively.

With the interactions obtained in [1], a thorough analysis of the properties of the deuteron and of many features of nucleon–nucleon systems was performed in [2], and a comparison was drawn in [5] between the results of this analysis and the corresponding results for other known potentials. A three-body calculation of the ^{3}H binding energy yielded values falling within the range 7.6–7.7 MeV and depending on the specific version of the interaction [14], the experimental value being 8.48 MeV.

At the same time, the deuteron form factors and the tensor polarizations in elastic *ed* scattering have not yet been calculated with the Nijmegen potentials. This can be done by using the wave functions obtained in [1]; their numerical values can be found in [15], but they are given there with a variable step in the range 0–25 MeV. Since this complicates the calculations, it is desirable to approximate analytically the wave function specified numerically, in which case we would have at our disposal its value at any required point.

To approximate the numerical wave functions from [15], it is convenient to use the following series in terms of Gaussian functions [16]:

$$R_L(r) = r^L \sum_k C_k \exp(-\alpha_k r^2). \quad (1)$$

Here, C_k are coefficients, while α_k are parameters in the expansion of the radial wave function, which is taken to be $R_0(r) = u(r)/r$ and $R_2 = w(r)/r$, $u(r)$ and $w(r)$ being, respectively, the *S*- and *D*-wave solutions to the standard radial equation. Summation in (1) was performed up to $N = 13$. For the wave function in question, this made it possible to achieve a comparatively accurate approximation in the range 0–10 fm. In constructing this approximation, the coefficients in (1) were chosen

* e-mail: serg@mail.kz

Deuteron features calculated with the precise and approximate wave functions for various versions of the Nijmegen potentials [$\Delta E(S)$ and $\Delta E(D)$ are the average errors in the approximation of the S- and D-wave functions, respectively]

Deuteron features	Nijm-1 [1]	Nijm-1 with the approximate wave function	Nijm-2 [1]	Nijm-2 with the approximate wave function	Nijm-93 [1]	Nijm-93 with the approximate wave function	Reid-93 [1]	Reid-93 with the approximate wave function	Experimental data from [9]
P_d, %	5.664	5.648	5.635	5.637	5.754	5.740	5.699	5.698	5.67
Q_d, fm^2	0.2719	0.2707	0.2707	0.2708	0.2706	0.2700	0.2703	0.2706	0.271(1)
R_d, fm	1.967	1.966	1.968	1.967	1.966	1.965	1.969	1.967	1.9676(10)
$\Delta E(S)$, %		2×10^{-3}		4×10^{-3}		2.5×10^{-3}		2.6×10^{-3}	
$\Delta E(D)$, %		7×10^{-3}		1×10^{-2}		8.0×10^{-3}		1.2×10^{-2}	

in such a way as to ensure the normalization of the overall wave function to unity. In calculating the features of the deuteron, our approximate wave function was matched, at large distances, with the corresponding asymptotic expressions [1, 9]

$$u(r) \longrightarrow A_S \exp(-r/R),$$

$$w(r) \longrightarrow A_D\{1 + 3R/r + 3(R/r)^2\}\exp(-r/R),$$

where $R = 4.319$ fm and $A_D = \eta A_S$, the asymptotic constants being $A_S = 0.8845(8)$ and $\eta = 0.0253(2)$ [9]. The calculated features of the deuteron are quoted in the table, along with corresponding values obtained with the precise wave functions from [1]. Also displayed in the table are averaged relative errors characterizing the deviation of the approximate wave function from the precise numerical results [15]. The values obtained with the approximate wave function are seen to comply well with the results presented in [1].

The solid curve in Fig. 1 represents the precise wave function for the Nijm-1 version of the potential [1, 15], the approximate wave function being graphically indiscernible from it. The asymptotic behavior of the wave function is shown by the dashed curve. It can be seen that, from 9 (or 10) fm, the asymptotic curve virtually coincides with the precise solution and its approximation both for the S and for the D wave (upper and lower pairs of the curves, respectively).

Apart from integrated characteristics of the deuteron like the radius or the quadrupole moment, we can compare the results for the momentum distributions. The momentum distributions presented in [15] were obtained with the precise wave functions for the various versions of the potential. For the momentum distributions of nucleons in the deuteron, the results obtained with the approximate wave functions are shown in Fig. 2, the dash-dotted and the dashed curve corresponding to the Nijm-1 and the Nijm-93 version, respectively. For the sake of comparison, the analogous distributions according to the precise results from [15] are also shown in Fig 2 by the dotted and the solid curve, respectively. It can be seen that some difference is observed only in the case of Nijm-93. The results for the soft-core Reid potential [3] are represented by the dash-and-double-dot curve. Each distribution displayed in this figure was normalized to unity at zero momentum transfer.

These results demonstrate that, for all potential versions under consideration, the features of the deuteron that were calculated with the approximate wave functions agree well with those calculated with the precise wave functions from [15]. It therefore seems reasonable to use our approximate wave functions in calculating the deuteron form factors.

To calculate the form factors, we made use of the expressions [17]

$$\frac{d\sigma}{d\Omega} = \left(\frac{d\sigma_M}{d\Omega}\right)\left[A + B\tan^2\left(\frac{\theta}{2}\right)\right],$$

$$A = G_0^2 + G_2^2 + \frac{2}{3}\eta(1+\eta)G_M^2,$$

$$B = \frac{4}{3}\eta(1+\eta)^2 G_M^2,$$

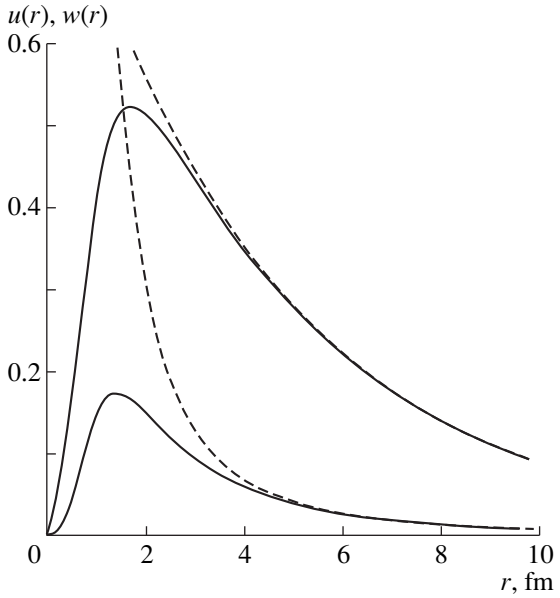

Fig. 1. Wave function for the Nijm-1 potential.

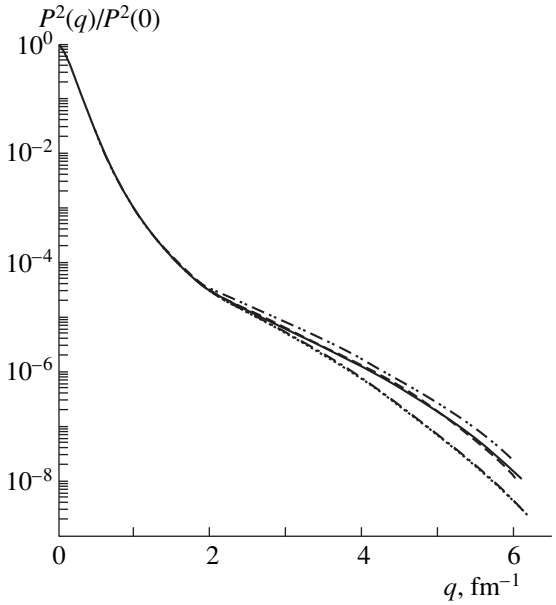

Fig. 2. Momentum distributions for the Nijm-1 and Nijm-93 potentials.

$$G_0 = 2G_E C_E,$$

$$G_2 = 2G_E C_Q,$$

$$G_M = \frac{M_d}{M_p}(2G_{M_0} C_S + G_E C_L),$$

$$2G_E = G_{E_p} + G_{E_n}, \quad 2G_{M_0} = G_{M_p} + G_{M_n},$$

$$\eta = \frac{(\hbar c q)^2}{4M_d^2} = 0.002767q^2,$$

$$x = \frac{qr}{2},$$

$$C_E = \int (u^2 + w^2) j_0(x) dr,$$

$$C_Q = 2\int w\left(u - \frac{w}{\sqrt{8}}\right) j_2(x) dr,$$

$$C_L = \frac{3}{2}\int w^2 (j_0(x) + j_2(x)) dr,$$

$$C_S = \int\left(u^2 - \frac{w^2}{2}\right) j_0(x) dr + \frac{1}{\sqrt{2}}\int w\left(u + \frac{w}{\sqrt{2}}\right) j_2(x) dr,$$

where $u(r)$ and $w(r)$ are the radial wave functions of the bound state, while j_L are spherical Bessel functions. For the nucleon masses, we used the values of M_p = 938.28 MeV and M_n = 939.57 MeV [10]; the deuteron mass was set to 1875.63 MeV. The charge form factor for the neutron was assumed to be zero, while the charge form factor for the proton was parametrized as [18]

$$G_{E_p} = \frac{1}{(1 + 0.054844q^2)^2},$$

where q is the momentum transfer in fm^{-1} units and where the magnetic form factors for the nucleon were determined on the basis of the scaling law: $G_{M_p} = \mu_p G_{E_p}$ and $G_{M_n} = \mu_n G_{E_p}$ [18].

The nonrelativistic formulas for the form factors were used previously in [17, 19]; in [20], the relativistic and the nonrelativistic impulse approximation were compared for the case of the Argonne potential. (The form factors for the Argonne potential virtually coincide with those for the Paris potential.) It was shown that relativistic effects become sizable only at comparatively high momentum transfers (5 or 6 fm^{-1}), slightly increasing the form factors. However, the contribution of meson-exchange currents is opposite in sign to that of relativistic effects, nearly canceling them (see Figs. 7 and 12 in [20]). Similar results were obtained for the tensor polarization t_{20} in elastic *ed* scattering [20]. The relativistic corrections and effects of meson-exchange currents were also considered in [21], where it was shown that they do not make a significant contribution at momentum-transfer values below 5 or 6 fm^{-1}: their magnitude in this range is within the experimental errors. It follows that, in the momentum-transfer range being considered, the use of the nonrelativistic impulse approximation is quite legitimate, so that the choice of potential model is a key point in describing the form factors and polarizations in *ed* scattering.

The form factors calculated in the present study are displayed in Fig. 3, along with experimental data from [17]. The dotted and the dashed curve in Fig. 3*a* represent the results obtained with the Reid-68 (RSCA) [3] and the Nijm-1 potential, respectively. The Nijm-2 and Nijm-93 potentials produce nearly coincident results, which are depicted by the solid curve. The results for Reid-93 (dash-dotted curve) show virtually no deviations from the solid curve. In Fig. 3*b*, the dotted curve represents the results for Reid-93, which are graphically indiscernible from the results for Reid-68. The dashed and the solid curve illustrate the results for Nijm-2 and Nijm-93, respectively, while the dash-dotted curve, which is almost coincident with the solid curve, corresponds to Nijm-1. It can be seen that the best description of the form factor $B(q)$ is achieved with Nijm-93 and Nijm-1: the corresponding curves do not go beyond the error bars.

The tensor polarizations t_{20}, t_{21}, and t_{22} in elastic *ed* scattering [20, 21] that were calculated for all versions of the Nijmegen potentials are presented in Fig. 4. The dash-and-double-dot, solid, dashed, dash-dotted, and dotted curves show the results for Nijm-1, Nijm-2, Nijm-93, Reid-93, and Reid-68 (RSCA), respectively. The experimental data were borrowed from [20]. We can see the following: (i) The potentials Nijm-1 and Nijm-93 yield very close results, and so do the potentials Nijm-2 and Reid-93. (ii) By and large, the description of the polarizations t_{22} and t_{21} is quite satisfactory. (iii) The results of the calculation for t_{20} fall somewhat

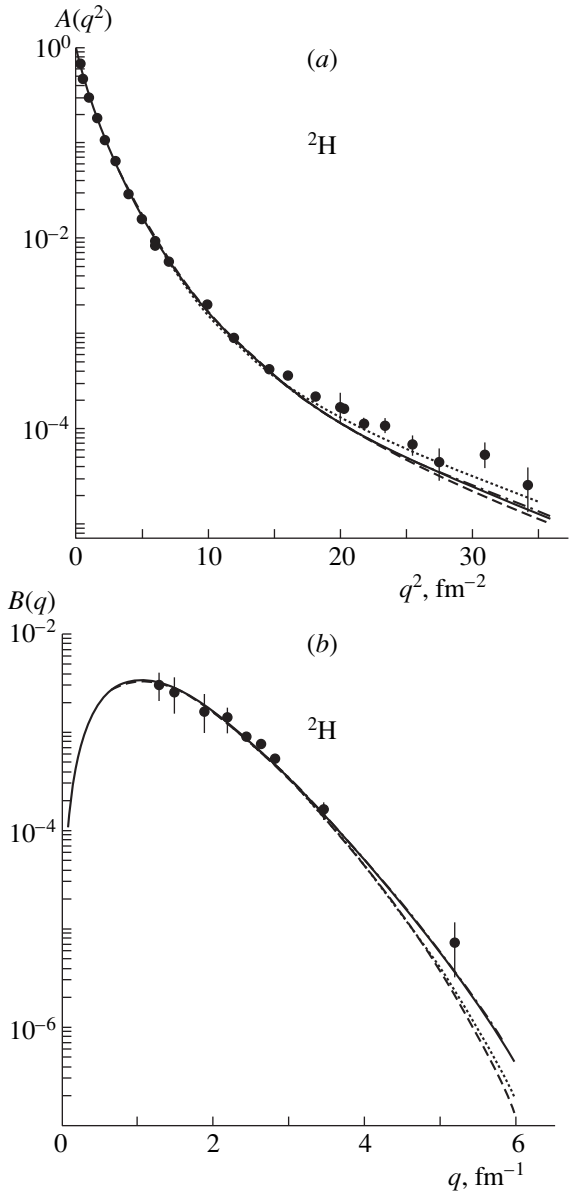

Fig. 3. Deuteron form factors for the various versions of the Nijmegen potential. The experimental data were borrowed from [17].

short of the experimental values. (iv) The best description of this quantity is provided by Reid-68.

Thus, we can conclude from the above that the approximate wave functions constructed here faithfully reproduce the behavior of the numerical wave functions for all versions of the Nijmegen potentials. The features of the deuteron that have been calculated with the approximate wave functions comply well with those found with the precise wave functions. For the deuteron form factors and the tensor polarizations in elastic *ed* scattering, the approximate wave function yields results that agree by and large with available experimental data and, in the momentum-transfer region

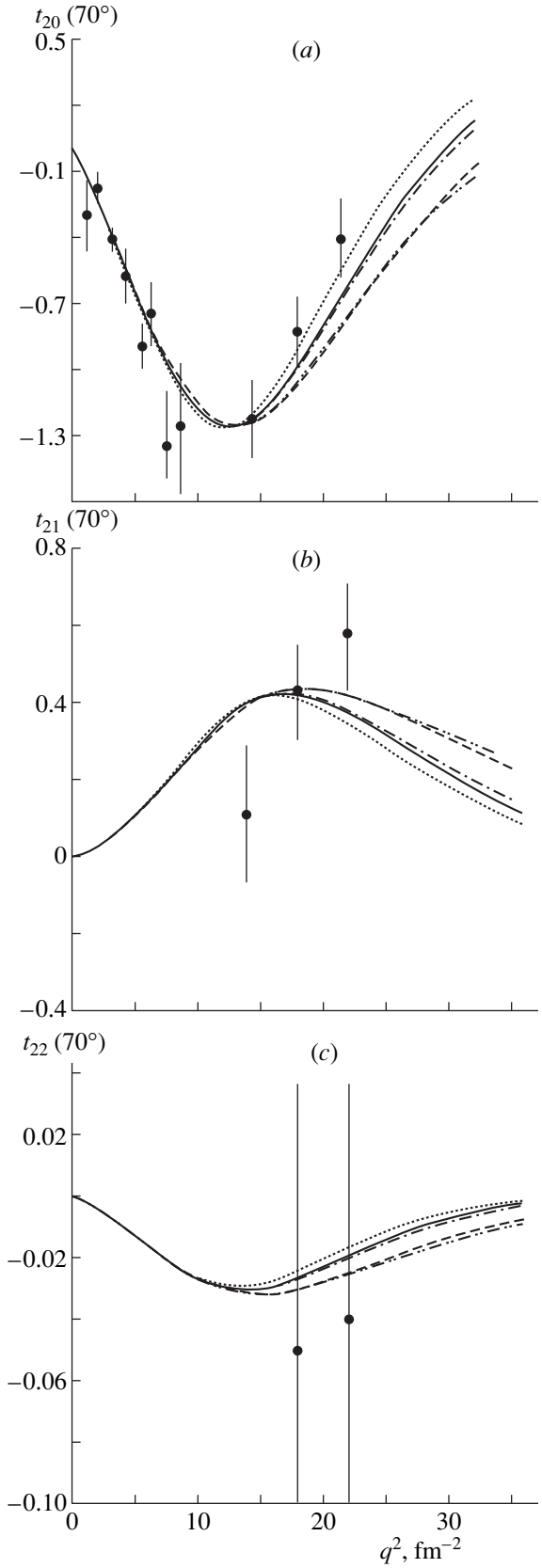

Fig. 4. Tensor polarizations in elastic *ed* scattering for the various versions of the Nijmegen potential. The experimental data were taken from [20].

being considered, show only modest variations in going over from one version of the Nijmegen potential to another.

ACKNOWLEDGMENTS

I am grateful to I.I. Strakovsky for valuable information and enlightening discussion on the results of the present study.

This work was supported in part by the Kazakh Academy of Sciences.

REFERENCES

1. V. G. J. Stoks, R. A. M. Klomp, C. P. F. Terheggen, and J. J. de Swart, Phys. Rev. C **49**, 2950 (1994); J. J. de Swart, R. A. M. Klomp, M. C. M. Rentmeester, and Th. A. Rijken, Few-Body Syst. (Suppl.) **8**, 437 (1995); nucl-th/9406039.
2. R. A. M. Klomp, V. G. J. Stoks, and J. J. de Swart, Phys. Rev. C **44**, R1258 (1991); V. G. J. Stoks, R. A. M. Klomp, M. C. M. Rentmeester, and J. J. de Swart, Phys. Rev. C **48**, 792 (1993).
3. R. V. Reid, Ann. Phys. (N.Y) **50**, 411 (1968).
4. M. Lacombe *et al.*, Phys. Rev. C **21**, 861 (1980).
5. V. G. J. Stoks and J. J. de Swart, Phys. Rev. C **52**, 1698 (1995); nucl-th/9411002.
6. R. B. Wiringa, R. A. Smith, and T. L. Ainsworth, Phys. Rev. C **29**, 1207 (1984).
7. R. A. Arndt, I. I. Strakovsky, and R. L. Workman, Phys. Rev. C **50**, 2731 (1994).
8. R. A. Arndt, Chang-Heon Oh, I. I. Strakovsky, *et al.*, Phys. Rev. C **56**, 3005 (1997).
9. J. J. de Swart, C. P. F. Terheggen, and V. G. J. Stoks, in *Proceedings of Third International Symposium "Deuteron 95," Dubna, 1995*; nucl-th/9509032.
10. T. E. O. Ericson and M. Rosa-Clot, Nucl. Phys. A **416**, 281 (1984); **405**, 497 (1983); Annu. Rev. Nucl. Part. Sci. **35**, 271 (1985).
11. J. Rahm *et al.*, Phys. Rev. C **57**, 1077 (1998).
12. R. A. Arndt, I. I. Strakovsky, R. L. Workman, and M. M. Pavan, Phys. Rev. C **52**, 2120 (1995); nucl-th/9505040; http://www.phys.vt.edu/~igor/appl.html
13. R. A. Arndt, I. I. Strakovsky, and R. L. Workman, Phys. Rev. C **52**, 2246 (1995).
14. J. L. Friar, G. L. Payne, V. G. J. Stoks, and J. J. de Swart, Phys. Lett. B **311**, 4 (1993).
15. V. G. J. Stoks, B. A. M. Klomp, C. P. E. Terheggen, *et al.*, http://nn-online.sci.kun.nl/NN/inde.html
16. V. I. Kukulin *et al.*, Nucl. Phys. A **417**, 128 (1984); **453**, 365 (1986); **517**, 221 (1990); S. B. Dubovichenko and A. V. Dzhazairov-Kakhramanov, Yad. Fiz. **57**, 784 (1994) [Phys. At. Nucl. **57**, 733 (1994)].
17. D. Benaksas, D. Drickey, and D. Frerejacque, Phys. Rev. **148**, 1327 (1966); C. D. Buchanan and M. R. Yearian, Phys. Rev. Lett. **15**, 303 (1965); J. E. Ellias *et al.*, Phys. Rev. **177**, 2075 (1969); R. G. Arnold *et al.*, Phys. Rev. Lett. **35**, 776 (1975); S. Galster *et al.*, Nucl. Phys. B **32**, 221 (1971).
18. A. M. Baldin, in *Electromagnetic Interactions and Structure of Elementary Particles* (Mir, Moscow, 1969), p. 5.
19. V. I. Kukulin, V. M. Krasnopolsky, V. N. Pomerantsev, and P. B. Sazonov, Phys. Lett. B **165**, 7 (1985); N. J. McGurk and H. Fideldey, Nucl. Phys. A **281**, 310 (1977).
20. M. Garson *et al.*, Phys. Rev. C **49**, 2516 (1994).
21. D. R. Phillips, S. J. Wallace, and N. K. Devine, Phys. Rev. C **58**, 2261 (1998); nucl-th/9802067.

Translated by R. Rogalyov

Physics of Atomic Nuclei, Vol. 63, No. 5, 2000, pp. 739–751. Translated from Yadernaya Fizika, Vol. 63, No. 5, 2000, pp. 809–820.

NUCLEI
Theory

Electron Charge Form Factors and Static Properties of Extremely Light 1*p*-Shell Nuclei within the Anisotropic-Oscillator Model Involving Projections

A. L. Savchenko, V. K. Tartakovsky, and A. V. Fursaev

Taras Shevchenko Kiev University, ul. Glushkova 6, Kiev, 252127 Ukraine

Received February 11, 1998; in final form, May 7, 1999

Abstract—The mirror odd nuclei ^{7}Li and ^{7}Be and the neutron-rich nucleus ^{6}He are considered within a microscopic approach relying on the variational principle. The binding energies of the nuclei, their root-mean-square radii, and the electron charge $C0$ and $C2$ form factors are calculated. The resulting form factors are compared with the predictions of the independent-particle model that assumes intermediate coupling. The sensitivity of the nuclear properties obtained here to the choice of nucleon–nucleon potential, to deviations of the nuclear deformation from that which follows from a variation of the total-energy functionals, and to taking projections onto states characterized by definite values of the total angular momentum and its projection is analyzed. A comparison with experimental data is performed. *© 2000 MAIK "Nauka/Interperiodica".*

1. INTRODUCTION

The use of the variational principle in studying the structure of nuclei [1] makes it possible to describe their properties in a wide range of mass numbers. This approach provides effective tools for inquiries [2, 3] into heavy and superheavy helium isotopes and other nuclei, primarily even–even ones. Neutron-poor and neutron-rich exotic nuclei, as well as unusual phenomena that can occur in the neighborhood of nuclear drip lines [4], are of interest in connection with constructing facilities for the production of beams of radioactive nuclei [5, 6] and with investigating the anomalous structure of unstable nuclei. Obviously, this requires evolving new theoretical frameworks and refining traditional models [1, 7]. From a comparison of theoretical results with experimental data, it is possible to deduce an answer to the question of whether a microscopic variational approach employing deformed single-particle orbitals and projections onto states characterized by specific values of the angular momentum and its projections can form a basis for a self-consistent calculation of static and dynamical nuclear properties in general and for a calculation of the properties of odd and exotic nuclei in particular.

2. BASIC EQUATIONS AND CONVENTIONS

The wave function of the ground state of a nucleus,

$$\Psi_{(\mathrm{in})K} = \frac{1}{\sqrt{A!}}\det\|\varphi_\nu(j)\|, \quad j, \nu = 1, \ldots, A, \qquad (1)$$

is constructed from the single-particle deformed oscillator orbitals [8, 9]

$$\varphi_\nu(j) = \chi_{s_\nu^z t_\nu^z}(j)\prod_{k=1}^{3} H_{n_\nu^k}\left(\frac{x_j^k}{a_\nu^k}\right)\frac{\exp\left(-\dfrac{(x_j^k)^2}{2(a_\nu^k)^2}\right)}{\sqrt{\pi^{1/2}(a_\nu^k \times 2^{n_\nu^k})n_\nu^k!}} \qquad (2)$$
$$\equiv \Phi_\nu(j)\chi_\nu(j),$$

where $\{a_\nu^1, a_\nu^2, a_\nu^3\} \equiv \{a_\nu, b_\nu, c_\nu\}$ are variational parameters, $\{x_j^1, x_j^2, x_j^3\} \equiv \{x_j, y_j, z_j\}$ are the coordinates of the jth particle, $\{n_\nu^1, n_\nu^2, n_\nu^3\} \equiv \{n_\nu^x, n_\nu^y, n_\nu^z\}$, $\chi_\nu(j) \equiv \chi_{s_\nu^z t_\nu^z}(j)$, and the subscript s_ν^z (t_ν^z) denotes the spin (isospin) projection for the jth nucleon. The function in (1) is determined by minimizing the total energy of the nucleus as represented by the functional [10]

$$E = \frac{\int D_{KK}^{J^*}(\Omega)\langle\Psi_{(\mathrm{in})K}|\hat{H}|\hat{R}(\Omega)\Psi_{(\mathrm{in})K}\rangle d\Omega}{\int D_{KK}^{J^*}(\Omega)\langle\Psi_{(\mathrm{in})K}|\hat{R}(\Omega)\Psi_{(\mathrm{in})K}\rangle d\Omega}, \qquad (3)$$

where $\hat{H} = \hat{T} + \hat{U} + \hat{U}_{\mathrm{Coul}}$ is the Hamiltonian of an A-nucleon nucleus in the notation adopted in [1] (we note that this Hamiltonian satisfies the condition $[\hat{H}, \hat{R}(\Omega)] = 0$), while $\mathbf{J} = \mathbf{L} + \mathbf{S}$ is the total angular momentum, $\mathbf{L}$ and $\mathbf{S}$ being, respectively, the orbital angular momentum and the spin moment.

For the odd mirror nuclei ^{7}Li and ^{7}Be ($\nu = 1, \ldots, 7$) and the even–odd neutron-rich nucleus ^{6}He ($\nu = 1, \ldots, 6$), we took the configurations presented in Table 1 and subjected them to the subsidiary condition $a_\nu = b_\nu$ for

1063-7788/00/6305-0739$20.00 © 2000 MAIK "Nauka/Interperiodica"

Table 1. Configurations for the ^{7}Li and ^{7}Be nuclei

ν	n_ν^x	n_ν^y	n_ν^z	s_ν^z	t_ν^z
1	0	0	0	+1/2	+1/2 (–1/2)
2	0	0	0	–1/2	+1/2 (–1/2)
3	0	0	0	+1/2	–1/2 (+1/2)
4	0	0	0	–1/2	–1/2 (+1/2)
5	0	0	1	+1/2	–1/2 (+1/2)
6	0	0	1	–1/2	–1/2 (+1/2)
7	0	0	1	+1/2	+1/2 (–1/2)

the orbital given by (2). The wave function (1) appears to be an eigenfunction of the operator $\hat{J}_{Z'}$ of the total-angular-momentum projection onto the Z' axis of the intrinsic reference frame, the corresponding eigenvalue being $K = 1/2$ for the ^{7}Li and ^{7}Be nuclei and $K = 0$ for the ^{6}He nucleus. In order to simplify the calculations, we retain the conventional constraints $\Phi_1 = \Phi_2$, $\Phi_3 = \Phi_4$, and $\Phi_5 = \Phi_6$ (see [1–3]), which are usually used for even–even nuclei. Since the orbitals presented in Table 1 are orthogonal to one another, we can recast the expression on the right-hand side of (3) into the form

$$E = \sum_{\nu > \nu' = 1}^{A} (E_{\nu\nu'}^{(NN)} + E_{\nu\nu'}^{(\mathrm{Coul})} + E_{\nu\nu'}^{(\mathrm{kin.ex})}) + \sum_{\nu = 1}^{A} E_\nu^{(\mathrm{kin})}, \quad (4)$$

where

$$E_{\nu\nu'}^{(NN)} = \frac{1}{N_J}\int D_{KK}^{J^*}(\Omega) h_{\nu\nu'}^{(NN)}(\Omega) d\Omega$$

with $N_J = \int D_{KK}^{J^*}(\Omega) \prod_{\nu = 1}^{A} \langle \nu|\tilde{\nu}\rangle d\Omega$ and $h_{\nu\nu'}^{(NN)}(\Omega) = \frac{1}{N_J}\xi_{\nu\nu'}(\langle \nu;\, \nu'|w_{\nu\nu'}^{(+)}|\tilde{\nu};\, \tilde{\nu}'\rangle - \langle \nu;\, \nu'|w_{\nu\nu'}^{(-)}|\tilde{\nu}';\, \tilde{\nu}\rangle)$, the as-yet-undefined quantities on the right-hand side of the last equality being given by $w_{\nu\nu'}^{(\pm)} \equiv (V_{33} \times 2^{s_- + t_-} \pm V_{31} t_+ \times 2^{s_-} \pm V_{13} s_+ \times 2^{t_-} + V_{11} s_+ t_+)/4$. The components of the effective central exchange nucleon–nucleon potential $\hat{U}$ are parametrized as [1]

$$\hat{U} = \sum_{i > j = 1}^{A} \sum_{n = 1}^{n_{\max}} \sum_{S,\, T = 0}^{1} V_{2S+1,\, 2T+1}^{(n)} \times \exp\left(-\frac{(\mathbf{r}_i - \mathbf{r}_j)^2}{(nr_0)^2}\right) \hat{P}_S \hat{P}_T. \quad (5)$$

The remaining quantities are parametrized in a similar way; that is,

$$h_{\nu\nu'}^{(\mathrm{Coul})}(\Omega) = t_- \xi_{\nu\nu'}(\langle \nu;\, \nu'|e^2/r|\tilde{\nu};\, \tilde{\nu}'\rangle - s_- \langle \nu;\, \nu'|e^2/r|\tilde{\nu}';\tilde{\nu}\rangle)\delta_{2t_\nu^z,\, 1},$$

$$h_{\nu\nu'}^{(\mathrm{kin.ex})}(\Omega) = -s_- t_- \xi_{\nu\nu'} \langle \nu|\nabla|\tilde{\nu}'\rangle \langle \nu'|\nabla|\tilde{\nu}\rangle/mA,$$

$$h_\nu^{(\mathrm{kin})}(\Omega) = (1 - A)\langle \nu|\nabla^2|\tilde{\nu}'\rangle \xi_\nu/2mA,$$

where m is the nucleon mass, $|\tilde{\nu}\rangle = \hat{R}(\Omega)|\nu\rangle \equiv \hat{R}(\Omega)|\Phi_\nu\rangle$, $s_\pm \equiv \delta_{s_{\nu'}^z \pm s_\nu^z,\, 0}$, $t_\pm \equiv \delta_{t_{\nu'}^z \pm t_\nu^z,\, 0}$, $\xi_{\nu\nu'} = \prod_{\nu'' = 1}^{A} \langle \nu''|\tilde{\nu}''\rangle$ ($\nu'' \neq \nu$, $\nu'' \neq \nu'$), and $\xi_\nu = \prod_{\nu' = 1}^{A} \langle \nu'|\tilde{\nu}'\rangle$ ($\nu' \neq \nu$).

For the nuclear states (1) minimizing the functional in (3), we find the static properties and the electron charge form factors $F_{C\Lambda}^2(q^2)$ for the nuclei being studied [11, 12]. Here, Λ is the rank of the tensor operator under consideration (multipole order), while q is the momentum transfer.

We have also calculated the form factors $F_{C\Lambda}^2(q^2)$ on the basis of the independent-particle model that assumes intermediate coupling. Within this model, the result obtained by antisymmetrizing the normalized wave function for the nuclear configuration $(n_1 l_1^{k_1})(n_2 l_2^{k_2})$ in all $A = k_1 + k_2$ nucleons can be represented as [13]

$$|J\rangle = \left\{\frac{k_1! k_2!}{A!}\right\}^{1/2} \sum_{\eta_2} C_{EJ_2T_2}^{k_2}(\eta_2) \times \hat{A}[|l_1^{k_1}\xi_1 J_1\rangle |l_2^{k_2}\xi_2 J_2\rangle]_{M_J M_T}^{JT} = \left\{\frac{k_1! k_2!}{A!}\right\}^{1/2} [J_1][J_2] \times \sum_{\eta_2 LS} C_{EJ_2T_2}^{k_2}(\eta_2)[L][S] \begin{Bmatrix} L_1 & S_1 & J_1 \\ L_2 & S_2 & J_2 \\ L & S & J \end{Bmatrix} \times \sum_{M_L M_S} \langle L M_L S M_S | J M_J\rangle \hat{A}[|l_1^{k_1}\xi_1\rangle |l_2^{k_2}\xi_2\rangle]_{M_L M_S M_T}^{LST}, \quad (6)$$

where $E = -E_b$, $\eta_j = \{[f_j], \alpha_j, L_j, S_j\}$, $\xi_j = \{\eta_j, T_j\}$ are the quantum numbers of the pure $l_j^{k_j}$ configuration, $\mathbf{J}_i = \mathbf{L}_i + \mathbf{S}_i$, and $[j] \equiv (2j + 1)^{1/2}$. The quantities $C_{EJ_2T_2}^{k_2}(\eta_2)$ are coefficients of the basis states $|l_2^{k_2}\xi_2 J_2\rangle$ in the superposition that represents the wave function of the $1p$ shell within the intermediate-coupling scheme [14].

In calculating the reduced matrix elements of the irreducible tensor operator $F(\kappa_1\kappa_2\kappa_3,\ q_1q_2q_3) = \sum_{i=1}^{A} f_i(\kappa_1\kappa_2\kappa_3,\ q_1q_2q_3)$, where κ_1, κ_2, and κ_3 are the ranks in, respectively, orbital, spin, and isospin spaces, between the states specified in (6), we obtained, instead of expressions (I.22) from [15] for F_1 and F_2, the more compact expressions

$$F_1 = k_1\delta_{\xi_2}^{\xi_2'}(-1)^{L+S+T+L_2+S_2+T_2+l_1+1}[L][S][T][L'] \times [S'][T'][L_1][S_1][T_1][L_1'][S_1'][T_1'] \times \left\langle l_1\frac{1}{2}\frac{1}{2}\| f(\kappa_1\kappa_2\kappa_3)\| l_1\frac{1}{2}\frac{1}{2}\right\rangle \times \begin{Bmatrix} L_1' & L_1 & \kappa_1 \\ L & L' & L_2 \end{Bmatrix}\begin{Bmatrix} S_1' & S_1 & \kappa_2 \\ S & S' & S_2 \end{Bmatrix}\begin{Bmatrix} T_1' & T_1 & \kappa_3 \\ T & T' & T_2 \end{Bmatrix} \times \sum_{\xi_1''}\langle l_1^{k_1}\xi_1|\}l_1^{k_1-1}\xi_1''\rangle\langle l_1^{k_1}\xi_1'|\}l_1^{k_1-1}\xi_1''\rangle(-1)^{L_1''+S_1''+T_1''} \times \begin{Bmatrix} L_1' & L_1 & \kappa_1 \\ l_1 & l_1 & L_1'' \end{Bmatrix}\begin{Bmatrix} S_1' & S_1 & \kappa_2 \\ \frac{1}{2} & \frac{1}{2} & S_1'' \end{Bmatrix}\begin{Bmatrix} T_1' & T_1 & \kappa_3 \\ \frac{1}{2} & \frac{1}{2} & T_1'' \end{Bmatrix}, \quad (7)$$

$$F_2 = k_2\delta_{\xi_1}^{\xi_1'} \times (-1)^{L_1+S_1+T_1+L_2+S_2+T_2+L_2'+S_2'+T_2'+L'+S'+T'+l_2+1} \times [L][S][T][L'][S'][T'][L_2][S_2][T_2][L_2'][S_2'][T_2'] \times \left\langle l_2\frac{1}{2}\frac{1}{2}\| f(\kappa_1\kappa_2\kappa_3)\| l_2\frac{1}{2}\frac{1}{2}\right\rangle \times \begin{Bmatrix} L_2' & L_2 & \kappa_1 \\ L & L' & L_1 \end{Bmatrix}\begin{Bmatrix} S_2' & S_2 & \kappa_2 \\ S & S' & S_1 \end{Bmatrix}\begin{Bmatrix} T_2' & T_2 & \kappa_3 \\ T & T' & T_1 \end{Bmatrix} \times \sum_{\xi_2''}\langle l_2^{k_2}\xi_2|\}l_2^{k_2-1}\xi_2''\rangle\langle l_2^{k_2}\xi_2'|\}l_2^{k_2-1}\xi_2''\rangle(-1)^{L_2''+S_2''+T_2''} \times \begin{Bmatrix} L_2' & L_2 & \kappa_1 \\ l_2 & l_2 & L_2'' \end{Bmatrix}\begin{Bmatrix} S_2' & S_2 & \kappa_2 \\ \frac{1}{2} & \frac{1}{2} & S_2'' \end{Bmatrix}\begin{Bmatrix} T_2' & T_2 & \kappa_3 \\ \frac{1}{2} & \frac{1}{2} & T_2'' \end{Bmatrix}, \quad (8)$$

where $\delta_{\xi_i}^{\xi_i'} = \delta_{[f_i'][f_i]}\delta_{\alpha_i'\alpha_i}\delta_{L_i'L_i}\delta_{S_i'S_i}\delta_{T_i'T_i}$. Expressions (7) and (8) were then used to calculate the electron charge form factors $F_{C\Lambda}^2(q^2)$ within the independent-particle model.

3. RESULTS OF THE CALCULATIONS

We have performed numerical calculations with fifteen nucleon–nucleon potentials $\hat{U}$ of the form (5). Of these, the first 11 were described in detail in [16], their numbering here being coincident with that from [16]. The nucleon–nucleon potentials nos. 12–15 were proposed in [17] and were used (see [2]) in calculations for a large number of even–even isotopes from He to Ca inclusive. In [1], the structure of the bound states of He and Be isotopes was considered by assuming the nucleon–nucleon potential no. 15. For the parameters of the nucleon–nucleon potentials nos. 12–15, the values extracted from data reported in [17] are displayed in Table 2. Table 3 presents the values obtained here for the parameters a_ν, b_ν, and c_ν by minimizing the functional in (3). Also shown in this table are the binding energies E_b calculated for the ^{7}Li and ^{7}Be nuclei with the nucleon–nucleon potential no. 15 either without going over to relevant projections (first row for each ν) or by taking such projections (second row for each ν). These results are listed for three options of single-particle orbitals (oscillator basis):

$$\begin{aligned} &\text{(A)} \quad a_\nu^o = b_\nu^o \neq c_\nu^o \quad \text{for each } \nu, \\ &\text{(B)} \quad a_\nu^{oeq} = b_\nu^{oeq} = c_\nu^{oeq} \quad \text{for each } \nu, \\ &\text{(C)} \quad a_\nu = b_\nu = c_\nu = a \quad \text{for all } \nu. \end{aligned} \quad (9)$$

The corresponding values for the ^{7}Be nucleus are given parenthetically in Table 3.

For the ^{7}Li and ^{7}Be nuclei, Table 4 quotes the binding energies $E_b \equiv -\langle\hat{H}\rangle$, the root-mean-square charge radii $R_Z \equiv \langle R_Z^2\rangle^{1/2}$, the neutron radii $R_N \equiv \langle R_N^2\rangle^{1/2}$, and the mass radii $R \equiv \langle R^2\rangle^{1/2}$ calculated with the nucleon–nucleon potentials nos. 1–15. For each nucleon–nucleon potential, the results obtained by calculating E_b, R_Z, R_N, and R without taking relevant projections are displayed in the second and the first row for the cases where the calculations employ, respectively, the basis (A) and the basis (B) from (9). For the same bases, the corresponding results produced by the procedure employing the above projections are given in the fourth [for (A)] and the third [for (B)] row. The analogous results for the ^{7}Be nucleus are given parenthetically. We used data from [18] as experimental values of E_b and data from [19] as experimental values of R_Z, R_N, and R.

The $E_{\nu\nu'}^{(NN)}$, $E_{\nu\nu'}^{(\mathrm{Coul})}$, $E_{\nu\nu'}^{(\mathrm{kin.ex})}$, and $E_\nu^{(\mathrm{kin})}$ values calculated with the nucleon–nucleon potential no. 15 by going over to relevant projections are presented in Table 5 for the case of $a_\nu = b_\nu \neq c_\nu$ {basis (A) from (9)}. For $\nu = 1$, we then have $E_1^{(\mathrm{kin})} = E_2^{(\mathrm{kin})}$. Taking into account symmetry under the interchange of the subscripts ν and ν' and using data from Table 5, we can

Table 2. Parameters of potentials nos. 12–15 used in the present calculations (the strengths $V^{(n)}_{2S+1,2T+1}$ and the radii r_0 are given in MeV and fm, respectively; the data in the table were calculated on the basis of the results reported in [17])

n	no. 12	no. 13	no. 14	no. 15
		$V^{(n)}_{33} = V^{(n)}_{11}$		
1	293.13	684.46	–229.11	390.744
2	–13.14	7.31	253.38	–169.171
3		–18.96	–75.83	332.699
4			–0.25	–270.834
5				82.331
		$V^{(n)}_{31} = V^{(n)}_{13}$		
1	37.32	414.77	1345.28	894.605
2	–44.68	–243.31	–612.36	22.138
3		60.81	149.01	–553.072
4			–0.42	475.756
5				–145.740
r_0	1.0	0.9	0.775	0.7
n_{max}	2	3	4	5

Table 3. Results obtained by minimizing the functional of the total energy E of the ^{7}Li nucleus with potential no. 15 in an anisotropic basis with $a_\nu = b_\nu \neq c_\nu$, in an isotropic basis with $a_\nu = b_\nu = c_\nu$, and in an isotropic basis where $a_\nu = b_\nu = c_\nu = a$ for all orbitals

ν	(A) $a^o_\nu = b^o_\nu \neq c^o_\nu$		(B) $a^{oeq}_\nu = b^{oeq}_\nu = c^{oeq}_\nu$	(C) $a_\nu = b_\nu = c_\nu = a$
	$a^o_\nu = b^o_\nu$	c^o_ν	a^{oeq}_ν	a
1(2)	1.384 (1.381)	1.898 (1.890)	1.508 (1.504)	1.639 (1.642)
	1.342 (1.339)	2.121 (2.113)	1.506 (1.502)	1.664 (1.667)
3(4)	1.395 (1.400)	1.887 (1.895)	1.515 (1.519)	1.639 (1.642)
	1.350 (1.354)	2.107 (2.119)	1.512 (1.516)	1.664 (1.667)
5(6)	1.573 (1.582)	1.933 (1.946)	1.836 (1.854)	1.639 (1.642)
	1.497 (1.504)	2.052 (2.065)	1.865 (1.881)	1.664 (1.667)
7	1.579 (1.575)	1.942 (1.935)	1.849 (1.842)	1.639 (1.642)
	1.501 (1.497)	2.061 (2.054)	1.877 (1.869)	1.664 (1.667)
E_b, MeV	33.31(31.94)		27.24 (25.92)	24.01 (22.57)
	37.73(36.14)		29.56 (28.23)	25.41 (23.97)

Note: For each ν value, the results obtained by going over to relevant projections are given in the second row, while the results computed without doing this are presented in the first row. The corresponding results for the ^{7}Be nucleus are given parenthetically. The values of the variational parameters a_ν, b_ν, and c_ν are quoted in fm.

obtain the energies of nucleon separation from the state with number ν (the results are listed in Table 6),

$$E^{(sep)}_\nu = -\sum_{\substack{\nu'=1\\ \nu'\neq\nu}}^{A}(E^{(NN)}_{\nu\nu'} + E^{(Coul)}_{\nu\nu'} + E^{(kin.ex)}_{\nu\nu'}) - E^{(kin)}_\nu. \quad (10)$$

Also given in Table 6 are the experimental values of $E^{(sep)}_\nu$ for the ^{7}Li nucleus [20] and the values of $E^{(sep)}_\nu$ that were calculated with the nucleon–nucleon potentials nos. 1 and 7.

We have also calculated the effect of the Coulomb repulsion of protons on the energies $E_{NN} \equiv \langle \hat{U} \rangle$, $T \equiv \langle \hat{T} \rangle$, and $E \equiv \langle \hat{H} \rangle = -E_b$ (see Table 7). This effect manifests itself as changes in the a_ν, b_ν, and c_ν values as obtained from a variational procedure versus the pres-

Table 4. Binding energies (E_b) and charge, neutron, and mass root-mean-square radii ($R_Z \equiv \langle R_Z^2 \rangle^{1/2}$, $R_N \equiv \langle R_N^2 \rangle^{1/2}$, and $R \equiv \langle R^2 \rangle^{1/2}$, respectively) computed for the ^{7}Li nucleus with the nucleon–nucleon potentials nos. 1–15

no.	E_b, MeV	R_Z, fm	R_N, fm	R, fm
1	–	–	–	–
	19.97 (18.41)	1.99 (2.14)	2.12 (2.00)	2.06 (2.08)
	–	–	–	–
	28.75 (27.10)	2.00 (2.14)	2.12 (2.00)	2.07 (2.08)
2	–	–	–	–
	15.26 (13.71)	2.01 (2.16)	2.13 (2.01)	2.08 (2.10)
	–	–	–	–
	23.95 (22.31)	2.00 (2.14)	2.12 (2.00)	2.07 (2.08)
3	28.25 (26.82)	2.03 (2.18)	2.16 (2.02)	2.10 (2.11)
	32.24 (30.81)	2.11 (2.26)	2.23 (2.10)	2.18 (2.19)
	29.67 (28.23)	2.05 (2.20)	2.17 (2.04)	2.12 (2.13)
	36.56 (35.14)	2.18 (2.33)	2.30 (2.16)	2.25 (2.26)
4	26.79 (25.44)	2.12 (2.28)	2.26 (2.12)	2.20 (2.21)
	31.32 (29.94)	2.18 (2.33)	2.31 (2.17)	2.26 (2.26)
	28.28 (26.91)	2.13 (2.29)	2.27 (2.12)	2.21 (2.22)
	35.85 (34.48)	2.25 (2.40)	2.37 (2.23)	2.32 (2.33)
5	27.10 (25.70)	2.06 (2.21)	2.19 (2.05)	2.14 (2.14)
	31.32 (29.91)	2.14 (2.29)	2.26 (2.12)	2.21 (2.22)
	28.55 (27.13)	2.07 (2.23)	2.20 (2.07)	2.15 (2.16)
	35.75 (34.35)	2.20 (2.36)	2.33 (2.19)	2.28 (2.29)
6	26.43 (25.12)	2.19 (2.35)	2.33 (2.18)	2.27 (2.28)
	31.21 (29.87)	2.25 (2.40)	2.38 (2.23)	2.32 (2.33)
	27.95 (26.63)	2.19 (2.35)	2.34 (2.18)	2.28 (2.28)
	35.66 (34.32)	2.31 (2.47)	2.44 (2.30)	2.39 (2.40)
7	35.76 (34.62)	2.49 (2.66)	2.63 (2.47)	2.57 (2.58)
	40.61 (39.45)	2.59 (2.75)	2.72 (2.56)	2.66 (2.67)
	36.90 (35.76)	2.50 (2.68)	2.65 (2.48)	2.59 (2.60)
	44.36 (43.21)	2.64 (2.82)	2.79 (2.63)	2.73 (2.74)
8	44.96 (43.76)	2.38 (2.53)	2.50 (2.35)	2.45 (2.46)
	49.13 (47.93)	2.48 (2.64)	2.61 (2.46)	2.56 (2.57)
	45.91 (44.71)	2.40 (2.56)	2.53 (2.38)	2.48 (2.48)
	52.49 (51.31)	2.56 (2.73)	2.69 (2.53)	2.64 (2.65)
9	45.00 (43.77)	2.33 (2.49)	2.46 (2.31)	2.40 (2.41)
	49.57 (48.34)	2.44 (2.60)	2.56 (2.41)	2.51 (2.52)
	46.05 (44.81)	2.35 (2.51)	2.48 (2.33)	2.43 (2.43)
	53.31 (52.09)	2.51 (2.68)	2.64 (2.48)	2.59 (2.60)
10	37.59 (36.35)	2.32 (2.49)	2.46 (2.32)	2.40 (2.42)
	43.74 (42.48)	2.43 (2.59)	2.57 (2.42)	2.51 (2.52)
	38.91 (37.66)	2.33 (2.50)	2.47 (2.33)	2.41 (2.43)
	48.72 (47.45)	2.48 (2.64)	2.62 (2.47)	2.56 (2.57)
11	–	–	–	–
	1.62 (0.42)	2.41 (2.61)	2.55 (2.40)	2.49 (2.52)
	–	–	–	–
	5.73 (4.51)	2.47 (2.66)	2.61 (2.46)	2.55 (2.58)
12	25.97 (24.77)	2.36 (2.54)	2.53 (2.36)	2.46 (2.47)
	30.88 (29.63)	2.40 (2.57)	2.55 (2.40)	2.49 (2.50)
	27.34 (26.12)	2.36 (2.53)	2.52 (2.36)	2.45 (2.46)
	35.38 (34.10)	2.45 (2.61)	2.60 (2.44)	2.54 (2.54)

Table 4. (Contd.)

no.	E_b, MeV	R_Z, fm	R_N, fm	R, fm
13	26.07 (24.78)	2.21 (2.38)	2.37 (2.21)	2.30 (2.31)
	32.56 (31.22)	2.26 (2.42)	2.41 (2.26)	2.35 (2.35)
	27.98 (26.69)	2.23 (2.40)	2.39 (2.23)	2.32 (2.33)
	37.27 (35.93)	2.31 (2.47)	2.46 (2.31)	2.40 (2.40)
14	26.74 (25.41)	2.14 (2.31)	2.30 (2.14)	2.23 (2.24)
	33.90 (32.54)	2.20 (2.36)	2.35 (2.20)	2.29 (2.29)
	29.07 (27.73)	2.16 (2.33)	2.32 (2.16)	2.25 (2.26)
	38.65 (37.28)	2.25 (2.41)	2.41 (2.25)	2.34 (2.34)
15	27.24 (25.92)	2.16 (2.33)	2.32 (2.15)	2.25 (2.25)
	33.31 (31.94)	2.20 (2.36)	2.35 (2.20)	2.29 (2.29)
	29.56 (28.23)	2.17 (2.35)	2.34 (2.17)	2.27 (2.27)
	37.73 (36.14)	2.25 (2.41)	2.41 (2.25)	2.34 (2.34)
Experimental data	39.2459 ± 0.0009	2.39 ± 0.03		2.405 ± 0.020
	(37.6016 ± 0.0009)	2.35 ± 0.10	2.38 (2.25)	2.33 (2.31)
		2.27 (2.36)		

Note: For each nucleon–nucleon potential, the results presented in the first and second (third and fourth) rows were obtained from the calculations performed in, respectively, an isotropic ($a_\nu = b_\nu = c_\nu$) and an anisotropic ($a_\nu = b_\nu \neq c_\nu$) basis without going to over to relevant projections (by using these projections). The corresponding results for the ^{7}Be nucleus are given parenthetically. The experimental data were borrowed from [18, 19].

Table 5. Energies (in MeV) $E^{(NN)}_{\nu\nu'}$ (first row) for each ν', $E^{(\mathrm{Coul})}_{\nu\nu'}$ (second row), $E^{(\mathrm{kin.\,ex})}_{\nu\nu'}$ (third row), and $E^{(\mathrm{kin})}_{\nu}$ as calculated for the ^{7}Li nucleus with potential no. 15 by going over to relevant projections

ν / ν'	2	3	4	5	6	7
1	–10.34 (–10.39)	–10.34 (–10.32)	–10.34 (–10.32)	–5.27 (–5.21)	–5.27 (–5.21)	–0.61 (–0.60)
	0.73 (0.00)					0.43 (0.00)
						0.55 (0.56)
2		–10.34 (–10.32)	–10.34 (–10.32)	–5.27 (–5.21)	–5.27 (–5.21)	–5.23 (–5.26)
						0.57 (0.00)
3			–10.33 (–10.26)	–0.60 (–0.62)	–5.24 (–5.20)	–5.21 (–5.25)
			0.00 (0.73)	0.00 (0.43)	0.00 (0.57)	
				0.57 (0.56)		
4				–5.24 (–5.20)	–0.60 (–0.62)	–5.21 (–5.25)
				0.00 (0.57)	0.00 (0.43)	
					0.57 (0.56)	
5					–5.75 (–5.74)	–5.75 (–5.75)
					0.00 (0.56)	
6						–5.75 (–5.75)
$E^{(\mathrm{kin})}_{\nu}$	11.49 (11.55)	11.42 (11.34)	11.42 (11.34)	13.81 (13.66)	13.81 (13.66)	13.71 (13.80)

Note: For $\nu = 1$, we have $E^{(\mathrm{kin})}_1 = E^{(\mathrm{kin})}_2$; the quantities $E^{(NN)}_{\nu\nu'}$, $E^{(\mathrm{Coul})}_{\nu\nu'}$, and $E^{(\mathrm{kin.\,ex})}_{\nu\nu'}$ are symmetric under the interchange of the subscripts ν and ν' ($\nu \neq \nu'$). The corresponding values for the ^{7}Be nucleus are given parenthetically.

Table 6. Nucleon separation energies $E_\nu^{(\mathrm{sep})}$ (in MeV)

ν	1	2	3 (4)	5 (6)	7
no. 1	32.66 (33.67)	39.11 (40.34)	32.47 (30.54)	14.12 (12.23)	15.96 (16.86)
no. 7	26.66 (27.40)	32.48 (33.37)	27.20 (25.72)	14.13 (12.81)	13.26 (14.02)
no. 15	28.97 (29.94)	34.00 (35.16)	30.07 (28.34)	13.50 (11.95)	12.50 (13.50)
Experimental data ^{7}Li	$nl_j = 1s_{1/2}$, protons				$1p_{3/2}$, protons
from [20]	23.5 ± 0.7				10.0 ± 1.4
	24.1 ± 1.5				10.1 ± 1.4
	25.8 ± 0.6				11.3 ± 0.5
	23.0 ± 1.5				10.2 ± 1.6
	25.5 ± 0.4				11.8 ± 0.3
	26.0 ± 0.2				10.1 ± 0.1

Table 7. Effect of taking into account Coulomb interaction in the Hamiltonian of the nucleus

Energies, MeV	^{7}Li	^{7}Be	Without Coulomb repulsion	Energies, MeV	^{7}Li	^{7}Be	Without Coulomb repulsion
E_{NN}	–128.30	–128.01	–128.62	T	88.84	88.58	89.16
E_{Coul}	1.73	3.29	0.00	$E = -E_b$	–37.73	–36.14	–39.46

ence or the absence of the term $\hat{U}_{\mathrm{Coul}}$ in the Hamiltonian $\hat{H}$. The values of the energies $E_{\mathrm{Coul}} = \langle \hat{U}_{\mathrm{Coul}} \rangle$ for the ^{7}Li and ^{7}Be nuclei are also included in Table 7.

The energies E, E_{NN}, E_{Coul}, and T calculated here by using the nucleon–nucleon potential no. 15 and by taking relevant projections are displayed in Fig. 1*a* versus the parameter ξ characterizing the deviation of the nuclear deformation from the equilibrium deformation corresponding to the minimal energy as determined in varying the functional in (3). The parameter ξ is introduced through the relations

$$\begin{aligned} a_\nu(\xi) &= b_\nu(\xi) = a + \xi(a_\nu^o - a), \\ c_\nu(\xi) &= a + \xi(c_\nu^o - a), \quad \nu = 1, \ldots, 7, \end{aligned} \tag{11}$$

with the values of a, a_ν^o, and c_ν^o being taken from Table 3 [in Table 3, the values of $\xi = 1$ and $\xi = 0$ correspond, respectively, to the version (A) and to the version (B) in (9)]. Curves *1*, *2*, *3*, and *4* represent, respectively, the dependences $\Delta W_1 \equiv E(\xi) - E$, $\Delta W_2 \equiv E_{NN}(\xi) - E_{NN}$, $\Delta W_3 \equiv T(\xi) - T$, and $\Delta W_4 \equiv [E_{\mathrm{Coul}}(\xi) - E_{\mathrm{Coul}}] \times 10^2$ for the ^{7}Li nucleus; for these dependences, we have used the values $E \equiv E(\xi = 1)$, $E_{NN} \equiv E_{NN}(\xi = 1)$, $T \equiv T(\xi = 1)$, and $E_{\mathrm{Coul}} \equiv E_{\mathrm{Coul}}(\xi = 1)$ from Table 7. Figure 1*b* shows the dependences $\Delta W_k^{(\mathrm{Be})}(\xi) - \Delta W_k^{(\mathrm{Li})}(\xi)$, $k = 1$, 2, 3, and $[E_{\mathrm{Coul}}^{(\mathrm{Be})}(\xi) - E_{\mathrm{Coul}}^{(\mathrm{Be})}] - [E_{\mathrm{Coul}}^{(\mathrm{Li})}(\xi) - E_{\mathrm{Coul}}^{(\mathrm{Li})}]$, the last dependence corresponding to curve *4*. Figures 1*c* and 1*d* display the same dependences, but for a different parametrization of the deformation, namely,

$$\begin{aligned} a_\nu(\eta) &= b_\nu(\eta) = a_\nu^{oeq} + \eta(a_\nu^o - a_\nu^{oeq}), \\ c_\nu(\eta) &= a_\nu^{oeq} + \eta(c_\nu^o - a_\nu^{oeq}), \quad \nu = 1, \ldots, 7. \end{aligned} \tag{12}$$

The root-mean-square radius R calculated here for the ^{7}Li nucleus by using the nucleon–nucleon potential no. 15 and by taking relevant projections (left scale) is shown in Fig. 2 versus the deformation parameters ξ from (11) (curve *1*) and η from (12) (curve *2*). Curve *3* represents the dependence $\delta(\xi) \equiv [R_{\mathrm{Be}}(\xi) - R_{\mathrm{Li}}(\xi)] \times 10^3$; the curve corresponding to the dependence $\delta(\eta)$ virtually coincides with curve *3*. Also illustrated in Fig. 2 (right scale) is the sensitivity of the energy $E = -E_b$ for the ^{7}Li nucleus to deviations of the parameters a_ν, b_ν, and c_ν for individual groups of orbitals (one of the first three pairs or the last orbital in Table 1) from their values resulting from applying the variational procedure. The deformation parameter ζ corresponding to curve *4* is determined by the relations

$$\begin{aligned} a_\nu(\zeta) &= b_\nu(\zeta) = \begin{cases} a + \zeta(a_\nu^o - a) \\ a_\nu^o, \end{cases} \\ c_\nu(\zeta) &= \begin{cases} a + \zeta(c_\nu^o - a), & \nu = 1, 2 \\ c_\nu^o, & \text{remaining values of } \nu. \end{cases} \end{aligned} \tag{13}$$

Curves *5* and *6* correspond to the replacement of the subscript pair (1, 2) by, respectively, (3, 4) and (5, 6) in relations (13), while curve *7* is associated with the subscript value of $\nu = 7$ in (13). The parameters ξ, η, and ζ vary within identical limits. In Fig. 2, they are plotted along the same axis (abscissa). Similar results were obtained for the ^{7}Be nucleus.

The states of $1p$ nucleons within the independent-particle model are very similar [14] to the $[3]^{22}P_{3/2}$ states in the ^{7}Li and ^{7}Be nucleus and to the $[2]^{31}S_0$ states in the ^{6}He nucleus. The coefficients $C_{EJ_2T_2}^{k_2}$ (here,

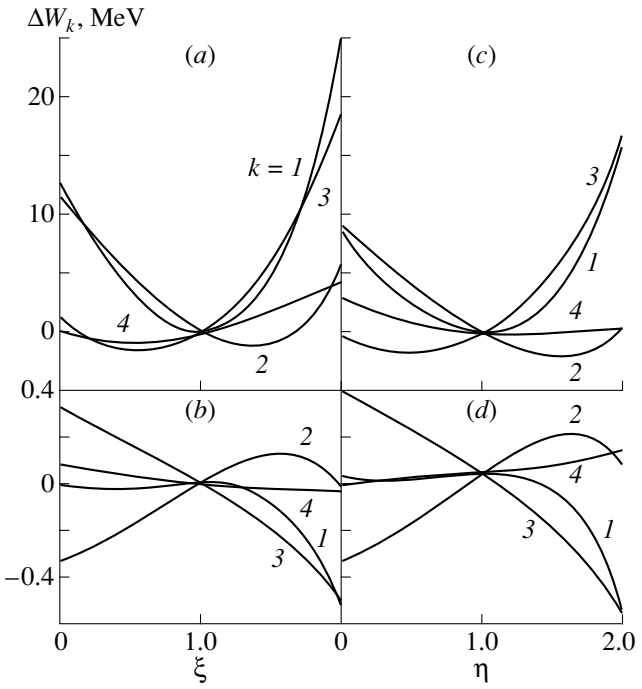

Fig. 1. Energies E, E_{NN}, E_{Coul}, and T for the ^{7}Li and ^{7}Be nuclei as functions of the parameter (a, b) ξ or (c, d) η [see equations (11) or (12) in the main body of the text] specifying deviations of the nuclear deformation from the equilibrium deformation found in varying the total-energy functional (3).

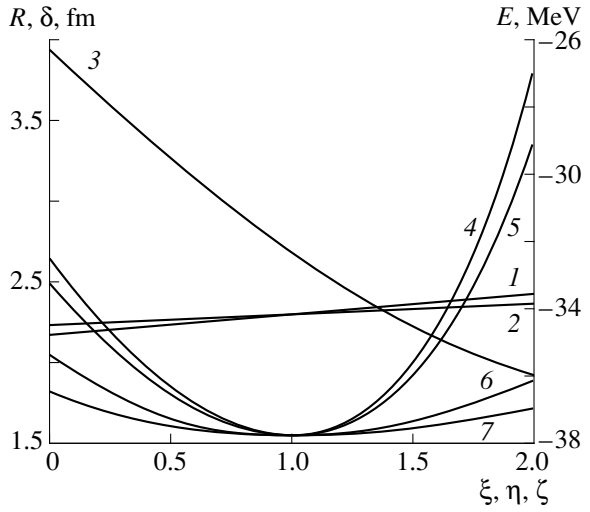

Fig. 2. Dependences of (left scale; curves *1*, *2*, *3*) the radii $R \equiv \langle R^2 \rangle^{1/2}$ of the ^{7}Li and ^{7}Be nuclei on the parameters ξ and η [see equations (11) or (12) in the main body of the text] and (right scale; curves *4–7*) the energy $E = -E_b$ of the ^{7}Li nucleus on the parameter ζ [see equation (13) in the main body of the text] specifying deviations of the deformation of individual groups of orbitals from the equilibrium deformation found in varying the total-energy functional (3). The results for the ^{7}Be nucleus are similar. In calculating curves *4*, *5*, *6*, and *7*, the deformation was changed only for the orbitals 1 and 2, 3 and 4, 5 and 6, and 7 from Table 1, respectively. The parameters ξ, η, and ζ were changed in the same range and are plotted along the same axis (abscissa).

$E = -E_b$), which are associated with these states and which appear in (6), are very close to unity. In Figs. 3*a* and 3*b*, curves *1*, *2*, and *3* represent the form factors $F^2_{C0}(q^2)$ and $F^2_{C2}(q^2)$ calculated for the ^{7}Li nucleus with the nucleon–nucleon potential no. 15. Curves *1* and *2*, computed with deformed orbitals ($a^o_\nu = b^o_\nu \neq c^o_\nu$), differ in that the former (latter) was obtained by taking relevant projections (without doing this). Curve *3* corresponds to the calculations with isotropic orbitals ($a^{oeq}_\nu = b^{oeq}_\nu = c^{oeq}_\nu$), in which case the results obtained by going over to the above projections virtually coincide with those for which projections were not used. The calculation of $F^2_{C2}(q^2)$ with isotropic orbitals was performed without employing projected states. In Figs. 3*a* and 3*b*, the results of the calculations for the ^{7}Li nucleus that were based on the independent-particle model are depicted by curve *4* for the oscillator-parameter value of $a_o = 2$ fm from [12] and by curve *5* for the oscillator-parameter value of $a_o = 1.755$ fm obtained in [21]. (Experimental data were borrowed from [21].) Curve *6* (obtained from a variational calculation employing deformed orbitals and projected states) in Fig. 3*a* represents the total ($C0 + C2$) electron charge form factor for the ^{7}Li nucleus as a function of q^2.

In Fig. 3*a*, curves *7* and *8* show the form factor $F^2_{C0}(q^2)$ calculated for the ^{6}He nucleus with, respectively, the deformed ($a^o_\nu = b^o_\nu \neq c^o_\nu$) and the isotropic ($a^{oeq}_\nu = b^{oeq}_\nu = c^{oeq}_\nu$) orbitals by using a variational procedure with the nucleon–nucleon potential no. 15. In either case, the results corresponding to the projected and unprojected states agree. Curve *9* represents the form factor $F^2_{C0}(q^2)$ calculated for the ^{6}He nucleus on the basis of the independent-particle model with the oscillator-parameter value of $a_o = 1.6$ fm.

The corresponding calculation for the ^{7}Be nucleus leads to analogous results. We do not display here the entire body of these results, showing only the q^2 dependences of the ratios F^2_{C0} (^{7}Be)/F^2_{C0} (^{7}Li) in Fig. 4, where the notation for the curves corresponds to that in Fig. 3.

4. DISCUSSION AND CONCLUSIONS

Investigation of nuclear structures within microscopic approaches is based on choosing an effective nuclear nucleon–nucleon potential that must lead to correct values for the simplest nuclear features like binding energies and nuclear dimensions. A variational calculation of these nuclear features is quite straightforward for the case where the trial wave function for the

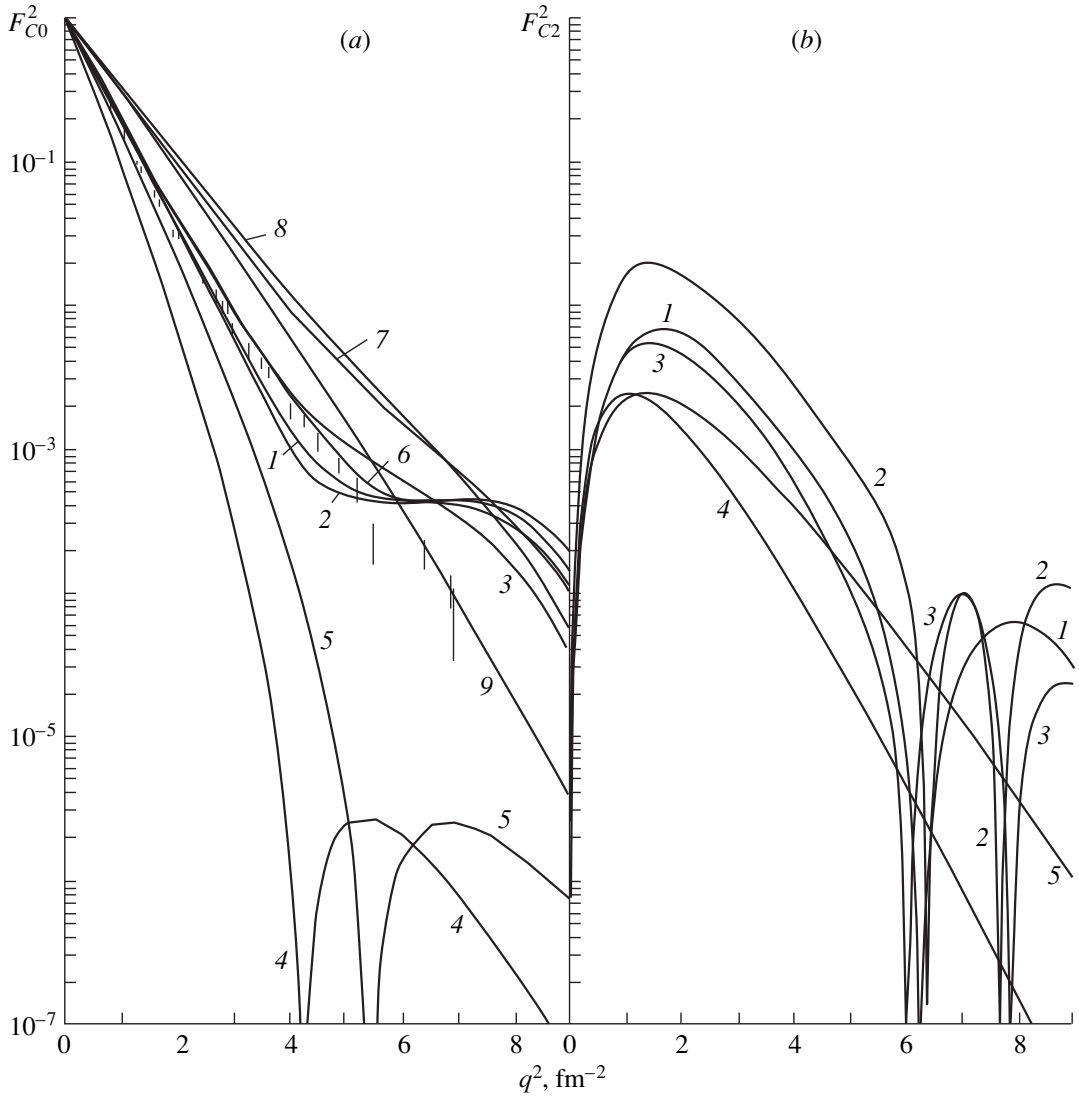

Fig. 3. Form factors (*a*) F^2_{C0} for the ^{7}Li and ^{6}He nuclei and (*b*) F^2_{C2} for the ^{7}Li nucleus. In Figs. 3*a* and 3*b*, curves *1* (*2*) represent the result of the calculation for $a^o_\nu = b^o_\nu \neq c^o_\nu$ within the variational procedure that involves (does not involve) going over to relevant projections; curve *3* corresponds to the calculations for $a^{oeq}_\nu = b^{oeq}_\nu = c^{oeq}_\nu$ (here, the results obtained by going over to relevant projections are virtually coincident with those computed without doing this); and curves *4* and *5* show the results obtained on the basis of the independent-particle model with a_o = 2 and 1.755 fm, respectively. Curve *6* in Fig. 3*a* was plotted for the sum of the form factors in question ($C0 + C2$ curve) and is contrasted against experimental data from [21] for the ^{7}Li nucleus. On the same panel (3*a*), curves *7*, *8*, and *9* represent our results for the ^{6}He nucleus, corresponding to, respectively, the calculation with $a^o_\nu = b^o_\nu \neq c^o_\nu$, the calculation with $a^{oeq}_\nu = b^{oeq}_\nu = c^{oeq}_\nu$ (in the cases illustrated by curves *7* and *8*, the results are virtually independent of whether the procedure used involves taking relevant projections or not), and the calculation based on the independent-particle model with a_o = 1.6 fm.

ground nuclear state is constructed in terms of single-particle orbitals. Within this framework, the energy of a specific nucleus is varied with respect to the parameters of the potential of a preset form. This implementation of the variational principle replaces the Hartree–Fock method, which could probably ensure a higher precision, but which involves considerable computational difficulties. It should be borne in mind that the ^{6}He, ^{7}Li, and ^{7}Be nuclei belong to the beginning of the filling of the 1*p* shell; therefore, these nuclei are inevitably deformed. In order to avoid possible problems associated with degeneracy, it is therefore natural to choose, for single-particle

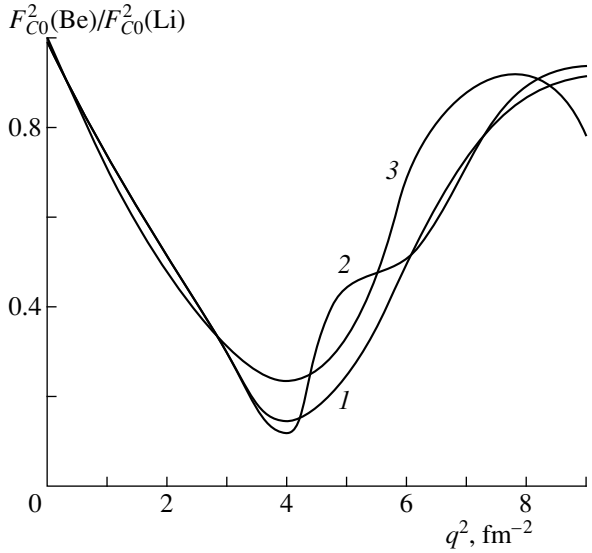

Fig. 4. Ratio of the squared form factors F^2_{C0} for the ^{7}Be and ^{7}Li nuclei. The notation for curves *1*, *2*, and *3* is identical to that in Fig. 3.

orbitals, one-nucleon wave functions in the field of an anisotropic oscillator (not a spherically symmetric one) generally featuring three different frequencies.

In view of the attractive character of nuclear forces, the configuration that corresponds to the ground nuclear state must obey the rule (see [22]) of maximally compact filling (allowed by the Pauli exclusion principle) with the orbitals (2) of the Slater determinant in expression (1). The quantum numbers of inner ($\nu = 1$–4) orbitals correspond to an alpha-particle cluster. In our case of the one-quantum orbitals (2) of valence nucleons, the maximal overlap of single-particle wave functions (that is, minimal energy) is achieved when the only quantum corresponding to the orbitals in (2) is associated, for all three (or two in the case of the ^{6}He nucleus) orbitals in (2), with the same coordinate axis chosen here for the *z* axis. The orientation of the unpaired-nucleon spin (for ^{7}Li and ^{7}Be nuclei) does not affect the energy of the nucleus. For the configuration constructed in this way (see Table 1), the *x* and *y* axes are equivalent, which implies the axial symmetry of the nucleus.

A great number of studies devoted to the problem being discussed were performed by different authors in different periods of time. In [16], this range of investigations was characterized by a list including 11 well-known potentials, but by no means is this list exhaustive. As the problems that the researchers of these realms addressed became more intricate, it was necessary to invoke more complicated effective nucleon–nucleon potentials. The calculations performed in [17] resulted (see Table 2) in multicomponent nucleon–nucleon potentials (nos. 12–15) that describe a wide range of nuclear properties. Of these, the nucleon–nucleon potential no. 15, which is used predominantly in the present calculations, is the best one. It was shown in [17] that, within the *SU*(3) microscopic model, this multicomponent [$n_{\max} = 5$] potential makes it possible to reproduce the binding energies and the root-mean-square radii of the ^{4}He, ^{16}O, and ^{40}Ca nuclei; in addition, it meets the saturation condition and respects many important features of nuclear matter, such as the energy per nucleon $E(k_F)/A$, the compressibility modulus $(k_F^2/A)d^2E/dk_F^2$, and the condition of minimum of the function $E(k)/A$ at $k = k_F$ (k_F is the Fermi momentum). This nucleon–nucleon potential is characterized by a moderate repulsion at small distances (soft core) and by a comparatively slow decrease at large distances.

For the oscillator lengths and the root-mean-square radii, a variational calculation of ^{6}He static properties that was performed by using the nucleon–nucleon potential no. 15 and by taking relevant projections yielded the values of (in fm) $a_1^o = b_1^o = 1.331$, $c_1^o = 1.972$, $a_2^o = b_2^o = 1.345$, $c_2^o = 1.985$, $a_3^o = b_3^o = 1.599$, $c_3^o = 1.992$, $R_Z = 1.746$, $R_N = 2.340$, and $R = 2.160$. The corresponding binding energy was found to be $E_b = 29.682$ MeV (the experimental value from [19] is $E_b^{(\text{expt})} = 29.267$ MeV). Here, the success achieved in calculating the binding energy was due, in our opinion, to two factors: first, the nucleon–nucleon potential no. 15 was fitted to the properties of precisely even–even nuclei; second, clustering in the ^{6}He nucleus is characterized by the dominance of the $\alpha + (nn)$ and $\alpha + n + n$ structures, which have close binding energies. This suggests that clustering has only a slight effect (the binding energy of the dineutron cluster is very small) on the binding energy of the ^{6}He nucleus; assuming the $\alpha + n + n$ structure, we can then use efficiently the $\nu = 1$–6 orbitals from Table 1. If we similarly assume $\alpha + {}^3$H clustering for the ^{7}Li nucleus and $\alpha + {}^3$He clustering for the ^{7}Be nucleus, the binding energies of the nuclei will depend greatly on the type of clustering. Owing to the sizable binding energies of the ^{3}H and ^{3}He clusters, the above structures are nonequivalent in binding energy to structures of the $\alpha + p + n + n$ and $\alpha + p + p + n$ types. Thus, the assumption that the three valence nucleons are not clustered in the field of the alpha-particle cluster leads to an underestimated binding energy of the ^{7}Li and ^{7}Be nuclei.

In order to study the possibility of self-consistently describing various static and dynamical nuclear features, we have used the nucleon–nucleon potentials that were presented in [16, 17] and which differ by the number of components and by their strengths. Mirror nuclei provide a convenient testing ground for theoretical models. These nuclei may play the role of a core in studying [23, 24] nuclides characterized by anomalous

values of the ratio N/Z. Beams of ^{7}Li and ^{7}Be nuclei can be used in experiments devoted to nucleus–nucleus scattering [25–28]. All this motivated our interest in the possibility of describing the ^{7}Li and ^{7}Be nuclei in the variational-approach version discussed here. Our calculations have revealed that the results depend sizably on the presence of short-range repulsion and of long-range attraction at larger distances in various components of the nucleon–nucleon potentials used. By way of example, we indicate that, for the nucleon–nucleon potentials nos. 1, 2, and 11, the ^{7}Li and ^{7}Be nuclear systems treated with the aid of the isotropic basis feature no bound states both in the case where a transition to relevant projections is performed and in the case where this is not done (Table 4). For the case of an anisotropic basis, the calculation that relies on the nucleon–nucleon potential no. 7 and which does not use projected states leads to reasonable, albeit somewhat overestimated, binding energies and to excessively large values for the radii R_Z, R_N, and R. As to the nucleon–nucleon potential no. 10, the calculation in the isotropic basis with this potential yields reasonable values for E_b and R_Z, but overestimated values for R_N and R, irrespective of whether we go over to projections onto relevant states or not. Similar listing could be continued, but we can already state that, whilst some nucleon–nucleon potentials from Table 4 are capable of reproducing individual nuclear parameters, the nucleon–nucleon potential no. 15 makes it possible to describe fairly well the entire body static nuclear features.

In calculating the data in Table 6, which is based on Table 5 and which makes it possible to compare various contributions to the separation energy $E_\nu^{(\mathrm{sep})}$, we have also used the nucleon–nucleon potential no. 15 within the procedure employing projections onto relevant states. We note that, because of constraints (see Table 2) on the components $V^{(n)}_{2S+1,\,2T+1}$ from (5) and on the orbitals Φ_ν, some of the results in Table 5 coincide. In addition to the experimental values from [20], Table 6 also presents the results obtained by calculating $E_\nu^{(\mathrm{sep})}$ for the nucleon–nucleon potentials nos. 1 and 7. This makes it possible to assess the sensitivity of the method to the choice of form for the potential $\hat{U}$. That we compare precisely these potentials is motivated by the circumstance that they lead to the minimal (no. 1) and the maximal (no. 7) nuclear sizes. Although the calculation with the nucleon–nucleon potential no. 15 leads to a somewhat overestimated value of $E^{(\mathrm{sep})}$ for proton separation from the core, the result is qualitatively consistent with experimental data.

In Fig. 1, the deviations from the optimal values of the energies E, E_{NN}, E_{Coul}, and T for two (of many possible ones) different parametrizations of the nuclear density are characterized by moderately high stability. This is quite surprising because the dimensionality of the space spanned by the parameters of the problem is rather high. Figure 2 shows deviations of the radii R (left scale) in response to changes in the nuclear deformation. We can see that these deviations are characterized by a similar stability. An analysis of deviations of the ^{7}Li binding energy E_b (right scale) that are caused by the deformation of the individual groups of orbitals shows, as might have been expected in advance, a tendency common to the ^{6}He, ^{7}Li, and ^{7}Be nuclei: the dominant contribution to the change in the binding energy E_b comes from the deformation of the $n_\nu^z = 0$ ($\nu = 1, \ldots, 4$) orbitals from Table 1—that is, from the deformation of inner orbitals corresponding to the alpha-particle cluster.

In contrast to the independent-particle model, which fails to reproduce (see Fig. 3) experimental data from [21] in the region $q^2 \geq 1.5$ fm^{-2}, our variational calculations of the electron charge form factor for the ^{7}Li nucleus lead to satisfactory agreement with experimental data for $q^2 \leq 5$ fm^{-2}. At higher momentum transfers, the calculated form-factor values are still overly great. To improve the agreement with experimental data, we can choose the nucleon–nucleon potential more thoroughly and take into account the properties of odd nuclei in fitting the potential parameters. The effect of the choice of potential on nuclear form factors—sometimes, the effect of this choice is quite sizable—was revealed in our calculations. In principle, we can also abandon the idea of imposing constraints on the single-particle orbitals and on the components of the nucleon–nucleon potential. In all probability, the most effective way to improve the agreement with experimental data is to take into account more consistently the cluster degrees of freedom of nuclei.

Figure 4 shows that, within each version of the calculation from those listed for Fig. 3, the squares of the monopole form factors for the mirror nuclei ^{7}Li and ^{7}Be may have a scatter at $q \sim 2$ fm^{-1} within a factor of five. The maximal distinction between the results of the calculation performed without taking projections to relevant states (curves *2*, *3*) and the results represented by curve *1* is about 20% both for the deformed and for the isotropic basis. Since the contribution of the $C2$ form factor is small, the behavior of the ratio $[F^2_{C0}(\mathrm{Be}) + F^2_{C2}(\mathrm{Be})]/[F^2_{C0}(\mathrm{Li}) + F^2_{C2}(\mathrm{Li})]$ as a function of q^2 is similar to the behavior of curves *1*, *2*, and *3*.

In summary, the basic results of the present study are as follows:

(i) It has been shown that main static and dynamical features of extremely light 1*p*-shell nuclei can be described, at least qualitatively, within a multiparticle variational approach taking into account the Pauli exclusion principle, using independent deformations of single-particle orbitals, and implementing a transition to projections onto states characterized by definite values of the total nuclear angular momentum and its projection (in contrast to what was done in [1], projections

are constructed here without any simplifying assumptions).

(ii) The use of the same multicomponent effective exchange nucleon–nucleon potential no. 15 (which was proposed in [17]) for the ^{7}Li and ^{7}Be nuclei in a variational calculation employing a one-determinant intrinsic wave function has enabled us to attain fairly good agreement with experimental data on the binding energy, the proton separation energy, and the root-mean-square radii for either nuclear species, as well as with the experimental values of the electron charge form factor for the ^{7}Li nucleus. Only some individual properties of the nuclei being considered can be reproduced with the other nucleon–nucleon potentials.

(iii) It has been established that many nuclear features, such as the energies E, E_{NN}, E_{Coul}, and T and the root-mean-square radii R, as determined in the variational calculations, are weakly sensitive to the shift that the point corresponding, in the eight-dimensional space of the variational parameters, to the minimum of the total-energy functional for the nuclei being considered undergoes in response to variations in the form of parametrization of the nuclear deformation.

(iv) The effect that changes in the deformation of individual groups of single-particle oscillator orbitals that was obtained in the variational calculation—these changes correspond to shifts in the relevant planes of the parameter space—may exert on the nuclear binding energies has been investigated, and it has been found that the binding energy of each nuclear species considered here is highly sensitive, as might have been expected, to changes in the deformation of inner orbitals associated with an alpha-particle cluster.

(v) It has been shown that the wave functions of nucleons in the field of an anisotropic harmonic oscillator (rather than of a spherical one) represent an optimal choice of single-particle orbitals for variational calculations of the static and dynamical features of nonmagic nuclei.

(vi) It has been found that the calculated electron charge form factors for the ^{6}He, ^{7}Li, and ^{7}Be nuclei depend sizably on the choice of nucleon–nucleon potential. The results corresponding to the use of the nucleon–nucleon potentials nos. 1 and 7, which lead, respectively, to the minimal and to the maximal root-mean-square radii of the nuclei, show the greatest deviations from the optimal results obtained with the nucleon–nucleon potential no. 15.

(vii) A comparison has been drawn between the results of the variational calculations of the static and dynamical features of the mirror nuclei ^{7}Li and ^{7}Be. It has been found that, in the region around $q \sim 2$ fm^{-1}, the calculated values of the squared form factors for these nuclear species may exhibit more than fivefold distinctions (for example, this is so for the monopole form factor).

(viii) To the best of our knowledge, the above consistent variational calculation of static and dynamical nuclear features has been applied to odd nuclei for the first time ever. That the entire body of the properties of the ^{7}Li and ^{7}Be nuclei has been described qualitatively on a unified basis gives sufficient ground to believe that the method used here can be applied more widely to odd and exotic nuclei.

(ix) By means of intermediate summations over the projections of the angular momenta, we have been able to obtain compact expressions used in calculating the reduced matrix elements of irreducible single-particle tensor operators between the states of the two-shell mixed configuration. These results have a wide range of application and make it possible to simplify considerably computations within the independent-particle model assuming intermediate coupling.

(x) The charge form factors calculated for the ^{6}He, ^{7}Li, and ^{7}Be nuclei by the variational method that employs the nucleon–nucleon potential no. 15 and which involves going over to projection onto relevant states have been compared with the corresponding results obtained on the basis of the independent-particle model assuming intermediate coupling. It has been shown that the results begin to deviate substantially from $q^2 \sim 1.5$–2.0 fm^{-2}; with increasing q, this difference grows, reaching one order of magnitude for the ^{6}He nucleus and two orders of magnitudes for the ^{7}Li and ^{7}Be nuclei at $q^2 \sim 6$–8 fm^{-2}.

(xi) The reasons that the experimental values of the electron charge form factor for the ^{7}Li nucleus cannot be described adequately within our variational method have been discussed. We hope that the agreement with experimental data can be improved considerably through the abandonment of the constraints that are usually imposed on the single-particle orbitals and on the components of the nucleon–nucleon potentials for even–even nuclei and through the inclusion of data on odd nuclei and of cluster degrees of freedom in the variational calculation.

ACKNOWLEDGMENTS

We are indebted to G.F. Filippov and A.I. Steshenko for stimulating discussions and enlightening comments.

REFERENCES

1. A. I. Steshenko, Yad. Fiz. **60**, 599 (1997) [Phys. At. Nucl. **60**, 520 (1997)].
2. A. I. Steshenko, I. V. Simenog, and V. I. Avramenko, Ukr. Fiz. Zh. **40**, 268 (1995).
3. A. I. Steshenko and A. L. Savchenko, Ukr. Fiz. Zh. **42**, 288 (1997).
4. A. I. Baz', V. I. Gol'danskiĭ, V. Z. Goldberg, and Ya. B. Zeldovich, *Light and Medium-Mass Nuclei near the Nucleon Drip Line* (Nauka, Moscow, 1972).
5. *Proceedings of the First International Conference on Radioactive Nuclear Beams, Berkeley*, Ed. by W. D. Meyers, J. M. Nitschke, and E. B. Noeman (Singapore, World Sci., 1990).

6. A. T. Rudchik, Yu. M. Tchuvil'sky, and V. A. Ziman, in *Proceedings of the Second INR International School on Nuclear Physics, Kiev, 1991*, Ed. by A. T. Rudchik (Institute for Nuclear Research, Kiev, 1992), p. 338.
7. M. V. Evlanov, A. M. Sokolov, and V. K. Tartakovskii, Yad. Fiz. **58**, 1010 (1995) [Phys. At. Nucl. **58**, 937 (1995)].
8. L. Pauling and E. B. Wilson, Jr., *Introduction to Quantum Mechanics with Applications to Chemistry* (McGraw-Hill, New York, 1935).
9. V. K. Tartakovskiĭ and A. V. Fursaev, Vestn. Kiev. Univ., Ser. Fiz.-Mat., No. 1, 138 (1993).
10. K. Wildermuth and Y. C. Tang, *A Unified Theory of the Nucleus* (Vieweg, Braunschweig, 1977).
11. V. K. Luk'yanov and Yu. S. Pol', Fiz. Elem. Chastits At. Yadra **5**, 955 (1974) [Sov. J. Part. Nucl. **5**, 385 (1974)].
12. V. K. Tartakovskiĭ and A. V. Fursaev, Yad. Fiz. **15**, 51 (1972) [Sov. J. Nucl. Phys. **15**, 31 (1972)].
13. V. K. Tartakovsky and A. V. Fursaev, Ukr. Fiz. Zh. (Russ. Ed.) **18**, 1331 (1973).
14. A. N. Boyarkina, *Structure of 1p-Shell Nuclei* (Mosk. Gos. Univ., Moscow, 1973).
15. V. G. Neudatchin and Yu. F. Smirnov, *Nucleon Clusters in Light Nuclei* (Nauka, Moscow, 1969).
16. A. I. Steshenko, Yad. Fiz. **23**, 44 (1976) [Sov. J. Nucl. Phys. **23**, 23 (1976)].
17. I. V. Simenog and A. I. Steshenko, Ukr. Fiz. Zh. **38**, 505 (1993).
18. V. A. Kravtsov, *Atomic Masses and Nuclear Binding Energies* (Atomizdat, Moscow, 1974).
19. F. Ajzenberg-Selove, Nucl. Phys. A **413**, 1 (1984).
20. R. C. Barrett and D. F. Jackson, *Nuclear Sizes and Structure* (Clarendon, Oxford, 1977).
21. L. R. Suelzle, M. R. Yearian, and H. Crannell, Phys. Rev. **162**, 992 (1967).
22. G. F. Filippov, Yad. Fiz. **41**, 1141 (1985) [Sov. J. Nucl. Phys. **41**, 729 (1985)].
23. K. Varga, Y. Suzuki, and I. Tanihata, Nucl. Phys. A **588**, 157 (1995).
24. L. Jarczyk, B. Kamys, M. Kistryn, *et al.*, Phys. Rev. C **54**, 1302 (1996).
25. H. T. Fortune and J. R. Powers, Phys. Rev. C **30**, 843 (1984).
26. H. T. Fortune, Phys. Rev. C **30**, 848 (1984).
27. M. F. Vineyard, J. Cook, K. W. Kemper, and M. N. Stephens, Phys. Rev. C **30**, 916 (1984).
28. R. J. Smith, J. J. Kolata, K. Lamkin, *et al.*, Nucl. Instrum. Methods Phys. Res., Sect. A **294**, 26 (1990).

Translated by A. Isaakyan

Physics of Atomic Nuclei, Vol. 63, No. 5, 2000, pp. 752–757. Translated from Yadernaya Fizika, Vol. 63, No. 5, 2000, pp. 821–827.

NUCLEI
Theory

Level-Density Parameters in the Back-Shifted Fermi Gas Model

V. I. Plyaskin and R. A. Kosilov

Institute of Nuclear Power Engineering, Obninsk, Kaluga oblast, 249020 Russia

Received April 26, 1999; in final form, October 13, 1999

Abstract—The parameters a and δ_{eff} appearing in the back-shifted Fermi gas model are determined for about 3000 nuclei on the basis of modern estimated experimental data and the proposed systematics. For 272 of these nuclei, the parameters are deduced from experimental data on the cumulative numbers of low-lying levels and on mean spacings between S-wave neutron resonances at the neutron binding energy in the nuclei. For 952 nuclei, the parameter δ_{eff} is calculated by using the cumulative numbers of low-lying levels and values of the parameter a that were obtained via an interpolation from the points corresponding to the aforementioned 272 nuclei. For the remaining nuclei, the parameters a and δ_{eff} are obtained on the basis of the proposed systematics. An expression is constructed for taking into account the damping of shell effects with increasing excitation energy of nuclei. The results are compared with those from other studies. © *2000 MAIK "Nauka/Interperiodica".*

1. INTRODUCTION

Various modifications of the Fermi gas model are extensively used to calculate nuclear level densities [1–4]. Despite substantial limitations of the model [5], it provides a convenient basis for constructing simple systematics by fitting the energy dependences of nuclear level densities to data on the cumulative numbers of low-lying levels and on mean spacings ($\overline{D}_0$) between S-wave neutron resonances at the neutron binding energies (B_n) in nuclei.

The systematics relying on the studies of Vonach and Huizenga [2] and Dilg *et al.* [4] is used most frequently. It is assumed in this systematics that the two sets of experimental data are described by relations based on the Fermi gas model, but the level-density parameter a and the excitation-energy shift δ_{eff} caused by even–odd distinctions between nuclei are treated there as free parameters. Since δ_{eff} values appear to be negative for odd–odd nuclei, this framework is referred to as the back-shifted Fermi gas model.

All systematics constructed within the back-shifted Fermi gas model (see [4, 6]), which contain information about the parameters a and δ_{eff} for approximately 300 nuclei (there are no data on mean spacings between S-wave neutron resonances for a wider range of nuclei), have the following disadvantages:

(i) There are no straightforward recipes for correctly parametrizing the dependence $\delta_{\text{eff}} = f(A)$, because it is difficult to disentangle shell, collective, and pairing effects within the conceptual framework in question.

(ii) The damping of shell effects at high nuclear excitations is not taken into account in the level-density parameter a.

The investigation reported in the present article resulted in constructing a database including level-density parameters in the back-shifted Fermi gas model for about 3000 nuclei. An expression has been proposed for phenomenologically describing the damping of shell effects in the parameter a with increasing excitation energy. Errors that arise in a and δ_{eff} because of uncertainties in data on the mean spacings between neutron resonances have been determined. The sensitivity of the level-density parameters being discussed to variations in the number of low-lying levels included in the input data set has been analyzed. The parameters a and δ_{eff} have been obtained for two values of the nuclear moment of inertia: $F = F_{\text{rig}}$ and $F = 0.5F_{\text{rig}}$, where F_{rig} is the rigid-body value of the nuclear moment of inertia.

2. DESCRIPTION OF THE PROCEDURE USED TO DETERMINE LEVEL-DENSITY PARAMETERS

The procedure for deducing the parameters a and δ_{eff} from experimental data on the cumulative numbers N_0 of low-lying levels and on the mean spacing $\overline{D}_0$ between S-wave neutron resonances is similar to that proposed in [4].

For the spin-dependent and the total level density, we use the expressions

$$\rho(U, J) = \frac{1}{24\sqrt{2}}\frac{2J+1}{\sigma^3 a^{1/4}} \times \frac{\exp[2\sqrt{a(U-\delta_{\text{eff}})} - J(J+1)/2\sigma^2]}{(U-\delta_{\text{eff}}+t)^{5/4}}, \quad (1)$$

$$\rho(U) = \frac{1}{12\sqrt{2}\sigma a^{1/4}}\frac{1}{(U-\delta_{\text{eff}}+t)^{5/4}}\exp[2\sqrt{a(U-\delta_{\text{eff}})}], \quad (2)$$

1063-7788/00/6305-0752$20.00

where U is the nuclear excitation energy, J is the total angular momentum, a is the level-density parameter related to the density of single-particle states near the Fermi energy, δ_{eff} is an adjustable parameter appearing in the back-shifted Fermi gas model, t is the thermodynamic temperature determined from the equation

$$U - \delta_{\text{eff}} = at^2 - t, \tag{3}$$

and σ is the spin-cutoff parameter in the level density. In our calculations, the quantity σ_{rig} was taken to be

$$\sigma_{\text{rig}}^2 = \frac{F_{\text{rig}}t}{\hbar^2} \approx 0.015A^{5/3}t, \tag{4}$$

where F_{rig} is the rigid-body value of the nuclear moment of inertia.

In order to determine the parameters a and δ_{eff}, we used the equations

$$\frac{1}{\overline{D}_0} = \begin{cases} \frac{1}{2}\left(\rho\left(B_n + \frac{1}{2}\Delta E, I_0 + \frac{1}{2}\right)\right. \\ \left. + \rho\left(B_n + \frac{1}{2}\Delta E, I_0 - \frac{1}{2}\right)\right) \quad \text{for } I_0 \neq 0 \\ \frac{1}{2}\rho\left(B_n + \frac{1}{2}\Delta E, \frac{1}{2}\right) \quad \text{for } I_0 = 0, \end{cases} \tag{5}$$

$$N_0 = \int_0^{U_0} \rho(U)dU, \tag{6}$$

where B_n is the neutron binding energy, ΔE is the energy interval where resonances were studied, I_0 is the target-nucleus spin, and $\overline{D}_0$ is the mean spacing between nuclear levels for S-wave neutrons. The coefficient 1/2 reflects the fact that the S-wave neutrons form resonances with definite parity, while N_0 is the number of low-lying levels in the nucleus being analyzed that occur in the energy range between zero and U_0.

The recommended experimental values of the parameters $\overline{D}_0 \pm \delta\overline{D}_0$, N_0, and U_0 were taken from [7]. The parameters a and δ_{eff} were determined for two values of the nuclear moment of inertia, $F = F_{\text{rig}}$ and $F = 0.5F_{\text{rig}}$. The errors that arise in the parameters a and δ_{eff} because of uncertainties in $\overline{D}_0$ were calculated as follows: for each nucleus, the parameters a and δ_{eff} were determined from equations (5) and (6) for three $\overline{D}_0$ values: $\overline{D}_0$, $\overline{D}_0 + \delta\overline{D}_0$, and $\overline{D}_0 - \delta\overline{D}_0$. The averaged values of the parameter a for $F = F_{\text{rig}}$ are displayed in Fig. 1 below.

Level-density parameters a and δ_{eff} versus N_0 and U_0

N_0	U_0, MeV	a, MeV^{-1}	δ_{eff}, MeV
	^{63}Ni		
61	4.106	8.87	0.92
80(+20%)	4.106	8.52	0.57
41(–20%)	4.106	9.37	1.38
40	3.52	8.43	0.47
28	3.01	8.1	0.09
20	2.519	7.82	–0.26
15	2.15	7.64	–0.5
	^{102}Ru		
53	3.086	13.65	1.0
63(+20%)	3.086	13.51	0.88
43(–20%)	3.086	13.82	1.12
27	2.56	13.31	0.73
15	2.19	13.16	0.6
10	1.84	12.9	0.4
	^{184}W		
48	1.894	19.61	0.37
58(+20%)	1.894	19.43	0.29
38(–20%)	1.894	19.82	0.46
30	1.61	19.27	0.21
20	1.42	19.12	0.14
12	1.25	19.09	0.13

3. EFFECT OF UNCERTAINTIES IN $\overline{D}_0$ AND N_0 ON THE DETERMINATION OF THE LEVEL-DENSITY PARAMETERS

A straightforward analysis of expressions (1) and (2), which yields

$$\left(\frac{\delta a}{a}\right) = \frac{1}{0.7\sqrt{A}}\frac{\delta\rho(U)}{\rho(U)},$$

reveals that the uncertainties in $\overline{D}_0$ values affect only slightly the level-density parameter a. The uncertainties in $\overline{D}_0$ have a minor effect on the absolute values of δ_{eff} as well.

The choice of N_0 and U_0 has a more pronounced effect on the extracted level-density parameters. Data that make it possible to estimate this effect are quoted in the table, which illustrates the dependence of a and δ_{eff} on the errors in the N_0 value and on the choice of U_0 for the ^{63}Ni, ^{102}Ru, and ^{184}W nuclei, which belong to different mass intervals. For each element, the first row corresponds to the N_0 and U_0 values used in the present calculations, while the next two rows contain the results contained for the case of ±20% errors in N_0. The remaining rows correspond to various N_0 and U_0

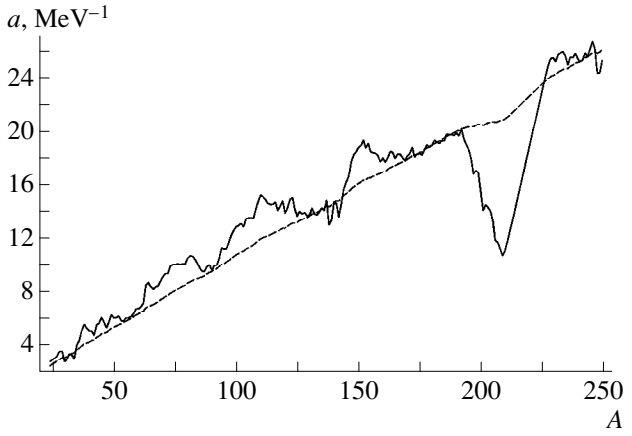

Fig. 1. Level-density parameter a as a function of the mass number: (solid curve) averaged values deduced from data on the cumulative numbers of low-lying levels and the density of S-wave neutron resonances and (dashed curve) values at an excitation energy of 100 MeV. The damping of shell effects was calculated by formula (10).

options based on an analysis of the schemes of levels in the nuclides being considered.

This example demonstrates that distinctions between the level-density parameters obtained by different authors are associated primarily with the choice of the number N_0 of low-lying levels for the nuclide under analysis.

4. EXCITATION-ENERGY DEPENDENCE OF THE LEVEL-DENSITY PARAMETER a

The level density determined for a Fermi gas of independent particles characterized by an equidistant spectrum of single-particle levels cannot naturally describe shell effects. The shell structure of nuclei leads to a nonlinear mass-number dependence of the level-density parameter (recall that the Fermi gas model predicts a linear dependence). Shell effects in the level density are washed out with increasing excitation energy; therefore, the mass-number dependence of the parameter a tends to that obtained in the Fermi gas model as the energy becomes sufficiently high (about 100 MeV). These features of the level-density parameter can be explained in general terms by using the shell-correction method. To do this, experimental information about a well-pronounced correlation between shell corrections and the ratio a/A, where A is the mass number, is used to construct a phenomenological systematics of variations in the level-density parameter obtained in the Fermi gas model [8]. This systematics is based on the relation

$$a(U, Z, A) = \tilde{a}(A)\left\{1 + \delta\varepsilon_0(Z, A)\frac{f(U)}{U}\right\}, \qquad (7)$$

where $\delta\varepsilon_0$ is the shell correction defined as the difference of the experimental value of the mass defect (M_{expt}) and its liquid-drop value (M_{ld}) calculated at the equilibrium deformation β, $\delta\varepsilon_0 = M_{\text{expt}}(Z, A) - M_{\text{ld}}(Z, A, \beta)$; $\tilde{a}$ is the asymptotic value of the level-density parameter at high excitation energies; and $f(U)$ is a dimensionless function that determines the energy dependence of the level-density parameter at low excitation energies. The form of this function,

$$f(U) = 1 - \exp(-\gamma U), \qquad (8)$$

was found by fitting the thermodynamic functions calculated for nuclei with the spectrum of levels in the shell potential [8].

The analysis of experimental data that was performed in [8] yielded the optimum values of $\tilde{a}/A = 0.154$ MeV^{-1} and $\gamma = 0.054$ MeV^{-1} for the parameters in the above forms. In constructing a systematics on the basis of experimental data on the neutron-resonance density in $A \geq 150$ nuclei, Ignatyuk *et al.* [9], who took into account an increase in the nuclear level density owing to collective effects, found that the values of $\tilde{a}/A = 0.0931$ MeV^{-1} and $\gamma = 0.064$ MeV^{-1} provided the best fit to the correlation between the energy dependence of the level-density parameters and the shell correction.

Ramamurthy *et al.* [10] and Schmidt *et al.* [11] showed that, in the parameter γ, it is necessary to introduce a slight mass-number dependence of the form

$$\gamma = \gamma_0 A^{-1/3}, \qquad (9)$$

where the recommended value of γ_0 is about 0.35 MeV^{-1}.

Figure 1 shows the a values obtained in the present study. Shell effects are seen there to be pronounced, but they cannot be taken adequately into account by relation (7). In view of this, we propose here taking into account the damping of shell effects with increasing excitation energy via the formula

$$a(U, Z, A) = \tilde{a}(A)\left\{1 + \frac{a(B_n, Z, A) - \tilde{a}(A)}{\tilde{a}(A)} \times \exp[-\gamma_1(U - B_n)\theta(U - B_n)]\right\}, \qquad (10)$$

where $a(B_n, Z, A)$ is the level-density parameter obtained in a given systematics, B_n is the neutron binding energy, and $\theta(U - B_n)$ is the step function

$$\theta(U - B_n) = \begin{cases} 1 & \text{for} \quad (U - B_n) \geq 0 \\ 0 & \text{for} \quad (U - B_n) < 0. \end{cases}$$

The parameter γ_1 was chosen by requiring optimal agreement between the rates of shell-effect damping according to (7) and (10) and was estimated at $\gamma_1 = 0.12A^{-1/3}$. By fitting data on nuclei far from those with

closed shells, the asymptotic value of the level-density parameter, $\tilde{a}$, was found to be $A/9.5$, which is consistent with the values of $\tilde{a} = (0.105 \pm 0.005)A$ and $\tilde{a} = (0.090 \pm 0.005)A$ calculated in [12] for the spectrum of single-particle states in the Nilsson and the Woods–Saxon potential, respectively.

Figure 1 shows the values of $a(U, Z, A)$ for the excitation energy of $U = 100$ MeV. They agree well with the results calculated in [5] with allowance for the discrete shell structure of single-particle levels.

5. LEVEL-DENSITY PARAMETERS IN THE CASE WHERE THERE IS NO EXPERIMENTAL INFORMATION ABOUT THE NUCLEI BEING CONSIDERED OTHER THAN DATA ON LOW-LYING LEVELS IN THEM

It should be noted that the mass-number dependence of the parameter δ_{eff} is governed by an intricate interplay of shell, collective, and pairing effects. In the model under consideration, the systematics constructed for the parameter δ_{eff} on the basis of data on 272 nuclei for which the parameters a and δ_{eff} were obtained with the aid of relations (5) and (6) does not seem reliable. For this reason, the parameter δ_{eff} was additionally determined here for 952 more nuclei by using the method that was proposed in [13] and which can be applied to the case where there are no data on the neutron-resonance density, but where there is information about low-lying levels (that is, the parameters N_0 and U_0 are known). In this case, covering many nuclei, the parameter δ_{eff} was deduced as follows: (a) The parameter a was determined by means of interpolation (for details, see below) between the values obtained from relations (5) and (6). (b) The parameter δ_{eff} was calculated from relation (6).

Figure 1 displays the averaged dependence $a(B_n, Z, A) = f(A)$ obtained for all mass numbers in the interval $24 \le A \le 250$ by using the a values as determined from experimental data on the cumulative numbers of low-lying levels and densities of S-wave neutron resonances. In the case of nuclei for which the neutron-resonance densities have not yet been determined experimentally, the parameter a was evaluated on the basis of relation (7). In particular, the unknown parameter $a_1(B_{n1}, Z_1, A)$ for the (Z_1, A) nucleus was calculated by the formula

$$a_1(B_{n1}, Z_1, A) = a(B_n, Z, A)\left\{\frac{1 + K_1\delta\varepsilon_{01}(Z_1, A)}{1 + K\delta\varepsilon_0(Z, A)}\right\}, \quad (11)$$

where $a(B_n, Z, A)$ is the level-density parameter taken from the dependence $a(B_n, Z, A) = f(A)$ displayed in Fig. 1; $\delta\varepsilon_{01}(Z_1, A)$ and $\delta\varepsilon_0(Z, A)$ are shell corrections for the (Z_1, A) and the (Z, A) nucleus, respectively; and $K_1 = \{1 - \exp(-\gamma B_{n1})\}/B_{n1}$ and $K = \{1 - \exp(-\gamma B_n)\}/B_n$ are the coefficients reflecting energy dependence of the parameter a for low excitation energies. In the expressions for these coefficients, we have set $\gamma = 0.35A^{-1/3}$ MeV^{-1} and denoted by B_{n1} and B_n the neutron binding energies in the (Z_1, A) and the (Z, A) nucleus, respectively.

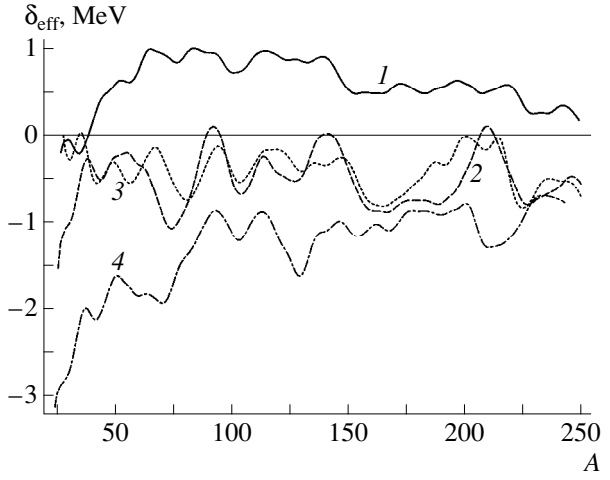

Fig. 2. Averaged mass-number dependences of the parameter δ_{eff} obtained with allowance for the parities of the numbers of intranuclear protons and neutrons. Curves *1*, *2*, *3*, and *4* represent the results obtained for even–even, even–odd, odd–even, and odd–odd nuclei, respectively.

6. LEVEL-DENSITY PARAMETERS IN THE CASE WHERE THERE ARE NO DATA ON THE NUCLEI BEING CONSIDERED

In some problems—for example, in astrophysics—it is necessary to know level-density parameters for a large number of nuclei for which we have at our disposal neither experimental information on low-lying levels nor data on the neutron-resonance density. In order to deduce information about the level-density parameters for such nuclei, we constructed a systematics for averaged parameters δ_{eff} (see Fig. 2).

That we determined the parameter δ_{eff} for more than 1200 nuclei whose low-lying levels are known from experiments made it possible to obtain the dependences $\delta_{\text{eff}} = f(A)$ averaged over a great number of nuclei for even–even, even–odd, odd–even, and odd–odd nuclides separately.

For these nuclei, the level-density parameter was calculated according to following algorithm: (a) The parameter $a_1(B_{n1}, Z_1, A)$ for the (Z_1, A) nucleus was determined on the basis of expression (11) by using a method similar to that described in the preceding section. (b) The parameter δ_{eff} was found from one of the dependences $\delta_{\text{eff}} = f(A)$ for a given value of the mass number A, the parities of the numbers of the intranuclear protons and neutrons being taken into account.

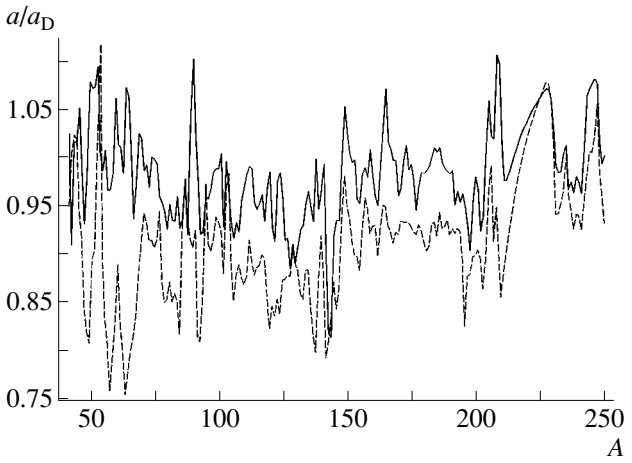

Fig. 3. Ratio $a/a_D = f(A)$ of the level-density parameter a as determined (solid curve) in the present study or (dashed curve) in [6] to that (a_D) taken from [4] as a function of the mass number.

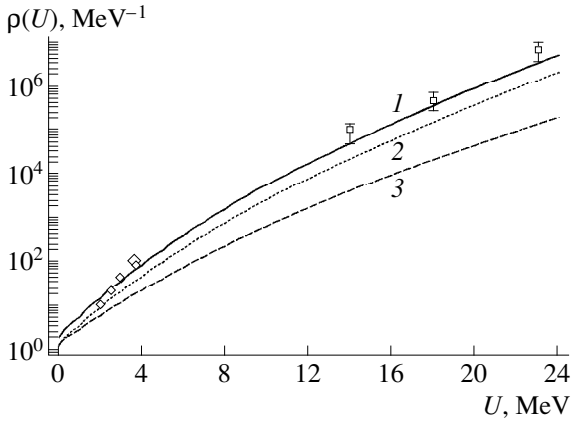

Fig. 4. Calculated and experimental values of the level density in the ^{55}Mn nucleus. Curves *1*, *2*, and *3* represent the results of the calculations with the parameters values from the present study, [4], and [6], respectively. Experimental data were taken from (□) [14] and (◇) [7].

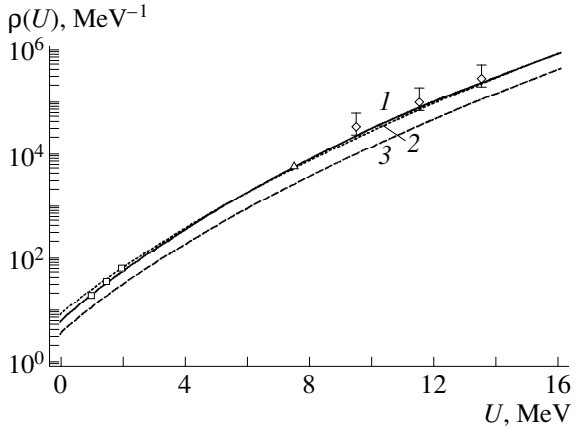

Fig. 5. As in Fig. 4, but for the ^{60}Co nucleus. The notation for the curves is identical to that in Fig. 4. Experimental data were taken from (□, △) [7] and (◇) [15].

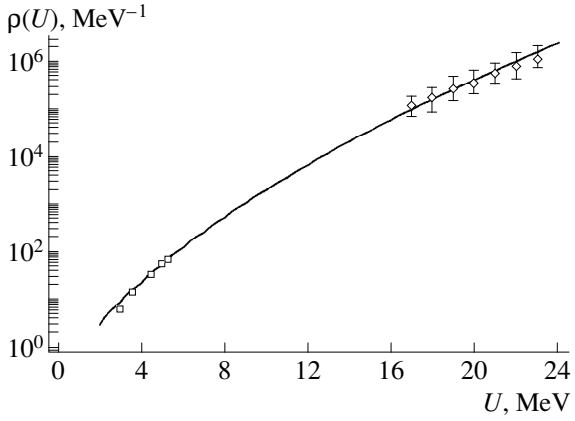

Fig. 6. As in Fig. 4, but for the ^{56}Fe nucleus. Only those calculated values that were obtained with the parameters determined in the present study are displayed in the figure. Experimental data were taken from (□) [7] and (◇) [16].

7. CONSTRUCTING A DATABASE OF THE LEVEL-DENSITY PARAMETERS FOR NUCLEI IN THE MASS-NUMBER RANGE $24 \le A \le 250$ ON THE BASIS OF THE BACK-SHIFTED FERMI GAS MODEL

Relying on the level-density parameters a and δ_{eff} as obtained by the methods described above, we compiled a database for 3000 nuclei. The level-density parameters included in this database can be broken down into three groups.

These are (i) the parameters a and δ_{eff} obtained from experimental data on low-lying levels and neutron-resonances densities (for 272 nuclei); (ii) the parameters a determined on the basis of formula (11) from the averaged dependence $a(B_n, Z, A)$ and the parameters δ_{eff} obtained from experimental data on low-lying levels (for 952 nuclei); and (iii) the parameters a and δ_{eff} determined by formula (11) from the averaged dependences $a(B_n, Z, A) = f(A)$ and $\delta_{\text{eff}} = f(A)$ with allowance for the parity of the numbers of intranuclear protons and neutrons (for all the remaining nuclei).

It should be noted that the accuracy in the first and the second group is obviously higher than the accuracy in the third group. For this reason, it is more reasonable to compile a database of parameters than to use a unified systematics that provides an averaged description even for nuclei whose parameters were obtained from experimental data.

8. COMPARISON WITH THE RESULTS OBTAINED ELSEWHERE

The parameters determined in the present study can be compared with corresponding results from [4, 6].

Figure 3 shows the mass-number dependence of the ratio $a/a_D = f(A)$, where a stands for the averaged values of the parameter a calculated in this study and in [6], while a_D is the analogous parameter from [4].

The scatter of the data determined in the different studies seems to reflect the current level of knowledge in this field. The greatest distinctions (of about 25%) are observed in the region around $A = 60$. For this reason, the level densities $\rho(U)$ for the ^{55}Mn and ^{60}Co nuclei were calculated here for excitation energies higher than the neutron binding energies in the respective nuclides. The results of the calculations are displayed in Figs. 4 and 5. It can be seen that the results obtained with the parameters taken from [6] are smaller than the experimental values and than the level densities calculated with the parameters found in this study and in [4].

The level densities for the ^{55}Mn and ^{56}Fe nuclei (Figs. 4 and 6) were calculated with the averaged parameters a and δ_{eff} determined with the aid of (6) from the cumulative numbers of low-lying levels. In either case, the results of the calculations agree well with experimental data.

9. CONCLUSION

On the basis of the constructed systematics and of currently available experimental data [7] on the cumulative numbers of low-lying levels and mean spacings between S-wave neutron resonances, we have determined the level-density parameters a and δ_{eff} for about 3000 nuclei within the back-shifted Fermi gas model. The parameters for 272 of these nuclei have been obtained from experimental data on the cumulative numbers of low-lying levels and mean spacings between S-wave neutron resonances at the neutron binding energies in relevant nuclei. For 952 nuclei, the parameter δ_{eff} has been deduced from data on the cumulative numbers of low-lying levels by using a values found by means of interpolation of the a values obtained for the 272 nuclei mentioned immediately above. For the remaining nuclei, the parameters a and δ_{eff} have been evaluated on the basis of our systematics. Thus, we have created a database that comprises the level-density parameters for a wide range of nuclei and which can be used in various problems that require describing the formation and decay of compound nuclei.

A formula has been proposed for taking into account the damping of shell effects in the parameter a. Errors arising in a and δ_{eff} because of the uncertainties in data on the mean spacings between neutron resonances have been determined. The sensitivity of the level-density parameters to variations in the number of low-lying levels included in the analysis has been explored.

ACKNOWLEDGMENTS

This work was supported by the Foundation for Basic Research at the Ministry of Higher Education of the Russian Federation (grant no. 97-25-5.3-518) and the Russian Foundation for Basic Research (project no. 00-07-90376).

REFERENCES

1. A. Gilbert and A. G. W. Cameron, Can. J. Phys. **43**, 1446 (1965).
2. H. K. Vonach and J. K. Huizenga, Phys. Rev. **138**, 1372 (1965).
3. A. V. Malyshev, *Level Density and Nuclear Structure* (Atomizdat, Moscow, 1965).
4. W. Dilg, W. Schantl, H. Vonach, and M. Uhl, Nucl. Phys. A **217**, 269 (1973).
5. A. V. Ignatyuk, *Statistical Properties of Excited Nuclei* (Énergoatomizdat, Moscow, 1983).
6. Huang Zhongfu, He Ping, Su Zongdi, and Zhou Chunmey, Chin. J. Nucl. Phys. **13**, 147 (1991).
7. *Handbook for Calculations of Nuclear Reaction Data*, Report IAEA-TECDOC-1034 (International Atomic Energy Agency, Vienna, 1998).
8. A. V. Ignatyuk, G. N. Smirenkin, and A. S. Tishin, Yad. Fiz. **21**, 485 (1975) [Sov. J. Nucl. Phys. **21**, 255 (1975)].
9. A. V. Ignatyuk, K. K. Istekov, and G. N. Smirenkin, Yad. Fiz. **29**, 875 (1979) [Sov. J. Nucl. Phys. **29**, 450 (1979)].
10. V. S. Ramamurthy, S. K. Kataria, and S. S. Kapoor, in *Proceedings of IAEA Advisory Group Meeting on Basic and Applied Problems of Nuclear Level Densities, New York*, Report BNL-NCS-51694 (Brookhaven National Laboratory, Upton, NY, 1983).
11. K. H. Schmidt, H. Delagrange, J. P. Dufour, *et al.*, Z. Phys. A **308**, 215 (1982).
12. A. V. Ignatyuk, V. S. Stavinskiĭ, and Yu. N. Shubin, in *Proceedings of Second International Conference on Nuclear Data for Reactors* (IAEA, 1970), p. 885.
13. V. M. Bychkov, O. T. Grudzevich, and V. I. Plyaskin, Vopr. At. Nauki Tekh., Ser. Yad. Konstanty, No. 3, 14 (1987).
14. A. A. Katsanos, R. W. Show, Jr., R. Vandenbosch, *et al.*, Phys. Rev. C **1**, 594 (1970).
15. D. Kopsch and S. Cierjaks, in *Statistical Properties of Nuclei* (Plenum, New York, 1972), p. 455.
16. J. K. Huizenga *et al.*, Phys. Rev. **182**, 1149 (1969).

Translated by R. Tyapaev

Physics of Atomic Nuclei, Vol. 63, No. 5, 2000, pp. 758–759. From Yadernaya Fizika, Vol. 63, No. 5, 2000, pp. 828–829.

NUCLEI
Theory

Semiempirical Formula for Describing Neutron Shell Effects in the Resonance-Level Density for *s*-Wave Resonances*

M. Kaczmarczyk and M. Przytuła**

Department of Nuclear Physics, Łódź University, Łódź, Poland

Received September 2, 1999

Abstract—A simple formula for the resonance-level density for *s*-wave resonances is found by fitting the assumed function of the number of neutrons to numerous experimental data. To describe shell effects, demonstrated as strong decreases in experimental data at the magic numbers of neutrons, the dependence of the assumed function on the "complexity" of a compound nucleus is introduced. The resulting function describes quite well the character of changes in the resonance-level density with the number of neutrons, including the regions of the magic numbers. © *2000 MAIK "Nauka/Interperiodica".*

1. INTRODUCTION

Available experimental data on resonance-level densities reveal strong shell effects that can be clearly observed in the dependence of the resonance-level density on the number of neutrons, N, especially in regions around the magic numbers of N_m = 82 and 126. The commonly used formula for the resonance-level density (Gilbert and Cameron [1]) cannot describe these effects if the level-density parameter a is assumed to be proportional to the mass number A (according to theoretical prediction based on the Fermi gas model). Rohr [2] considered the relation between the resonance-level density and "the hierarchy of the compound state." The hierarchy can be characterized by the number of particles or holes (or both) that may be excited in a composite nucleus in a resonance reaction. In [3], it was proposed to classify various states of an excited composite nucleus by the number of nucleons raised above the Fermi level. The maximum number k of particles that may be raised at a given excitation energy is referred to as "complexity." According to [2], we can expect that there is a relation between the resonance-level density and k. The structure of the N dependence of k seems to confirm this expectation since shell effects are quite obvious there (Fig. 1).

In this study, we presents a simple semiempirical formula, obtained from the above idea, that can describe shell effects in the resonance-level density.

2. SEMIEMPIRICAL FORMULA

After a preliminary analysis of available data on the resonance-level density for *s*-wave resonances, we decided to perform fitting in terms of the function

$$\rho = 10^b k^c. \quad (1)$$

According to [3], the complexity k is

$$k = E\{1-(g\Delta)/2 + \frac{1}{2}\sqrt{(g\Delta-2)^2+4[z(g\Delta-1)+gU]}\}. \quad (2)$$

Here, $g = (A/13)$ MeV^{-1} is the single-particle level density at the Fermi level; Δ is the shell energy gap given in Table 1; $U = S_n - P(N) - P(Z)$, where S_n is the neutron separation energy for a composite nucleus; and $P(N)$ and $P(Z)$ are the neutron and the proton pairing energy, respectively. If N_t is the number of neutrons in the target nucleus and if N_m is the nearest magic number of neutrons, then we have

$$z = \begin{cases} |N_t - N_m| & \text{for} \quad N_t < N_m \\ |N_t - N_m| + 1 & \text{for} \quad N_t \geq N_m. \end{cases}$$

Experimental data subjected to our analysis were taken from [4]. They are energy-normalized to S_n = 8 MeV and

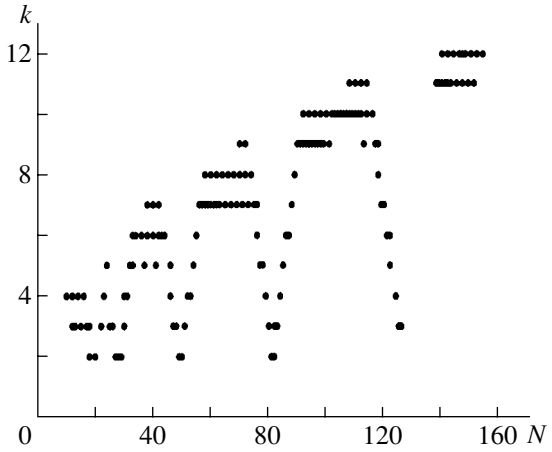

Fig. 1. Complexity k of excited composite nuclei for S_n = 8 MeV as a function of the number N of neutrons.

* This article was submitted by the authors in English.

** e-mail: MaryKacz@Krysia.Uni.Lodz.Pl

1063-7788/00/6305-0758$20.00 © 2000 MAIK "Nauka/Interperiodica"

Table 1. Shell energy gaps

N_m	20	28	50	82	126
Δ, MeV	5.12	4.26	4.18	3.66	3.09

Table 2. Fitted parameters for (1)

α	β	γ	δ	ε
-9.21×10^{-4}	0.127	–1.27	0.391	2.14×10^{-2}

spin-reduced to $J = 1/2$ for even–even target nuclei (to $J = 0$ and 1 for other nuclei). The normalization and spin reduction performed to alleviate fitting was based on the formula [1]

$$\rho(U, J) = \frac{2J+1}{24\sqrt{2}\sigma^3 a^{1/4}U^{5/4}} \times \exp\left[-\left(J+\frac{1}{2}\right)^2/2\sigma^2\right]\exp(2\sqrt{aU}), \quad (3)$$

where

$$\sigma^2 = 0.145A^{2/3}\sqrt{aU}.$$

The pairing energies were taken from [1], while the values of a were calculated on the basis of experimental data.

The analysis that employed data on 284 nuclides showed that the optimal and simple form of neutron-number dependence for both exponents in formula (1) is

$$b = \alpha N^2 + \beta N + \gamma, \quad (4)$$

$$c = \delta\exp(\varepsilon N). \quad (5)$$

The fitting of the function in (1) to the set of normalized and reduced experimental values of the resonance-level density yielded the adjusted-parameter values quoted in Table 2.

Finally, we have

$$b = -0.000921N^2 + 0.127N - 1.27,$$

$$c = 0.391\exp(0.0214N).$$

Then, ρ is expressed in MeV^{-1}.

A comparison of calculated and reduced values of the neutron-resonance-level densities is presented in Fig. 2.

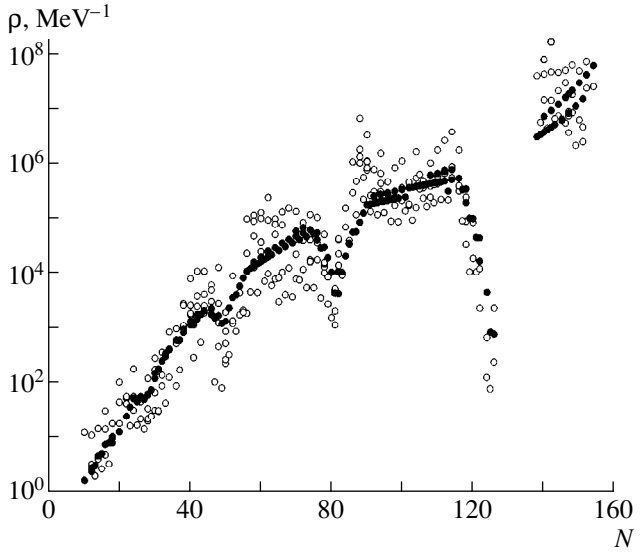

Fig. 2. Calculated (black circles) and reduced experimental values (open circles) of the neutron-resonance-level densities.

3. REMARKS

The semiempirical formula obtained here can reasonably describe the general form of the N dependence of the resonance-level density, including shell effects. The idea to relate the resonance-level density to the highest hierarchy of excited composite nucleus (compound nucleus), given by complexity k, proved to be justified. But we should not expect that this formula can describe detailed values of the resonance-level density for individual nuclides since it was fitted to dispersed experimental values in the form of a smooth function. The purpose of our study was to show how the complexity of a compound nucleus affects the resonance-level density.

ACKNOWLEDGMENTS

We would like to thank Dr. G. Rohr for kindly placing recent data at our disposal. One of us (M. Kaczmarczyk) wishes to thank Dr. L. Łasoń for enlightening discussions on the subject.

REFERENCES

1. A. Gilbert and A. G. W. Cameron, Can. J. Phys. **43**, 1446 (1965).
2. G. Rohr, Z. Phys. A **318**, 299 (1984).
3. M. Kaczmarczyk and M. Przytuła, Z. Phys. A **323**, 465 (1986).
4. S. F. Mughabghab, M. Divadeenam, and N. E. Holden, *Neutron Cross Sections* (BNL, New York, 1981), Vol. 1, Part A; S. F. Mughabghab, *Neutron Cross Sections* (BNL, New York, 1984), Vol. 1, Part B; and data obtained by courtesy of G. Rohr.

Physics of Atomic Nuclei, Vol. 63, No. 5, 2000, pp. 760–766. Translated from Yadernaya Fizika, Vol. 63, No. 5, 2000, pp. 830–836.

NUCLEI
Theory

Λααα Cluster Model for the $^{13}_{\Lambda}$C Nucleus

I. N. Filikhin*

Institute of Physics (Petrodvorets Branch), St. Petersburg State University, Ul'yanovskaya ul. 1, Petrodvorets, 198904 Russia

Received March 10, 1999; in final form, June 22, 1999

Abstract—The $^{13}_{\Lambda}$C hypernucleus is treated as a $(1/2)^+$ bound state of the Λααα system. The *s*-wave model is used on the basis of differential equations for the corresponding Yakubovsky components. No account is taken of 2 + 2 clustering in the system. Phenomenological potentials are used to simulate the αα and αΛ interactions. The system as a whole is bound owing to the additional potential of three-body interaction between the alpha-particle clusters. The differential equations for the Yakubovsky components are solved numerically by the cluster-reduction method. The binding energies are calculated for the ground and the first excited state of the $^{13}_{\Lambda}$C hypernucleus. It is shown that the dominant type of clustering in the system is (Λαα)α. © *2000 MAIK "Nauka/Interperiodica".*

1. INTRODUCTION

A three-body potential of interaction between alpha-particles makes it possible to describe the properties of the light nuclei ^{12}C and ^{16}O within, respectively, the three- and the four-body cluster models [1–3]. These models are based on the concept that there are alpha-cluster correlations in these nuclei, which is confirmed experimentally. The parameters of the three-body potential that binds the system of three alpha particles were evaluated in [3]. This was done by fitting the experimental values of the binding energy and the root-mean-square radius of the ^{12}C nucleus. The analysis in [3] relied on the differential forms of the Faddeev and Yakubovsky equations for, respectively, the 3α and the 4α system [4]. In the case of identical particles, the set of Faddeev–Yakubovsky equations takes the simplest form. The situation is more involved when we are dealing with systems featuring nonidentical particles. Such cases are exemplified by the Λαα and Λααα systems ($^{9}_{\Lambda}$Be and $^{13}_{\Lambda}$C hypernuclei, respectively). In the relevant equations, it is then necessary to take into account various versions of clustering in the subsystems, whereby the number of coupled equations is increased. As a result, the requirements upon computational facilities for numerically solving such equations prove to be more stringent. The cluster-reduction method for the Yakubovsky equations that was proposed in [5] removes some of the difficulties encountered in directly solving these equations. In the present study, the cluster-reduction method is used to analyze the Λααα system. Previously, this method was applied only to systems of identical particles [5, 6]. The Λααα system is also interesting in that it provides the possibility of testing the potential that was proposed in [3] to simulate the three-body interaction of alpha-particle clusters.

Earlier, cluster models of the $^{13}_{\Lambda}$C hypernucleus were considered by Hiyama *et al.* [7] and by Bodmer *et al.* [8]. The former group of authors invoked a microscopic approach that relies on realistic Λ*N* potentials, but which reduces to the Λααα cluster model where Λα interaction is simulated by a nonlocal potential and where, in the 3α subsystem, there is an additional repulsive three-body potential. The latter [8] studied the ^{12}C + Λ cluster system. In order to determine the intercluster interaction, they proposed averaging the Λ*N* and Λ*NN* potentials by using the distribution of nucleon density that was obtained for the ^{12}C nucleus from experimental data.

2. DESCRIPTION OF THE FORMALISM

For the system of four particles, the differential equations for the Yakubovsky components are given by [4]

$$(H_0 + V_{a_3} + V^{\mathrm{Coul}} - E)\Psi_{a_3a_2} + V_{a_3}\sum_{(c_3\neq a_3)\subset a_2}\Psi_{c_3a_2} = -V_{a_3}\sum_{d_2\neq a_2}\sum_{(d_3\neq a_3)\subset a_2}\Psi_{d_3d_2}. \quad (1)$$

In all, there are 18 Yakubovsky components $\Psi_{a_3a_2}$. Each component corresponds to a specific partition of the four-particle system into two or three clusters (a_2, a_3). There are two types of partitions into two clusters (3 + 1 and 2 + 2 ones). For systems involving identical particles, some Yakubovsky components can be expressed in terms of the others by using the operators of particle permutations. In particular, the Λααα sys-

* e-mail: filikhin@cph10.phys.spbu.ru

tem consists of three identical bosons and a fermion. The corresponding set of equations can be reduced to five equations determining the wave-function components U_1, U_2, W_1, Y_1, and Y_2, where the subscripts 1 and 2 label the component types 3 + 1 and 2 + 2, respectively. Specifically, we have

$$\begin{aligned}
&(H_0 + V_{12} + V^{\mathrm{Coul}} + V_3 - E)U_1 + V_{12}(P_4^+ + P_4^-)U_1 \\
&\quad = -V_{12}[(P_{23} + P_{13})W_1 + (P_{23} + P_{13})U_2], \\
&(H_0 + V_{12} + V^{\mathrm{Coul}} + V_3 - E)U_2 + V_{12}Y_2 \\
&\quad = -V_{12}(Y_1 + P_{12}Y_1), \\
&(H_0 + V_{12} + V^{\mathrm{Coul}} + V_3 - E)W_1 + V_{12}(P_4^- + P_{23})Y_1 \\
&\quad = -V_{12}[(P_4^+ + P_{13})Y_1 + (P_{23} + P_{13})Y_2], \\
&(H_0 + V_{34} + V^{\mathrm{Coul}} + V_3 - E)Y_1 + V_{34}(P_{13}Y_1 + P_{23}W_1) \\
&\quad = -V_{34}(P_{23}U_1 + P_4^+Y_1 + P_{23}U_2 + P_{13}Y_2), \\
&(H_0 + V_{34} + V^{\mathrm{Coul}} + V_3 - E)Y_2 + V_{34}U_2 \\
&\quad = -V_{34}(U_1 + W_1),
\end{aligned} \tag{2}$$

where the numbers 1, 2, and 3 label identical particles; the number 4 labels the fourth, nonidentical, particle; V_{12} is the pair potential of interaction between the identical particles of the system; V_{34} is the pair potential of interaction between the nonidentical particle and the remaining particles of the system; V^{Coul} is the Coulomb interaction potential; V_3 is the three-body potential; H_0 is the kinetic-energy operator; P_{ik} is the operator permuting the ith and the kth particle for $i, k = 1, 2, 3$; and $P_i^{\pm}$ stands for the operators of cyclic permutations of three particles, the subscript labeling the particle not involved in a given permutation.

The wave function of the system can be represented as

$$\Psi = \Psi_1 + \Psi_2, \tag{3}$$

where

$$\begin{aligned}
\Psi_1 &= (I + P_4^+ + P_4^-)U_1 + (I + P_{23} + P_{13})W_1 \\
&\quad + (I + P_4^+ + P_4^- + P_{12} + P_{23} + P_{13})Y_1, \\
\Psi_2 &= (I + P_{23} + P_{13})U_2 + (I + P_{23} + P_{13})Y_2.
\end{aligned}$$

In configuration space, the system is described with the aid of the Jacobi coordinates $\mathbf{X}^A = \{\mathbf{x}^A, \mathbf{y}^A, \mathbf{z}^A\}$, where the superscript A labels the Jacobi coordinates corresponding to the various types of partitions of the system in question ($A = U_1$, U_2, W_1, and Y_1). The Jacobi coordinates are expressed in terms of the particle radius vectors $\mathbf{r}_k$, $k = 1, 2, 3, 4$, as

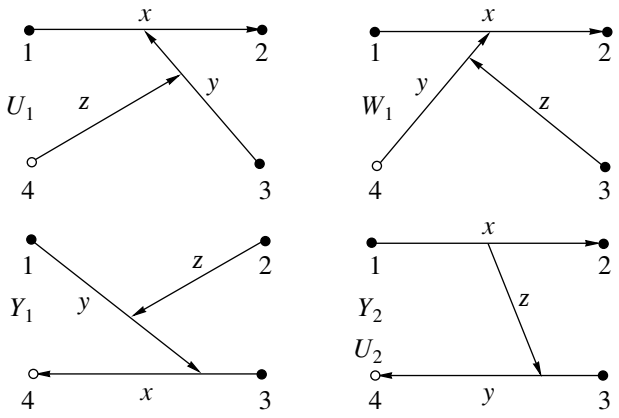

Fig. 1. Jacobi coordinates in the Λααα system (shown in the figure are the Yakubovsky components corresponding to each set of the Jacobi coordinates).

$$\begin{aligned}
&\mathbf{x}^{U_1} = \mathbf{r}_2 - \mathbf{r}_1, \quad \mathbf{y}^{U_1} = \frac{\mathbf{r}_1 + \mathbf{r}_2}{2} - \mathbf{r}_3, \\
&\mathbf{z}^{U_1} = \frac{\mathbf{r}_1 + \mathbf{r}_2 + \mathbf{r}_3}{3} - \mathbf{r}_4, \\
&\mathbf{x}^{U_2} = \mathbf{r}_2 - \mathbf{r}_1, \quad \mathbf{y}^{U_2} = \mathbf{r}_4 - \mathbf{r}_3, \\
&\mathbf{z}^{U_2} = \frac{\mathbf{r}_1 + \mathbf{r}_2}{2} - \frac{m\mathbf{r}_3 + m_4\mathbf{r}_4}{m + m_4}, \\
&\mathbf{x}^{W_1} = \mathbf{r}_2 - \mathbf{r}_1, \quad \mathbf{y}^{W_1} = \frac{\mathbf{r}_1 + \mathbf{r}_2}{2} - \mathbf{r}_4, \\
&\mathbf{z}^{W_1} = \frac{m\mathbf{r}_1 + m\mathbf{r}_2 + m_4\mathbf{r}_4}{2m + m_4} - \mathbf{r}_3, \\
&\mathbf{x}^{Y_1} = \mathbf{r}_4 - \mathbf{r}_3, \quad \mathbf{y}^{Y_1} = \frac{m\mathbf{r}_3 + m_4\mathbf{r}_4}{m + m_4} - \mathbf{r}_1, \\
&\mathbf{z}^{Y_1} = \frac{m\mathbf{r}_1 + m\mathbf{r}_3 + m_4\mathbf{r}_4}{2m + m_4} - \mathbf{r}_2,
\end{aligned}$$

where we have considered that $m_1 = m_2 = m_3 = m$. For the four-particle system being considered, the Jacobi coordinates are illustrated in Fig. 1.

3. DESCRIPTION OF THE MODEL

We consider a bound system that consists of three alpha-particle clusters and a Λ hyperon. The angular momentum of the entire system and the angular momentum of each of its subsystems are taken to be zero; that is, our consideration is restricted to the s-wave approximation. The interaction between the Λ hyperon and each alpha particle is simulated here by

the potential that was proposed in [9] and which is given by

$$V_{\Lambda\alpha}(r) = V_0 \exp\left(-\frac{r^2}{\beta_0^2}\right), \quad (4)$$

where V_0 = –47.97 MeV and β_0 = 1.566 fm. For the potential of the pair interaction between the alpha particles, we use the *s*-wave component of the potential from [10],

$$V_{\alpha\alpha}(r) = V_1 \exp\left(-\frac{r^2}{\beta_1^2}\right) + V_2 \exp\left(-\frac{r^2}{\beta_2^2}\right), \quad (5)$$

where V_1 = 120.0 MeV, β_1 = 1.53 fm, V_2 = –30.18 MeV, and β_2 = 2.85 fm. Since the pair potential (5) does not bind the system of three alpha particles because of strong Coulomb repulsion, it is reasonable to introduce, in just the same wave as in [1, 2], a three-body potential, V_3. It is taken here in the form

$$V_3(\rho) = V \exp[-(\rho/\beta)^2], \quad (6)$$

where $\rho^2 = \sum_{i=1}^{i=3} \mathbf{r}_i^2$, $\mathbf{r}_i$ being the radius vector of the *i*th particle in the c.m. frame; V = –24.32 MeV; and β = 3.795 fm. The values of the parameters V and β were chosen in such a way as to reproduce the experimental results for the binding energy and the root-mean-square radius of the ^{12}C nucleus [3].

The model is supplemented with the assumption specifying the character of clustering within the system. As was shown in [7], the probability of 2 + 2 clustering is small in the system being considered: only an insignificant correction arises there in the computed binding energy of the $^{13}_{\Lambda}$C hypernucleus upon taking into account this type of clustering. For this reason, the components U_2 and Y_2, which correspond to 2 + 2 clustering, are discarded here in the eventual equations. The *s*-wave differential equations for the coordinate parts $\mathcal{U}_1$, $\mathcal{W}_1$, and $\mathcal{Y}_1$ of the Yakubovsky components are presented in the Appendix.

4. METHOD FOR SOLVING EQUATIONS (3)

Equations (3) for the relevant Yakubovsky components were solved numerically by the cluster-reduction method. Within this method, a solution to the original equations is represented as an expansion in bases formed by eigenfunctions of the Hamiltonians of the three-particle subsystems:

$$\Psi_{a_3 a_2}(\mathbf{X}) = \sum_{k=0}^{\infty} \psi^{a_3}_{a_2,k}(\mathbf{x}_{a_2}) F^k_{a_2}(\mathbf{z}_{a_2}). \quad (7)$$

Here, the unknown amplitudes $F^k_{a_2}(\mathbf{z}_{a_2})$ depend only on the vector $\mathbf{z}_{a_2}$ of the relative coordinate of the clusters in the partition a_2; by $\mathbf{x}_{a_2}$, we denote the internal coordinates of the clusters in this partition. The basis $\psi^{a_3}_{a_2,k}(\mathbf{x}_{a_2})$, $k = 1, 2, \ldots$, is complete, but it is not orthogonal. A biorthogonal basis is formed by the eigenfunctions of conjugate Hamiltonians for the three-particle subsystems [11]. By taking relative projections onto the basis functions, we arrive at a set of equations for functions that describe the relative motion of the clusters. The dimensionality of each equation in this set is smaller by unity than the dimensionality of the original equations. A detailed account of the reduction outlined immediately above is given in [6]. In numerically solving the equations in question, a finite number N of terms is retained in expansion (7). The number N is a parameter that determines the efficiency of the method, since this parameter specifies the dimension of the algebraic problem to which we go over from the problem of numerically solving the reduced equations. The cluster-reduction method was used in [5, 6] to compute bound states and low-energy scattering in systems comprising three and four particles.

5. RESULTS OF THE CALCULATIONS

The cluster-reduction method specifies a general scheme for numerically solving the *s*-wave differential equations (A.1) for the Yakubovsky components. In configuration space, the parameters R_x, R_y, and R_z determine a rectangular parallelepiped Ω (in the present study, each of these parameters is taken to be 25 fm). In solving equations (A.1), zero boundary conditions are imposed at the boundary of the region Ω. Within this region, the basis functions are determined as the eigenfunctions of the boundary-value problems for the Faddeev equations describing the 3α and $\Lambda\alpha\alpha$ subsystems. These eigenfunctions are numbered in the order of increasing eigenvalues that correspond to them. In particular, the functions $\psi^{a_3}_{a_2,k}(\mathbf{x}_{a_2})$ that are assigned the number k = 1 describe the bound states in the 3α and $\Lambda\alpha\alpha$ systems. The bound states of these systems can be associated with the ground states of the ^{12}C nucleus and the $^{9}_{\Lambda}$Be hypernucleus in the three-body cluster models being considered [3, 12]. The results of our calculations for the binding energy and the root-mean-square radii of the 3α and $\Lambda\alpha\alpha$ systems governed by the potentials (4)–(6) are listed in Table 1. By applying the procedure of cluster reduction to the problem specified by equation (A.1), we go over to the problem of solving effective equations for the functions describing the relative motion of the clusters forming the system being considered. A numerical solution to the resulting equations is constructed by means of a finite-difference approximation on an equidistant mesh.

For the binding energy of the $\Lambda\alpha\alpha\alpha$ system, the results of our calculations are presented in Table 2. The *s*-wave potential model used in the present study has

Table 1. Binding energy E_B and root-mean-square radii R of the 3α and Λαα systems (^{12}C nucleus and $^{9}_{\Lambda}$Be hypernucleus, respectively)

	$E_B(^{12}C)$, MeV	$R(^{12}C)$, fm	$E_B(^{9}_{\Lambda}Be)$, MeV	$R_\Lambda(^{9}_{\Lambda}Be)$, fm
This study	–7.26	2.47	–5.6	3.0
Experiment	–7.27	2.47	–6.62	–

Note: The energy is reckoned from the threshold for the breakup of the system into constituent particles. Here and in Table 2, $R_\Lambda(^{9}_{\Lambda}Be)$ is the root-mean-square radius of the Λ-hyperon distribution in the Λαα system.

Table 2. Binding energies and root-mean-square radii of the Λ-hyperon distribution in the $^{13}_{\Lambda}$C hypernucleus for its ground state (E_B and R_Λ, respectively) and the first excited state (E_B^* and R_Λ^*)

	E_B, MeV	R_Λ, fm	E_B^*, MeV	R_Λ^*, fm
[7]	–21.34	2.09	–7.73	2.73
[8]	–20.37	–	–	–
[13]	–16.75	–	–	–
This study	–18.7	2.56	–7.8	4.7
Experiment	–18.96	–	–	–

Note: Presented in the first row are the values of R_Λ, E_B^*, and R_Λ^* as obtained in [7] upon correcting the Λα potential in order to reproduce the binding energy of the $^{13}_{\Lambda}$C hypernucleus.

two bound $(1/2)^+$ states, the ground and the first excited state. As can be seen from Table 2, the results of our calculations approximate closely the experimental value of the energy of the ground state of the $^{13}_{\Lambda}$C hypernucleus. The results of the calculations performed in [7, 8, 13] are also presented in Table 2 for the sake of comparison. As was mentioned above, the calculations from [7, 8] were based on cluster models; in contrast to this, a microscopic approach featuring a realistic (Jülich) Λ*N* interaction was employed in [13].

Proceeding to study clustering in the Λαααα system, we will first dwell on the problem of convergence of a calculation within the cluster-reduction method. It should be emphasized that the rate of convergence within the cluster-reduction method gives a hint as to whether there is (or there is no) clustering in the subsystems of the system being considered [3]. Table 3 displays the calculated binding energy of the Λαααα system versus the number N of terms retained in expansions (7) in basis functions. We can see that a convergent result is obtained by retaining the first six of nine basis functions, the contribution of the last five being no more than 4% of the total result. At the same time, the disregard of the component U_1, which corresponds to the 3α + Λ clustering, in the equations being considered increases the calculated binding energy only by 0.2 MeV. Thus, we can state that the ground state of the system is determined primarily by the (Λαα)α cluster state. Considering that the calculation of the binding energy of the $^{9}_{\Lambda}$Be hypernucleus within the Λαα model employing the pair potentials (4) and (5) underestimates the absolute value of the binding energy of this hypernucleus in the ground state by 1 MeV [12], we arrive at the conclusion that the above clustering of the Λαααα system is not identical to the cluster representation $^{9}_{\Lambda}$Be + α. In this connection, it

Table 3. Calculated binding energies in the ground and the first excited state of the Λαααα system versus the number N of basis functions taken into account in the calculation (illustration of the convergence of the cluster-reduction method)

N	E_B, MeV	E_B^*, MeV
1	–18.0	–7.0
2	–17.9	–7.0
3	–18.2	–7.1
4	–18.6	–7.4
5	–18.6	–7.6
6	–18.7	–7.8
7	–18.7	–7.8
8	–18.7	–7.8
9	–18.7	–7.8

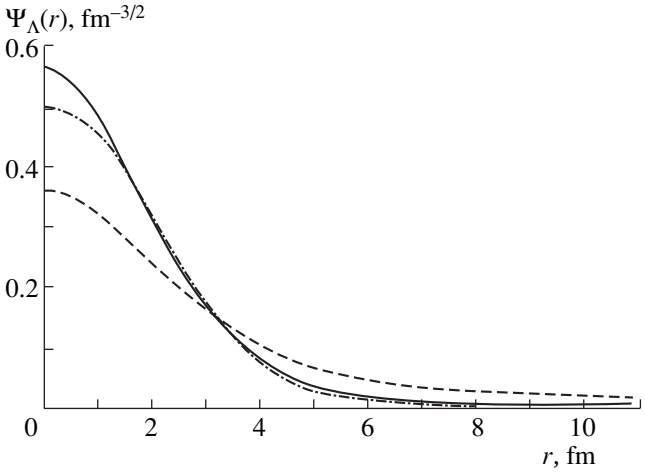

Fig. 2. Calculated distributions of the Λ hyperon in (solid curve) the ground state of the $^{13}_{\Lambda}$C hypernucleus, (dashed curve) the first excited state of the $^{13}_{\Lambda}$C hypernucleus, and (dash-dotted curve) the ground state of the $^{17}_{\Lambda}$O hypernucleus (according to the results of the calculations from [14]).

should be noted that attempts at simultaneously describing the $^{9}_{\Lambda}$Be and $^{13}_{\Lambda}$C hypernuclei on the basis of the Λαα and Λααα cluster models employing the Λα potential that makes it possible to reproduce faithfully the binding energy of $^{9}_{\Lambda}$Be hypernucleus lead to an overestimation of the binding energy of the Λααα system ($^{13}_{\Lambda}$C hypernucleus) [7, 8].

The (3α + Λ) clustering of the Λααα system plays a crucial role in the formation of the excited $(1/2)^+$ state. Without taking into account this type of clustering (that is, without the component U_1), there is no excited bound state in the Λααα system.

In connection with investigations into clustering phenomena, it is worth noting that the result obtained here for the ground state—namely, the dominance of (Λαα)α clustering in the system being considered—is at odds with the corresponding result from [7], where clustering of the (ααα)Λ type was found to be dominant. For the excited state of the system, the results of the two studies are closer. The excited state of $^{13}_{\Lambda}$C considered in [7] is formed via a core excitation in the $^{12}C(0^+_2) + \Lambda$ model. An analysis of the convergence of our calculation for the binding energy of the excited state (see Table 3) reveals that no less than five basis functions must be retained in order to obtain this state. Thus, we can see that, for an excited state to be realized in the Λααα system, an excitation in the 3α subsystem must be taken into account in the present model as well.

The spatial distribution of the Λ hyperon in the Λααα system can be investigated by calculating the wave function (3) of our system. Denoting by $\rho_\Lambda(r)$ the density of the hyperon probability distribution in the system, we introduce the function $\Psi_\Lambda(r) = \sqrt{\rho_\Lambda(r)}$ satisfying the normalization condition

$$\int_0^\infty \Psi^2_\Lambda(r) r^2 dr = 1.$$

The distribution function $\Psi_\Lambda(r)$ is displayed in Fig. 2 for the ground state of the $^{13}_{\Lambda}$C hypernucleus (solid curve) and for its excited state (dashed curve). For the sake of comparison, this figure also shows the distribution of the Λ hyperon in the $^{17}_{\Lambda}$O hypernucleus (dash-dotted curve) from [14]. The root-mean-square radius of this distribution is 2.47 fm, the corresponding hyperon-separation energy being close to its experimental value.

6. CONCLUSION

The $^{13}_{\Lambda}$C nucleus has been considered here within the Λααα cluster model. The Λααα system is a four-particle system involving one nonidentical particle. The differential equations for the relevant Yakubovsky components have been presented. On the basis of these equations, an *s*-wave potential model has been proposed that takes into account, in addition to the pair Λα and αα potentials, the potential of three-body interaction between the alpha-particle clusters (the potential parameters were determined in [3]). For the binding energy of the $^{13}_{\Lambda}$C hypernucleus, this model yields results that agree with the results of calculations performed by other authors and with experimental data. An analysis of the present calculations has revealed that the ground state of the system is dominated by the (Λαα)α type of clustering. In addition, the potential model considered here admits an excited bound state, which receives a significant contribution from (ααα)Λ clustering. The results of the present study for the excited state in question are consistent with the results presented in [7]. The use of the cluster-reduction method for numerically solving the Yakubovsky equations has made it possible, first, to relax requirements on computational facilities and, second, to reveal the types of clustering in the Λααα system.

ACKNOWLEDGMENTS

I am grateful to S.L. Yakovlev for enlightening discussions on the results of this study.

This work was supported in part by the Contest Center at the Ministry for Higher Education of the Russian Federation (grant no. 97-0-14.3-23).

APPENDIX

The *s*-wave differential equations for the coordinate parts $\mathcal{U}_1$, $\mathcal{W}_1$, and $\mathcal{Y}_1$ of the Yakubovsky components are given by

$$
\begin{aligned}
&(h_0^{U_1} + V_{\alpha\alpha}(x) + V_{\mathrm{Coul}}^{U_1}(x,y,z) + V_3^{U_1}(\rho) - \varepsilon)\mathcal{U}_1(x,y,z) \\
&\quad + V_{\alpha\alpha}(x)\int_{-1}^{1} dv\,\frac{xy}{x'y'}\mathcal{U}_1(x',y',z) \\
&\quad = -\frac{1}{2}V_{\alpha\alpha}(x)\int_{-1}^{1}du\int_{-1}^{1}dv\,\frac{xyz}{x_3y_3z_3}\mathcal{W}_1(x_3,y_3,z_3), \\
&(h_0^{W_1} + V_{\alpha\alpha}(x) + V_{\mathrm{Coul}}^{W_1}(x,y,z) + V_3^{W_1}(\rho) - \varepsilon)\mathcal{W}_1(x,y,z) \\
&\quad + V_{\alpha\alpha}(x)\int_{-1}^{1} dv\,\frac{xy}{x'y_1'}\mathcal{Y}_1(x',y_1',z) \\
&\quad = -\frac{1}{2}V_{\alpha\alpha}(x)\int_{-1}^{1}du\int_{-1}^{1}dv\,\frac{xyz}{x_4y_4z_4}\mathcal{Y}_1(x_4,y_4,z_4), \\
&(h_0^{Y_1} + V_{\Lambda\alpha}(x) + V_{\mathrm{Coul}}^{Y_1}(x,y,z) + V_3^{Y_1}(\rho) - \varepsilon)\mathcal{Y}_1(x,y,z) \\
&\quad + \frac{1}{2}V_{\Lambda\alpha}(x)\int_{-1}^{1} dv\left(\frac{xy}{x_1y_1}\mathcal{W}_1(x_1,y_1,z)\right. \\
&\quad \left. + \frac{xy}{x_2y_2}\mathcal{Y}_1(x_2,y_2,z)\right) = -\frac{1}{4}V_{\Lambda\alpha}(x)\int_{-1}^{1}du\int_{-1}^{1}dv\left(\frac{xyz}{x_5y_5z_5}\right. \\
&\quad \left. \times\mathcal{U}_1(x_5,y_5,z_5) + \frac{xyz}{x_6y_6z_6}\mathcal{Y}_1(x_6,y_6,z_6)\right),
\end{aligned}
\tag{A.1}
$$

where

$$
\begin{aligned}
h_0^{U_1} &= -\left(\partial_x^2 + \frac{3}{4}\partial_y^2 + \frac{1}{2}\frac{ad}{b}\partial_z^2\right), \\
h_0^{W_1} &= -\left(\partial_x^2 + \frac{1}{2}\frac{a}{b}\partial_y^2 + \frac{3}{4}d\partial_z^2\right), \\
h_0^{Y_1} &= -\left(\frac{1}{2b}\partial_x^2 + \frac{3}{4}a\partial_y^2 + \frac{3}{4}d\partial_z^2\right), \\
a &= \frac{1}{2}\frac{m_4+2m}{m_4+m}, \quad b = \frac{m}{m_4+m}, \\
d &= \frac{2}{3}\frac{m_4+3m}{m_4+2m}, \quad c = \frac{m}{m+m_4},
\end{aligned}
$$

m is the alpha-particle mass, and m_4 is the Λ-hyperon mass. The coordinates in equations (A.1) are transformed as

$$
\begin{aligned}
x' &= \left(\frac{1}{4}x^2 + y^2 + xyv\right)^{1/2}, \\
y' &= \left[\left(\frac{3}{4}x\right)^2 + \frac{1}{4}y^2 - \frac{3}{4}xyv\right]^{1/2}, \\
y_1' &= [(ax)^2 + (by)^2 - 2abxyv]^{1/2}, \\
x_1 &= [(bx)^2 + y^2 + 2bxyv]^{1/2}, \\
y_1 &= \left[(ax)^2 + \frac{1}{4}y^2 - axyv\right]^{1/2}, \\
x_2 &= [(cx)^2 + y^2 + 2cxyu]^{1/2}, \\
y_2 &= [4(abx)^2 + (cy)^2 - 4abcxyu]^{1/2}, \\
x_3 &= x', \quad y_3 = \left[(y'/3)^2 + z^2 + \frac{2}{3}zy'u\right]^{1/2}, \\
z_3 &= \left[(dy')^2 + \left(\frac{b}{2a}z\right)^2 - \frac{bd}{a}y'zu\right]^{1/2}, \\
x_4 &= x', \quad y_4 = \left[\left(\frac{c}{a}y_1'\right)^2 + z^2 - \frac{b}{c}zy_1'u\right]^{1/2}, \\
z_4 &= \left[\left(\frac{3}{4}\frac{d}{a}y_1'\right)^2 + \left(\frac{c}{2a}z\right)^2 + \frac{3}{4}\frac{bd}{ac}y_1'zu\right]^{1/2}, \\
x_5 &= x_1, \quad y_5 = \left[\left(\frac{b}{2a}y_1\right)^2 + z^2 - \frac{b}{a}zy_1u\right]^{1/2}, \\
z_5 &= \left[(dy_1)^2 + \left(\frac{1}{3}z\right)^2 + \frac{2}{3}by_1zu\right]^{1/2}, \\
x_6 &= x_2, \quad y_6 = \left[\left(\frac{c}{a}y_2\right)^2 + z^2 + \frac{b}{c}zy_2u\right]^{1/2}, \\
z_6 &= \left[\left(\frac{3}{4}\frac{d}{a}y_2\right)^2 + \left(\frac{c}{2a}z\right)^2 - \frac{3}{4}\frac{bd}{ac}y_2zu\right]^{1/2}.
\end{aligned}
$$

The *s*-wave projections of the Coulomb interaction in equations (A.1) are given by

$$
\begin{aligned}
V_{\mathrm{Coul}}^{U_1} &= \frac{n}{x} + 2\frac{n}{r_>}, \quad r_> = \max\left\{\frac{x}{2}, y\right\}, \\
V_{\mathrm{Coul}}^{W_1} &= \frac{n}{x} + \frac{n}{2}\int_{-1}^{1}du\int_{-1}^{1}dv\,\frac{1}{\tilde{x}_2}, \\
V_{\mathrm{Coul}}^{Y_1} &= \frac{n}{x} + \frac{n}{4}\int_{-1}^{1}du\int_{-1}^{1}dv\,\frac{1}{\tilde{x}_3} + \frac{n}{2}\int_{-1}^{1}du\int_{-1}^{1}dv\left(\frac{1}{\tilde{x}_1} + \frac{1}{x_1}\right),
\end{aligned}
$$

where

$$
n = \frac{4me^2}{\hbar^2},
$$

$$\tilde{x}_1 = \left[\left(\frac{1}{2a}y\right)^2 + z^2 - \frac{1}{a}yzu\right]^{1/2},$$

$$\tilde{x}_2 = \left[\left(\frac{1}{2a}y_1'\right)^2 + z^2 + \frac{1}{a}y_1'zu\right]^{1/2},$$

$$\tilde{x}_3 = \left[\left(\frac{1}{2a}y_2\right)^2 + z^2 + \frac{1}{a}y_2zu\right]^{1/2}.$$

The short-range potential of interaction between two alpha particles, $v_{\alpha\alpha}(x)$, is calculated by formula (5) with allowance for the fact that $v_{\alpha\alpha}(x) = V_{\alpha\alpha}(x)m/\hbar^2$. The $\Lambda\alpha$-interaction potential $v_{\Lambda\alpha}(x)$ is given by (4) [$v_{\Lambda\alpha}(x) = V_{\Lambda\alpha}(x)m/\hbar^2$]. The potential of three-body interaction, $v_3^A(\rho)$, has the form

$$v_3^A(\rho) = \frac{1}{8}\int_{-1}^{1}\int_{-1}^{1}\int_{-1}^{1} dv\,du\,dw\,v_3(\rho_A),$$

where the superscript A stands for U_1, W_1, and Y_1, while ρ_A^2 is expressed in terms of the Jacobi coordinates as

$$\rho_A^2 = \frac{2}{3}\xi_A^2 + \frac{1}{2}\eta_A^2,$$

where

$$\xi_{U_1}^2 = y^2, \quad \eta_{U_1}^2 = x^2,$$

$$\xi_{W_1}^2 = \left(\frac{b}{2a}y\right)^2 + z^2 + \frac{b}{a}yzu, \quad \eta_{W_1}^2 = x^2,$$

$$\eta_{Y_1}^2 = \left(\frac{1}{2a}y\right)^2 + z^2 - \frac{1}{a}yzv,$$

$$\xi_{Y_1}^2 = (\tilde{\tilde{y}})^2 + \left(\frac{1}{2}\eta_{Y_1}\right)^2 + \eta_{Y_1}\tilde{\tilde{y}}w$$

with

$$\tilde{\tilde{y}}^2 = (bx)^2 + (cy)^2 - 2bcxyu.$$

REFERENCES

1. K. Fukatsu, K. Kato, and H. Tanaka, Prog. Theor. Phys. **81**, 736 (1989); O. Portilho and S. A. Coon, Z. Phys. A **290**, 93 (1979); H. Ogasawara and J. Hiura, Prog. Theor. Phys. **59**, 655 (1978).
2. D. V. Fedorov and A. S. Jensen, Phys. Lett. B **389**, 631 (1996).
3. I. N. Filikhin and S. L. Yakovlev, Yad. Fiz. **63**, 409 (2000) [Phys. At. Nucl. **63**, 343 (2000)].
4. S. P. Merkuriev and S. L. Yakovlev, Dokl. Akad. Nauk SSSR **262**, 591 (1982); Teor. Mat. Fiz. **56**, 60 (1983); S. P. Merkuriev and L. D. Faddeev, *Quantum Scattering Theory for Few-Particle Systems* (Nauka, Moscow, 1985).
5. S. L. Yakovlev and I. N. Filikhin, Yad. Fiz. **56** (12), 98 (1993) [Phys. At. Nucl. **56**, 1676 (1993)]; Yad. Fiz. **58**, 817 (1995) [Phys. At. Nucl. **58**, 754 (1995)].
6. S. L. Yakovlev and I. N. Filikhin, Yad. Fiz. **60**, 1962 (1997) [Phys. At. Nucl. **60**, 1794 (1997)]; Few-Body Syst. (Suppl.) **10**, 37 (1999); nucl-th/9809041.
7. E. Hiyama, M. Kamimura, T. Motoba, *et al.*, Prog. Theor. Phys. **97**, 881 (1997).
8. A. R. Bodmer, Q. N. Usmani, and J. Carlson, Phys. Rev. C **29**, 684 (1984).
9. H. Bando, K. Ikeda, and T. Motobu, Prog. Theor. Phys. **66**, 344 (1981); **67**, 508 (1982).
10. S. Ali and A. R. Bodmer, Nucl. Phys. **88**, 99 (1966).
11. S. L. Yakovlev, Teor. Mat. Fiz. **107**, 513 (1996); **102**, 323 (1995); V. A. Rudnev and S. L. Yakovlev, Yad. Fiz. **58**, 1762 (1995) [Phys. At. Nucl. **58**, 1662 (1995)].
12. I. N. Filikhin and S. L. Yakovlev, Yad. Fiz. **63**, 402 (2000) [Phys. At. Nucl. **63**, 336 (2000)].
13. I. Vidana, A. Polls, A. Ramos, and M. Hjorth-Jensen, Nucl. Phys. A **644**, 201 (1998); nucl-th/9805032.
14. M. Hjorth-Jensen, A. Polls, A. Ramos, and H. Muther, Nucl. Phys. A **605**, 458 (1996); nucl-th/9604028.

Translated by A. Isaakyan

Physics of Atomic Nuclei, Vol. 63, No. 5, 2000, pp. 767–773. Translated from Yadernaya Fizika, Vol. 63, No. 5, 2000, pp. 837–843.

NUCLEI
Theory

T Invariance and Polarization Effects in the Reactions $p + {}^3\mathrm{He} \longrightarrow \pi^+ + {}^4\mathrm{He}$ and $\pi^+ + {}^4\mathrm{He} \longrightarrow p + {}^3\mathrm{He}$

V. V. Lyuboshitz and V. L. Lyuboshitz*

Joint Institute for Nuclear Research, Dubna, Moscow oblast, 141980 Russia

Received April 9, 1999; in final form, July 8, 1999

Abstract—On the basis of *T* invariance, it is established that the dependence of the effective cross section for a binary reaction of the $a + b \longrightarrow c + d$ type on the polarization vectors of primary particles *a* and *b* determines completely the polarization vectors and spin correlations for the same particles in the inverse reaction $c + d \longrightarrow a + b$ induced by collisions between unpolarized primary particles *c* and *d*. By using the formalism of helicity amplitudes, polarization effects are studied in the process $p + {}^3\mathrm{He} \longrightarrow \pi^+ + {}^4\mathrm{He}$ and in the inverse process $\pi^+ + {}^4\mathrm{He} \longrightarrow p + {}^3\mathrm{He}$. It is shown that, in the reaction $\pi^+ + {}^4\mathrm{He} \longrightarrow p + {}^3\mathrm{He}$, the spins of the final-state particles (proton and ^{3}He nucleus) are strongly correlated. An expression for the correlation tensor is obtained for arbitrary values of the (p, ^{3}He) emission angle. © *2000 MAIK "Nauka/Interperiodica".*

Polarization effects in the scattering of spin-1/2 particles on an unpolarized target were discussed in [1] on the basis of the *T* invariance of the differential cross section for elastic scattering. In the present study, a similar approach is used to analyze implications of *T* invariance for the effective cross sections for direct and inverse binary reactions involving two spin-1/2 particles in the initial or the final state. Specifically, polarization effects are investigated in detail for the reactions $p + {}^3\mathrm{He} \longrightarrow \pi^+ + {}^4\mathrm{He}$ and $\pi^+ + {}^4\mathrm{He} \longrightarrow p + {}^3\mathrm{He}$.

1. Let us consider a binary reaction of the $a + b \longrightarrow c + d$ type. Let the initial particles *a* and *b* both have a spin of 1/2, and let the final particles have arbitrary spins. We denote by $\mathbf{k}_a = -\mathbf{k}_b$ the primary momentum in the reaction c.m. frame, by $\mathbf{k}_c = -\mathbf{k}_d$ the final momentum in the c.m. frame, by θ the angle between the momenta $\mathbf{k}_a$ and $\mathbf{k}_c$, and by *E* the total energy in the c.m. frame. We further introduce three mutually orthogonal unit vectors (of these, two lie in the reaction plane, while the third is aligned with the normal to the reaction plane)

$$\mathbf{l} = \frac{\mathbf{k}_a}{k_a}, \quad \mathbf{m} = \frac{\mathbf{l}' - \mathbf{l}(\mathbf{l}' \cdot \mathbf{l})}{\sin\theta}, \quad \mathbf{n} = \frac{\mathbf{l} \times \mathbf{l}'}{\sin\theta}, \qquad (1)$$

where

$$\mathbf{l}' = \frac{\mathbf{k}_c}{k_c}, \quad k_a = |\mathbf{k}_a|, \quad k_c = |\mathbf{k}_c|, \quad \theta = \arccos(\mathbf{l} \cdot \mathbf{l}').$$

If parity is conserved and if invariance under rotations in three-dimensional space and the fact that quantum theory is linear are taken into account, the quantity obtained by summing the effective cross section for the $a + b \longrightarrow c + d$ process over the projections of the final-particle spins must be a scalar linear in the initial-particle polarization vectors $\mathbf{P}^{(a)}$ and $\mathbf{P}^{(b)}$. In accordance with this, the structural formula for the differential cross section in the c.m. frame takes the form (see also [2])

$$\begin{aligned}
&\sigma_{a+b\to c+d}(\mathbf{k}_a, \mathbf{P}^{(a)}, \mathbf{P}^{(b)}; \mathbf{k}_c) \\
&= \sigma_0(E, \theta)\{1 + A(E, \theta)(\mathbf{P}^{(a)} \cdot \mathbf{n}) + B(E, \theta)(\mathbf{P}^{(b)} \cdot \mathbf{n}) \\
&+ C(E, \theta)(\mathbf{P}^{(a)} \cdot \mathbf{P}^{(b)}) + D(E, \theta)(\mathbf{P}^{(a)} \cdot \mathbf{l})(\mathbf{P}^{(b)} \cdot \mathbf{l}) \\
&+ F(E, \theta)(\mathbf{P}^{(a)} \cdot \mathbf{m})(\mathbf{P}^{(b)} \cdot \mathbf{m}) \\
&+ G(E, \theta)(\mathbf{P}^{(a)} \cdot \mathbf{l})(\mathbf{P}^{(b)} \cdot \mathbf{m}) \\
&+ H(E, \theta)(\mathbf{P}^{(a)} \cdot \mathbf{m})(\mathbf{P}^{(b)} \cdot \mathbf{l})\},
\end{aligned} \qquad (2)$$

where $\sigma_0(E, \theta)$ is the effective cross section for the $a + b \longrightarrow c + d$ reaction induced by a collision of unpolarized primary particles, while *A*, *B*, *C*, *D*, *F*, *G*, and *H* are dimensionless functions of energy and of the emission angle θ, the vectors $A(E, \theta)\mathbf{n}$ and $B(E, \theta)\mathbf{n}$ having the meaning of analyzing powers for particles *a* and *b*, respectively.

It is obvious that, at $\theta = 0$, the functions *A*, *B*, *F*, *G*, and *H* vanish by virtue of axial symmetry; the expression for the differential reaction cross section is then simplified to become

$$\begin{aligned}
&\sigma_{a+b\to c+d}(k_a\mathbf{l}, \mathbf{P}^{(a)}, \mathbf{P}^{(b)}; k_c\mathbf{l}) \\
&= \sigma_0(E, 0)\{1 + C(E, 0)(\mathbf{P}^{(a)} \cdot \mathbf{P}^{(b)}) \\
&+ D(E, 0)(\mathbf{P}^{(a)} \cdot \mathbf{l})(\mathbf{P}^{(b)} \cdot \mathbf{l})\}.
\end{aligned} \qquad (3)$$

At $\theta = \pi$, the effective cross section for the reaction in question has the same structure. Taking into account expressions (1), we find that, at very small values of the

* e-mail: lyubosh@sunhe.jinr.ru

emission angle, the above dimensionless functions are given by

$$A(E,\theta) = a(E)\theta, \quad B(E,\theta) = b(E)\theta,$$
$$G(E,\theta) = g(E)\theta, \quad H(E,\theta) = h(E)\theta, \qquad (4)$$
$$F(E,\theta) = f(E)\theta^2,$$

where the functions $a(E)$, $b(E)$, $f(E)$, $g(E)$, and $h(E)$ do not vanish in general. For small deviations of the emission angle from π, we have limiting relations of the form (4) that feature different functions of E and the angle $\Delta\theta = \pi - \theta$ in place of θ.

Let us now integrate the effective cross section for the $a + b \longrightarrow c + d$ reaction with respect to the azimuthal angle. It can easily be seen that the following relations hold:

$$\int_0^{2\pi} (\mathbf{P}^{(a)} \cdot \mathbf{n}) d\varphi = \int_0^{2\pi} (\mathbf{P}^{(b)} \cdot \mathbf{n}) d\varphi = 0,$$
$$\int_0^{2\pi} (\mathbf{P}^{(a)} \cdot \mathbf{m}) d\varphi = \int_0^{2\pi} (\mathbf{P}^{(b)} \cdot \mathbf{m}) d\varphi = 0, \qquad (5)$$
$$\int_0^{2\pi} (\mathbf{P}^{(a)} \cdot \mathbf{m})(\mathbf{P}^{(b)} \cdot \mathbf{m}) d\varphi$$
$$= \pi[(\mathbf{P}^{(a)} \cdot \mathbf{P}^{(b)}) - (\mathbf{P}^{(a)} \cdot \mathbf{l})(\mathbf{P}^{(b)} \cdot \mathbf{l})].$$

Taking them into account, we then arrive at

$$\sigma_{a+b\to c+d}(E,\theta,\mathbf{P}^{(a)},\mathbf{P}^{(b)}) = 2\pi\sigma_0(E,\theta)$$
$$\times\left\{1 + \left(C(E,\theta) + \frac{1}{2}F(E,\theta)\right)(\mathbf{P}^{(a)} \cdot \mathbf{P}^{(b)}) \right. \qquad (6)$$
$$\left. + \left(D(E,\theta) - \frac{1}{2}F(E,\theta)\right)(\mathbf{P}^{(a)} \cdot \mathbf{l})(\mathbf{P}^{(b)} \cdot \mathbf{l})\right\}.$$

2. Assuming T invariance and using expression (2), we can obtain a general expression for the effective cross section for the inverse reaction $c + d \longrightarrow a + b$ involving unpolarized particles c and d and resulting in the formation of final-state particles with fixed polarizations $\boldsymbol{\zeta}^{(a)}$ and $\boldsymbol{\zeta}^{(b)}$. By $\boldsymbol{\zeta}^{(a)}$ and $\boldsymbol{\zeta}^{(b)}$, we mean the analyzing powers of corresponding detectors, in which case we have $|\boldsymbol{\zeta}^{(a)}| \le 1$ and $|\boldsymbol{\zeta}^{(b)}| \le 1$. Considering that the inversion of time leads to the reversal of the polarization-vector and momentum directions and using the principle of detailed balance [3], we obtain

$$\sigma_{c+d\to a+b}(\mathbf{k}_c; \mathbf{k}_a, \boldsymbol{\zeta}^{(a)}, \boldsymbol{\zeta}^{(b)})$$
$$= \frac{k_a^2}{k_c^2(2j_c+1)(2j_d+1)} \qquad (7)$$
$$\times \sigma_{a+b\to c+d}(-\mathbf{k}_a, -\boldsymbol{\zeta}^{(a)}, -\boldsymbol{\zeta}^{(b)}; -\mathbf{k}_c).$$

Thus, the effective cross section for the $c + d \longrightarrow a + b$ reaction in the c.m. frame of particles c and d has the form

$$\sigma_{c+d\to a+b}(\mathbf{k}_c; \mathbf{k}_a, \boldsymbol{\zeta}^{(a)}, \boldsymbol{\zeta}^{(b)}) = \frac{1}{4}\tilde{\sigma}_0(E,\theta)$$
$$\times\{1 - A(E,\theta)(\boldsymbol{\zeta}^{(a)} \cdot \mathbf{n}) - B(E,\theta)(\boldsymbol{\zeta}^{(b)} \cdot \mathbf{n})$$
$$+ C(E,\theta)(\boldsymbol{\zeta}^{(a)} \cdot \boldsymbol{\zeta}^{(b)}) + D(E,\theta)(\boldsymbol{\zeta}^{(a)} \cdot \mathbf{l})(\boldsymbol{\zeta}^{(b)} \cdot \mathbf{l}) \qquad (8)$$
$$+ F(E,\theta)(\boldsymbol{\zeta}^{(a)} \cdot \mathbf{m})(\boldsymbol{\zeta}^{(b)} \cdot \mathbf{m})$$
$$+ G(E,\theta)(\boldsymbol{\zeta}^{(a)} \cdot \mathbf{l})(\boldsymbol{\zeta}^{(b)} \cdot \mathbf{m})$$
$$+ H(E,\theta)(\boldsymbol{\zeta}^{(a)} \cdot \mathbf{m})(\boldsymbol{\zeta}^{(b)} \cdot \mathbf{l})\},$$

where

$$\tilde{\sigma}_0(E,\theta) = \frac{4k_a^2}{k_c^2(2j_c+1)(2j_d+1)}\sigma_0(E,\theta) \qquad (9)$$

is the quantity obtained by summing the effective reaction cross section for the unpolarized initial particles c and d over the projections of the spins of the final-state particles a and b.

It should be emphasized that, in expressions (8) and (9), the quantities $A(E,\theta)$, $B(E,\theta)$, $C(E,\theta)$, $D(E,\theta)$, $F(E,\theta)$, $G(E,\theta)$, $H(E,\theta)$, and $\sigma_0(E,\theta)$ are the same functions of energy E and the angle of final-particle emission as in expression (2) and that the unit vectors appearing in (8) are expressed in terms of the momenta $\mathbf{k}_a$ and $\mathbf{k}_c$ according to (1).

From the fact that relation (8) holds for any fixed values of the final-state polarizations $\boldsymbol{\zeta}^{(a)}$ and $\boldsymbol{\zeta}^{(b)}$ measured by two analyzers, it follows that the spin density matrix for the system of two final-state spin-1/2 particles formed in the $c + d \longrightarrow a + b$ reaction induced by a collision between the unpolarized initial particles c and d can be obtained by replacing the vectors $\boldsymbol{\zeta}^{(a)}$ and $\boldsymbol{\zeta}^{(b)}$ by the Pauli operators $\hat{\boldsymbol{\sigma}}^{(a)}$ and $\hat{\boldsymbol{\sigma}}^{(b)}$, respectively. As a result, the two-body spin density matrix $\hat{\rho}^{(1,2)}$ satisfying the normalization condition

$$\mathrm{tr}_{(1,2)}\hat{\rho}^{(1,2)} = 1$$

assumes the form

$$\hat{\rho}^{(a,b)} = \frac{1}{4}[\hat{I}^{(a)} \otimes \hat{I}^{(b)} + (\mathbf{P}^{(a)}(E,\theta) \cdot \hat{\boldsymbol{\sigma}}^{(a)}) \otimes \hat{I}^{(b)}$$
$$+ \hat{I}^{(a)} \otimes (\mathbf{P}^{(b)}(E,\theta) \cdot \hat{\boldsymbol{\sigma}}^{(b)}) \qquad (10)$$
$$+ \sum_{i=1}^{3}\sum_{k=1}^{3} T_{ik}(E,\theta)\hat{\sigma}_i^{(a)} \otimes \hat{\sigma}_k^{(b)}],$$

where $\hat{I}^{(a)}$ and $\hat{I}^{(b)}$ are the two-row identity matrices; the symbol $\otimes$ denotes the tensor product of matrices;

and the quantities $\mathbf{P}^{(a,\,b)}(E,\,\theta)$ entering into expression (10) and having the form

$$\begin{aligned}\mathbf{P}^{(a)}(E,\,\theta) &= -A(E,\,\theta)\mathbf{n},\\ \mathbf{P}^{(b)}(E,\,\theta) &= -B(E,\,\theta)\mathbf{n}\end{aligned} \tag{11}$$

are the polarization vectors of particles *a* and *b* produced in the $c + d \longrightarrow a + b$ reaction. The double sum in (10) involves the coefficients T_{ik} appearing to be

$$\begin{aligned}T_{ik}(E,\,\theta) &= C(E,\,\theta)\delta_{ik} + D(E,\,\theta)l_i l_k\\ &+ F(E,\,\theta)m_i m_k + G(E,\,\theta)l_i m_k + H(E,\,\theta)m_i l_k,\end{aligned} \tag{12}$$

where l_i and l_k (m_i and m_k) are components of the unit vector $\mathbf{l}$ (**m**), and forming a correlation tensor that describes spin correlations in the two-particle (*a*, *b*) system.

In accordance with (10)–(12), we can state that, if, in the measurement process, a detector selects a spin state of particle *a* with a polarization vector $\boldsymbol{\zeta}^{(a)}$ (for example, as the result of secondary scattering), the polarization vector of particle *b* produced in association with particle *a* in the same event of collisions between particles *c* and *d* has the components (see also [2, 4])

$$\tilde{P}_k^{(b)}(\boldsymbol{\zeta}^{(a)}) = \frac{P_k^{(b)} + \sum_{i=1}^{3} T_{ik}(E,\,\theta)\zeta_i^{(a)}}{1 + \mathbf{P}^{(a)}(E,\,\theta)\boldsymbol{\zeta}^{(a)}}, \tag{13}$$

where $\mathbf{P}^{(a)}$ and $\mathbf{P}^{(b)}$ are the polarization vectors of the final particles *a* and *b* under the condition that spin states are not fixed by detectors [see (11)]. Obviously, we have

$$\mathbf{P}^{(b)} = \frac{1}{2}(1 + \mathbf{P}^{(a)}\cdot\boldsymbol{\zeta}^{(a)})\tilde{\mathbf{P}}^{(b)}(\boldsymbol{\zeta}^{(a)})$$

$$\frac{1}{2}(1 - \mathbf{P}^{(a)}\cdot\boldsymbol{\zeta}^{(a)})\tilde{\mathbf{P}}^{(b)}(-\boldsymbol{\zeta}^{(a)}).$$

It can easily be seen that, in the absence of correlations—that is, under the conditions $T_{ik} = P_i^{(a)} P_k^{(b)}$—the quantity $\tilde{\mathbf{P}}^{(b)}(\boldsymbol{\zeta}^{(a)}) = \mathbf{P}^{(b)}$ is independent of the vector $\boldsymbol{\zeta}^{(a)}$.

It should be noted that, at the values of the angle θ that are equal to 0 and π, the polarization vectors vanish by virtue of relations (4) and (11), and spin effects are determined completely by the correlation tensor T_{ik}; that is,

$$\tilde{P}_k^{(b)} = \sum_{i=1}^{3} T_{ik}\zeta_i^{(a)}, \tag{14}$$

where

$$T_{ik} = C\delta_{ik} + Dl_i l_k. \tag{15}$$

That the spin state of one of the particles depends on the character of measurements performed for the other particle in the way specified by equations (13) and (14) is a manifestation of the general correlation effect in recording multiparticle quantum states by single-particle detectors that was predicted in the well-known study of Einstein, Podolsky, and Rosen [5].

Thus, we can see that, by virtue of *T* invariance, the dependence of the effective cross section for the direct reaction $a + b \longrightarrow c + d$ on the polarizations of initial particles completely determines spin correlations between the same particles in the inverse reaction $c + d \longrightarrow a + b$ induced by a collision of unpolarized initial particles.[1)] From *T* invariance, we have also inferred that the left–right azimuthal asymmetries $A(E,\,\theta)$ and $B(E,\,\theta)$ in the direct reaction $a + b \longrightarrow c + d$ induced by a collision between the polarized particles *a* and *b* are related by the simple equations (11) to the polarization vectors of the same particles formed in the inverse reaction $c + d \longrightarrow a + b$ induced by a collision between the unpolarized particles *c* and *d*.

3. Let us now consider polarization effects in the specific reaction $p + {}^3\mathrm{He} \longrightarrow \pi^+ + {}^4\mathrm{He}$ and in the inverse reaction $\pi^+ + {}^4\mathrm{He} \longrightarrow p + {}^3\mathrm{He}$. Previously, it was shown that the effective cross section for the reaction $p + {}^3\mathrm{He} \longrightarrow \pi^+ + {}^4\mathrm{He}$ depends sizably on the polarizations of the proton and the ^{3}He nucleus. The reaction $p({}^3\mathrm{He},\,{}^4\mathrm{He})\pi^+$ occurring on a polarized hydrogen target can in principle be used to measure the polarization of a ^{3}He beam [6].[2)] Thus, *T* invariance leads to a tight correlation between the polarizations of the proton and the ^{3}He nucleus in the inverse reaction $\pi^+ + {}^4\mathrm{He} \longrightarrow p + {}^3\mathrm{He}$.

Let us proceed somewhat further along these lines. From angular-momentum and parity conservation, it follows that, in reactions of the $1/2 + 1/2 \longrightarrow 0 + 0$ type (where two spin-1/2 fermions are converted into two spinless bosons), transitions from the singlet state of

[1)] Listed below are errors made in analyzing the implications of *T* invariance for direct and inverse reactions in [2]. Relations (46) must have the form

$$\mathbf{k}_a \longrightarrow -\mathbf{k}_a,\quad \mathbf{k}_c \longrightarrow -\mathbf{k}_c,$$
$$\mathbf{P}^{(a)} \longrightarrow -\boldsymbol{\zeta}^{(a)},\quad \mathbf{P}^{(b)} \longrightarrow -\boldsymbol{\zeta}^{(b)}.$$

The clause following these relations should read "and $\mathbf{n} \longrightarrow \mathbf{n}$." In accordance with this, the following changes should be made in equations (47), (49), and (50): the tensor $\tilde{M}_{ik}$ should be replaced by the tensor M_{ik} appearing in (44), and the functions *A* and *B* should be taken with the reversed sign. In addition, the expression on the right-hand side of (47) should be multiplied by a factor of 1/4. The definition of the tensor $\tilde{M}_{ik}$ should be omitted.

[2)] The reaction $p + {}^3\mathrm{He} \longrightarrow \pi^+ + {}^4\mathrm{He}$ and the inverse reaction $\pi^+ + {}^4\mathrm{He} \longrightarrow p + {}^3\mathrm{He}$ were investigated experimentally by many authors (see, for example, [7–10]), but they did not consider polarization effects. From these experimental data, it follows that, when neither a beam nor a target is polarized, the differential cross section for the process $^3\mathrm{He} + p \longrightarrow {}^4\mathrm{He} + \pi^+$ at proton kinetic energies of 300–600 MeV in the laboratory frame is 10–15 μb/sr in the reaction c.m. frame at small angles of $(\pi^+,\,{}^4\mathrm{He})$ emission.

the fermions (that is, from the state with zero total spin) are forbidden if the product of the intrinsic parities of the initial particles is opposite in sign to the product of the intrinsic parities of the final particles [11–13]. Since the reaction $p + {}^3\mathrm{He} \longrightarrow \pi^+ + {}^4\mathrm{He}$ belongs to the above type (π^+ is a pseudoscalar meson, ^{4}He is a spinless nucleus, and the proton and ^{3}He nucleus are spin-1/2 objects), it can occur only if the total spin of the (p, ^{3}He) system is equal to unity.

Let us choose the z axis, the axis of total-spin quantization, along the direction of the vector $\mathbf{l} = \mathbf{k}_p/k_p$, where $\mathbf{k}_p$ is proton momentum in the reaction c.m. frame. We take the remaining two axes, x and y, to be aligned with the directions of, respectively, the unit vectors $\mathbf{m}$ and $\mathbf{n}$ given by expressions (1) with $\mathbf{l}' = \mathbf{k}_\pi/k_\pi$, where $\mathbf{k}_\pi$ is the π^+-meson momentum in the c.m. frame. The triplet states of the (p, ^{3}He) system that are characterized by the spin projections onto the quantization axis of +1, –1, and 0 are given by

$$
\begin{aligned}
|+1, \mathbf{l}\rangle &= |+1/2, \mathbf{l}\rangle^{(p)}|+1/2, \mathbf{l}\rangle^{(\mathrm{He})},\\
|-1, \mathbf{l}\rangle &= |-1/2, \mathbf{l}\rangle^{(p)}|-1/2, \mathbf{l}\rangle^{(\mathrm{He})},\\
|0, \mathbf{l}\rangle &= \frac{1}{\sqrt{2}}(|+1/2, \mathbf{l}\rangle^{(p)}|-1/2, \mathbf{l}\rangle^{(\mathrm{He})}\\
&\quad + |-1/2, \mathbf{l}\rangle^{(p)}|+1/2, \mathbf{l}\rangle^{(\mathrm{He})}).
\end{aligned}
\tag{16}
$$

Let $\mathbf{P}^{(p)}$ and $\mathbf{P}^{(\mathrm{He})}$ be independent polarization vectors of the proton and the ^{3}He nucleus, respectively. The two-particle spin density matrix for the initial state can then be represented in the form of the tensor product of the single-particle spin density matrices for the proton and the ^{3}He nucleus; that is,

$$
\begin{aligned}
&\hat{\rho}^{(p,\mathrm{He})}\\
&= \frac{1}{4}(\hat{I}^{(p)} + \mathbf{P}^{(p)}\cdot\hat{\boldsymbol{\sigma}}^{(p)}) \otimes (\hat{I}^{(\mathrm{He})} + \mathbf{P}^{(\mathrm{He})}\cdot\hat{\boldsymbol{\sigma}}^{(\mathrm{He})}).
\end{aligned}
\tag{17}
$$

We denote by $R_\lambda(E, \theta)$ the expression in the c.m. frame for the amplitude of the direct reaction $p + {}^3\mathrm{He} \longrightarrow \pi^+ + {}^4\mathrm{He}$ proceeding from the $|\lambda, \mathbf{l}\rangle$ state. Here, E is the total energy of the proton and the ^{3}He nucleus in the c.m. frame; θ is the angle between the vectors $\mathbf{k}_p$ and $\mathbf{k}_\pi$; and the parameter λ can take values of +1, –1, and 0. In this case, the differential cross section for the reaction $p + {}^3\mathrm{He} \longrightarrow \pi^+ + {}^4\mathrm{He}$ has the form

$$
\begin{aligned}
&\sigma_{p + {}^3\mathrm{He} \to \pi^+ + {}^4\mathrm{He}}(\mathbf{k}_p, \mathbf{P}^{(p)}, \mathbf{P}^{(\mathrm{He})}; \mathbf{k}_\pi)\\
&= \sum_\lambda \sum_{\lambda'} R_\lambda(E, \theta)\langle\lambda, \mathbf{l}|\hat{\rho}^{(p,\mathrm{He})}|\lambda', \mathbf{l}\rangle R^*_{\lambda'}(E, \theta)\\
&= \langle\Psi|\hat{\rho}^{(p,\mathrm{He})}|\Psi\rangle,
\end{aligned}
\tag{18}
$$

where

$$
|\Psi\rangle = \sum_{\lambda = \pm 1, 0} R^*_\lambda(E, \theta)|\lambda, \mathbf{l}\rangle \tag{19}
$$

has the meaning of the unnormalized initial two-particle spin state that is selected by the reaction being studied.

If we consider that, for the particles participating in the process $p + {}^3\mathrm{He} \longrightarrow \pi^+ + {}^4\mathrm{He}$, the product of the intrinsic parities is $\eta = -1$ and that the total spins of these particles in the initial and the final state are, respectively, 1 and 0, parity conservation leads to the equality

$$
R_\lambda(E, \theta) = (-1)^{|\lambda|} R_{-\lambda}(E, \theta), \tag{20}
$$

which can be derived easily by using the formalism of helicity amplitudes [14, 15]. Thus, we have

$$
R_{+1}(E, \theta) = -R_{-1}(E, \theta) \equiv R_1(E, \theta). \tag{21}
$$

From relations (19) and (21), it follows that the reaction $p + {}^3\mathrm{He} \longrightarrow \pi^+ + {}^4\mathrm{He}$ can proceed only from the $|+1, \mathbf{n}\rangle$ and $|-1, \mathbf{n}\rangle$ triplet states of the initial system that are characterized by the total-spin projections onto the normal to the reaction plane that are equal to +1 and –1. We then have

$$
\begin{aligned}
|\Psi\rangle &= \left(R^*_1(E, \theta) - \frac{i}{\sqrt{2}}R^*_0(E, \theta)\right)|+1, \mathbf{n}\rangle\\
&\quad + \left(R^*_1(E, \theta) + \frac{i}{\sqrt{2}}R^*_0(E, \theta)\right)|-1, \mathbf{n}\rangle.
\end{aligned}
\tag{22}
$$

The states $|\lambda, \mathbf{n}\rangle$ with the total-spin projections onto the normal to the reaction plane that take the values of $\lambda = \pm 1, 0$ represent orthogonal superpositions of the triplet states in (16); that is,

$$
\begin{aligned}
|+1, \mathbf{n}\rangle &= \frac{1}{2}|+1, \mathbf{l}\rangle + \frac{i}{\sqrt{2}}|0, \mathbf{l}\rangle - \frac{1}{2}|-1, \mathbf{l}\rangle,\\
|-1, \mathbf{n}\rangle &= \frac{1}{2}|+1, \mathbf{l}\rangle - \frac{i}{\sqrt{2}}|0, \mathbf{l}\rangle - \frac{1}{2}|-1, \mathbf{l}\rangle,\\
|0, \mathbf{n}\rangle &= \frac{i}{\sqrt{2}}(|+1, \mathbf{l}\rangle + |-1, \mathbf{l}\rangle).
\end{aligned}
\tag{23}
$$

It should be emphasized that the result presented in (22) is consistent with the well-known rule of A. Bohr [15],

$$
\eta = (-1)^{M - M'}.
$$

Here, η is the product of the intrinsic parities of four particles participating in the binary reaction, while M and M' are the projections of the total spin in the initial and final states onto the normal to the reaction plane.

The expansion of the amplitude $R_\lambda(E, \theta)$ in the total angular momenta has the form

$$R_\lambda(E, \theta) = \sum_J (2J+1)\gamma^{(J)}(E) d^{(J)}_{0\lambda}(\theta),$$

where $d^{(J)}_{0\lambda}(\theta)$ are Wigner functions (see, for example, [15]). We have $|d^{(J)}_{0\lambda}(\theta)| \sim \theta^{|\lambda|}$ for very small angles and $|d^{(J)}_{0\lambda}(\theta)| \sim \Delta\theta^{|\lambda|}$ for $\Delta\theta = (\pi - \theta) \ll 1$. Thus, we see that, both for $\theta \longrightarrow 0$ and for $\theta \longrightarrow \pi$, the amplitude $R_1(E, \theta)$ vanishes, which corresponds to the conservation of the angular-momentum projection onto the reaction axis.

In order to calculate the differential cross section for the reaction $p + {}^3\mathrm{He} \longrightarrow \pi^+ + {}^4\mathrm{He}$ by formula (18), we will first find the expectation values of the Pauli matrices and of their tensor products in the two-particle spin state $|\Psi\rangle$. Taking into account equations (16) and (21), we can recast expression (19) for $|\Psi\rangle$ into the form

$$\begin{aligned}|\Psi\rangle &= R_1^*(E, \theta)(|+1/2, z\rangle^{(p)}|+1/2, z\rangle^{(\mathrm{He})} \\ &\quad - |-1/2, z\rangle^{(p)}|-1/2, z\rangle^{(\mathrm{He})}) \\ &+ \frac{1}{\sqrt{2}} R_0^*(E, \theta)(|+1/2, z\rangle^{(p)}|-1/2, z\rangle^{(\mathrm{He})} \\ &\quad + |-1/2, z\rangle^{(p)}|+1/2, z\rangle^{(\mathrm{He})}),\end{aligned} \tag{24}$$

where the z axis coincides with the reaction axis $\mathbf{l}$ (see above). By using the explicit form of the Pauli matrices, it can be shown easily that the following relations hold:

$$\begin{aligned}\langle\Psi|\hat\sigma_z^{(p)} \otimes \hat I^{(\mathrm{He})}|\Psi\rangle &= \langle\Psi|\hat I^{(p)} \otimes \hat\sigma_z^{(\mathrm{He})}|\Psi\rangle \\ = \langle\Psi|\hat\sigma_x^{(p)} \otimes \hat I^{(\mathrm{He})}|\Psi\rangle &= \langle\Psi|\hat I^{(p)} \otimes \hat\sigma_x^{(\mathrm{He})}|\Psi\rangle = 0, \\ \langle\Psi|\hat\sigma_y^{(p)} \otimes \hat I^{(\mathrm{He})}|\Psi\rangle &= \langle\Psi|\hat I^{(p)} \otimes \hat\sigma_y^{(\mathrm{He})}|\Psi\rangle \\ &= 2\sqrt{2}\,\mathrm{Im}(R_1(E, \theta)R_0^*(E, \theta));\end{aligned} \tag{25}$$

$$\begin{aligned}\langle\Psi|\hat\sigma_z^{(p)} \otimes \hat\sigma_z^{(\mathrm{He})}|\Psi\rangle &= 2|R_1(E, \theta)|^2 - |R_0(E, \theta)|^2, \\ \langle\Psi|\hat\sigma_x^{(p)} \otimes \hat\sigma_x^{(\mathrm{He})}|\Psi\rangle &= -2|R_1(E, \theta)|^2 + |R_0(E, \theta)|^2, \\ \langle\Psi|\hat\sigma_y^{(p)} \otimes \hat\sigma_y^{(\mathrm{He})}|\Psi\rangle &= 2|R_1(E, \theta)|^2 + |R_0(E, \theta)|^2;\end{aligned} \tag{26}$$

$$\begin{aligned}\langle\Psi|\hat\sigma_x^{(p)} \otimes \hat\sigma_y^{(\mathrm{He})}|\Psi\rangle &= \langle\Psi|\hat\sigma_y^{(p)} \otimes \hat\sigma_x^{(\mathrm{He})}|\Psi\rangle \\ = \langle\Psi|\hat\sigma_z^{(p)} \otimes \hat\sigma_y^{(\mathrm{He})}|\Psi\rangle &= \langle\Psi|\hat\sigma_y^{(p)} \otimes \hat\sigma_z^{(\mathrm{He})}|\Psi\rangle = 0, \\ \langle\Psi|\hat\sigma_z^{(p)} \otimes \hat\sigma_x^{(\mathrm{He})}|\Psi\rangle &= \langle\Psi|\hat\sigma_x^{(p)} \otimes \hat\sigma_z^{(\mathrm{He})}|\Psi\rangle \\ &= 2\sqrt{2}\,\mathrm{Re}(R_1(E, \theta)R_0^*(E, \theta)).\end{aligned} \tag{27}$$

Substituting (17) and (24)–(27) into expression (18) for the effective cross section for the reaction $p + {}^3\mathrm{He} \longrightarrow \pi^+ + {}^4\mathrm{He}$ and considering that the relations $\hat\sigma_z = \hat{\boldsymbol\sigma} \cdot \mathbf{l}$, $\hat\sigma_x = \hat{\boldsymbol\sigma} \cdot \mathbf{m}$, and $\hat\sigma_y = \hat{\boldsymbol\sigma} \cdot \mathbf{n}$ hold by definition, we arrive at the structural formula (2), where the proton, the ^{3}He nucleus, the π^+ meson, and the ^{4}He nucleus play the roles of particles a, b, c, and d, respectively, and where the functions σ_0, A, B, C, etc., appear to be bilinear combinations of the amplitudes $R_1(E, \theta)$ and $R_0(E, \theta)$:

$$\begin{aligned}\sigma_0(E, \theta) &= \frac{1}{4}\langle\Psi|\Psi\rangle = \frac{1}{4}(|R_0(E, \theta)|^2 + 2|R_1(E, \theta)|^2), \\ A(E, \theta) &= B(E, \theta) \\ &= \frac{1}{\sqrt{2}\sigma_0(E, \theta)}\mathrm{Im}(R_1(E, \theta)R_0^*(E, \theta)), \\ C(E, \theta) &= 1; \quad D(E, \theta) = -\frac{|R_0(E, \theta)|^2}{2\sigma_0(E, \theta)}, \\ F(E, \theta) &= -\frac{|R_1(E, \theta)|^2}{\sigma_0(E, \theta)}, \\ G(E, \theta) &= H(E, \theta) \\ &= \frac{1}{\sqrt{2}\sigma_0(E, \theta)}\mathrm{Re}(R_1(E, \theta)R_0^*(E, \theta)).\end{aligned} \tag{28}$$

At $\theta = 0$ and $\theta = \pi$, the amplitude $R_1(E, \theta)$ vanishes, and the dependence of the effective cross section for the reaction $p + {}^3\mathrm{He} \longrightarrow \pi^+ + {}^4\mathrm{He}$ on the polarization vectors of the proton and the ^{3}He nucleus takes the much simpler form [2, 6]

$$\begin{aligned}\sigma_{p + {}^3\mathrm{He} \to \pi^+ + {}^4\mathrm{He}} &= \frac{1}{4}|R_0|^2(1 + (\mathbf{P}^{(p)} \cdot \mathbf{P}^{(\mathrm{He})}) \\ &\quad - 2(\mathbf{P}^{(p)} \cdot \mathbf{l})(\mathbf{P}^{(\mathrm{He})} \cdot \mathbf{l})).\end{aligned} \tag{29}$$

Let us integrate the effective cross section for the reaction $p + {}^3\mathrm{He} \longrightarrow \pi^+ + {}^4\mathrm{He}$ with respect to the azimuthal angle. Taking into account relations (6) and (28), we obtain (see also [6])

$$\begin{aligned}\sigma_{p + {}^3\mathrm{He} \to \pi^+ + {}^4\mathrm{He}}(E, \theta, \mathbf{P}^{(p)}, \mathbf{P}^{(\mathrm{He})}) &= \frac{\pi}{2}|R_0(E, \theta)|^2 \\ &\times (1 + (\mathbf{P}^{(p)} \cdot \mathbf{P}^{(\mathrm{He})}) - 2(\mathbf{P}^{(p)} \cdot \mathbf{l})(\mathbf{P}^{(\mathrm{He})} \cdot \mathbf{l})) \\ &+ \pi|R_1(E, \theta)|^2(1 + (\mathbf{P}^{(p)} \cdot \mathbf{l})(\mathbf{P}^{(\mathrm{He})} \cdot \mathbf{l})).\end{aligned} \tag{30}$$

We can see that, in the effective cross section for the reaction in question, the terms that are proportional to $A(E, \theta)$, $B(E, \theta)$, $G(E, \theta)$, and $H(E, \theta)$ and which correspond to the interference of states characterized by different total-spin projections onto the momentum direction vanish upon integration with respect to azimuthal angle. It is obvious that the total reaction cross section has the same structure (30).

4. Let us now address the inverse reaction $\pi^+ + {}^4\mathrm{He} \longrightarrow p + {}^3\mathrm{He}$. In this reaction, a transition to the singlet ground state is forbidden, and the total spin of the (p, ^{3}He) system is equal to unity. We retain the notation $\mathbf{k}_p$ and $\mathbf{k}_\pi$ for the proton and π^+-meson momenta in the reaction c.m. frame and choose the z axis, the quantization axis for the total spin of the (p, ^{3}He) system, to be aligned with the direction of the final-proton momentum $\mathbf{k}_p$. We further introduce the same set of mutually orthogonal unit vectors as in the case of the direct reaction $p + {}^3\mathrm{He} \longrightarrow \pi^+ + {}^4\mathrm{He}$—that is, the same vectors $\mathbf{l} = \mathbf{k}_p/k_p$, $\mathbf{m}$, and $\mathbf{n}$ given by equations (1) with $\mathbf{l}' = \mathbf{k}_\pi/k_\pi$.

Taking into account the general relations (8)–(12), which follow from T invariance, and expressions (28) for the functions that determine the spin dependence of the effective cross section for the process $p + {}^3\mathrm{He} \longrightarrow \pi^+ + {}^4\mathrm{He}$, we find that the quantity obtained by summing the effective cross section for the reaction $\pi^+ + {}^4\mathrm{He} \longrightarrow p + {}^3\mathrm{He}$ in the c.m. frame over the spin projections in the final state can be represented as

$$\sigma_{\pi^+ + {}^4\mathrm{He} \to p + {}^3\mathrm{He}} = (k_p^2/k_\pi^2)(|R_0(E,\theta)|^2 + 2|R_1(E,\theta)|^2). \tag{31}$$

For the polarization parameters of the (p, ^{3}He) system, calculations along similar lines yield

$$\mathbf{P}^{(p)}(E,\theta) = \mathbf{P}^{(\mathrm{He})}(E,\theta) = -2\sqrt{2}\frac{\mathrm{Im}(R_1(E,\theta)R_0^*(E,\theta))}{|R_0(E,\theta)|^2 + 2|R_1(E,\theta)|^2}\mathbf{n}, \tag{32}$$

$$T_{ik}(E,\theta) = \delta_{ik} - \frac{2}{|R_0(E,\theta)|^2 + 2|R_1(E,\theta)|^2} \times [|R_0(E,\theta)|^2 l_i l_k + 2|R_1(E,\theta)|^2 m_i m_k - \sqrt{2}\mathrm{Re}(R_1(E,\theta)R_0^*(E,\theta))(l_i m_k + m_i l_k)], \tag{33}$$

where l_i and l_k (m_i and m_k) are, as before, the components of the vector $\mathbf{l}$ ($\mathbf{m}$).

In the above expressions, $R_0(E,\theta)$ and $R_1(E,\theta)$ are the same amplitudes as those for the process $p + {}^3\mathrm{He} \longrightarrow \pi^+ + {}^4\mathrm{He}$, E and θ being, respectively, as before, the total energy and the angle between the π^+-meson and proton 3-momenta in the reaction c.m. frame. According to (32) and (33), the polarization of the ^{3}He nucleus along the normal to the reaction plane is identical to that of the proton, and the tensor $T_{ik}(E,\theta)$, which describes spin correlations in the (p, ^{3}He) system, is symmetric. This is because the (p, ^{3}He) system is produced in a specific triplet state symmetric under the interchange of the spin quantum numbers of the proton and the ^{3}He nucleus. As functions of the energy E and the proton emission angle θ in the c.m. frame, this spin state, normalized to unity and obtained by taking into account relations (21), has the form

$$|\tilde{\Psi}\rangle = \frac{1}{(|R_0(E,\theta)|^2 + 2|R_1(E,\theta)|^2)^{1/2}} \times [R_1(E,\theta)(|+1/2,\mathbf{l}\rangle^{(p)}|+1/2,\mathbf{l}\rangle^{(\mathrm{He})} - |-1/2,\mathbf{l}\rangle^{(p)}|-1/2,\mathbf{l}\rangle^{(\mathrm{He})}) + \frac{1}{\sqrt{2}}R_0(E,\theta)(|+1/2,\mathbf{l}\rangle^{(p)}|-1/2,\mathbf{l}\rangle^{(\mathrm{He})} + |-1/2,\mathbf{l}\rangle^{(p)}|+1/2,\mathbf{l}\rangle^{(\mathrm{He})})]. \tag{34}$$

This expression corresponds to a superposition of those states in (23) that are characterized by the total-spin projections onto the normal to the reaction plane that are equal to +1 and –1:

$$|\tilde{\Psi}\rangle = \frac{1}{(|R_0(E,\theta)|^2 + 2|R_1(E,\theta)|^2)^{1/2}} \times \left[\left(R_1(E,\theta) - \frac{i}{\sqrt{2}}R_0(E,\theta)\right)|+1,\mathbf{n}\rangle + \left(R_1(E,\theta) + \frac{i}{\sqrt{2}}R_0(E,\theta)\right)|-1,\mathbf{n}\rangle\right]. \tag{35}$$

In contrast to expressions (22) and (24), which feature complex-conjugate amplitudes $R_0^*(E,\theta)$ and $R_1^*(E,\theta)$ and which describe the initial spin state $|\Psi\rangle$ that is selected by the reaction $p + {}^3\mathrm{He} \longrightarrow \pi^+ + {}^4\mathrm{He}$, expressions (34) and (35) refer to the final state in the time-inverted process $\pi^+ + {}^4\mathrm{He} \longrightarrow p + {}^3\mathrm{He}$.

By virtue of relations (34) and (35), the spins of the proton and the ^{3}He nucleus in the reaction $\pi^+ + {}^4\mathrm{He} \longrightarrow p + {}^3\mathrm{He}$ must be tightly correlated. In principle, this offers the possibility for preparing a beam of ^{3}He nuclei with a controllable spin polarization without applying brute force to this nuclei [2]. In order to demonstrate this explicitly, we will consider a proton that is produced in the reaction $\pi^+ + {}^4\mathrm{He} \longrightarrow p + {}^3\mathrm{He}$ and which is then scattered on a spinless or an unpolarized target (say, on a ^{12}C nucleus), the corresponding analyzing power being characterized by the vector

$$\boldsymbol{\zeta}^{(p)} = \alpha_p(\mathbf{k}_p,\theta_p)\mathbf{t}^{(p)}, \tag{36}$$

where $\alpha_p(\mathbf{k}_p,\theta_p)$ is the left–right asymmetry dependent on the secondary-scattering angle θ_p, while $\mathbf{t}^{(p)}$ is the unit vector aligned with the normal to the scattering plane [16]. The spin state of the unscattered ^{3}He nucleus formed in association with the scattered proton in the same event of a collision between a π^+ meson and a ^{4}He nucleus will then depend on the proton analyzing power.

The components of the polarization vector of the ^{3}He nucleus are determined by expression (13), where $\boldsymbol{\zeta}^{(a)}$, $\mathbf{P}^{(b)}$, $\mathbf{P}^{(a)}$, and $T_{ik}(E,\theta)$ are now taken to mean,

respectively, the proton analyzing power (36), the polarization vector of the ^{3}He nucleus, the proton polarization vector in the absence of secondary scattering [see expression (32)], and the correlation tensor (33).

The case where either the proton or the ^{3}He nucleus is emitted at zero angle with respect to the reaction axis was analyzed previously in [2, 4]. At $\theta = 0$, the proton and the ^{3}He nucleus are both produced in an unpolarized state, while the correlation tensor assumes the form

$$T_{ik}(E, \theta) = \delta_{ik} - 2l_i l_k. \quad (37)$$

If the proton is scattered on a target formed by ^{12}C nuclei, the ^{3}He nucleus produced in association with it appears to be polarized owing to spin correlation:

$$\tilde{\mathbf{P}}^{(\mathrm{He})} = \alpha_p(E_p, \theta_p)(\mathbf{t}^{(p)} - 2\mathbf{l}(\mathbf{l} \cdot \mathbf{t}^{(p)})). \quad (38)$$

In this case, we have $\left|\tilde{\mathbf{P}}^{(\mathrm{He})}\right| = |\alpha_p(E_p, \theta_p)|$, which corresponds to the maximal spin correlation.

ACKNOWLEDGMENTS

This work was supported by the Russian Foundation for Basic Research (project no. 97-02-16699).

REFERENCES

1. V. V. Lyuboshitz and V. L. Lyuboshitz, Preprint No. R4-98-88, JINR (Dubna, 1998); Yad. Fiz. **62**, 1404 (1999) [Phys. At. Nucl. **62**, 1323 (1999)].
2. V. L. Lyuboshitz and M. I. Podgoretsky, Yad. Fiz. **60**, 45 (1997) [Phys. At. Nucl. **60**, 39 (1997)].
3. L. D. Landau and E. M. Lifshitz, *Quantum Mechanics: Non-Relativistic Theory* (3rd ed., Pergamon, Oxford, 1977; 4th ed., Nauka, Moscow, 1989).
4. V. L. Lyuboshitz, Preprint No. E2-98-274, JINR (Dubna, 1998).
5. A. Einstein, B. Podolsky, and N. Rosen, Phys. Rev. **47**, 477 (1935); A. Einstein, in *Collected Works* (Moscow, Nauka, 1966), Vol. 3, p. 604.
6. V. L. Lyuboshitz, Preprint No. E2-93-397, JINR (Dubna, 1993); in *Proceedings of the International Symposium, Dubna, Deuteron-93* (JINR, Dubna, 1994), No. E2-94-95, p. 292.
7. K. Cabathuler *et al.*, Nucl. Phys. B **40**, 32 (1972).
8. B. Tatischeff *et al.*, Phys. Lett. B **63**, 158 (1976).
9. B. Höistad *et al.*, Phys. Rev. C **29**, 553 (1984).
10. J. Kallne, Phys. Rev. C **28**, 304 (1983).
11. S. M. Bylenky and R. M. Ryndin, Phys. Lett. **6**, 217 (1963).
12. S. M. Bylenky and R. M. Ryndin, Zh. Éksp. Teor. Fiz. **45**, 1192 (1963) [Sov. Phys. JETP **18**, 823 (1963)].
13. V. L. Lyuboshitz, Yad. Fiz. **12**, 199 (1970) [Sov. J. Nucl. Phys. **12**, 107 (1970)].
14. M. Yacob and G. C. Wick, Ann. Phys. (N.Y.) **7**, 404 (1959).
15. A. M. Baldin, V. I. Goldanskiĭ, and I. L. Rosental', *Kinematics of Nuclear Reactions*, Transl. of 1st Russ. ed. (Oxford Univ. Press, London, 1961; 2nd ed., Atomizdat, Moscow, 1968) [The 2nd Russ. ed. has an additional author V. M. Maksimenko].
16. L. Wolfenstein and J. Ashkin, Phys. Rev. **85**, 947 (1952).

Translated by A. Isaakyan

Physics of Atomic Nuclei, Vol. 63, No. 5, 2000, pp. 774–781. From Yadernaya Fizika, Vol. 63, No. 5, 2000, pp. 844–851.

NUCLEI
Theory

Sensitivity of Polarization Observables in Elastic *ed* Scattering to the Neutron Form Factors*

S. G. Bondarenko, V. V. Burov***, and S. M. Dorkin[1)]**

Joint Institute for Nuclear Research, Dubna, Moscow oblast, 141980 Russia

Received April 14, 1999

Abstract—The deuteron elastic form factors are calculated within the Bethe–Salpeter approach with separable interaction. The charge, quadrupole, and magnetic form factors [$F_C(q^2)$, $F_Q(q^2)$, and $F_M(q^2)$, respectively]; the structure functions $A(q^2)$ and $B(q^2)$; and the tensor polarization components $T_{20}(q^2)$, $T_{21}(q^2)$, and $T_{22}(q^2)$ are investigated up to $-q^2 = 50$ fm^{-2}. The role of relativistic effects is discussed, and a comparison with nonrelativistic calculations is performed. The effect of the neutron form factors on the deuteron form factors and especially on tensor polarization components is discussed too. © *2000 MAIK "Nauka/Interperiodica".*

1. INTRODUCTION

The deuteron electromagnetic form factors provide a direct way to study the properties of *NN* interaction and the electromagnetic characteristics of nucleons. These investigations are of great interest nowadays, especially in the context of relativistic treatment. The traditional nonrelativistic approach is based on the nonrelativistic impulse approximation with allowance for relativistic corrections, meson-exchange currents (MEC), and retardation effects. In [1–4] (for details, see [2]), it was shown that taking correctly into account these effects is necessary for describing experimental data. Generally, the deuteron elastic form factors are very sensitive to the choice of strong vertex form factors and to the way in which MECs are introduced. On the other hand, recent relativistic investigations of deuteron electrodisintegration show [5] that some of the MECs (in particular, the pair current) are automatically included in the relativistic impulse approximation. Apparently, this is valid for elastic electron–deuteron scattering as well. Therefore, a consistent relativistic approach even in the relativistic impulse approximation can reproduce the results of a nonrelativistic treatment with some of the MECs.

Recent experimental data at high-momentum transfers [6, 7] and the planned TJNAF (CEBAF) experiments E91-029 and E94-018 furnish different arguments for a consistent relativistic treatment because of the importance of relativistic effects in the high-momentum-transfer range.

Nowadays, several relativistic approaches to elastic electron–deuteron scattering are known; some of them are the quasipotential approach [8], light-front dynamics, and the approach based on the Bethe–Salpeter equation. The third was developed in [9], where the importance of various relativistic effects was shown. The first takes into account the effect coming from a Lorentz transformation of Bethe–Salpeter amplitudes and their arguments. Another one is the contribution of negative-energy states in the deuteron Bethe–Salpeter amplitude.

Another interesting aspect of the investigation of the deuteron elastic form factors is the effect of the nucleon form factors on the deuteron form factors. Theoretical and phenomenological models yield different sets of the on-shell nucleon form factors $G_E(q^2)$ and $G_M(q^2)$. Some models predict a nonzero neutron electric form factor. If some of the observables in elastic electron–deuteron scattering depend sizably on the nucleon form factors, then this could be a test for nucleon-form-factor models. If, on the other hand, there is no appreciable dependence on the nucleon form factor, this could be a test for *NN*-interaction dynamics or other effects.

The main goal of this study is to analyze relativistic effects and the influence of the nucleon form factors in elastic electron–deuteron scattering, especially for polarization observables.

The article is organized as follows. After basic formulas are given for kinematics and for cross sections in Section 2, the decomposition of the Bethe–Salpeter amplitude and the *NN* potential is discussed in Section 3. In Section 4, formulas for the deuteron-current matrix element in the relativistic impulse approximation are given, and the technique of analytic calculations is described. The results of our numerical calculations and the discussion of these results are presented in Section 5.

2. RELATIVISTIC KINEMATICS

The differential cross section for unpolarized elastic electron–deuteron scattering is expressed in terms of

* This article was submitted by the authors in English.

** e-mail: bondaren@thsun1.jinr.ru

*** e-mail: burov@thsun1.jinr.ru

[1)] Far Eastern State University, Vladivostok, 690000, Russia.

the Mott cross section and the deuteron structure functions (the electron mass is neglected) as

$$\frac{d\sigma}{d\Omega_e'} = \left(\frac{d\sigma}{d\Omega_e'}\right)_{\text{Mott}} \left[A(q^2) + B(q^2)\tan^2\frac{\theta_e}{2}\right]. \quad (1)$$

Here, θ_e is the electron scattering angle;

$$\left(\frac{d\sigma}{d\Omega_e'}\right)_{\text{Mott}} = \frac{\alpha^2\cos^2\theta_e/2}{4E_e^2(1 + 2E_e/M\sin^4\theta_e/2)}, \quad (2)$$

where M is the deuteron mass and E_e is the incident-electron energy; and

$$A(q^2) = F_C^2(q^2) + \frac{8}{9}\eta^2F_Q^2(q^2) + \frac{2}{3}\eta F_M^2(q^2),$$
$$B(q^2) = \frac{4}{3}\eta(1 + \eta)F_M^2(q^2), \quad (3)$$

with $\eta = -q^2/4M^2$. The electric $[F_C(q^2)]$, quadrupole $[F_Q(q^2)]$, and magnetic $[F_M(q^2)]$ form factors are normalized as

$$F_C(0) = 1, \quad F_Q(0) = M^2Q_d, \quad F_M(0) = \mu_d\frac{M}{m}, \quad (4)$$

where m is the nucleon mass, while Q_d and μ_d are, respectively, the quadrupole and the magnetic moment of the deuteron. The components of the tensor polarization of the final deuteron in this reaction are expressed in terms of the deuteron form factors as

$$T_{20}\left[A + B\tan^2\frac{\theta_e}{2}\right] = -\frac{1}{\sqrt{2}}\left\{\frac{8}{3}\eta F_CF_Q + \frac{8}{9}\eta^2F_Q^2 + \frac{1}{3}\eta\left(1 + 2(1 + \eta)\tan^2\frac{\theta_e}{2}\right)F_M^2\right\},$$

$$T_{21}\left[A + B\tan^2\frac{\theta_e}{2}\right] = \frac{2}{\sqrt{3}}\eta\left(\eta + \eta^2\sin^2\frac{\theta_e}{2}\right)^{1/2}F_MF_Q\sec\frac{\theta_e}{2}, \quad (5)$$

$$T_{22}\left[A + B\tan^2\frac{\theta_e}{2}\right] = -\frac{1}{2\sqrt{3}}\eta F_M^2.$$

Equation (1) is due to the one-photon approximation and can be obtained, by using the standard technique [10], from the reaction amplitude

$$M_{\text{fi}} = ie^2\bar{u}_{m'}(k_e')\gamma^\mu u_m(k_e)\frac{1}{q^2}\langle D'\mathcal{M}'|j_\mu|D\mathcal{M}\rangle, \quad (6)$$

where $u_m(k_e)$ is the free-electron spinor for a 4-momentum k_e and a spin projection m; $q = k_e - k_e' = P' - P$ is the 4-momentum transfer, $P(P')$ being the initial (final) deuteron momentum; $|D\mathcal{M}\rangle$ is the deuteron state characterized by the total-angular-momentum projection $\mathcal{M}$; and j_μ is the electromagnetic-current operator.

The deuteron-current matrix element is usually parametrized as

$$\langle D'\mathcal{M}'|j_\mu|D\mathcal{M}\rangle = -\xi^*_{\alpha\mathcal{M}'}(P')\xi_{\beta\mathcal{M}}(P) \times\left\{(P' + P)_\mu\left[g^{\alpha\beta}F_1(q^2) - \frac{q^\alpha q^\beta}{2M^2}F_2(q^2)\right] - (q^\alpha g_\mu^\beta - q^\beta g_\mu^\alpha)G_1(q^2)\right\}, \quad (7)$$

where $\xi_{\mathcal{M}}(P)$ and $\xi^*_{\mathcal{M}'}(P')$ are the polarization 4-vectors of the initial and the final deuteron, respectively. The form factors $F_{1,2}(q^2)$ and $G_1(q^2)$ are related to $F_C(q^2)$, $F_Q(q^2)$, and $F_M(q^2)$ by the equations

$$F_C = F_1 + \frac{2}{3}\eta[F_1 + (1 + \eta)F_2 - G_1],$$
$$F_Q = F_1 + (1 + \eta)F_2 - G_1, \quad F_M = G_1.$$

The normalization condition for the deuteron-current matrix element has the form

$$\lim_{q^2\to 0}\langle D'\mathcal{M}'|j_\mu|D\mathcal{M}\rangle = 2P_\mu\delta_{\mathcal{M}\mathcal{M}'}.$$

To calculate the deuteron form factors, we must use a particular reference frame. In the laboratory frame, the 4-vectors are given by (the z axis is directed along the photon momentum)

$$P = (M, \mathbf{0}), \quad P' = [M(1 + 2\eta), 0, 0, 2\sqrt{\eta}\sqrt{1 + \eta}],$$
$$q = [2M\eta, 0, 0, 2M\sqrt{\eta}\sqrt{1 + \eta}], \quad (8)$$

$$\xi_{\mathcal{M}=+1}(P) = \xi_{\mathcal{M}=+1}(P') = -\frac{1}{\sqrt{2}}(0, 1, i, 0),$$
$$\xi_{\mathcal{M}=-1}(P) = \xi_{\mathcal{M}=-1}(P') = \frac{1}{\sqrt{2}}(0, 1, -i, 0),$$
$$\xi_{\mathcal{M}=0}(P) = (0, 0, 0, 1), \quad (9)$$
$$\xi_{\mathcal{M}=0}(P') = (2\sqrt{\eta}\sqrt{1 + \eta}, 0, 0, 1 + 2\eta).$$

Using expressions (9) and the parametrization in (7), we can obtain

$$\langle\mathcal{M}'|j_0|\mathcal{M}\rangle = 2M(1 + \eta) \times\{F_1\delta_{\mathcal{M}\mathcal{M}'} + 2\eta[F_1 + (1 + \eta)F_2 - G_1]\delta_{\mathcal{M}'0}\delta_{\mathcal{M}0}\}, \quad (10)$$

$$\langle\mathcal{M}'|j_x|\mathcal{M}\rangle = \frac{2M}{\sqrt{2}}\sqrt{\eta}\sqrt{1 + \eta}G_1(\delta_{\mathcal{M}'\mathcal{M}+1} - \delta_{\mathcal{M}'\mathcal{M}-1}).$$

To calculate the deuteron form factors, we must therefore know three matrix elements with different total-angular-momentum projections and current components.

3. BETHE–SALPETER AMPLITUDE

3.1. Partial-Wave Decomposition

The main object of the approach used is the Bethe–Salpeter amplitude (or wave function), which is usually decomposed into the sum of direct products of free Dirac spinors. Since the Bethe–Salpeter equation is solved in the rest frame, the decomposition of the Bethe–Salpeter amplitude can be represented as

$$\chi_{\mathcal{M}}(P, p) = \sum_{\alpha} \phi_{\alpha}(p_0, |\mathbf{p}|)\Gamma^{\alpha}_{\mathcal{M}}(\mathbf{p}), \tag{11}$$

where P is the total momentum of the system [in the rest frame, we have $P = (M, \mathbf{0})$] and $p = (p_0, \mathbf{p})$ is the relative momentum. The decomposition is performed in terms of quantum numbers—namely, the relative orbital angular momentum L, the total spin S, and the ρ spin briefly denoted by α [11]. The radial components of the amplitude are denoted by $\phi_{\alpha}(p_0, |\mathbf{p}|)$, and the spin–angular-momentum components are $\Gamma^{\alpha}_{\mathcal{M}}(\mathbf{p})$.

In the deuteron channel, the Bethe–Salpeter amplitude involves eight states: ${}^3S_1^{++}$, ${}^3S_1^{--}$, ${}^3D_1^{++}$, ${}^3D_1^{--}$, ${}^3P_1^{e}$, ${}^3P_1^{o}$, ${}^1P_1^{e}$, and ${}^1P_1^{o}$. Below, only the ${}^3S_1^{++}$ and ${}^3D_1^{++}$ states will be used. The radial functions for these waves will be denoted by $\phi_L(p_0, |\mathbf{p}|)$ with $L = S, D$.

In practice, however, it is more convenient to use the covariant form of the Bethe–Salpeter amplitude instead of the partial-wave decomposition (11). Introducing eight Lorentz invariant functions $h_i(Pp, p^2)$, we can write

$$\begin{aligned}\chi_{\mathcal{M}}(P, p) &= h_1\hat{\xi}_{\mathcal{M}} + h_2\frac{(p\xi_{\mathcal{M}})}{m} \\ &+ h_3\left(\frac{\hat{p}_1 - m}{m}\hat{\xi}_{\mathcal{M}} + \hat{\xi}_{\mathcal{M}}\frac{\hat{p}_2 + m}{m}\right) \\ &+ h_4\left(\frac{\hat{p}_1 + \hat{p}_2}{m}\right)\frac{(p\xi_{\mathcal{M}})}{m} + h_5\left(\frac{\hat{p}_1 - m}{m}\hat{\xi}_{\mathcal{M}} - \hat{\xi}_{\mathcal{M}}\frac{\hat{p}_2 + m}{m}\right) \\ &+ h_6\left(\frac{\hat{p}_1 - \hat{p}_2 - 2m}{m}\right)\frac{(p\xi_{\mathcal{M}})}{m} \\ &+ \frac{\hat{p}_1 - m}{m}\left(h_7\hat{\xi}_{\mathcal{M}} + h_8\frac{(p\xi_{\mathcal{M}})}{m}\right)\frac{\hat{p}_2 + m}{m},\end{aligned} \tag{12}$$

where $p_{1,2} = P/2 \pm p$.

If only the ${}^3S_1^{++}$ and ${}^3D_1^{++}$ states are taken into account, the relation between functions $h_i(Pp, p^2)$ and $\phi_L(p_0, |\mathbf{p}|)$ has the form

$$\begin{aligned}h_1 &= \frac{1}{16}a_1 D_1^-[\sqrt{2}\phi_S - \phi_D], \\ h_2 &= \frac{1}{16}a_1\left[\sqrt{2}a_3 D_3^-\phi_S + \frac{1}{m}a_2^2 D_4^+\phi_D\right], \\ h_3 &= 0, \quad h_4 = \frac{1}{4}a_1 p_0[\sqrt{2}a_3 m\phi_S - a_2^2(E_p + 2m)\phi_D], \\ h_5 &= -\frac{1}{2}a_1 m^2[\sqrt{2}\phi_S - \phi_D], \\ h_6 &= \frac{1}{8}a_1[\sqrt{2}a_3 m D_6^-\phi_S + a_2^2 D_7^+\phi_D], \\ h_7 &= \frac{1}{4}a_1 m^2[\sqrt{2}\phi_S - \phi_D], \\ h_8 &= -\frac{1}{4}a_1 m[\sqrt{2}a_3 m\phi_S - a_2^2(2E_p + m)\phi_D],\end{aligned} \tag{13}$$

where

$$\begin{aligned}&a_1 = 1/ME_p, \quad a_2 = m/|\mathbf{p}|, \quad a_3 = m/(E_p + m), \\ &D_1^{\pm} = (M \pm 2E_p)^2 - 4(4m^2 + p_0^2), \\ &D_3^{\pm} = (M \pm 2E_p \pm 4m)^2 - 4p_0^2, \\ &D_4^{\pm} = [(M \pm 2E_p)^2 - 4p_0^2](2E_p + m) - 16(m \pm M)\mathbf{p}^2, \\ &D_6^{\pm} = 4m + 2E_p \pm M, \\ &D_7^{\pm} = \pm M(E_p + 2m) + 2(2m^2 + 2mE_p - E_p^2), \\ &p_0 = \frac{(Pp)}{M}, \quad |\mathbf{p}| = \sqrt{\frac{(Pp)^2}{M^2} - p^2}, \quad E_p = \sqrt{\mathbf{p}^2 + m^2}.\end{aligned}$$

3.2. Separable Potential

It is well known from the nonrelativistic approach that, for a separable potential, the relevant integral equation (for instance, the Lippmann–Schwinger equation) reduces to a set of linear equations. For a separable potential of rank N,

$$\begin{aligned}&V_{L'L}(p_0', |\mathbf{p}'|; p_0, |\mathbf{p}|) \\ &= \sum_{i,j}^{N}\lambda_{ij}g_i^{(L')}(p_0', |\mathbf{p}'|)g_j^{(L)}(p_0, |\mathbf{p}|), \quad \lambda_{ij} = \lambda_{ji},\end{aligned} \tag{14}$$

Table 1. Parameters of the covariant Graz II potential

γ_1	28.69550	GeV^{-2}	β_{12}	5.21705×10^{-1}	GeV	γ_{11}	2.718930×10^{-4}	GeV^6	λ_{22}	16.52393	GeV^2
γ_2	64.9803	GeV^{-2}	β_{21}	7.94907×10^{-1}	GeV	γ_{12}	-7.16735×10^{-2}	GeV^4	λ_{23}	0.28606	GeV^4
β_{11}	2.31384×10^{-1}	GeV	β_{22}	1.57512×10^{-1}	GeV	λ_{13}	-1.51744×10^{-3}	GeV^6	λ_{33}	3.48589×10^{-3}	GeV^6

the radial functions of the Bethe–Salpeter amplitude are given by ($s = M^2$)

$$\phi_L(p_0, |\mathbf{p}|) = S(p_0, |\mathbf{p}|, s)\sum_{i,j=1}^{N}\lambda_{ij}g_i^{(L)}(p_0, |\mathbf{p}|)c_j(s),$$

$$S(p_0, |\mathbf{p}|, s) \tag{15}$$

$$= [(\sqrt{s}/2 + p_0 - E_p + i\epsilon)(\sqrt{s}/2 - p_0 - E_p + i\epsilon)]^{-1},$$

where the coefficients $c_j(s)$ satisfy the following set of linear algebraic equations:

$$c_i(s) - \sum_{k,j}^{N} H_{ik}(s)\lambda_{kj}c_j(s) = 0,$$

$$H_{ik} = \frac{i}{2\pi^2}\sum_{L=S,D}\int dp_0|\mathbf{p}|^2 d|\mathbf{p}|$$

$$\times S(p_0, |\mathbf{p}|, s)g_i^{(L)}(p_0, |\mathbf{p}|)g_k^{(L)}(p_0, |\mathbf{p}|).$$

In this case, the partial-wave T-matrix series has the form

$$T_{L'L}(p_0', |\mathbf{p}'|; p_0, |\mathbf{p}|, s)$$

$$= \sum_{ij}^{N}(\tau(s))_{ij}g_i^{(L')}(p_0', |\mathbf{p}'|)g_j^{(L)}(p_0, |\mathbf{p}|), \tag{16}$$

$$(\tau^{-1}(s))_{ij} = (\lambda^{-1})_{ij} - H_{ij}(s).$$

The on-shell T matrix

$$T_{L'L}^{(\mathrm{os})} \equiv T_{L'L}(0, |\mathbf{p}^*|; 0, |\mathbf{p}^*|; s),$$

$$|\mathbf{p}^*| = \sqrt{\frac{s}{4} - m^2} = \sqrt{\frac{1}{2}mE_{\mathrm{lab}}}, \tag{17}$$

where $|\mathbf{p}^*|$ is the relative momentum in the c.m. frame and E_{lab} is the energy in the laboratory frame, is related to the $^3S_1$ and $^3D_1$ phase shifts (δ_S and δ_D) and the mixing parameter ϵ as

$$T^{(\mathrm{os})} = \frac{-2i}{|\mathbf{p}^*|\sqrt{s}}$$

$$\times\begin{pmatrix} \cos 2\epsilon e^{2i\delta_S} - 1 & i\sin 2\epsilon e^{i(\delta_S+\delta_D)} \\ i\sin 2\epsilon e^{i(\delta_S+\delta_D)} & \cos 2\epsilon e^{2i\delta_D} - 1 \end{pmatrix}. \tag{18}$$

The calculations were performed with a covariant generalization of the separable Graz II potential [12]. For the relativistic Graz II (rank-3) potential, the functions g_i are given by [13]

$$g_1^{(S)}(p_0, |\mathbf{p}|) = \frac{1-\gamma_1(p_0^2-\mathbf{p}^2)}{(p_0^2-\mathbf{p}^2-\beta_{11}^2)^2},$$

$$g_2^{(S)}(p_0, \mathbf{p}) = -\frac{(p_0^2-\mathbf{p}^2)}{(p_0^2-\mathbf{p}^2-\beta_{12}^2)^2},$$

$$g_3^{(D)}(p_0, |\mathbf{p}|) = \frac{(p_0^2-\mathbf{p}^2)(1-\gamma_2(p_0^2-\mathbf{p}^2))}{(p_0^2-\mathbf{p}^2-\beta_{21}^2)(p_0^2-\mathbf{p}^2-\beta_{22}^2)^2}, \tag{19}$$

$$g_1^{(D)}(p_0, |\mathbf{p}|) = g_2^{(D)}(p_0, |\mathbf{p}|) = g_3^{(S)}(p_0, |\mathbf{p}|) \equiv 0.$$

The parameters for these functions are given in Table 1.

The results of the calculations for basic properties of the deuteron (D-wave weights p_D, binding energy ϵ_d, quadrupole moment Q_d, magnetic moment μ_d, and $\rho_{D/S}$ ratio) and the parameters of low-energy $^3S_1$ scattering (effective range r_0 and scattering length a) are displayed in Table 2. For the sake of comparison, the results obtained with the nonrelativistic Graz II potential are also presented.

The $^3S_1$ and $^3D_1$ phase shifts are shown in Fig. 1.

4. RELATIVISTIC IMPULSE APPROXIMATION

In the relativistic impulse approximation, the deuteron-current matrix element $\langle D'\mathcal{M}'|j_\mu|D\mathcal{M}\rangle$ can be represented as

$$\langle D'\mathcal{M}'|j_\mu|D\mathcal{M}\rangle \tag{20}$$

$$= i\int\frac{d^4p}{(2\pi)^4}\mathrm{tr}\left\{\bar{\chi}_{\mathcal{M}'}(P', p')\Gamma_\mu^{(S)}(q)\chi_{\mathcal{M}}(P, p)\left(\frac{\hat{P}}{2} - \hat{p} + m\right)\right\},$$

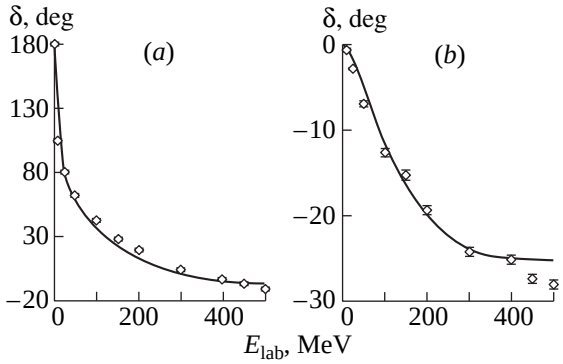

Fig. 1. (*a*) $^3S_1$ and (*b*) $^3D_1$ phase shifts. Experimental data were borrowed from [14].

Table 2. Deuteron properties and parameters of low-energy $^3S_1$ scattering

	p_D, %	ϵ_d, MeV	Q_d, fm^{-2}	μ_d, $e/2m$	$\rho_{D/S}$	r_0, fm	a, fm
Covariant Graz II	4	2.225	0.2484	0.8279	0.02408	1.7861	5.4188
Nonrelativistic Graz II	4.82	2.225	0.2812	0.8522	0.0274	1.78	5.42
Experiment		2.2246	0.286	0.8574	0.0263	1.759	5.424

where $\chi_{\mathcal{M}}(P, p)$ is the Bethe–Salpeter amplitude for the deuteron, $P' = P + q$, and $p' = p + q/2$. The vertex of γNN interaction,

$$\Gamma_\mu^{(S)}(q) = \gamma_\mu F_1^{(S)}(q^2) - \frac{\gamma_\mu \hat{q} - \hat{q}\gamma_\mu}{4m} F_2^{(S)}(q^2),$$

is chosen to be on the mass shell. The isoscalar form factors for the nucleon, $F_{1,2}^{(S)}(q^2)$, appear owing to summation over the two nucleons.

First, the trace was evaluated in (20) with the aid of the analytic calculation package MAPLE V. The covariant form was used for the Bethe–Salpeter amplitudes (12). After tracing, the scalar products of 4-momenta (P, p, q) and deuteron polarization 4-vectors ($\xi_{\mathcal{M}}$, $\xi^*_{\mathcal{M}'}$) with definite spin projections were inserted. Then, using equations (13), the functions h_i were expressed in terms of ϕ_S and ϕ_D. All scalar products were evaluated in the laboratory frame.

The resulting expressions for the deuteron-current matrix element can be represented as

$$\langle D'\mathcal{M}'|j_\mu|D\mathcal{M}\rangle$$

$$= \mathcal{J}_{1\mu}^{\mathcal{M}'\mathcal{M}}(q^2) F_1^{(S)}(q^2) + \mathcal{J}_{2\mu}^{\mathcal{M}'\mathcal{M}}(q^2) F_2^{(S)}(q^2),$$

$$\mathcal{J}_{1,2\mu}^{\mathcal{M}'\mathcal{M}}(q^2) = i\int dp_0 |\mathbf{p}|^2 d|\mathbf{p}| d(\cos\theta) \qquad (21)$$

$$\times \sum_{L', L = S, D} \phi_{L'}(p'_0, |\mathbf{p}'|)\phi_L(p_0, |\mathbf{p}|)$$

$$\times I_{1,2,\mathcal{M}'\mathcal{M}\mu}^{L', L}(p_0, |\mathbf{p}|, \cos\theta, q^2),$$

where the function $I_{1,2,\mathcal{M}'\mathcal{M}\mu}^{L', L}(p_0, |\mathbf{p}|, \cos\theta, q^2)$ emerged as the result of calculating the trace and substituting the scalar products into (20). It has a very cumbersome form and is omitted in the article.

In (21), the radial part of the Bethe–Salpeter amplitude for the outgoing deuteron, $\phi_{L'}(p'_0, |\mathbf{p}'|)$, depends on the components of the 4-vector p' calculated in the rest frame. To go over from the vectors in the rest frame to those in the laboratory frame, we must make a Lorentz transformation; that is,

$$P'_{\text{lab}} = \mathcal{L}P'_{\text{rest}} = \mathcal{L}(M, \mathbf{0}), \quad p'_{\text{lab}} = \mathcal{L}p'_{\text{rest}}, \qquad (22)$$

where the Lorentz transformation matrix $\mathcal{L}$ has the form

$$\mathcal{L} = \begin{pmatrix} 1+2\eta & 0 & 0 & 2\sqrt{\eta}\sqrt{1+\eta} \\ 0 & 1 & 0 & 0 \\ 0 & 0 & 1 & 0 \\ 2\sqrt{\eta}\sqrt{1+\eta} & 0 & 0 & 1+2\eta \end{pmatrix}. \qquad (23)$$

To simplify the notation, the components of the 4-vector p'_{rest} are denoted by $p' \equiv p'_{\text{rest}} = (p'_0, p'_x, p'_y, p'_z)$ and $|\mathbf{p}'| = |\mathbf{p}'_{\text{rest}}| = \sqrt{p'^2_x + p'^2_y + p'^2_z}$. Using relations (8), (22), and (23), we arrive at

$$p'_0 = (1+2\eta)p_0 - 2\sqrt{\eta}\sqrt{1+\eta}\,p_z - M\eta, \qquad (24)$$

$$p'_x = p_x, \quad p'_y = p_y,$$

$$p'_z = (1+2\eta)p_z - 2\sqrt{\eta}\sqrt{1+\eta}\,p_0 + M\sqrt{\eta}\sqrt{1+\eta}, \qquad (25)$$

where p_0, p_x, p_y, and p_z are the components of the 4-vector p in the laboratory frame.

5. CALCULATIONS AND RESULTS

The radial part of the Bethe–Salpeter amplitude in (21) has the form $\phi_L(p_0, |\mathbf{p}|) = S(p_0, |\mathbf{p}|)g_L(p_0, |\mathbf{p}|)$ [see equation (15)], where $g_L(p_0, |\mathbf{p}|)$ is the radial part of the vertex function. Thus, the Bethe–Salpeter amplitude involves singularities in the p_0 plane, which are infinitesimally close to the real axis. Some of the singularities are from the propagator, while the others are from the radial part of the vertex function—in other words, from the functions $g_i^{(L)}$.

For the initial deuteron, the singularities do not depend on q^2 (or η) and always remain in the same quadrant:

$p_0 = \pm M/2 \mp \sqrt{\mathbf{p}^2 + m^2} \pm i\epsilon$ for the propagator,

$p_0 = \pm\sqrt{\mathbf{p}^2 + \beta_i^2} \mp i\epsilon$ for the functions $g_i^{(L)}$.

A different situation occurs for the final deuteron. Due to the boost of the arguments of the amplitude in (25), the singularities depend on q^2 (or η) and can go across the imaginary axis and appear in another quadrant (mobile singularities). The positions of the singularities are the following:

$$p_0 = -(1+4\eta)M \pm \sqrt{\mathbf{p}^2 + m^2 + 4\sqrt{\eta(1+\eta)}M|\mathbf{p}|\cos\theta + 4\eta^2(1+\eta)^2M^2} \mp i\epsilon$$

for the propagator and

$$p_0 = -\eta M \pm \sqrt{\mathbf{p}^2 + \beta_i^2 + 2\sqrt{\eta(1+\eta)}M|\mathbf{p}|\cos\theta + \eta^2(1+\eta)^2M^2} \mp i\epsilon$$

for the functions $g_i^{(L)}$.

The mobility of the singularities does not affect the calculations if the Cauchy residue theorem is applied. But for the Wick rotation procedure, this means that the additional contributions (the residues at these mobile singularities) must be taken into account. The minimal value of q^2 for which the imaginary axis is traversed is $-q^2 = M(2m - M) \approx 0.107$ fm^{-2} for propagator and $-q^2 = 4M\beta_i \approx 30$ fm^{-2} for the functions $g_i^{(L)}$. The contributions of the residues from the functions $g_i^{(L)}$ are negligible (about 1%) in the region $-q^2 < 50$ fm^{-2}, but the contri-

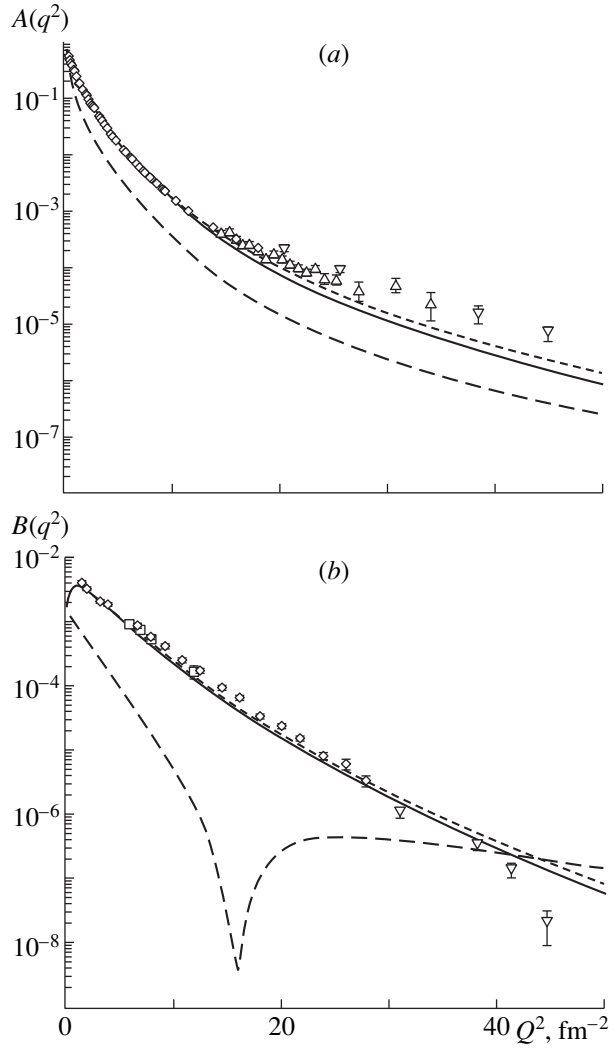

Fig. 2. (*a*) Structure function $A(q^2)$. Long dashes represent the calculation without the contribution of moving poles. The solid curve shows the results of the full calculation. Short dashes correspond to the nonrelativistic calculation (nonrelativistic Graz II potential). Experimental data were borrowed from (◇) [15], (△) [16], and (▽) [6]. (*b*) Structure function $B(q^2)$. The notation for the curves is identical to that in Fig. 2*a*. Experimental data were borrowed from (◇) [15], (□) [17], and (▽) [18].

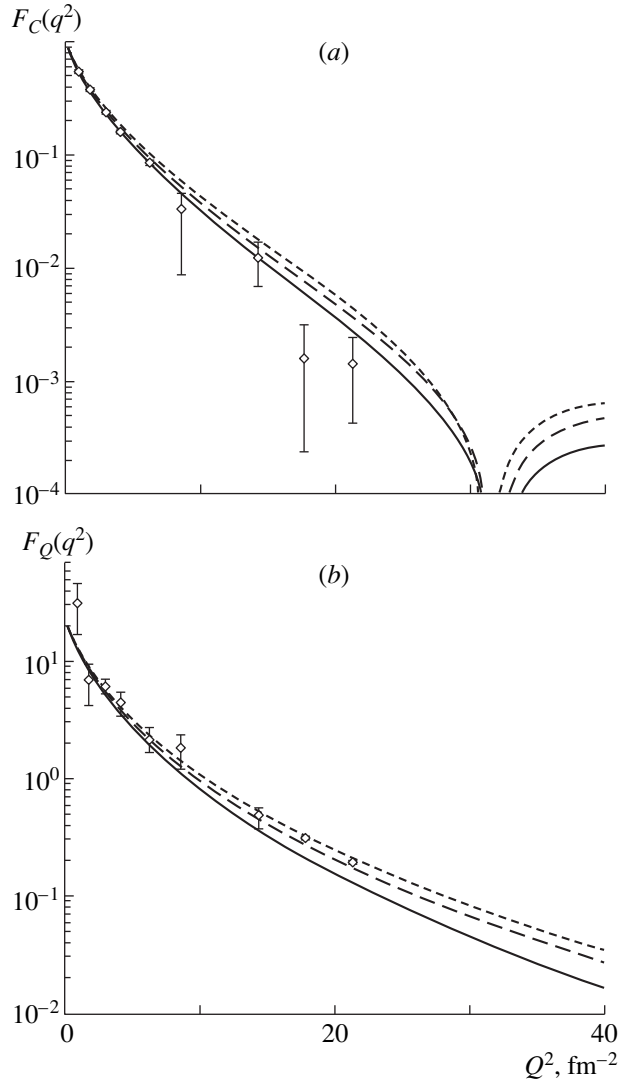

Fig. 3. (*a*) Charge form factor $F_C(q^2)$. Long and short dashes represent the calculations with, respectively, the VMDM and the RHOM nucleon form factors. The solid curve corresponds to the dipole fit. The experimental data were borrowed from [15]. (*b*) Quadrupole form factor $F_Q(q^2)$. The notation is identical to that in Fig. 3*a*, and experimental data originate from the same source.

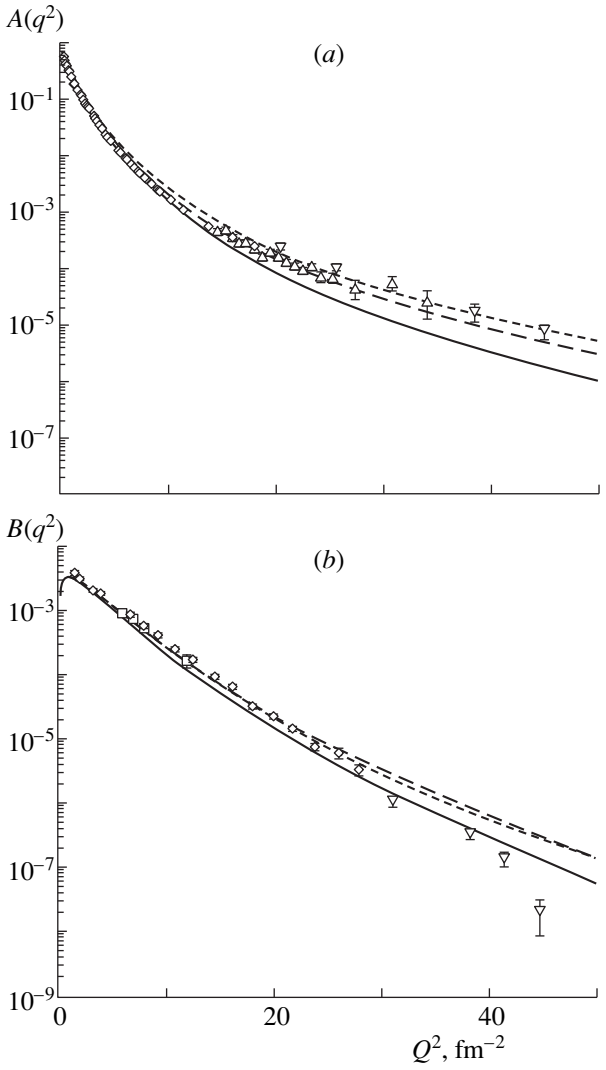

Fig. 4. (*a*) Structure function $A(q^2)$. The notation is identical to that in Fig. 3*a*. Experimental data originate from the same source as in Fig. 2*a*. (*b*) Structure function $B(q^2)$. The notation is identical to that in Fig. 3*b*. Experimental data originate from the same source as in Fig. 2*b*.

bution of the residue from the propagator is too large and can even modify the curves significantly.

The contribution of the residue from the propagator is shown in Fig. 2 for the functions $A(q^2)$ and $B(q^2)$. We can see that this contribution is sufficiently large both for the function $A(q^2)$ and for the function $B(q^2)$ [for the function $B(q^2)$, this contribution fills the minimum, which does not exist in the experimental data]. This result can be considered as a specific relativistic effect caused by the Lorentz transformation for arguments of the Bethe–Salpeter amplitude (vertex functions and propagator).

Yet another interesting result of the investigations is the dependence of the deuteron form factors on the nucleon form factors—in particular, on the neutron electric form factor. The electric and magnetic form

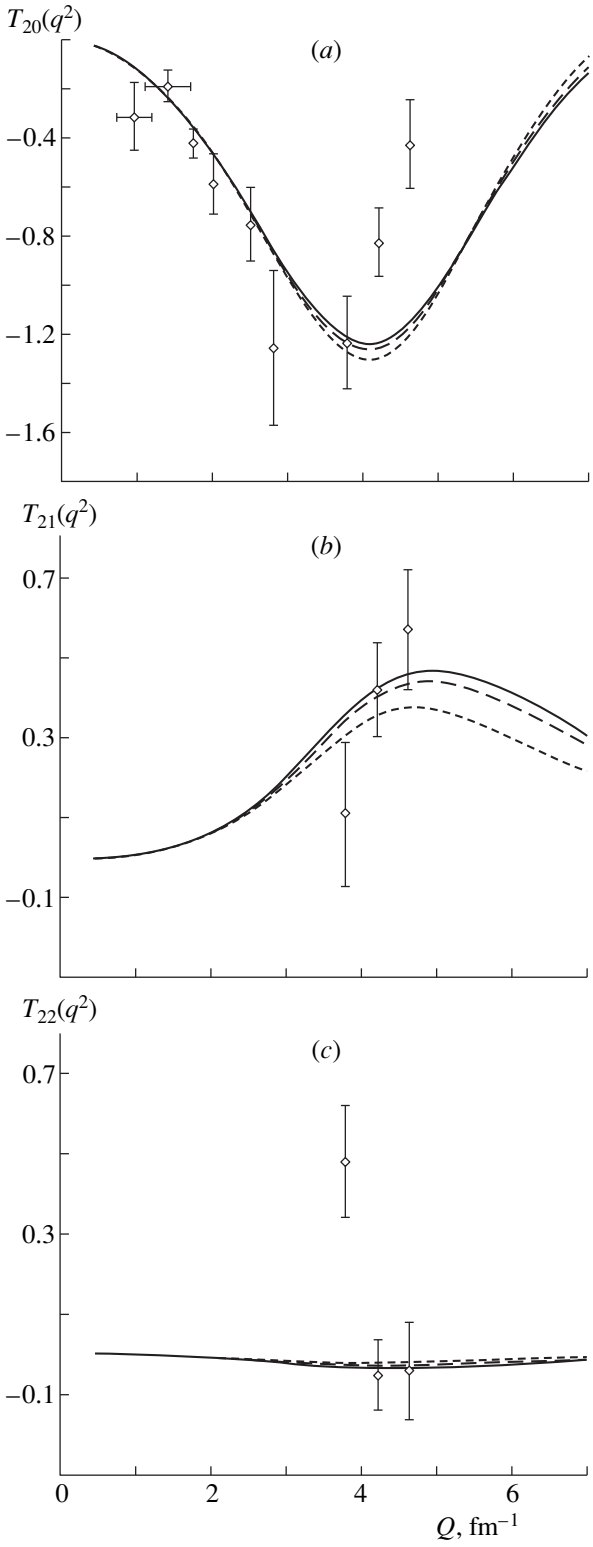

Fig. 5. (*a*) Tensor polarization component $T_{20}(q^2)$ (θ_e = 70°). The notation is identical to that in Fig. 3*a*. Experimental data were borrowed from [22]. (*b*) Tensor polarization component $T_{21}(q^2)$ (θ_e = 78.7°). The notation is identical to that in Fig. 3*a*. Experimental data were borrowed from [21]. (*c*) Tensor polarization component $T_{22}(q^2)$ (θ_e = 78.7°). The notation is identical to that in Fig. 3*a*. Experimental data originate from the same source as in Fig. 5*b*.

factors for nucleons [$G_E(q^2)$ and $G_M(q^2)$, respectively] are related to the Dirac and Pauli form factors [$F_1(q^2)$ and $F_2(q^2)$, respectively] by the equations

$$G_E(q^2) = F_1(q^2) + \frac{q^2}{4m^2}F_2(q^2),$$
$$G_M(q^2) = F_1(q^2) + F_2(q^2). \quad (26)$$

Three sets of the nucleon form factors were used in the calculations. The first set is the so-called dipole fit

$$G_M^p(q^2) = (1+\kappa_p)G_E^p(q^2), \quad G_M^n = \kappa_n G_E^p(q^2),$$
$$G_E^n(q^2) = 0, \quad G_E^p(q^2) = (1 - q^2/0.71(\text{GeV})^2)^{-2}, \quad (27)$$

where $\kappa_p = 1.7928$ and $\kappa_n = -1.9130$ are the anomalous magnetic moments of the nucleons. The second set is that from the vector-meson-dominance model (VMDM) [19], whereas the third set is that from the relativistic harmonic-oscillator model (RHOM) [20]. The first model assumes that the neutron electric form factor is equal to zero, but the second and third ones lead to a nonzero value for it.

Figure 3 shows the charge and the quadrupole form factors [$F_C(q^2)$ and $F_Q(q^2)$, respectively]. The zero of the form factor $F_C(q^2)$ is in the range of Q^2 between 32 and 33 fm^{-2}, but experimental data yield $Q^2 = 17.81$–21.34 fm^{-2} [21]. This is because of the specific type of the separable Graz II potential [in the calculations with the nonrelativistic Graz II potential, the zero of $F_C(q^2)$ is shifted too]. The nucleon form factors do not shift the zero of the form factor $F_C(q^2)$. The nucleon form factors with the nonzero electric form factor for the neutron (VMDM and RHOM) are more suitable for fitting the experimental data on the quadrupole form factor $F_Q(q^2)$. The structure functions $A(q^2)$ and $B(q^2)$ are shown in Fig. 4.

Figure 5 shows the tensor polarization components $T_{20}(q^2)$, $T_{21}(q^2)$, and $T_{22}(q^2)$ for the final deuteron. It can be seen that the tensor polarization components depend on the nucleon form factors. For $T_{20}(q^2)$ and $T_{22}(q^2)$, this dependence is very weak, but, for $T_{21}(q^2)$, it is more pronounced [this is because the nucleon form factors affect sizably the quadrupole form factor (Fig. 3*b*)]. This result can be used to choose between the models for the nucleon form factors. Unfortunately, large uncertainties in experimental data give no way to choose one of the sets, and future experiments to measure the component $T_{21}(q^2)$ can be very useful for this.

Note that the calculated function $T_{20}(q^2)$ differs from the experimental indications in the region $Q > 4$ fm^{-1}. This fact, apparently, could be explained by several reasons. It is necessary to improve the description of the zero of the charge form factor $F_C(q^2)$ by changing the separable kernel of *NN* interaction and by taking into account the negative-energy states of the Bethe–Salpeter amplitude for the deuteron. It is also important to investigate the contribution of the two-body electromagnetic current. Information about the effect of these factors will provide a powerful tool for studying the on- and off-shell behavior of the nucleon form factors in elastic *ed* scattering.

ACKNOWLEDGMENTS

This work was supported in part by the Russian Foundation for Basic Research (project no. 96-15-96423). One of the authors (S.G. Burov) is grateful to the Russian Academy of Sciences for a scholarship for young scientists.

REFERENCES

1. M. Gari and H. Hyuga, Nucl. Phys. A **262**, 409 (1976); Z. Phys. A **277**, 291 (1976); Nucl. Phys. A **278**, 372 (1977); M. Gari, H. Hyuga, and B. Sommer, Phys. Rev. C **14**, 2196 (1976).
2. V. V. Burov, V. N. Dostovalov, and S. É. Sus'kov, Fiz. Élem. Chastits At. Yadra **23**, 721 (1992) [Sov. J. Part. Nucl. **23**, 317 (1992)].
3. V. V. Burov, V. N. Dostovalov, and S. É. Sus'kov, Pis'ma Zh. Éksp. Teor. Fiz. **44**, 357 (1986) [JETP Lett. **44**, 457 (1986)]; V. V. Burov and V. N. Dostovalov, Z. Phys. A **326**, 254 (1987); V. V. Burov, A. A Goi, and V. N. Dostovalov, Yad. Fiz. **45**, 994 (1987) [Sov. J. Nucl. Phys. **45**, 616 (1987)].
4. R. F. Wagendrunn and W. Plessas, Few-Body Syst. (Suppl.) **8**, 181 (1995).
5. B. Desplanques, V. A. Karmanov, and J.-F. Mathiot, Nucl. Phys. A **589**, 697 (1995).
6. R. G. Arnold *et al.*, Phys. Rev. Lett. **35**, 776 (1975).
7. R. G. Arnold *et al.*, Phys. Rev. Lett. **58**, 1723 (1987).
8. F. Gross, Phys. Rev. **142**, 1025 (1966); Nucl. Phys. A **358**, 215 (1981).
9. M. J. Zuilhof and J. A. Tjon, Phys. Rev. C **24**, 736 (1981); G. Rupp and J. A. Tjon, Phys. Rev. C **37**, 1729 (1988).
10. J. D. Bjorken and S. D. Drell, *Relativistic Quantum Mechanics* (McGraw-Hill, New York, 1964; Nauka, Moscow, 1978).
11. J. J. Kubis, Phys. Rev. D **6**, 547 (1972).
12. L. Mathelitsch, W. Plessas, and W. Schweiger, Phys. Rev. C **26**, 65 (1982).
13. G. Rupp and J. A. Tjon, Phys. Rev. C **41**, 472 (1990).
14. R. A. Arndt, J. S. Hyslop, and L. D. Roper, Phys. Rev. D **35**, 128 (1987).
15. J. E. Elias *et al.*, Phys. Rev. **177**, 2075 (1969).
16. S. Platchkov *et al.*, Nucl. Phys. A **510**, 285 (1990).
17. C. D. Buchanan *et al.*, Phys. Rev. Lett. **15**, 303 (1965).
18. R. G. Arnold *et al.*, Phys. Rev. Lett. **54**, 649 (1985).
19. F. Iachello, A. D. Jackson, and A. Lande, Phys. Lett. B **43**, 191 (1973).
20. V. V. Burov, A. De Pace, S. M. Dorkin, and P. Saracco, Europhys. Lett. **24**, 443 (1993).
21. M. Garcon *et al.*, Phys. Rev. C **49**, 2516 (1994).
22. I. The *et al.*, Phys. Rev. Lett. **67**, 173 (1991).

Physics of Atomic Nuclei, Vol. 63, No. 5, 2000, pp. 782–794. Translated from Yadernaya Fizika, Vol. 63, No. 5, 2000, pp. 852–864.

NUCLEI
Theory

Analysis of Elastic Proton–Nucleus Scattering on the Basis of the Glauber–Sitenko Approach with Allowance for Intermediate Excitations of Nuclei

V. I. Kuprikov and V. V. Pilipenko*, 1)

National Research Center, Kharkov Institute for Physics and Technology, Akademicheskaya ul. 1, Kharkov, 310108 Ukraine
Received December 29, 1998; in final form, May 7, 1999

Abstract—On the basis of the Glauber–Sitenko approach, the cross sections and spin observables for proton–nucleus scattering at intermediate energies are calculated with allowance for intermediate excitations of target nuclei. The calculations are performed by using the Hartree–Fock and model-independent nuclear densities and nucleon–nucleon amplitudes determined from partial-wave analyses. It is shown that the inclusion of intermediate excitations of nuclei strongly affects the behavior of observables in the region of moderately small scattering angles. *© 2000 MAIK "Nauka/Interperiodica".*

1. The Glauber–Sitenko theory of multiple diffractive scattering [1, 2], where the amplitude for proton–nucleus scattering is expressed in terms of nucleon–nucleon amplitudes and the wave function of the target nucleus, underlies one of the most popular approaches to theoretically describing collisions between protons with energies of a few hundred MeV and nuclei. This theory was successfully used by many authors to study such processes. As a rule, calculations within this framework for medium-mass and heavy nuclei disregard correlations of intranuclear nucleons, treating the nuclei under investigation in terms of single-particle nucleon densities. (For the studies that are free from this limitation and which attempt to take into account various correlations, we can indicate, by way of example, those in [3–8].) Such calculations usually employ the following simplifications of the model: the distinctions between the proton–proton and the proton–neutron amplitudes and between the neutron and the proton densities are ignored—the averaged proton–nucleon amplitude and the averaged nuclear density are used instead of them, respectively; the optical limit is used; no account is taken of the Z ordering of noncommuting operators in the expression for the pA amplitude; explicit approximations of the proton–nucleon amplitude are sometimes used, which imposes some restrictions on its form; and the zero-range approximation for nuclear forces is invoked in some cases.

Along with an analysis of differential cross sections for scattering processes, an investigation of spin observables (such as polarizations and spin-rotation functions), which form, together with cross sections, a complete set of quantities for describing elastic proton scattering on spinless nuclei, is also of considerable interest, since spin observables exhibit quite a high sensitivity to the choice of model and model parameters. In some studies, a good description of cross sections and spin variables was achieved via an explicit use of free parameters in proton–nucleon amplitudes and model nuclear densities. Fitting procedures for determining the densities and the parameters of the proton–nucleon amplitudes were also invoked (see, for example, [9]). However, a theoretical description of data that is obtained in this way can be questioned because of ambiguities in the fits and because of the above simplifications of the model.

At present, we have a vast body of information at our disposal that comes from partial-wave analyses of nucleon–nucleon scattering and which refines substantially our knowledge of nucleon–nucleon amplitudes, including their dependence on nucleon spins. The results of theoretical investigations of the structure of nuclei—in particular, the results of Hartree–Fock calculations with effective Skyrme forces—and data on proton densities from a model-independent analysis of electron scattering create preconditions for the use of realistic nuclear densities. In view of this, it is of great interest to describe proton–nucleus scattering on the basis of the Glauber–Sitenko theory of multiple diffractive scattering by employing realistic nucleon–nucleon amplitudes and nuclear densities without oversimplifying the model.

In the present study, we calculate the cross sections and spin observables for elastic proton scattering on spinless nuclei, relying on the above theory of multiple diffractive scattering. In this calculation, we take into account two-body nucleon correlations that are due to intermediate excitations of nuclei in successive rescatterings on target nucleons and use Hatree–Fock or model-independent nuclear densities and proton–

* e-mail: berezhnoy@pem.kharkov.ua
1) Research and Technological Center for Electrophysical Processing, National Academy of Sciences of Ukraine, ul. Chernyshevskogo 28, Kharkov, 310002 Ukraine.

nucleon amplitudes determined from a partial-wave analysis. As a result, we obtain new expressions for the amplitudes of *pA* scattering without invoking the above simplifying assumptions.

2. According to the theory of multiple diffractive scattering, the expression for the amplitude of elastic *pA* scattering has the form

$$F_e = \frac{ik}{2\pi}\int d^2b e^{i\mathbf{q}\cdot\mathbf{b}}\Omega_e(\mathbf{b}) = \frac{ik}{2\pi}\int d^2b e^{i\mathbf{q}\cdot\mathbf{b}}\left\{1-\left\langle 0\left|\hat{Z}\prod_{j=1}^{A}S_j(\mathbf{b}-\mathbf{s}_j)\right|0\right\rangle\right\}, \quad (1)$$

where k is the wave vector; $\Omega_e(\mathbf{b})$ is the nucleon–nucleus profile function describing elastic scattering; $\mathbf{q}$ and $\mathbf{b}$ are, respectively, the 3-momentum transfer and the impact-parameter vector, which lie in the plane orthogonal to the beam direction; $\mathbf{s}_j$ is the projection of the radius vector of jth nucleon onto this plane; $|0\rangle$ is the ground-state vector of the target nucleus; and A is the mass number of the target nucleus. For scattering on intranuclear nucleons, the operator $\hat{Z}$ ensures the Z ordering [10] of the scattering matrices $S_j(\mathbf{b})$, which are expressed in terms of the proton–nucleon amplitude $f_j(\mathbf{q})$ as

$$S_j(\mathbf{b}) = 1-\frac{1}{2\pi ik}\int d^2q e^{-i\mathbf{q}\cdot\mathbf{b}}f_j(\mathbf{q}). \quad (2)$$

In the expression for the amplitude $f_j(\mathbf{q})$, we will take into account only the central and the spin–orbit term [$f_c^{(j)}(q)$ and $f_s^{(j)}(q)$, respectively], disregarding the remaining components, which involve the target-nucleon-spin operators and which therefore contribute insignificantly to the amplitude of scattering on spinless nuclei [11]; that is, we set $f_j(\mathbf{q}) = f_c^{(j)}(q) + f_s^{(j)}(q)\boldsymbol{\sigma}\cdot\mathbf{n}$, where $\boldsymbol{\sigma}$ stands for the Pauli matrices and $\mathbf{n} = \mathbf{k}_i\times\mathbf{k}_f/|\mathbf{k}_i\times\mathbf{k}_f|$ (here, $\mathbf{k}_i$ and $\mathbf{k}_f$ are, respectively, the initial and final wave vectors).

The amplitude in the form (1) takes fully into account nucleon correlations in the nucleus. A description of a nucleus in terms of single-particle densities $\rho_0^{(j)}(r)$ in the ground state corresponds to replacing the identity operators between the operators S_j by the projection operator $|0\rangle\langle 0|$. In this case, it is assumed that successive events of proton scattering on the nucleons of a nucleus leave this nucleus in the ground state, intermediate excitations being ignored. Here, we take into account the possibility of the single intermediate nuclear excitations of various multipole orders. This means that, in (1), we retain terms of the form

$$\langle 0|S_A|0\rangle\cdots\langle 0|S_j|\alpha; I, M\rangle\cdots\langle\alpha; I, M|S_j|0\rangle\cdots\langle 0|S_1|0\rangle. \quad (3)$$

According to the pattern corresponding to the expression in (3), the excitation of the state $|\alpha; I, M\rangle$ of multipolarity I (here, M is the projection of the spin $\mathbf{I}$, while α stands for the remaining quantum numbers of the state) in scattering on the jth nucleon is followed by deexcitation in scattering on the ith nucleon. The structure of the correction terms (3) suggests that the main contribution is expected to come from states associated with inelastic processes whose relative probabilities are high (since the corresponding cross sections are large). These are predominantly low-lying collective nuclear states. In specific calculations of observables, we will therefore restrict ourselves to taking into account intermediate excitations of natural parity for some low values of I, retaining the contributions of only the few most important states for each multipolarity. It should be noted that this approach corresponds to representing the two-particle correlation function $C_2^{(i,j)}(\mathbf{r}_i, \mathbf{r}_j)$ in the form of a special expansion in terms of spherical harmonics:

$$C_2^{(i,j)}(\mathbf{r}_i, \mathbf{r}_j) = \sum_{\alpha}\sum_{I,M}\rho_{\alpha I}^{(i)}(r_i)\rho_{\alpha I}^{(j)}(r_j)Y_{IM}(\hat{\mathbf{r}}_i)Y_{IM}^{*}(\hat{\mathbf{r}}_j) = \frac{1}{4\pi}\sum_{\alpha, I}(2I+1)\rho_{\alpha I}^{(i)}(r_i)\rho_{\alpha I}^{(j)}(r_j)P_I(\hat{\mathbf{r}}_i\cdot\hat{\mathbf{r}}_j). \quad (4)$$

Here, the transition density for the excitation of the intermediate state $|\alpha; I, M\rangle$ has the form $\tilde{\rho}_{\alpha IM}^{(j)}(\mathbf{r}) = \rho_{\alpha I}^{(j)}(r)Y_{IM}(\hat{\mathbf{r}})$, where $\rho_{\alpha I}^{(j)}(r)$ is the radial transition density; $Y_{IM}(\hat{\mathbf{r}}) \equiv Y_{IM}(\theta, \varphi)$ is a spherical harmonic; and $P_I(\hat{\mathbf{r}}_i\cdot\hat{\mathbf{r}}_j)$ is the Legendre polynomial of degree I. In addition to two-particle correlations that result from taking into account intermediate states proper, we will similarly include center-of-mass correlations associated with the motion of the center of mass of the target nucleus. The corresponding correlation function has a form similar to that obtained in [6, 7]; that is,

$$C_{\text{c.m.}}^{(i,j)}(\mathbf{r}_i, \mathbf{r}_j) = -\frac{3\mathbf{r}_i\cdot\mathbf{r}_j}{Nr_m^{(n)2}+Zr_m^{(p)2}}\rho_0^{(i)}(r_i)\rho_0^{(j)}(r_j), \quad (5)$$

where $r_m^{(n,p)} \equiv \langle r_{n,p}^2\rangle^{1/2}$ represents either the neutron (for the index n) or the proton (for the index p) root-mean-square radius for the densities $\rho_0^{(n,p)}(r_{n,p})$, while N and Z are the numbers of, respectively, neutrons and protons in the target nucleus. The expression in (5) formally corresponds to the $I = 1$ intermediate excitation characterized by a transition density of the form

$$\rho_{\text{c.m.}}^{(j)}(r) = i\sqrt{\frac{4\pi}{Nr_m^{(n)2}+Zr_m^{(p)2}}}r\rho_0^{(j)}(r). \quad (6)$$

As a result, the nucleon–nucleus profile function appearing in (1) can be represented in the convenient form

$$\Omega_e(\mathbf{b}) = \Omega_c(b) + i\boldsymbol{\sigma}\cdot\mathbf{B}\Omega_B(b) = \Omega_{c0}(b) + i\boldsymbol{\sigma}\cdot\mathbf{B}\Omega_{B0}(b) + \Omega^{(\mathrm{exc})}(\mathbf{b}).$$

For the profile functions Ω_{c0} and Ω_{B0} describing the scattering without excitation, we have

$$\Omega_{c0}(b) = 1 - C^{(+)}_{N,Z}(b),\ \ \Omega_{B0}(b) = iC^{(-)}_{N,Z}(b), \quad (7)$$

where

$$C^{(\pm)}_{N,Z}(b) = \frac{1}{2}\{[1 - E_0^{(n)} + iE_s^{(n)}]^N[1 - E_0^{(p)} + iE_s^{(p)}]^Z \pm [1 - E_0^{(n)} - iE_s^{(n)}]^N[1 - E_0^{(p)} - iE_s^{(p)}]^Z\} \quad (8)$$

with

$$E^{(j)}_{0,s}(b) = -\frac{i}{k}\int_0^\infty dqqJ_{0,1}(qb)f^{(j)}_{c,s}(q)Q^{(j)}_0(q). \quad (9)$$

Here, $J_m(x)$ is a cylindrical Bessel function, while $Q^{(j)}_0(q)$ is the form factor for the ground state of the nucleus being considered,

$$Q^{(j)}_0(q) = 4\pi\int_0^\infty drr^2 j_0(qr)\rho^{(j)}_0(r), \quad (10)$$

where $j_m(x)$ is a spherical Bessel function.

For the profile function $\Omega^{(\mathrm{exc})}(\mathbf{b})$ taking into account intermediate excited states, we have

$$\Omega^{(\mathrm{exc})}(\mathbf{b}) = -\sum_{\alpha,I,M}(-1)^M\int\prod_{j=1}^A dz_j \times\sum_{n=1}^{A-1}\sum_{m=n+1}^{A}\sum_{\{i\}} H_0^{(i_1)}(\mathbf{b},z_{i_1})\ldots H_0^{(i_{n-1})}(\mathbf{b},z_{i_{n-1}}) \times H^{(\alpha,i_n)}_{I,M}(\mathbf{b},z_{i_n})H_0^{(i_{n+1})}(\mathbf{b},z_{i_{n+1}})\ldots H_0^{(i_{m-1})}(\mathbf{b},z_{i_{m-1}}) \times H^{(\alpha,i_m)}_{I,-M}(\mathbf{b},z_{i_m})H_0^{(i_{m+1})}(\mathbf{b},z_{i_{m+1}})\ldots H_0^{(i_A)}(\mathbf{b},z_{i_A}) \theta(z_{i_1}-z_{i_2})\ldots\theta(z_{i_{A-1}}-z_{i_A}), \quad (11)$$

where $\theta(z)$ is the Heaviside step function associated with the Z-ordering procedure [10]; the symbol $\sum_{\{i\}}$ denotes that summation over the permutations of the nucleon numbers $i_1, \ldots, i_A$ is performed; and the operators $H_0^{(j)}(\mathbf{b},z)$ and $H^{(\alpha,j)}_{IM}(\mathbf{b},z)$ as functions of the spin variables are given by

$$H_0^{(j)}(\mathbf{b},z) = \int d^2s\rho_0^{(j)}(r)S_j(\mathbf{b}-\mathbf{s}) = H^{(j)}_{c0}(b,z) + iH^{(j)}_{B0}(b,z)\boldsymbol{\sigma}\cdot\mathbf{B}, \quad (12)$$

$$H^{(\alpha,j)}_{IM}(\mathbf{b},z) = \int d^2s\tilde{\rho}^{(j)}_{\alpha IM}(\mathbf{r})S_j(\mathbf{b}-\mathbf{s}) = e^{iM\varphi_b}[H^{(\alpha,j)}_{cIM}(b,z) + iH^{(\alpha,j)}_{BIM}(b,z)\boldsymbol{\sigma}\cdot\mathbf{B} + H^{(\alpha,j)}_{bIM}(b,z)\boldsymbol{\sigma}\cdot\hat{\mathbf{b}}]. \quad (13)$$

Here, φ_b is the azimuthal angle of the vector $\mathbf{b}$ and $\mathbf{B} = \hat{\mathbf{b}}\times\hat{\mathbf{k}}$, where $\hat{\mathbf{b}} = \mathbf{b}/b$ and $\hat{\mathbf{k}} = \mathbf{k}/k$. The operator $\Omega^{(\mathrm{exc})}(\mathbf{b})$ can be broken down into two components. The first, $\Omega^{(\mathrm{exc})}_1(\mathbf{b}) = \Omega^{(\mathrm{exc})}_{c1}(b) + i\boldsymbol{\sigma}\cdot\mathbf{B}\Omega^{(\mathrm{exc})}_{B1}(b)$, involves only the first two terms from (13) (no noncommuting operators appear in this component), which feature $H^{(\alpha,j)}_{cIM}$ and $H^{(\alpha,j)}_{BIM}$ [expression (11) is taken into account here]. The second, $\Omega^{(\mathrm{exc})}_2(\mathbf{b}) = \Omega^{(\mathrm{exc})}_{c2}(b) + i\boldsymbol{\sigma}\cdot\mathbf{B}\Omega^{(\mathrm{exc})}_{B2}(b)$, involves only that term from (13) which is proportional to $H^{(\alpha,j)}_{bIM}$.

For the profile functions $\Omega^{(\mathrm{exc})}_{c1}(b)$, $\Omega^{(\mathrm{exc})}_{B1}(b)$, $\Omega^{(\mathrm{exc})}_{c2}(b)$, and $\Omega^{(\mathrm{exc})}_{B2}(b)$, calculations similar to those described in [12] for the inelastic-scattering amplitude yield

$$\Omega^{(\mathrm{exc})}_{c1}(b) = -\sum_{\alpha,I,M}Y^2_{IM}\left(\frac{\pi}{2},0\right)\sum_{\nu=0}^{2}k_\nu\Big\{C^{(+)}_{N-\nu,Z-2+\nu}\Big[E^{(\alpha,i_\nu)}_{IM}E^{(\alpha,j_\nu)}_{IM} - \left(\frac{d}{db}E^{(\alpha,i_\nu)}_{sIM}\right)\left(\frac{d}{db}E^{(\alpha,j_\nu)}_{sIM}\right)\Big] + iC^{(-)}_{N-\nu,Z-2+\nu}\Big[E^{(\alpha,i_\nu)}_{IM}\frac{d}{db}E^{(\alpha,j_\nu)}_{sIM} + E^{(\alpha,j_\nu)}_{IM}\frac{d}{db}E^{(\alpha,i_\nu)}_{sIM}\Big]\Big\}, \quad (14)$$

$$\Omega^{(\mathrm{exc})}_{B1}(b) = \sum_{\alpha,I,M}Y^2_{IM}\left(\frac{\pi}{2},0\right)\sum_{\nu=0}^{2}k_\nu\Big\{iC^{(-)}_{N-\nu,Z-2+\nu} \times\Big[E^{(\alpha,i_\nu)}_{IM}E^{(\alpha,j_\nu)}_{IM} - \left(\frac{d}{db}E^{(\alpha,i_\nu)}_{sIM}\right)\left(\frac{d}{db}E^{(\alpha,j_\nu)}_{sIM}\right)\Big] - C^{(+)}_{N-\nu,Z-2+\nu}\Big[E^{(\alpha,i_\nu)}_{IM}\frac{d}{db}E^{(\alpha,j_\nu)}_{sIM} + E^{(\alpha,i_\nu)}_{IM}\frac{d}{db}E^{(\alpha,j_\nu)}_{sIM}\Big]\Big\}, \quad (15)$$

$$\Omega^{(\mathrm{exc})}_{c2}(b) = \sum_{\alpha,I,M}\sum_{\nu=0}^{2}k_\nu\int_{-\infty}^{\infty}dz_1\int_{-\infty}^{\infty}dz_2H^{(\alpha,i_\nu)}_{bIM}(b,z_1) \times H^{(\alpha,j_\nu)}_{bIM}(b,z_2)[D^{(+)}_{N-\nu,Z-2+\nu}(b,z_1,z_2)\theta(z_1-z_2) + D^{(+)}_{N-\nu,Z-2+\nu}(b,z_2,z_1)\theta(z_2-z_1)], \quad (16)$$

$$\Omega_{B2}^{(\mathrm{exc})}(b) = -i\sum_{\alpha, I, M}\sum_{\nu=0}^{2} k_\nu \int_{-\infty}^{\infty} dz_1 \int_{-\infty}^{\infty} dz_2 H_{bIM}^{(\alpha, i_\nu)}(b, z_1) \times H_{bIM}^{(\alpha, j_\nu)}(b, z_2)[D_{N-\nu, Z-2+\nu}^{(-)}(b, z_1, z_2)\theta(z_1 - z_2) + D_{N-\nu, Z-2+\nu}^{(-)}(b, z_2, z_1)\theta(z_2 - z_1)], \quad (17)$$

where the explicit expressions for the coefficients k_ν are $k_0 = Z(Z-1)/2$, $k_1 = NZ$, and $k_2 = N(N-1)/2$; the subscripts i_ν and j_ν take the values $i_2 = i_1 = j_2 = n$ and $i_0 = j_1 = j_0 = p$ (n and p label quantities associated with neutrons and protons, respectively); and the functions appearing in (14)–(17) are determined by (8) and (9) and by the expressions

$$E_{IM}^{(\alpha, j)}(b) = -\frac{i}{k}\int_0^\infty dq q J_M(qb) f_c^{(j)}(q) Q_{\alpha I}^{(j)}(q),$$
$$E_{sIM}^{(\alpha, j)}(b) = -\frac{i}{k}\int_0^\infty dq J_M(qb) f_s^{(j)}(q) Q_{\alpha I}^{(j)}(q), \quad (18)$$

$$D_{N,Z}^{(\pm)}(b, z_1, z_2) = \frac{1}{2}\{[1 - E_0^{(n)}(b) + i\varepsilon_s^{(n)}(b, z_1, z_2)]^N \times [1 - E_0^{(p)}(b) + i\varepsilon_s^{(p)}(b, z_1, z_2)]^Z \pm [1 - E_0^{(n)}(b) - i\varepsilon_s^{(n)}(b, z_1, z_2)]^N \times [1 - E_0^{(p)}(b) - i\varepsilon_s^{(p)}(b, z_1, z_2)]^Z\}, \quad (19)$$

$$\varepsilon_s^{(j)}(b, z_1, z_2) = E_s^{(j)}(b) + \frac{2i}{\pi k}\int_0^\infty dq q J_1(qb) f_s^{(j)}(q) \times \int_0^\infty \frac{dt}{t}(\sin tz_1 - \sin tz_2) Q_0^{(j)}(\sqrt{q^2 + t^2}), \quad (20)$$

$$H_{bIM}^{(\alpha, j)}(b, z) = i^{I-M-1}\frac{M}{2\pi k b}\int_0^\infty dq J_M(qb) f_s^{(j)}(q) \times \int_{-\infty}^{\infty} dt e^{-itz} Y_{IM}\left(\arctan\frac{q}{t}, 0\right) Q_{\alpha I}^{(j)}(\sqrt{q^2 + t^2}). \quad (21)$$

Here, the transition nuclear form factor $Q_{\alpha I}^{(j)}(q)$ is given by

$$Q_{\alpha I}^{(j)}(b) = 4\pi\int_0^\infty dr r^2 j_I(qr)\rho_{\alpha I}^{(j)}(r). \quad (22)$$

Expressions (16) and (17) for the functions $\Omega_{c2}^{(\mathrm{exc})}(b)$ and $\Omega_{B2}^{(\mathrm{exc})}(b)$, respectively, are overly cumbersome for numerical calculations. In addition, they yield only small corrections to the elastic-scattering amplitude. For these functions, we can therefore employ the approximate expressions that follow from (11) if we assume that all factors commute with one another:

$$\Omega_{c2}^{(\mathrm{exc})}(b) \approx \sum_{\alpha, I, M} Y_{IM}^2\left(\frac{\pi}{2}, 0\right)\frac{M^2}{b^2} \times \sum_{\nu=0}^{2} k_\nu E_{sIM}^{(\alpha, i_\nu)} E_{sIM}^{(\alpha, j_\nu)} C_{N-\nu, Z-2+\nu}^{(+)}, \quad (23)$$

$$\Omega_{B2}^{(\mathrm{exc})}(b) \approx -i\sum_{\alpha, I, M} Y_{IM}^2\left(\frac{\pi}{2}, 0\right)\frac{M^2}{b^2} \times \sum_{\nu=0}^{2} k_\nu E_{sIM}^{(\alpha, i_\nu)} E_{sIM}^{(\alpha, j_\nu)} C_{N-\nu, Z-2+\nu}^{(-)}. \quad (24)$$

Numerically, the distinctions between the results that are obtained with expressions (16) and (17) and those that are obtained with expressions (23) and (24) are vanishingly small.

It should be emphasized that, by summing the contributions from the most significant intermediate excitations, we can take into account only a part of rather long-range nucleon correlations in target nuclei. It was indicated in [7] that, for fully taking into account correlations in a model-independent way, it is necessary to sum the contributions of all intermediate states, including those from the continuous spectrum, but this is impossible in practice. In addition to the aforementioned corrections, we will therefore include short-range correlations associated with the repulsion between nucleons in a model-dependent way. For this, we can employ the simple correlation function (see [3, 4, 6–8])

$$C_{\mathrm{sr}}^{(i, j)}(\mathbf{r}_i, \mathbf{r}_j) = -g(|\mathbf{r}_i - \mathbf{r}_j|)\rho_0^{(i)}(r_i)\rho_0^{(j)}(r_j), \quad (25)$$

where the function $g(r)$ is taken in the form $g(r) = \exp(-\pi r^2/4l_{\mathrm{cor}}^2)$ (l_{cor} is the correlation length). Formally, this form of short-range correlations corresponds to taking into account transitions into the continuous spectrum with the transition density $\tilde{\rho}_{\mathrm{sr}}^{(j)}(\mathbf{u}, \mathbf{r}) = \rho_0^{(j)}(r)\exp(-i\mathbf{u}\cdot\mathbf{r})$, and summation over the states in (11) takes the form

$$\sum_{\alpha, I, M} \ldots \longrightarrow (-1)/(2\pi)^3 \int d^3u \zeta(u)\ldots,$$

where $\zeta(u)$ is the Fourier transform of the function $g(r)$. Expression (25) is not self-consistent [6, 7], because the condition $\int d^3r \tilde{\rho}_{\mathrm{sr}}^{(j)}(\mathbf{u}, \mathbf{r}) = 0$ is not satisfied for it. For this reason, we will use the function $\tilde{\rho}_{\mathrm{sr}}^{(j)}(\mathbf{u}, \mathbf{r}) = \rho_0^{(j)}(r)[\exp(-i\mathbf{u}\cdot\mathbf{r}) - Q_0^{(j)}(u)]$, which meets this condi-

tion. This choice of the density corresponds to the self-consistent form of the correlation function from [6, 7]. In calculating the relevant corrections, we assumed that $l_{\rm cor} \ll r_m$ and $a_{NN} \ll r_m$, where a_{NN} is the range of nucleon–nucleon interaction (see, for example, [7]). Within this assumption, we performed an expansion up to second-order terms in a_{NN}/r_m. The corrections to the profile functions (14)–(17) due short-range correlations are given by

$$\Omega_{c1}^{(\rm sr)}(b) = \sum_{\nu=0}^{2} k_\nu [G_0^{(\nu)}(b) C_{N-\nu, Z-2+\nu}^{(+)} + iG_B^{(\nu)}(b) C_{N-\nu, Z-2+\nu}^{(-)}], \tag{26}$$

$$\Omega_{B1}^{(\rm sr)}(b) = -\sum_{\nu=0}^{2} k_\nu [iG_0^{(\nu)}(b) C_{N-\nu, Z-2+\nu}^{(-)} - G_B^{(\nu)}(b) C_{N-\nu, Z-2+\nu}^{(+)}], \tag{27}$$

$$\Omega_{c2}^{(\rm sr)}(b) = -\sum_{\nu=0}^{2} k_\nu G_b^{(\nu)}(b) C_{N-\nu, Z-2+\nu}^{(+)}, \tag{28}$$

$$\Omega_{B2}^{(\rm sr)}(b) = i\sum_{\nu=0}^{2} k_\nu G_b^{(\nu)}(b) C_{N-\nu, Z-2+\nu}^{(-)}. \tag{29}$$

Since the expressions for the functions $G_0^{(\nu)}$, $G_B^{(\nu)}$, and $G_b^{(\nu)}$ are rather cumbersome, we present here simpler formulas for them, those that satisfy the definition in (25) and which correspond to the zero-order approximation in a_{NN}/r_m (in numerical calculations, the resulting distinctions are insignificant):

$$G_0^{(\nu)}(b) = -\frac{\pi}{k^2}\left\{\int_0^\infty dq q \zeta(q)[2 f_c^{(i_\nu)}(q) f_c^{(j_\nu)}(q) - f_s^{(i_\nu)}(q) f_s^{(j_\nu)}(q)] \int_{-\infty}^{\infty} dz \rho_0^{(i_\nu)}(r) \rho_0^{(j_\nu)}(r) - 2\int_0^\infty dq q^{-1} \zeta(q) f_s^{(i_\nu)}(q) f_s^{(j_\nu)}(q) \times \int_{-\infty}^{\infty} dz \left[\frac{\partial}{\partial b}\rho_0^{(i_\nu)}(r)\right]\left[\frac{\partial}{\partial b}\rho_0^{(j_\nu)}(r)\right]\right\}, \tag{30}$$

$$G_B^{(\nu)}(b) = -\frac{2\pi}{k^2}\left[\int_0^\infty dq \zeta(q) f_c^{(i_\nu)}(q) f_s^{(j_\nu)}(q) \times \int_{-\infty}^{\infty} dz \rho_0^{(i_\nu)}(r) \frac{\partial}{\partial b}\rho_0^{(j_\nu)}(r) + (i_\nu \longleftrightarrow j_\nu)\right], \tag{31}$$

$$G_b^{(\nu)}(b) = -\frac{\pi}{k^2}\int_0^\infty dq q \zeta(q) f_s^{i_\nu}(q) f_s^{j_\nu}(q) \times \int_{-\infty}^{\infty} dz \rho_0^{(i_\nu)}(r) \rho_0^{(j_\nu)}(r). \tag{32}$$

Here, $r = \sqrt{b^2 + z^2}$ and the $(i_\nu \longleftrightarrow j_\nu)$ term in (31) is obtained from the preceding term by the interchange of the indices indicated in the parentheses.

In calculating the *pA* amplitude, we also took into account electromagnetic interaction, along with its spin–orbit part. We note that, in the partial-wave analysis, the expressions for the proton–nucleon amplitudes contain the terms describing the electromagnetic interaction of nucleons and the distorting Coulomb phase shift in the sum over the sought partial waves. However, these terms cannot be directly substituted into equations (9) and (18)–(21). Following [7, 13, 14], we therefore take into account Coulomb interaction via the macroscopic proton–nucleus Coulomb phase shift and choose the proton–nucleon amplitudes as $f_c^{(j)}(q) = f_{cN}^{(j)}(q)$, $f_s^{(n)}(q) = f_{sN}^{(n)}(q)$, and $f_s^{(p)}(q) = f_{sN}^{(p)}(q) + f_{s,\rm em}^{(p)}(q)$, where $f_{cN}^{(j)}(q)$ and $f_{sN}^{(j)}(q)$ are the nuclear components of the amplitudes. These nuclear components are calculated on the basis of the nuclear phase shifts found from a partial-wave analysis, neither electromagnetic terms nor the distorting Coulomb phase shift being taken into account in this calculations. In accordance with a similar term in the partial-wave analysis from [15], the electromagnetic correction to the spin–orbit part of the proton–proton amplitude can be represented as {in contrast to [15], we use here the non-symmetrized expression for $f_{s,\rm em}^{(p)}(q)$}

$$f_{s,\rm em}^{(p)}(q) = \frac{i\hbar^2 \xi_{pp} k^2}{2m_p^2 c^2}(3 + 4\mu_\alpha)\frac{1}{q}\left(\sqrt{1 - \frac{q^2}{4k^2}} \times \left[1 - \frac{q^2}{2k^2}\sum_{l=1}^{l_{\max}} \frac{2l+1}{l(l+1)} P_l'(1 - q^2/2k^2)\right]\right), \tag{33}$$

where m_p and $\mu_a = 1.79$ are, respectively, the proton mass and the anomalous magnetic moment of the proton; $\zeta_{pp} = e^2/\hbar v$ is the Coulomb parameter for proton–proton scattering; $l_{\max}$ is the maximum value of the orbital angular momentum for partial-wave amplitudes in the partial-wave analysis; and $P_l'(x)$ stands for the first derivatives of Legendre polynomials. The sum over l in (33) eliminates the $l \le l_{\max}$ partial waves from $f_{s,\rm em}^{(p)}(q)$ because the corresponding effects are included in the sought phase shifts. The disregard of

this sum has virtually no effect on the calculated observables for *pA* scattering.

The central and spin–orbit components of the *pA* amplitude [$A(q)$ and $B(q)$, respectively] are expressed in terms of the proton–nucleus profile functions as

$$A(q) = A_C(q) + ik\int_0^\infty dbbJ_0(qb) \times \{e^{i\chi_0(b)} + e^{i\chi_1(b)}[\Omega_c(b) - 1]\}, \quad (34)$$

$$B(q) = B_C(b) - ik\int_0^\infty dbbJ_1(qb) \times [e^{i\chi_0(b)}\chi_{0s}(b) + e^{i\chi_1(b)}\Omega_B(b)]. \quad (35)$$

Here, $\chi_0(b) = 2\xi\ln(kb)$ and $\chi_{0s}(b) = 2\xi\kappa/b$ are the eikonal expressions for the central and spin–orbit phase shifts for the scattering of two pointlike charges, the corresponding central and spin–orbit components of the scattering amplitude being given by [11]

$$A_C(q) = -\frac{2\xi k\Gamma(1+i\xi)}{q^2\Gamma(1-i\xi)}\exp\left(-2i\xi\ln\frac{q}{2k}\right), \quad B_C(q) = -i\kappa qA_C(q), \quad (36)$$

where $\xi = Ze^2/\hbar v$ is the Coulomb parameter for *pA* scattering. The parameter κ, which characterizes the values of the phase shift $\chi_{0s}(b)$ and of the amplitude $B_C(b)$, is evaluated on the basis of the asymptotic behavior of the profile function $\Omega_B(b)$ for $b \longrightarrow \infty$. The eikonal Coulomb phase shift $\chi_1(b)$ for scattering on the volume distribution of the nuclear charge has the form [14]

$$\chi_1(b) = \chi_0(b) + 8\pi\xi\int_b^\infty drr^2\rho_0^{(p)}(r) \times \left[\ln\left(\frac{(1+\sqrt{1-b^2/r^2})}{b/r}\right) - \sqrt{1-b^2/r^2}\right]. \quad (37)$$

It should be noted that, in contrast to the popular approach described in [11], where the interaction of the proton magnetic moment with the nuclear field is taken into account by introducing the spin–orbit correction to the macroscopic proton–nucleus Coulomb phase shift $\chi_1(b)$, we include it microscopically through the proton–nucleon amplitudes.

3. We have calculated the differential cross sections and various spin observables for the elastic scattering of 800-MeV protons on ^{40}Ca, ^{54}Fe, and ^{208}Pb nuclei. In the calculations, the proton–nucleon amplitudes were approximated as $f_{cN}^{(j)}(q) = 2ik(g_{cj} + h_{cj}q^2)\exp(-a_{cj}q^2)$ and $f_{sN}^{(j)}(q) = 2ik(g_{sj} + h_{sj}q^2)\exp(-a_{sj}q^2)$, with the parameter values being determined from the solutions of the partial-wave analyses from [15–17]. Presented below are the results of the calculations with the proton–nucleon amplitudes featuring parameters obtained in [18] from the partial-wave analysis performed in [15]. Specifically, we used the values of $g_{cp} = 4.84 + i0.03$ (GeV/c)$^{-2}$, $h_{cp} = 8.33 + i12.24$ (GeV/c)$^{-4}$, and $a_{cp} = 5.82 - i0.85$ (GeV/c)$^{-2}$; $g_{sp} = -2.29 - i6.15$ (GeV/c)$^{-2}$, $h_{sp} = 0$, and $a_{sp} = 3.70 + i0.19$ (GeV/c)$^{-2}$; $g_{cn} = 3.91 + i1.40$ (GeV/c)$^{-2}$, $h_{cn} = 5.52 - i5.64$ (GeV/c)$^{-4}$, and $a_{cn} = 4.87 - i3.0$ (GeV/c)$^{-2}$; and $g_{sn} = -2.55 - i4.51$ (GeV/c)$^{-2}$, $h_{sn} = 0$, and $a_{sp} = 3.93 + i0.47$ (GeV/c)$^{-2}$. The results of the calculations with the proton–nucleon amplitudes from the solutions of the partial-wave analyses performed in [16, 17] differ only slightly from those mentioned immediately above.

The Hartree–Fock densities that we used here were calculated with various Skyrme forces, including Sk1 and Sk2 [19], SkT [20], Ska [21], and SkM [22]. For the ^{40}Ca nucleus, we also present the results of the calculations with the densities determined from the model-independent charge density [23] found from an analysis of electron scattering. In this case, we took into account the charge form factor for the proton and assumed that the proton densities are identical to the neutron densities.

For the specific calculations, we need the $|0\rangle \longrightarrow |\alpha; I, M\rangle$ transition densities. We use a macroscopic model and express the transition densities in terms of the derivatives of ground-state densities $\rho_0^{(j)}(r)$ as $\rho_{\alpha I}^{(j)}(r) = -\delta_{\alpha I}/\sqrt{2I+1}\,(\partial\rho_0^{(j)}/\partial r)$. It is well known that this model appears to be the most appropriate one for low-lying collective states. However, we assume that, for our purposes, it is legitimate to use it for all intermediate states included in our analysis, since inelastic transitions are well known to be predominantly superficial, irrespective of the nature of the final states. The deformation length $\delta_{\alpha I}$ was evaluated either by using the relation $\delta_I = B(EI)^{1/2}/[Ze\int_0^\infty(\partial\rho_0^{(p)}/\partial r)\,r^{I+2}dr]$ with the reduced probabilities $B(EI)$ for corresponding transitions from [24, 25] or by using the results of the studies—[26, 27] for ^{40}Ca, [27, 28] for ^{54}Fe, and [29–31] for ^{208}Pb—where these transitions were analyzed within a similar macroscopic model. Some details are given immediately below. For ^{40}Ca, we took into account the $I^\pi = 2^+$ states at 3.90 MeV [$B(E2) = 96e^2$ fm^4], 6.91 MeV ($\delta_2 = 0.49$ fm), 7.87 MeV (0.28 fm), and four more states corresponding to weaker transitions with $\delta_2 = 0.15$–0.18 fm; the $I^\pi = 3^-$ states at 3.74 MeV [$B(E3) = 20\,400e^2$ fm^6), 6.29 MeV ($\delta_3 = 0.46$ fm), and 6.58 MeV (0.41 fm); the $I^\pi = 4^+$ states at 5.28 MeV ($\delta_4 = 0.16$ fm), 6.51 MeV (0.18 fm), 7.46 MeV (0.2 fm), 7.56 MeV (0.23 fm), and 7.92 MeV (0.34 fm); and the $I^\pi = 5^-$ states at 4.49 MeV ($\delta_5 = 0.91$ fm) and 8.54 MeV

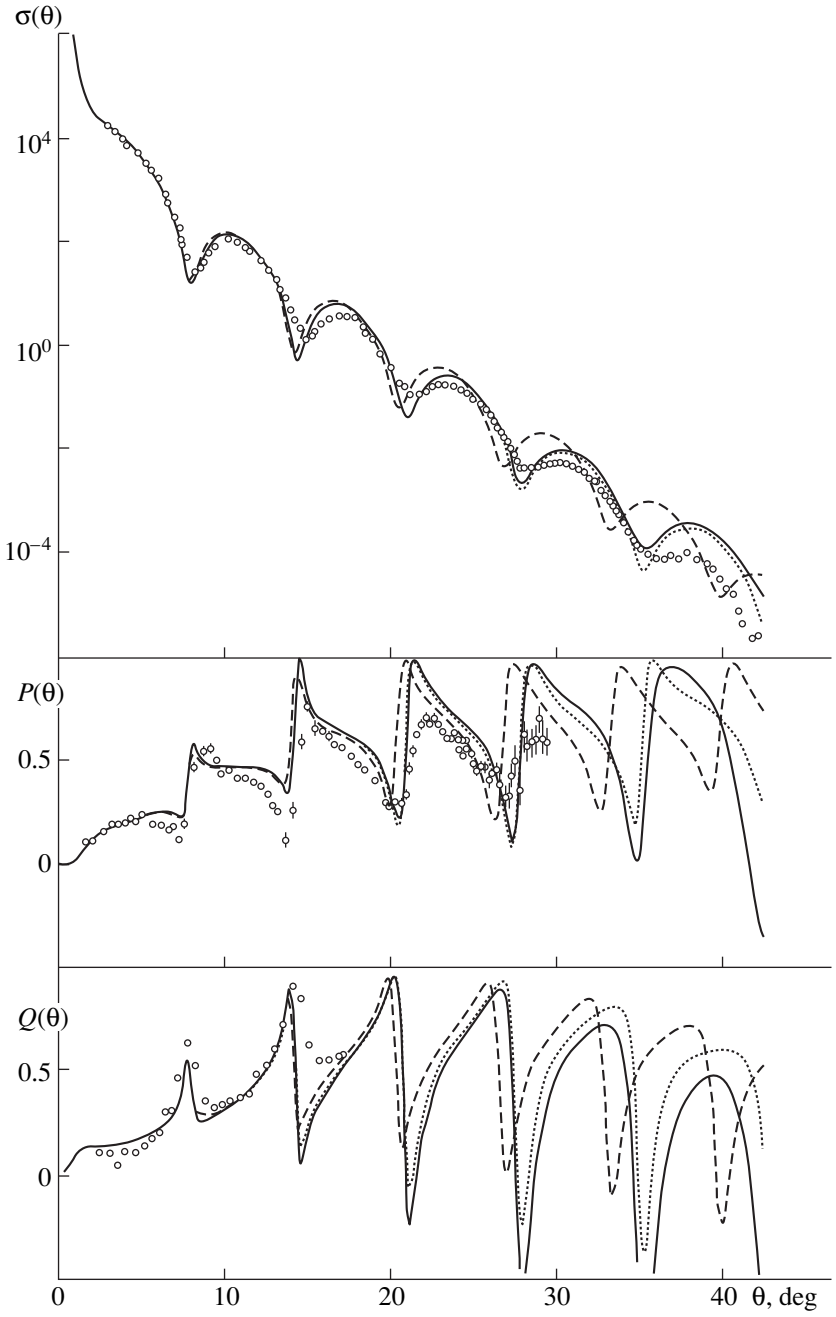

Fig. 1. Differential cross section σ(θ) (in mb/sr), polarization $P(\theta)$, and spin-rotation function $Q(\theta)$ for the elastic scattering of 800-MeV protons on ^{40}Ca nuclei: (solid curves) results of the calculation employing the Hartree–Fock densities for the Sk1 Skyrme forces and taking into account c.m. correlations, short-range correlations, and intermediate excitations; (dotted curves) results of the calculations taking no account of short-range correlations; and (dashed curves) results of the calculations taking into account only c.m. correlations. Experimental data were borrowed from [9, 32].

(0.23 fm). For ^{54}Fe, we took into account the $I^\pi = 2^+$ states at 1.41 MeV [$B(E2) = 620e^2$ fm^4], 2.96 MeV (δ_2 = 0.51 fm), 3.17 MeV (0.3 fm), 4.58 MeV (0.17 fm), and 6. 43 MeV (0.2 fm); the $I^\pi = 3^-$ states at 4.78 MeV [$B(E3) = 4390e^2$ fm^6], 6.34 MeV (δ_3 = 0.63 fm), 7.27 MeV (0.31 fm), 8.01 MeV (0.21 fm), 8.47 MeV (0.19 fm), and 14 additional states with δ_3 = 0.10–0.17 fm; and the $I^\pi = 4^+$ states at 2.54 MeV (δ_4 = 0.36 fm), 3.30 MeV (0.22 fm), 3.83 MeV (0.43 fm), 4.26 MeV (0.35 fm), and ten additional states with δ_4 = 0.10–0.15 fm. For ^{208}Pb, we took into account the $I^\pi = 2^+$ states at 4.09 MeV [$B(E2) = 2900e^2$ fm^4] and 11 additional states with $\delta_2 = 0.05 \pm 0.12$ fm; the $I^\pi = 3^-$ states at 2.61 MeV [$B(E3) = 611000e^2$ fm^6], 5.35 MeV

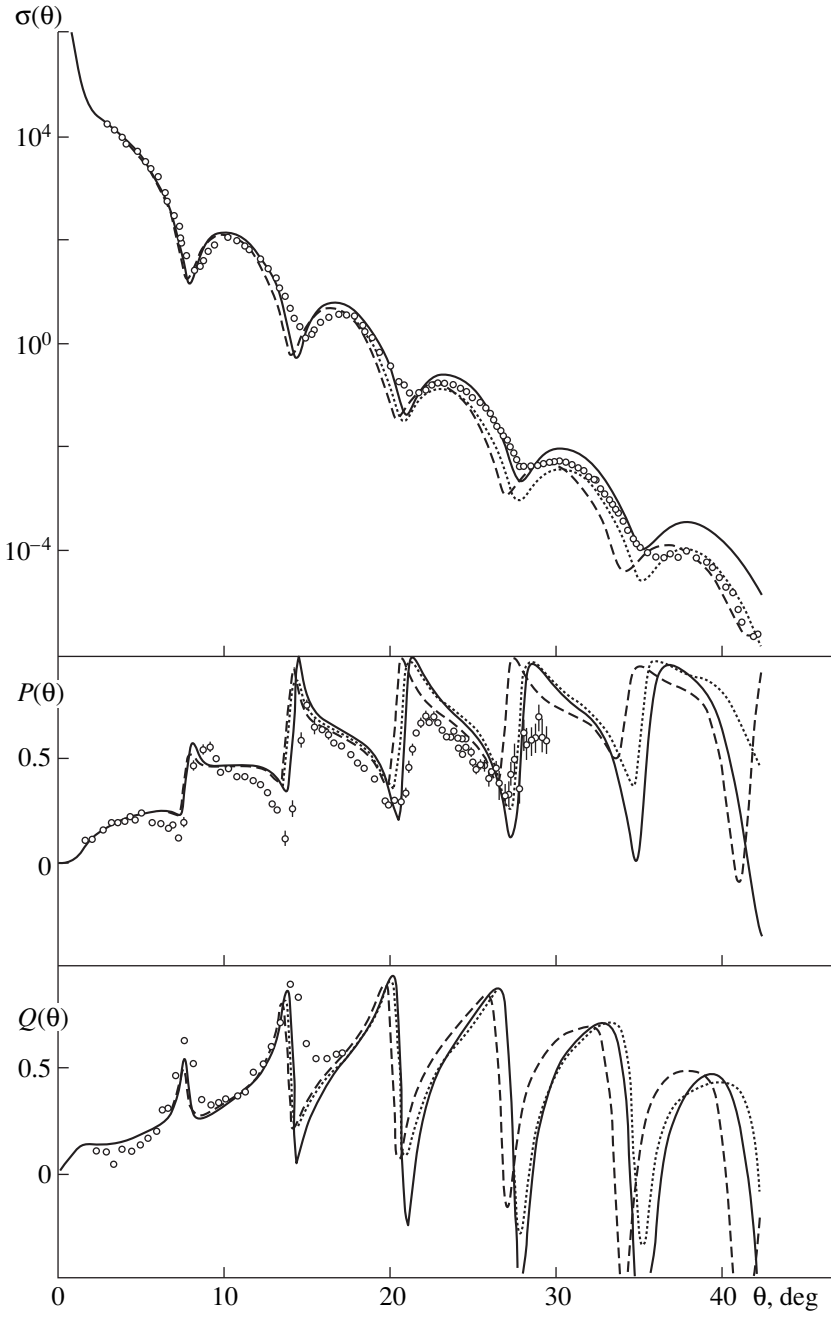

Fig. 2. Differential cross section σ(θ) (in mb/sr), polarization $P(\theta)$, and spin-rotation function $Q(\theta)$ for the elastic scattering of 800-MeV protons on ^{40}Ca nuclei: (solid curves) results of the calculation employing the Sk1 Skyrme forces and taking into account all kinds of correlations considered in this study, (dashed curves) results of the calculation employing the SkT Skyrme forces and taking into account all kinds of correlations considered in this study, and (dotted curves) results of the calculation employing the model-independent densities.

(δ_3 = 0.25 fm), and 22 additional states with δ_3 = 0.05–0.20 fm; the $I^\pi = 4^+$ states at 4.32 MeV (δ_4 = 0.55 fm), 5.69 MeV (0.32 fm), and four additional states with δ_4 = 0.10–0.15 fm; and the $I^\pi = 5^-$ states at 3.20 MeV (δ_5 = 0.40 fm), 3.71 MeV (0.28 fm), 5.48 MeV (0.32 fm), 6.69 MeV (0.29 fm), and four additional states with δ_5 = 0.10–0.15 fm. For short-range correlations, we used the value of l_{cor} = 0.55 fm [6, 7]. It should be noted that the contribution of low-lying collective excitations to the cross section for elastic proton scattering on nuclei was estimated previously in a number of studies (see, for example, [4, 7, 14]), but this contribution is usually disregarded for spherical target nuclei, because it is assumed to be small.

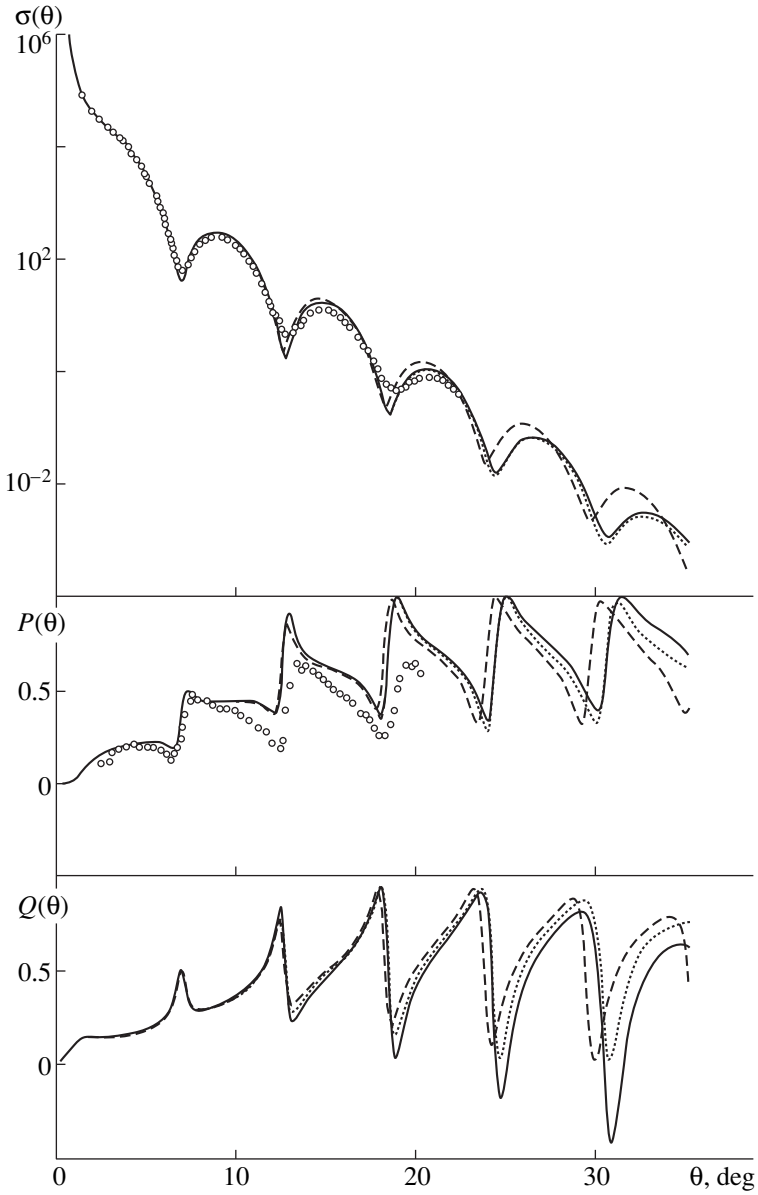

Fig. 3. As in Fig. 1, but for ^{54}Fe target nuclei. Experimental data were borrowed from [33].

For the cases of proton–nucleus scattering that were studied here, Figs. 1–6 display the results obtained from various versions of the calculation of the differential cross sections $\sigma(\theta)$, the polarizations $P(\theta)$, and the spin-rotation functions $Q(\theta)$. The effect of taking into account intermediate excitations on the computed observables is demonstrated by considering the results of the calculations with the nuclear densities for the Sk1 Skyrme forces (see Figs. 1, 3, and 5). In the calculations with other densities, the effects of intermediate excitations have just the same character. From Figs. 1, 3, and 5, it can be seen that the effect of intermediate excitations is enhanced as the scattering angle becomes larger, reaching quite a sizable degree at sufficiently large values of θ, where it leads to noticeable shifts of diffraction maxima and minima in the cross sections and spin observables toward larger scattering angles and suppresses further the cross section maxima with increasing θ. In the case of p^{40}Ca scattering, the inclusion of intermediate excitations reduces the height of the fifth cross-section maximum at $\theta \sim 30°$ by a factor greater than two. It was indicated in number of studies (see, for example, [35–37]) that, in describing *pA* scattering on the basis of the Glauber–Sitenko theory of multiple diffractive scattering with Hartree–Fock densities, there arise characteristic deviations from experimental data: the positions of the diffraction maxima and minima in the observables computed theoretically are shifted toward smaller values of the scattering angle, while the slope of the envelope of the cross-sec-

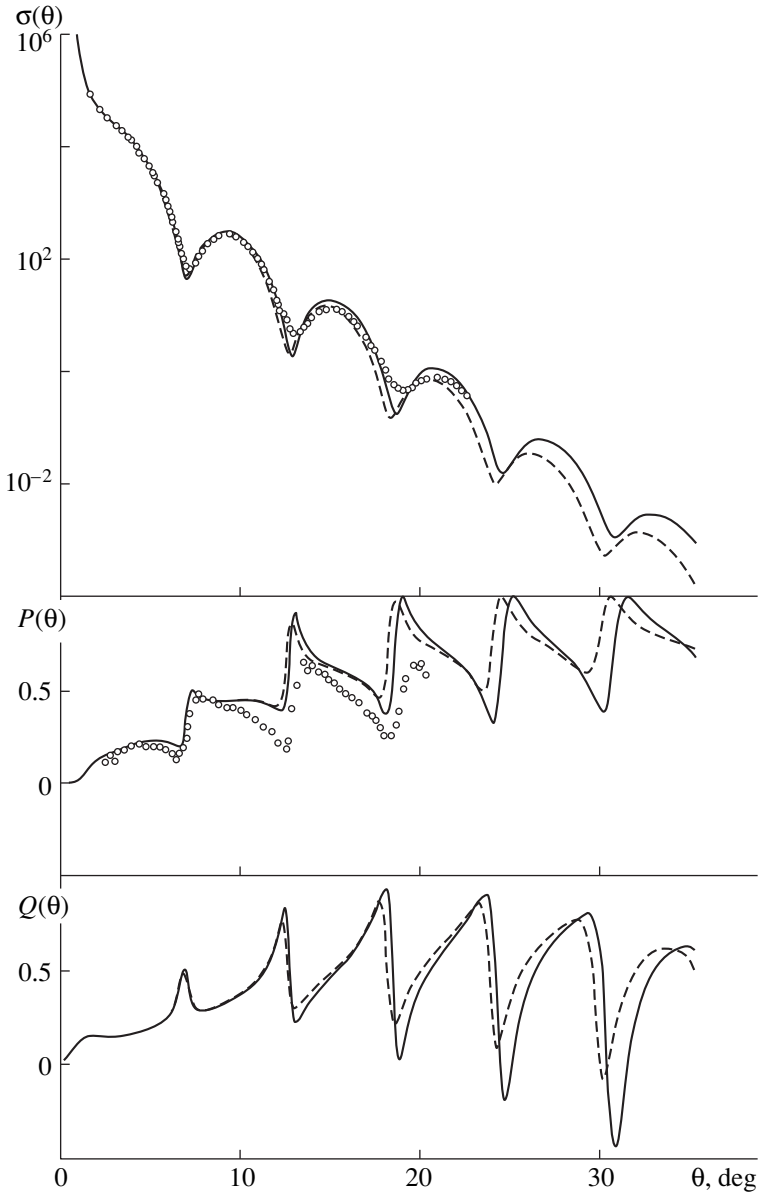

Fig. 4. As in Fig. 3, but the results of the calculations performed with the Hartree–Fock densities and with allowance for all types of correlations considered in the present article are depicted by the solid and dashed curves for the cases of, respectively, the Sk1 and the SkT Skyrme forces.

tion maxima is smaller than the value obtained experimentally. Thus, the data presented in Figs. 1, 3, and 5 show that the above discrepancies between the calculated and measured values are reduced upon taking into account intermediate excitations. In the cases being considered, the contribution of short-range correlations is relatively small. They have the strongest effect on the spin-rotation function $Q(\theta)$ at sufficiently large values of the angle θ.

The results of the calculations employing the various nuclear densities and taking into account all the correlations considered above are compared in Figs. 2, 4, and 6. Of all Hartree–Fock densities, we present the results only for the Sk1 and SkT versions. The calculations performed with the remaining Hartree–Fock densities lead to results similar to those obtained by using the SkT version. From Figs. 2, 4, and 6, it can be seen that, in the case of the Sk1 forces, the inclusion of intermediate excitations removes completely the above shift of the computed positions of the diffractive maxima and minima in the observables in question with respect to their experimental positions, but that, for the SkT version (as well as for all other versions), there remains some shift toward small angles. At the same time, the calculations for the Sk1 version yield overestimated values for cross-section maxima at large scattering

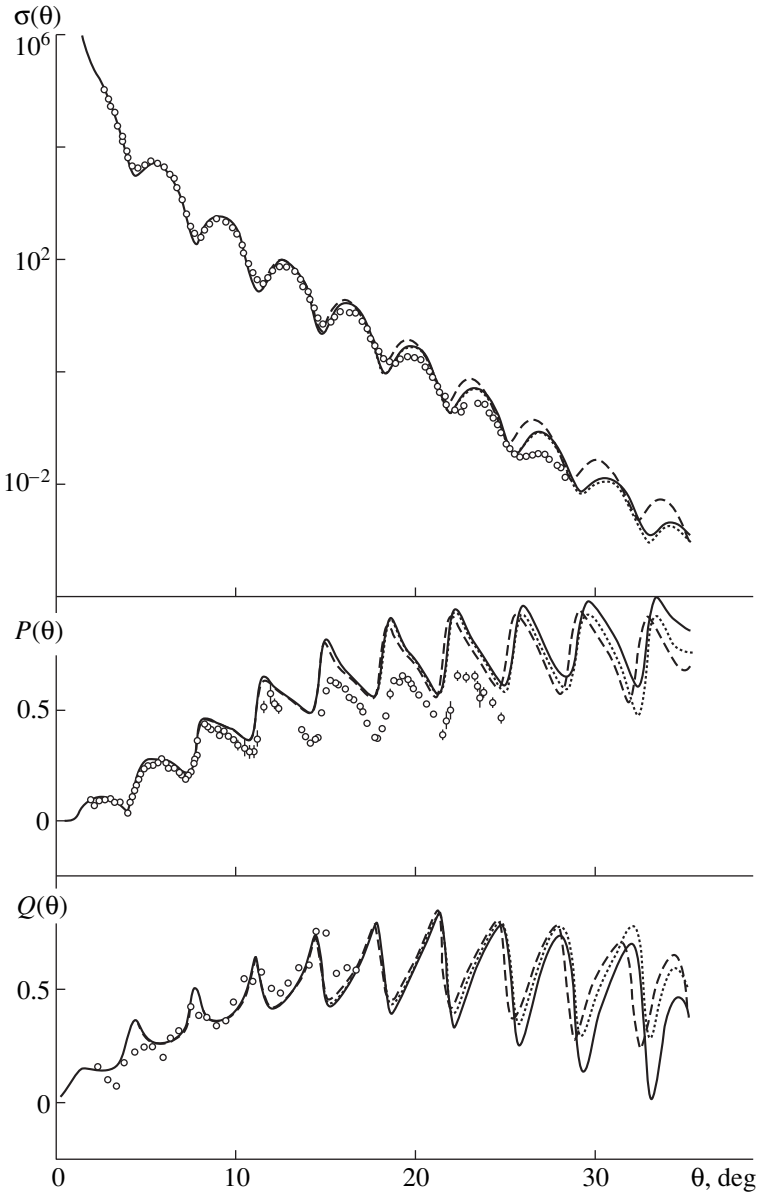

Fig. 5. As in Fig. 1, but for ^{208}Pb target nuclei. Experimental data were borrowed from [32, 34].

angles. In the calculations with model-independent densities for p^{40}Ca scattering (see Fig. 2), the inclusion of intermediate excitations also removes completely the shift of the diffraction maxima and minima in the computed observables. In that case, the maxima of the computed cross section are lower than those for the Sk1 version. We note that, in each quoted version of the calculations, there is some specific discrepancy between the calculated and measured spin observables that is peculiar to this version. By way of example, we indicate that, at not overly small values of the scattering angle, the polarization $P(\theta)$ computed theoretically exceeds systematically the measured polarization. This may suggest the need for taking into account corrections to the standard Glauber–Sitenko approach.

4. By taking into account spin–orbit interaction, intermediate excitations of the target nucleus, short-range nucleon correlations in nuclei, the distinctions between the proton–proton and the proton–neutron amplitudes and between the proton and the neutron densities, electromagnetic effects, and Z ordering, we have obtained here the expressions for the amplitudes of elastic pA scattering. On the basis of these expressions, we have computed the cross sections and the spin observables for the elastic scattering of 800-MeV protons on ^{40}Ca, ^{54}Fe, and ^{208}Pb nuclei by using the proton–nucleon amplitudes found from partial-wave analyses, as well as the Hartree–Fock and the model independent densities. A satisfactory description of experimental data has been obtained. It has been shown

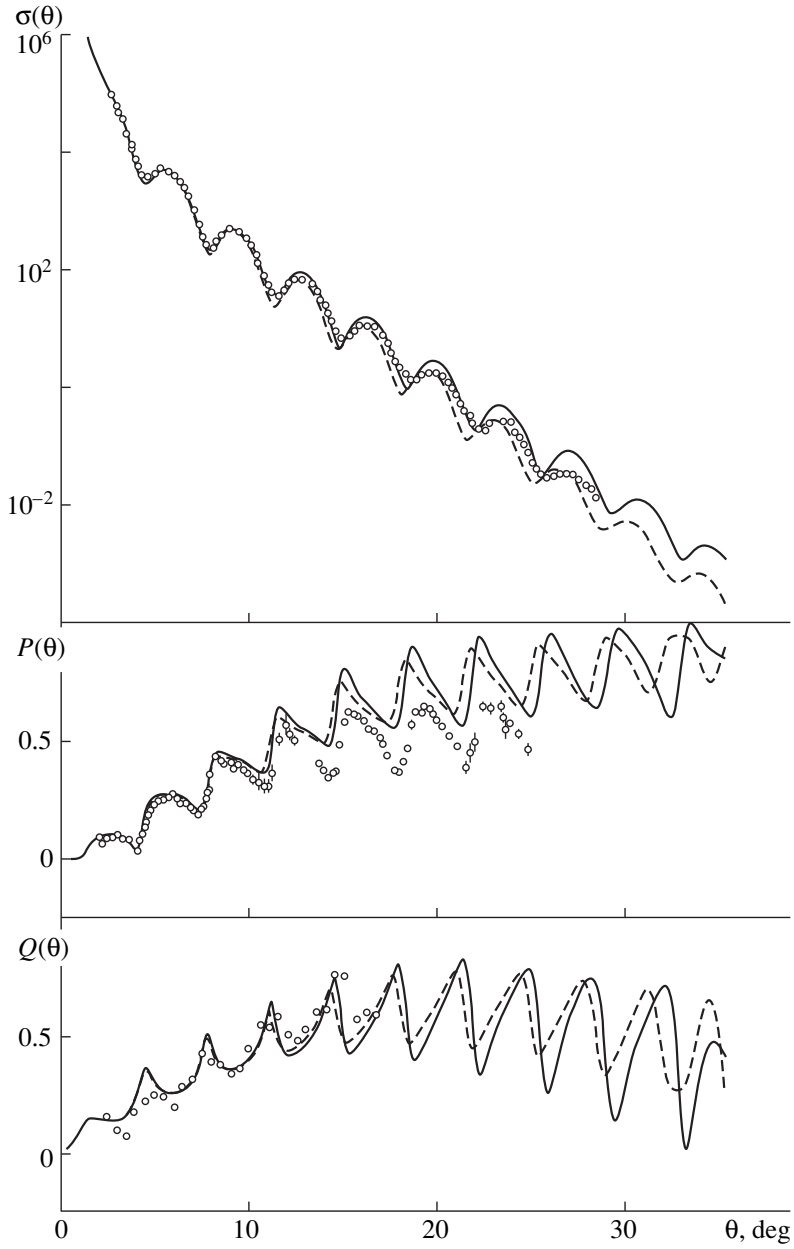

Fig. 6. As in Fig. 5, but the results of the calculations performed with the Hartree–Fock densities and with allowance for all types of correlations considered in the present article are depicted by the solid and dashed curves for the cases of, respectively, the Sk1 and the SkT Skyrme forces.

that the inclusion of intermediate excitations affects considerably the behavior of observables, shifting the positions of diffractive maxima and minima toward larger scattering angles and enhancing the reduction of cross-section maxima. The effect of intermediate excitations appears to be commensurate with the distinctions between the results of the calculations with the different versions of the nuclear densities or even to exceed them. Therefore, a comparison of different versions of data descriptions is meaningless without taking such effects into account.

ACKNOWLEDGMENTS

We are grateful to Yu.A. Berezhnoy, I.N. Kudryavtsev, and A.P. Soznik for stimulating discussions.

REFERENCES

1. R. J. Glauber, in *Lectures in Theoretical Physics*, Ed. by W. E. Brittin and L. G. Dunham (Interscience, New York, 1959), Vol. 1, p. 315.
2. A. G. Sitenko, Ukr. Fiz. Zh. (Russ. Ed.) **4**, 152 (1959).

3. J. J. Ullo and H. Feshbach, Ann. Phys. (N.Y.) **82**, 156 (1974).
4. V. E. Starodubsky, Nucl. Phys. A **219**, 525 (1974).
5. I. Ahmad, Phys. Lett. B **36**, 301 (1971).
6. G. D. Alkhazov, Nucl. Phys. A **280**, 330 (1977).
7. G. D. Alkhazov, S. I. Belostocky, and A. A. Vorobyov, Phys. Rep. **42**, 89 (1978).
8. D. R. Harrington and G. K. Varma, Nucl. Phys. A **306**, 477 (1978).
9. E. Bleszynski *et al.*, Phys. Rev. C **25**, 2563 (1982).
10. R. J. Glauber and V. Franko, Phys. Rev. **156**, 1685 (1967).
11. P. Osland and R. J. Glauber, Nucl. Phys. A **326**, 255 (1979).
12. V. V. Pilipenko, Vestn. Khar'k. Univ., Ser. Fiz., No. 421, 27 (1998).
13. R. J. Glauber and G. Matthiae, Nucl. Phys. B **21**, 135 (1970).
14. I. Ahmad, Nucl. Phys. A **247**, 418 (1975).
15. J. Bystricky *et al.*, J. Phys. (Paris) **48**, 199 (1987).
16. R. Arndt *et al.*, Phys. Rev. D **28**, 97 (1983).
17. R. Arndt *et al.*, Phys. Rev. D **35**, 128 (1987).
18. I. N. Kudryavtsev and A. P. Soznik, J. Phys. G **15**, 1377 (1989).
19. D. Vautherin and D. M. Brink, Phys. Rev. C **5**, 626 (1972).
20. F. Tondeur, Phys. Lett. B **123**, 139 (1983).
21. H. S. Köhler, Nucl. Phys. A **258**, 301 (1976).
22. J. Bartel *et al.*, Nucl. Phys. A **386**, 79 (1982).
23. H. De Vries *et al.*, At. Data Nucl. Data Tables **36**, 495 (1987).
24. S. Raman *et al.*, At. Data Nucl. Data Tables **36**, 1 (1987).
25. R. H. Spear, At. Data Nucl. Data Tables **42**, 55 (1989).
26. C. R. Gruhn *et al.*, Phys. Rev. C **6**, 915 (1972).
27. G. S. Adams *et al.*, Phys. Rev. C **21**, 2485 (1980).
28. M. Fujiwara *et al.*, Phys. Rev. C **32**, 830 (1985).
29. D. K. McDaniels *et al.*, Nucl. Phys. A **467**, 557 (1987).
30. Y. Fujita *et al.*, Phys. Rev. C **32**, 425 (1985).
31. W. T. Wagner *et al.*, Phys. Rev. C **12**, 757 (1975).
32. R. W. Fergerson *et al.*, Phys. Rev. C **33**, 239 (1986).
33. G. W. Hoffmann *et al.*, Phys. Lett. B **79**, 376 (1978).
34. G. W. Hoffmann *et al.*, Phys. Rev. C **21**, 1488 (1980).
35. A. Chaumeaux *et al.*, Ann. Phys. (N.Y.) **116**, 247 (1978).
36. V. E. Starodubsky and V. R. Shaginyan, Preprint No. 387, LNPI (Leningrad Nuclear Physics Inst., USSR Academy of Sciences, 1978).
37. V. I. Kuprikov and A. P. Soznik, Ukr. Fiz. Zh. (Russ. Ed.) **32**, 994 (1987).

Translated by A. Isaakyan

Physics of Atomic Nuclei, Vol. 63, No. 5, 2000, pp. 795–800. From Yadernaya Fizika, Vol. 63, No. 5, 2000, pp. 865–870.

NUCLEI
Theory

Cross Sections and Asymmetries for Elastic π^3He Scattering in the Energy Region around the Δ Resonance*

M. A. Braun and V. M. Suslov

Institute of Physics (Petrodvorets Branch), St. Petersburg State University, Ul'yanovskaya ul. 1, Petrodvorets, 198904 Russia

Received February 4, 1999

Abstract—For a polarized target, π^3He interaction is studied in the fixed-center approximation with all rescatterings included. Only the P_{33} wave is taken for the πN interaction. The nuclear wave function is taken either as a sum of Gaussian functions or as a Faddeev wave function in the *s*-wave approximation. The differential cross sections and asymmetries for elastic π^{+3}He scattering at the laboratory energies of T_π = 142, 180, and 256 MeV are calculated. The results are compared with experimental data. © *2000 MAIK "Nauka/Interperiodica".*

1. INTRODUCTION

Investigation of pion scattering off light nuclei requires its reliable theoretical description. An exact relativistic treatment of systems with four or more particles is beyond the present computational possibilities, so that simplifications are unavoidable. Current studies of π–trinucleon reactions are mostly performed on the basis of the optical potential model [1], which treats the nucleus as a single particle interacting with the pion via some effective potential. This may be a good approach at low energies when the pion wavelength λ_π is larger than the internucleon distance *R*. However, at energies above 100 MeV, when $\lambda_\pi \le R$, the optical potential model does not seem natural, and alternative approaches deserve attention. A viable alternative seems to be the fixed-scattering-center model, which emerges in the limit $m_\pi/m_N \longrightarrow 0$. In this model, all intermediate nuclear states are taken into account, although the variation of their energies is neglected. If one retains only the ground state in the sum over intermediate nuclear states in the fixed-center model, then the optical-model results are recovered (without the contribution of the nucleus to the energy denominators). Thus, the fixed-center model represents an improvement of the optical potential model in that it takes into account intermediate nuclear states.

From the study of πd scattering, where more sophisticated techniques can also be applied, it is known that the fixed-center model gives an accuracy of about 10–20%, which naturally becomes poorer with increasing momentum transfer [2]. For that, the fixed-center model is well-behaved in the ultraviolet region, involving no cutoff parameter, in contrast to all models that take the nucleon recoil into account.

For practical application of the fixed-center model, the energy region of the Δ resonance seems particularly favorable. At these energies, the πN interaction can be well approximated by a P_{33} wave (i.e., it is simple and essentially reduces to a separable form, which simplifies the calculations substantially). On the other hand, the pion energy still remains considerably smaller than the nucleon energy. Therefore, one can hope that neglecting the nucleon recoil might be a reasonable approximation.

In [3], we introduced a model that is based on the fixed-center approximation for elastic π^3H and π^3He interactions and which takes completely into account multiple pion rescattering. A simple Gaussian wave function for the nuclear ground-state was used. The present paper reports on the calculations with the Faddeev ground-state wave functions and also on the application of the model to polarized targets.

2. GENERAL FORMALISM

In the fixed-center approximation, the determination of the amplitude of the interaction with a nucleus reduces to evaluating the sum of the diagrams shown in Fig. 1.

The exact treatment of these graphs requires the introduction of 216 amplitudes. In the present calculations, the spin-tensor interaction in the elementary block of Fig. 2 was replaced by an averaged one. As a result, the number of independent amplitudes was reduced to 27.

The basic Faddeev-like amplitudes are M_{ik}, where *i* and *k* refer to the number of initial and final nucleons (*i*, *k* = 1, 2, 3). Each M_{ik} is a 3×3 matrix in both spin and isospin. The final system of linear equations for the amplitudes M_{ik} has the form

$$M_{ik} = R_1 P^{(i)} \delta_{ik} + R_1 \sum_{l \neq i} P^{(i)} W_{il} M_{lk}, \qquad (1)$$

* This article was submitted by the author in English.

1063-7788/00/6305-0795$20.00 © 2000 MAIK "Nauka/Interperiodica"

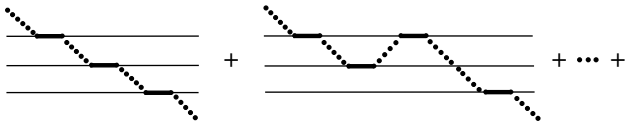

Fig. 1. Successive rescatterings of a π meson with the production of a Δ_{33} resonance: (dotted lines) π meson, (thick lines) Δ_{33} resonance, and (thin lines) nucleons.

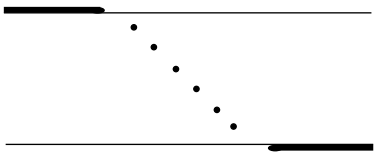

Fig. 2. Potential W_{ik}. The notation is identical to that in Fig. 1.

where $R_1(E) = (m_\Delta - m_N + \varepsilon_b - k_0 - i0)^{-1}$, k_0 is the pion energy, and $P^{(i)}$ stands for the operators of projection onto the $I = J = 3/2$ states for the *pion plus the i*th *nucleon* system.

The "potentials" W_{ik} describe intermediate-pion propagation, and they are complex:

$$W(r) = \frac{\lambda^2}{3(2\pi)^2}\int d^3q \frac{\mathbf{q}^2 \exp(i\mathbf{q}\cdot\mathbf{r})}{\mathbf{q}^2 + m_\pi^2 - (k_0 - \varepsilon_b)^2 - i0}, \qquad \lambda^2 = \frac{6\pi\Gamma_\Delta}{k_{\text{res}}^3}. \tag{2}$$

Here, ε_b is the binding energy of the $A = 3$ nucleus. The solution of equation (1) provides us with scattering amplitudes with given total spin and isospin and spin–isospin variables of pairs of nucleons. For the π*A* amplitudes of total isospin *T*, we obtain the expression

$$\mathcal{A}^{(T)} = \frac{3\lambda^2}{\sqrt{2k_0 2k_0'}} \sum_{S = 1/2,\, 3/2} (\mathbf{k}' P^{(S)} \mathbf{k}) \int d^3r_1 d^3r_2 \Psi_A^*(\mathbf{r}_{ik}) \times (\exp(i(\mathbf{k} - \mathbf{k}')\cdot\mathbf{r}_1) M_{11(T,S)} + 2\exp(i(\mathbf{k}\cdot\mathbf{r}_1 - \mathbf{k}'\cdot\mathbf{r}_2)) M_{21(T,S)}) \Psi_A(\mathbf{r}_{ik}). \tag{3}$$

Here, Ψ_A is the wave function of the ^{3}H (^{3}He) nucleus, and the relative coordinates are defined as $\mathbf{r}_{ik} = \mathbf{r}_i - \mathbf{r}_k$ ($\mathbf{r}_3 = -\mathbf{r}_1 - \mathbf{r}_2$). To make partial integrations with respect to angles possible, we represent the π*A* amplitude as the sum $\mathcal{A}^{(T)} = \mathcal{A}_1^{(T)} + \mathcal{A}_2^{(T)}$, where

$$\mathcal{A}_1^{(T)} = \frac{3\lambda^2}{\sqrt{2k_0 2k_0'}} \sum_{S = 1/2,\, 3/2} (\mathbf{k}' P^{(S)} \mathbf{k}) \times \int d^3r_1 d^3r_2 (\exp(i(\mathbf{k} - \mathbf{k}')\cdot\mathbf{r}_1)) F_{(T,S)}(\mathbf{r}_{ik}),$$

$$\mathcal{A}_2^{(T)} = \frac{3\lambda^2}{\sqrt{2k_0 2k_0'}} \sum_{S = 1/2,\, 3/2} (\mathbf{k}' P^{(S)} \mathbf{k}) \times \int d^3r_1 d^3r_2 \exp(i(\mathbf{k}\cdot\mathbf{r}_1 - \mathbf{k}'\cdot\mathbf{r}_2)) G_{(T,S)}(\mathbf{r}_{ik}) \tag{4}$$

with

$$F_{(T,S)}(\mathbf{r}_{ik}) = \Psi_A^*(\mathbf{r}_{ik}) M_{11(T,S)}(\mathbf{r}_{ik}) \Psi_A(\mathbf{r}_{ik}),$$
$$G_{(T,S)}(\mathbf{r}_{ik}) = 2\Psi_A^*(\mathbf{r}_{ik}) M_{21(T,S)}(\mathbf{r}_{ik}) \Psi_A(\mathbf{r}_{ik}). \tag{5}$$

The formula for the amplitude $\mathcal{A}$ can be represented in a form similar to that for the case of π*N* interaction,

$$\mathcal{A}^{(T)} = a^{(T)}(\mathbf{k}'\cdot\mathbf{k}) + ib^{(T)}(\boldsymbol{\sigma}\cdot\mathbf{k}'\times\mathbf{k}), \tag{6}$$

$$a^{(T)} = \frac{1}{3}(\mathcal{A}^{(\mathcal{T})}_{1,S=1/2} + \mathcal{A}^{(\mathcal{T})}_{2,S=1/2} + 2(\mathcal{A}^{(\mathcal{T})}_{1,S=3/2} + \mathcal{A}^{(\mathcal{T})}_{2,S=3/2})),$$
$$b^{(T)} = \frac{1}{3}(\mathcal{A}^{(\mathcal{T})}_{1,S=1/2} + \mathcal{A}^{(\mathcal{T})}_{2,S=1/2} - (\mathcal{A}^{(\mathcal{T})}_{1,S=3/2} + \mathcal{A}^{(\mathcal{T})}_{2,S=3/2})). \tag{7}$$

The amplitudes $\mathcal{A}_{i,S}^{(T)}$, which results from integration with respect to the angles in (4), are determined by triple integrals of the form

$$\mathcal{A}_{1,S}^{(T)} = \frac{24\pi^2\lambda^2}{\kappa\sqrt{2k_0 2k_0'}} \int_0^\infty r_1 dr_1 \sin(\kappa r_1) \times \int_0^\infty r_2^2 dr_2 \int_{-1}^{+1} dz F_{(T,S)}(r_1, r_2, z),$$

$$\mathcal{A}_{2,S}^{(T)} = \frac{12\pi^2\lambda^2}{\sqrt{2k_0 2k_0'}} \int_0^\infty r_1^2 dr_1 \int_0^\infty r_2^2 dr_2 \times \int_{-1}^{+1} dz_2 G_{(T,S)}(r_1, r_2, z_2) D(kr_1, \kappa r_2, \cos\delta, z_2). \tag{8, 9}$$

In these expressions, the variables z and z_2 are $\cos(\widehat{r_1, r_2})$ and $\cos(\widehat{r_{12}, r_2})$, respectively, and the notation $\cos\delta = -\sqrt{\frac{1 - \cos\theta_\pi}{2}}$ and $\kappa = -2k\cos\delta$, where θ_π is the c.m. angle of the pion, is used. The function *D*,

which emerges as the result of integration with respect to the angles in the second equation (4), has the form

$$D(kr_1, \kappa r_2, \cos\delta, z_2) = \int_{-1}^{+1} du J_0(kr_1\sqrt{1-u^2}\sin\delta) \times J_0(\kappa r_2\sqrt{1-u^2}\sqrt{1-z_2^2})\exp(-iu(kr_1\cos\delta + \kappa r_2 z_2)), \quad (10)$$

where J_0 stands for Bessel functions.

The differential cross section for the unpolarized target is given by

$$\frac{d\sigma}{d\theta_\pi} = \frac{k_0^2\mathbf{k}^4}{4\pi^2}(|a^{(T)}|^2\cos^2\theta_\pi + |b^{(T)}|^2\sin^2\theta_\pi). \quad (11)$$

The asymmetry for the polarized target is

$$A_y = \frac{\sigma\uparrow - \sigma\downarrow}{\sigma\uparrow + \sigma\downarrow},$$
$$A_y = -\frac{2\sin\theta_\pi\cos\theta_\pi \mathrm{Im}(a^{(T)}b^{*(T)})}{|a^{(T)}|^2\cos^2\theta_\pi + |b^{(T)}|^2\sin^2\theta_\pi}. \quad (12)$$

3. ^{3}He GROUND-STATE WAVE FUNCTION

As a first step, it is natural to choose the initial and final nuclear states Ψ_A in (3) without taking into account tensor forces—i.e., in the form of the product of a coordinate wave function symmetric in all variables and a spin–isospin wave function χ antisymmetric in all nucleons. We take the square of the coordinate wave function Ψ of the ground state of ^{3}He as the sum of two Gaussian functions,

$$|\Psi|^2 = \sum_{j=1,2} N_j \exp\left(-\alpha_j \sum_{i<k} r_{ik}^2\right). \quad (13)$$

The parameters α_j were chosen to give the best fit to the elastic cross section at large angles. Obviously, the spin–isospin wave function χ should have the form

$$\chi = \sqrt{1/2}[\eta(1/2, 0)\xi(1/2, 1) - \eta(1/2, 1)\xi(1/2, 0)], \quad (14)$$

where $\xi(s, s_{ij})$ $[\eta(t, t_{ij})]$ are the eigenfunctions of the total spin s (isospin t) with a given value s_{ij} of the spin (isospin t_{ij}) for the pair of the nucleons i and j. In this case, the quantities $F_{(T,S)}$ and $G_{(T,S)}$ in (5) have the form

$$F_{(T,S)}(\mathbf{r}_{ik}) = |\Psi_A(\mathbf{r}_{ik})|^2\langle M_{11(T,S)}\rangle,$$
$$G_{(T,S)}(\mathbf{r}_{ik}) = 2|\Psi_A(\mathbf{r}_{ik})|^2\langle M_{21(T,S)}\rangle, \quad (15)$$

where $\langle M_{ik}\rangle$ are the amplitudes averaged over the values of the spin and isospin of the ^{3}He (^{3}H) nucleus ($\langle M_{ik}\rangle = \chi^* M_{ki}\chi$; for details, see [3]).

At the next step, the solution of the three-body Faddeev equations are used as the wave function Ψ in order to render the predictions of our model more accurate. It is natural to start from the *s*-wave approximation for *NN* interaction. In polar coordinates [4], these equations then have the form

$$\left\{-\frac{\partial^2}{\partial\rho^2} - \frac{1}{\rho}\frac{\partial}{\partial\rho} - \frac{1}{\rho^2}\frac{\partial^2}{\partial\theta^2} + V^1_{\mathrm{Coul}}(\rho, \theta) + V^t(\rho, \theta) - E\right\}\Psi^t(\rho, \theta) = -\frac{1}{4}V^t(\rho, \theta)$$
$$\times \int_{-1}^{+1} du \frac{\sin\theta\cos\theta}{\sin\theta'\cos\theta'}(\Psi^t(\rho, \theta') - 3\Psi^s(\rho, \theta')),$$
$$\left\{-\frac{\partial^2}{\partial\rho^2} - \frac{1}{\rho}\frac{\partial}{\partial\rho} - \frac{1}{\rho^2}\frac{\partial^2}{\partial\theta^2} + V^2_{\mathrm{Coul}}(\rho, \theta) + V^s(\rho, \theta) - E\right\}\Psi^s(\rho, \theta) = -\frac{1}{4}V^s(\rho, \theta)$$
$$\times \int_{-1}^{+1} du \frac{\sin\theta\cos\theta}{\sin\theta'\cos\theta'}(-3\Psi^t(\rho, \theta') + \Psi^s(\rho, \theta')), \quad (16)$$

where

$$\cos^2\theta'(u, \theta) = \frac{1}{4}\cos^2\theta - \frac{\sqrt{3}}{2}\cos\theta\sin\theta u + \frac{3}{4}\sin^2\theta. \quad (17)$$

In (16), the Coulomb potential $V^{(1,2)}_{\mathrm{Coul}}(\rho, \theta)$ has the form

$$V^1_{\mathrm{Coul}}(\rho, \theta) = \begin{cases} \dfrac{2n}{\sqrt{3}\rho\sin\theta}, & \theta > 30^\circ \\ \dfrac{2n}{\rho\cos\theta}, & \theta \le 30^\circ, \end{cases} \quad (18)$$
$$V^2_{\mathrm{Coul}}(\rho, \theta) = \frac{1}{3}\left(\frac{2n}{\rho\cos\theta} + V^1_c(\rho, \theta)\right),$$

and we have used the strongly repulsive MT I–III potentials $V^{t,s}(\rho, \theta)$ [5] corrected in [6]; that is,

$$V^s(\rho, \theta) = \frac{m}{\hbar^2}\frac{1}{\rho\cos\theta} \times [-513.969\exp(-1.55\rho\cos\theta) + 1438.72\exp(-3.11\rho\cos\theta)],$$
$$V^t(\rho, \theta) = \frac{m}{\hbar^2}\frac{1}{\rho\cos\theta} \times [-626.885\exp(-1.55\rho\cos\theta) + 1438.72\exp(-3.11\rho\cos\theta)], \quad (19)$$

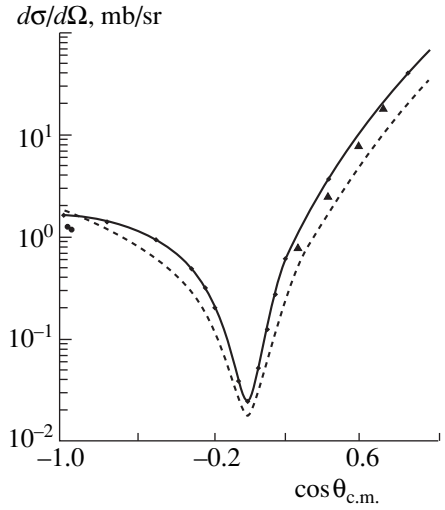

Fig. 3. Differential cross section for π^{+3}He elastic scattering at T_π = 142 MeV in the laboratory frame, with $|\Psi|^2$ taken as (solid line) the Faddeev wave function or (dashed line) as the sum of two Gaussian forms. In either case, all pion rescatterings are taken into account. The experimental data taken from [7] and [8] are shown by closed circles and triangles, respectively.

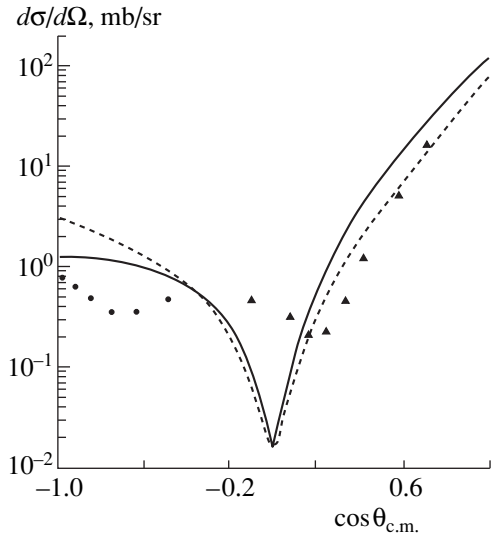

Fig. 4. Differential cross section for π^{+3}He elastic scattering at T_π = 180 MeV in the laboratory frame. The notation is identical to that in Fig. 3.

where $\hbar^2/m$ = 41.47 MeV fm^2, $n = me^2/\hbar^2$, and e^2 = 1.44 MeV fm. The potentials $V^{s,t}$ act only in the singlet $^1S_0$ and triplet $^3S_0$ s waves, respectively, and are given by a superposition of attractive and repulsive Yukawa terms.

To solve the eigenvalue problem in the region $\rho \in [0, \infty]$, $\theta \in [0, \pi/2]$, equation (16) must be supplemented with the boundary conditions

$$\Psi^{(t,s)}(0,\theta) = \Psi^{(t,s)}(\infty,\theta) = 0,$$
$$\Psi^{(t,s)}(\rho,0) = \Psi^{(t,s)}(\rho,\pi/2) = 0. \quad (20)$$

Moreover, we must substitute, instead of the quantities $F_{(T,S)}$ and $G_{(T,S)}$ in (5), the new ones

$$F_{(T,S)}(\mathbf{r}_{ik}) = \sum_{ab,\,pq=1,2} \Psi_{ap}(\mathbf{r}_{ik})\Psi_{bq}(\mathbf{r}_{ik})M_{11(T,S)ab,\,pq},$$
$$G_{(T,S)}(\mathbf{r}_{ik}) = 2\sum_{ab,\,pq=1,2} \Psi_{ap}(\mathbf{r}_{ik})\Psi_{bq}(\mathbf{r}_{ik})M_{21(T,S)ab,\,pq}. \quad (21)$$

Here, $\Psi_{ap}(\mathbf{r}_{ik})$ are the components of the total Faddeev wave function of ^{3}He that correspond to different spin–isospin states:

$$\Psi_{11} = \sqrt{3}[(\Psi_2^s - \Psi_3^s) + (\Psi_2^t - \Psi_3^t)],$$
$$\Psi_{22} = -\sqrt{3}[(\Psi_2^s - \Psi_3^s) + (\Psi_2^t - \Psi_3^t)] = -\Psi_{11},$$
$$\Psi_{12} = [3(\Psi_1^t - \Psi_2^s - \Psi_3^s) + (\Psi_1^t + \Psi_2^t + \Psi_3^t)], \quad (22)$$
$$\Psi_{21} = [3(\Psi_1^s - \Psi_2^t - \Psi_3^t) + (\Psi_1^s + \Psi_2^s + \Psi_3^s)].$$

In (22), the coordinate functions $\Psi_i^{t,s}$ are related to solutions of equation (16) by the formula

$$\Psi_i^{t,s} = \frac{2}{\sqrt{3}}\rho^{-5/2}\frac{\Psi^{t,s}(\rho,\theta_i)}{\cos\theta_i \sin\theta_i}. \quad (23)$$

Here, it is necessary to note the relations $\rho^2 = x_i^2 + \frac{4}{3}y_i^2$ and $\tan\theta_i = \frac{2}{\sqrt{3}}\frac{y_i}{x_i}$ for any i = 1, 2, 3, which allow us to express the coordinates ρ and θ_i in terms of the coordinates $\mathbf{r}_1$ and $\mathbf{r}_2$ by using the definition of the Jacobi vectors $\mathbf{x_i}$ and $\mathbf{y_i}$ from [4]. The total Faddeev wave function $\hat{\Psi}$ has the form

$$\hat{\Psi} = \Psi_{11}\xi(1/2,0)\eta(1/2,0) + \Psi_{12}\xi(1/2,1)\eta(1/2,0)$$
$$+ \Psi_{21}\xi(1/2,0)\eta(1/2,1) + \Psi_{22}\xi(1/2,1)\eta(1/2,1), \quad (24)$$

where, ξ (η) are the eigenfunctions of the total spin s (isospin t) from (14). It is normalized by the condition

$$\int d^3r_1 d^3r_2 d^3r_3 \delta^3(\mathbf{r}_1 + \mathbf{r}_2 + \mathbf{r}_3)|\hat{\Psi}|^2 = 1.$$

4. NUMERICAL RESULTS AND DISCUSSION

We begin by recalling that our model does not involve any free parameter, so that our results reflect the true content of the approximations used.

In Figs. 3–5, the calculated differential cross sections for π^{+3}He interaction at the pion laboratory energies of T_π = 142, 180, and 256 MeV for unpolarized ^{3}He are shown along with experimental data from [7–9]. The solid curves were obtained with the Faddeev wave functions, and the dashed curves, with a wave function as the sum of two Gaussian forms. Inspection of these

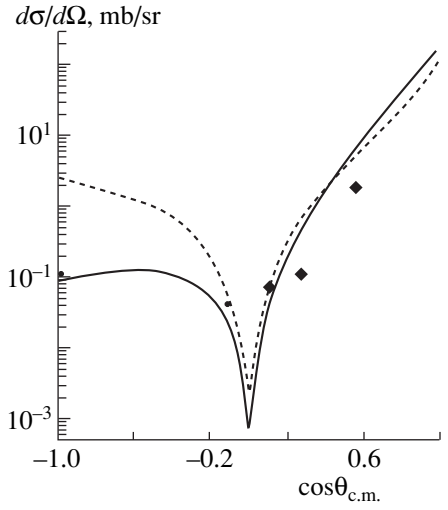

Fig. 5. Differential cross section for π^{+3}He elastic scattering at T_π = 256 MeV in the laboratory frame. The notation for the curves is identical to that in Fig. 3. The experimental data taken from [7] and [9] are shown by closed circles and diamonds, respectively.

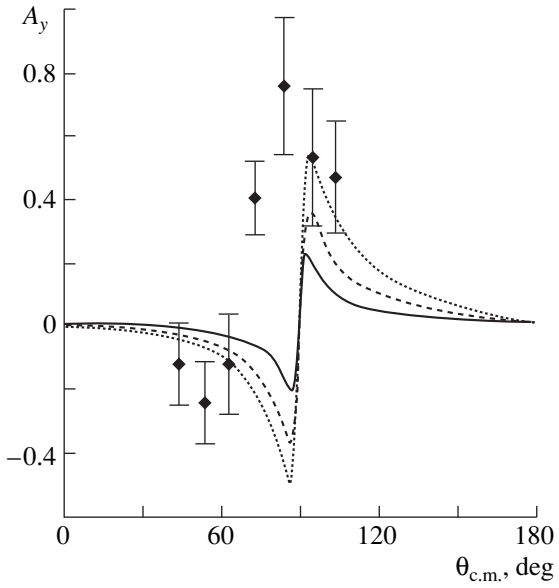

Fig. 6. Asymmetry for π^{+3}He interaction at the pion laboratory energy of T_π = 142 MeV, with $|\Psi|^2$ taken as (solid lines) the Faddeev wave function and as (dashed line) the sum of two Gaussian forms. In either case, all pion rescatterings are taken into account. The dotted line corresponds to two pion rescatterings taken into account in the case of the sum of two Gaussian forms. The experimental data were taken from [10].

results shows that introducing the sophisticated Faddeev wave functions is essential for the backward hemisphere, where this considerably improves the agreement with the experimental data. In the forward hemisphere, the effect is weaker; moreover, it leads to changes in the wrong direction (as clearly seen at 180 MeV). A noticeable dip at 90° that is obtained in our calculations, but which is not observed experimentally, is due to our neglect of the πN interaction in the s wave. Hopefully, it will be filled once this interaction is taken into account.

In Figs. 6–8, the asymmetries calculated for π^{+3}He interactions at the pion laboratory energies of T_π = 142, 180, and 256 MeV are shown along with experimental data from [10]. To demonstrate the effect of multiple π rescatterings, the results that take into account only two rescatterings are also shown (for the wave function as the sum of two Gaussian forms). First, from the figures, we observe a large effect of multiple rescatterings. For lower energies, the inclusion of multiple rescatterings substantially reduces the asymmetry and, at 256 MeV, even completely changes its behavior. The introduction of the Faddeev wave functions does not again seem to modify the results in any significant manner.

The agreement with the asymmetry data is found to be considerably poorer than that for the differential cross sections. This is not surprising since, as was emphasized in many previous publications on the problem, the asymmetry is extremely sensitive to the details of the interaction.

For energies of 142 and 180 MeV, the calculated asymmetry follows the experimental pattern shifted toward larger angles. This is not surprising too. In our approximation (pure P_{33} πN interaction, infinite mass

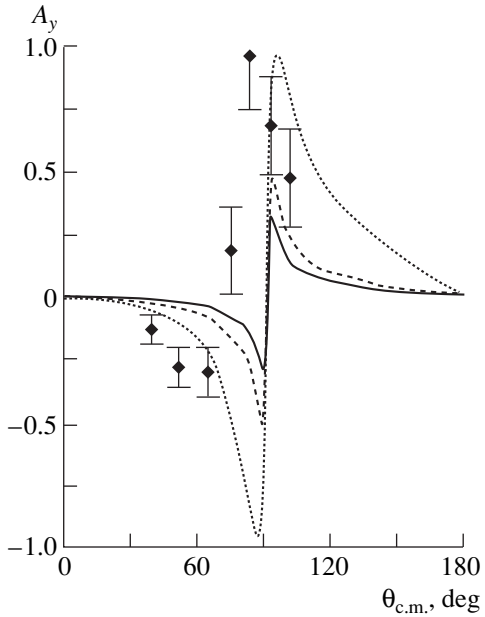

Fig. 7. Asymmetry for π^{+3}He interaction at pion laboratory energy T_π = 180 MeV. The notation is identical to that in Fig. 6.

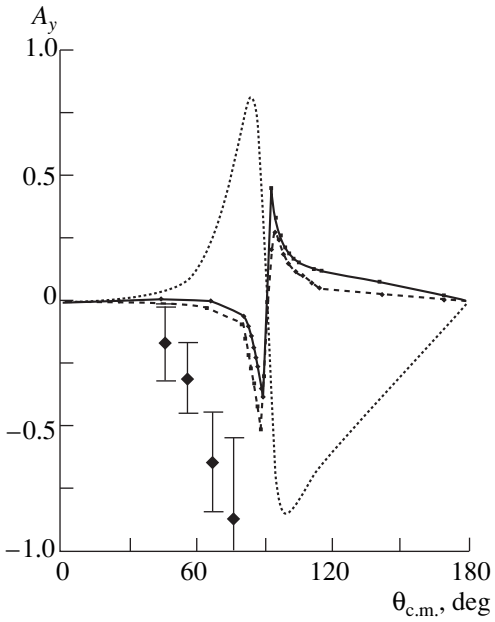

Fig. 8. Asymmetry for π^{+3}He interaction at pion laboratory energy T_π = 256 MeV. The notation is identical to that in Fig. 6.

m_N), the amplitude f vanishes at $\theta = 90°$. The addition of the s-wave interaction and kinematical corrections for the finite m_N would both shift this zero toward smaller angles, thereby rendering the agreement with the experimental data quite satisfactory.

For the energy of 256 MeV, there seems to be no agreement with the experimental data at all. However, as was found in [1], the fact that the angular dependence of the asymmetry is modified drastically at this energy is actually due to quite a small shift in the position of the zeros of the complex amplitude f. It was also found there that this shift could be achieved effectively by introducing a small angle-independent term in f. Thus, we believe that the inclusion of the s-wave πN interaction will make the situation at 256 MeV much better.

In conclusion, we have found that the use of the Faddeev wave functions for the nuclear ground state considerably improves predictions for the differential cross sections in the backward hemisphere, but that this produces a small effect for the forward hemisphere and asymmetries. The overall agreement of the model with experimental data is satisfactory for the cross sections. It is much poorer for the asymmetries. A further improvement of the model and especially of its application to the asymmetry requires the introduction of the s-wave πN interaction and finite m_N kinematics. The work in this direction is now in progress.

REFERENCES

1. C. Benhold *et al.*, Nucl. Phys. A **540**, 621 (1992).
2. M. A. Braun *et al.*, Yad. Fiz. **27**, 135 (1978) [Sov. J. Nucl. Phys. **27**, 72 (1978)].
3. M. A. Braun and V. M. Suslov, Yad. Fiz. **54**, 404 (1991) [Sov. J. Nucl. Phys. **54**, 244 (1991)].
4. A. A. Kvitsinskiĭ, Yu. A. Kurepin, *et al.*, Fiz. Élem. Chastits At. Yadra **17**, 267 (1986) [Sov. J. Part. Nucl. 17, 113 (1986)].
5. R. A. Malfliet *et al.*, Nucl. Phys. A **127**, 161 (1969).
6. G. L. Payne *et al.*, Phys. Rev. C **26**, 1385 (1982).
7. S. K. Matthews *et al.*, Phys. Rev. C **51**, 2534 (1995).
8. B. M. K. Nefkens *et al.*, Phys. Rev. C **41**, 2770 (1990).
9. B. L. Berman *et al.*, Few-Body Syst. (Suppl.) **9**, 83 (1995).
10. O. Hüsser *et al.*, Few-Body Syst. (Suppl.) **9**, 69 (1995).

Physics of Atomic Nuclei, Vol. 63, No. 5, 2000, pp. 801–811. Translated from Yadernaya Fizika, Vol. 63, No. 5, 2000, pp. 871–880.

NUCLEI
Theory

Near-Threshold Amplitude of Pion–Deuteron Scattering: One-Loop Contributions

V. E. Tarasov, V. V. Baru, and A. E. Kudryavtsev

Institute of Theoretical and Experimental Physics, Bol'shaya Cheremushkinskaya ul. 25, Moscow, 117259 Russia

Received March 25, 1999

Abstract—The one-loop expression for the absorptive correction to the πd scattering length is discussed. Relevant Feynman diagrams are calculated both in the relativistic and in the nonrelativistic formalism. A simple expression is obtained for the one-loop correction that arises in the πd scattering length owing to the Fermi motion of the nucleons in the deuteron. This correction includes absorption effects. Fulfillment of the unitarity relation is verified explicitly. © *2000 MAIK "Nauka/Interperiodica".*

1. INTRODUCTION

At present, there are a great number of theoretical studies devoted to calculating the πd scattering length. In recent years, interest in the problem has been rekindled in connection with the emergence of new experimental data on the shifts and widths of the S levels of the $\pi^- p$ and $\pi^- d$ atoms [1–4]. A global analysis of such data for the pionic hydrogen and deuterium atoms makes it possible to extract the πN scattering length. This is of particular interest in connection with testing the predictions of chiral perturbation theory [5, 6].

Usually, the πd scattering length is calculated by summing a series of diagrams for multiple pion scattering on the nucleons of the deuteron. In this approach, the amplitudes for on-energy-shell pion–nucleon interaction are assumed to be known and are extracted from experimental data, whereas off-mass-shell effects are taken into account via the pion–nucleon potential or via phenomenological form factors. A detailed discussion of the approach in question, as well as references to earlier studies, can be found, for example, in [7]. In this method for calculating the πd scattering length, taking into account the effect of absorption in the system on the real part of the amplitude (here, we mean the deuteron-breakup process $\pi^- d \longrightarrow nn$ and its effect on the amplitude of elastic πd scattering) involves the greatest uncertainties. The inclusion of absorption within the multichannel system by means of solving Faddeev-type equations was discussed in [8, 9]. The main difficulty in allowing for absorption is associated with the need for avoiding the double-counting problem in dealing with pion rescatterings on the nucleons of the deuteron. Indeed, let us consider the diagram that describes elastic pion scattering on a deuteron through a two-nucleon intermediate state (Fig. 1). Even at zero pion energy, this diagram has both an imaginary and a real part. The imaginary part of the diagram is calculated unambiguously in terms of the cross section for the reaction $\pi d \longrightarrow NN$, but the real part of the diagram can be reconstructed, for example, with the aid of the dispersion relation. The problem, however, consists in that the real part of the diagram in Fig. 1 is partly contained in multiple-scattering diagrams. Therefore, a mere addition of the real part of the diagram in Fig. 1 to the πd scattering length computed by the method of multiple scattering leads to double counting.

In the present study, we will discuss the problem of taking into account absorption within a diagrammatic approach. The elementary pion–nucleon amplitudes will be calculated here on the basis of a semiphenomenological model. Many attempts have been undertaken by now to construct a model of pion–nucleon amplitudes in terms of exchanges of various mesons. In particular, the amplitudes of pion–nucleon scattering in the energy region below the delta isobar were successfully reproduced in [10] by considering t-channel sigma- and rho-meson exchanges supplemented with Compton pion–nucleon scattering with allowance for intermediate nucleons and delta isobars. Since the Compton s-channel diagram for pion–nucleon scattering represents the only elementary amplitude making a nonzero contribution to the imaginary part of the pion–deuteron scattering length, we will try to single out precisely this diagram and to include it directly in the series of multiple scattering. In the following, it is therefore assumed that the near-threshold amplitude for pion–nucleon scattering is determined by the sum of two Feynman diagrams in Fig. 2 that are supplemented with additional contributions providing correct values for the

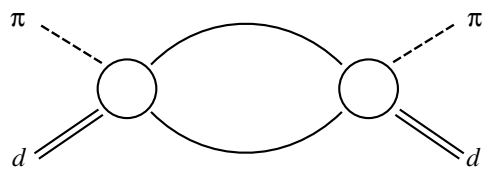

Fig. 1.

1063-7788/00/6305-0801$20.00

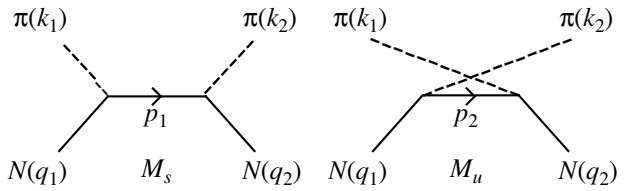

Fig. 2.

low-energy parameters of the *S* and *P* waves. Here, the *P* waves are assumed to be fixed and are determined by fitting experimental data, the main problem of the present analysis being a reconstruction of the *S*-wave scattering lengths. The on-mass-shell amplitude for pion–nucleon scattering near the threshold can be parametrized as

$$f_{\pi N} = \tilde{b}_0 + \tilde{b}_1 \boldsymbol{\tau}\cdot\mathbf{I} + ((\tilde{c}_0 + \tilde{c}_1 \boldsymbol{\tau}\cdot\mathbf{I})\mathbf{k}'\cdot\mathbf{k} + i(\tilde{d}_0 + \tilde{d}_1 \boldsymbol{\tau}\cdot\mathbf{I})\boldsymbol{\sigma}\cdot[\mathbf{k}'\times\mathbf{k}]) + f_s + f_u, \quad (1)$$

where the quantities f_s and f_u are determined by the Feynman diagrams in Fig. 2. Taking into account the contributions to the *P* waves from the amplitudes f_s and f_u, we can determine the constants $\tilde{c}_{0,1}$ and $\tilde{d}_{0,1}$ from a fit of the *P*-wave scattering volumes to experimental data. The constants $\tilde{b}_0$ and $\tilde{b}_1$ are to be determined from an analysis of data on the shifts of the levels in the pionic hydrogen and deuterium atoms. The pion–nucleon scattering lengths are reconstructed here on the basis of the expression $\tilde{b}_0 + \tilde{b}_1 \boldsymbol{\tau}\cdot\mathbf{I} + f_s + f_u$ at zero energy. The amplitude of pion–deuteron scattering is determined in terms of the off-mass-shell pion–nucleon amplitudes, which in turn are related to the amplitude in (1) as follows: the amplitudes f_s and f_u are specified by the diagrams in Fig. 2 for off-mass-shell nucleons as well, the off-mass-shell effects in the remaining part of the amplitude being determined phenomenologically as before.

The present study is aimed at a precision calculation of the pion–deuteron scattering length in terms of pion–nucleon scattering lengths with an eye to subsequently extracting the latter from experimental data on the pionic hydrogen and deuterium atoms. This in turn requires accurately evaluating diagrams for single and double pion scattering on the nucleons of the deuteron. Since the nucleon spin is flipped in pion-absorption processes, it is necessary to take relativistic corrections into account in these calculations. In the present study, we will restrict our analysis to computing the contributions of the amplitudes f_s and f_u to the one-loop diagrams that determine the amplitude of pion–deuteron scattering. We present two versions of the calculation that rely on either the nonrelativistic or the relativistic formalism. As a check upon our results, we also calculate the deuteron-breakup amplitude and verify fulfillment of the unitarity condition. The reason behind the resulting discrepancy between the nonrelativistic and relativistic results is discussed. The two-loop contributions will be taken into account elsewhere.

We note that, even in the nonrelativistic case, we must take into account spin variables since pion absorption entails nucleon-spin flip. The nonrelativistic diagram technique as applied to calculations on direct nuclear reactions was developed in the studies of I.S. Shapiro and his disciples and is expounded in the monograph [11] and in the review article [12]. In computing spin features, the diagrammatic approach is usually supplemented with the formalism of a graphical summation of Wigner 3*j* coefficients [13–15]. In the present study, we make use of an alternative approach that is more economical, at least in dealing with reaction featuring deuterons, and which makes it possible, in principle, to calculate spin effects in multiloop diagrams as well. The present approach is based on an invariant representation of spin vertex functions and the amplitudes of virtual processes. The inclusion of spin effects reduces here to evaluating traces of the products of σ matrices, whereby the computational procedure in question is simplified considerably.

2. PION–NUCLEON SCATTERING AMPLITUDE WITH A NUCLEON POLE

Let us consider pion–nucleon scattering amplitudes corresponding to the tree diagrams in Fig. 2. We will make use of pseudovector πNN coupling corresponding to the Lagrangian

$$L_{\pi N} = \frac{g}{2m}\bar{\psi}\gamma_\mu\gamma_5\boldsymbol{\tau}\psi\partial_\mu\boldsymbol{\pi}. \quad (2)$$

The amplitudes are then given by[1)]

$$M_{s,u} = \frac{g^2}{4m^2}\frac{\bar{u}(q_2)\gamma_5\hat{k}_{2,1}(\hat{p}_{1,2}+m)\hat{k}_{1,2}\gamma_5 u(q_1)}{p_{1,2}^2 - m^2}T_{s,u}. \quad (3)$$

Here, the 4-momenta $k_{1,2}$, $q_{1,2}$, and $p_{1,2}$ are specified in Fig. 2 ($p_1 = k_1 + q_1$, $p_2 = q_2 - k_1$); $u(q_{1,2})$ are four-component spinors normalized by the condition $\bar{u}u \equiv u^+\gamma_0 = 2m$; $T_{s,u} = \chi_2^+\tau_{b,a}\tau_{a,b}\chi_1$ are isotopic factors, where $\chi_{1,2}$ are the isospinors of the initial and the final nucleon ($\chi^+\chi = 1$) and *a* and *b* are the Cartesian isospin subscripts of the initial and the final pion (in the charge representation, the matrices τ_a and τ_b are given in Appendix 1); *m* is the nucleon mass; and $\hat{k} = k_\mu\gamma_\mu$. Going over to the two-component spinors w_1 and w_2, in which case we have

$$u(q_i) = [(\varepsilon_i + m)^{1/2}w_i, (\varepsilon_i + m)^{-1/2}(\mathbf{q}_i\cdot\boldsymbol{\sigma})w_i],$$

$$q_i = (\varepsilon_i, \mathbf{q}_i),\ w^+w = 1,$$

[1)]We perform our consideration in terms of the invariant amplitudes *M* defined as $M = 8\pi\sqrt{s}f$ ($\sqrt{s}$ is the total energy in the reaction c.m. frame), the differential cross section for scattering being $d\sigma/d\Omega = |f|^2$.

we find that, in the reaction c.m. frame (where $\varepsilon_1 = \varepsilon_2 \equiv \varepsilon$), the amplitude M_s is given by

$$M_s = \frac{-g^2}{4m^2}\frac{w_2^+[(\varepsilon+m)^2(\sqrt{s}-m)^3 + (\sqrt{s}+m)^3(\mathbf{q}_2\cdot\boldsymbol{\sigma})(\mathbf{q}_1\cdot\boldsymbol{\sigma})]w_1}{(\varepsilon+m)(s-m^2)}T_{s,u}, \quad (4)$$

where ε, $\mathbf{q}_1$, and $\mathbf{q}_2$ are, respectively, the total energy, the initial nucleon momentum, and the final nucleon momentum, while $s = (\varepsilon + \omega)^2$, ω being the total pion energy. For $\omega \ll m$, the right-hand side of equation (4) can be represented as

$$M_{s,u} = \frac{-g^2}{4m^2\omega} \times w_2^+[\omega^3 \pm 2m(\mathbf{q}_{2,1}\cdot\boldsymbol{\sigma})(\mathbf{q}_{1,2}\cdot\boldsymbol{\sigma})]w_1 T_{s,u}. \quad (5)$$

In the amplitudes given by (4) and (5), the first and the second term correspond to the contributions of the *S* and the *P* wave, respectively, and these contributions are commensurate at $q^2 \sim \omega^3/(2m)$. (In this case, we have $\omega \simeq \mu$, where μ is the pion mass.) In the nonrelativistic limit, the Hamiltonian corresponding to the Lagrangian in (2) has the form [16]

$$H_{\pi NN} = -g\left(\boldsymbol{\sigma}\cdot\left[\nabla_\pi - \frac{\omega}{2m}(\vec{\nabla}_N - \overleftarrow{\nabla}_N)\right]\right)(\boldsymbol{\tau}\cdot\boldsymbol{\pi}), \quad (6)$$

where we have taken into account the leading nonstatic corrections. The Hamiltonian in (6) involves the operator $\vec{\nabla}_N$ ($\overleftarrow{\nabla}_N$) acting to the right (left) on a single nucleon and the total energy ω of the absorbed pion. This Hamiltonian reconstructs only the *P*-wave part of the amplitude in (3), taking no account of the *S* wave. Formally, the *S*-wave components of the diagrams in Fig. 2 are obtained from a consistent relativistic approach, and their presence is associated with the impossibility to apply the free Dirac equation [which is used in going over from the four-component to two-component spinors in order to obtain expressions (6) and (2)] to the intermediate virtual state.[2)] At the threshold, the contribution of the *S* wave is proportional to μ^2/m^2, so that it vanishes in the chiral limit $\mu/m \longrightarrow 0$.

Let us estimate the *S*-wave contribution from the diagrams in Fig. 2 to the amplitude of $\pi^- d$ scattering near the threshold. In the approximation of the nucleons at rest, we have

$$f_{\pi^- d}(0) = \frac{1+\mu/m}{1+\mu/m_d}(f_{\pi^- p} + f_{\pi^- n}) = -0.0225\,\mu^{-1}. \quad (7)$$

Here, $f_{\pi^- p, \pi^- n} = M_{s,u}/8\pi(m+\mu)$, where $M_{s,u} = -g^2\mu^2/m(2m \pm \mu)$ ($g^2/4\pi = 14.6$) according to equation (4) (it is considered here that $T_s = T_u = 2$ because of charge exchange in the πNN vertices). The value in (7) is commensurate with the experimental $\pi^- d$ scattering length [4]

$$a_{\pi^- d} = (-0.0259 \pm 0.0011)\mu^{-1}. \quad (8)$$

From the above, it follows that, in the reaction on a deuteron, it is of paramount importance to take into account the *S* waves in the amplitudes represented by Fig. 2. At the same time, the *P*-wave contributions of these diagrams at zero angle compensate each other to a considerable extent. Going over to an analysis of $\pi^- d$ scattering and using the diagrams in Fig. 2 for the relevant subprocess, we arrive at the diagrams M_1 and M_2 in Fig. 3. At first glance, it seems that a nonrelativistic calculation of these diagrams is possible by taking into account expression (5) for pion–nucleon amplitudes, which already contain *S*-wave effects. However, this gives no way to include correctly the contribution of the real intermediate nucleon–nucleon state. This is due to the following reasons. First, expressions (5) were written for free nucleon legs, and their use will lead to the absence of an imaginary part in the amplitude M_1 (Fig. 3), but this is not correct. Second, the antisymmetrization of the intermediate nucleon–nucleon state in the *s* channel requires supplementing the diagram M_1 with the diagram M_3 in Fig. 3 (the presence of the diagrams M_2 and M_3 ensures antisymmetry in the *u* channel as well). Here, the imaginary part $\mathrm{Im}M_1$ ($\mathrm{Im}M_3$) must correspond to the contribution of the sum of the squares (interference) of the diagrams $M_1^{(b)}$ and $M_2^{(b)}$ to the cross section for the breakup process $\pi^- d \longrightarrow nn$ (see Fig. 4). In this approach, however, the question of the emergence of "*S*-wave" effects from the πNN vertex (2) in the amplitude M_3 and the question of taking these effects into account within the nonrelativistic formalism remain open.

Thus, we conclude that, in order to take correctly into account the pion–nucleon interaction (2), $\pi^- d$ scattering must be considered on the basis of the relativistic formalism.

3. EVALUATION OF ONE-LOOP DIAGRAMS

Let us make use of the deuteron wave function in the relativistic form (see, for example, [19, 20])

$$\Psi_d = e_\nu \bar{u}(k_2)O_\nu(k_1,k_2)U_c\tilde{\bar{u}}(k_1)X,$$
$$O_\nu(k_1,k_2) = f_1\frac{(k_1-k_2)_\nu}{2m^2} + f_2\frac{\gamma_\nu}{m}, \quad X = \chi_2^+\frac{\tau_2}{\sqrt{2}}\chi_1^*, \quad (9)$$

[2)] The presence of the *S*-wave contribution of the diagrams in Fig. 2 was also discussed in the monograph [17] for the case of pseudoscalar πNN coupling. If we consider that a virtual fermion has no definite parity [18], the following interpretation is possible: the interaction in (2) is of a *P*-wave character in the case of real nucleons, which do not change parity; as to the *S* wave, it seems to take into account the effect of "nucleon-parity reversal" upon the absorption (emission) of a pseudoscalar pion.

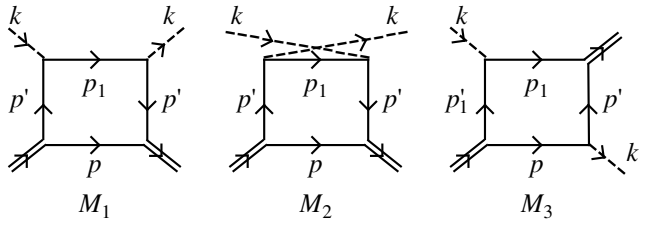

Fig. 3.

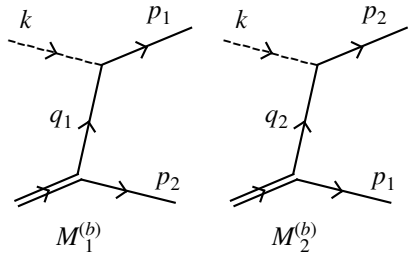

Fig. 4.

where $U_c = \gamma_2\gamma_0$ is the charge-conjugation matrix, e_ν is the deuteron polarization 4-vector, $u(k_{1,2})$ are the relevant four-component spinors ($\bar{u}\,u = 2m$), X is the isotopic component of the deuteron wave function, and $\chi_{1,2}$ are isospinors. Everywhere, with the exception of expression (1), the tilde sign denotes the transposition operation. The expression in (9) represents a relativistic generalization of the deuteron wave function in the nonrelativistic form (see [21, 22])

$$\Psi_d^{(\mathrm{non})}(\mathbf{p}) = w_2^+(\boldsymbol{\epsilon}\cdot\mathbf{O}^{(n)}(\mathbf{p}))\sigma_2 w_1^* X \quad (w_{1,2}^+ w_{1,2} = 1),$$
$$\mathbf{O}^{(n)}(\mathbf{p}) = \frac{u}{\sqrt{2}}\boldsymbol{\sigma} - \frac{w}{2}\left(\frac{3(\mathbf{p}\cdot\boldsymbol{\sigma})}{\mathbf{p}^2}\mathbf{p} - \boldsymbol{\sigma}\right), \tag{10}$$

where $\boldsymbol{\epsilon}$ is the deuteron polarization 3-vector (in this approximation, the expectation value of the deuteron-spin vector is $\langle\mathbf{S}\rangle = i[\boldsymbol{\epsilon}^*\times\boldsymbol{\epsilon}]$); $\mathbf{p}$ is the relative momentum of the nucleons in the deuteron; and $u \equiv u(|\mathbf{p}|)$ and $w \equiv w(|\mathbf{p}|)$ are, respectively, the S- and D-wave components of the deuteron wave function.[3)]

In the nonrelativistic limit, the equality of expressions (9) and (10) in the deuteron rest frame determines the relations between the functions f_1 and f_2, on one hand, and the S- and D-wave functions (u and w, respectively), on the other hand. Specifically, we have

$$f_1 = \frac{m^2}{2\mathbf{p}^2}\left[\left(1 - \frac{m}{\varepsilon(\mathbf{p})}\right)\frac{u}{\sqrt{2}} - \left(1 + \frac{m}{2\varepsilon(\mathbf{p})}\right)w\right],$$
$$f_2 = \frac{m}{4\varepsilon(\mathbf{p})}(\sqrt{2}u + w), \tag{11}$$

where $\varepsilon(\mathbf{p}) = \sqrt{m^2 + \mathbf{p}^2}$. The rules of the diagram technique as formulated with a deuteron wave function of the form (9) or (10), normalizations, and some other relevant information are presented in Appendices 1 and 2.

Yet another circumstance is worthy of special note. We will clarify it by considering the example in which the scalar form factor for the deuteron, $F_d(q)$, is calculated at zero momentum $q = 0$. It is obvious that, because of the normalization condition, a correct calculation must yield $F_d(0) = 1$. Let us write the relativistic expression for the corresponding triangle diagram (Fig. 5) by using the deuteron wave function in the form (9). Further, we go over to the nonrelativistic limit (in the integral, we take into account the pole at a positive energy and retain second-order terms in the intermediate 3-momentum $\mathbf{p}$) and express the result in terms of the functions u and w according to (11). Specifically, we have

$$F_d(0) = \int\frac{d^3\mathbf{p}}{(2\pi)^3}\frac{m^3}{\varepsilon^3}\left[u^2 + w^2 + \frac{\mathbf{p}^2}{m^2}\left(-\frac{\sqrt{2}}{2}uw + \frac{5}{8}w^2\right)\right],$$

where $\varepsilon = m + p^2/2m$. We can see that $F_d(0) \neq 1$ because of the presence of the second term in the integrand (this term is proportional to $\mathbf{p}^2/m^2$). The reason for this discrepancy is that, in equations (11), which relate the functions f_1 and f_2 to u and w, both nucleons in the dpn vertex are on the energy shell. In fact, however, we can see that, if one of the nucleons is real, the off-energy-shellness of the second nucleon is determined by the quantity $-\mathbf{p}^2/m$ (we take here no account of the deuteron binding energy). In calculating the amplitudes M_1, M_2, and M_3 (Fig. 4) in the ensuing analysis, we therefore disregard $\mathbf{p}^2/m^2$ terms against terms on the order of unity (by including the former, we would go beyond the accuracy adopted here), but we retain terms of order $\mathbf{p}^2/m\mu$. This approach assumes fulfillment of the condition $\mu \ll m$. Taking the above into account, we can simplify relations (11) significantly and arrive at

$$f_1 = -\frac{3m^2}{4\mathbf{p}^2}w, \quad f_2 = \frac{1}{4}(\sqrt{2}u + w). \tag{12}$$

Let us now evaluate the diagrams for the amplitudes M_1, M_2, and M_3 in Fig. 3 within both the relativistic and the nonrelativistic approach. In the relativistic approach, we first use a consistent relativistic representation for the relevant matrix elements (see Appendix 1) and then discard $\mathbf{p}^2/m^2$ terms by virtue of the above argument. By the nonrelativistic approach, we mean

[3)]Expression (10) is the amplitude of the probability that, in the deuteron at rest occurring in a state that is determined by the polarization vector $\boldsymbol{\epsilon}$, the nucleons have a relative momentum $\mathbf{p}$ and are in the spin (isospin) states described by the spinors w_1 and w_2 (isospinors χ_1 and χ_2). From the identities $w_2^+\boldsymbol{\sigma}\sigma_2 w_1^* \equiv w_1^+\boldsymbol{\sigma}\sigma_2 w_2^*$ and $\chi_2^+\tau_2\chi_1^* \equiv -\chi_1^+\tau_2\chi_2^*$, it follows that the states in question are symmetric (antisymmetric) in spin (isospin) variables; that is, the deuteron wave function (10) corresponds to a nucleon–nucleon state having a spin value of unity and zero isospin. In [22], it is shown that the second term in the deuteron wave function (10)—that is the term that involves w—corresponds to the D wave.

that in which the analogous diagrams are calculated nonrelativistically (see Appendix 2) with the pion–nucleon interaction specified by expression (6).

In calculating the amplitudes M_1, M_2, and M_3, the integral with respect to the energy ε (see the notation in Fig. 3) is determined by the residues at the poles in the lower half-plane (we take into account only those poles that correspond to $\varepsilon > 0$). The amplitudes M_1 and M_2 are determined by the contribution of one pole at $\varepsilon = \varepsilon_0$ ($\varepsilon_0 = \sqrt{m^2 + \mathbf{p}^2} - i0$), while M_3 is determined by the poles at $\varepsilon = \varepsilon_0$ and $\varepsilon = \varepsilon_0 + \mu$. For these amplitudes, we eventually obtain the expressions

$$M_{1,2} = 2T_{1,2}\left(1 \pm \frac{\mu}{2m}\right)^{-1}\int\frac{d^3\mathbf{p}}{(2\pi)^3}\frac{S_{1,2}}{\mathbf{p}^2 \mp m\mu - i0}, \quad (13)$$

$$M_3 = 2T_3\int\frac{d^3\mathbf{p}}{(2\pi)^3}\frac{\mathbf{p}^2}{m\mu}\left[\frac{S_3^{(1)}}{\mathbf{p}^2 - m\mu - i0} - \frac{S_3^{(2)}}{\mathbf{p}^2 + m\mu - i0}\right],$$

where

$$S_{1,2} = \frac{-g^2}{4m^2}\{O_\mu(p, p')(\hat{p}' + m)\gamma_5\hat{k}(\hat{p}_1 + m)$$
$$\times\hat{k}\gamma_5(\hat{p}' + m)O_\nu(p, p')(\hat{p} - m)\}e_\mu^* e_\nu,$$

$$S_3 = \frac{-g^2}{4m^2}\{O_\mu(p', p_1)(\hat{p}_1 + m)\hat{k}\gamma_5(\hat{p}_1' + m)$$
$$\times O_\nu(p, p_1')(\hat{p} - m)\hat{k}\gamma_5\hat{k}(\hat{p}_1' - m)\}e_\mu^* e_\nu.$$

Here, {…} stands for the trace of the braced expression; the 4-momenta k, p, p', p_1, and p_1' are specified in Fig. 3; and the isotopic factors are given by $T_{1,2} = \{\tau_2\tau_\mp\tau_2\tau_\pm\} = 1$ and $T_3 = \{\tau_2\tau_-\tau_2\tilde{\tau}_+\} = -1$, where $\tau_\pm = (\tau_1 \pm i\tau_2)/2$ and $\tilde{\tau}_\pm = \tau_\mp$).[4] The expressions for S_1 and S_2 differ by the 4-momentum p_1 ($p_1 = p' \pm k$). The quantities $S_3^{(1)}$ and $S_3^{(2)}$ are determined by the expression for S_3 at $p = (\varepsilon_0, \mathbf{p})$ and $p = (\varepsilon_0 + \mu, \mathbf{p})$, respectively. We note that S_2 and $S_3^{(2)}$ are obtained from S_1 and $S_3^{(1)}$, respectively, upon the substitution $\mu \longrightarrow -\mu$. For the amplitudes M_1, M_2, and M_3 considered for zero initial momentum and for the polarization vectors $e_{1,2} = (0, \boldsymbol{\epsilon}_{1,2})$, the calculations that assume the initial and the final deuteron to be at rest and which take into account relations (9) and (12) yield

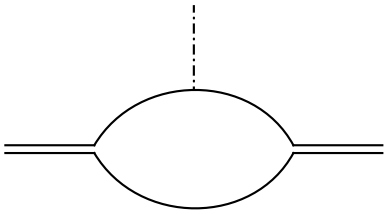

Fig. 5.

$$M_{1,2} = \frac{2g^2\mu^3}{2m \pm \mu}(\boldsymbol{\epsilon}_2^* \cdot \boldsymbol{\epsilon}_1)\int\frac{d^3\mathbf{p}}{(2\pi)^3}\left[\pm(u^2 + w^2)\right.$$
$$\left. + \frac{\mathbf{p}^2}{m\mu}\left(u^2 + \sqrt{2}uw - \frac{1}{4}w^2\right)\right]\frac{1}{\mathbf{p}^2 \mp m\mu - i0},$$

$$M_3 = \frac{g^2\mu^3}{12m}(\boldsymbol{\epsilon}_2^* \cdot \boldsymbol{\epsilon}_1)\int\frac{d^3\mathbf{p}}{(2\pi)^3}\frac{\mathbf{p}^2}{m\mu} \quad (14)$$
$$\times(8u^2 + 20\sqrt{2}uw + 7w^2)$$
$$\times\left[\frac{1}{\mathbf{p}^2 - m\mu - i0} + \frac{1}{\mathbf{p}^2 + m\mu - i0}\right].$$

The factor $(\boldsymbol{\epsilon}_2^* \cdot \boldsymbol{\epsilon}_1)$ in (14) demonstrates that the deuteron polarization remains unchanged, which is obvious since the external 3-momenta vanish at the threshold. In the following, we will therefore omit the factor $(\boldsymbol{\epsilon}_2^* \cdot \boldsymbol{\epsilon}_1)$. We will also present expressions for the imaginary parts of the amplitudes in (14). They are given by[5]

$$\mathrm{Im}M_1 = \frac{g^2\mu^3 p}{4\pi m}\left(2u^2 + \sqrt{2}uw + \frac{3}{4}w^2\right),$$
$$\mathrm{Im}M_2 = 0 \quad (p = \sqrt{m\mu}),$$
$$\mathrm{Im}M_3 = \frac{g^2\mu^3 p}{48\pi m}(8u^2 + 20\sqrt{2}uw + 7w^2), \quad (15)$$
$$\mathrm{Im}M = \mathrm{Im}(M_1 + M_2 + M_3) = \frac{g^2\mu^3 p}{3\pi m}(\sqrt{2}u + w)^2.$$

4. AMPLITUDE OF THE BREAKUP PROCESS $\pi^- d \longrightarrow nn$: UNITARITY RELATION

Since formulas (14) for the amplitudes M_1, M_2, and M_3 were obtained from very cumbersome expressions,

[4] The amplitudes $M_{1,2}$ involve a μ/m correction [the factor $(1 \pm \mu/2m)^{-1}$] caused by the presence of the propagator for the intermediate nucleon with a 4-momentum p_1, since $\varepsilon_1 = m_d \pm \mu - \varepsilon$ and $\varepsilon_1^2 - \mathbf{p}^2 - m^2 + i0 = -2(1 \pm \mu/2m)(\mathbf{p}^2 - m\mu - i0)$ for $\varepsilon = \varepsilon_0 \approx m + \mathbf{p}^2/2m$. Upon the evaluation of the integral with respect to the energy, the amplitude M_3 develops a $(\mu/m)^2$ correction [the factor $(1 - \mu^2/4m^2)^{-1}$], but we disregard this correction here.

[5] Here, we neglect μ/m corrections because, at $p = \sqrt{m\mu}$, the discarded $\mathbf{p}^2/m^2$ terms are of the same order of smallness.

it is desirable to verify fulfillment of the unitarity condition in the one-loop approximation. It should be noted that the relativistic procedure for calculating the breakup amplitude is of interest in and of itself.

In the tree approximation, the breakup amplitude $M_{\pi d\to NN} = M_1^{(b)} + M_2^{(b)}$ receives contributions from those diagrams in Fig. 4 that correspond to the expressions

$$\begin{aligned} M_1^{(b)} &= +\frac{g}{\sqrt{m}}\bar{u}(p_1)\hat{k}\gamma_5(\hat{p}_1-\hat{k}+m)\\ &\times O_\mu(p_2, p_1-k)\gamma_2 u^*(p_2)e_\mu,\\ M_2^{(b)} &= -\frac{g}{\sqrt{m}}\bar{u}(p_2)\hat{k}\gamma_5(\hat{p}_2-\hat{k}+m)\\ &\times O_\mu(p_1, p_2-k)\gamma_2 u^*(p_1)e_\mu. \end{aligned} \tag{16}$$

Going over to two-component spinors and considering the case of the reaction with the initial pion at rest, we obtain

$$\begin{aligned} M_1^{(b)} &= \frac{4g\mu}{m\sqrt{m}}w_1^+ A_1\sigma_2 w_2^*,\\ M_2^{(b)} &= -\frac{4g\mu}{m\sqrt{m}}w_2^+ A_2\sigma_2 w_1^*, \end{aligned} \tag{17}$$

where

$$A_{1,2} = f_1 E(\mathbf{p}_{1,2}\cdot\boldsymbol{\epsilon}) + f_2 m(\mathbf{p}_{1,2}\cdot\boldsymbol{\sigma})(\boldsymbol{\epsilon}\cdot\boldsymbol{\sigma}).$$

Here, $E = \mathbf{p}^2/2m$ ($\mathbf{p} = \mathbf{p}_1 = -\mathbf{p}_2$); from (12), it follows that $f_1 E = -3mw/8$. Evaluating the sum $M_1^{(b)} + M_2^{(b)}$, we arrive at (we have transformed the expression for $M_2^{(b)}$ by using the relations $w_2^+ A_2\sigma_2 w_1^* = w_1^+\tilde{\sigma}_2\tilde{A}_2 w_2^*$, $\tilde{\sigma}_2 = -\sigma_2$, and $\sigma_2\tilde{\sigma} = -\sigma\sigma_2$)

$$\begin{aligned} M_{\pi d\to NN} &= \frac{4g\mu}{\sqrt{m}}f_2 w_1^+\\ &\times[(\mathbf{p}_1\cdot\boldsymbol{\sigma})(\boldsymbol{\epsilon}\cdot\boldsymbol{\sigma}) - (\boldsymbol{\epsilon}\cdot\boldsymbol{\sigma})(\mathbf{p}_1\cdot\boldsymbol{\sigma})]\sigma_2 w_2^*. \end{aligned} \tag{18}$$

The total amplitude in (18) depends on f_2; that is, $M_{\pi d\to NN}\sim(\sqrt{2}\,u + w)$. The probability of the deuteron-breakup reaction is given by

$$\begin{aligned} W_{\pi d\to NN} &= W_{11} + W_{22} + W_{12}\\ &= \frac{p}{32\pi^2 s}\int\overline{|M_{\pi d\to NN}|^2}\,d\Omega. \end{aligned} \tag{19}$$

The quantities W_{11}, W_{22}, and W_{12} stand for, respectively, the contribution of the square of the amplitude $M_1^{(b)}$, contribution of the square of the amplitude $M_2^{(b)}$, and the contribution of the interference of these amplitudes.

We will calculate the imaginary parts of the elastic-scattering amplitudes in (14) by using the unitarity conditions

$$\begin{aligned} \mathrm{Im}M_1 &= \frac{1}{\sqrt{s}}(W_{11}+W_{22}),\quad \mathrm{Im}M_3 = \frac{W_{12}}{\sqrt{s}},\\ \mathrm{Im}M &= \frac{W_{\pi d\to NN}}{\sqrt{s}}. \end{aligned} \tag{20}$$

By evaluating the quantities W_{ij} according to (18) and (19) (we set here $\sqrt{s} = 2m + \mu \approx 2m$ and consider that $\mathbf{p}^2 = m\mu$), we arrive at expressions (15). Thus, the calculations of the breakup and scattering processes in the relativistic approximation prove to be consistent at the level of the optical theorem.

5. COMPARISON WITH NONRELATIVISTIC EXPRESSIONS

By using the Hamiltonian in (6), we will now calculate the amplitudes represented by the diagrams in Fig. 3. We denote these amplitudes by M_1^{non}, M_2^{non}, and M_3^{non}. With the aid of the rules presented in Appendix 2, we obtain

$$\begin{aligned} M_{1,2}^{\mathrm{non}} &= \frac{2g^2\mu^2}{m^2}\int\frac{d^3\mathbf{p}}{(2\pi)^3}\frac{\mathbf{p}^2(u^2+w^2)}{\mathbf{p}^2\mp m\mu - i0},\\ M_3^{\mathrm{non}} &= \frac{2g^2\mu^2}{3m^2}\int\frac{d^3\mathbf{p}}{(2\pi)^3}\mathbf{p}^2(u^2+4\sqrt{2}uw-w^2)\\ &\times\left[\frac{1}{\mathbf{p}^2-m\mu-i0}+\frac{1}{\mathbf{p}^2+m\mu-i0}\right],\\ M^{\mathrm{non}} &= \frac{4g^2\mu^2}{3m^2}\int\frac{d^3\mathbf{p}}{(2\pi)^3}\mathbf{p}^2(\sqrt{2}u+w)^2\\ &\times\left[\frac{1}{\mathbf{p}^2-m\mu-i0}+\frac{1}{\mathbf{p}^2+m\mu-i0}\right], \end{aligned} \tag{21}$$

where $M^{\mathrm{non}} = M_1^{\mathrm{non}} + M_2^{\mathrm{non}} + M_3^{\mathrm{non}}$ [as in (14), the isotopic factors correspond here to the reaction $\pi^- d \longrightarrow \pi^- d$]. For the imaginary parts, we have

$$\begin{aligned} \mathrm{Im}M_1^{\mathrm{non}} &= \frac{g^2\mu^3 p}{2\pi m}(u^2+w^2),\\ \mathrm{Im}M_2^{\mathrm{non}} &= 0\quad (p=\sqrt{m\mu}),\\ \mathrm{Im}M_3^{\mathrm{non}} &= \frac{g^2\mu^3 p}{6\pi m}(u^2+4\sqrt{2}uw-w^2),\\ \mathrm{Im}M^{\mathrm{non}} &= \frac{g^2\mu^3 p}{3\pi m}(\sqrt{2}u+w)^2. \end{aligned} \tag{22}$$

Let us compare the relativistic and the nonrelativistic expressions [(14) and (21), respectively]. In contrast to the amplitudes M_1^{non} and M_2^{non}, the amplitudes M_1 and M_2 in (14) feature the S-wave contribution [the terms $\pm(u^2 + w^2)$ in the integrand] from the pole diagrams of pion–nucleon scattering. For $\mu \longrightarrow 0$ ($\mathbf{p}^2/m\mu \longrightarrow \infty$), this contribution vanishes, and only the P-wave contributions survive in the amplitudes M_1 and M_2 (14).

The imaginary parts $\mathrm{Im}M$ (15) and $\mathrm{Im}M^{\text{non}}$ (22) coincide, although the contributions of the individual diagrams may be different in the relativistic and nonrelativistic approximations, for example,

$$\mathrm{Im}M_1 \neq \mathrm{Im}M_1^{\text{non}}.$$

By no means is the coincidence of the imaginary part $\mathrm{Im}M$ of the sum of the relativistic amplitudes and the imaginary part $\mathrm{Im}M^{\text{non}}$ of the sum of the nonrelativistic amplitudes accidental. Indeed, it can be shown that the amplitudes M and M^{non} differ only by a real-valued constant having a simple physical meaning. Let us first recast the S-wave component of expression (14) for M_1 into the form

$$M_1^{(S)} = \frac{2g^2\mu^3}{2m+\mu}\int\frac{d^3\mathbf{p}}{(2\pi)^3}(u^2+w^2) \times\left[-\frac{1}{m\mu}+\frac{\mathbf{p}^2}{m\mu(\mathbf{p}^2-m\mu-i0)}\right]. \quad (23)$$

The second term in the bracketed expression on the right-hand side of (23) has the same structure as the P-wave contribution to M_1 (14). In the leading approximation in m/μ, we therefore have

$$M_1 = -\frac{g^2\mu^2}{m^2}+\frac{g^2\mu^3}{m}\int\frac{d^3\mathbf{p}}{(2\pi)^3}\frac{\mathbf{p}^2}{m\mu} \times\frac{2u^2+\sqrt{2}uw+(3/4)w^2}{\mathbf{p}^2-m\mu-i0}. \quad (24)$$

In a similar way, we transform the expression for M_2. As a result, the sum $M = M_1 + M_2 + M_3$ can be reduced to the form

$$M = M^{(S)} + M^{(P)}, \quad M^{(S)} = -\frac{2g^2\mu^2}{m^2},$$

$$M^{(P)} = \frac{4g^2\mu^3}{3m}\int\frac{d^3\mathbf{p}}{(2\pi)^3}\frac{\mathbf{p}^2}{m\mu}(\sqrt{2}u+w)^2 \times\left[\frac{1}{\mathbf{p}^2-m\mu-i0}+\frac{1}{\mathbf{p}^2+m\mu+i0}\right]. \quad (25)$$

The first term in (25), $M^{(S)}$, coincides with the contribution to the pion–nucleon scattering length from the S-wave components of the pion–nucleon scattering amplitude that are associated with the Compton diagrams in Fig. 2; that is, $M^{(S)} = 2(M_s + M_u)$ (the factor of 2 emerges from a normalization of the amplitudes M). The second term in (25), $M^{(P)}$, represents a correction to this result due to the Fermi motion of the nucleons in the deuteron. It can be seen that this term is identical to expression (21) for M^{non}! For this reason, the correction for the Fermi motion of the nucleons in loop diagrams can be calculated according to the rules of the nonrelativistic diagram technique by using the P-wave interaction.

At the same time, the S-wave contribution $M^{(S)}$ to the pion–deuteron scattering length is determined by the Compton amplitudes of pion scattering on a free nucleon at zero energy. This contribution does not involve corrections associated with nucleon off-mass-shell effects in the deuteron. Thus, the S-wave contribution to the pion–deuteron scattering length is not affected either by off-mass-shell effects or by the Fermi motion. This was not obvious from the outset.

6. CONCLUSION

We have considered the contribution of pion absorption (emission) by a nucleon to the near-threshold amplitude for pion–deuteron scattering and have obtained expressions for one-loop diagrams. The formulas presented above have been derived on the basis of the relativistic Lagrangian (2), but they are not relativistic, since we have disregarded terms of order $\mathbf{p}^2/m^2$ against $O(1)$ terms. The main objective of the present study was to take correctly into account, in the pion–deuteron scattering amplitude, the S-wave component that emerges in the pion–nucleon component from Lagrangian (2). Expression (25) for the Compton amplitude of pion–deuteron scattering is the main outcome of our analysis. The first term in (25), a constant, is determined by the sum of the Compton amplitudes for scattering on a free neutron and on a free proton at zero energy. This contribution is commensurate with the pion–deuteron scattering length. A renormalization of this expression due to nucleon off-mass-shell effects in the deuteron, the Fermi motion, and absorption are determined by the second term in (25). This term can be calculated easily according to the rules of the nonrelativistic diagram technique. A numerical calculation of the $\pi^- d$ scattering length by formula (25) yields

$$f_{\pi^- d} = \frac{M}{8\pi(2m+\mu)} = [-0.02238 + (0.00038 + i\times 0.00015)]\mu^{-1},$$

where the value in parentheses corresponds to the P-wave term $M^{(P)}$ in (25) (we used here the value of $g^2/4\pi = 14.6$ and the deuteron wave function for the Bonn potential with the parameter values from Table 11 of the review article by Machleidt *et al.* [25]). We see

that the contribution of this term is comparatively small.

The above formulas take correctly into account the antisymmetric character of the intermediate nucleon–nucleon state. It should of course be recalled that the inclusion of only one-loop diagrams is by far insufficient for describing pion–deuteron scattering. For example, the imaginary part of the amplitude then allows only for the contribution of tree diagrams in the breakup reaction $\pi d \longrightarrow NN$, where double interaction plays an important role [16] (pion rescattering on one nucleon and pion absorption on the other one).

In a subsequent study, we plan to take phenomenologically into account additional *S*- and *P*-wave contributions to the pion–nucleon amplitude that are not associated with pion absorption [see Introduction and equation (1)] and to consider two-loop diagrams for pion–deuteron scattering.

ACKNOWLEDGMENTS

We are grateful to A. Baderschter, B. Birbrair, A. Gridnev, S. Kamalov, V.A. Karmanov, B.O. Kerbikov, V.M. Kolybasov, V.G. Ksendzov, and V.E. Markushin for stimulating discussions.

This work was supported in part by the Russian Foundation for Basic Research (project nos. 98-02-17618 and 96-15-96578).

APPENDIX 1

Here, we give an account of the rules for describing the relativistic matrix elements in pion–deuteron interactions. In contrast to what occurs in conventional field theory, the vector field of the deuteron is not converted, in our case, into a particle–antiparticle pair—it is a composite object decaying into two nucleons. Because of this, the rules of the diagram technique are somewhat different here from standard rules and can formally be obtained from the interaction Lagrangian

$$L = L_{dNN}(x) + L_{\pi NN}(x), \tag{A.1}$$

where

$$L_{dNN}(x) = \frac{1}{\sqrt{2}} A_\mu(x)\bar{\psi}(x) \times \left[\frac{ig_1}{2m^2}(\overleftarrow{\partial} - \overrightarrow{\partial})_\mu + \frac{g_2}{m}\gamma_\mu\right]\frac{\tau_2}{\sqrt{2}}\psi^c(x) + \text{h.c.} \tag{A.2}$$

Here, we have introduced the following notation: $\psi^c = U_c\tilde{\bar{\psi}} = \gamma_2\psi^*$, where $U_c = \gamma_2\gamma_0$; $A_\mu(x)$ is the deuteron vector field; $\overleftarrow{\partial}_\mu$ ($\overrightarrow{\partial}_\mu$) is an operator acting on $\bar{\psi}(x)$ [$\psi^c(x)$]; τ_2 is an isospin Pauli matrix; and $L_{\pi NN}$ is an arbitrary Lagrangian of πN interaction. A direct interaction of the deuteron field A_μ with the pion is not introduced here. We will employ the commonly accepted normalization [18] of the invariant amplitudes *M* related to the differential cross sections ($d\sigma$) by the equations

$$d\sigma = \frac{1}{4q\sqrt{s}}|M|^2 d\tau_n,$$
$$d\tau_n = (2\pi)^4\delta^{(4)}(P_i - P_f)\frac{d^3\mathbf{p}_1}{(2\pi)^3 2\varepsilon_1}\ldots\frac{d^3\mathbf{p}_n}{(2\pi)^3 2\varepsilon_n}, \tag{A.3}$$

where q and s are, respectively, the colliding-particle momentum and the square of the total energy in the reaction c.m. frame, while $d\tau_n$ is an element of the phase space of the final state of n particles (ε_i are their total energies). The rules for constructing the matrix elements will be illustrated for the example of the pseudovector interaction $L_{\pi N}$ (2).

(i) We choose the directions of the nucleon lines in the diagrams in such a way that the vertex of initial-deuteron breakup (final-deuteron formation) or final-antideuteron formation (initial-antideuteron breakup) involves only outgoing (incoming) nucleon lines, in which case the final-nucleon (initial-nucleon) or initial-antinucleon (final-antinucleon) line is treated as an outgoing (incoming) line. The notation for the relevant 4-momenta is chosen in accordance with this (see, for example, Fig. 3). The direction of motion is chosen arbitrarily along a continuous sequence of nucleon lines. This determines the order of writing expressions (from left to right) for the diagram elements representing the factors in the product of these expressions that appears in the quantity iM. In the diagrams, the motion along some lines occurs in the directions antiparallel to the directions of these lines (we refer to these lines as ordinary ones), while the motion along the other lines proceeds along the directions of these lines (we refer to them as charge-conjugate lines). Each *dNN* vertex is connected with two nucleon lines of the different types.

(ii) With the vertex *dNN*, we associate the expression $i\Gamma_\mu(p_2, p_1)\tau_2/\sqrt{2}$ with

$$\Gamma_\mu(p_2, p_1) = \frac{g_1}{2m^2}(p_2 - p_1)_\mu + \frac{g_2}{m}\gamma_\mu,$$

where p_1 (p_2) is the 4-momentum of the ordinary (charge-conjugate) nucleon line connected to the *dNN* vertex in question.

(iii) With an external line of the initial (final) deuteron or final (initial) antideuteron, we associate the polarization 4-vector e_μ (e_μ^*) satisfying the condition $e_\mu e_\mu = -1$.

(iv) With each nucleon line carrying the 4-momentum p, we associate the propagator $iG(p)$ (for an ordinary line) or $iG^c(p)$ (for a charge-conjugate line); by definition, we have

$$G(p) = \frac{\hat{p} + m}{p^2 - m^2 + i0}.$$

For an arbitrary matrix, we use here the notation $A^c = U_c \tilde{A} U_c$, where the transposition operator acts on the spinor and isotopic matrices in the expression for A [the following useful relations associated with these operations hold: $1^c \equiv U_c \times 1 U_c = 1$, $\gamma_\mu^c = -\gamma_\mu$ ($\mu = 0, 1, 2, 3$), $\gamma_5^c = \gamma_5$, and $(AB)^c = B^c A^c$]. We also have $G^c(p) \equiv G(-p)$.

(v) In the case of an ordinary (charge-conjugate) nucleon line, there is the factor iA (iA^c) at each vertex of boson coupling to a nucleon. For the πNN vertex from the interaction Lagrangian (2), we have $A = (g/2m) i\hat{k}\gamma_5\tau_a$ and $A^c = (g/2m) i\hat{k}\gamma_5\tilde{\tau}_a$ (a is an isospin subscript), where the pion 4-momentum k is directed from the vertex. For a real $\pi^{+,-,0}$ meson, $\tau_a = (\sqrt{2}\,\tau_-, \sqrt{2}\,\tau_+, \tau_3)$ in the case of pion emission and $\tau_a = (\sqrt{2}\,\tau_+, \sqrt{2}\,\tau_-, \tau_3)$ in the case of pion absorption.

(vi) With an initial (final) nucleon having a 4-momentum p, we associate the factor $u(p)\chi$ ($\bar{u}(p)\chi^+$) for an ordinary line and the factor $\bar{u}^c(p)\tilde{\chi}$ ($u^c(p)\chi^*$) for a charge-conjugate line. Here, $u(p)$ is a four-component spinor, χ is an isospinor, $u^c(p) = U_c\tilde{\bar{u}}(p) = \gamma_2 u^*(p)$, and $\bar{u}^c(p) = -\tilde{u}(p)U_c$.

(vii) Prescriptions for the remaining elements of the diagrams (which do not involve nucleon lines connected to dNN vertices or nucleon lines featuring such vertices) are identical to conventional rules [18]. A closed contour formed by nucleon lines yields a product of traces (of expressions involving gamma matrices and isospin tau matrices), implies integration $(2\pi)^{-4}\int d^4p$ with respect to the intermediate 4-momentum p, and contains the factors of (–1) and 2 (the latter stems from the permutation of internal nucleon lines).

Further, we restrict our consideration to the case of nonrelativistic nucleons—that is, we assume that $\mathbf{p}^2/m \ll m$, where $\mathbf{p}$ is the relative momentum of the nucleons in the dNN vertex. The procedure of evaluating the amplitudes in this approximation on the basis of the above rules is referred to here as a "relativistic" approach. It is precisely this approach that is used in the present article.

The quantities Γ_μ, g_1, and g_2 [see item (ii)] are related to O_μ, f_1, and f_2 [see (9)] by the equations

$$\Gamma_\mu(p_2, p_1) = 4\sqrt{m}(\mathbf{p}^2 + \alpha^2)O_\mu(p_2, p_1),$$
$$g_{1,2} = 4\sqrt{m}(\mathbf{p}^2 + \alpha^2) f_{1,2}, \quad \alpha^2 = m\varepsilon_d, \tag{A.4}$$

where ε_d is the deuteron binding energy.

By way of example, we indicate that the amplitude for $\pi^- d$ scattering at the threshold and the amplitudes for the processes $\pi^- d \longrightarrow nn$ and $pp \longrightarrow \pi^+ d$, which correspond to some of the diagrams in Figs. 3–5, are given by

$$M_3 = 2iT_3\left(\frac{g}{2m}\right)^2 e_\mu^* e_\nu \int \frac{d^4p}{(2\pi)^4} \times \{\Gamma_\mu(p', p_1)G(p_1)\hat{k}\gamma_5 G(p_1') \times \Gamma_\nu(p, p_1')G(-p)\hat{k}\gamma_5 G(-p')\}, \tag{A.5a}$$

$$M_{1,2}^{(b)} = \pm iT_{1,2}^{(b)}\frac{g}{2m} e_\nu \bar{u}(p_{1,2})\hat{k}\gamma_5 G(p_{1,2} - k) \times \Gamma_\nu(p_{2,1}, p_{1,2} - k)u^c(p_{2,1}), \tag{A.5b}$$

$$M_{1,2}^{(f)} = \mp iT_{1,2}^{(f)}\frac{g}{2m} e_\mu^* \bar{u}^c(p_{2,1})\Gamma_\mu(p_{2,1}, p_{1,2} - k) \times G(p_{1,2} - k)\hat{k}\gamma_5 u(p_{1,2}), \tag{A.5c}$$

$$T_3 = \{\tau_2\tau_-\tau_2\tilde{\tau}_+\} = -1, \quad T_{1,2}^{(b)} = \chi_{1,2}^+ \tau_-\tau_2\chi_{2,1}^* = -i, \quad T_{1,2}^{(f)} = \tilde{\chi}_{2,1}\tau_2\tau_-\chi_{1,2} = -i. \tag{A.5d}$$

In order to antisymmetrize a specific amplitude in external nucleons, this amplitude must be supplemented with the analogous expression with the reversed sign and permuted nucleon variables. For example, the expression for $M_2^{(b)}$ must be added to $M_1^{(b)}$ (A.5b) [the factor of $1/\sqrt{2}$ has already been taken into account in expressions (A.5b)]. The expressions for M_3 and $M_{1,2}^{(b)}$ [formulas (13) and (16) of the present article] are obtained here by substituting (A.4) into (A.5a) and (A.5b) (upon performing integration with respect to energy in M_3).

APPENDIX 2

The rules for constructing nonrelativistic matrix elements are the following [the amplitudes are normalized according to (A.3), the total energies of the nucleons and the deuterons being replaced by their masses]:

(i) See item (i) in Appendix 1.

(ii) With the dNN vertex, we associate the expression $i\Gamma_j^{(n)}(\mathbf{p})\tau_2/\sqrt{2}$, where $\mathbf{p}$ is the relative momentum of the nucleons in the dNN vertex, while j is a vectorial subscript.

(iii) With the external line of the initial (final) deuteron, we associate the polarization 3-vector $\boldsymbol{\epsilon}$ ($\boldsymbol{\epsilon}^*$) satisfying the condition $\boldsymbol{\epsilon}\cdot\boldsymbol{\epsilon} = 1$.

(iv) With the internal nucleon line carrying a 4-momentum $p = (m + E, \mathbf{p})$, we associate the nonrelativistic propagator $iG(E, \mathbf{p})$ (for an ordinary line) and $iG^c(E, \mathbf{p})$ (for a charge-conjugate line), where $G(E, \mathbf{p}) = 1/(2mE - \mathbf{p}^2 + i0)$. Here, we have introduced the opera-

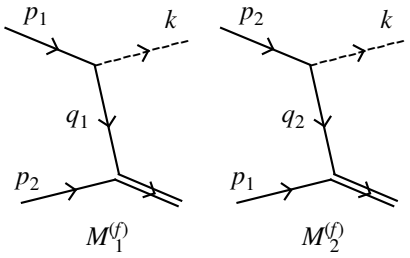

Fig. 6.

tion $A^c = -\sigma_2 \tilde{A} \sigma_2$ [the following useful relations associated with these operations hold: $1^c \equiv -\sigma_2 \times 1 \sigma_2 = -1$, $\sigma_j^c = \sigma_j$ (j = 1, 2, 3), and $(AB)^c = -B^c A^c$]. We also have $G^c(E, \mathbf{p}) = -G(E, \mathbf{p})$.

(v) With each vertex of boson–nucleon coupling, we associate the factor iA (iA^c) in the case of an ordinary (charge-conjugate) nucleon line. For the P-wave pion–nucleon interaction [see expression (6)], we have $A = g(\boldsymbol{\sigma}[\mathbf{k} - (\omega/(2m))(\mathbf{p}_1 + \mathbf{p}_2)])\tau_a$ and $A^c = g(\boldsymbol{\sigma} \cdot [\mathbf{k} - (\omega/(2m))(\mathbf{p}_1 + \mathbf{p}_2)])\tilde{\tau}_a$. Here, ω and $\mathbf{k}$ are, respectively, the total energy and the 3-momentum of the pion, its 4-momentum k [$k = (\omega, \mathbf{k})$] being directed from the vertex; $\mathbf{p}_1$ and $\mathbf{p}_2$ are the nucleon 3-momenta in the vertex; and a is the isospin subscript. The matrices τ_a in the charge representation are presented in item (v) of Appendix 1.

(vi) With each initial (final) nucleon, we associate the factor $w\chi$ ($w^+\chi^+$) for an ordinary line and the factor $w^{c+}\tilde{\chi}$ ($w^c\chi^*$) for the charge-conjugate line. Here, w is a spinor ($w^+w = 1$), χ is an isospinor, $w^c = \sigma_2 w^*$, and $w^{c+} = \tilde{w}\sigma_2$.

(vii) This item is perfectly analogous to item (vii) in Appendix 1. The only exception is that traces contain sigma matrices instead of gamma matrices, while the integral $(2\pi)^{-4}\int d^4p$ with respect to the 4-momentum of the intermediate nucleon is replaced by $(2\pi)^{-4}\int dE\, d^3\mathbf{p}$ [$p = (m + E, \mathbf{p})$].

The equation relating the vertices $\Gamma_j^{(n)}(\mathbf{p})$ [see item (ii)] to the quantities $O_j(\mathbf{p})$ [see equation (10)] and the normalization used in this article for the deuteron wave function (10) are given by

$$\Gamma_j^{(n)}(\mathbf{p}) = 4\sqrt{m}(\mathbf{p}^2 + \alpha^2)O_j^{(n)}(\mathbf{p}),$$
$$\int d^3\mathbf{p}(u^2(\mathbf{p}) + w^2(\mathbf{p})) = (2\pi)^3. \quad \text{(A.6)}$$

Let us present expressions for the amplitudes M_3, $M_{1,2}^{(b)}$, and $M_{1,2}^{(f)}$ (see diagrams 3, 4, and 6). The amplitude M_3 will be considered only for zero pion energy—that is, for $\mathbf{k} = 0$, $\omega = \mu$ (in this case, only the nonstatic term in the πNN vertex is operative), and $\mathbf{p}_1 = -\mathbf{p}_2$. The amplitudes $M_{1,2}^{(b)}$ ($M_{1,2}^{(f)}$) will be written in the c.m. frame of the initial (final) deuteron. Specifically, we have

$$M_3^{(\text{non})} = 2iT_3 g^2 \frac{\mu^2}{m^2}\epsilon_k^*\epsilon_j \int \frac{dE\, d^3\mathbf{p}}{(2\pi)^4} \times \{\Gamma_k^{(n)}(\mathbf{p})(\boldsymbol{\sigma}\cdot\mathbf{p})\Gamma_j^{(n)}(\mathbf{p})(\boldsymbol{\sigma}\cdot\mathbf{p})\} \times G(E_1, \mathbf{p})G(E_1', \mathbf{p})G(E, \mathbf{p})G(E', \mathbf{p}), \quad \text{(A.7a)}$$

$$M_{1,2}^{(b)} = \mp iT_{1,2}^{(b)} g\epsilon_j w_{1,2}^+ \left(\boldsymbol{\sigma}\cdot\left[\mathbf{k} - \frac{\omega}{2m}(\mathbf{p}_{1,2} + \mathbf{q}_{1,2})\right]\right) \times G(E_{q1,q2}, \mathbf{q}_{1,2})\Gamma_j^{(n)}(\mathbf{p}_{2,1})w_{2,1}^c, \quad \text{(A.7b)}$$

$$M_{1,2}^{(f)} = \pm iT_{1,2}^{(f)} g\epsilon_j^* w_{2,1}^{c+}\Gamma_j^{(n)}(\mathbf{p}_{2,1}) \times G(E_{q2,q1}, \mathbf{q}_{2,1})\left(\boldsymbol{\sigma}\cdot\left[\mathbf{k} - \frac{\omega}{2m}(\mathbf{p}_{1,2} + \mathbf{q}_{1,2})\right]\right)w_{1,2}. \quad \text{(A.7c)}$$

Here, we have denoted by E_{q1} and E_{q2} the nonrelativistic energies of virtual nucleons in Figs. 4 and 6, respectively, with 4-momenta $q_i = (m + E_{qi}, \mathbf{q}_i)$ (i = 1, 2). The expressions for the isospin factors T_3, $T_{1,2}^{(b)}$, and $T_{1,2}^{(f)}$ are presented in Appendix 1 [see (A.5d)]. The procedure of antisymmetrization with respect to external nucleons is also explained there. Expression (21) for $M_3^{(\text{non})}$ is obtained in this study upon integration with respect to energy and substitution of (A.6). In the case of the primary pion at rest, the amplitudes $M_{1,2}^{(b)}$ in (A.7b) do not reduce individually to the corresponding expressions in (17) (this was indicated in Section 5 for the imaginary parts), but their sum coincides with the right-hand side of equation (18).

REFERENCES

1. D. Sigg *et al.*, Phys. Rev. Lett. **75**, 3245 (1995).
2. D. Sigg *et al.*, Nucl. Phys. A **609**, 269 (1996).
3. D. Chatellard *et al.*, Phys. Rev. Lett. **74**, 4157 (1995).
4. D. Chatellard *et al.*, Nucl. Phys. A **625**, 855 (1997).
5. V. Bernard, N. Kaiser, and Ulf-G. Meissner, Phys. Lett. B **309**, 421 (1993); Int. J. Mod. Phys. E **4**, 193 (1995); Phys. Rev. C **52**, 2185 (1995).
6. S. R. Beane, V. Bernard, T.-S. H. Lee, *et al.*, Phys. Rev. C **57**, 424 (1998).
7. V. V. Baru and A. E. Kudryavtsev, Yad. Fiz. **60**, 1620 (1997) [Phys. At. Nucl. **60**, 1475 (1997)].
8. A. W. Thomas and R. H. Landau, Phys. Rep. **58**, 121 (1980).
9. D. S. Koltun and T. Mizutani, Ann. Phys. (N.Y.) **109**, 1 (1977).
10. P. F. A. Goudsmit *et al.*, Nucl. Phys. A **575**, 673 (1994).

11. I. S. Shapiro, *The Theory of Direct Nuclear Reactions* (Atomizdat, Moscow, 1963).
12. I. S. Shapiro, Usp. Fiz. Nauk **92**, 549 (1967) [Sov. Phys. Usp. **10**, 515 (1967)].
13. A. P. Yutsis, I. B. Levinson, and V. V. Vaganas, *Mathematical Apparatus of the Theory of Angular Momentum* (Gospolitnauchizdat, Vilnius, 1960; Israel Program for Scientific Transl., Jerusalem, 1962).
14. E. El Baz and B. Castel, *Graphical Methods of Spin Algebras in Atomic, Nuclear, and Particle Physics* (Dekker, New York, 1972; Mir, Moscow, 1974).
15. V. M. Kolybasov, *General Properties of the Scattering Matrix and Polarization Effects in Direct Nuclear Reactions* (Izd. MIFI, Moscow, 1971).
16. T. E. O. Ericson and W. Weise, *Pions and Nuclei* (Clarendon, Oxford, 1988; Nauka, Moscow, 1991).
17. J. D. Bjorken and S. D. Drell, *Relativistic Quantum Fields* (McGraw-Hill, New York, 1965; Nauka, Moscow, 1978).
18. V. B. Berestetskiĭ, E. M. Lifshitz, and L. P. Pitaevskiĭ, *Relativistic Quantum Theory* (Russ. original, Part 1, Nauka, Moscow, 1968; Pergamon, Oxford, 1971).
19. V. A. Karmanov and A. V. Smirnov, Nucl. Phys. A **575**, 520 (1994).
20. C. Fayard, G. Lamot, B. Kerbikov, *et al.*, Strangeness Photoproduction on Deuteron (to be published).
21. F. Gross, Phys. Rev. B **136**, 140 (1964); **140**, 410 (1965).
22. G. D. Alkhazov, V. V. Anisovich, and P. É. Volkovitskiĭ, *Diffractive Hadron–Nucleus Interactions at High Energies* (Nauka, Leningrad, 1991).
23. R. Machleidt *et al.*, Phys. Rep. **149**, 1 (1987).

Translated by A. Isaakyan

Physics of Atomic Nuclei, Vol. 63, No. 5, 2000, pp. 812–819. Translated from Yadernaya Fizika, Vol. 63, No. 5, 2000, pp. 881–889.

NUCLEI
Theory

Green's Functions and Strength Functions for Stationary Quantum Systems

S. G. Kadmensky and M. M. Lesnykh

Voronezh State University, Universitetskaya pl. 1, Voronezh, 394693 Russia

Received December 25, 1998; in final form, June 23, 1999

Abstract—By using the analytic properties of the retarded Green's function for a stationary quantum system, the strength function that coincides with the energy distribution of an unperturbed state of the system over its exact states in a perturbing field is constructed. It is shown that, in general, this strength function has the form of a Breit–Wigner distribution with energy-dependent parameters and that its moments are determined by the expectation values of various powers of the exact Hamiltonian for the wave function of the unperturbed state. The strength function averaged over a certain energy interval is calculated, and its properties are investigated for a global regime of averaging. The resulting strength functions are used to determine the mean field and the optical potential for nucleons in nuclei and to investigate conditions under which quantum chaos emerges in various systems. *© 2000 MAIK "Nauka/Interperiodica".*

1. INTRODUCTION

The features of a quantum system can be calculated if its exact Green's function is known [1–5]. With the aid of the Green's function, we can determine strength functions that describe the character of fragmentation of comparatively simple states associated with the unperturbed Hamiltonian of the system over states of more complicated nature that correspond to the exact Hamiltonian, which takes fully into account perturbations in the system. Knowledge of the energy moments and widths of strength functions makes it possible to deduce important information about the dynamical and static properties of the system—in particular, about the probabilities of the decay of quasistationary states, as well as about conditions under which quantum chaos can emerge in the system [6–8].

In [9–11], the properties of the exact single-particle Green's function, of the mass operator, and of strength functions for fermions were investigated for open Fermi systems, which are exemplified by many-electron atoms and atomic nuclei. An analysis of nucleon strength functions in nuclei revealed that, in the case of a global regime of averaging, the self-consistent potential for nucleons and the real part of the optical potential for nucleons coincide with the Hartree–Fock potential generated by realistic nucleon–nucleon forces.

The objective of the present study is to apply the methods developed in [2, 9–11] to investigating the properties of retarded Green's functions and strength functions for arbitrary quantum systems.

2. RETARDED GREEN'S FUNCTION FOR A STATIONARY SYSTEM

The behavior of an arbitrary stationary quantum system governed by a Hamiltonian $H(x)$, where x is a complete set of coordinates of the system, is described [1] by the wave functions $\Psi_s(x) \equiv |s\rangle$ satisfying the time-independent Schrödinger equation

$$(H(x) - E_s)|s\rangle = 0, \tag{1}$$

where E_s are the corresponding energies. The subscript s characterizing the state $|s\rangle$ of the system includes both the eigenvalues of the Hamiltonian $H(x)$ of the system and the eigenvalues of all basic integrals of the motion of the system in involution [the operators corresponding to such integrals of the motion commute not only with the Hamiltonian $H(x)$ of the system but also with one another], since the wave function $|s\rangle$ of the system is an eigenfunction not only of the Hamiltonian $H(x)$ but also of the operators of the above integrals of the motions—that is, $s \equiv \bar{s}, E_s$. In general, the set of states s includes states $s_0 = \bar{s}_0, E_{s_0}$ characterized by discrete energies E_{s_0} and wave functions $|s_0\rangle$ normalized to unity and states s, E_s characterized by continuous energies $E_s \geq E_0$ (E_0 is the lower continuum threshold) and wave functions $|\bar{s}, E_s\rangle$ normalized to the delta function of energy. The functions $|s\rangle$ satisfy the completeness condition

$$\sum_s \Psi_s(x)\Psi_s^*(x') = \sum_s |s\rangle\langle s| = \delta(x - x'), \tag{2}$$

where the symbol $\sum_s$ is spelled out as

$$\sum_s = \sum_{s_0} + \sum_{\bar{s}} \int_{E_0}^{\infty} dE_s, \tag{3}$$

1063-7788/00/6305-0812$20.00

and the orthonormalization condition

$$\langle s|s_1\rangle = \delta_{ss_1}, \tag{4}$$

where the symbol δ_{ss_1} coincides with the ordinary Kronecker delta symbol for $s = \bar{s}_0$, E_{s_0} and $s_1 = \bar{s}_{10}$, $E_{s_{10}}$ and with the symbol $\delta_{\bar{s}\bar{s}_1}\delta(E_s - E_{s_1})$ for $s = \bar{s}$, E_s.

Let us represent the Hamiltonian $H(x)$ in the form

$$H(x) = H_0(x) + V(x), \tag{5}$$

where $H_0(x)$ is the Hamiltonian of the unperturbed system and $V(x)$ is the perturbation operator. We also introduce wave functions $|k\rangle$ with energies ε_k for the unperturbed system with the Hamiltonian $H_0(x)$:

$$[H_0(x) - \varepsilon_k]|k\rangle = 0. \tag{6}$$

Among the states k, there are states k_0 with discrete energies ε_{k_0} and states $\bar{k}$, ε_k with continuous energies $\varepsilon_k > \varepsilon_0$.

The wave functions $|k\rangle$ form a complete orthonormalized basis in accordance with the conditions of the type (2) and (4). We can expand a function $|k\rangle$ in a series in the functions $|s\rangle$ as

$$|k\rangle = \sum_s C_s^k |s\rangle, \tag{7}$$

where the expansion coefficients $C_s^k = \langle s|k\rangle$, which have the meaning of the wave function $|k\rangle$ in the s representation, satisfy the equation

$$[\varepsilon_k - E_s]C_s^k + \sum_{s_1}\langle s|V|s_1\rangle C_{s_1}^k = 0 \tag{8}$$

and the orthonormalization and completeness conditions

$$\sum_s (C_s^k)^* C_s^{k_1} = \delta_{kk_1}, \quad \sum_k (C_s^k)^* C_{s_1}^k = \delta_{ss_1}. \tag{9}$$

Let us now determine the retarded Green's function [3] $G(xt, x't')$ for the perturbed system. This Green's function satisfies the equation

$$\left(i\hbar\frac{\partial}{\partial t} - H(x)\right)G(xt, x't') = \delta(x - x')\delta(t - t').$$

The Green's function $G^0(xt, x't')$ for the unperturbed system is determined by the similar equation with the Hamiltonian $H(x)$ replaced by the Hamiltonian $H_0(x)$. By using condition (2), we can represent the solution for the retarded Green's function $G(xt, x't')$ as

$$G(xt, x't') = \frac{i}{\hbar}\sum_s \Psi_s(x)\Psi_s^*(x')e^{-i/\hbar E_s(t-t')}\theta(t - t'),$$

where the function $\theta(t)$ is equal to unity and zero for $t > 0$ and $t < 0$, respectively. The Fourier transform of this function in the variable $\tau = t - t'$ is given by

$$G(x, x', \varepsilon) = \int_{-\infty}^{+\infty} e^{(i/\hbar)\varepsilon\tau - \delta|\tau|}G(xt, x't')d\tau,$$

where the infinitesimal quantity $\delta \longrightarrow 0+$ is introduced to regularize the relevant integral. This function and the Fourier transform of the analogous unperturbed Green's function $G^0(xt, x't')$ can be represented in the symbolic form

$$\begin{aligned} G(\varepsilon, x) &= \frac{1}{\varepsilon - H(x) + i\delta}, \\ G^0(\varepsilon, x) &= \frac{1}{\varepsilon - H_0(x) + i\delta}. \end{aligned} \tag{10}$$

Let us consider the matrix elements of the type $\langle k|G(\varepsilon, x)|k_1\rangle \equiv G_{kk_1}(\varepsilon)$ for the Green's functions $G(\varepsilon, x)$ and $G^0(\varepsilon, x)$ (10) in the k representation of these Green's functions,

$$\begin{aligned} G_{kk_1}(\varepsilon) &= \left\langle k\left|\frac{1}{\varepsilon - H(x) + i\delta}\right|k_1\right\rangle, \\ G^0_{kk_1}(\varepsilon) &= \left\langle k\left|\frac{1}{\varepsilon - H_0(x) + i\delta}\right|k_1\right\rangle. \end{aligned} \tag{11}$$

If we express the above matrix elements in terms of the complete orthonormalized bases of the eigenfunctions $|s\rangle$ and $|k\rangle$ of the Hamiltonians $H(x)$ (1) and $H_0(x)$ (6), respectively, the functions $G_{kk_1}(\varepsilon)$ and $G^0_{kk_1}(\varepsilon)$ (11) can be represented as

$$\begin{aligned} G_{kk_1}(\varepsilon) &= \sum_s \frac{(C_s^k)^* C_s^{k_1}}{\varepsilon - E_s + i\delta} \\ &= \sum_{s_0}\frac{(C_{s_0}^k)^* C_{s_0}^{k_1}}{\varepsilon - E_{s_0} + i\delta} + \sum_{\bar{s}}\int_{E_0}^{\infty} dE_s \frac{(C_s^k)^* C_s^{k_1}}{\varepsilon - E_s + i\delta}, \end{aligned} \tag{12}$$

$$G^0_{kk_1}(\varepsilon) = \frac{\delta_{kk_1}}{\varepsilon - \varepsilon_k + i\delta} \equiv G_k^0\delta_{kk_1}. \tag{12a}$$

We further make use of the well-known relation (see, for example, [1])

$$\frac{1}{x + i\delta} = P\frac{1}{x} - i\pi\delta(x) \tag{13}$$

and write explicitly the real and the imaginary part of the Green's function $G_{kk_1}(\varepsilon)$:

$$\begin{aligned} \mathrm{Re}\, G_{kk_1}(\varepsilon) &= P\sum_s \frac{(C_s^k)^* C_s^{k_1}}{\varepsilon - E_s}, \\ \mathrm{Im}\, G_{kk_1}(\varepsilon) &= -\pi\sum_s (C_s^k)^* C_s^{k_1}\delta(\varepsilon - E_s). \end{aligned} \tag{14}$$

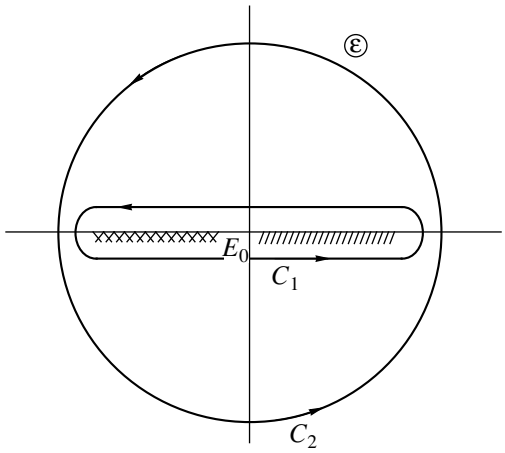

Positions of the poles (crosses) and cuts (hatching) for the Green's function on the physical sheet of the variable ε. Closed solid lines with arrows represent contours of integration that are used in evaluating relevant integrals.

From here, we obtain the dispersion relation [3]

$$G_{kk_1}(\varepsilon) = -\frac{1}{\pi}\int_{-\infty}^{+\infty}\frac{\mathrm{Im}\,G_{kk_1}(\varepsilon_1)}{\varepsilon-\varepsilon_1+i\delta}d\varepsilon_1, \qquad (15)$$

which makes it possible to reconstruct the complete Green's function from its imaginary part $\mathrm{Im}\,G_{kk_1}(\varepsilon)$.

By analogy with a consideration of the analytic properties of the exact single-particle Green's function for open Fermi systems in [11], we will now investigate the analytic properties of the Green's function $G_{kk_1}(\varepsilon)$ in the complex plane of the variable ε. As can be seen from (12), $G_{kk_1}(\varepsilon)$ is a two-sheeted function. On the first (physical) sheet, this function has discrete poles on the real axis at $\varepsilon = E_{s_0} < E_0$ and the branch point at $\varepsilon = E_0$, from which we can draw a cut along the real axis to infinity ($E_0 \le \varepsilon \le \infty$). Upon going over from the lower ($\varepsilon = \mathrm{Re}\varepsilon - i\alpha$, where $\alpha > \delta$ and $\alpha \longrightarrow 0+$) to the upper ($\varepsilon = \mathrm{Re}\varepsilon + i\alpha$) bank of the cut, the function $G_{kk_1}(\varepsilon)$ undergoes the discontinuity

$$\Delta G_{kk_1}(\varepsilon) = -2i\pi\sum_s (C_s^k)^* C_s^{k_1}\delta(\varepsilon-E_s). \qquad (16)$$

The properties of the function $G_{kk_1}(\varepsilon)$ on the physical sheet are illustrated in the figure. On the second (unphysical) sheet of the variable ε, whose upper and lower half-planes are joined with, respectively, the lower and the upper bank of the cut on the physical sheet, the function $G_{kk_1}(\varepsilon)$ has poles that occur on the real axis for $\varepsilon < E_0$ and correspond to virtual and antibound states; in addition, it has pairs of poles at $\mathrm{Re}\varepsilon \ge E_0$ and $\mathrm{Im}\varepsilon = +\Gamma, -\Gamma$ ($\Gamma > 0$), which correspond to the quasistationary states of the system.

The equations for the matrix elements $G_{kk_1}(\varepsilon)$ can be derived by expanding the Green's function $G(\varepsilon, x)$ (10) in a series in the potential $V(x)$ and by subsequently summing some terms of this series. As the result, we find that the Green's function $G(\varepsilon, x)$ satisfies the equation [3]

$$\begin{aligned} G(\varepsilon,x) &= G^0(\varepsilon,x) + G^0(\varepsilon,x)V(x)G^0(\varepsilon,x) \\ &+ G^0(\varepsilon,x)V(x)G^0(\varepsilon,x)V(x)G^0(\varepsilon,x) + \ldots \\ &= G^0(\varepsilon,x) + G^0(\varepsilon,x)V(x)G(\varepsilon,x), \end{aligned} \qquad (17)$$

whence we obtain an equation for the Green's function $G_{kk_1}(\varepsilon)$ in the k representation:

$$G_{kk_1}(\varepsilon) = G_k^0\delta_{kk_1} + G_k^0\sum_{k_2}\langle k|V|k_2\rangle G_{k_2k_1}(\varepsilon). \qquad (18)$$

For a discrete state $k_1 = k_0$, the diagonal matrix element $G_{k_0k_0}(\varepsilon)$ is determined by the equation

$$G_{k_0k_0}(\varepsilon) = G_{k_0}^0 + G_{k_0}^0\sum_{k_2}\langle k_0|V|k_2\rangle G_{k_2k_0}(\varepsilon). \qquad (19)$$

If we use equation (18), the result obtained by iterating the right-hand side of (19) and by explicitly isolating the diagonal element $G_{k_0k_0}(\varepsilon)$ is given by [2]

$$\begin{aligned} G_{k_0k_0}(\varepsilon) &= G_{k_0}^0 + G_{k_0}^0\Bigg\{\langle k_0|V|k_0\rangle \\ &+ \sum_{k_1\ne k_0}\langle k_0|V|k_1\rangle G_{k_1}^0(\varepsilon)\langle k_1|V|k_0\rangle \\ &+ \sum_{k_1\ne k_0}\langle k_0|V|k_1\rangle G_{k_1}^0(\varepsilon) \\ &\times \sum_{k_2\ne k_0}\langle k_1|V|k_2\rangle G_{k_2}^0(\varepsilon)\langle k_2|V|k_0\rangle + \ldots\Bigg\}G_{k_0k_0}(\varepsilon). \end{aligned}$$

This formula can be represented in the compact form

$$\begin{aligned} G_{k_0k_0}(\varepsilon) &= G_{k_0}^0 + G_{k_0}^0\Bigg\{\langle k_0|V|k_0\rangle \\ &+ \left\langle k_0\left|V\frac{1}{\varepsilon-\tilde{H}+i\delta}V\right|k_0\right\rangle\Bigg\}G_{k_0k_0}(\varepsilon), \end{aligned} \qquad (20)$$

where the Hamiltonian $\tilde{H}$ differs from the Hamiltonian H in that the former is defined in the space of eigenfunctions $|\tilde{s}\rangle$,

$$[E_{\tilde{s}} - \tilde{H}]|\tilde{s}\rangle = 0, \quad (21)$$

which are orthogonal to the wave function $|k_0\rangle$ of the unperturbed system, $\langle k_0|\tilde{s}\rangle = 0$. For $E_{\tilde{s}} < \tilde{E}_0$, the states $|\tilde{s}\rangle = |\tilde{s}_0\rangle$ have discrete energies, while, for $E_{\tilde{s}} \geq \tilde{E}_0$, the states $|\tilde{s}\rangle$ belong to the continuous spectrum. Following the ideology of the projection-operator technique [11, 12], we can introduce the projection operator $\hat{P}_{k_0} \equiv |k_0\rangle\langle k_0|$ ($\hat{P}_{k_0} = (\hat{P}_{k_0})^2$) and the complementary operator $\hat{Q} = 1 - \hat{P}_{k_0}$. Within this framework, the Hamiltonian $\tilde{H}$ can be represented in the form $\tilde{H} = \hat{Q}H\hat{Q}$. Introducing a complete orthonormalized basis of eigenfunctions $|\tilde{s}\rangle$ of Hamiltonian (21) and using equation (20), we can reduce the diagonal matrix element $G_{k_0k_0}(\varepsilon)$ to the form

$$G_{k_0k_0}(\varepsilon) = [\varepsilon - \varepsilon_{k_0} - \langle k_0|V|k_0\rangle - \tilde{M}_{k_0}(\varepsilon) + i\delta]^{-1}, \quad (22)$$

where $\tilde{M}_{k_0}(\varepsilon)$ is an analog of the retarded (energy-dependent) part of the mass operator [3]:

$$\tilde{M}_{k_0}(\varepsilon) \equiv \sum_{\tilde{s}} \frac{|\langle k_0|V|\tilde{s}\rangle|^2}{\varepsilon - E_{\tilde{s}} + i\delta}. \quad (23)$$

For the continuum states $|k\rangle$ and $|k_1\rangle$, there is the problem of a limiting transition from the off-diagonal matrix element $G_{kk_1}(\varepsilon)$ to the diagonal one. The point is that, upon a formal substitution of the subscript $k_1 = k$ into $G_{kk_1}(\varepsilon)$, the resulting quantity involves a term proportional to $\delta_{kk} = \delta(\varepsilon_k - \varepsilon_{k_1})$ for $\varepsilon_{k_1} \longrightarrow \varepsilon_k$ and is therefore divergent. Instead of the divergent matrix element $G_{kk}(\varepsilon)$, we will make use of the quantity $\bar{G}_{kk}(\varepsilon)$ defined as

$$\bar{G}_{kk}(\varepsilon) = \int G_{\bar{k}\varepsilon_k, \bar{k}\varepsilon_{k_1}}(\varepsilon)d\varepsilon_{k_1},$$
$$\bar{G}^0_{kk}(\varepsilon) = \int G^0_{\bar{k}\varepsilon_k, \bar{k}\varepsilon_{k_1}}(\varepsilon)d\varepsilon_{k_1} = G^0_k(\varepsilon), \quad (24)$$

where the integral with respect to ε_{k_1} receives the main contribution from a small vicinity $\delta\varepsilon_k$ of the point $\varepsilon_{k_1} = \varepsilon_k$. For the function $\bar{G}_{kk}(\varepsilon)$, equation (22) then holds upon the replacement of the subscript k_0 by k; the projection operator $\hat{P}_{k_0} \equiv |k_0\rangle\langle k_0|$ by the projection operator $P_k \equiv \int |k\rangle\langle k|d\varepsilon_k$ ($P_k^2 = P_k$); and the quantities $\langle k_0|V|k_0\rangle$ and $\tilde{M}_{k_0}$ by $\int \langle k|V|k_1\rangle d\varepsilon_{k_1}$ and $\int d\varepsilon_{k_1} \sum_{\tilde{s}} \frac{\langle k|V|\tilde{s}\rangle\langle\tilde{s}|V|k_1\rangle}{\varepsilon - E_{\tilde{s}} + i\delta}$, respectively, where the integrals with respect to ε_{k_1} are determined by a small vicinity $\delta\varepsilon_k$ of the point $\varepsilon_{k_1} = \varepsilon_k$. For potentials $V(x)$ decreasing with increasing distance between the interacting parts of the system, we can disregard all terms involving $V(x)$ in formulas for the Green's function $\bar{G}_{kk}(\varepsilon)$ that are similar to (22), whereby $\bar{G}_{kk}(\varepsilon)$ becomes coincident with G^0_k (12a).

3. STRENGTH FUNCTION OF THE STATE k

Let us consider the energy distribution $S_{kk_1}(\varepsilon)$ of the coefficients C^k_s, which is given by

$$S_{kk_1}(\varepsilon) = -\frac{1}{\pi}\mathrm{Im}\,G_{kk_1}(\varepsilon) = \sum_s (C^k_s)^* C^{k_1}_s \delta(\varepsilon - E_s). \quad (25)$$

In the diagonal case, it reduces to the function

$$S_k(\varepsilon) \equiv S_{kk}(\varepsilon) = \sum_s |C^k_s|^2 \delta(\varepsilon - E_s), \quad (26)$$

which is referred to as the strength function for the state k [9, 13]. The strength function $S_k(\varepsilon)$ specifies the energy distribution of the unperturbed state k over the states s of the perturbed system. For a discrete state k_0, the strength function S_{k_0} is determined by the imaginary part of the Green's function $G_{k_0k_0}(\varepsilon)$ (22). Separating the real $[\Delta_{k_0}(\varepsilon)]$ and the imaginary $\left(-\frac{1}{2}\Gamma_{k_0}(\varepsilon)\right)$ parts of the function $\tilde{M}_{k_0}(\varepsilon)$ (23) with the aid of (13),

$$\Delta_{k_0}(\varepsilon) = P\sum_{\tilde{s}} \frac{|\langle k_0|V|\tilde{s}\rangle|^2}{\varepsilon - E_{\tilde{s}}},$$
$$\Gamma_{k_0}(\varepsilon) = 2\pi\sum_{\tilde{s}} |\langle k_0|V|\tilde{s}\rangle|^2 \delta(\varepsilon - E_{\tilde{s}}), \quad (27)$$

and determining the imaginary part of the Green's function $G_{k_0k_0}(\varepsilon)$ (22), we can deduce an explicit expression for the strength function $S_{k_0}(\varepsilon)$ by using the definition in (26). The result is

$$S_{k_0}(\varepsilon) = \frac{\Gamma_k(\varepsilon)}{2\pi\left[(\varepsilon - \varepsilon_{k_0} - \langle k_0|V|k_0\rangle - \Delta_{k_0}(\varepsilon))^2 + \frac{(\Gamma_{k_0}(\varepsilon))^2}{4}\right]}. \quad (28)$$

Formula (28) has a Breit–Wigner form, but it was obtained without invoking an averaging procedure usually used in deriving similar expressions [13].

Let us now analyze this formula in some detail. For $\varepsilon < \tilde{E}_0$, the width $\Gamma_{k_0}(\varepsilon)$ (27) has a delta-function character at ε values coincident with the energies $E_{\tilde{s}_0}$ of the discrete states. At these ε values, however, the strength function $S_{k_0}(\varepsilon)$ vanishes. At nonzero values of $S_{k_0}(\varepsilon)$, the quantity $\Gamma_{k_0}(\varepsilon)$ can therefore be set to zero in (28). Formula (28) then reduces to that part of formula (26) which is determined by the sum over the discrete states s_0 under the condition $E_0 = \tilde{E}_0$, the energies E_{s_0} of the corresponding states being determined by the equation

$$E_{s_0} = \varepsilon_{k_0} + \langle k_0|V|k_0\rangle + \Delta_{k_0}(E_{s_0}). \tag{29}$$

For the quantities $\left|C_{s_0}^{k_0}\right|^2$, we have

$$\left|C_{s_0}^{k_0}\right|^2 = \left(1 - \frac{d\Delta_{k_0}(\varepsilon)}{d\varepsilon}\bigg|_{\varepsilon = E_{s_0}}\right)^{-1}. \tag{30}$$

For $\varepsilon \geq \tilde{E}_0$, the width $\Gamma_{k_0}(\varepsilon)$ becomes nonzero owing to the contribution of the continuum states $\tilde{s}$:

$$\Gamma_{k_0}(\varepsilon) = 2\pi\sum_{\tilde{s}}\left|\langle k_0|V|\bar{\tilde{s}}, \varepsilon\rangle\right|^2. \tag{31}$$

In (28), the poles are simultaneously shifted from the real axis of ε to the unphysical sheet of complex values of this variable.

If the state k belongs to the continuous spectrum, it is natural to use the function $\bar{G}_{kk}(\varepsilon)$ (24), which is equal to $G_k^0(\varepsilon)$, instead of the divergent diagonal matrix element $G_{kk}(\varepsilon)$ of the Green's function (see above). Instead of the strength function S_k, we can make use of the strength function $\bar{S}_k = \int S_{kk_1}d\varepsilon_{k_1}$, which coincides with $\delta(\varepsilon - \varepsilon_k)$.

4. ENERGY MOMENTS OF THE STRENGTH FUNCTION

Let us consider the energy moments $J_{kk_1}^{(l)}$ of the distribution $S_{kk_1}(\varepsilon)$ that are given by

$$J_{kk_1}^{(l)} = \int\varepsilon^l S_{kk_1}(\varepsilon)d\varepsilon = \sum_s (C_s^k)^* C_s^{k_1} E_s^l. \tag{32}$$

By using the relation between the strength function $S_{kk_1}(\varepsilon)$ and the Green's function $G_{kk_1}(\varepsilon)$, the energy moments can be expressed [13] in terms of integrals along the contour C_1 that corresponds to transition from the lower ($\varepsilon = \mathrm{Re}\varepsilon - i\alpha$, where $\alpha > \delta$ and $\alpha \longrightarrow 0+$) to the upper ($\varepsilon = \mathrm{Re}\varepsilon + i\alpha$) bank of the cut for the function $G_{kk_1}(\varepsilon)$ and which is depicted in the figure:

$$J_{kk_1}^{(l)} = \frac{1}{2\pi i}\oint_{C_1}\varepsilon^l G_{kk_1}(\varepsilon)d\varepsilon. \tag{33}$$

Since the integrand in (33) involves analytic functions, the contour C_1 can be deformed into a circle of infinitely large radius (contour C_2 in the figure). From (11), it follows that, for $\varepsilon \longrightarrow \infty$, we have

$$G_{kk_1}(\varepsilon) \longrightarrow G_k^0(\varepsilon)\delta_{kk_1} \longrightarrow \frac{1}{\varepsilon}\delta_{kk_1}. \tag{34}$$

As a result, the zeroth moment $J_{kk_1}^{(0)}$, which is determined by calculating the relevant integral along the contour C_2 in (28), appears to be

$$J_{kk_1}^{(0)} = \sum_s (C_s^k)^* C_s^{k_1} = \delta_{kk_1}, \tag{35}$$

which is consistent with the orthonormalization condition (9).

In order to calculate the first moment $J_{kk_1}^{(1)}$ [see (33)], we consider the integral

$$\frac{1}{2\pi i}\oint_{C_2}\varepsilon[G_{kk_1}(\varepsilon) - G_{kk_1}^{(0)}(\varepsilon)]d\varepsilon. \tag{36}$$

With the aid of equations (18) and (29), the limiting form of the bracketed expression in (36) for $\varepsilon \longrightarrow \infty$ can be represented as $\frac{\langle k|V|k_1\rangle}{\varepsilon^2}$. The integral in (36) then assumes the form $\langle k|V|k_1\rangle$. If we consider that $\frac{1}{2\pi i}\oint_{C_2}\varepsilon G_{kk_1}^0(\varepsilon)d\varepsilon = \varepsilon_k\delta_{kk_1}$, the relation

$$J_{kk_1}^{(1)} = \sum_s (C_s^k)^* C_s^{k_1} E_s = \varepsilon_k\delta_{kk_1} + \langle k|V|k_1\rangle \tag{37}$$

follows from expression (36) for the first moment $J_{kk_1}^{(1)}$, which coincides with the energy centroid of the distribution $S_{kk_1}(\varepsilon)$.

In order to calculate the second moment $J_{kk_1}^{(2)}$ [see (32)], we consider the integral

$$\frac{1}{2\pi i}\oint_{C_2}\varepsilon^2\Bigg[G_{kk_1}(\varepsilon) - G_{kk_1}^{(0)}(\varepsilon) - G_k^0\sum_{k_2}\langle k|V|k_2\rangle G_{k_2k_1}^0(\varepsilon)\Bigg]d\varepsilon. \tag{38}$$

By means of equations (18) and (29), the limiting form of the bracketed expression in (38) for $\varepsilon \longrightarrow \infty$ can be reduced to $\frac{\langle k|V^2|k_1\rangle}{\varepsilon^3}$. The integral in (38) then assumes the form $\langle k|V^2|k_1\rangle$. From (38), we find, by additionally taking into account the relations

$$\frac{1}{2\pi i}\oint_{C_2}\varepsilon^2 G^0_{kk_1}(\varepsilon)d\varepsilon = \varepsilon_k^2\delta_{kk_1},$$

$$\frac{1}{2\pi i}\oint_{C_2}\varepsilon^2 G^0_k(\varepsilon)\langle k|V|k_1\rangle G^0_{k_1}d\varepsilon = 2\varepsilon_k\langle k|V|k_1\rangle,$$

that the second moment $J^{(2)}_{kk_1}$ can be represented as

$$\begin{aligned} J^{(2)}_{kk_1} &= \sum_s (C^k_s)^* C^{k_1}_s E^2_s \\ &= \varepsilon_k^2\delta_{kk_1} + 2\varepsilon_k\langle k|V|k_1\rangle + \langle k|V^2|k_1\rangle. \end{aligned} \tag{39}$$

Pursuing our calculations further along similar lines, we obtain the following generic expression for the moment $J^{(l)}_{kk_1}$:

$$J^{(l)}_{kk_1} = \langle k|(\varepsilon_k + V)^l|k_1\rangle = \langle k|H^l(x)|k_1\rangle. \tag{40}$$

This formula reflects high symmetry: the *l*th moment of the distribution $S_{kk_1}(\varepsilon)$ is determined by the matrix element of the *l*th power of the Hamiltonian of the perturbed system between the states $|k\rangle$ and $|k_1\rangle$. It is therefore natural to make an attempt at deriving this formula within a more general formalism. For this, we consider the Green's function $G(\varepsilon, x)$ (10) as a function of energy ε and the operator $H(x)$. We define the operator strength function $\hat{S}(\varepsilon)$ as

$$\hat{S}(\varepsilon) = -\frac{1}{\pi}\mathrm{Im}\,G(\varepsilon, x) = \delta(\varepsilon - H(x)). \tag{41}$$

Its matrix element between the states k and k_1 coincides with the distribution $S_{kk_1}(\varepsilon)$ (25). We further introduce the operator moments $\hat{J}^{(l)}$ of the operator strength function $\hat{S}(\varepsilon)$ as

$$\hat{J}^{(l)} = \int\varepsilon^l\hat{S}(\varepsilon)d\varepsilon = \frac{1}{2\pi i}\oint_{C_2}\varepsilon^l G(\varepsilon, x)d\varepsilon. \tag{42}$$

The integral in (42) can be calculated straightforwardly by using expression (10) for $G(\varepsilon, x)$. The result is

$$\hat{J}^{(l)} = (H(x))^l. \tag{43}$$

The matrix element of the operator $\hat{J}^{(l)}$ between the states k and k_1 coincides with the moment $J^{(l)}_{kk_1}$ calculated above [see (40)].

Let us now consider the quantity

$$K = \frac{1}{4\pi i}\oint_{C_1}\left[\tilde{M}_{k_0}(\varepsilon) + \tilde{M}^*_{k_0}(\varepsilon)\right]G_{k_0k_0}(\varepsilon)d\varepsilon,$$

where $\tilde{M}^*_{k_0}(\varepsilon)$ is the complex conjugate of $\tilde{M}_{k_0}(\varepsilon)$ not only for real values of the variable ε but also for its complex values. Taking into the account the definitions of the functions $\tilde{M}_{k_0}(\varepsilon)$ and $G_{k_0k_0}(\varepsilon)$ [formulas (23) and (22), respectively], we can evaluate the integral in the expression for K along the contour C_1. This yields

$$K = \int_{-\infty}^{+\infty}\Delta_{k_0}(\varepsilon)S_{k_0}(\varepsilon)d\varepsilon.$$

On the other hand, we can see that, owing to the analyticity of the integrand in the definition of K on the physical sheet beyond the contour C_1, the quantity K can be represented as an integral along the contour C_2:

$$K = \frac{1}{4\pi i}\oint_{C_2}\left[\tilde{M}_{k_0}(\varepsilon) + \tilde{M}^*_{k_0}(\varepsilon)\right]G_{k_0k_0}(\varepsilon)d\varepsilon.$$

Since this integral is equal to zero, we arrive at the important conclusion that the function $\Delta_{k_0}(\varepsilon)$ (23) averaged over the distribution in (28) vanishes; that is,

$$\int_{-\infty}^{+\infty}\Delta_{k_0}(\varepsilon)S_{k_0}(\varepsilon)d\varepsilon = 0. \tag{44}$$

This conclusion makes it possible to clarify the reason why the quantity $\Delta_{k_0}(\varepsilon)$ does not appear in expression (37) for the first moment $J^{(1)}_{kk_1}$ of the strength function. Using the methods of the above analysis, we can derive the inverse strength function $S_{s_0}(\varepsilon)$, which determines the energy distribution of the perturbed discrete state s_0 over the states k of the unperturbed system:

$$S_{s_0}(\varepsilon) = \sum_k\left|C^{s_0}_k\right|^2\delta(\varepsilon - \varepsilon_k). \tag{45}$$

For this, we must make the substitution $k \rightleftharpoons s$ in all the formulas obtained above and reverse the sign of the potential $V(x)$.

5. AVERAGED STRENGTH FUNCTION AND GLOBAL REGIME OF AVERAGING

Let us consider the case where a discrete state k_0 corresponds to a sufficiently high excitation energy, so that the main contribution to the strength function $S_{k_0}(\varepsilon)$ (26) comes from the states s characterized by a

significant energy density ρ_s. In this case, we can introduce [9, 13] the strength function

$$\langle S_{k_0}(\varepsilon)\rangle = \int_{-\infty}^{+\infty} f_\Delta(\varepsilon-\varepsilon_1)S_{k_0}(\varepsilon_1)d\varepsilon_1 = \sum_s \left|C_{k_0}^s\right|^2 f_\Delta(\varepsilon-E_s), \quad (46)$$

averaged over the energy range Δ satisfying the condition $\rho_s\Delta \gg 1$. The quantity $f_\Delta(y)$ in integrand in (46)—the function with which the averaging is performed—is a normalized (to unity) even function that has a maximum at $y = 0$ and which decreases fast beyond the interval of averaging. It immediately follows from the definition of this function that the zeroth and first moments of the averaged strength function $\langle J_{k_0}^{(l)}\rangle$ coincide with the corresponding moments of the exact strength function $S_{k_0}(\varepsilon)$ (26):

$$\langle J_{k_0}^{(0)}\rangle = 1, \quad \langle J_{k_0}^{(1)}\rangle = \varepsilon_{k_0} + \langle k_0|V|k_0\rangle. \quad (47)$$

The averaged strength function $\langle S_{k_0}(\varepsilon)\rangle$ (46) can also be expressed in terms of an integral in the complex plane along the contour C_1 [13]:

$$\langle S_{k_0}(\varepsilon)\rangle = \frac{1}{2\pi i}\oint_{C_1} f_\Delta(\varepsilon-\varepsilon_1)G_{k_0k_0}(\varepsilon_1)d\varepsilon_1. \quad (48)$$

We choose the averaging function in the form of the Breit–Wigner distribution [13]

$$f_\Delta(y) = \frac{\Delta}{2\pi\left(y^2+\left(\frac{\Delta}{2}\right)^2\right)}, \quad (49)$$

which has two poles in the complex plane of y at $y = \pm i\Delta/\sqrt{2}$ and which decreases in proportion to $1/y^2$ for $|y| \longrightarrow \infty$. Therefore, this function has only two finite moments, those corresponding to $l = 0$ and $l = 1$. For this case, relation (48) can be recast into the form [9, 13]

$$\langle S_{k_0}(\varepsilon)\rangle = \frac{1}{2\pi i}\oint_{C_3} f_\Delta(\varepsilon-\varepsilon_1)G_{k_0k_0}(\varepsilon_1)d\varepsilon_1, \quad (50)$$

where the contour C_3 is formed by two circles of small radius that circumvent the poles of the function $f_\Delta(y)$ in the counterclockwise direction. Upon calculating the integral in (50), we can reduce the function $\langle S_{k_0}(\varepsilon)\rangle$ to a form similar to that of (28). Specifically, we have

$$\langle S_{k_0}(\varepsilon)\rangle = \frac{\langle\Gamma_{k_0}(\varepsilon)\rangle+\Delta}{2\pi\left[\left(\varepsilon-\varepsilon_{k_0}-\langle k_0|V|k_0\rangle-\langle\Delta_{k_0}(\varepsilon)\rangle\right)^2+\frac{\left(\langle\Gamma_{k_0}(\varepsilon)\rangle+\Delta\right)^2}{4}\right]}, \quad (51)$$

where

$$\langle\Delta_{k_0}(\varepsilon)\rangle = \sum_{\tilde{s}}\frac{|\langle k_0|V|\tilde{s}\rangle|^2(\varepsilon-E_{\tilde{s}})}{(\varepsilon-E_{\tilde{s}})^2+\frac{\Delta^2}{4}} = \int dE_{\tilde{s}}\rho_{\tilde{s}}\frac{|\langle k_0|V|\tilde{s}\rangle|^2(\varepsilon-E_{\tilde{s}})}{(\varepsilon-E_{\tilde{s}})^2+\frac{\Delta^2}{4}}, \quad (52)$$

$$\langle\Gamma_{k_0}(\varepsilon)\rangle = \sum_{\tilde{s}}\frac{|\langle k_0|V|\tilde{s}\rangle|^2\Delta}{(\varepsilon-E_{\tilde{s}})^2+\frac{\Delta^2}{4}} = \int dE_{\tilde{s}}\rho_{\tilde{s}}\frac{|\langle k_0|V|\tilde{s}\rangle|^2\Delta}{(\varepsilon-E_{\tilde{s}})^2+\frac{\Delta^2}{4}}. \quad (53)$$

In formulas (52) and (53), we went over from summation over states $\tilde{s}$ to integration by using the density $\rho_{\tilde{s}}$ of these states. From formulas (47) for the zeroth and the first moment of the distribution in (51) and from (45), it follows that, in the region where the function $\langle S_{k_0}(\varepsilon)\rangle$ is nonzero, the changes in the quantities $\langle\Delta_{k_0}(\varepsilon)\rangle$ and $\langle\Gamma_{k_0}(\varepsilon)\rangle$ are correlated and that their values averaged over this region are equal to zero and Γ_{k_0}, respectively. Further, we choose the averaging interval Δ_0 in such a way as to ensure fulfillment of the following relations to a high precision:

$$\langle\Delta_{k_0}(\varepsilon)\rangle = 0, \quad (54)$$

$$\langle\Gamma_{k_0}(\varepsilon)\rangle = \Gamma_{k_0}. \quad (55)$$

In this case, the expression for the averaged strength function is simplified significantly to become

$$\langle S_{k_0}(\varepsilon)\rangle = \frac{\Gamma_{k_0}+\Delta_0}{2\pi\left[\left(\varepsilon-\varepsilon_{k_0}-\langle k_0|V|k_0\rangle\right)^2+\frac{\left(\Gamma_{k_0}+\Delta_0\right)^2}{4}\right]}. \quad (56)$$

This regime of averaging—it results in the vanishing of all quantities that oscillate on the interval of averaging

(Δ_0)—is referred to as a global regime of averaging [11]. Experience gained in solving specific problems of quantum mechanics and nuclear physics (see, for example, [13, 14]) reveals that the width Δ_0 of the interval of averaging depends on the form of the potential $V(x)$ and on the energy and the structure of the state k_0. At sufficiently high excitation energies of the state k_0, however, Δ_0 proves to be much less than the width Γ_{k_0}, so that it can be disregarded in (56).

6. STRENGTH FUNCTION AND QUANTUM CHAOS

The conditions under which quantum chaos arises in stationary quantum systems were investigated in [6–8]. A stationary system that is described by a Hamiltonian $H_0(x)$ has a regular character [8] if the number of the coordinates x of the system coincides with the number of operators of basic integrals of the motion of the system in involution. For the emergence of quantum chaos in the system [8], it is necessary (but not sufficient) that the Hamiltonian $H_0(x)$ be supplemented with a perturbing potential $V(x)$ that violates symmetries associated with one or several basic integrals of the motion and which removes the degeneracy of states $|k\rangle$ of the unperturbed Hamiltonian. Quantum chaos arises in the system if the coefficients C_s^k in the expansion of the ensemble of the wave functions $\Psi_s(x) \equiv |s\rangle$ of the total Hamiltonian $H(x)$ of the system in the unperturbed states $|k\rangle$ become random numbers described by an equiprobable Wigner distribution [13].

From the viewpoint of the strength function $S_k(\varepsilon)$ (28) and its averaged representation $\langle S_k(\varepsilon)\rangle$ (56), quantum chaos is equivalent to equiprobability in the distribution of the coefficients C_s^k. For an ensemble of excited states $\Psi_s(x)$ with a sufficiently high density, this regime is realized [8] under the condition $\Gamma_k \geq D_k$, where D_k is the mean spacing between the neighboring states k for the unperturbed Hamiltonian $H_0(x)$. A similar criterion as implemented with an approximate representation for strength functions was used in [6–8], where it was shown that the conditions for the emergence of quantum chaos in some mechanical systems coincide with the conditions under which classical types of chaotic motion arise in these systems when they are described within classical mechanics.

7. CONCLUSION

The above investigation has made it possible to establish some important integral properties of the coefficients C_k^s that describe a transition from one orthonormalized basis of the wave functions of a stationary quantum system to another. These properties are very useful for testing accuracies in perturbative calculations and in approaches relying on expansions of exact wave functions of the system in the functions of the unperturbed system. Of particular importance are these properties for the vigorously developing line of investigations that address the problem of conditions under which chaos emerges in quantum systems.

ACKNOWLEDGMENTS

This work was supported in part by the Foundation "Russian Universities: Basic Research."

REFERENCES

1. L. D. Landau and E. M. Lifshitz, *Quantum Mechanics: Non-Relativistic Theory* (Pergamon, Oxford, 1977; 4th ed., Nauka, Moscow, 1989).
2. M. L. Goldberger and K. M. Watson, *Collision Theory* (Wiley, New York, 1964; Mir, Moscow, 1967).
3. A. A. Abrikosov, L. P. Gor'kov, and I. E. Dzyaloshinskiĭ, *Methods of Quantum Field Theory in Statistical Physics* (Fizmatgiz, Moscow, 1962; Prentice-Hall, Englewood Cliffs, 1963).
4. L. D. Landau, Zh. Éksp. Teor. Fiz. **32**, 59 (1957) [Sov. Phys. JETP **5**, 101 (1957)].
5. A. B. Migdal, *Theory of Finite Fermi Systems and Applications to Atomic Nuclei*, transl. of the 1st Russ. ed. (Interscience, New York, 1967; 2nd ed., Nauka, Moscow, 1982).
6. V. E. Bunakov, I. B. Ivanov, and R. B. Panin, Preprint No. 2255, PNPI (Petersburg Nuclear Physics Institute, St. Petersburg, 1998).
7. V. E. Bunakov, F. F. Valiev, and Yu. M. Tchuvilski, Phys. Lett. B **243**, 288 (1998).
8. V. E. Bunakov, in *Lecture Notes of XXX PNPI Winter School, St. Petersburg*, 1966, p. 135.
9. S. G. Kadmensky and P. A. Luk'yanovich, Yad. Fiz. **49**, 1285 (1989) [Sov. J. Nucl. Phys. **49**, 800 (1989)]; **51**, 650 (1990) [**51**, 411 (1990)].
10. S. G. Kadmensky, Fiz. Élem. Chastits At. Yadra **28**, 391 (1997) [Phys. Part. Nuclei **28**, 159 (1997)].
11. S. G. Kadmensky, Yad. Fiz. **62**, 236 (1999) [Phys. At. Nucl. **62**, 201 (1999)].
12. H. Feshbach, Ann. Phys. (N.Y.) **5**, 357 (1958).
13. A. Bohr and B. R. Mottelson, *Nuclear Structure*, Vols. 1, 2 (Benjamin, New York, 1969, 1975; Mir, Moscow, 1971, 1977).
14. M. Ya. Amus'ya and A. S. Kheĭfets, Zh. Éksp. Teor. Fiz. **86**, 1217 (1984) [Sov. Phys. JETP **59**, 710 (1984)].

Translated by A. Isaakyan

Physics of Atomic Nuclei, Vol. 63, No. 5, 2000, pp. 820–823. Translated from Yadernaya Fizika, Vol. 63, No. 5, 2000, pp. 890–893.

ELEMENTARY PARTICLES AND FIELDS
Experiment

New Method for Measurement of a *T*-Violating Muon Polarization in K^+ Decays*

Yu. G. Kudenko and A. N. Khotjantsev**

Institute for Nuclear Research, Russian Academy of Sciences, pr. Shestidesyatiletiya Oktyabrya 7a, Moscow, 117312 Russia

Received March 23, 1999

Abstract—A new method is proposed for measuring a *T*-violating muon polarization in the decays $K^+ \longrightarrow \pi^0\mu^+\nu$ and $K^+ \longrightarrow \mu^+\nu\gamma$. The method is based on a complete reconstruction of kinematics in these decays by using a high-resolution π^0 detector, an active muon polarimeter, and a nearly 4π efficient photon veto system. A high acceptance of the detector allows one to reach a statistical sensitivity to the *T*-violating muon polarization of less than 10^{-4} in an experiment with stopped K^+ mesons. © *2000 MAIK "Nauka/Interperiodica".*

1. INTRODUCTION

One of the few observables that have good prospects for detecting *CP* violation beyond the Standard Model (SM) is the transverse muon polarization (P_T) in the decays $K^+ \longrightarrow \pi^0\mu^+\nu$ ($K_{\mu 3}$) and $K^+ \longrightarrow \mu^+\nu\gamma$ ($K_{\mu 2\gamma}$). It vanishes in the SM, but it is particularly sensitive to scalar or pseudoscalar interactions in the case of $K_{\mu 3}$ decay [1, 2]. The decay $K^+ \longrightarrow \mu^+\nu\gamma$ can have even more sources (effective pseudoscalar, vector, and axial-vector four-fermion interactions [3]) that might give rise to P_T. The transverse muon polarization can easily reach a level of 10^{-3} in the three-Higgs-doublet model and in the leptoquark model without conflicting with existing experimental constraints [4]. Measurement of a nonzero transverse muon polarization in these decays would be a clear indication of physics beyond the SM and provide some insights into the origin of *CP* violation. The contribution to the transverse muon polarization from electromagnetic final-state interaction (FSI) is on the order of 10^{-6}; that is, it is negligible in the case of $K_{\mu 3}$ decay [5]. The FSI contribution to the polarization could be as large as 10^{-3} for $K^+ \longrightarrow \mu^+\nu\gamma$ [6], but it can be reliably calculated [7].

The on-going E246 experiment at KEK [8] is designed for P_T measurements at a level of about 10^{-3} in the $K_{\mu 3}$ decay of stopped K^+. In this experiment, the kinematics of the $K_{\mu 3}$ decay is reconstructed by using the muon momentum measured in a toroidal magnet and a π^0 measurement provided by a CsI calorimeter. A suppression of instrumental systematic effects is attained through the azimuthal symmetry of the apparatus and by taking a double ratio between events with forward- and backward-going π^0 mesons relative to the direction of the kaon beam. An important feature of this technique is that the detector systematics is, to the first order, independent of the characteristics of the kaon beam. The major limitation of the experiment is the low detector acceptance to $K_{\mu 3}$ events [about $(0.7–0.8) \times 10^{-5}$ per incident kaon]. The sensitivity of the E246 experiment is basically limited by this factor.

The new experiment E923, which is planned at BNL [9], uses in-flight K^+ decays. A cylindrical active polarimeter around the kaon beam and an electromagnetic calorimeter will be used to reconstruct $K_{\mu 3}$ decays and suppress background. The detector acceptance to $K_{\mu 3}$ events is about $(2.5–2.7) \times 10^{-5}$ per 2-GeV/c kaons. The advantage of the in-flight experiment is thus the relatively high detector acceptance, but systematics associated with the kaon beam can be a major problem of the method compared to the stopped-kaon approach. Moreover, the common problem for the two experiments is that they cannot measure P_T in the decay $K^+ \longrightarrow \mu^+\nu\gamma$ with a high sensitivity because of an inefficient rejection of the background from the decays $K^+ \longrightarrow \pi^0\mu^+\nu$, $K^+ \longrightarrow \pi^0\pi^+$, and $K^+ \longrightarrow \pi^+\pi^0\pi^0$.

2. DESCRIPTION OF THE METHOD

A new method of measurement of a *T*-odd polarization in the decays $K^+ \longrightarrow \pi^0\mu^+\nu$ and $K^+ \longrightarrow \mu^+\nu\gamma$ is discussed below. The basic principles can be briefly formulated as follows: (i) a high-resolution measurement of π^0 from the $K_{\mu 3}$ decay of stopped K^+; (ii) an active muon polarimeter, which also provides the muon momentum measurement, and photon detection; and (iii) a highly efficient photon veto covering nearly a full solid angle.

The energy of the neutral pion can be defined as

$$E_{\pi^0}^2 = \frac{2m_{\pi^0}^2}{(1-\cos\eta)(1-X^2)},$$

* This article was submitted by the authors in English.

** e-mail: kudenko@wocup.inr.troitsk.ru

1063-7788/00/6305-0820$20.00

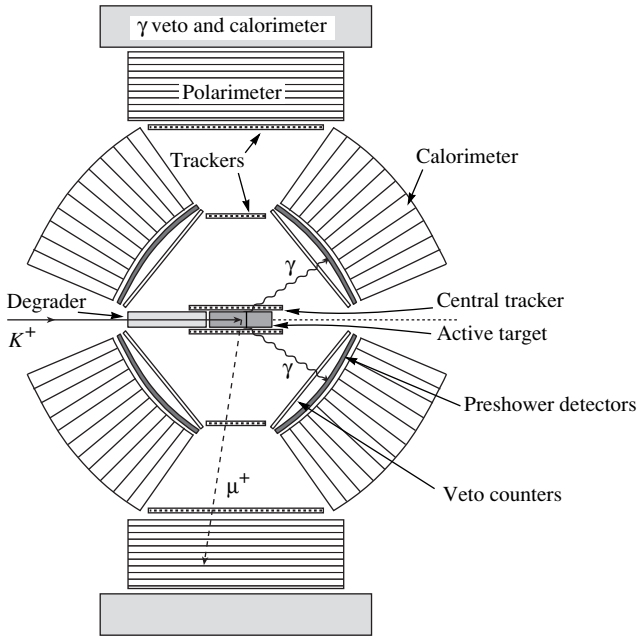

Fig. 1. Schematic side view of the detector.

where η is the opening angle between the momenta of the two photons from the decay $\pi^0 \longrightarrow \gamma\gamma$, while E_1 and E_2 are the laboratory photon energies, which yield the ratio $X = \dfrac{E_1 - E_2}{E_1 + E_2}$. If the photon energies are nearly equal, X^2 is small, and an accurate measurement of η provides a high energy resolution for π^0. The contribution to the pion energy resolution from the uncertainty in the reconstruction of η (σ_η) is given by

$$\Delta E^{\eta}_{\pi^0}(\text{r.m.s.}) = \frac{m_{\pi^0}}{2}\gamma^2\beta\sigma_\eta,$$

where $\beta = p/E$ and $\gamma = E/m_{\pi^0}$. In the case of $E_1 \approx E_2$ [10], the π^0 energy resolution due to the uncertainty in the photon energies (σ_{E_γ}) is

$$\Delta E^{\gamma}_{\pi^0}(\text{r.m.s.}) = \sqrt{3}\frac{\sigma^2_{E_\gamma}}{E_{\pi^0}}.$$

Assuming that the above-mentioned quantities are independent and that the parameters of a photon detector are $\sigma_\eta \sim 5$ mrad and $\sigma_{E_\gamma} \sim 0.015/\sqrt{E(\text{GeV})}$, we can find that σ_p/p is 1 to 2% ($|X| \le \beta$) for pions from $K_{\pi 2}$ decay. Such a momentum resolution for π^0 is expected to provide a narrow peak for $K_{\pi 2}$ decay, which can be rejected to give a good selection of the $K_{\mu 3}$ mode.

Figure 1 shows a schematic view of the proposed setup. The kaon beam is stopped in the scintillating fiber target. The π^0 mesons from $K_{\mu 3}$ decays at rest are detected by both the preshower detector and the photon

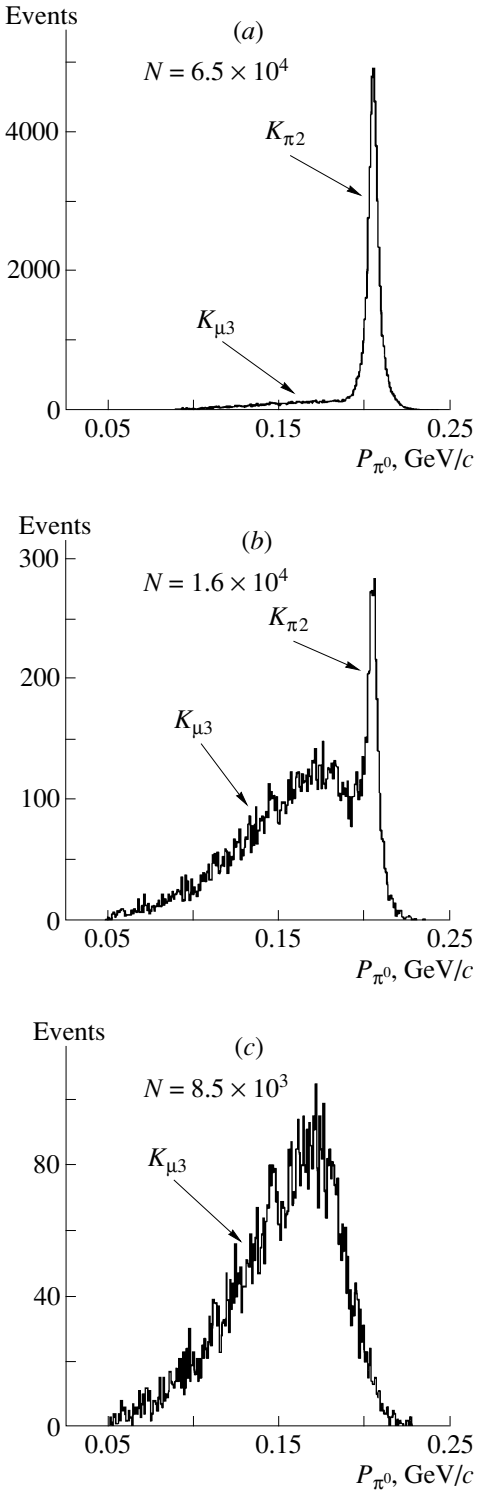

Fig. 2. Reconstructed π^0 momentum spectra for events which pass the requirements that $|X| \le \beta$ and that μ^+ stops in the polarimeter; only $K_{\mu 3}$ and $K_{\pi 2}$ modes are shown: (*a*) total spectrum (intensities of the modes are proportional to their branching ratios), (*b*) events with the opening angle between charged and neutral particles less than 175° are accepted, and (*c*) only events with forward- and backward-going pions and opening angle ≤175° are accepted.

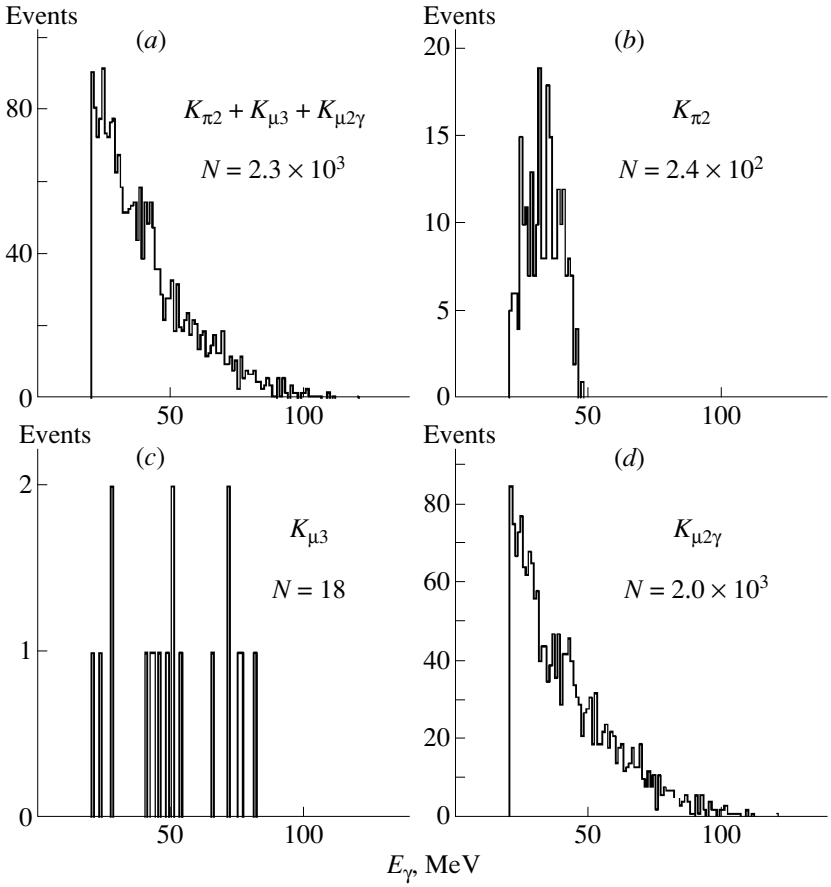

Fig. 3. Monte Carlo simulation of the energy spectra of photons for 10^6 K^+ decays at rest; events in which only one photon is detected in the calorimeter and which passed the cuts $E_\mu \geq 200$ MeV and $20 \leq E_\gamma \leq 200$ MeV and have the opening angle of $\leq 100°$ between photon and muon momenta are accepted. Intensities of the modes are proportional to their branching ratios. Shown in the figure are (*a*) the total spectrum, (*b*) $K_{\pi 2}$ events, (*c*) $K_{\mu 3}$ events, and (*d*) $K_{\mu 2\gamma}$ events.

calorimeter providing a separate measurement of the photon-momentum direction and the photon energy. The momentum of the muon is determined through its range in the segmented active polarimeter (Al plates + MWPCs + plastic counters). The polarization of stopped muons is measured by detecting the positron from the decay $\mu^+ \longrightarrow e^+\nu\bar{\nu}$, which is emitted preferentially in the muon-spin direction. The polarimeter, which also serves as a photon veto detector, is surrounded by an additional photon veto system. Charged-particle tracking is provided by fiber trackers and wire chambers. The *T*-violating muon polarization is defined by $\mathbf{s}_\mu \cdot (\mathbf{p}_{\pi^0} \times \mathbf{p}_\mu)$, where $\mathbf{p}_{\pi^0}$ and $\mathbf{p}_\mu$ are the momentum vectors of the π^0 and μ^+ mesons, respectively, and $\mathbf{s}_\mu$ is the muon spin. The transverse muon polarization P_T is directed in a screw sense around the beam axis and will generate an asymmetry $A = \dfrac{N_{cw} - N_{ccw}}{N_{cw} + N_{ccw}}$ in the counting rate between clockwise (cw) and counterclockwise (ccw) emitted positrons. The sign of P_T in forward-going π^0 events is opposite to that in backward-going π^0 events. This allows us to take a double ratio between these two types of events, which is of importance for reducing of systematic errors.

The results of Monte Carlo simulations of $K_{\mu 3}$, $K_{\pi 2}$, and $K_{\mu 2\gamma}$ modes of 10^6 K^+ decays at rest using the GEANT3.21 code with the detector parameters $\sigma_\eta \sim$ 5 mrad and $\sigma_{E_\gamma} \sim 1.5\%$ at 1 GeV are shown in Figs. 2 and 3. Figure 2*a* shows the momentum spectrum of π^0 mesons for $K_{\mu 3}$ and $K_{\pi 2}$ events. The numbers of events simulated for these modes are proportional to their branching ratios, and no cuts were applied. The separation of $K_{\mu 3}$ events from those of $K_{\pi 2}$ is achieved by requiring that the angle between the momenta of the charged and neutral particle be less than 175°, as is seen in Fig. 2*b*. An additional cut on the π^0 direction (selection of $K_{\mu 3}$ events with forward- and backward-going pions, $\theta \leq 70°$ and $\geq 100°$, respectively) completely eliminates the $K_{\pi 2}$ mode, as is shown in Fig. 3*c*. It should be noted that muons from the in-flight π^+ decays of the $K_{\pi 2}$ mode, accepted as muons from $K_{\mu 3}$ decays in the case of charged-particle momentum measurement,

will be completely removed from the accepted $K_{\mu 3}$ events after the requirement that the neutral-pion momentum be less than 190 MeV/c. After applying these cuts, $K_{\mu 3}$ events are virtually free from the background due to other K^+-decay modes. The $K_{\pi 3}$ background is removed by using an efficient photon veto.

The apparatus in question is also able to measure the transverse muon polarization in the decay $K^+ \longrightarrow \mu^+\nu\gamma$. The background events for this decay appear from the $K_{\mu 3}$ and $K_{\pi 2}$ modes when one photon is missed. To suppress these events, an additional photon veto detector consisting of alternating layers of lead and plastic can be installed to detect photons traversing the polarimeter. In the Monte Carlo simulations, an average photon-detection inefficiency of the veto detector in the energy range 10–250 MeV was assumed to be 2%, which is even larger than that of the E787 experiment at BNL [11]. The photon spectra detected by the photon detector after applying the cuts $E_\mu \geq 200$ MeV and $20 \leq E_\gamma \leq 200$ MeV and the requirement that the opening angle between the photon and muon momenta not exceed 100° are shown in Fig. 3. The signal-to-background ratio of about 8 is obtained; i.e., the physical background from copious $K_{\mu 3}$ and $K_{\pi 2}$ decays is suppressed by a factor of about 10^2–10^3. The main contribution to the background comes from the $K_{\pi 2}$ mode, which cannot produce a spurious P_T and only dilutes the detector sensitivity to polarization in the decay $K^+ \longrightarrow \mu^+\nu\gamma$. The E_γ threshold of 50 MeV eliminates $K_{\pi 2}$ events, and we have very clear $K_{\mu 2\gamma}$ events in the region 50–200 MeV, but at the expense of the detector acceptance. The background from $K_{\mu 3}$ events is found to be at very safe level of less than 1%, as is seen from Fig. 3*c*.

3. SENSITIVITY

The detector acceptance to $K_{\mu 3}$ events obtained from a Monte Carlo simulation is about 1.9%. This includes the muon stopping efficiency in the polarimeter of 0.85–90, the photon conversion and reconstruction efficiency of about 0.3, and the efficiency of positron detection of 0.75–0.80. Since the branching ratio for the $K_{\mu 3}$ decay is 3.18% and since the kaon-stopping efficiency is obtained to be about 0.3 for a 800-MeV/c kaon momentum, the total detector acceptance ϵ per incident K^+ is about 2.0×10^{-4}; i.e., it is greater than the acceptance of the KEK E246 and BNL E923 detectors by a factor of 20 and 6, respectively. The statistical sensitivity to P_T that can be obtained in this experiment is given by

$$\delta P_T = \frac{1}{Af\sqrt{\epsilon N_{K^+}}},$$

where the detector analyzing power A is 0.2 and the attenuation factor f is 0.70. For a kaon intensity of 10^7 K^+/s, which can be available in the BNL low-energy separated beam, for example, and a running time of 10^7 s, we obtain $\delta P_T \sim 5.5 \times 10^{-5}$. For the decay $K^+ \longrightarrow \mu^+\nu\gamma$, a similar estimation gives $\delta P_T \sim 0.9 \times 10^{-4}$.

Owing to simple detector geometry, which provides good azimuthal symmetry, and to the use of an active muon polarimeter, it also seems possible, within this method, to suppress systematic errors below a level of 10^{-4}. In addition, such an efficient tool as the double ratio between forward- and backward-going pions will be applied to reduce systematics further.

4. CONCLUSION

A new approach to a search for T violation in K^+ decays by using a high-resolution π^0 measurement has been discussed. A high detector acceptance and an efficient veto system allow us to reach a statistical sensitivity to T-violating muon polarization of less than 10^{-4} for either of the decays $K^+ \longrightarrow \pi^0\mu^+\nu$ and $K^+ \longrightarrow \mu^+\nu\gamma$.

ACKNOWLEDGMENTS

This work was supported in part by the Russian Foundation for Basic Research (project no. 96-02-16081).

REFERENCES

1. M. Leurer, Phys. Rev. Lett. **62**, 1967 (1989).
2. P. Castoldi, J. M. Frère, and G. L. Kane, Phys. Rev. D **39**, 2633 (1989).
3. C. Q. Geng and S. K. Lee, Phys. Rev. D **51**, 99 (1995); M. Kobayashi, T. T. Lin, and Y. Okada, Prog. Theor. Phys. **95**, 361 (1996); G. H. Wu and John N. Ng, Phys. Rev. D **55**, 2806 (1997).
4. G. Bélanger and C. Q. Geng, Phys. Rev. D **44**, 2789 (1991).
5. A. R. Zhitnitskiĭ, Yad. Fiz. **31**, 1024 (1980) [Sov. J. Nucl. Phys. **31**, 529 (1980)].
6. G. S. Adkins, Phys. Rev. D **28**, 2885 (1983).
7. V. P. Efrosinin and Yu. G. Kudenko, Yad. Fiz. **62**, 1054 (1999) [Phys. At. Nucl. 62, 987 (1999)]
8. J. Imazato *et al.*, Preprint No. KEK 91-8 (1991).
9. M. Diwan *et al.*, AGS Proposal E923, 1996.
10. H. W. Baer *et al.*, Nucl. Instrum. Methods **180**, 445 (1981).
11. M. S. Atia *et al.*, Nucl. Instrum. Methods Phys. Res. A **321**, 129 (1992).

Physics of Atomic Nuclei, Vol. 63, No. 5, 2000, pp. 824–833. Translated from Yadernaya Fizika, Vol. 63, No. 5, 2000, pp. 894–903.

ELEMENTARY PARTICLES AND FIELDS
Experiment

Polarization in the Quasielastic Scattering of 1-GeV/*c* Protons on Light Nuclei

O. V. Miklukho, N. P. Aleshin, S. L. Belostotski, O. G. Grebenyuk, O. Ya. Fedorov, A. A. Izotov, A. Yu. Kisselev, Yu. G. Naryshkin, V. V. Nelyubin, A. N. Prokofiev, D. A. Prokofiev, Yu. A. Shcheglov, A. V. Shvedchikov, V. V. Vikhrov, A. A. Zhgun, and A. A. Zhdanov

Petersburg Nuclear Physics Institute, Russian Academy of Sciences, Gatchina, 188350 Russia

Received March 24, 1999

Abstract—Polarization measurements in the $A(p, 2p)B$ reactions on ^{6}Li, ^{7}Li, and ^{28}Si nuclei at a proton-beam energy of 1 GeV were performed in a kinematically complete experiment. By using a two-arm magnetic spectrometer, two secondary protons were recorded in coincidence at asymmetric scattering angles of $\theta_1 = 15°–26°$ and $\theta_2 = 58.6°$ for residual-nucleus momenta in the range $K_B = 0–150$ MeV/c. Either arm of the spectrometer was equipped with polarimeters based on proportional chambers. The data coming from this experiment are analyzed within the distorted-wave impulse approximation. It is shown that the polarization of recoil protons formed at angle θ_2 in the interaction featuring a proton from the P shell of the ^{7}Li nucleus can be described under the assumption of an effective intranuclear-proton polarization by using the single-particle shell-model wave function of the nucleus. Our data on the polarizations of the two protons from the reaction $(p, 2p)$ on a ^{28}Si nucleus also suggest the effective polarization of the protons in the D shell of the ^{28}Si nucleus. It is found that, for high recoil-nucleus momenta of $K_B \geq 90$ MeV/c, the effective polarization of the protons in the P shell of the ^{6}Li nucleus—this polarization was discovered in studying the polarization of recoil protons in the reaction $^6\text{Li}(p, 2p)^5\text{He}$—cannot be described within the shell model assuming LS coupling. As might have been expected, the polarization of recoil protons knocked out from the S shells of the ^{6}Li and ^{7}Li nuclei comply well with the predictions obtained in the impulse approximation with allowance for the depolarization effect alone.

1. INTRODUCTION

In studying quasielastic-scattering reactions of the $(p, 2p)$ type on nuclei at intermediate energies [1], a nonzero effective polarization (P_{eff}) can be observed for intranuclear protons occurring in states belonging to shells with nonzero orbital angular momenta. According to [2], the effective polarization is due to spin–orbit interaction and to the absorption of knock-on protons in nuclear matter and is manifested experimentally only under asymmetric kinematical conditions.

Owing to a strong spin dependence of the matrix element for proton–proton scattering, the effective polarization can be measured in experiments with a polarized proton beam [2–4]. The results of such experiments (see [5, 6]) that measured the asymmetry of scattering suggest a sizable polarization of intranuclear nucleons. Data on effective nucleon polarization in ^{16}O and ^{40}Ca nuclei at a proton-beam energy of 200 MeV [6] are in reasonable agreement with the results of the calculations from [2, 4, 6], which relied on the distorted-wave impulse approximation (DWIA) and which employed the single-particle shell model of the nucleus.

Since the emergence of effective polarization is due to a correlation between the spins and orbits of intranuclear nucleons, investigation of this polarization may furnish direct information about the structure of the ground state of the target nucleus or of the residual nucleus. In particular, it was shown in [7] that the polarization P_{eff} is highly sensitive to nucleon–nucleon correlations in a nucleus.

Measurement of secondary-proton polarization in experiments with unpolarized proton beams provides another possibility for discovering P_{eff}. Within the DWIA, which is a good approximation at sufficiently high energies of incident protons, the polarizations of secondary protons (P_1 and P_2) from reactions of the $A(p, 2p)B$ type are related to the relevant effective polarization by the equations

$$P_1 = \frac{P + K_{nn}P_{\text{eff}}}{1 + PP_{\text{eff}}}, \quad (1)$$

$$P_2 = \frac{P + D_{nn}P_{\text{eff}}}{1 + PP_{\text{eff}}}, \quad (2)$$

where P, D_{nn}, and K_{nn} are, respectively, the polarization, the depolarization parameter, and the factor of polarization transfer in elastic proton–proton scattering. The subscript "2" corresponds to the recoil proton. In the pure impulse approximation without distortions (IA), we have $P_{\text{eff}} = 0$ and $P_1 = P_2 = P$.

1063-7788/00/6305-0824$20.00

The objective of the present study was to measure the polarizations of secondary protons from $A(p, 2p)B$ reactions on light nuclei at 1 GeV. We also make an attempt at describing the results of this experiment in terms of the effective polarization on the basis of the single-particle shell model of the nucleus. We have measured primarily the polarization of the recoil protons, P_2, formed in the $(p, 2p)$ reactions involving the protons from the P and S shells of the ^{6}Li [8] and ^{7}Li nuclei. Since the effective polarization of the protons from the S shell must be zero, data on scattering off protons belonging to this shell could be used to estimate depolarization and off-mass-shell effects. In 1998, we obtained the first data on the polarizations of two secondary protons (P_1 and P_2) from the $(p, 2p)$ reactions on ^{6}Li and ^{28}Si nuclei.

2. EXPERIMENTAL PROCEDURE

Polarizations were investigated at asymmetric angles of secondary-proton emission ($\theta_1 = 15$–$26°$, $\theta_2 = 58.6°$) from $A(p, 2p)B$ reactions under the conditions of the coplanar geometry of scattering and of a full reconstruction of reaction kinematics. We have measured the momenta K_1 and K_2 of secondary protons and their scattering angles θ_1 and θ_2. By using the measured values of these kinematical variables and the known value of the proton-beam momentum, K_0, the energy of intranuclear-proton separation, ΔE, and the residual-nucleus momentum $\mathbf{K}_B$ have been calculated for each $(p, 2p)$ event. In the IA, the latter is equal in magnitude to the intranuclear-proton momentum $\mathbf{K}$ prior to interaction ($\mathbf{K}_B = -\mathbf{K}$). In our experiment, the resolution in the recoil-proton momentum was ±12 MeV/c.

The layout of our experimental setup is displayed in Fig. 1. A proton beam extracted from the synchrocyclotron installed at the Petersburg Nuclear Physics Institute (PNPI, Gatchina) was focused on the unpolarized target T1 of a two-arm spectrometer (magnetic spectrometers MAP and LES, low-energy spectrometer). For targets, we used samples made from ^{6}Li, ^{7}Li, ^{28}Si, and polyethylene (CH_2). The beam intensity, which was varied between 5×10^{10} and 1×10^{11} proton/(s cm^2), was monitored by the M1–M3 scintillation telescope. The two-arm spectrometer was used to record, in coincidence, protons from the $(p, 2p)$ reactions and to measure their momenta and emission angles. The recoil-proton polarization P_2 was measured by a polarimeter positioned in the focal plane of the low-energy spectrometer LES. The polarimeter consisted of a carbon analyzer T3 of thickness 72.5 mm and proportional chambers PC5–PC8. In order to measure the polarization P_1 of high-energy protons from the $A(p, 2p)B$ reactions, the MAP spectrometer was also equipped, in 1998, with a polarimeter that consisted of proportional chambers PC1–PC4 and a carbon analyzer T2 170 mm thick. The basic parameters of the two-arm spectrometer [9] are listed in Table 1.

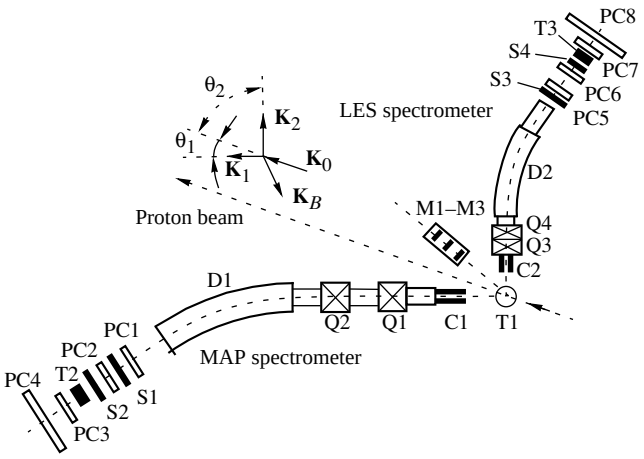

Fig. 1. Layout of the experimental setup: (T1) target of the two-arm spectrometer, (Q1–Q4) quadrupole lenses, (D1, D2) magnetic dipoles, (C1, C2) collimators, (S1–S4 and M1–M3) scintillation counters, (PC1–PC4, T2) proportional chambers and carbon analyzer of the high-energy polarimeter, and (PC5–PC4, T3) proportional chambers and carbon analyzer of the low-energy polarimeter. Presented separately above is the kinematics of $(p, 2p)$ reactions.

The recoil-particle spectrometer (LES) was arranged at a fixed angle of $\theta_2 = 58.6°$. The momentum tuning of the MAP and LES spectrometers was not changed in the course of the experiment either. The two spectrometers were tuned to the kinematics of the $(p, 2p)$ reactions, which is close to the kinematics of elastic proton–proton scattering at angles of $\theta_1 = 21.75$ and $\theta_2 = 58.6°$. Various values of the recoil-nucleus momentum K_B were obtained by changing the angular position (θ_1) of the MAP spectrometer. The experimental conditions were chosen in such a way that, in the regions $\theta_1 < 21.75°$ and $\theta_2 > 21.75°$, the signs of the scalar product ($\mathbf{K}_0 \cdot \mathbf{K}_B$) and, hence, the signs of the effective polarizations of intranuclear protons in the P shell were opposite.

In order to identify correlation events in the $A(p, 2p)B$ reactions and to monitor the level of the background from random coincidences, we measured,

Table 1. Parameters of the magnetic spectrometers used

Spectrometer	LES	MAP
Boundary momentum $(K/Z)^{max}$, GeV/c	1.0	1.7
Radius of the axial trajectory, ρ, m	3.03	5.5
Angle of deflection by a magnet, β, deg	42.2	24.0
Dispersion in the focal plane, D_f, mm/%	16	22
Angular acceptance Ω, sr	4.5×10^{-3}	4.0×10^{-4}
Momentum acceptance ΔK, MeV/c	40	150
Energy resolution (FWHM), MeV	~2.0	~1.5

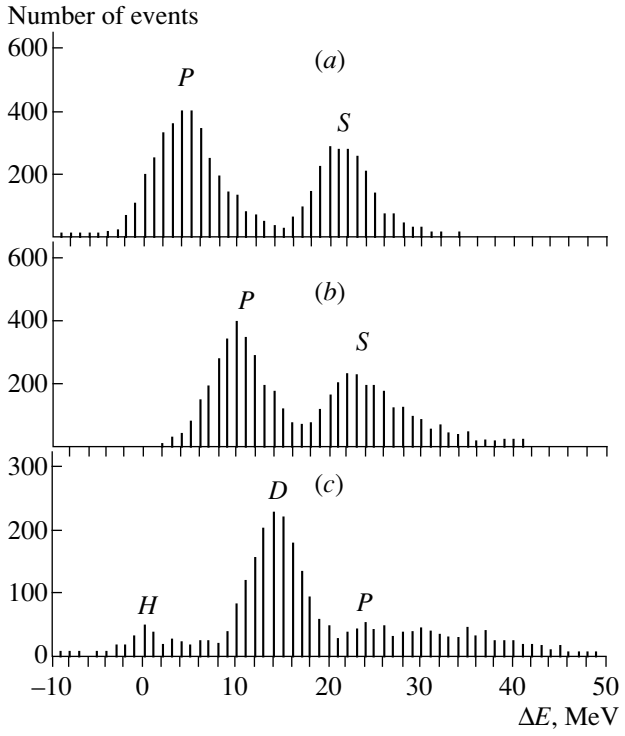

Fig. 2. Spectra of proton-separation energies in the reactions (*a*) ^{6}Li(*p*, 2*p*)^{5}He, (*b*) ^{7}Li(*p*, 2*p*)^{6}He, and (*c*) ^{28}Si(*p*, 2*p*)^{27}Al. Events labeled with the symbol "*H*" are those of elastic proton–proton scattering.

in our experiment, the difference of the proton time of flight from the target T1 to the counter S1 and the analogous time of flight from the target T1 to the counter S4. We recorded events from two neighboring microbunches of the beam, one corresponding to purely background events. In processing our data, we used these events to estimate the polarization of the background and the contribution of the background from the main beam microbunch producing correlation (*p*, 2*p*) events.

In order to determine the polarizations (P_1, P_2) of two secondary protons from the (*p*, 2*p*) reactions, the azimuthal and polar scattering angles ($\phi_{s1,2}$ and $\theta_{s1,2}$, respectively) for the interaction of these protons with the analyzers T2 and T3 were calculated by using the track coordinates in the proportional chambers PC1–PC4 and PC5–PC8.

The polarizations were then determined by the formula

$$P_{1,2} = \frac{\epsilon_{1,2}}{A_{1,2}} = \frac{2\langle \cos\phi_{s1,2}\rangle}{\langle A(\theta_{s1,2}, K_{1,2})\rangle}, \qquad (3)$$

where ϵ_1 and ϵ_2 are the azimuthal asymmetries for proton scattering on the analyzers T2 and T3 (these asymmetries were found by averaging $\cos\phi_{s1,2}$ over sets of events recorded in the operating angular ranges θ_{s1} = 3°–14° and θ_{s2} = 5.5°–16° of the MAP and LES polarimeters, respectively), while A_1 and A_2 are the quantities obtained by averaging the analyzing powers of the carbon analyzers T2 and T3 over the same sets of events. In calculating A_1 and A_2, we invoked data on the analyzing power $A(\theta_{s1,2}, K_{1,2})$ from [10, 11]. In our experiment, the contribution of the random-event background whose effect on the polarization was taken into account (see [9]) did not exceed 15%.

By using the data from Fig. 2, which shows the spectra of proton-separation energies for the (*p*, 2*p*) reactions on ^{6}Li, ^{7}Li, and ^{28}Si nuclei, we were able to assess the resolution of nuclear shells that was achieved in the present experiment.

3. EXPERIMENTAL RESULTS AND THEIR DISCUSSION

For the $A(p, 2p)B$ reactions involving the *P*- and *S*-shell protons of ^{6}Li and ^{7}Li nuclei and for the analogous reactions involving the *D*-shell protons of ^{28}Si nuclei, the results obtained by measuring the polarizations P_2 and P_1 of, respectively, the recoil proton and the scattered proton from these reactions are displayed in Figs. 3, 4, and 6 (see also Tables 2–4), along with the results of the corresponding calculations. Figure 5 shows averaged data on the polarization of the recoil protons from the above reactions featuring the *S*-shell protons of ^{6}Li and ^{7}Li nuclei. In the figures being discussed, the point at θ_1 = 21.75° corresponds to the polarization P_2 of recoil protons in elastic proton–proton scattering; solid curves represent the results of the IA calculations performed under the assumption that the protons of the target nucleus are unpolarized ($P_{\text{eff}} = 0$).

Within the IA, the polarizations P_1 and P_2 in the $A(p, 2p)B$ reactions being considered are both equal to the polarization *P* for off-energy-shell elastic proton–proton scattering. In our calculations, we assumed that $P_{1,2} = P = P(W_{\text{lab}}, \theta_{\text{c.m.}})$, where $P(W_{\text{lab}}, \theta_{\text{c.m.}})$ is the polarization in on-mass-shell elastic proton–proton scattering. Here, W_{lab} is the total collision energy for the interaction of the beam and intranuclear protons in the laboratory frame, while $\theta_{\text{c.m.}}$ is their scattering angle in the c.m. frame. These two quantities were computed by the formulas[1)]

$$W_{\text{lab}} = \frac{s - 4m^2}{2m}, \qquad (4)$$

$$\cos\theta_{\text{c.m.}} = \frac{t - u}{\sqrt{(s - 4m^2)\left[\dfrac{(4m^2 - t - u)^2}{s} - 4m^2\right]}}. \qquad (5)$$

In expressions (4) and (5), *m* is the proton mass, while $s = (k_0 + k)^2$, $t = (k_0 - k_1)^2$, and $u = (k_0 - k_2)^2$ are the Mandelstam variables, k_0, k_1, k_2, and *k* being the

[1)]We note that, in contrast to what we have in the case of free proton–proton scattering, $s^2 \neq (4m^2 - t - u)^2$ for off-energy-shell kinematics.

Table 2. Polarizations $P_{1,2}$ of secondary protons (quantities referring to the scattered and the recoil proton are labeled with the subscripts 1 and 2, respectively) from the reaction ^{6}Li(p, $2p$)^{5}He (at 1 GeV) involving the *P*- and the *S*-shell protons of the ^{6}Li nucleus versus the scattered-proton emission angle θ_1, the recoil-proton emission angle θ_2 being fixed at 58.6°

θ_1, deg	K_1, MeV/c	K_2, MeV/c	K_B, MeV/c	P_2	P_1
			P shell		
15.75	1464.39	630.39	146.52	0.2892 ± 0.0635	0.3093 ± 0.1016
17.75	1466.40	629.6	94.78	0.3753 ± 0.0419	0.4107 ± 0.0733
19.75	1466.76	630.58	44.39	0.4200 ± 0.0564	
20.75	1471.21	624.18	12.49	0.3664 ± 0.0626	
22.75	1469.82	626.06	37.02	0.3616 ± 0.0526	
23.75	1467.94	628.47	60.27	0.3456 ± 0.0340	
24.25	1468.68	626.97	74.57	0.3511 ± 0.0807	
25.75	1465.89	629.94	110.01	0.3638 ± 0.0493	
			S shell		
15.75	1444.82	629.40	146.56	0.4047 ± 0.0781	0.3842 ± 0.1372
17.75	1446.98	628.52	95.58	0.2447 ± 0.0497	0.4260 ± 0.0922
19.75	1447.84	628.56	47.28	0.3016 ± 0.0620	
20.75	1452.58	621.74	20.62	0.2087 ± 0.0880	
22.75	1452.69	621.25	45.26	0.2935 ± 0.0860	
23.87	1452.27	621.27	72.44	0.1948 ± 0.0688	
25.75	1446.73	628.21	113.25	0.2432 ± 0.0773	

Table 3. Polarization of the recoil proton formed at angle $\theta_2 = 58.6°$ in the reaction ^{7}Li(p, $2p$)^{6}He (at 1 GeV) involving the *P*- and the *S*-shell protons of the ^{7}Li nucleus versus the scattered-proton emission angle θ_1

θ_1, deg	K_1, MeV/c	K_2, MeV/c	K_B, MeV/c	P_2
		P shell		
15.75	1459.24	629.38	145.56	0.4122 ± 0.0628
17.75	1459.89	630.32	95.52	0.3023 ± 0.0635
19.75	1459.93	631.38	45.90	0.2697 ± 0.0625
20.75	1462.52	627.76	17.40	0.3235 ± 0.0525
22.75	1462.38	627.81	35.92	0.3056 ± 0.0619
23.75	1463.89	625.08	63.80	0.3608 ± 0.0700
25.75	1461.03	628.06	111.96	0.3780 ± 0.0625
		S shell		
15.75	1441.73	628.93	146.53	0.1838 ± 0.0747
17.75	1443.00	628.95	96.85	0.1987 ± 0.0613
19.75	1443.34	629.53	50.16	0.2779 ± 0.0377
20.75	1444.68	627.77	29.48	0.2844 ± 0.0366
22.75	1443.91	628.79	42.50	0.2776 ± 0.0420
23.75	1448.90	620.71	70.93	0.3160 ± 0.0980
25.75	1442.25	629.55	112.73	0.1500 ± 0.0720

4-momenta of, respectively, the beam proton, the scattered proton, the recoil proton, and the intranuclear proton prior to interaction. The proton polarization $P(W_{\rm lab}, \theta_{\rm c.m.})$ was determined on the basis of the partial-wave analysis performed by Arndt *et al.* [12], the energy $W_{\rm lab}$ being calculated by using the beam-proton and intranuclear-proton momenta prior to collision event [13]. Our estimates show that, in the kinematical region being studied, the off-mass-shellness-induced uncertainty in the IA calculation

Table 4. Polarizations $P_{1,2}$ of secondary protons (quantities referring to the scattered and the recoil proton are labeled with the subscripts 1 and 2, respectively) from the reaction ^{28}Si(p, $2p$)^{27}Al (at 1 GeV) involving the D-shell protons of the ^{28}Si nucleus for two values of the scattered-proton emission angle θ_1, the recoil-proton emission angle θ_2 being fixed at 58.6°

θ_1, deg	K_1, MeV/c	K_2, MeV/c	K_B, MeV/c	P_2	P_1
19.75	1456.72	629.36	44.78	0.3838 ± 0.0960	0.4541 ± 0.1028
23.75	1455.81	630.68	59.33	0.2012 ± 0.0971	0.2076 ± 0.1079

of the proton polarization P does not exceed 0.02 [14].

Figures 3–6 show that, in the pure IA, it is impossible to describe data on the polarization P_2 of recoil protons. An unsatisfactory description of data in the case of scattering on the S-shell protons of the ^{6}Li and ^{7}Li nuclei (Figs. 4, 5) cannot be explained in terms of the effective polarization of the S-shell protons since their orbital angular momentum is zero. It is more probable that the discrepancy revealed here is associated with the depolarization of recoil protons because of their rescattering on intranuclear nucleons. It is interesting to note

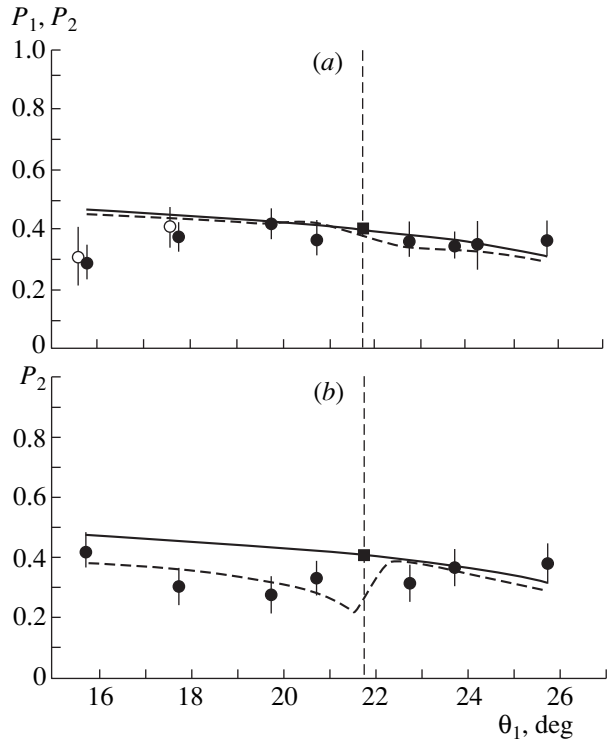

Fig. 3. (*a*) Polarizations (●) P_2 and (○) P_1 of secondary protons (quantities referring to the scattered and the recoil proton are labeled with the subscripts 1 and 2, respectively) from the reaction ^{6}Li(p, $2p$)^{5}He involving the P-shell proton of the ^{6}Li nucleus versus the scattered-proton emission angle θ_1 (the recoil-proton emission angle θ_2 is fixed at 58.6°): (solid curve) results of the calculation in the impulse approximation ($P_1 = P_2$), (dashed curve) recoil-proton polarization P_2 calculated in the distorted-wave impulse approximation on the basis of the shell model assuming LS coupling (with allowance for depolarization corrections), and (closed box) polarization P_2 measured in elastic proton–proton scattering at $\theta_1 = 21.75°$. (*b*) As in Fig. 3*a*, but for the polarization P_2 of recoil protons from the reaction ^{7}Li(p, $2p$)^{6}He. The dashed curve represents the results of the calculations in the distorted-wave impulse approximation on the basis of the shell model assuming jj coupling (with allowance for depolarization corrections).

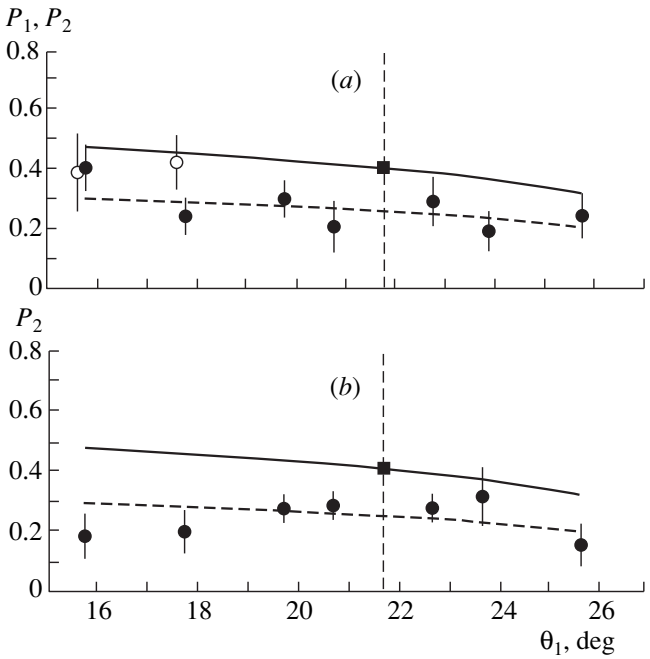

Fig. 4. (*a*) As in Fig. 3*a*, but for the reaction ^{6}Li(p, $2p$)^{5}He involving the S-shell protons of the ^{6}Li nucleus: (solid curve) results of the calculation in the impulse approximation ($P_1 = P_2$), (dashed curve) results of fitting the quantities $(P^i_{2\text{expt}} - P^i_{2\text{IA}})/P^i_{2\text{IA}}$ in terms of the function $f(\theta_1) = \lambda^S_{\text{IA}}$, where λ^S_{IA} is a constant, and (closed box) polarization P_2 measured in elastic proton–proton scattering at $\theta_1 = 21.75°$. (*b*) As in Fig. 4*a*, but for the polarization P_2 of recoil protons from the reaction ^{7}Li(p, $2p$)^{6}He.

that, at recoil-proton energies close to 190 MeV, even single rescatterings at small angles can reduce significantly the polarization of recoil protons. In the approximation of single rescattering, the relative depolarization $\Delta P/P$ can be defined as

$$\frac{\Delta P}{P} = -\frac{L}{L_{\text{free}}}\alpha(1-D), \qquad (6)$$

where L, L_{free}, and α are, respectively, the proton range in a nucleus, the range with respect to elastic scattering, and the probability of elastic proton scattering within the angular acceptance of the spectrometer, while D is the depolarization parameter characterizing the depolarization properties of elastic proton–nucleon scattering. In the case of rescattering in the plane of the $(p, 2p)$ reaction, the depolarization parameter D is virtually coincident with the depolarization parameter D_{nn} in elastic proton–nucleon scattering. All the variables appearing in (6) depend on the proton energy; only the quantity L depends additionally on the geometry of the experiment. The calculations within the DWIA revealed that, for all shells studied here, L is virtually constant in the range of θ_1 values covered in the present experiment. This, together with the fact that the energies of secondary protons were fixed in the present experiment, gives sufficient ground to assume that the relative depolarization $\Delta P/P$ is constant in the kinematical region studied here. From a DWIA calculation of the spin-flip amplitude A_{sf} for a polarized proton moving in a spin–orbit nuclear optical potential [2], we obtained a similar result. This amplitude is related to the relative depolarization by the simple equation $\Delta P/P = 2|A_{\text{sf}}|^2$.

In Figs. 4 and 5, the dashed curves represent the results of fitting $(P^i_{2\text{expt}} - P^i_{2\text{IA}})/P^i_{2\text{IA}}$ values calculated on the basis of data on scattering off the *S*-shell protons of the ^{6}Li and ^{7}Li nuclei to the function $f = \lambda^S_{\text{IA}}$, which is independent of the scattering angle θ_1. The figures show that the experimental dependence of the recoil-proton polarization P_2 on the angle θ_1 complies with the theoretical predictions obtained under the assumption that the relative depolarization $(\Delta P/P)$ is constant in the angular range studied here. The values of λ^S_{IA} for the reactions involving the *S*-shell protons of the ^{6}Li and ^{7}Li nuclei are –0.360 ± 0.062 and –0.384 ± 0.046, respectively.

The data on the polarizations in scattering on the *P*-shell protons of ^{6}Li and ^{7}Li nuclei and on the *D*-shell protons of a ^{28}Si nucleus (Figs. 3 and 6, respectively) cannot be described in terms of the depolarization effect alone. We also took into account the influence of the effective polarization P_{eff} of intranuclear protons on polarization observables by using equations (1) and (2). In these equations, the polarization parameters P, D_{nn}, and K_{nn} for elastic proton–proton scattering were determined on the basis of the partial-wave analysis performed by Arndt *et al.* [12]. For the reaction ^{6}Li$(p, 2p)^5$He involving the *P*-shell proton, the behavior of these parameters as functions of the scattering angle θ_1 is illustrated in Fig. 7. Under the kinematical conditions of the present experiment, the parameters P, D_{nn}, and K_{nn} depend only slightly on the atomic number of the nucleus and on the missing energy in the $A(p, 2p)B$ reactions. The effective polarization P_{eff} was calculated on the basis of the DWIA by using the single-particle shell-model wave functions of the nuclei.

In a specific coplanar geometry of $A(p, 2p)B$ reactions, the effective polarization is orthogonal to the scattering plane and can be calculated by the formu-

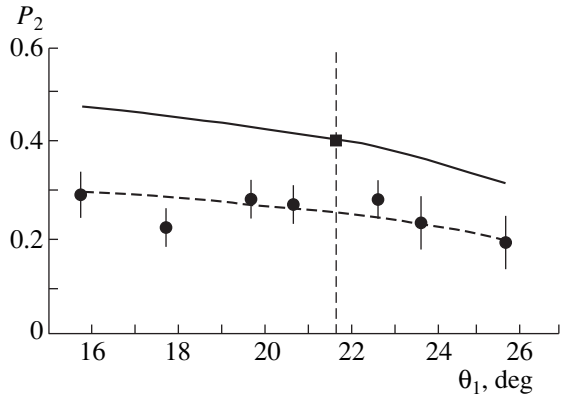

Fig. 5. Recoil-proton polarization P_2 averaged over data on the $(p, 2p)$ reactions involving the *S*-shell protons of the ^{6}Li and ^{7}Li nuclei. The notation is identical to that in Fig. 4.

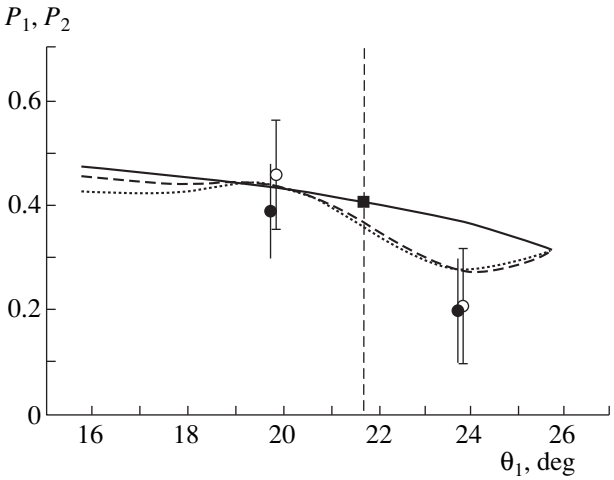

Fig. 6. As in Fig. 3*a*, but for the reaction ^{28}Si$(p, 2p)^{27}$Al involving the *D*-shell protons of the ^{28}Si nucleus: (solid curve) results of the calculation in the impulse approximation ($P_1 = P_2$), (dashed and dotted curve) results of the calculations for, respectively, P_1 and P_2 in the distorted-wave impulse approximation on the basis of the shell model assuming *jj* coupling, and (closed box) polarization P_2 measured in elastic proton–proton scattering at $\theta_1 = 21.75°$.

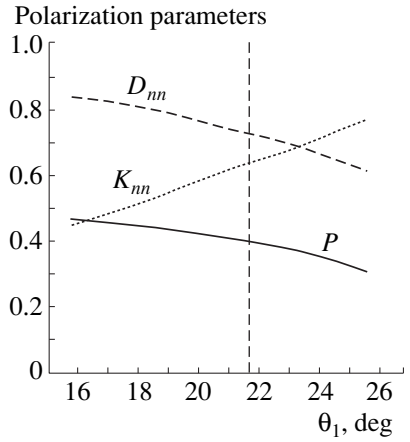

Fig. 7. Polarization parameters P, D_{nn}, and K_{nn} for elastic proton–proton scattering that are calculated for the kinematical region corresponding to the present investigation of the $(p, 2p)$ reaction involving the P-shell proton of the ^{6}Li nucleus.

la [3, 7]

$$P_{\text{eff}} = \frac{\sum_{m_f m_i}\left(\left|g'^{(+)}_{m_f m_i}(\mathbf{k})\right|^2 - \left|g'^{(-)}_{m_f m_i}(\mathbf{k})\right|^2\right)}{\sum_{m_f m_i}\left(\left|g'^{(+)}_{m_f m_i}(\mathbf{k})\right|^2 + \left|g'^{(-)}_{m_f m_i}(\mathbf{k})\right|^2\right)}, \quad (7)$$

where $g'^{(\pm)}_{m_f m_i}(\mathbf{k})$ is the distorted amplitude for the transition from the initial to the final state. This amplitude can be represented as

$$g'^{(\pm)}_{m_f m_i}(\mathbf{k}) = (2\pi)^{-3/2}\int e^{-i\mathbf{k}\cdot\mathbf{r}}\prod_n D_n(\mathbf{r}) \times \langle j_f m_f; B|a^{(\pm)}(\mathbf{r})|j_i m_i; A\rangle d^3\mathbf{r}, \quad (8)$$

where $|j_i m_i; A\rangle$ and $|j_f m_f; B\rangle$ are the nuclear wave functions of, respectively, the initial and the final state characterized by the total angular momentum j_i and its projection m_i for the former and the total angular momentum j_f and its projection m_f for the latter, while $a^{(\pm)}(\mathbf{r})$ are the operators annihilating a nucleon having a radius vector $\mathbf{r}$ and $(\pm)$ spin projections. For all angular momenta, the quantization axis is aligned with the direction of the vector $\mathbf{K}_2 \times \mathbf{K}_1$. The distorting factors $D_n(\mathbf{r})$ $(n = 0, 1, 2)$ that take into account the effect of multiple rescatterings of the primary $(n = 0)$ and secondary $(n = 1, 2)$ protons in the nucleus were computed in the Wentzel–Kramers–Brillouin approximation:

$$D_0(\mathbf{r}) = \exp\left\{-i\frac{E_0}{\hbar^2 c^2 K_0}\int_{-\infty}^{0} U_0(\mathbf{r} + s\hat{k}_0)ds\right\}, \quad (9)$$

$$D_n(\mathbf{r}) = \exp\left\{-i\frac{E_n}{\hbar^2 c^2 K_n}\int_{0}^{\infty} U_n(\mathbf{r} + s\hat{k}_n)ds\right\}. \quad (10)$$

Here, E_0 is the total energy of the beam proton, E_1 and E_2 are the total energies of the secondary protons from the $(p, 2p)$ reaction, and $U_n(\mathbf{r}) = V_n(\mathbf{r}) + iW_n(\mathbf{r})$ $(n = 0, 1, 2)$ are complex optical potentials.

In the shell-model calculations for the ^{6}Li nucleus, we used an oscillator wave function with an oscillator length chosen in such a way as to reproduce the root-mean-square nuclear radius $R_{\text{rms}} = 2.54$ fm measured in an experiment devoted to elastic electron scattering [16]. The same parameter value was used in the calculations for the ^{7}Li nucleus [17]. The radial wave function of the D-wave state of the ^{28}Si nucleus was determined by solving the Schrödinger equation for the square potential well of size $R_\omega = \sqrt{5/3}\,R_{\text{rms}} = 3.92$ fm (in accordance with data obtained by investigating electron scattering [18]) and depth chosen in such a way as to reproduce the energy of proton separation from the D state (13.97 MeV [19]).

It was assumed that, in the ground state of the ^{6}Li nucleus, there are a valence neutron and a valence proton, whose total orbital angular momentum and total spin are equal to zero and unity, respectively. The result of composing them into the nuclear spin is $j_i = 1$ [20]. The $(p, 2p)$ reaction involving the P-shell proton of the ^{6}Li nucleus leads to the formation of the residual nucleus ^{5}He ($j_f = 3/2$), which has one neutron above the filled S shell. In the calculation of the effective polarizations P_{eff} for the reactions ^{7}Li$(p, 2p)^6$He and ^{28}Si$(p, 2p)^{27}$Al, we employed the shell model assuming jj coupling. The total angular momentum of two neutrons in the P shell of the ^{7}Li nucleus was taken to be zero, so that the total spin of the nucleus ($j_i = 3/2$) was determined by the angular momentum of the valence proton, whose knockout led to the formation of a ^{6}He nucleus in the ground state ($j_f = 0$). It was assumed that the spin of the ^{28}Si nucleus ($j_i = 0$) results from the composition of the angular momenta of the $D_{5/2}$ proton and the ^{27}Al core ($j_f = 5/2$) of this nucleus.

The calculations were performed in the inert-core approximation [7]. It was assumed that the position of the center of mass of the system coincides with the position of the center of mass of the residual nucleus and that it does not change in the process of nucleon knockout. This approximation simplifies substantially the calculations, but it leads to the error of about A^{-1} in determining the squares of the overlap integrals (8) (here, A is the atomic number). The error in calculating the effective polarization P_{eff} decreases significantly since P_{eff} depends only on the ratio of the momentum distributions [see equation (7)].

The optical potentials $U_n(\mathbf{r}) = V_n(\mathbf{r}) + iW_n(\mathbf{r})$ $(n = 0, 1, 2)$ in (9) and (10) were assumed to be spin-independent and were taken in the form of square wells [$V_n(\mathbf{r}) = V_n^0$, $W_n(\mathbf{r}) = W_n^0$] of dimensions $R_d = \sqrt{5/3}R_{\text{rms}} = 3.28$ fm for the ^{6}Li and ^{7}Li nuclei and $R_d = 3.92$ fm for the ^{28}Si nucleus. The integration in (8) was performed over the

classical trajectories of the incident proton and over the classical trajectories of the secondary protons under the assumption that neither refraction nor reflection occurs. The potential depths for the recoil protons (V_2^0, W_2^0) that are formed in the (p, $2p$) reactions on ^{6}Li and ^{7}Li nuclei and which have kinetic energies of $T_{K_2} \approx 190$ MeV were determined from the potential volumes used in [3, 21–23]. For the ^{28}Si nucleus, these parameters were calculated on the basis of data on the ^{16}O and ^{40}Ca nuclei [2] by using the equations from [24] that relate V_n^0 to the real part of the amplitude for forward nucleon–nucleon scattering and W_n^0 to the imaginary part of this amplitude. The optical potentials for the protons that originated from the (p, $2p$) reactions at the angle θ_1 with energy $T_{K_1} \approx 800$ MeV and for beam protons were assumed to be pure imaginary quantities. The depths of the potentials W_1^0 and W_0^0 were determined from the optical potentials at the energy of 190 MeV by using the aforementioned relations from [24]. In doing this, the relativistic effect of a finite range of the nucleon–nucleon interaction [25] was partly taken into account. The V_n^0 and W_n^0 values used in our calculations are listed in Table 5.

The calculated effective polarizations are illustrated in Fig. 8. In the calculations for the ^{6}Li and ^{7}Li nuclei, we took into account the finite angular and momentum acceptances of the MAP and LES spectrometers. We have studied the dependence of the effective polarization on the depths of the optical potentials. It turned out that, when the imaginary and real parts of the optical potentials for the recoil protons (W_2^0 and V_2^0, respectively) were varied within reasonable limits, no strong effect arose. The depolarization ratio $\Delta P_{\text{eff}}/P_{\text{eff}}$ for the reaction ^{7}Li(p, $2p$)^{6}He did not exceed 0.1 when W_2^0 or V_2^0 changed by 20%. The dependence of the effective polarization P_{eff} on the high-energy potentials is still weaker. The ratio $\Delta P_{\text{eff}}/P_{\text{eff}}$ is less than 0.1 when W_1^0 and W_0^0 are simultaneously varied within 30%.

The dashed curve in Fig. 3*b* represents the results of the DWIA calculations (allowing for the depolarization effect) of the polarization P_2 of the recoil proton from the reaction ^{7}Li(p, $2p$)^{6}He involving the P-shell proton. We assumed that the deviation of the polarization P^i_{2DWIA} computed by formula (2) from the experimental values P^i_{2expt} is due to the depolarization of recoil protons. The values of the ratio $(P^i_{\text{2expt}} - P^i_{\text{2DWIA}})/P^i_{\text{2DWIA}}$ were fitted to the function $f(\theta_1) = \lambda^P_{\text{DWIA}}$ in accordance with the aforementioned depolarization law ($\Delta P/P$ = const). As a result, we obtained λ^P_{DWIA} values varying between –0.1405 and 0.0602. From the data in Fig. 3*b*, it follows that the assumption of the effective polarization of intranuclear nucleons leads to a satisfactory description of experimental data. This assumption is also supported by the results obtained by studying the (p, $2p$) reaction involving the D-shell protons of the ^{28}Si nucleus (Fig. 6). The calculations within the DWIA reveal that the effective polarization of D-shell protons is close to zero at $\theta_1 = 19.75°$ and reaches a maximum negative value at $\theta_1 = 23.75°$ (Fig. 8). In addition, it is interesting to note that, in the angular range $\theta_1 = 22°$–$25°$, the sign of P_{eff} for the D-shell protons of the ^{28}Si nucleus is opposite to the corresponding sign for the P-shell proton of the ^{7}Li nucleus. We have also measured the polarizations of both secondary protons from the reaction ^{28}Si(p, $2p$)^{27}Al at the aforementioned values of the scattering angle ($\theta_1 = 19.75°$, $23.75°$). The results of

Table 5. Parameters of the optical potentials used in the present calculations

Energy, MeV	^{6}Li, $1P_{3/2}$	^{7}Li, $1P_{3/2}$	^{28}Si, $1D_{5/2}$
T_{K_0}	1000	1000	1000
W_0^0	18.9	21.4	48.6
T_{K_1}	803	798	794
W_1^0	18.2	20.6	46.7
T_{K_2}	191	191	192
W_2^0	6.3	7.5	17.3
V_2^0	6.7	7.8	13.9

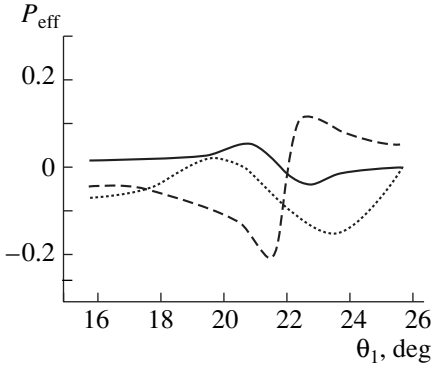

Fig. 8. Effective polarizations P_{eff} of the P-shell protons of (solid curve) the ^{6}Li and (dashed curve) the ^{7}Li nucleus and of (dotted curve) the D-shell protons of the ^{28}Si nuclei as calculated in the distorted-wave impulse approximation by using single-particle shell-model wave functions.

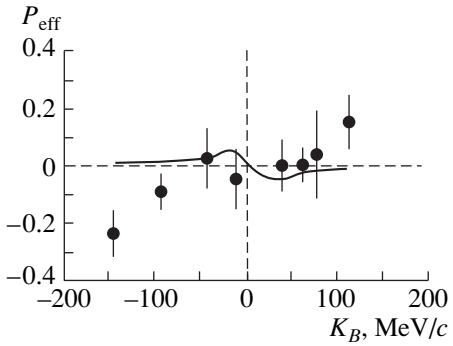

Fig. 9. Effective polarization P_{eff} of the *P*-shell proton of the ^{6}Li nucleus versus the momentum K_B of the residual nucleus [the sign of K_B corresponds to the sign of the scalar product $(\mathbf{K}_0 \cdot \mathbf{K}_B)$]. The solid curve represents the results of the calculation in the distorted-wave impulse approximation on the basis of the shell model assuming *LS* coupling.

these measurements are compatible with the DWIA predictions (Fig. 6).

The results of the DWIA calculations for the polarization P_2 of the recoil protons from the $(p, 2p)$ reaction involving the *P*-shell proton of the ^{6}Li nucleus are displayed in Fig. 3*a* (dashed curve). Corrections for the depolarization were introduced by analogy with what was done for the reaction on the ^{7}Li nucleus. The resulting values of the ratio $(P^i_{2\text{expt}} - P^i_{2\text{DWIA}})/P^i_{2\text{DWIA}}$ were then fitted as above in the angular interval $\theta_1 = 19.75°$–$23.75°$. For the depolarization parameter, this yielded $\lambda^P_{\text{DWIA}} = -0.0413 \pm 0.0620$. It can be seen from the data in Fig. 3*a* that the single-particle shell model that assumes *LS* coupling and which was used in the DWIA calculations of the ^{6}Li nucleus gives no way to describe experimental data over the entire kinematical region studied here. It should be emphasized, however, that this model makes it possible to reproduce closely the magnetic moment of the ^{6}Li nucleus and yields a quadrupole-moment value ($Q_{\text{theor}} = 0$) close to the experimental value [20].

By using expression (2) and the measured values of the recoil-proton polarization P_2 that were corrected for depolarization, the effective polarization P_{eff} of the *P*-shell proton of the ^{6}Li nucleus can be calculated as a function of the recoil-proton momentum K_B. It seems (see Fig. 3*a*) that, in the angular range $19.75° \le \theta_1 \le 23.75°$, the effective polarization P_{eff} is close to zero and that the deviation of the experimental values of the recoil-proton polarization P_2 from the values predicted within the IA is due exclusively to the depolarization effect. In this case, the fitting of the experimental data within the above angular range yields the depolarization parameter λ^P_{IA} ranging between –0.0523 and 0.0612. The P_{eff} values calculated with the depolarization parameter λ^P_{IA} are displayed in Fig. 9. The solid curve in this figure represents the results of the aforementioned DWIA calculations. It can be seen from the figure that, in the region $K_B \ge 90$ MeV/c, the effective polarization P_{eff} computed on the basis of experimental data is finite. That a nonzero effective polarization was observed for the protons in the unfilled shell of the ^{6}Li nucleus is at odds with the assumption that this shell corresponds to a pure $2S$ state [20], since the effective polarization of the *S*-shell protons, which have zero orbital angular momentum, must be equal to zero. It is conceivable that the emergence of a nonzero effective polarization of intranuclear protons at high values of K_B is due to the contribution of the *D*-wave state to the wave function of the ^{6}Li nucleus.

In conclusion, we would like to discuss the possible reasons behind the levels of the depolarizations of the recoil protons knocked out from the *P* and *S* shells of the ^{6}Li and ^{7}Li nuclei—in particular, we recall that, for the ^{7}Li nucleus, the ratio $\lambda^S_{\text{IA}}/\lambda^P_{\text{DWIA}}$ amounts to 2.7. If we assume that the spin-flip amplitude is finite in recoil-nucleon rescattering on all nucleons of the residual nucleus, the depolarization must not depend greatly on the shell from which the knock-on proton originates. There is, however, one argument against the last statement: the point is that the recoil protons that are knocked out from the *S* shell travel a larger distance in nuclear matter than the recoil protons that are knocked out from the *P* shell. Owing to absorption in nuclei, however, $(p, 2p)$ reactions occur primarily in the small region close to the nuclear boundary. For this reason, the difference between the ranges of the protons knocked out from the *P* and *S* shells cannot be as great (according to our estimates, this difference is less than 25%) as that which would account for the large value of the ratio $\lambda^S_{\text{IA}}/\lambda^P_{\text{DWIA}}$. This value is explicable if we assume that the spin of the proton knocked out from the *P* shell cannot be flipped in rescatterings on *S*-wave nucleons because of the Pauli exclusion principle and that its depolarization is determined exclusively by collisions with one (two) *P*-shell neutron(s) of the ^{6}Li (^{7}Li) nucleus. As to the proton knocked out from the *S* shell, its depolarization is determined by the interaction with one *S*-shell proton and with all nucleons in the *P* shell of the residual nucleus. That the polarization of the recoil protons knocked out from the *S* shell is observed to be much less than the value predicted within the IA [see Figs. 4, 5] may also be due, at least partly, to in-medium modifications of the nucleon–nucleon interaction [26–28]. But in this case, we have to assume that, under the conditions of our experiment, the kinematical dependences of effects associated with the in-medium modifications of the nucleon–nucleon interaction are similar to the kinematical dependences of the depolarization effects.

ACKNOWLEDGMENTS

This work was supported in part by the Russian Foundation for Basic Research (project nos. 93-02-17085 and 97-02-17085) and by the program Fundamental Nuclear Physics (grant nos. 1.4 144.03 and 1.2 122.03).

REFERENCES

1. T. Berggren *et al.*, Annu. Rev. Nucl. Sci. **16**, 153 (1966).
2. G. Jacob *et al.*, Nucl. Phys. A **257**, 517 (1976).
3. Th. A. J. Maris, Nucl. Phys. **9**, 577 (1958/59).
4. G. Jacob *et al.*, Phys. Lett. B **45**, 181 (1973).
5. V. S. Nadejdin *et al.*, Preprint No. E1-7559, JINR (Dubna, 1973); Preprint No. E1-10820, JINR (Dubna, 1977).
6. P. Kitching *et al.*, Phys. Rev. Lett. **37**, 1600 (1976); Nucl. Phys. A **340**, 423 (1980).
7. F. Fernández *et al.*, Phys. Lett. B **106**, 15 (1981).
8. O. V. Miklukho *et al.*, in *Proceedings of the International Conference "SPIN-97," Dubna, 1997* (JINR, Dubna, 1997), No. E2-97-413, p. 246.
9. N. P. Aleshin *et al.*, Preprint No. 1971, PINP (Gatchina, 1994).
10. O. Ya. Fedorov, Preprint No. 484, LNPI (Leningrad, 1979).
11. G. Waters *et al.*, Nucl. Instrum. Methods **153**, 401 (1978).
12. R. A. Arndt *et al.*, Phys. Rev. D **28**, 97 (1983).
13. E. F. Redish *et al.*, Phys. Rev. C **2**, 1665 (1970).
14. C. L. Belostotskiĭ *et al.*, Yad. Fiz. **42**, 1427 (1985) [Sov. J. Nucl. Phys. **42**, 904 (1985)].
15. Th. A. J. Maris *et al.*, Nucl. Phys. A **322**, 461 (1979).
16. A. Arima *et al.*, Adv. Nucl. Phys. **5**, 345 (1972).
17. L. R. B. Elton and A. Swift, Nucl. Phys. A **94**, 52 (1967).
18. R. Hofstadter, Annu. Rev. Nucl. Sci. **7**, 231 (1957).
19. A. A. Vorob'ev *et al.*, Yad. Fiz. **57**, 3 (1994) [Phys. At. Nucl. **57**, 1 (1994)].
20. P. E. Nemirovski, in *Nuclear Models* (Compton Printing Works, Kings College, London, 1962), p. 36.
21. A. Johansson and Y. Sakamoto, Nucl. Phys. **42**, 625 (1963).
22. T. Berggren and G. Jacob, Phys. Lett. **1**, 258 (1962).
23. G. R. Satchler and R. M. Maybron, Phys. Lett. **11**, 313 (1964).
24. A. K. Kerman *et al.*, Ann. Phys. (N.Y.) **8**, 551 (1959).
25. T. Berggren and G. Jacob, Nucl. Phys. **47**, 481 (1963).
26. G. Krein *et al.*, Phys. Rev. C **51**, 2646 (1995).
27. T. Noro *et al.*, in *Proceedings of the RCNP International Mini Workshop on Nuclear Medium Effect via Nucleon-Induced Reactions, Kyoto, 1997*, Shiran-kaikan **42** (1), 59 (1997).
28. C. J. Horowitz and D. F. Murdock, Phys. Rev. C **37**, 2032 (1988).

Translated by A. Isaakyan

Physics of Atomic Nuclei, Vol. 63, No. 5, 2000, pp. 834–838. Translated from Yadernaya Fizika, Vol. 63, No. 5, 2000, pp. 904–908.

ELEMENTARY PARTICLES AND FIELDS
Experiment

Multiplicity of Charged Secondaries Emitted in Association with Neutral Strange Particles in Antiproton–Nucleus Collisions at 40 GeV/*c*

K. G. Akhobadze, T. S. Grigalashvili, L. D. Chikovani, E. Sh. Ioramashvili*, L. A. Khizanishvili, E. S. Mailian, M. I. Nikoladze, and L. V. Shalamberidze

Institute of Physics, Academy of Sciences of Georgia, ul. Tamarashvili 6, GE-380077 Tbilisi, Republic of Georgia

Received January 25, 1999; in final form, May 12, 1999

Abstract—In collisions of 40-GeV/*c* antiprotons with D, Li, C, S, Cu, and Pb nuclei, mean multiplicities of various secondary particles are investigated as functions of the mass number *A*. The mass-number dependence of the mean multiplicities of positively charged particles suggests that the effect of intranuclear cascades is strong for the emission of Λ hyperons, but that it is relatively weak for the emission of either K^0 or $\bar{\Lambda}$. Also measured are the yields of various neutral strange particles with respect to those of charged secondaries. © *2000 MAIK "Nauka/Interperiodica".*

1. INTRODUCTION

Investigation of strange-particle production in hadron–nucleus collisions is of importance for obtaining deeper insights into the underlying mechanisms of strong interactions. The point is that, because of the presence of a strange quark, strange particles appear to be a convenient object of experiments aimed at this. In the hadron–hadron and hadron–nucleus interactions induced by nonstrange projectiles, the emission of strange particles signals the formation of an $s\bar{s}$ pair, which subsequently undergoes hadronization to secondaries with open strangeness. The mechanisms governing the formation and hadronization of strange-quark pairs in hadron–nucleus collisions can be revealed by studying the formation of strange particles and, in particular, the characteristics of other particles in the final state.

Any effect due to the quark content of the projectile may be estimated by comparing data on $\pi^- A$, pA, and $\bar{p}A$ collisions. Antiproton–proton collisions at incident momenta of 22.4 and 32 GeV/*c* (see [1] and [2], respectively) lead to larger multiplicities of charged secondaries and of neutral strange particles than proton–proton collisions at comparable energies. Likewise, $\bar{p}A$ collisions at 200 GeV prove to yield more neutral strange particles and more negatively charged secondaries produced in associations with them than pA collisions [3].

In this article, we analyze the multiplicities of charged secondaries originating, along with neutral strange particles, from collisions of 40-GeV/*c* antiprotons with a broad variety of target nuclei *A* (D, Li, C, S, Cu, and Pb). The data subjected to this analysis were collected by using a relativistic ionization streamer chamber (RISC) [4], which is capable of detecting secondaries from hadron–hadron and hadron–nucleus collisions over a full solid angle.

2. EXPERIMENTAL PROCEDURE AND METHOD FOR DATA ANALYSIS

A 5-m streamer chamber placed in a magnetic field of strength $H = 1.5$ kG plays the role of one of the main detectors of the apparatus. The streamer chamber may house a few nuclear targets, whereby different nuclei are irradiated under identical conditions, so that systematic errors are largely eliminated.

A 130-m-long magnetic optical channel (see [5] for details) formed a beam of 40-GeV/*c* negatively charged particles produced by protons on an internal target of the accelerator used. The momentum spread of the beam was 1%. Beam particles were identified by a system of four gas Cherenkov counters that operated in the threshold mode. The π^-, K^-, and antiproton fractions in the unseparated beam amounted to 0.980, 0.017, and 0.003, respectively. This beam successively traversed a few nuclear targets spaced by 30 cm, the thickness of each target being less than 1% of the nuclear-collision range.

The relatively large "memory time" of the streamer chamber, 1 to 2 μs, effectively restricted the number of triggers to 1 to 2 per spill. The sensitive volume of the chamber was scanned by eight optical cameras that had an image-reduction factor of 56 and which formed four stereopairs with opening angles of 17°. The system of electronic triggering, whereby the cameras were activated, fixed the type of a primary (π^-, K^-, or $\bar{p}$) and rejected noninteracted primaries and events character-

* e-mail: etheri@ipnhepi.edu.ge

ized by low momentum transfers [$t \le 0.05$ (GeV/c)^2]. The latter selection eliminated the bulk of elastic collisions and only 3% of inelastic ones. The primary particle was identified at the triggering stage. In further detail, the detector is described in [4–6].

The photographic film was viewed on the BPS-75 table with a magnification of 1 : 4.5 with respect to the live image. Four films were viewed simultaneously. Frames featuring tracks of poor quality, as well as those where there was no auxiliary information, were dropped. The films were viewed two times independently. If the results for some frame proved to be inconsistent, the frame was viewed for the third time. In all, nearly 18000 frames were viewed for events with no less than three charged secondaries, and 7489 inelastic collisions of antiprotons with deuterium, lithium, carbon, sulfur, copper, and lead nuclei were found and measured. For each target-nucleus species, the total number of detected collisions and the corresponding number of events involving detected strange neutral particles are listed in Table 1.

For each detected event, we analyzed here the following quantities: N_{ch}, the multiplicity of all charged secondaries; N^+ and N^-, the multiplicities of, respectively, positive and negative secondaries; N_{sl} and N_F, the multiplicities of, respectively, slow and fast negative secondaries with momenta below and above 500 MeV/c; and N_p, the multiplicity of slow protons with momenta below 500 MeV/c and a visible ionization of $I \ge 2I_0$, where I_0 denotes the ionization induced by a primary particle. The number of fast protons Q_R with momenta above 500 MeV/c was estimated as the difference of the numbers of positive and negative particles,

$$\langle Q_R \rangle = \langle N^+ \rangle - \langle N^- \rangle - \langle N_p \rangle + 1,$$

with the charge of the projectile being taken into account by adding unity on the right-hand side.

Neutral strange particles were detected and identified by characteristic two-body decays (vees) in the fiducial volume of the streamer chamber, and their momenta and emission angles were then reconstructed. Further details of the selection and identification of neutral strange particles can be found in [7], where their yields were measured as functions of the target mass number.

In the present article, we analyze experimental data on the multiplicities of charged secondaries emitted in the antiproton-induced reactions

$$\bar{p}A \longrightarrow X, \quad (1)$$

$$\bar{p}A \longrightarrow K^0(K^0Y, K\bar{K}) + X, \quad (2)$$

$$\bar{p}A \longrightarrow \Lambda(\Sigma^0) + X, \quad (3)$$

$$\bar{p}A \longrightarrow \bar{\Lambda}(\bar{\Sigma}^0) + X. \quad (4)$$

In (2), Y stands for Λ, $\bar{\Lambda}$, Σ^0, or $\Sigma^\pm$, so that K^0 is emitted in association with either a hyperon or another neutral kaon.

Table 1. Total number of events of inelastic collisions for each target-nucleus species and numbers of events with neutral strange particles detected in the final state

A	N_{int}	$N_{K^0_S}$	N_Λ	$N_{\bar{\Lambda}}$
D	1741	35	23	27
Li	1149	36	22	20
C	1053	30	16	16
S	1197	47	36	24
Cu	1346	42	34	14
Pb	1003	29	28	17

The mean multiplicities were corrected for the conversion of photons from the decays of π^0 mesons and Dalitz pairs, as well as for the reinteractions of charged secondaries in the target. Since thin targets were used, these corrections proved to be relatively small. Depending on the target-nucleus species, the total correction to the mean multiplicity ranged between 5% and 12%, the main contribution (about 90%) to this correction being due to photon conversions.

The results of Monte Carlo simulations suggest that nearly 95% of secondary protons with momenta below 180 MeV/c do not leave the target of origin; therefore, they are undetectable. In other words, the multiplicity N_p (see above) actually refers to secondary protons with momenta between 180 and 500 MeV/c.

3. MEAN MULTIPLICITIES OF CHARGED SECONDARIES AS FUNCTIONS OF THE TARGET MASS NUMBER

For each of the reactions in (1)–(4), the measured values of $\langle N_{ch} \rangle$, $\langle N^+ \rangle$, and $\langle N^- \rangle$ are plotted in Fig. 1 as functions of the target mass number A. For the same reactions, the observed A dependences of the mean multiplicities of fast and slow negatively charged particles ($\langle N_f \rangle$ and $\langle N_{sl} \rangle$) are illustrated in Fig. 2, while the analogous dependences for the multiplicities of fast and slow protons ($\langle Q_R \rangle$ and $\langle N_p \rangle$) are displayed in Fig. 3. The solid curves in Figs. 1–3 represent fits of the above multiplicities in terms of the exponential form aA^α. For the best fit, the values of the parameters a and α, as well as the values of χ^2/NDF, are listed in Table 2. We can see that reactions (1) and (3) [(2) and (4)] are characterized by very similar A dependences of each multiplicity considered here, but these dependences for reactions (1) and (3) are basically different from those for reactions (2) and (4). All four reactions show very similar A dependences of the fast negatively charged particles, so that any distinctions between the A dependences for negative particles are due to the contribution of slow negatively charged secondaries.

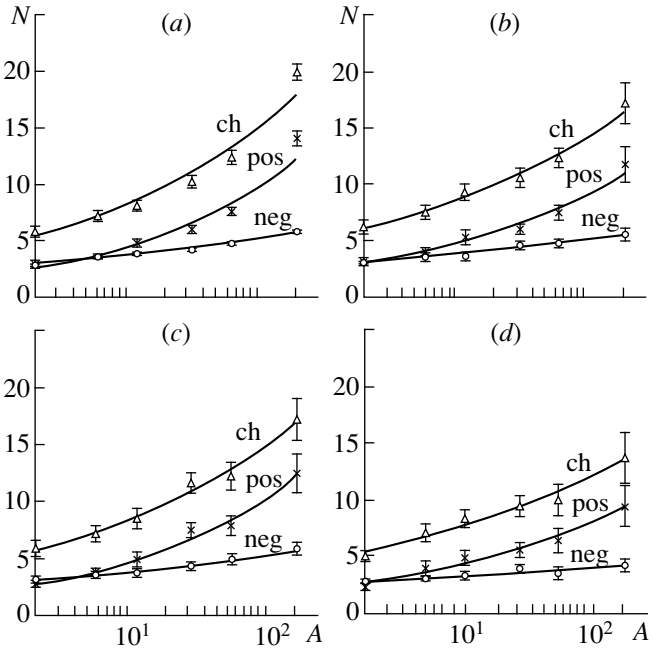

Fig. 1. Mean multiplicities of charged secondaries as functions of the mass number A for the reactions (*a*) $\bar{p}A \longrightarrow X$, (*b*) $\bar{p}A \longrightarrow K^0X$, (*c*) $\bar{p}A \longrightarrow \Lambda X$, and (*d*) $\bar{p}A \longrightarrow \bar{\Lambda}X$. Here and in the figures that follow, solid curves represent fits that are described in the main body of the text.

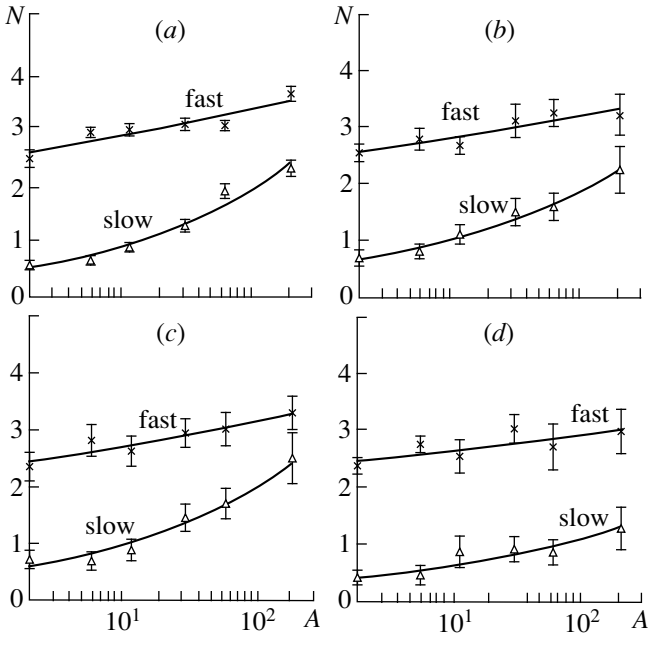

Fig. 2. Mean multiplicities of fast and slow negatively charged secondaries as functions of the mass number A for the reactions (*a*) $\bar{p}A \longrightarrow X$, (*b*) $\bar{p}A \longrightarrow K^0X$, (*c*) $\bar{p}A \longrightarrow \Lambda X$, and (*d*) $\bar{p}A \longrightarrow \bar{\Lambda}X$.

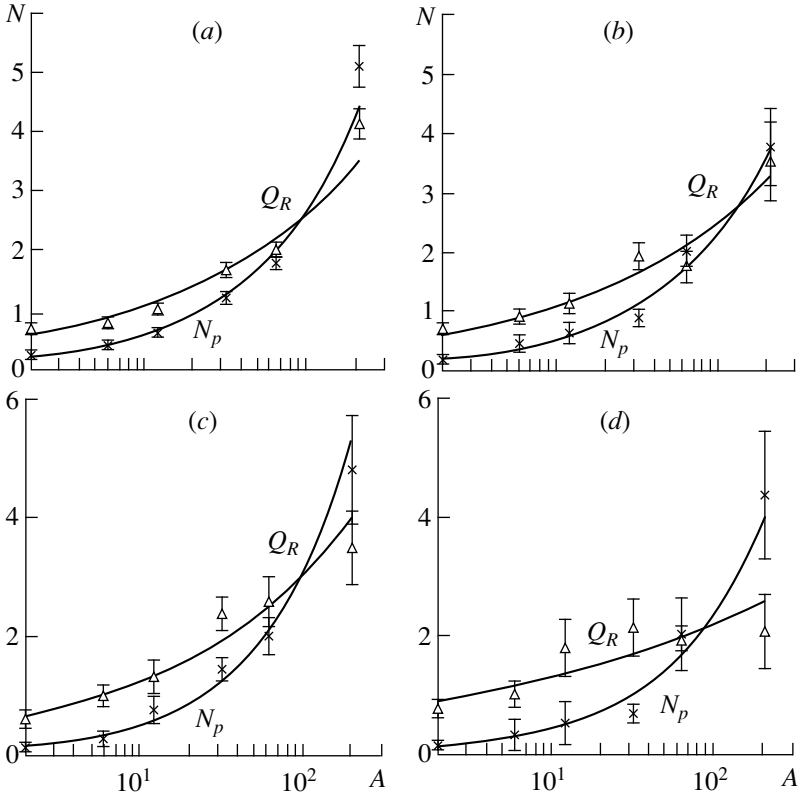

Fig. 3. Mean multiplicities of fast and slow secondary protons as functions of the mass number A for the reactions (*a*) $\bar{p}A \longrightarrow X$, (*b*) $\bar{p}A \longrightarrow K^0X$, (*c*) $\bar{p}A \longrightarrow \Lambda X$, and (*d*) $\bar{p}A \longrightarrow \bar{\Lambda}X$.

4. COMPARISON OF THE YIELDS OF NEUTRAL STRANGE PARTICLES WITH THE YIELDS OF NEGATIVELY CHARGED MESONS AND FAST PROTONS AND THE DEPENDENCES OF THESE YIELDS ON THE TARGET MASS NUMBER

The yields of neutral strange particles in $\bar{p}A$ collisions at 40 GeV/c were measured in [7] for reactions (2)–(4). The A dependences of these yields were fitted to

$$\langle N_K\rangle \sim (0.179 \pm 0.004)A^{(0.155 \pm 0.003)},$$

$$\langle N_\Lambda\rangle \sim (0.054 \pm 0.003)A^{(0.202 \pm 0.007)},$$

$$\langle N_{\bar{\Lambda}}\rangle \sim (0.060 \pm 0.002)A^{(0.074 \pm 0.004)}.$$

In this section, the multiplicities of neutral strange particles relative to that of negatively charged secondaries and to that of fast protons, $\langle N_{V^0}\rangle/\langle N^-\rangle$ and $\langle N_{V^0}\rangle/\langle Q_R\rangle$, are analyzed as functions of the target mass number A. The resulting A dependences of these ratios are illustrated in Fig. 4, where the solid curves represent fits to the data in terms of the exponential form aA^α (the fitted values of a and α are quoted in Table 3, along with the χ^2/NDF values). The ratio $\langle N_{K^0}\rangle/\langle N^-\rangle$ is seen to be virtually independent of A, while the ratio $\langle N_\Lambda\rangle/\langle N^-\rangle$ ($\langle N_{\bar{\Lambda}}\rangle/\langle N^-\rangle$) increases (decreases) with increasing A. At the same time, the yield of each neutral-strange-particle species relative to that of fast protons decreases with increasing A. The falloff with A is the strongest for K^0 emission and the weakest for Λ emission, that for $\bar{\Lambda}$ emission being intermediate between the above two.

5. DISCUSSION OF THE RESULTS AND CONCLUSIONS

The mean multiplicities of various secondaries from reactions (1)–(4) induced by antiproton–nucleus collisions at 40 GeV/c have been analyzed here as functions of the target mass number. For the mechanism of antiproton–nucleus interactions, the implications of this analysis can be summarized as follows.

(i) The resulting A dependences of the mean multiplicities of all charged, all positively charged, and slow negatively charged secondaries suggest that intranuclear cascades contribute to the interactions in question, but reactions (2) and (4) appear to be less affected by intranuclear cascades than reactions (1) and (3).

(ii) In all four reactions considered here—and especially in reactions (2) and (4)—the multiplicity of fast negatively charged secondaries shows but a slow increase with A. This may imply that fast negatively charged secondaries are largely formed outside of the target nucleus.

(iii) By studying the A dependences of the yields of neutral strange particles relative to that of negatively

Table 2. Values of the coefficients a and α in the fits of the mean multiplicities of charged secondaries in terms of the power-law form aA^α and corresponding χ^2 values

Reaction	a	α	χ^2/NDF
	$\langle N_{ch}\rangle$		
$\bar{p}A \longrightarrow X$	4.6 ± 0.3	0.255 ± 0.009	5.1
$\bar{p}A \longrightarrow K^0X$	5.3 ± 0.2	0.212 ± 0.005	0.3
$\bar{p}A \longrightarrow \Lambda X$	4.8 ± 0.2	0.237 ± 0.005	0.3
$\bar{p}A \longrightarrow \bar{\Lambda}X$	4.8 ± 0.3	0.197 ± 0.008	0.5
	$\langle N^+\rangle$		
$\bar{p}A \longrightarrow X$	2.1 ± 0.2	0.33 ± 0.01	5.8
$\bar{p}A \longrightarrow K^0X$	2.5 ± 0.2	0.28 ± 0.01	0.7
$\bar{p}A \longrightarrow \Lambda X$	2.1 ± 0.1	0.32 ± 0.01	0.8
$\bar{p}A \longrightarrow \bar{\Lambda}X$	2.3 ± 0.3	0.27 ± 0.01	1.0
	$\langle N^-\rangle$		
$\bar{p}A \longrightarrow X$	2.72 ± 0.05	0.140 ± 0.002	0.4
$\bar{p}A \longrightarrow K^0X$	2.93 ± 0.08	0.129 ± 0.003	0.3
$\bar{p}A \longrightarrow \Lambda X$	2.7 ± 0.1	0.138 ± 0.004	0.2
$\bar{p}A \longrightarrow \bar{\Lambda}X$	2.6 ± 0.2	0.09 ± 0.01	0.5
	$\langle N_f\rangle$		
$\bar{p}A \longrightarrow X$	2.4 ± 0.1	0.067 ± 0.005	2.3
$\bar{p}A \longrightarrow K^0X$	2.4 ± 0.1	0.057 ± 0.005	0.5
$\bar{p}A \longrightarrow \Lambda X$	2.3 ± 0.1	0.066 ± 0.006	0.4
$\bar{p}A \longrightarrow \bar{\Lambda}X$	2.4 ± 0.1	0.046 ± 0.007	0.8
	$\langle N_{sl}\rangle$		
$\bar{p}A \longrightarrow X$	0.41 ± 0.04	0.33 ± 0.01	2.6
$\bar{p}A \longrightarrow K^0X$	0.55 ± 0.04	0.264 ± 0.008	0.2
$\bar{p}A \longrightarrow \Lambda X$	0.470 ± 0.007	0.31 ± 0.02	0.7
$\bar{p}A \longrightarrow \bar{\Lambda}X$	0.35 ± 0.06	0.25 ± 0.02	0.4
	$\langle Q_R\rangle$		
$\bar{p}A \longrightarrow X$	0.44 ± 0.06	0.39 ± 0.02	4.6
$\bar{p}A \longrightarrow K^0X$	0.52 ± 0.07	0.34 ± 0.02	1.0
$\bar{p}A \longrightarrow \Lambda X$	0.50 ± 0.06	0.39 ± 0.01	0.9
$\bar{p}A \longrightarrow \bar{\Lambda}X$	0.7 ± 0.1	0.23 ± 0.03	0.9
	$\langle N_p\rangle$		
$\bar{p}A \longrightarrow X$	0.13 ± 0.01	0.67 ± 0.01	2.3
$\bar{p}A \longrightarrow K^0X$	0.12 ± 0.02	0.65 ± 0.02	1.1
$\bar{p}A \longrightarrow \Lambda X$	0.08 ± 0.02	0.79 ± 0.06	3.2
$\bar{p}A \longrightarrow \bar{\Lambda}X$	0.08 ± 0.01	0.73 ± 0.05	1.2

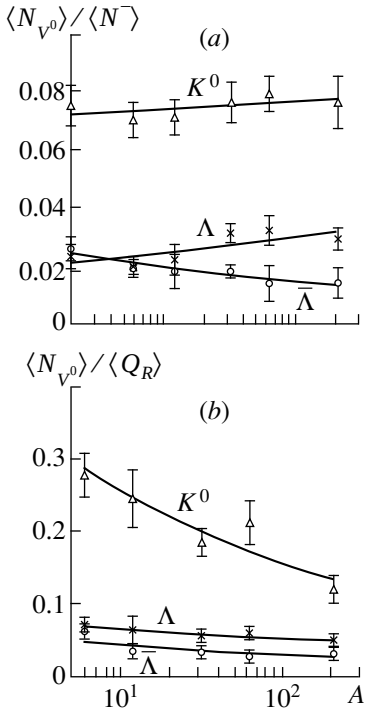

Fig. 4. Ratio of the mean multiplicities of neutral strange particles to that of negative secondaries (*a*), $\langle N_{V^0}\rangle/\langle N^-\rangle$, and to that of fast protons (*b*), $\langle N_{V^0}\rangle/\langle Q_R\rangle$, as functions of the mass number *A*.

charged secondaries and to that of fast protons, $\langle N_{V^0}\rangle/\langle N^-\rangle$ and $\langle N_{V^0}\rangle/\langle Q_R\rangle$, respectively, we found the following:

(a) The ratio $\langle N_{K^0}\rangle/\langle N^-\rangle$ is virtually independent of *A*; the ratio $\langle N_\Lambda\rangle/\langle N^-\rangle$ increases with *A* (this suggests that some slow K^0 mesons are rescattered inside the nucleus, forming Λ hyperons); and the ratio $\langle N_{\bar{\Lambda}}\rangle/\langle N^-\rangle$ decreases with increasing *A* (this is consistent with the conjecture that, because of the relatively high energy threshold for the production of $\bar{\Lambda}$ particles, they are formed predominantly in the primary collision rather than in subsequent reinteractions).

(b) With increasing *A*, the ratios $\langle N_{K^0}\rangle/\langle Q_R\rangle$ and $\langle N_{\bar{\Lambda}}\rangle/\langle Q_R\rangle$ decrease at approximately the same rate (within the errors), while the ratio $\langle N_\Lambda\rangle/\langle Q_R\rangle$ decreases more slowly (since the quantity $\langle Q_R\rangle$ is proportional to the number of collisions suffered by the projectile inside the target nucleus, and the experimental results being discussed suggest that, in contrast to Λ hyperons, which can be produced in any collision event because of the low production threshold, K^0 mesons and $\bar{\Lambda}$ hyperons are largely formed in the primary collision).

After many years of investigations into the physics of $\bar{p}p$ interactions, it was established that, because of annihilation, such interactions yield more secondary mesons than *pp* collisions [8]. In $\bar{p}A$ collisions at 40 GeV/*c*, the fraction of annihilation events increases with the target mass number from 15% for hydrogen to 44% for lead [9]. This effect is consistent with the observed *A* dependences of the ratios $\langle N_{K^0}\rangle/\langle N^-\rangle$ (which is virtually independent of *A*) and $\langle N_{\bar{\Lambda}}\rangle/\langle N^-\rangle$ (which decreases with *A*).

Table 3. Values of the coefficients *a* and α in the fits of the ratios of the mean multiplicity of neutral strange particles to that of negative particles, $\langle N_{V^0}\rangle/\langle N^-\rangle$, and to that of fast protons, $\langle N_{V^0}\rangle/\langle Q_R\rangle$, in terms of the power-law form aA^α and corresponding χ^2 values

Type of ratio	*a*	α	χ^2/NDF
$\langle N_{K^0}\rangle/\langle N^-\rangle$	0.071 ± 0.003	0.015 ± 0.005	0.3
$\langle N_\Lambda\rangle/\langle N^-\rangle$	0.020 ± 0.003	0.090 ± 0.020	1.1
$\langle N_{\bar{\Lambda}}\rangle/\langle N^-\rangle$	0.026 ± 0.002	−0.13 ± 0.01	0.3
$\langle N_{K^0}\rangle/\langle Q_R\rangle$	0.42 ± 0.07	−0.22 ± 0.01	0.9
$\langle N_\Lambda\rangle/\langle Q_R\rangle$	0.082 ± 0.007	−0.09 ± 0.01	0.3
$\langle N_{\bar{\Lambda}}\rangle\langle Q_R\rangle$	0.06 ± 0.02	−0.17 ± 0.03	1.0

ACKNOWLEDGMENTS

We wish to thank our colleagues in the RISC collaboration for their contributions to collecting and processing the data analyzed here.

This work was supported in part by the Academy of Sciences of Georgia (grant no. 2.11).

REFERENCES

1. B. V. Batyunya *et al.*, Yad. Fiz. **39**, 1182 (1984) [Sov. J. Nucl. Phys. **39**, 746 (1984)].
2. M. Yu. Bogolyubskiĭ *et al.*, Yad. Fiz. **46**, 1680 (1987) [Sov. J. Nucl. Phys. **46**, 1002 (1987)].
3. I. Derado *et al.*, Z. Phys. C **50**, 31 (1991).
4. A. Javrishvili *et al.*, Nucl. Instr. Methods **177**, 381 (1980).
5. N. K. Vishnevskiĭ *et al.*, Yad. Fiz. **20**, 694 (1974) [Sov. J. Nucl. Phys. **20**, 400 (1974)].
6. A. V. Bannikov *et al.*, Preprint no. R1-89-119, JINR (Joint Institute for Nuclear Research, Dubna, 1989).
7. T. Grigalashvili *et al.*, Eur. Phys. J. C **10**, 265 (1999).
8. L. N. Smirnova, Yad. Fiz. **47**, 419 (1988) [Sov. J. Nucl. Phys. **47**, 265 (1988)].
9. RISC Collab., Report no. E1-83-449, JINR (Joint Institute for Nuclear Research, Dubna, 1983).

Translated by A. Asratyan

Physics of Atomic Nuclei, Vol. 63, No. 5, 2000, pp. 839–844. Translated from Yadernaya Fizika, Vol. 63, No. 5, 2000, pp. 909–914.

ELEMENTARY PARTICLES AND FIELDS
Experiment

Analyzing the Features of π^- Mesons and Protons from *A*C Interactions at a Momentum of $p = 4.2$ GeV/c per Projectile Nucleon on the Basis of the FRITIOF Model

Ts. Baatar[1)], A. I. Bondarenko[2)], R. A. Bondarenko[2)], B. Ganhuyag, E. N. Kladnitskaya, A. A. Kuznetsov, O. V. Rogachevskiĭ, G. P. Toneeva, and V. V. Uzhinkiĭ

Joint Institute for Nuclear Research, Dubna, Moscow oblast, 141980 Russia

Received March 16, 1999

Abstract—The mean multiplicities of π^- mesons and protons originating from *p*C, *d*C, αC, and CC interactions at a momentum of $p = 4.2$ GeV/c per projectile nucleon and the distributions of these particles in kinematical variables are presented. These experimental distributions are compared with the corresponding predictions obtained on the basis of the FRITIOF model. It is shown that the FRITIOF version used in the present analysis describes satisfactorily our experimental data. *© 2000 MAIK "Nauka/Interperiodica".*

1. INTRODUCTION

In order to reveal the mechanism of hadron–nucleus and nucleus–nucleus interactions, experimental results are frequently compared with predictions based on existing theoretical models like the cascade–evaporation model (CEM), the model of quark–gluon strings (QGS model, also known as QGSM), and the FRITIOF model.

In the energy range 2–5 GeV per projectile nucleon, nucleus–nucleus collisions have been traditionally analyzed on the basis of the CEM. This model qualitatively describes existing experimental data, but there are quantitative discrepancies. In particular, the CEM underestimates the transverse momenta of product pions and overestimates their multiplicity [1–4].

On the whole, a comparison of experimental data on *A*C interactions with QGSM predictions showed satisfactory agreement [5–7]. At the same time, serious discrepancies between experimental data and predictions of this model were revealed in describing the properties of *A*Ta interactions [8]. There is yet another popular model referred to as FRITIOF [9]. This model is extensively used at high energies, but it is commonly believed to fail at intermediate energies since the concept of quantum-string generation and decay becomes inapplicable in this energy region. By taking accurately into account kinematical constraints and by including the Fermi motion of nucleons in a Lorentz invariant way, it becomes possible [10] to reduce the formal limit below which the model ceases to be applicable and to describe satisfactorily, as is shown below, basic features of nucleus–nucleus interactions.

In the present study, experimental data on protons and π^- mesons originating from *A*C interactions are analyzed within a modified version of the FRITIOF model.

2. EXPERIMENTAL DATA

Data used in the present analysis come from the 2-m propane bubble chamber installed at the Laboratory of High Energies at the Joint Institute for Nuclear Research (JINR, Dubna) and irradiated with protons, deuterons, alpha particles, and carbon nuclei accelerated to a momentum of 4.2 GeV/c per projectile nucleon by the JINR synchrophasotron. At present, the eventual statistics of events occurring on propane have been obtained.

In the total ensembles of interactions that light nuclei suffer in the propane chamber, inelastic interactions with carbon nuclei, *p*C, *d*C, αC, and CC, were isolated in [11]. However, the criteria used in [11] separate about 70% of the total number of nucleus–carbon events that was estimated by using known cross sections for *Ap* and *A*C interactions and the proton–carbon ratio in the propane molecule. The remaining interactions were broken down statistically into *Ap* and *A*C events by introducing relevant weights. The weights were determined in such a way that the numbers of events occurring on carbon and hydrogen corresponded to the numbers expected on the basis of the known cross sections for inelastic interactions [12]. The number of secondaries and their distributions were refined by introducing corrections for missed particles that were emitted in the direction close to the direction of the optical axis of the camera (strongly inclined tracks) and for particles whose momenta could not be determined because of a small length of their tracks. In addition, all positively charged particles with momenta in excess of 0.5 GeV/c

[1)] Institute for Physics and Technology, Academy of Sciences of Mongolia, Ulan Bator, Mongolia.
[2)] Institute of Nuclear Physics, Uzbek Academy of Sciences, pos. Ulughbek, UZ-702132, Tashkent, Republic of Uzbekistan.

were assigned weights determining the probability that a given particle is a proton or a π^+ meson (for momenta below 0.5 GeV/*c*, protons and π^+ mesons are reliably identified by ionization along the tracks of these particles).

The details of the procedure for correcting experimental data included in the complete set of nucleus–propane interactions were described in [11]. As in [1, 6, 7, 13, 14], we compared the multiplicities and distributions of π^- mesons and participant protons with the predictions of the modified FRITIOF model. From this comparison, we excluded evaporation protons ($p <$ 0.3 GeV/*c*) and stripping projectile fragments ($p >$ 3 GeV/*c*; $\theta < 4°$).

3. FRITIOF MODEL

The FRITIOF model [9] assumes the two-body kinematics of inelastic hadron–hadron interactions, which are schematically represented as $a + b \longrightarrow a' + b'$, where a' and b' are some excited states of hadrons a and b, respectively. These excited states are characterized by a mass. In order to choose it in the case being considered, we proceed as follows. In the c.m. frame of colliding hadrons, the law of energy–momentum conservation can be represented as

$$\begin{aligned} E_a + E_b &= E_{a'} + E_{b'} = \sqrt{s_{ab}}, \\ p_{az} + p_{bz} &= p_{a'z} + p_{b'z} = 0, \\ 0 &= \mathbf{p}_{a'\perp} + \mathbf{p}_{b'\perp}, \end{aligned} \tag{1}$$

where E_a and E_b ($E_{a'}$ and $E_{b'}$) are the energies of the initial (final) hadrons a and b (a' and b'), while p_{az} and p_{bz} are the corresponding longitudinal momentum components (momentum projections onto the interaction axis). The rest of the notation is obvious.

Taking the sum and the difference of the first two equations in (1), we arrive at

$$\begin{aligned} P_a^+ + P_b^+ &= P_{a'}^+ + P_{b'}^+, \\ P_a^- + P_b^- &= P_{a'}^- + P_{b'}^-, \\ 0 &= \mathbf{p}_{a'\perp} + \mathbf{p}_{b'\perp}, \end{aligned} \tag{2}$$

where $P^+ = E + p_z$ and $P^- = E - p_z$.

The model employs the following distributions in $P_{a'}^-$ and $P_{b'}^+$:

$$\begin{aligned} dW &\sim dP_{a'}^-/P_{a'}^-, \\ dW &\sim dP_{b'}^+/P_{b'}^+. \end{aligned} \tag{3}$$

The admissible ranges of $P_{a'}^-$ and $P_{b'}^+$ are defined as

$$[P_a^-, P_b^-], \quad [P_b^+, P_a^+]. \tag{4}$$

In the case of hadron–nucleus interactions, the kinematics that is specified by equations (2)–(4) is used for the first collision of the incident hadron a with some intranuclear nucleon ($a + N_1 \longrightarrow a' + N_1'$). Similar equations are used for the second collision ($a' + N_2 \longrightarrow a'' + N_2'$), but the condition in (4) is replaced, in this case, by the condition

$$[P_{a'}^-, P_{N_2}^-], \quad [P_{N_2}^+, P_{a'}^+]. \tag{5}$$

As a result, the mass of the hadron a increases steadily in successive collisions, provided that transverse-momentum transfers are low.

The same approach is used in simulating nucleus–nucleus collisions, where the reactions being considered are schematically represented as $a' + b' \longrightarrow a'' + b''$. The distributions in $P_{a''}^-$ and $P_{b''}^+$ are taken in the former form, while the admissible ranges of these variable are defined as

$$[P_{a'}^-, P_{b'}^-], \quad [P_{b'}^+, P_{a'}^+]. \tag{6}$$

The distribution in the transverse-momentum exchange between colliding nucleons was taken in the form

$$dW = b^2 e^{-Bp_T^2} p_T dp_T, \quad B = 6.7 \text{ GeV}/c^{-2}.$$

In the model version used here, we introduced the following modifications to the original FRITIOF model (see also [15]):

(i) The lower boundary of the mass spectrum of excited nucleons was set to 1.1 GeV.

(ii) In the case of the two-body decay of strings whose mass is less than 1.7 GeV, the isotropic divergence of particles is simulated in the string rest frame.

(iii) Charge exchange between colliding nucleons is admitted in 50% cases of two-vertex diffraction.

(iv) The mean square of transverse-momentum exchange between colliding nucleons is 0.15 GeV/c^2.

All these modifications were introduced in the model in order to achieve a satisfactory description of the distributions of π^- mesons and protons from *np* interactions within the momentum range 1–5 GeV/*c* [15]. Further, the FRITIOF model subjected to these modifications was used in a comparison with experimental data on a wide range of nucleon–nucleus and nucleus–nucleus interactions [16–18]. The set of simulated events that is used in the present study is grouped according to the collision types, individual groups containing from 6000 (*d*C) to 20000 (CC) events. This database was written in the form of a summary data tape and was processed by using the same procedures as for live events.

4. RESULTS OF THE ANALYSIS

Let us begin by considering the features of product π^- mesons. The mean multiplicities of these mesons versus the projectile mass are presented in Table 1,

Table 1. Mean multiplicities of π^- mesons in inelastic pC, dC, αC, and CC interactions at a momentum of p = 4.2 GeV/c per projectile nucleon

Statistics	Interaction type			
	p + C	d + C	α + C	C + C
Number of events	8371	5807	13318	20594
Experiment	0.407 ± 0.006	0.686 ± 0.009	0.968 ± 0.007	1.439 ± 0.007
FRITIOF	0.408 ± 0.002	0.703 ± 0.003	1.003 ± 0.001	1.505 ± 0.002

along with the values computed on the basis of the above FRITIOF version. It can be seen that, for pC, dC, αC, and CC interactions, the model predictions agree with experimental data to within 5%.

Table 2 presents the mean values of the kinematical features of π^- mesons originating from pC, dC, αC, and CC interactions at a momentum of p = 4.2 GeV/c per projectile nucleon. The greatest distinction between the experimental and the model results, which is observed for pC and dC interactions, does not exceed 6%. With increasing projectile mass, the agreement between the experimental and calculated values of the quantities under comparison is improved substantially. The distributions of π^- mesons in the kinematical variables p, p_T, y, and θ are displayed in Fig. 1, along with the results of the calculations based on the FRITIOF model, these distributions being normalized to the total number of π^- mesons. Figure 1*a* shows the momentum distributions of π^- mesons from CC interactions at a momentum of p = 4.2 GeV/c per projectile nucleon. The model predictions are seen to overestimate experimental values at momenta in the range 0.2–0.6 GeV/c. At higher

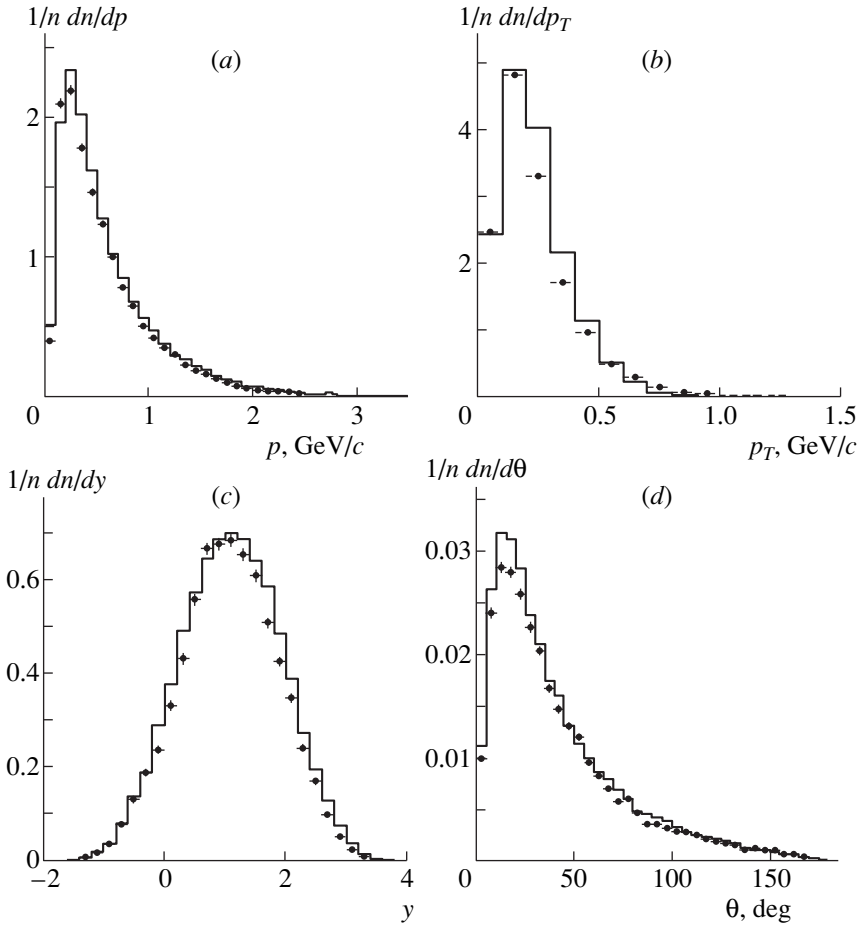

Fig. 1. Distribution of π^- mesons in kinematical variables for CC interactions at a momentum of 4.2 GeV/c per projectile nucleon (normalization is performed to the number of π^- mesons): (points) experimental data and (histograms) results of the calculation on the basis of the FRITIOF model.

Table 2. Mean values of the kinematical variables of π^- mesons from *p*C, *d*C, αC, and CC interactions at a momentum of $p = 4.2$ GeV/*c* per projectile nucleon

Interaction type	Mean values of kinematical variables			
	p_{lab}, GeV/*c*	θ_{lab}, deg	p_T, GeV/*c*	rapidity, *y*
*p*C (experiment)	0.503 ± 0.007	50.8 ± 0.6	0.248 ± 0.003	0.832 ± 0.013
*p*C (FRITIOF)	0.480 ± 0.003	49.1 ± 0.3	0.236 ± 0.001	0.860 ± 0.002
*d*C (experiment)	0.557 ± 0.007	46.0 ± 0.5	0.255 ± 0.003	0.941 ± 0.011
*d*C (FRITIOF)	0.540 ± 0.002	44.6 ± 0.2	0.240 ± 0.001	0.970 ± 0.003
αC (experiment)	0.583 ± 0.004	44.1 ± 0.3	0.250 ± 0.001	1.000 ± 0.006
αC (FRITIOF)	0.570 ± 0.002	43.4 ± 0.3	0.240 ± 0.001	1.010 ± 0.001
CC (experiment)	0.592 ± 0.003	41.0 ± 0.2	0.241 ± 0.001	1.071 ± 0.004
CC (FRITIOF)	0.600 ± 0.001	40.9 ± 0.1	0.240 ± 0.001	1.090 ± 0.003

momenta, the discrepancy between the experimental and the model results decreases. The transverse-momentum distributions are displayed in Fig. 1*b*. Here, the calculated values exceed experimental ones in the range $p_T \approx 0.2$–0.5 GeV/*c*. Figure 1*c* illustrates a comparison of the rapidity distributions: for nucleon–nucleon interactions, the experimental and computed rapidity distributions peak at the same rapidity value of $y_0 \sim y_{c.m.} \approx 1.1$. The calculated values exceed the experimental ones in the nuclear-fragmentation regions (*y* values between –0.5 and 0.5 and between 1.5 and 2.5). Figure 1*d* shows the angular distributions of π^- mesons. It can be seen that the model overestimates the multiplicity of mesons at small angles ($\theta \sim 0°$–$30°$). Conceivably, the inclusion of π^--meson absorption in residual nuclei, which is disregarded in the present version of the model, may improve the description of the experimentally observed regularities.

On the whole, the model reproduces faithfully the single-particle distributions of π^- mesons in kinematical variables. This gives sufficient ground to believe that this model can be used further in performing a more detailed analysis and in estimating meson yields in heavy-ion collisions.

The mean multiplicities of participant protons from *A*C interactions at a momentum 4.2 GeV/*c* per projectile nucleon are quoted in Table 3, along with the results of the calculations within the FRITIOF model.

Table 3. Mean multiplicities of participant protons in inelastic *p*C, *d*C, αC, and CC interactions at a momentum of $p = 4.2$ GeV/*c* per projectile nucleon

Statistics	Interaction type			
	p + C	*d* + C	α + C	C + C
Number of events	8371	5807	13318	20593
Experiment	1.82 ± 0.01	2.10 ± 0.02	2.90 ± 0.01	4.43 ± 0.02
FRITIOF	1.99 ± 0.02	2.05 ± 0.03	2.77 ± 0.01	4.13 ± 0.03

The greatest discrepancy (within 10%) is observed for *p*C interactions.

Table 4 displays the mean values of the kinematical features of participant protons from *A*C interactions at a momentum 4.2 GeV/*c* per projectile nucleon. The most pronounced discrepancies are observed in the mean emission angles and the mean momenta for *p*C interactions (within 10%).

Figure 2 shows the experimental and calculated distributions of protons in kinematical variables for CC interactions, these distributions being normalized to the number of protons. The momentum distributions of protons are displayed in Fig. 2*a*. An excess of the experimental values over the calculated ones is observed at momentum values in the range $p = 0.4$–1.0 GeV/*c*. The discrepancy between the experimental and the calculated values at $p_{lab} \sim 3$ GeV/*c* can be tentatively associated with selections for identifying stripping protons. Figure 2*b* shows the transverse-momentum distributions of participant protons. The model underestimates experimental results at $p_T \sim 0.3$–0.4 GeV/*c*.

Figure 2*c* shows the rapidity distributions of protons. It can be seen that the experimental distribution has two maxima (at $y \sim 0.2$ and 1.5) and one minimum (at $y \sim 1.1$). The asymmetry of the rapidity distributions of protons is due to a small admixture (10%) of deuterons, which shift the spectrum toward higher rapidities when assigned the proton mass. The calculated distribution have no such asymmetry. We can see that the model underestimates the yield of slow protons in the regions of nuclear fragmentation. Figure 2*d* displays the angular distributions of participant protons. A small discrepancy between the experimental and the calculated values is observed over a broad range of angles.

Despite discrepancies between the shapes of the experimental and the calculated distributions, the above comparison of the experimental inclusive distributions of protons in kinematical variables for *p*C, *d*C, αC, and CC interactions with the corresponding distributions

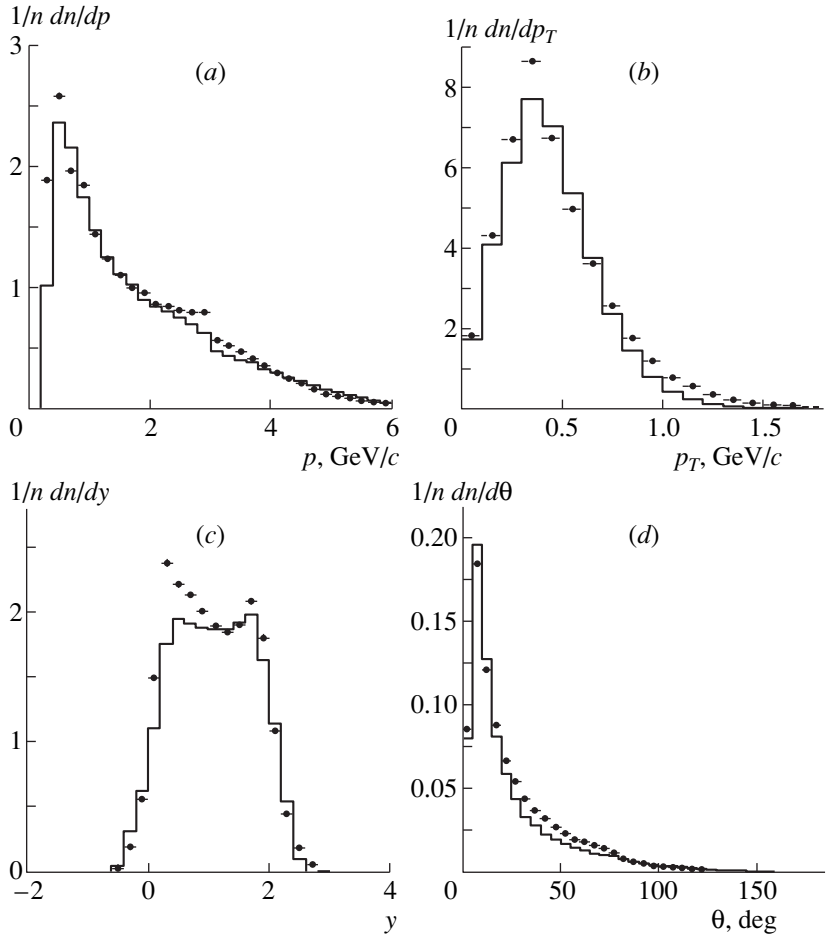

Fig. 2. Distribution of protons in kinematical variables for CC interactions at a momentum of 4.2 GeV/*c* per projectile nucleon (normalization is performed to the number of the protons): (points) experimental data and (histograms) results of the calculation on the basis of the FRITIOF model.

obtained on the basis of the FRITIOF model suggests that, by and large, the FRITIOF model provides a qualitative description of experimental data on *A*C interactions.

In summary, we have arrived at the following conclusions:

(i) The FRITIOF model version used here faithfully reproduces the mean features of π^- mesons and protons originating from inelastic *A*C interactions.

(ii) The model provides a qualitative description of the distributions of π^- mesons.

Table 4. Mean values of the kinematical variables of protons from *p*C, *d*C, αC, and CC interactions at a momentum of p = 4.2 GeV/*c* per projectile nucleon

Interaction type	Mean values of kinematical variables			
	p_{lab}, GeV/*c*	θ_{lab}, deg	p_T, GeV/*c*	rapidity, y
*p*C (experiment)	1.292 ± 0.007	36.1 ± 0.2	0.443 ± 0.002	0.775 ± 0.004
*p*C (FRITIOF)	1.170 ± 0.003	39.3 ± 0.3	0.420 ± 0.001	0.720 ± 0.004
*d*C (experiment)	1.289 ± 0.008	36.5 ± 0.2	0.437 ± 0.002	0.765 ± 0.005
*d*C (FRITIOF)	1.250 ± 0.002	38.4 ± 0.2	0.440 ± 0.001	0.750 ± 0.003
αC (experiment)	1.541 ± 0.005	33.0 ± 0.1	0.464 ± 0.001	0.887 ± 0.003
αC (FRITIOF)	1.450 ± 0.002	33.6 ± 0.3	0.408 ± 0.001	0.817 ± 0.003
CC (experiment)	1.857 ± 0.004	27.5 ± 0.1	0.476 ± 0.001	1.051 ± 0.002
CC (FRITIOF)	1.808 ± 0.001	26.8 ± 0.1	0.440 ± 0.001	1.070 ± 0.004

(iii) A detailed description of the distribution of protons in the regions of nuclear fragmentation still presents a problem.

ACKNOWLEDGMENTS

We are grateful to the members of the collaboration that has been performing experiments at the 2-m propane bubble chamber of JINR (Dubna) and to the technical staff for viewing relevant films and for measuring events. Thanks are also due to L.A. Ratnikova for assistance in the preparation of the manuscript.

REFERENCES

1. G. N. Agakishiev *et al.*, Yad. Fiz. **40**, 1209 (1984) [Sov. J. Nucl. Phys. **40**, 767 (1984)].
2. A. I. Bondarenko *et al.*, Yad. Fiz. **62**, 1612 (1999) [Phys. At. Nucl. **62**, 1513 (1999)].
3. G. N. Agakishiev *et al.*, Yad. Fiz. **34**, 1517 (1981) [Sov. J. Nucl. Phys. **34**, 842 (1981)].
4. G. N. Agakishiev *et al.*, Yad. Fiz. **51**, 758 (1990) [Sov. J. Nucl. Phys. **51**, 481 (1990)].
5. S. Backovic *et al.*, Phys. Rev. C **46**, 1501 (1992).
6. R. N. Bekmirzaev *et al.*, Yad. Fiz. **58**, 63 (1995) [Phys. At. Nucl. **58**, 58 (1995)].
7. R. N. Bekmirzaev *et al.*, Yad. Fiz. **58**, 1642 (1995) [Phys. At. Nucl. **58**, 1548 (1995)].
8. R. N. Bekmirzaev *et al.*, Yad. Fiz. **58**, 1822 (1995) [Phys. At. Nucl. **58**, 1721 (1995)].
9. B. Andersson *et al.*, Nucl. Phys. B **281**, 289 (1987); B. Nilsson-Almquist and E. Stenlund, Comput. Phys. Commun. **43**, 387 (1987)
10. V. V. Uzhinskiĭ, Preprint No. E2-96-102, JINR (Dubna, 1996).
11. A. I. Bondarenko *et al.*, Soobshch. Ob'edin. Inst. Yad. Issled., No. R1-98-292 (Dubna, 1998).
12. G. N. Agakishiev *et al.*, Soobshch. Ob'edin. Inst. Yad. Issled., No. 1-83-662 (Dubna, 1983).
13. D. Armutliysky *et al.*, Yad. Fiz. **45**, 1047 (1987) [Sov. J. Nucl. Phys. **45**, 649 (1987)]; D. Armutliysky, Z. Phys. A **328**, 455 (1987).
14. A. I. Bondarenko *et al.*, Preprint No. R1-96-447, JINR (Dubna, 1996); Yad. Fiz. **60**, 2004 (1997) [Phys. At. Nucl. **60**, 1833 (1997)].
15. B. Ganhuyag, Soobshch. Ob'edin. Inst. Yad. Issled., No. R2-98-26 (Dubna, 1998).
16. B. Ganhuyag and V. V. Uzhinskiĭ, Soobshch. Ob'edin. Inst. Yad. Issled., No. R2-96-419 (Dubna, 1996); Czech. J. Phys. **47**, 913 (1997).
17. B. Ganhuyag and V. V. Uzhinskiĭ, Soobshch. Ob'edin. Inst. Yad. Issled., No. R1-97-315 (Dubna, 1997).
18. B. Ganhuyag and V. V. Uzhinskiĭ, Soobshch. Ob'edin. Inst. Yad. Issled., No. R2-97-397 (Dubna, 1997).

Translated by A. Isaakyan

Physics of Atomic Nuclei, Vol. 63, No. 5, 2000, pp. 845–849. Translated from Yadernaya Fizika, Vol. 63, No. 5, 2000, pp. 915–919.

ELEMENTARY PARTICLES AND FIELDS
Theory

Proton Polarizability and Lamb Shift in the Muonic Hydrogen Atom

A. P. Martynenko and R. N. Faustov[1)]

Samara State University, ul. Akad. Pavlova 1, Samara, 443011 Russia

Received May 5, 1999

Abstract—The corrections that the structure of the proton and its polarizability induce in the Lamb shift in the muonic and the conventional hydrogen atom are calculated on the basis of up-to-date experimental data on the structure functions in deep-inelastic scattering. Numerically, the contribution from proton polarizability to the $2P$–$2S$ shift in the muonic hydrogen atom is 4.4 GHz. © *2000 MAIK "Nauka/Interperiodica".*

The muonic hydrogen atom (μp atom) is a two-particle bound state of a proton and a muon. The energy levels of this system can be determined in the same way as for the conventional hydrogen atom [1]. However, some QED effects and corrections associated with the structure of the proton and its polarizability are more important for the muonic hydrogen atom [2, 3], because the electron-to-muon mass ratio is as small as $m_e/m_\mu = 4.836332 \times 10^{-3}$. In particular, the leading contribution to the Lamb shift in the muonic hydrogen atom comes from the electron polarization of the vacuum—in contrast to what is observed for conventional hydrogen—because the electron Compton wavelength is on the same order of magnitude as the Bohr radius for the muonic hydrogen atom: $\hbar/m_e c : \hbar^2/m_\mu e^2 = 0.737386$. Measurement of the $2P$–$2S$ Lamb shift in the muonic hydrogen atom would make it possible to determine more precisely the charge radius of the proton $R_p = \sqrt{\langle r^2 \rangle}$ [4], an extremely important feature of the proton indeed. Major contributions to the Lamb shift in the muonic hydrogen atom were studied theoretically in [2, 3]; information about currently known corrections is compiled in [5]. The sixth-order contribution to the Lamb shift in the muonic hydrogen atom due to vacuum polarization was calculated in [6]. In the present study, we consider the contribution of proton polarizability to the Lamb shift in the muonic hydrogen atom. In just the same way as in calculating hyperfine splitting in the muonic hydrogen atom [7, 8], we rely here on the local quasipotential equation in describing the two-particle bound states of the μp system [9].

The contribution of proton polarizability is determined by the amplitude of muon–proton interaction that is mediated by two photons (see Fig. 1) and which involves Compton scattering on a muon. The amplitude of this Compton scattering can be represented as the sum of direct and crossed 2γ diagrams:

$$M^{(\mu)}_{\mu\nu} = \bar{u}(q_1)\left[\gamma_\mu \frac{\hat{p}_1 + \hat{k} + m_1}{(p_1 + k)^2 - m_1^2 + i\epsilon}\gamma_\nu + \gamma_\nu \frac{\hat{p}_1 - \hat{k} + m_1}{(p_1 - k)^2 - m_1^2 + i\epsilon}\gamma_\mu\right]u(p_1). \quad (1)$$

Neglecting the momenta of the relative motion of the particles in the initial and in the final state (that is, setting $\mathbf{p} = \mathbf{q} = 0$), we can represent the amplitude of virtual Compton scattering on a proton as [10, 11]

$$M^{(p)}_{\mu\nu} = \bar{v}(p_2)\left\{\frac{1}{2}C_1\left(-g_{\mu\nu} + \frac{k_\mu k_\nu}{k^2}\right) + \frac{1}{2m_2^2}C_2\left(p_{2\mu} - \frac{m_2\nu}{k^2}k_\mu\right)\left(p_{2\nu} - \frac{m_2\nu}{k^2}k_\nu\right) + \frac{1}{2m_2}H_1([\gamma_\nu, \hat{k}]p_{2\mu} - [\gamma_\mu, \hat{k}]p_{2\nu} + [\gamma_\mu, \gamma_\nu]k^2) + \frac{1}{2}H_2([\gamma_\nu, \hat{k}]k_\mu - [\gamma_\mu, \hat{k}]k_\nu + [\gamma_\mu, \gamma_\nu]k^2)\right\}v(q_2), \quad (2)$$

where $\nu = k_0$ is the virtual-photon energy. The tensor in (2) involves the symmetric part determined by the structure functions $C_{1,2}(\nu, k^2)$ and the antisymmetric

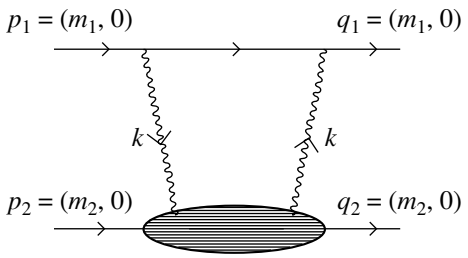

Fig. 1. Correction for proton polarizability.

[1)] Scientific Council for Cybernetics, Russian Academy of Sciences, ul. Vavilova 40, Moscow, 117967 Russia.

1063-7788/00/6305-0845$20.00

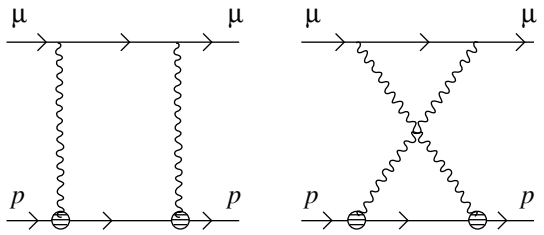

Fig. 2. $(Z\alpha)^5$ correction for the finite proton size.

part determined by the functions $H_{1,2}(\nu, k^2)$. The former and the latter contribute, respectively, to the Lamb shift and to the hyperfine splitting of the S-wave energy levels. In order to isolate that part of the quasipotential which is responsible for the hyperfine splitting, $V^{\rm hfs}$, it is convenient to use the projections for the muon and the proton onto the $S = 0$ and $S = 1$ states [$V(^1S_0)$ and $V(^3S_1)$, respectively], the generic expression for the corresponding projection operators being

$$\hat{\Pi} = u(p_1)\bar{v}(p_2) = \frac{1}{2\sqrt{2}}(1+\gamma_0)\hat{\epsilon}(\gamma_5). \qquad (3)$$

The quasipotential contributing to the Lamb shift of the S-wave levels can be constructed either by averaging the amplitudes in (1) and (2) over the muon and proton spins [12] or by applying the projection operators (3) in order to construct the particle-interaction operator in the form

$$V^{\rm Ls} = V(^1S_0) + \frac{3}{4}V^{\rm hfs}. \qquad (4)$$

Taking the product of the amplitudes in (1) and (2) and isolating the parts of the quasipotential that correspond to hyperfine splitting (hfs) and the Lamb shift (Ls), we obtain

$$(M^{(\mu)}_{\mu\nu}M^{(p)}_{\mu\nu})^{\rm hfs} = -\frac{16}{3}\frac{k^2}{k^4-4k_0^2m_1^2} \times [m_2(k_0^2+2k^2)H_1 + 3k_0k^2H_2], \qquad (5)$$

$$(M^{(\mu)}_{\mu\nu}M^{(p)}_{\mu\nu})^{\rm Ls} = \frac{2m_1}{k^4-4k_0^2m_1^2} \times [-(2k_0^2+k^2)C_1 + (k^2-k_0^2)C_2]. \qquad (6)$$

Expression (5) was used in [13–15] to calculate hyperfine splitting. Here, we employ formula (6) to calculate the Lamb shift. Using the dispersion relations for the structure functions $C_i(k_0, k^2)$ and isolating the contribution of the one-nucleon intermediate state shown in Fig. 2, we arrive at

$$C_i(k_0,k^2) = C_i^p(k_0,k^2) + \frac{1}{\pi}\int_{\nu_0}^{\infty}\frac{d\nu^2}{(\nu^2-k_0^2)}{\rm Im}C_i(\nu,k^2), \qquad (7)$$
$$\nu_0 = m_\pi + \frac{1}{2m_2}(Q^2+m_\pi^2), \quad Q^2 = -k^2.$$

For the integrand in (7) to have a correct asymptotic behavior in ν, the function $C_1(k_0, k^2)$ must satisfy a dispersion relation with one subtraction.

The proton vertices in the two-photon amplitudes in Fig. 2 are determined by the form factors F_1 and F_2 [16]:

$$\Gamma^\mu = \gamma^\mu F_1 + \frac{i}{2m_2}\sigma^{\mu\nu}k_\nu F_2. \qquad (8)$$

The contribution of the relevant diagrams to the Lamb shift $\Delta E_p^{\rm Ls}$ can be represented in the form

$$\Delta E_p^{\rm Ls} = -|\psi(0)|^2\frac{(Z\alpha)^2}{\pi^2}\int d^4k\frac{1}{(k^2)^2}\frac{1}{2m_1} \times m_2(k^4+4m_1^2k_0^2)\frac{1}{(k^4+4m_2^2k_0^2)}[4m_2^2(k^4+2k_0^4)F_1^2 - 2k^4(k^2+2k_0^2)F_1F_2 - 3k_0^2k^4F_2^2], \qquad (9)$$

where, upon the substitution $k_0 \longrightarrow ik_0$, the integral is taken over four-dimensional Euclidean space. It should be noted that the integral in (9) involves an infrared divergence. In order to eliminate it, the corrections associated with the iteration term of the quasipotential and, in the case of a pointlike proton, the contribution of the two-photon amplitudes are subtracted from expression (8). The contribution of the iteration part of the quasipotential has the form

$$\Delta E_{\rm iter}^{\rm Ls} = V_{1\gamma}\times G^f\times V_{1\gamma} \approx \frac{\mu^4(Z\alpha)^5}{m_2^2\pi n^3}\int_0^\infty\frac{dk}{k^2}[4m_2^2F_1'(0)+F_2(0)]. \qquad (10)$$

The iteration terms of the quasipotential cancel the infrared divergences in the hyperfine structure, provided that all effects of binding are disregarded for the particles involved [11]. It should be noted that the leading proton-structure-induced correction to the Lamb shift of the hydrogen-like atoms is determined by the one-photon term in the quasipotential, $V_{1\gamma} \sim G_E(k^2)/\mathbf{k}^2$ [17] (G_E is the Sachs form factor), and is given by [1]

$$E^{\rm Ls} = \frac{2\mu^3}{3n^3}(Z\alpha)^4R_p^2\delta_{l0}, \quad R_p^2 = \frac{1}{6G_E(0)}\frac{\partial G_E(k^2)}{\partial k^2}\bigg|_{k^2=0}, \qquad (11)$$

where R_p is the charge radius of the proton [4]. For a pointlike proton, the recoil correction ΔE_{nl} of order $(Z\alpha)^5$ is determined both by the domain of nonrelativistic momenta in the two-photon quasipotential $V_{2\gamma}$ and by the domain of relativistic momenta and is given by [1]

$$\Delta E_{nl} = \frac{\mu^3}{m_1 m_2}\frac{(Z\alpha)^5}{\pi n^3}\left[\frac{2}{3}\delta_{l0}\ln\left(\frac{1}{Z\alpha}\right)-\frac{8}{3}\ln k_0(n,l)\right.$$
$$-\frac{1}{9}\delta_{l0}-\frac{7}{3}a_n-\frac{2}{m_2^2-m_1^2} \qquad (12)$$
$$\left.\times\,\delta_{l0}\left(m_2^2\ln\frac{m_2}{\mu}-m_1^2\ln\frac{m_2}{\mu}\right)\right],$$

$$a_n = -2\left[\ln\frac{2}{n}+\left(1+\frac{1}{2}+\ldots+\frac{1}{n}\right)+1-\frac{1}{2n}\right]\delta_{l0} \qquad (13)$$
$$+\frac{1-\delta_{l0}}{l(l+1)(2l+1)}.$$

Taking into account expressions (10) and (12), we can represent the infrared-safe contribution of the two-photon diagrams to the Lamb shift in the hydrogen-like atom in the form

$$\Delta E_{2\gamma}^{\mathrm{Ls}} = -\frac{\mu^3}{\pi n^3}\delta_{l0}(Z\alpha)^5\int_0^\infty\frac{dk}{k}V(k), \qquad (14)$$

$$V(k) = \frac{2(F_1^2-1)}{m_1 m_2}+\frac{8m_1[F_2(0)+4m_2^2F_1'(0)]}{m_2(m_1+m_2)k}$$
$$+\frac{k^2}{2m_1^3m_2^3}[2(F_1^2-1)(m_1^2+m_2^2)+4F_1F_2m_1^2+3F_2^2m_1^2]$$
$$+\frac{\sqrt{k^2+4m_1^2}}{2m_1^3m_2(m_1^2-m_2^2)k}\left\{k^2[2(F_1^2-1)m_2^2\right.$$
$$+4F_1F_2m_1^2+3F_2^2m_1^2] \qquad (15)$$
$$\left.-8m_1^4F_1F_2+\frac{16m_1^4m_2^2(F_1^2-1)}{k^2}\right\}$$
$$-\frac{\sqrt{k^2+4m_2^2}m_1}{2m_2^3(m_1^2-m_2^2)k}\{k^2[2(F_1^2-1)+4F_1F_2+3F_2^2]$$
$$\left.-8m_2^2F_1F_2+\frac{16m_2^4(F_1^2-1)}{k^2}\right\}.$$

In calculating correction (14), we used the dipole parametrization of the proton form factors:

$$F_1(k^2) = \frac{G_E-\dfrac{k^2}{4m_2^2}G_M}{1-\dfrac{k^2}{4m_2^2}}, \quad F_2(k^2) = \frac{G_M-G_E}{1-\dfrac{k^2}{4m_2^2}}, \qquad (16)$$
$$G_M = \frac{1+\kappa}{\left(1-\dfrac{k^2}{\Lambda^2}\right)^2}, \quad G_E = \frac{1}{\left(1-\dfrac{k^2}{\Lambda^2}\right)^2}.$$

Here, the proton-structure parameter Λ was set to $\Lambda = 0.898m_2$ (this value was also used in calculating the hyperfine structure in the hydrogen atom [16]), while $\kappa = 1.792847$ is the anomalous magnetic moment of the proton. Numerically, the contribution in (14) to the Lamb shift is $\Delta E_{\mathrm{H}}^{\mathrm{Ls}}(2P\text{–}2S) = 4.25$ Hz in the case of conventional hydrogen and is as large as $\Delta E_{\mu p}^{\mathrm{Ls}} = 4.35$ GHz in the case of muonic hydrogen, in agreement with the results obtained in [5]. Let us now consider the effects of proton polarizability that are determined by the dispersion integral in (7). The imaginary parts of the amplitudes $C_i(k_0, k^2)$ are expressed in terms of the structure functions $F_i(x, Q^2)$ for deep-inelastic scattering as

$$\frac{1}{\pi}\mathrm{Im}C_1(x,Q^2) = \frac{F_1(x,Q^2)}{m_2},$$
$$\frac{1}{\pi}\mathrm{Im}C_2(x,Q^2) = \frac{F_2(x,Q^2)}{\nu}, \quad x = \frac{Q^2}{2m_2\nu}. \qquad (17)$$

In the limit $Q^2 \longrightarrow 0$, we have

$$F_2 = O(Q^2), \quad \frac{F_1}{m_2}-\frac{F_2\nu}{Q^2} = O(Q^2). \qquad (18)$$

These relations play an important role in parametrizing the structure functions $F_i(x, Q^2)$ [18]. Making use of relations (6) and (7) and performing integrations in loop amplitudes over four-dimensional Euclidean space with the aid of the formula

$$\int d^4k = 4\pi\int_0^\infty k^3dk\int_0^\pi\sin^2\phi\,d\phi, \quad k^0 = k\cos\phi, \qquad (19)$$

we can represent the photon-polarizability contribution to the Lamb shift in the muonic hydrogen atom as

$$\Delta E_{\mathrm{pol}}^{\mathrm{Ls}} = -\frac{16\mu^3(Z\alpha)^5m_1}{\pi^2n^3}\int_0^\infty\frac{dk}{k}\int_0^\pi\sin^2\phi\,d\phi$$
$$\times\int_{\nu_0}^\infty dy\frac{1}{(k^2+4m_1^2\cos^2\phi)}\,\frac{1}{(y^2+k^2\cos^2\phi)} \qquad (20)$$

Proton-polarizability contribution to the shifts of the *S*-wave levels in the conventional and in the muonic hydrogen atom

	(e^-p^+), Hz	(μ^-p^+), μeV	[22]		[23]	
1*S*	−94	−144	−72	−100	−95	−136
2*S*	−11.8	−18	−9	−13	−11.9	−17

$$\times\left[(1+2\cos^2\phi)\frac{\left(1+\frac{k^2}{y^2}\right)\cos^2\phi}{1+R(y,k^2)}+\sin^2\phi\right]F_2(y,k^2),$$

where $R(y, k^2) = \sigma_L/\sigma_T$ is the ratio of the cross sections for the absorption of longitudinally and transversely polarized photons by hadrons. In order to perform numerical calculations on the basis of (20), we need experimental data on the structure function $F_2(x, Q^2)$ and on the ratio $R(x, Q^2)$. There are several parametrizations of experimental data for the function $F_2(x, Q^2)$ over a wide range of the parameters Q^2 and x [18]. Here, we have used the parametrization proposed in [19], where the function F_2 was represented as the sum of the Pomeron and the Reggeon term (F_2^{P} and F_2^{R}, respectively):

$$F_2 = F_2^{\mathrm{P}} + F_2^{\mathrm{R}},$$

$$F_2^r = \frac{Q^2}{Q^2+m_0^2}C_r(t)x_r^{a_r(t)}(1-x)^{b_r(t)}, \quad r = \mathrm{P}, \mathrm{R}, \tag{21}$$

$$\frac{1}{x_r} = \frac{2m_2\nu + m_r^2}{Q^2+m_r^2}.$$

Recent efforts to extract $R(x, Q^2)$ from experimental data on deep-inelastic *ep* scattering [20] resulted in a six-parameter formula describing this ratio in the kinematical domain specified by the inequalities $0.005 \le x \le 0.86$ and $0.5\ \mathrm{GeV}^2 \le Q^2 \le 130\ \mathrm{GeV}^2$:

$$R = \frac{a_1}{\ln(Q^2/0.04)}\theta(x,Q^2) + \frac{a_2}{[Q^8+a_3^4]^{1/4}} \times[1+a_4x+a_5x^2]x^{a_6}, \tag{22}$$

$$\theta(x,Q^2) = 1 + 12\left(\frac{Q^2}{Q^2+1}\right)\left(\frac{0.125^2}{0.125^2+x^2}\right).$$

In the case of muonic hydrogen, the numerical value obtained on the basis of (20)–(22) for the proton-polarizability contribution to the $2P$–$2S$ Lamb shift is

$$\Delta E_{\mathrm{pol}}^{\mathrm{Ls}} = 4.4 \pm 0.5\ \mathrm{GHz}. \tag{23}$$

The analogous correction for the $1S$ state of the conventional hydrogen atom is -94 ± 10 Hz, in agreement with the results presented in [21–23]. The shifts of the $1S$ and $2S$ energy levels in the muonic and in the conventional hydrogen atom are quoted in the table. Our values are compared there with the results from [22, 23]; for convenience, the shifts in the muonic hydrogen atom are given in eV. It should be noted that parametrization (21), which is used here, complies with the asymptotic behavior (18) and makes an infrared-finite contribution to the energy spectrum. For this reason, the bulk of the error in our result stems from the uncertainty in the experimental data on the function $R(x, Q^2)$ for $Q^2 \le 0.5$ and from errors in the measurements of the structure function $F_2(x, Q^2)$ [18] rather than from the logarithmic approximation of an integral of the type in (20) as was in [21]. Thus, our correction (23) for the muonic hydrogen atom is on the same order of magnitude as the other contributions (12) and (14); therefore, it must be taken into account in extracting the charge radius R_p of the proton from a future experiment to measure the Lamb shift in the μp system.

ACKNOWLEDGMENTS

We are grateful to S.G. Karshenboĭm, V.A. Petrun'kin, R.A. Senkov, and I.B. Khriplovich for stimulating discussions and to J.R. Sapirsteĭn for sending us a reprint copy of the article quoted in [1].

This work was supported in part by the Russian Foundation for Basic Research (project no. 98-02-16185) and by the program Russian Universities: Basic Research (grant no. 2759).

REFERENCES

1. J. R. Sapirstein and D. R. Yennie, in *Quantum Electrodynamics*, Ed. by T. Kinoshita (World Sci., Singapore, 1990), p. 560.
2. A. Giacomo, Nucl. Phys. B **11**, 411 (1969).
3. E. Borie and G. A. Rinker, Rev. Mod. Phys. **54**, 67 (1982).
4. S. G. Karshenboim, in *Proceedings of International Workshop "Hadronic Atoms and Positronium in the Standard Model," Dubna, Russia, May 26–31, 1998* (Dubna, 1998), p. 224.
5. K. Pachucki, Phys. Rev. A **53**, 2092 (1996).
6. T. Kinoshita and M. Nio, Phys. Rev. Lett. **82**, 3240 (1999).
7. R. N. Faustov and A. P. Martynenko, Yad. Fiz. **61**, 534 (1998) [Phys. At. Nucl. **61**, 471 (1998)].
8. R. N. Faustov, A. P. Martynenko, and V. A. Saleev, Yad. Fiz. **62**, 2280 (1999) [Phys. At. Nucl. **62**, 2099 (1999)].
9. A. P. Martynenko and R. N. Faustov, Teor. Mat. Fiz. **64**, 179 (1985).
10. J. D. Bjorken, Phys. Rev. **148**, 1467 (1966).
11. G. M. Zinov'ev *et al.*, Yad. Fiz. **11**, 1284 (1970) [Sov. J. Nucl. Phys. **11**, 715 (1970)].

12. G. C. Bhatt and H. Grotch, Ann. Phys. (N.Y.) **178**, 1 (1987).
13. S. D. Drell and I. D. Sullivan, Phys. Rev. **154**, 1477 (1967).
14. F. Guerin, Nuovo Cimento A **50**, 1 (1967).
15. R. P. Feynman, *Photon–Hadron Interactions* (Benjamin, Reading, 1972; Mir, Moscow, 1975).
16. G. T. Bodwin and D. R. Yennie, Phys. Rev. D **37**, 498 (1988).
17. R. N. Faustov, Fiz. Élem. Chastits At. Yadra **3**, 238 (1972).
18. B. Badelek and J. Kwiecinski, Rev. Mod. Phys. **68**, 445 (1996).
19. H. Abramovicz and A. Levy, Preprint No. 97-251, DESY (1997).
20. K. Abe *et al.*, Preprint No. PUB-7927, SLAC (Stanford Linear Accelerator Center, 1998).
21. I. B. Khriplovich and R. A. Senkov, Phys. Lett. A **249**, 474 (1998); nucl-th/9903077.
22. S. A. Startsev, V. A. Petrun'kin, and A. L. Khomkin, Yad. Fiz. **23**, 1233 (1976) [Sov. J. Nucl. Phys. **23**, 656 (1976)].
23. R. Rosenfelder, hep-ph/9903352.

Translated by R. Rogalyov

Physics of Atomic Nuclei, Vol. 63, No. 5, 2000, pp. 850–858. From Yadernaya Fizika, Vol. 63, No. 5, 2000, pp. 920–928.

ELEMENTARY PARTICLES AND FIELDS
Theory

Cascade Transitions in Heavy Hadronic Hydrogen Atoms*

L. I. Men'shikov**

Russian Research Centre Kurchatov Institute, pl. Kurchatova 1, Moscow, 123182 Russia

Received March 25, 1999; in final form, August 9, 1999

Abstract—The majority of deexcited hadronic atoms (hX) ($h = K^-, \bar{p}, \ldots$ and $X = p, d, t$) are accelerated up to energies of about 100 eV due to Coulomb transitions. The diffusion model of Stark transitions is developed. The resulting nuclear capture rate is higher than that in Bethe–Leon theory by a factor not less than five. Thus, only nonaccelerated atoms can survive. Therefore, the yield Y of K_α x rays is significantly less (by a factor of about ten) than that calculated in standard cascade models and is approximately equal to 0.2% and 1.0% for (K^-p) atoms at hydrogen densities of $N = 2 \times 10^{21}$ and 5×10^{20} atom/cm^3, respectively. The scheme of a more accurate calculation of Y is also presented. © *2000 MAIK "Nauka/Interperiodica".*

1. INTRODUCTION

The mass M_h of a hadron in a hadronic atom (hX) for $h = K^-, \bar{p}, \Sigma^-, \ldots$ is comparable with the nuclear mass M_X (for the sake of definiteness, the (K^-p) atoms are considered below). Therefore, the behavior of such atoms in matter differs substantially from the cases of pionic and muonic atoms with the lighter particles in the orbit. This is the result of Coulomb transitions—that is, the inelastic ($n' < n$) reaction

$$(K^-p)_{nl} + p \longrightarrow (K^-p)_{n'l'} + p \qquad (1)$$

(for $n' = n$, it is a Stark mixing process). Hadrons are captured mainly from high orbits (see the review article of Batty [1] and below) with the principal quantum numbers

$$n = 4\text{–}7. \qquad (2)$$

Hence, pure classical mechanics is applicable, and it is preferable and much more reliable for large n than the rigorous quantum-mechanical approach. In each collision of the type (1), a significant fraction of the internal energy $E = -\mu/(2n^2)$ ($\mu^{-1} = M_h^{-1} + M_X^{-1}$) is converted into the kinetic energy of the hadronic atom ($\varepsilon = Mv^2/2$, $M = M_h + M_X$); therefore, we have

$$\bar{\varepsilon} \sim \xi|E|, \quad \xi \sim \exp\left(-\beta\sqrt{\frac{1}{\eta}}\right), \qquad (3)$$

where $\eta = M_h/M_X$ and $\beta \sim 1$. For the (K^-p) atom, $\xi \sim 0.2$. The estimate in (3) remains valid after taking into account Auger and radiative deexcitation in which the internal energy E is transferred to electrons and x rays. This estimate is confirmed by Monte Carlo simulations that will be published later.

For heavy atoms, it follows from (2) and (3) that $\bar{\varepsilon} \sim$ 100 eV. In the case of light (π^-X) and (μ^-X) atoms, there exist only a small (about 10%) fraction of accelerated atoms. This follows both from the classical and from quantum-mechanical estimates [2–4] (approximate conservation of adiabatic invariants, which is equivalent to small probabilities of quantum transitions in the adiabatic motion of nuclei). This follows also from experiments [5, 6]. A fraction of 45% obtained in [5, 6] for the liquid hydrogen density of $\varphi = 1$ ($\varphi = N/N_0$, $N_0 = 4.25 \times 10^{22}$ atom/cm^3) should be lowered by a factor of about five because incorrect values of the effective nuclear capture rate Γ were assumed in [5, 6] for accelerated (π^-p) atoms. The actual value of Γ is larger than that assumed in [5, 6] (see below). Thus, the same number of observed neutrons can be ejected by smaller fraction of (π^-p) atoms.

Nuclear capture occurs mainly from the ns state, and its rate Γ_{ns} is greater than the rate of (1) and other processes for all n from (2) and all kinds of hadronic atoms. The resulting nuclear capture rate Γ is determined [7, 8] by the rate λ_{st} of the "feeding" of ns states in Stark processes (bottleneck effect):

$$\Gamma \equiv \Gamma_n = Nv\int_0^\infty 2\pi\rho\, d\rho\, Q(\rho), \qquad (4)$$

$$Q(\rho) = \sum_{lm} f_{lm} P(nlm \longrightarrow n00). \qquad (5)$$

Here, ρ is the impact parameter of a collision, f_{lm} is the population of the lm states with the same n before the collision (it is normalized as $\sum_{lm} f_{lm} = 1$—one atom per n level), and $P(nlm \longrightarrow n00)$ is the probability of the Stark transition (nlm) $\longrightarrow$ ($n00$) in a collision with an impact parameter $\boldsymbol{\rho}$. Formulas (4) and (5) are based

* This article was submitted by the author in English.
** Pomorskiĭ State University, Arkhangel'sk, Russia.

[8] on the following well-grounded assumptions: quasistationary approximation

$$\Gamma_{ns} \gg \lambda \tag{6}$$

and the total depletion of hadrons from the *ns* state in the time interval between collisions $1/\nu_{\text{coll}}$,

$$\Gamma_{ns} \gg \nu_{\text{coll}}. \tag{7}$$

Here, λ is the maximal value of the rates of Auger, radiative, and Coulomb transitions. In accordance with (7), the *ns* state is empty before the collision ($f_{00} = 0$). The quantity $Q(\rho)$ in (5) is the population of the *ns* state immediately after the collision (before nuclear capture). Thus, before the collision, we have

$$f_{lm}(t) = \text{const}, \quad \sum_{lm} f_{lm} = 1, \quad f_{00} = 0. \tag{8}$$

Following the pioneering study of Leon and Bethe [8], all cascade calculations are based on the statistical-distribution assumption

$$f_{00} = 0, \quad f_{lm} = \frac{1}{n^2 - 1} \approx \frac{1}{n^2} \text{ at } l \neq 0. \tag{9}$$

Another assumption from [8] is that

$$Q(\rho) = \begin{cases} \dfrac{1}{n^2}, & \rho < \rho_s \\ 0, & \rho > \rho_s, \end{cases} \tag{10}$$

where $\rho_s \sim n^2/(\mu v)$ is the critical impact parameter defined in [8] (hereafter, atomic units are used: $\hbar = m_e = e = 1$). The approximation in (10) is invalid for the case of $v > v_0 = n/\mu$ (see below), because the large long-range ($\rho > \rho_s$) logarithmic contribution to Γ is omitted here. It was corrected in [9], but the assumption in (9) was admitted (note that the general theory of Stark transitions was independently developed in [10–13]). Below, it will be shown (this is the main result of our study) that the statistical distribution (9) is not valid for heavy hadronic atoms. This results in a significant deviation of Γ from the values Γ_{BL} obtained on the basis of [8, 9].

2. DIFFUSION REGIME OF STARK MIXING

Let us propose in advance that the main contribution to Γ comes from collisions with impact parameters that are larger than the radius of the hadronic orbit $r \sim n^2/\mu$:

$$\rho \gg n^2/\mu. \tag{11}$$

In any case [see (3)], we have

$$v < 1/n. \tag{12}$$

From (11) and (12), one concludes that the typical collision time ρ/v exceeds the period of orbital motion, $T = n^3/\mu$:

$$\frac{\rho}{v} \gg \frac{n^3}{\mu}. \tag{13}$$

In other words, the inequalities in (11) and (13) mean that perturbations of Keplerian orbits of the (K^-p) atom by the electric field $\mathbf{E} = \mathbf{R}/R^3$ of the other proton in (1) are small, that their relative velocity $\dot{\mathbf{R}}(t)$ is sufficiently small in relation to the high velocity $\dot{\mathbf{r}}(t)$ of the internal motion of a hadronic atom, and that the dipole approximation for the interaction between them is applicable. After averaging over fast internal motion, we can easily obtain equations well known in astronomy as "slow" motion (as the terms of "old" quantum mechanics, they were used in [14]):

$$\begin{aligned} \dot{\mathbf{l}} &= \mathbf{\Omega} \times \mathbf{u}, \\ \dot{\mathbf{u}} &= \mathbf{\Omega} \times \mathbf{l}, \\ \dot{n} &= 0, \quad (\dot{E} = 0). \end{aligned} \tag{14}$$

Here, $\mathbf{l} = \mathbf{r} \times \mu\dot{\mathbf{r}}$ is atomic orbital angular momentum; $\mathbf{\Omega} = \dfrac{3n}{2\mu}\mathbf{E}$; and $\mathbf{u} = n\mathbf{A}$, where $\mathbf{A}$ is the Runge–Lenz vector, directed from one Keplerian ellipse focus to the other, $|\mathbf{A}| = \varepsilon = \sqrt{1 - \dfrac{l^2}{n^2}}$ being the eccentricity of the Keplerian orbit. A completed set of equations for slow motion is obtained by adding, to (14), the third equation for the relative motion [15]. Our problem is much simpler because, at large energies (3), the approximation of straight-line trajectories for relative motion is applicable:

$$\mathbf{R} = \boldsymbol{\rho} + \mathbf{v}t. \tag{15}$$

It follows from (14) and (15) that the admissible regimes are

$$b \gg 1 \tag{16}$$

for "strong" collisions and

$$b \ll 1 \tag{17}$$

for "weak" collisions (or "diffusion" regime). Here, we denoted by

$$b = |\mathbf{b}| \sim \frac{n}{\mu v \rho} \tag{18}$$

the main dimensionless parameter of Stark mixing,

$$\mathbf{b} = \int_{-\infty}^{+\infty} \mathbf{\Omega} dt = \frac{3n}{\mu v \rho}\hat{\boldsymbol{\rho}}, \quad \hat{\boldsymbol{\rho}} = \boldsymbol{\rho}/\rho. \tag{19}$$

For $b \gg 1$, the orbit is deformed many times during the collision. This corresponds to the case of $\rho < \rho_s$ in Bethe–Leon theory. For $b \ll 1$, the perturbation of the orbit in one collision is small. In each collision, the extreme points of the vectors $\mathbf{l}$ and $\mathbf{A}$ undergo the small random jumps

$$\Delta\mathbf{l} = \mathbf{b} \times n\mathbf{A}, \quad n\Delta\mathbf{A} = \mathbf{b} \times \mathbf{l}; \tag{20}$$

i.e., the vector extreme points execute diffusion motion.

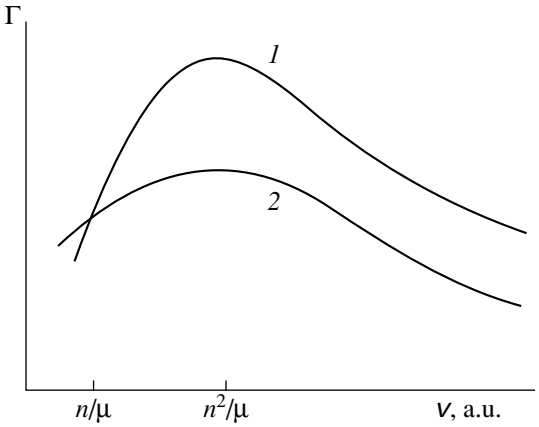

Qualitative dependences of effective nuclear-capture rates on the hadronic-atom velocity (in a.u.): (curve *1*) Γ from the diffusion formula (31) (valid for $v > n/\mu$) and (curve *2*) values Γ_{BL} from [8, 9] (valid only for $v < n/\mu$—that is, for "strong" collisions).

The regions of strong and diffusion collisions are, respectively, $\rho < \rho_0$ and $\rho > \rho_0$, where $\rho_0 = n/(\mu v)$. One should also take into account the screening due to electrons; that is,

$$\mathbf{E}(R) \approx \frac{\mathbf{R}}{R^3} e^{-2R}(1 + 2R + 2R^2). \tag{21}$$

This means that only collisions with impact parameters

$$\rho < 1 \tag{22}$$

are of importance. If $\rho_0 > 1$, which corresponds to

$$v < v_0, \quad v_0 = n/\mu, \tag{23}$$

then all important collisions are strong ones, the distribution f_{lm} is statistical (9), and the results from [8, 9] for Γ are true: $\Gamma \approx \Gamma_{BL}$. Note that, for the most important states (2), the values of the boundary kinetic energy $\varepsilon_0 = M v_0^2/2$ are the following:

$$\begin{aligned} &\text{for } (K^- p), (\bar{p} p) \quad \varepsilon_0 \sim 2 \text{ eV}, \\ &\text{for } (\pi^- p), (\mu^- p) \quad \varepsilon_0 \sim 7 \text{ eV}. \end{aligned} \tag{24}$$

The estimate in (24), together with (3), means that a major fraction of heavy hadronic atoms exist in the diffusion regime of Stark mixing. The distribution $f \equiv f_{lm}$ in this case is far from a statistical one and obeys the kinetic equation of the Fokker–Planck type (see Appendix 1):

$$\begin{aligned} &\frac{\partial f}{\partial t} = \frac{1}{l}\frac{\partial}{\partial l}\left(l D_0 \frac{\partial f}{\partial l}\right) + qf, \\ &D_0 = a\left(1 - \frac{l^2}{n^2}\right), \quad a = \frac{3\pi n^4 N \Lambda}{\mu^2 v}, \quad \Lambda = \ln\left(\frac{\mu v}{n}\right). \end{aligned} \tag{25}$$

Note that the main contribution to D_0 comes from large impact parameters satisfying condition (11)—this fact confirms the assumption in (11).

In (25), the symbol q is the difference between the atomic flow incoming to the n level (from upper Rydberg levels) and the outcoming (to lower Rydberg levels) one. This difference is equal to the diffusion flow

$$J(l) = 2 D_0 l \frac{\partial f}{\partial l} \tag{26}$$

of atoms with the same n to a region of low l values ($l < l_0 \approx 1$; see Appendix 2), where nuclear capture occurs. Taking into account the normalization to unity (8), one obtains:

$$\Gamma = J(l = l_0). \tag{27}$$

The boundary conditions to (25) are

$$f(l_0, t) = 0, \quad f(n, t) < \infty. \tag{28}$$

The former follows from (8). The latter is equivalent to $J(l = n) = 0$ [see (26)]; i.e., the value $l = n$ is the natural boundary of the problem—the region $l > n$ is an unphysical one and therefore does not exist. As we will see below, all physical quantities depend on l_0 only slightly, and we need not know it exactly. For computer simulations (see Appendix 2), the best value of l_0 is $l_0 = 1$.

In accordance with (8), it is sufficient to consider the steady regime, $\partial f/\partial t = 0$,

$$\frac{1}{l}\frac{d}{dl}\left(l D_0 \frac{df}{dt}\right) + qf = 0. \tag{29}$$

The solution to (29) is (Appendix 1)

$$f \approx \frac{1}{n^2}\left[1 - \frac{1}{\Lambda_1}\ln\left(\frac{n}{l}\right)\right] = \frac{1}{n^2 \Lambda_1}\ln\left(\frac{l}{l_0}\right), \tag{30}$$

where $\Lambda_1 = \ln(n/l_0) \approx \ln n$. From (26), (27), and (30), we have

$$\Gamma = \frac{6\pi n^2 \Lambda N}{\mu^2 \Lambda_1 v}. \tag{31}$$

Note that all quantum-mechanical effects are absorbed in the arguments of large logarithms, which confirms the applicability of a classical consideration.

A comparison of (31) with the Bethe–Leon values Γ_{BL} [8, 9] is presented in the figure. According to [8, 9], at $v \gg n^2/\mu$ we have

$$\Gamma_{BL} = \frac{2\pi n^2 N}{3\mu^2 v}\Lambda_{BL}, \quad \Lambda_{BL} = \ln\left(\frac{\mu v}{n^2}\right). \tag{32}$$

The simplest way to obtain the result in (32) is to use (4) and (5) and to calculate the probabilities P to the first order of perturbation theory in the dipole interaction $\hat{V} = \mathbf{r} \cdot \mathbf{E}(\mathbf{R})$ of $(K^- p)$ and p. Taking into account

the dipole selection rules and neglecting the screening, one obtains

$$\Gamma_{\mathrm{BL}} = \frac{Nv}{n^2-1}\int_0^\infty 2\pi\rho d\rho S(\rho) = \frac{2\pi n^2 N}{3\mu v}\ln\left(\frac{\rho_{\max}}{\rho_{\min}}\right),$$

$$S(\rho) = \sum_m P(n1m \longrightarrow n00)$$

$$\approx \sum_m \left|\int_{-\infty}^{+\infty} dt\hat{\mathbf{V}}_{n1m,\,n00}\right|^2 = \frac{n^2(n^2-1)}{3\mu^2 v^2\rho^2}.$$

Here, $\rho_{\max} \sim 1$ (because of screening) and $\rho_{\min} \sim n^2/(\mu v) \sim \rho_s$. The latter is obtained from the condition $P < 1$, which is violated at $\rho \sim \rho_{\min}$. It is worth mentioning that the result in (32), which is based on the incorrect assumption (9), is not true. It is presented here only in order to demonstrate the mistake one obtains using the results from [8, 9] in the high-energy region $\varepsilon > \varepsilon_0$ (this happened in interpretation of experiments [5, 6]):

$$\xi_0 = \frac{\Gamma}{\Gamma_{\mathrm{BL}}} = \frac{9\Lambda}{\Lambda_1\Lambda_{\mathrm{BL}}}.$$

By using (2) and (3), we get $\xi_0 \sim 5$–10. The reason for this difference is the distortion of the statistical distribution with respect to the angular momentum in the diffusion regime of Stark mixing [compare (30) and (9)].

3. PROBABILITY P TO ACHIEVE THE $2p$ STATE

This probability is important for planned experiments because it determines the total yield Y of K x rays per hadron stopped in the target:

$$Y \approx P. \tag{33}$$

A more rigorous way to calculate Y is presented in Appendix 2. Here, Y will only be estimated.

In the approximation of continuous n (appropriate for $n \gg 1$), we have

$$P = \exp(-S), \quad S = \int_0^\tau \Gamma dt = \int_2^{n_0}\Gamma\left(-\frac{dn}{dt}\right)dn. \tag{34}$$

Here, τ is the time interval for the cascade from initial states $n \sim n_0 = \sqrt{M_h}$ when the atom was formed,

$$-\frac{dn}{dt} = \Gamma_{\mathrm{A}} + \Gamma_\gamma + \Gamma_{\mathrm{C}}, \tag{35}$$

where Γ_{A}, Γ_γ, and Γ_{C} are the rates of Auger, radiative, and Coulomb deexcitation processes for the level n. A more rigorous formula for S is

$$S = \sum_{n=2}^{n_0} S_n, \quad S_n = \frac{\Gamma}{\Gamma_{\mathrm{A}} + \Gamma_\gamma + \Gamma_{\mathrm{C}}}. \tag{36}$$

The quasistationary approximation applied here is not true only at the first steps of the cascade just after atom formation, when the distribution f_{lm} is statistical. Shortly after, it becomes distorted and is defined by (30). It follows from (30) that the fraction of the hadrons captured during this nonstationary period is negligible ($\sim 1/\Lambda_1$)—approximately, it is equal to

$$\int_0^n 2ldl[f(n) - f(l)].$$

According to [8], for the Auger rate we get the expression

$$\Gamma_{\mathrm{A}} = \frac{16\pi N}{3p}\langle r^2\rangle \approx \frac{4n^{11/2}N}{\mu^{5/2}}, \tag{37}$$

where $p = \sqrt{2\omega_{fi}}$ is the momentum of the ejected electron, $\omega_{fi} = E_n - E_{n'} \approx \omega_k = \omega_k$, $k = n - n'$, and $\omega = n^3/\mu$. In formula (37), the following expression for the averaged square of the matrix element of the dipole transition was used [2]:

$$\langle r^2\rangle = \sum_{lm,\,l'm'} |\mathbf{r}_{nl'm',\,nlm}|^2 f_{lm} \approx 0.37\frac{n^4}{\mu^2 k^4}. \tag{38}$$

This formula is valid in the classical limit $n \gg 1$ and can be derived from the Bohr correspondence rule: for $n \gg 1$, the matrix element is approximately equal to the Fourier component. The main contribution to (38) comes from the range $l \sim n$, where the distortion of f_{lm} is negligible, and it can be replaced by the statistical distribution. In (37), only one-quantum Auger transitions ($n \longrightarrow n-1$, $k = 1$) were taken into account, others ($k \geq 2$) being neglected (an uncertainty is roughly 5%).

In the limiting case of $n \gg 1$, we have

$$\Gamma_\gamma = \sum_{k=1}^{n-1} k\frac{4\omega_{fi}^3}{3c^3}\langle r^2\rangle \approx \frac{\mu}{3c^3 n^4}. \tag{39}$$

The main contribution to Γ_γ comes from transitions to the deep states $k \sim n$—i.e., from small l values in (38), where the distortion of f_{lm} is sizable. This effect is taken into account in (39): it gives an additional factor of about 0.6 [for values n from (2)].

The rate Γ_{C} of Coulomb transitions in the denominator of (36) does not affect S_n values significantly. Below, we present only a rough estimate of Γ_{C}. The internal energy E is governed by the equation [compare with (3)]

$$\frac{d|E|}{dt} \approx \xi\lambda_{\mathrm{C}}|E|, \tag{40}$$

where

$$\lambda_{\mathrm{C}} = \pi\rho_{\mathrm{C}}^2 Nv = \frac{2\pi n^2 N}{M\mu v} \tag{41}$$

Table 1. Values of S_n at $\varphi = 0.05$ for accelerated protium kaonic atoms in hydrogen [probability of avoiding the capture into the level n is equal to $\exp(-S_n)$]

n	2	3	4	5	6	7	8	9	10	$\sum_{n=11}^{n_0}$
S_n	0.3	2.5	6.4	6	3.5	1.7	1.0	0.6	0.4	2

is the rate of inelastic Coulomb collision (1). Here, ρ_C is the critical impact parameter for the collision followed by the capture of a hadronic atom by a proton due to dipole–charge interaction:

$$\frac{d}{\rho_C^2} \sim \frac{Mv^2}{2}, \quad d = er \sim \frac{n^2}{\mu}.$$

Substituting the energy $|E| = \mu/(2n^2)$ into (40), one obtains

$$-\frac{dn}{dt} = \Gamma_C, \quad \Gamma_C = \xi\lambda_C n/2. \tag{42}$$

The values of S_n for (K^-p) atoms with the energy specified by (3) and the hydrogen density $\varphi = 0.05$ (conditions of the proposal from [16]) are presented in Table 1. It follows that $S = 24.4$; i.e., accelerated (K^-p) atoms entirely decay at high Rydberg states $n \sim 6$. This conclusion holds for all types of hadronic atoms, including the (π^-p) atom; for all reasonable densities, the latter is due to a very weak dependence on φ:

$$S \sim \varphi^{3/19}. \tag{43}$$

A general conclusion from above is that only nonaccelerated hadronic atoms can achieve the $n = 2$ state. More strictly speaking, only those atoms can survive that remain in the "strong" Stark collision region $\varepsilon < \varepsilon_0$, where Γ is less than the diffusion value ($\varepsilon > \varepsilon_0$). Just after formation in the process $K^- + H \longrightarrow (K^-p) + e$, atoms are in the region $\varepsilon < \varepsilon_0 = Mn_0^2/2\mu^2$. Similarly to (32), the probability to remain nonaccelerated (to remain "slow") is

$$P_s = \exp(-a), \quad a = \sum_{n=2}^{n_0} a_n,$$
$$a_n = \frac{\lambda_a^{(0)}(n)}{\Gamma_A + \Gamma_\gamma + \Gamma_C^{(0)}}. \tag{44}$$

Here, $\lambda_a^{(0)}(n)$ is the rate of acceleration due to Coulomb transitions (1) (the probability per unit time). A rough estimation yields

$$\lambda_a^{(0)} = \beta\lambda_C^{(0)}, \quad \beta \sim 0.5. \tag{45}$$

The subscript "zero" here indicates that the velocity $v = v_0 = n/\mu$ should be inserted into each formula.

The values of a_n for $\beta = 0.5$ and $\varphi = 0.05$ are presented in Table 2. This results in $a = 3.1$ and

$$P_s = 0.05. \tag{46}$$

For $\beta = 0.5$ and $\varphi = 0.01$, we similarly obtain

$$P_s = 0.15. \tag{47}$$

It is seen from the above that the theory from [8, 9] is applicable to "slow" atoms. From this theory, similarly to (34) and (36), we obtain, for slow atoms, $Y_s = 0.02$ (at $\varphi = 0.05$). This result is in agreement with the calculation from [17], which is based on [8, 9].

The resulting (observed) yield is

$$Y = Y_s P_s. \tag{48}$$

Taking into account the values from (46) and (47) and the dependence in (43), which is also true for slow atoms, we obtained the values presented in Table 3. Of course, the parameter β in (45) is determined with large uncertainty: $\beta = 0.3$–0.5. The appropriate results for $\beta = 0.5$ and $\beta = 0.3$ are presented in Table 3. The actual values are confined between these "boundary" values.

The effect of acceleration is less important for deuterium kaonic atoms than for (K^-p). In this case, we obtain the estimate $P_s \sim 0.5$. It means that, for (K^-d) atoms, the total yield is

$$Y \sim 0.5 Y_s, \tag{49}$$

where Y_s is the value calculated within the "standard" cascade model [17].

Table 2. Values of a_n at $\varphi = 0.05$ for protium kaonic atoms in hydrogen

n	2	3	4	5	6	7	$\sum_{n=8}^{n_0}$
a_n	0.07	0.5	0.6	0.6	0.5	0.3	0.5

Table 3. Values of P_s, Y_s, and Y for protium kaonic atoms at $\varphi = 0.05$ (Frascati proposal [16]) and $\varphi = 0.01$ (KEK [18]) for two values of the parameter β in (45)

		P_s	Y_s, %	Y, %
$\varphi = 0.05$	$\beta = 0.5$	0.05	2	0.1
	$\beta = 0.3$	0.14	2	0.3
$\varphi = 0.01$	$\beta = 0.5$	0.15	7	1
	$\beta = 0.3$	0.3	7	2

4. CONCLUSION

Nuclear capture in hadronic atoms of hydrogen isotopes essentially depends on their kinetic-energy distribution. Roughly speaking, there are two regions: $\varepsilon < \varepsilon_0$ and $\varepsilon > \varepsilon_0$. The majority of light atoms $(\mu^- X)$ and $(\pi^- X)$ (where $X = p, d, t$) correspond to energies from the first region ($\varepsilon < \varepsilon_0$); hence, such atoms are statistically distributed among (l, m) states. An accelerated fraction of them ($\varepsilon > \varepsilon_0$) is small (~10%), and the (l, m) distribution of such $(\pi^- p)$ atoms is distorted and considerably deviates from the statistical distribution as the result of a specific (diffusion) regime of Stark mixing. The resulting decay rates for these atoms are at least five times larger than those calculated within the standard Bethe–Leon theory [8, 9]. This provides a novel treatment of the experiments reported in [5, 6], which were devoted to direct measurements of the distribution of $(\pi^- p)$ atoms: the accelerated fraction is about 10%, and the rates of the Coulomb transitions are compatible with quantum-mechanical estimates [2–4]. In the opposite case of heavy atoms $(K^- X)$, $(\bar{p} X)$, …, the majority of them [about 90% for $(K^- p)$] at $\varphi = 0.05$) are accelerated to $\varepsilon > \varepsilon_0$ and are described by the nonstatistical distribution (30). Virtually all of them decay before reaching the $n = 2$ state. About 10% of atoms remain nonaccelerated. The capture rate for nonaccelerated atoms is moderate and about 2% of such $(K^- p)$ atoms at $\varphi = 0.05$ achieve the $n = 2$ state. Hence, the resulting yield of K x rays emitted in the $2p \longrightarrow 1s$ transition is about $Y = 0.1 \times 0.02 = 0.002$ (that is, 0.2%). At $\varphi = 0.01$ for $(K^- p)$ atoms, we have $1 < Y < 2\%$ (see Table 3).

Of course, a more detailed analysis of cascade processes is desirable. It is described in Appendix 2, and the appropriate results will be published later. The main result of this paper is to expose a new regime of Stark mixing resulting in the distortion of the angular-momentum distribution and increasing of effective nuclear-capture rates.

ACKNOWLEDGMENTS

The hospitality of Prof. W.H. Breunlich, who informed me about this problem, and the support of the Austrian Academy of Sciences and of the Institute of Medium Energy Physics are gratefully acknowledged.

APPENDIX 1

Deriving and Solving the Diffusion Equations (25) and (26)

To simplify the derivation, we introduce a new variable $\mathbf{r}$ $(0 < r < 1)$ instead of $\mathbf{l}$: $\mathbf{r} = \hat{\mathbf{l}}\,(l/n)^{2/3}$, where $\hat{\mathbf{l}} = \mathbf{l}/l$. The number of quantum states (lm) for the interval $(l, l + dl)$ is

$$dN_{\rm st} = 2l dl = n^2 \frac{4\pi r^2 dr}{V_0} = n^2 \frac{d^3 r}{V_0}, \qquad V_0 = \frac{4\pi}{3}. \tag{A.1}$$

From (A.1), the advantage of $\mathbf{r}$ is clear: quantum states are distributed uniformly over the $\mathbf{r}$ space, while the density of states is nonuniform over $\mathbf{l}$ space.

In order, to find the populations $f \equiv f_{lm}(t)$, one should generally write and solve the kinetic equation

$$\frac{\partial f_{lm}}{\partial t} = -f_{lm}\lambda_{lm} + \sum_{l'm'} \lambda_{l'm',\,lm} f_{l'm'}, \tag{A.2}$$

where $\lambda_{lm} = \sum_{l'm'} \lambda_{l'm',\,lm}$ and $\lambda_{l'm',\,lm}$ is the rate of the $(lm) \longrightarrow (l'm')$ transition. These rates can be calculated as in [9]. In this paper, we restrict ourselves to the diffusion regime (17). In this case, equation (A.2) becomes simpler; it is a Fokker–Planck equation for a standard Markov diffusion process of particles in $\mathbf{r}$ space:

$$\frac{\partial f}{\partial t} = -\frac{\partial j_\alpha}{\partial x_\alpha}, \quad j_\alpha = -D_{\alpha\beta}\frac{\partial f}{\partial x_\beta}. \tag{A.3}$$

Here and below, summation over dummy subscripts is performed. In (A.3) (see [19]),

$$D_{\alpha\beta} = \frac{1}{2}\left\langle \frac{\Delta x_\alpha \Delta x_\beta}{\tau} \right\rangle \tag{A.4}$$

are the diffusion coefficients, which, in general, are components of a tensor. Averaging over the possible collisions is performed in (A.4), τ is the time period between them, and $\mathbf{j}$ is the diffusion flow of particles.

Let us consider a region Ω in $\mathbf{r}$ space (or a corresponding sector in $\mathbf{l}$ space). The number of particles in this region is

$$N_p = \int_\Omega f dN_{\rm st} = \frac{n^2}{V_0}\int_\Omega f d^3 r = \int_\Omega 2l dl f. \tag{A.5}$$

In the last equality, we considered that f_{lm} does not depend on m. From (A.3) and (A.5), we obtain the balance equation

$$\frac{dN_p}{dt} = \frac{n^2}{V_0}\int_\Omega \frac{\partial f}{\partial t} d^3 r = -\frac{n^2}{V_0}\int_\Omega (\nabla \cdot \mathbf{j}) d^3 r = -\int_{\partial\Omega} \mathbf{J} \cdot \mathbf{df}, \tag{A.6}$$

where $\partial\Omega$ is the boundary of Ω, $\mathbf{df}$ is an external element of surface on this boundary, and $\mathbf{J} = \mathbf{j}n^2/V_0$ is a real flow of particles. If we have only one particle with a quantum number n, then

$$\int_{l_0 < l < n} f dN_{sl} = \frac{n^2}{V_0}\int f d^3 r = \int_{l_0}^{n} 2l dl f = 1, \tag{A.7}$$

and the flow **J** determines the number of particles coming into a capture region $l < l_0$ per unit time; i.e., the effective nuclear-capture rate is

$$\Gamma = -4\pi r^2 J_r(r) = -4\pi r^2 \frac{n^2}{V_0} D_{rr} \frac{\partial f}{\partial r} = -2D_0 l \frac{\partial f}{\partial l} \equiv J(r), \quad \text{(A.8)}$$

where $r \longrightarrow r_0 = (l_0/n)^{2/3}$, $l \longrightarrow l_0$,

$$D_{rr} = \hat{\mathbf{r}}_\alpha \hat{\mathbf{r}}_\beta D_{\alpha\beta}, \quad \hat{\mathbf{r}} = \mathbf{r}/r, \quad D_0 = \frac{1}{2}\left\langle \frac{(\Delta l)^2}{\tau} \right\rangle. \quad \text{(A.9)}$$

We have considered that

$$\frac{\partial f}{\partial x_\alpha} = \hat{\mathbf{r}}_\alpha \frac{\partial f}{\partial l}, \quad D_{\alpha\beta}\hat{\mathbf{r}}_\beta = D_{rr}\hat{\mathbf{r}}_\alpha.$$

Similarly to (A.8), (A.3) is transformed back to the variable l:

$$\frac{\partial f}{\partial t} = \frac{1}{l}\frac{\partial}{\partial l}\left(l D_0 \frac{\partial f}{\partial l} \right). \quad \text{(A.10)}$$

The steady-state regime is achieved owing to the resulting flow to our n level from other Rydberg levels. Hence, in a single collision, $|\Delta l| \ll n$, this flow is proportional to f, as in (25). Integration of (29) with respect to $2ldl$, as in (A.7), gives the balance condition

$$q = \Gamma. \quad \text{(A.11)}$$

After averaging over the directions of $\hat{\rho}$, we find from (19), (20), and (A.9) that

$$D_0 = \frac{1}{2}n^2\left\langle \frac{1}{\tau}(\hat{\mathbf{l}} \cdot (\mathbf{b} \times \mathbf{A}))^2 \right\rangle = \frac{1}{6}n^2 A^2 \left\langle \frac{b^2}{\tau} \right\rangle = \frac{1}{6}n^2\left(1 - \frac{l^2}{n^2}\right)\left\langle \frac{b^2}{\tau} \right\rangle,$$

$$\left\langle \frac{b^2}{\tau} \right\rangle = N v \int_0^{+\infty} 2\pi\rho d\rho \left(\frac{3n}{\mu v \rho}\right)^2 = \frac{18\pi n^2 N}{\mu^2 v}\Lambda, \quad \Lambda = \ln\left(\frac{\rho_{\max}}{\rho_{\min}}\right). \quad \text{(A.12)}$$

Here, $\rho_{\max} \sim 1$ (see the end of Section 1). Our considerations are true under the conditions $b \ll 1$ and $\rho \gg r = n^2/\mu$; therefore [see (12)]

$$\rho_{\min} = \max\left(\frac{n}{\mu v}, \frac{n^2}{\mu}\right) = \frac{n}{\mu v}, \quad \text{(A.13)}$$

and we obtain (26).

In accordance with (28), $f \longrightarrow f_0 < \infty$ for $l \longrightarrow n$. Since q is small, we therefore find a solution to (29) at $l \sim n$ in the form $f = f_0[1 + S(l)]$, where $S(n) = 0$, $|S| \ll 1$. Solving the equation for S,

$$\frac{1}{l}\frac{d}{dl}\left[l\left(1 - \frac{l^2}{n^2}\right)\frac{dS}{dl} \right] + \frac{q}{a} = 0,$$

one obtains

$$f = f_0\left[1 - \frac{qn^2}{2a}\ln\left(\frac{n}{l}\right)\right]. \quad \text{(A.14)}$$

Since q is small, we assume that

$$\frac{qn^2}{2a} \ll 1. \quad \text{(A.15)}$$

From (A.15), it follows that (A.14) holds also in the region $l \ll n$ (but not in the limit $l \longrightarrow l_0$).

Let us now consider the region

$$l \ll n, \quad \text{(A.16)}$$

where the ratio l^2/n^2 in the factor D_0 can be omitted, which leads to the Bessel equation

$$f = C_1 J_0(x) + C_2 Y_0(x), \quad x = l\sqrt{\frac{q}{a}}.$$

From (A.15) and (A.16), it follows that $x \ll 1$; hence, in the case (A.16), we arrive at

$$f = C_3 \ln\left(\frac{l}{l_0}\right) = C_3\Lambda_1\left[1 - \frac{1}{\Lambda_1}\ln\left(\frac{n}{l}\right)\right], \quad \text{(A.17)}$$

where $\Lambda_1 = \ln(n/l_0)$, and we take into account (28). The regions of applicability of (A.14) and (A.17) overlap; therefore, we can simply compare (A.14) and (A.17). This gives $C_3\Lambda_1 = f_0$ and

$$f = f_0\left[1 - \frac{1}{\Lambda_1}\ln\left(\frac{n}{l}\right)\right], \quad \text{(A.18)}$$

$$\frac{qn^2}{2a} = \frac{1}{\Lambda_1}. \quad \text{(A.19)}$$

Inequality (A.15) follows from (A.19). After integrating (A.7), it is easy to find f_0 and to obtain (30). Thus, the result in (31) follows directly from (A.8). Therefore, the accuracy of (31) is above $\sim 1/\Lambda_1$. Within this accuracy, the result in (31) remains true for q dependent on l.

APPENDIX 2

Scheme of a Purely Classical Calculation

The above calculations combine a quantum and a classical treatment. For large n, it seems reasonable to be restricted to a classical consideration. This makes it possible to obtain the more accurate results for the yield Y of K x rays and for other characteristics of the cascade.

All particles in reaction (1) (K^- and both protons) move along the classical trajectories. If the angular

momentum becomes small ($l < l_0$) after a collision, this is equivalent to the capture of a hadron by a nucleus. As we demonstrated in Appendix 1, the exact value of l_0 and all other quantum values are inoperative in the diffusion regime: all of them are contained in the arguments of large logarithms. The value of l_0 is important in the regime of strong collisions. In this sense, such a regime can be considered as more "quantum" than the first one. In the case of $v < v_0$, the angular distribution becomes statistical after each collision (see [8] and above), and collisions occur with average frequency $\nu_{\text{coll}} = \pi\rho_s^2 Nv$. The population of the *ns* state just after a collision will be

$$f_{00} = 1/n^2. \tag{A.20}$$

It is the quantum-mechanical picture for strong collisions.

In a classical picture, the distribution after a collision is microcanonical; i.e.,

$$dW = Ad^3pd^3r\delta\left(\frac{p^2}{2\mu} - \frac{1}{r} - E\right), \tag{A.21}$$

where $A = (\pi^3 r_0^{5/2}\sqrt{2\mu})^{-1}$ ($\int dW = 1$), $n = (\mu/2|E|)^{1/2}$, and $r_0 = 1/|E| = 2n^2/\mu$. Let us also determine the classical Keplerian frequency $\omega = \mu/n^3$.

It follows from (A.21) that, at each point, the motion is isotropic: the momentum vector $\mathbf{p}$ is uniformly distributed over the solid angles. The r distribution is obtained from (A.21) after integration with respect to d^3p:

$$dW_r = \frac{16}{\pi r_0^{5/2}}\sqrt{\frac{1}{r} - \frac{1}{r_0}}r^2 dr\theta(r_0 - r). \tag{A.22}$$

Using (A.21) and

$$dW_l = d(l^2)\int\delta[l^2 - (\mathbf{r}\times\mathbf{p})^2]dW$$

and performing integration with respect to $\mathbf{p}$ and $\mathbf{r}$, one obtains the statistical distribution $dW_l = (2ldl/n^2)\theta(n - l)$, as we hoped above. The probability to find the angular momenta in the capture region $0 < l < l_0$ is equal to $W_c = l_0^2/n^2$. Comparing this result with (A.20), we obtain

$$l_0 = 1. \tag{A.23}$$

At this value of l_0, classical and quantum considerations give the same results for Γ and Y (when *ns* nuclear capture dominates).

We saw above that Stark mixing in the classical picture reduces simply to a variation of $\mathbf{l}$ and $\mathbf{A}$ in a collision. In such calculations, it is impossible to separate inelastic Coulomb transitions and Stark mixing as was done, for example, in [20], where the effects of Stark mixing in ($\bar{p}p$) atoms were taken into account twice: in calculations of classical trajectories and next through a quantum-mechanical treatment enforced from outside rather artificially. The hypothesis of the statistical distribution f_{lm} was also adopted. As we have seen, it fails for the majority of ($\bar{p}p$) atoms, i.e., for accelerated atoms, which were not taken into account either.

At last, we introduce radiative and Auger processes in the classical picture. This can be done by adding friction forces to the equation of motion. The collision time is small in relation to the period between collisions. This allows us to assume that these forces act only on the particles of the hadronic atom (*h* and *X*) and not on the incident proton. In what follows, it will be important that internal motion in the hadronic atom is periodic over intervals between collisions.

The energy radiated per second (radiative power) is [21]

$$P_\gamma = \frac{\mu^2}{3c^3n^3l^5}\left(3 - \frac{l^2}{n^2}\right).$$

This power can be obtained if one imagines that the effective electric field of radiative friction is $\mathbf{E}_\gamma = B_\gamma\dot{\mathbf{r}}$. Thus, the radiative friction force is

$$\mathbf{F}_a^\gamma = e_a\mathbf{E}_\gamma. \tag{A.24}$$

Here, $e_h = -1$, $e_X = +1$ (atomic units), and $\mathbf{r} \equiv \mathbf{r}(t) = \mathbf{r}_h(t) - \mathbf{r}_X(t)$. The averaged power of radiation is $B_\gamma\langle\dot{\mathbf{r}}^2\rangle = \frac{1}{n^2}B_\gamma$; hence,

$$B_\gamma = \frac{\mu^2}{3c^3nl^5}\left(3 - \frac{l^2}{n^2}\right).$$

Note that it is impossible to use, in computations, the standard form of radiative friction field, $\mathbf{E} = \frac{2}{3c^3}\dddot{\mathbf{d}}$. The origin is the incorrect solutions with self-acceleration in this case [21].

According to (37), the work of Auger friction forces per second (friction power) is

$$\begin{aligned} P_{\text{A}} &= -\frac{16\pi N}{3\sqrt{2}}\sum_f\sqrt{\omega_{fi}}|\mathbf{r}_{fi}|^2 \\ &\approx -\frac{16\pi N}{3\sqrt{2}}\sum_{k=1}^{\infty}\sqrt{\omega_k}|\mathbf{r}_k|^2, \end{aligned} \tag{A.25}$$

where, in accordance with Bohr's correspondence principle, we replace ω_{fi} and matrix element $\mathbf{r}_{fi}$ by their classical values: the frequencies of Fourier harmonics, $\omega_k = \omega k$, and harmonics of the trajectory $\mathbf{r}_k$ for unperturbed Keplerian orbital motion of hadron $\mathbf{r}(t)$:

$$\mathbf{r}_k = \frac{1}{T}\int_0^T\mathbf{r}(t)e^{i\omega_k t}dt.$$

It is remarkable that (A.25) can be rewritten in the form

$$P_{\text{A}} = \langle\mathbf{F}(t)\dot{\mathbf{r}}(t)\rangle,$$

where the effective force of radiative friction is

$$\mathbf{F}(t) = \int_{-\infty}^{+\infty} Q(t-t')\dot{\mathbf{r}}(t')dt'. \qquad \text{(A.26)}$$

Here, averaging is performed over the Keplerian motion. Note that, in (A.26), **F** depends not only on the past but also on the future.

This causal contradiction is a consequence of our approximations and of the quantum-mechanical character of the ejected-electron motion. Because of the energy–time uncertainty principle $\Delta E\tau \sim \hbar$, we are not able to answer the question of what happens earlier: electron ejection or hadronic transition. To avoid this trouble, we neglect, in (A.25), the contributions for $k \geq 2$. This gives a tolerant error about 7%. Afterward, we will make corrections in final formulas. The next step is to introduce the additional electric field in (A.24): $\mathbf{E}_\gamma \longrightarrow \mathbf{E}_\gamma + \mathbf{E}_\mathrm{A}$. Here, $\mathbf{E}_\mathrm{A} = B\dot{\mathbf{r}}$ is the real physical (but approximate) electric field acting on the particles of the hadronic atom resident inside the electron cloud. The atom distorts this cloud; hence, the additional electric field arises. With allowance for this field, the equations of motion assume the form

$$M_h\ddot{\mathbf{r}}_h = -\mathbf{E}_\mathrm{A} - \frac{\mathbf{r}}{\mathbf{r}^3}, \quad M_X\ddot{\mathbf{r}}_X = \mathbf{E}_\mathrm{A} + \frac{\mathbf{r}}{\mathbf{r}^3}.$$

Thus, we have

$$\ddot{\mathbf{r}} = \ddot{\mathbf{r}}_h - \ddot{\mathbf{r}}_X = -\frac{1}{\mu}\left(\mathbf{E}_\mathrm{A} + \frac{\mathbf{r}}{\mathbf{r}^3}\right),$$

whence it follows that

$$\mu\ddot{\mathbf{r}}_h = -\mathbf{E}_\mathrm{A} - \frac{\mathbf{r}}{\mathbf{r}^3}.$$

This gives the friction power

$$P_\mathrm{A} = \left\langle \frac{d}{dt}\left(\frac{\mu\dot{\mathbf{r}}^2}{2}\right)\right\rangle = \langle \mu\ddot{\mathbf{r}}\dot{\mathbf{r}}\rangle = -B\langle\dot{\mathbf{r}}^2\rangle$$
$$= -B\sum_{k=-\infty}^{\infty}\omega_k^2|\mathbf{r}_k|^2 = -2B\sum_{k=1}^{\infty}\omega_k^2|\mathbf{r}_k|^2 \approx -2B\omega^2|\mathbf{r}_1|^2. \qquad \text{(A.27)}$$

A comparison with (A.25) (after neglecting there $k \geq 2$ terms) yields

$$B = \frac{4\pi\sqrt{2}N}{3\omega^{3/2}}.$$

From (38), it is easy to estimate the error in (A.27) and to correct it.

Finally, one concludes that radiative and Auger transitions are taken into account by introducing the electric field

$$\mathbf{E} = D\dot{\mathbf{r}}, \quad D = B_\gamma + \frac{4\pi\sqrt{2}N}{3\omega^{3/2}}\beta. \qquad \text{(A.28)}$$

This field acts only on the particles of hadronic atom. Here, $\beta \approx 2/3$ is a correction factor for either of the above two approximations.

REFERENCES

1. C. J. Batty, Yad. Fiz. **13**, 124 (1982) [Sov. J. Part. Nucl. **13**, 71 (1982)].
2. L. I. Men'shikov, Muon Catal. Fusion **2**, 173 (1988); Preprint No. IAE-4531/12 (Russian Research Centre Kurchatov Institute, Moscow, 1996).
3. W. Czaplinski, A. Gula, A. Kravtsov, *et al.*, Muon Catal. Fusion **5/6**, 59 (1990/91).
4. L. I. Ponomarev and E. A. Solov'ev, Preprint No. PSI-PR-96-18 (Villigen, 1996); Pis'ma Zh. Éksp. Teor. Fiz. **68**, 9 (1998) [JETP Lett. **68**, 7 (1998)].
5. J. E. Crawford, M. Daum, R. Frosch, *et al.*, Phys. Lett. B **213**, 391 (1988); Phys. Rev. D **43**, 46 (1991).
6. E. C. Aschenauer, K. Gabathuler, P. Hauser, *et al.*, Phys. Rev. A **51**, 1965 (1995).
7. T. B. Day, G. A. Snow, and J. Sucher, Phys. Rev. Lett. **3**, 61 (1959).
8. M. Leon and H. A. Bethe, Phys. Rev. **127**, 636 (1962).
9. J. L. Vermeulen, Nucl. Phys. B **12**, 506 (1969).
10. V. S. Lisitsa and G. V. Sholin, Zh. Éksp. Teor. Fiz. **61**, 912 (1971) [Sov. Phys. JETP **34**, 484 (1971)].
11. Yu. N. Demkov, V. N. Ostrovsky, and E. A. Solovjev, Zh. Éksp. Teor. Fiz. **66**, 125 (1974) [Sov. Phys. JETP **39**, 57 (1974)].
12. V. A. Abramov, F. F. Baryshnikov, and V. S. Lisitsa, Zh. Éksp. Teor. Fiz. **74**, 897 (1978) [Sov. Phys. JETP **47**, 469 (1978)].
13. A. K. Kazansky and V. N. Ostrovsky, Phys. Rev. A **52**, R 1811 (1995)
14. R. W. Pauli, *Lectures in Atomic Mechanics* (Nauka, Moscow, 1965).
15. L. I. Men'shikov and L. I. Ponomarev, Z. Phys. D **2**, 1 (1986).
16. R. Baldini, S. Bianco, F. L. Fabbri, *et al.*, DEAR Proposal. LNF-95/055 (IR) (Frascati,1995).
17. T. P. Terada and R. S. Hayano, Phys. Rev. C **55**, 73 (1997).
18. M. Iwasaki, R. S. Hayano, T. M. Ito, *et al.*, Phys. Rev. Lett. **78**, 3067 (1997).
19. E. M. Lifshitz and L. P. Pitaevskiĭ, *Physical Kinetics* (Nauka, Moscow, 1987; Pergamon, Oxford, 1981).
20. G. Raifenrother and E. Klempt, Nucl. Phys. A **503**, 885 (1989).
21. L. D. Landau and E. M. Lifshitz, *The Classical Theory of Fields* (Pergamon, Oxford, 1975; 6th ed., Nauka, Moscow, 1976).

Physics of Atomic Nuclei, Vol. 63, No. 5, 2000, pp. 859–869. From Yadernaya Fizika, Vol. 63, No. 5, 2000, pp. 929–939.

ELEMENTARY PARTICLES AND FIELDS
Theory

Can HERA Data Improve the LEP Constraints on the *WWV* Vertex?*

A. A. Likhoded and A. I. Onishchenko**, 1)**

Budker Institute of Nuclear Physics (Protvino Branch), Siberian Division, Russian Academy of Sciences, Protvino, Moscow oblast, 142284 Russia

Received May 19, 1999; in final form, August 17, 1999

Abstract—The combined results from $ep \longrightarrow \nu WX$, $ep \longrightarrow eWX$, and $ep \longrightarrow \nu\gamma X$ processes at HERA are used to constrain anomalous three-boson couplings. The effective model for anomalous couplings where there is no light Higgs boson and where interactions responsible for the breakdown of electroweak symmetry are strongly coupled is considered. Bounds on the couplings L_{9L} and L_{9R}, which parametrize contributions from the anomalous $WW\gamma$ (WWZ) vertices, attainable from an analysis of the distributions for the processes in question are presented. The results are compared with the bounds resulting from the LEP I and LEP II data. It is shown that the bounds coming from HERA significantly reduce the parameter region allowed by the analysis of the LEP I and LEP II data. © *2000 MAIK "Nauka/Interperiodica".*

1. INTRODUCTION

One of the main goals of the operating LEP II and of future next linear colliders is to measure the $WW\gamma$ and WWZ couplings. In the Standard Model (SM), these couplings are strictly fixed by the structure of $SU(2) \times U(1)$ symmetry, and any deviation of the couplings from the values predicted by the SM will definitively indicate the presence of new physics. It is convenient to describe the phenomenology of models with anomalous couplings in terms of the low-energy effective Lagrangians. Within this approach, effects of new physics manifest themselves as higher dimension operators modifying the couplings of observed particles, including anomalous boson couplings. This approach has a number of practical consequences in limiting the number of anomalous couplings to be studied.

In this article, we consider a class of models where interactions responsible for electroweak-symmetry breaking are strongly coupled and where there are no new particles light enough to be produced at energies below 500 GeV–1 TeV and study the effect of the lowest dimension operators that lead to anomalous contribution of the $WW\gamma(Z)$ vertex at HERA energies. Deviations from the boson self-couplings predicted by the minimal SM were studied extensively in the literature; in particular, they were discussed in the context of the HERA collider [1–6]. The main processes to probe the anomalous couplings at the HERA collider are $ep \longrightarrow \nu\gamma X$, $ep \longrightarrow eWX$, and $ep \longrightarrow \nu WX$, where X is a hadronic state. The first two processes reveal sizable cross sections, which allow one to reconstruct final states and to analyze relevant distributions for the processes. In turn, the cross section for the process $ep \longrightarrow \nu WX$ is too small, so that only isolated events can be observed at the present HERA luminosity. For this reason, the chance to probe the anomalous couplings via this process was usually neglected. We will show later, however, that this process is highly sensitive to anomalous contributions, permitting the inclusion of data on this process in the analysis as well.

There are two main distinctions between the present study and those that can be found in the literature. First, we apply the effective Lagrangian formalism allowing us to parametrize the anomalous gauge-boson interactions and to correlate them with the symmetry-breaking sector. Second, we perform a global analysis of all three processes, $ep \longrightarrow \nu\gamma X$ (eWX, νWX). Here, we pay special attention to the fact that the process $ep \longrightarrow \nu WX$, in spite of the small cross section, reveals a high sensitivity to anomalous terms and leads to bounds competitive with those from the process $ep \longrightarrow eWX$ and more stringent than those coming from the data on radiative charged-current scattering.

This article is organized as follows. In Section 2, we briefly summarize the effective Lagrangian formalism used to describe anomalous couplings. In Section 3, we present the results of our calculations for the HERA processes. In Section 4, we present bounds on the anomalous couplings parametrizing the triple boson vertex and compare these bounds with those coming from LEP I and LEP II data. Finally, we summarize our results.

* This article was submitted by the authors in English.

** e-mail: likhoded@mx.ihep.su
*** e-mail: onishchenko@heron.itep.ru
1) Institute for Theoretical and Experimental Physics, Bol'shaya Cheremushkinskaya ul. 25, Moscow, 117259 Russia.

2. FORMALISM FOR ANOMALOUS COUPLINGS

Introducing anomalous boson interactions, we want to describe the case where, for the electroweak-symmetry-breaking sector, there is no light Higgs boson and where the low-energy particle content is essentially the same as that in the minimal SM, provided that Higgs boson is taken to be very heavy. This model can be written as the usual Standard Model, but the scalar sector must then be replaced by the effective Lagrangian [7]

$$\mathcal{L}^{(2)} = \frac{v^2}{4}\mathrm{tr}(D^\mu\Sigma^\dagger D_\mu\Sigma).$$

Here, the matrix $\Sigma \equiv \exp(i\boldsymbol{\omega}\cdot\boldsymbol{\tau}/v)$ contains the would-be Goldstone bosons ω_i that give the gauge bosons their mass via the Higgs mechanism, the $SU(2)_L \times U(1)_Y$ covariant derivative is given by

$$D_\mu\Sigma = \partial_\mu\Sigma + \frac{i}{2}gW_\mu^i\tau^i\Sigma - \frac{i}{2}g'B_\mu\Sigma\tau_3,$$

and $v \approx 246$ GeV. This case was considered at length in the literature [7, 8], and we used it previously for processes incorporating triple [9] and quartic boson interactions [10]. In this model, anomalous gauge-boson couplings correspond to the contributions from higher dimension operators that are invariant under the $SU(2)_L \times U(1)_Y$ gauge group. The next-to-leading-order (NLO) effective Lagrangian that arises in the context of this model and the contributions of this Lagrangian to the anomalous couplings were discussed in the literature [7, 8].

It became common to write the most general C- and P-invariant VW^+W^- vertex (where $V = Z, \gamma$) in the form [11]

$$\begin{aligned}\mathcal{L}_{WWV} = &-ie\frac{c_\mathrm{W}}{s_\mathrm{W}}g_1^Z(W^\dagger_{\mu\nu}W^\mu - W_{\mu\nu}W^{\mu\dagger})Z^\nu \\ &- ieg_1^\gamma(W^\dagger_{\mu\nu}W^\mu - W_{\mu\nu}W^{\mu\dagger})A^\nu \\ &- ie\frac{c_\mathrm{W}}{s_\mathrm{W}}\kappa_Z W^\dagger_\mu W_\nu Z^{\mu\nu} - ie\kappa_\gamma W^\dagger_\mu W_\nu A^{\mu\nu},\end{aligned} \quad (1)$$

where s_W and c_W are the sine and the cosine of the Weinberg angle.

At the tree level and in the unitary gauge, the anomalous terms contribute to the processes under consideration only through the three-gauge-boson vertex WWV. Within the effective Lagrangian approach and under the assumption that whatever breaks electroweak symmetry has at least an approximate custodial symmetry, there are only three operators in the C- and P-preserving NLO effective Lagrangian that are relevant to the gauge sector:

$$\begin{aligned}\mathcal{L}^{(4)} = \frac{v^2}{\Lambda^2}\{&-gL_{9L}\mathrm{tr}(W^{\mu\nu}D_\mu\Sigma D_\nu\Sigma^\dagger) \\ &- ig'L_{9R}\mathrm{tr}(B^{\mu\nu}D_\mu\Sigma^\dagger D_\nu\Sigma) \\ &+ gg'L_{10}\mathrm{tr}(\Sigma B^{\mu\nu}\Sigma^\dagger W_{\mu\nu})\}.\end{aligned} \quad (2)$$

However, it was shown in [12] that the coupling L_{10}, being proportional to the parameter ϵ_3 measured at LEP I, is tightly constrained, $-1.1 \le L_{10}(M_Z) \le 1.5$; therefore, we will not consider the evolution of this coupling.[2)]

For the case of a strongly interacting symmetry-breaking sector, the approach of the effective Lagrangian allows one to relate the four couplings in (1) to those in (2):

$$\begin{aligned}g_1^Z &= 1 + \frac{e^2}{c_\mathrm{W}^2}\left(\frac{1}{2s_\mathrm{W}^2}L_{9L} + \frac{1}{(c_\mathrm{W}^2 - s_\mathrm{W}^2)}L_{10}\right)\frac{v^2}{\Lambda^2} + \ldots, \\ g_1^\gamma &= 1 + \ldots, \\ \kappa_Z &= 1 + e^2\left(\frac{1}{2s_\mathrm{W}^2c_\mathrm{W}^2}(L_{9L}c_\mathrm{W}^2 - L_{9R}s_\mathrm{W}^2)\right. \\ &\quad \left. + \frac{2}{(c_\mathrm{W}^2 - s_\mathrm{W}^2)}L_{10}\right)\frac{v^2}{\Lambda^2} + \ldots, \\ \kappa_\gamma &= 1 + \frac{e^2}{s_\mathrm{W}^2}\left(\frac{L_{9L} + L_{9R}}{2} - L_{10}\right)\frac{v^2}{\Lambda^2} + \ldots.\end{aligned} \quad (3)$$

In (3), the leading contribution to each anomalous coupling is presented, while the ellipses stand for contributions that arise in a higher order of $1/\Lambda^4$ or in the $1/\Lambda^2$ order with custodial $SU(2)$-symmetry breaking. It should be noted here that, in contrast to the anomalous couplings from [11], we do not have terms that correspond to the usual couplings λ_Z and λ_γ, because, within the model discussed, they only occur in higher orders in $1/\Lambda^2$.

In this paper, we will consider the processes $ep \longrightarrow \nu\gamma X$ (eWX, νWX) at the tree level and use the unitary gauge. In Figs. 1–3, one can see that new physics contributes to these processes via anomalous triple boson vertices, so that (adopting that L_{10} is severely constrained by LEP I data and that boson–fermion vertices remain unchanged) we are left with the set of anomalous couplings $g_1^{Z(\gamma)}$ and $\kappa_{Z(\gamma)}$ [in terms of (1)], or with the set of L_{9L} and L_{9R} [in terms of (2)].

3. PROCESSES WITH ANOMALOUS $WW\gamma(Z)$ COUPLINGS

In this section, we would like to discuss the possible manifestations of anomalous $WW\gamma(Z)$ couplings in the processes $ep \longrightarrow \nu\gamma X$ (eWX, νWX) at the HERA ep collider, where $E_e = 30$ GeV and $E_p = 820$ GeV, which corresponds to $\sqrt{s} = 314$ GeV. We adopt the integrated luminosity of 1000 pb^{-1}, which corresponds at least to five years of machine operation. We use a Monte Carlo

[2)]Within the model discussed, the anomalous couplings also affect the $Wf\nu$ and $Zf\bar{f}$ vertices through renormalization, but they do this only through the parameter L_{10} [12], and this contribution is neglected.

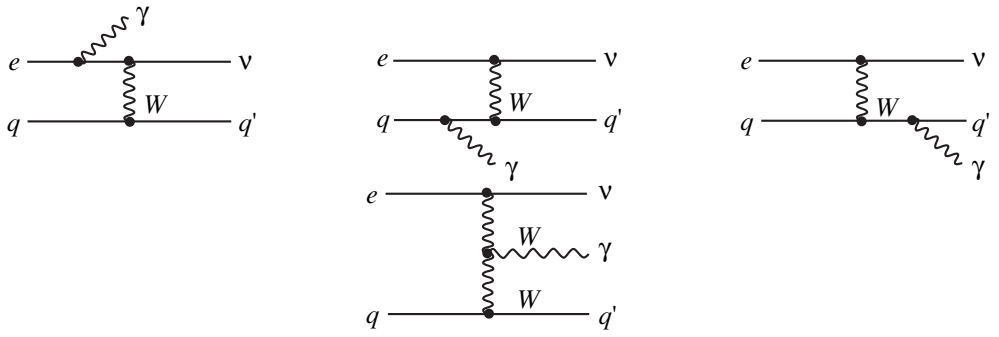

Fig. 1. Feynman diagrams for the process $ep \longrightarrow \nu\gamma X$.

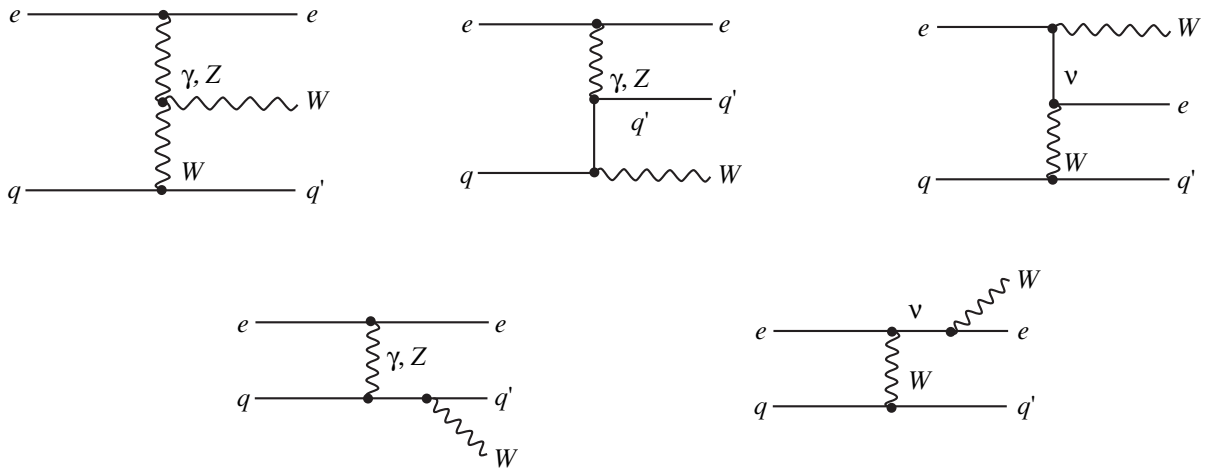

Fig. 2. Feynman diagrams for the process $ep \longrightarrow eWX$.

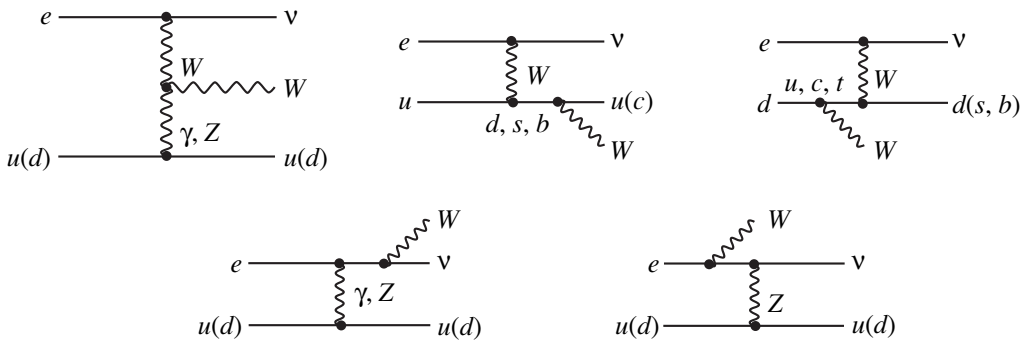

Fig. 3. Feynman diagrams for the process $ep \longrightarrow \nu WX$.

generator to simulate signal events and CTEQ4 parametrization [13] for the proton structure function. Standard sets of cuts on p_T^{jet}, p_T^{γ}, and p_T^{e}, as well as on the corresponding rapidities, were applied to satisfy the detector geometry and to reproduce the reconstruction efficiency. Uncertainties in the photon and jet energy measurements were taken into account by the Gaussian smearing of the 4-momenta. For our numerical study, we also use the following input parameter values:

$$M_W = 80.43 \text{ GeV}, \quad M_Z = 91.187 \text{ GeV},$$
$$\alpha = 1/128.8;$$

the values for CKM matrix elements were taken from the PDG review [14].

3.1. Process $ep \longrightarrow \nu\gamma X$

The following partonic subprocesses contribute to the process $ep \longrightarrow \nu\gamma X$:

$$eu \longrightarrow \nu\gamma d,$$

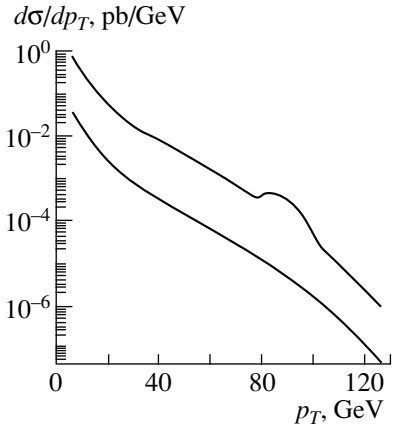

Fig. 4. The $ep \longrightarrow \nu\gamma X$ cross section as a function of the photon transverse momentum in the SM case.

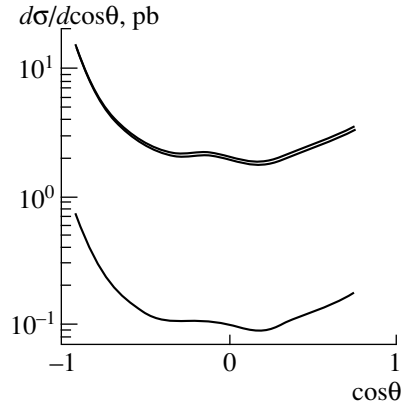

Fig. 5. Angular dependence of the $ep \longrightarrow \nu\gamma X$ cross section in the SM case.

$$eu \longrightarrow \nu\gamma s,$$
$$eu \longrightarrow \nu\gamma b.$$

For each of the cases, the corresponding Feynman diagrams are shown in Fig. 1. Since the signal topology for this process includes a jet, a photon, and missing energy, it is necessary to require the jet–photon separation (for example, by applying the cut on the relative pseudorapidity of the photon and jet, $\Delta\eta$, and their relative azimuthal angle, $\Delta\varphi$) and to impose the cut on the photon transverse momentum to get rid of the collinear and infrared singularities.

This process was studied in detail in the literature [1]; however, we will recall some of its main features to motivate our further choice of kinematical cuts that are aimed at improving the sensitivity of the process to anomalous couplings. We found that the cuts

$$p_T^\gamma \geq 0.5 \text{ GeV and } \sqrt{(\Delta\eta)^2 + (\Delta\varphi)^2} \geq 0.4 \qquad (4)$$

allow one to isolate the singularities and to separate the final photon and the jet. With these cuts, the cross sections for the relevant subprocess are

$$\sigma(eu \longrightarrow \nu\gamma d) = 8.72 \text{ pb},$$
$$\sigma(eu \longrightarrow \nu\gamma s) = 0.44 \text{ pb},$$
$$\sigma(eu \longrightarrow \nu\gamma b) = 1.06 \times 10^{-4} \text{ pb},$$

which corresponds to the $ep \longrightarrow \nu\gamma X$ total cross section of $\simeq 9.16$ pb. The contribution from the subprocess with a b quark in the final state is negligible, and we will not show it, while presenting differential distributions, but will keep it performing numerical estimates.

The differential distributions with respect to the photon transverse momentum, its scattering angle (relative to the electron-beam direction), and energy are shown in Figs. 4–6. In all three figures, the lowest curve represents the contribution from the subprocess with an s quark in the final state, while intermediate and upper curves represent, respectively, the contribution of the final d quark and the total contribution (in the cases of p_T and E distributions, the last two curves are indistinguishable on this scale). One can see that the bulk of the cross section is collected at low values of the photon transverse momentum and energy.

It is seen from the diagrams in Fig. 1 that the anomalous terms contribute to the process $ep \longrightarrow \nu\gamma X$ only through the $WW\gamma$ vertex. This means that, in terms of (3), the total cross section and the differential distributions that take into account anomalous interactions are functions of the combination $(L_{9L} + L_{9R})$ of anomalous couplings, which parametrize the $WW\gamma$ vertex. From Fig. 7, where the total cross section is shown as a function of $(L_{9L} + L_{9R})$, one can see that the total cross section has the highest sensitivity at negative values of $(L_{9L} + L_{9R})$; this is due to the constructive (destructive) interference between the anomalous and the Standard Model contributions at negative (positive) values of $(L_{9L} + L_{9R})$. Analyzing the process distributions, we found that stricter bounds on the anomalous couplings can be attained from the data on p_T distributions. Therefore, it seems interesting to study the behavior of $d\sigma/dp_T$ for nonvanishing anomalous couplings.

In Fig. 8, we present[3)] the relative contributions of the anomalous terms to the p_T distribution for $(L_{9L} + L_{9R}) = 500$ and -500[4)] (curves *1* and *2*, respectively). One can see that, for positive values of the anomalous couplings, the new-physics contribution is positive and corresponds to the high-p_T region, while, for negative values, it is distributed more or less uniformly over the region of moderate p_T. In either case, however, the region of small p_T is poorly sensitive to new-physics effects; i.e., it is mostly dominated by the SM contribution. This allows one to impose an extra cut on p_T, which should suppress the "background" SM contribution without losses of the effect due to anomalous terms. The optimal cut on p_T can be determined from

[3)]The appearance of sharp peaks in Figs. 8 and 9 is caused by a shortcoming in the spline algorithm.

[4)]These values of $(L_{9L} + L_{9R})$ were chosen for demonstration purposes only.

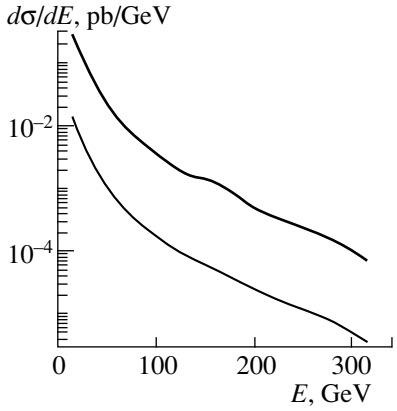

Fig. 6. Energy dependence of the $ep \longrightarrow \nu\gamma X$ cross section in the SM case.

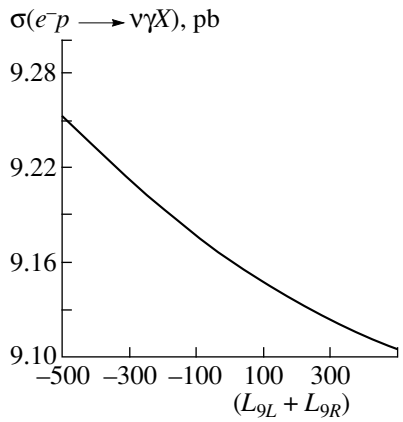

Fig. 7. $ep \longrightarrow \nu\gamma X$ total cross section as a function of anomalous couplings.

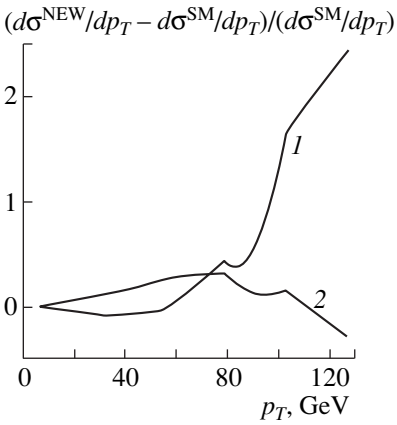

Fig. 8. Relative deviation of the p_T distribution for the process $ep \longrightarrow \nu\gamma X$ at nonvanishing anomalous couplings.

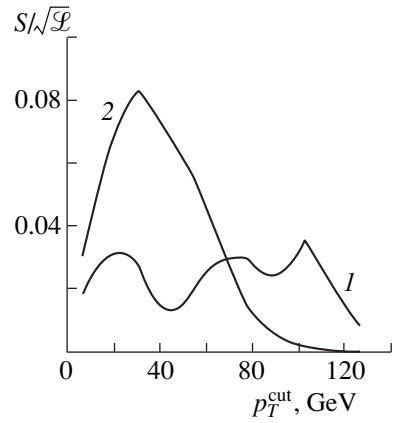

Fig. 9. Normalized sensitivity as a function of p_T^{cut}.

the so-called "sensitivity function," which is defined as

$$S = \frac{\left|\sigma^{\text{NEW}} - \sigma^{\text{SM}}\right|}{\sqrt{\sigma^{\text{SM}}}}\sqrt{\mathscr{L}}, \qquad (5)$$

where σ^{SM} and σ^{NEW} are the SM cross section and the cross section with allowance for the anomalous terms, respectively. The appearance of a peak in $S(p_T^{\text{cut}})$ corresponds to the optimal cut value. In Fig. 9, the sensitivity function is plotted against p_T^{cut} for the case of $(L_{9L} + L_{9R}) = 500$ and -500 (curves *1* and *2*, respectively). It should be noted that a variation of the couplings will change the absolute normalization of the curves, but this will not modify their line shape. One can see that, for negative coupling values, the sensitivity peaks are at $p_T^{\text{cut}} \simeq 30$ GeV, while for positive coupling values, there is no such pronounced peak behavior. Maximizing both *S* functions, one gets an optimal cut value, $p_T \geq 30$ GeV. Later, discussing the resulting bounds, we will use just this cut value. This cut does lead to a higher sensitivity of the cross section to anomalous couplings.

In Fig. 10, we again present the total cross section as a function of $(L_{9L} + L_{9R})$, but for the case where the cut $p_T \geq 30$ GeV is used. Of course, this cut reduces the cross section substantially; however, while, in the no-cut case (see Fig. 7), the cross section varies from 1 to –0.5%, for cut used, the cross section varies from 14 to –4.6% for the same range of $(L_{9L} + L_{9R})$ values.

3.2. Process $ep \longrightarrow eWX$

This process has a smaller cross section in relation to that for $ep \longrightarrow \nu\gamma X$, but it turns out to be very sensitive to the anomalous couplings. The following partonic subprocesses contribute to $ep \longrightarrow eWX$:

$$eu \longrightarrow eWd,$$
$$eu \longrightarrow eWs,$$
$$eu \longrightarrow eWb,$$
$$ed \longrightarrow eWu,$$
$$ed \longrightarrow eWc.$$

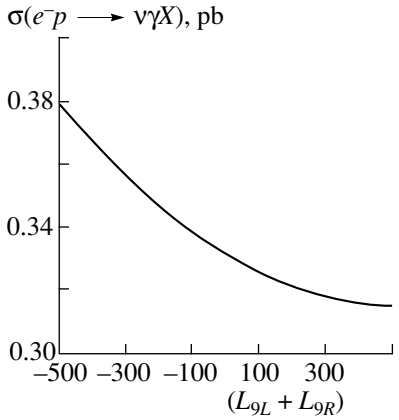

Fig. 10. $ep \longrightarrow \nu\gamma X$ total cross section as a function of anomalous couplings for $p_T \geq 30$ GeV.

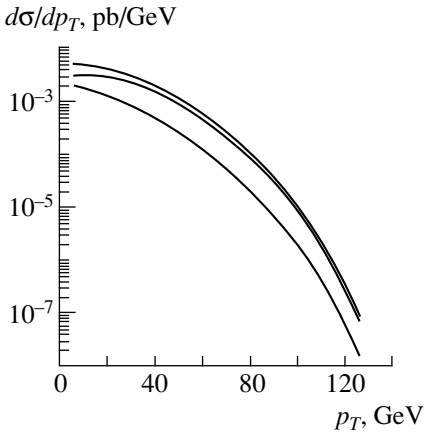

Fig. 11. $ep \longrightarrow eWX$ cross section versus the transverse momentum p_T of W in the SM case.

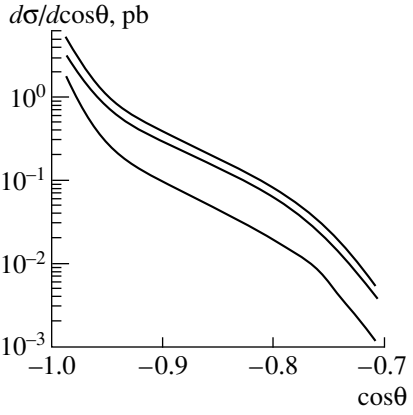

Fig. 12. $ep \longrightarrow eWX$ cross section versus the W scattering angle in the SM case.

The corresponding Feynman diagrams are shown in Fig. 2. For this process, the signal includes the scattered lepton, a jet, and final W-decay products. To regulate the singularities, it is necessary to impose a cut on the electron transverse momentum. This cut also solves, in part, the problem of the scattered electrons lost in the beam pipe. However, a cross-check cut on the polar angle of the scattered electrons is also needed, $-0.999 \leq \cos\theta_e \leq 0.998$, where θ_e is the angle of the scattered electron with respect to the electron-beam direction. It is also necessary to require the jet–electron separation, which could be done, for example, by applying the cut on the relative pseudorapidity of the electron and the jet and their azimuthal angle. In this case, we should identify final W by its decays into $l\nu$ or jets. The possible backgrounds to the leptonic W-decay mode are beam-induced processes, cosmic muons, charged-current events with a spurious electron, and the neutral-current background. As was shown in [6], these backgrounds can be reduced by imposing cuts on the position of the interaction vertex, by means of algorithms based on calorimeter and tracking information, by requiring an isolated electromagnetic cluster and a matched track, and by requiring an isolated missing p_T. It was found [6] that such cuts reduce the signal-to-background ratio up to 1/7 and lead to an acceptance of about 40–65% for $W \longrightarrow e\nu(\mu\nu, \tau\nu)$ events. For the hadronic decay modes of W, the dominant backgrounds are QCD processes from neutral-current DIS and photoproduction. Jet cuts and algorithms [6] being applied lead to a significant reduction of the background and give the signal-to-background ratio of 1/24.

To demonstrate the characteristic behavior of the $ep \longrightarrow eWX$ process distributions, we use a minimal set of cuts, $p_T^e \geq 2$ GeV and the cut on the electron-scattering angle discussed above. In this case, the subprocess cross sections are

$$\sigma(eu \longrightarrow eWd) = 1.39 \times 10^{-1} \text{ pb},$$
$$\sigma(eu \longrightarrow eWs) = 0.738 \times 10^{-2} \text{ pb},$$
$$\sigma(eu \longrightarrow eWb) = 1.694 \times 10^{-6} \text{ pb},$$
$$\sigma(ed \longrightarrow eWu) = 0.617 \times 10^{-1} \text{ pb},$$
$$\sigma(ed \longrightarrow eWc) = 0.32 \times 10^{-2} \text{ pb},$$

which corresponds to the total cross section for $ep \longrightarrow eWX$ of about 0.21 pb. In Figs. 11–14, we present the process differential distributions in the transverse momentum and scattering angle of W and the electron, respectively. In all these figures, the lowest curve represents the contribution from the d-quark subprocesses, while the intermediate and upper curves represent the u-quark and total contributions. Both the W-boson and electron p_T distributions are strongly peaked at small p_T. While produced W bosons are boosted along the proton direction, the angular distribution for electrons is not so sharp and they are scattered preferably along the electron-beam direction.

Anomalous couplings contribute to the process $ep \longrightarrow eWX$ through the WWZ and $WW\gamma$ vertices, and this implies that it is possible in principle to separate L_{9L} and L_{9R} dependences in the observables. The pro-

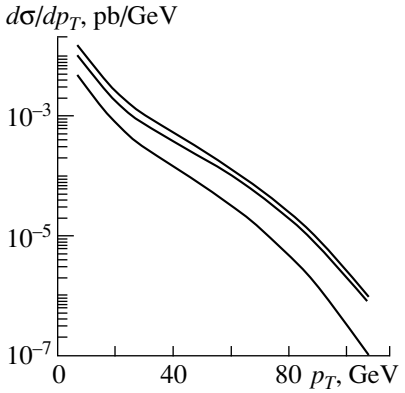

Fig. 13. $ep \longrightarrow eWX$ cross section versus the transverse momentum p_T of the electron in the SM case.

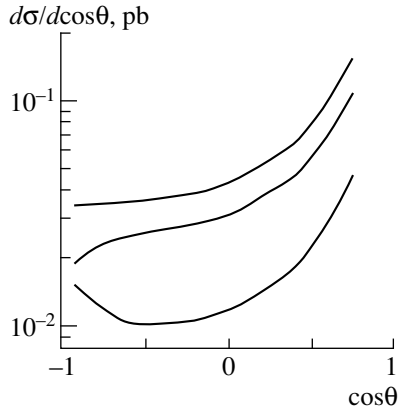

Fig. 14. $ep \longrightarrow eWX$ cross section versus the electron-scattering angle in the SM case.

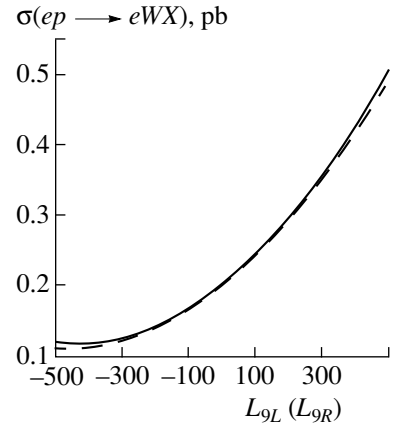

Fig. 15. $ep \longrightarrow eWX$ total cross section as a function of the couplings L_{9L} and L_{9R}.

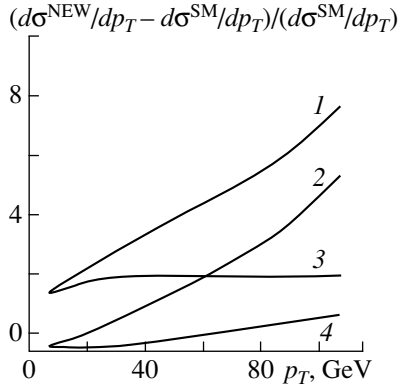

Fig. 16. Relative deviation of the electron p_T distribution for the $ep \longrightarrow eWX$ process at nonvanishing anomalous couplings.

cess cross section reveals a sensitivity to both couplings [see Fig. 15, which shows the total cross section as a function of the couplings L_{9L} (solid curve) and L_{9R} (dashed curve)], much higher than that for the $ep \longrightarrow \nu\gamma X$ case. We analyzed various observables and found that the most severe bounds on the anomalous parameters can be obtained from the differential distribution over the electron transverse momentum. In Fig. 16, we demonstrate the relative deviation of this distribution for nonvanishing values of the couplings L_{9L} and L_{9R}, where curve *1* (*2*) corresponds to the case of L_{9L} = 500 (–500), L_{9R} = 0, and curve *3* (*4*) corresponds to $L_{9L} = 0, L_{9R} = 500$ (–500). One can see that, for negative couplings, the deviation is less than that for the case of positive couplings, and it is negative for low p_T^e, which is due to the destructive interference with SM contribution. For both cases, the anomalous-coupling contribution reaches its maximum in the high p_T^e region. We used the sensitivity function defined in (5) to determine the p_T^e cut that makes the process be sensitive to anomalous contributions; however, it turned out that, due to the small cross section and, as a consequence, low statistics, such a cut does not lead to noticeable improvement of the resulting bounds.

3.3. Process $ep \longrightarrow \nu WX$

The last process to be considered is $ep \longrightarrow \nu WX$. The partonic subprocesses contributing to $ep \longrightarrow eWX$ are as follows:

$$eu \longrightarrow \nu Wc,$$
$$eu \longrightarrow \nu Wu,$$
$$ed \longrightarrow \nu Wd,$$
$$ed \longrightarrow \nu Ws,$$
$$ed \longrightarrow \nu Wb.$$

The corresponding Feynman diagrams are shown in Fig. 3. For this process, the signal includes the missing p_T, a jet, and final W-decay products. The cut $p_T \geq 5$ GeV on the transverse momentum of the struck quark jet allows one to get rid of singularities and to guarantee a

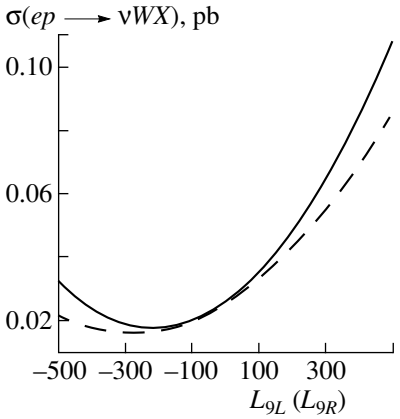

Fig. 17. $ep \longrightarrow \nu WX$ total cross section as a function of anomalous couplings.

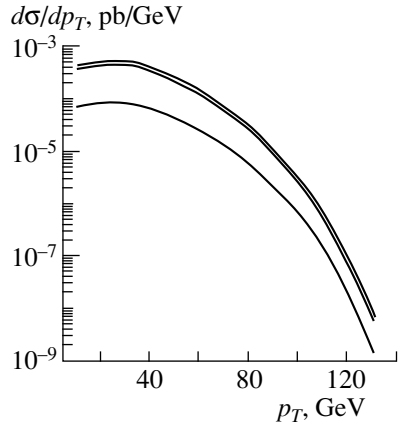

Fig. 18. $ep \longrightarrow \nu WX$ cross section versus the W transverse momentum.

high detection efficiency. As in the case of the process $ep \longrightarrow eWX$, one has to reconstruct the final W boson by its leptonic or jet final states. In doing this, all the methods and cuts necessary to reconstruct the final state and to suppress the background discussed in the preceding section are also applicable.

For the cut on the jet transverse momentum, $p_T \geq 5$ GeV, the partial cross sections the various partonic subprocesses are

$$\sigma(eu \longrightarrow \nu Wu) = 2.11 \times 10^{-2} \text{ pb},$$

$$\sigma(ed \longrightarrow \nu Wd) = 0.41 \times 10^{-2} \text{ pb},$$

and the subprocesses with a s, c, or b quark in the final state have cross sections that are negligibly small. The total cross section is about 2.5×10^{-2} pb, which is much smaller than that for the processes $ep \longrightarrow \nu\gamma X$ or $ep \longrightarrow eWX$. For an integrated luminosity of 1000 pb^{-1} and a realistic reconstruction efficiency, one could expect to have only isolated signal events, at max. However, this reaction is highly sensitive to an anomalous contribution.

In Fig. 17, which shows the total cross section as a function of anomalous couplings, one can see that the process cross section is highly sensitive to positive values of anomalous couplings. In Figs. 18 and 19, we present the distributions of the cross section with respect to the transverse momentum and W scattering angle. One can see that the bulk of the cross section is collected from the small p_T region and that final W bosons are strongly boosted along the proton-beam direction. Though both distributions are equally sensitive to an anomalous contribution, the fact that the process cross section is extremely small makes it reasonable to analyze the total cross section only, since the low statistics will hardly allow observation of the real distributions for this process.

4. BOUNDS ON ANOMALOUS COUPLINGS

In this section, we will discuss the bounds on the anomalous couplings that can be attained from the data on the processes $ep \longrightarrow \nu\gamma X$ (eWX, νWX). First of all, it is necessary to determine the efficiencies of the final-state reconstruction for each of the processes.

For the reaction $ep \longrightarrow \nu\gamma X$, which has a final-state topology of a jet and a photon plus missing energy, it should be noted that existing calorimeters allow one to detect energetic photons with the efficiency of about 60%. However, about 30% of all photons convert to electron–positron pairs on the detector material before entering the calorimeter. The reconstruction efficiency of such pairs is about 90%. Thus, the expected reconstruction efficiency for the photon is about 70%. Putting bounds on the anomalous couplings from this process, we use the cut set of (4), but with $p_T \geq 30$ GeV, as follows from the sensitivity-function analysis.

Studying the process $ep \longrightarrow eWX$, we adopt the algorithms and cuts used in [6], thus having the following acceptances for each of W-decay modes: 65% for $W \longrightarrow e\nu(\mu\nu)$, 40% for $W \longrightarrow \tau\nu$, and 20% for $W \longrightarrow$ jets. In addition, we check the cuts $p_T^e \geq 5$ GeV and $-0.999 \leq \cos\theta_e \leq 0.998$ to be satisfied, which ensures the scattered-electron detection.

For the process $ep \longrightarrow \nu WX$, we require $p_T \geq 5$ GeV for the struck quark and adopt the corresponding algorithms for reconstructing final W decay as discussed above.

For an integrated luminosity of 1000 pb^{-1}, we assume the uncertainty in the luminosity to be 2% and the systematics to be 1% for each of the acceptances.

Discussing the sensitivity of the processes to anomalous couplings, we will analyze the differential cross sections in the case of $ep \longrightarrow \nu\gamma X$ and $ep \longrightarrow eWX$ and the total cross section in the case of $ep \longrightarrow \nu WX$ (here, under the assumption of the Gaussian nature of the systematics, one can relate the deviations of σ_{tot} to the cor-

responding confidence level). We adopt the following philosophy to confine anomalous contributions: one uses the SM predictions as "experimental" data and considers possible effects due to new physics as small deviations. One then requires agreement between the predictions including new physics and the "experimental" values within expected experimental errors. Thus, the parameters representing new physics are bound by requiring that their effect on the observables not exceed the expected experimental errors.

Using differential cross sections (p_T or angular distributions), we apply the simplest χ^2 criterion defined as

$$\chi^2 = \sum_i \left(\frac{X_i - Y_i}{\Delta^i_{\text{exp}}} \right)^2, \qquad (6)$$

where, for example, for the case of the p_T distribution,

$$X_i = \int_{p_T^i}^{p_T^{i+1}} \frac{d\sigma^{\text{SM}}}{dp_T} dp_T, \quad Y_i = \int_{p_T^i}^{p_T^{i+1}} \frac{d\sigma^{\text{NEW}}}{dp_T} dp_T.$$

In the above expressions, $\sigma \equiv \sigma^{\text{SM}}$ represents the experimental data, σ^{NEW} are the new-model predictions, and Δ^i_{exp} are the appropriate experimental errors in bins including statistical and systematic errors. For binning, we subdivide the chosen kinematical range into equal bins. Here,

$$\Delta^i_{\text{exp}} = X_i \sqrt{\delta^2_{\text{stat}} + \delta^2_{\text{syst}}}.$$

In Fig. 20, we present the resulting allowed regions (for a 95% C.L. and $\Lambda = 2$ TeV) for the parameters L_{9L} and L_{9R} that can be attained from the data on the process $ep \longrightarrow \nu\gamma X$ (the area bounded by long-dashed lines), $ep \longrightarrow eWX$ (the domain bounded by the solid contour), and $ep \longrightarrow \nu WX$ (the area bounded by the short-dashed contour). One can see that, in the case of $ep \longrightarrow \nu\gamma X$, the resulting bounds on L_{9L} and L_{9R} have the form of a straight band oriented along the line $L_{9L} = -L_{9R}$. This is due to the fact that these couplings contribute to the process $ep \longrightarrow \nu\gamma X$ only through the parameter κ_γ of the anomalous $WW\gamma$ vertex, and κ_γ is proportional to the combination $(L_{9L} + L_{9R})$ [see (3)]. However, due to the different sensitivity of the data to the regions of negative and positive coupling values, this band is not symmetric with respect the line $L_{9L} = -L_{9R}$. In two other processes anomalous parameters contribute through both the $WW\gamma$ and the WWZ vertices; thus, the resulting bounds are less trivial.

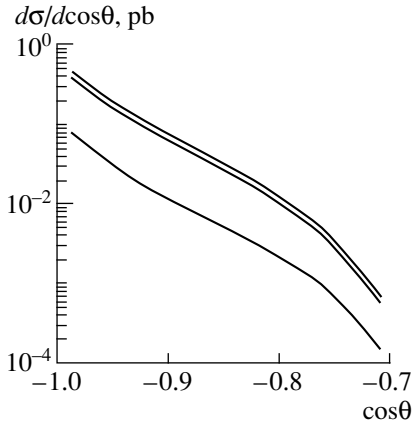

Fig. 19. $ep \longrightarrow \nu WX$ cross section versus the cosine of the W scattering angle.

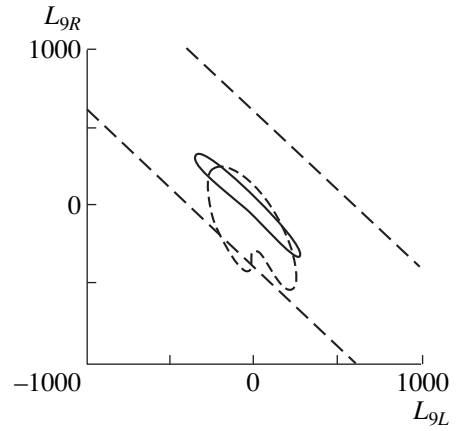

Fig. 20. Allowed region (at a 95% C.L.) for the couplings L_{9L} and L_{9R} from the data on $ep \longrightarrow \nu\gamma X$ (the area between long-dashed lines), $ep \longrightarrow eWX$ (domain within the solid contour), and $ep \longrightarrow \nu WX$ (domain within the short-dashed contour).

Thus, for $\mathcal{L} = 1000$ pb^{-1}, $\Lambda = 2$ TeV, and a 95% C.L., one gets the following two-parameter bounds from the individual processes:

Process	Bounds
$ep \longrightarrow \nu\gamma X$	$-390 \le L_{9L} + L_{9R} \le 600$
$ep \longrightarrow eWX$	$-340 \le L_{9L} \le 280$
	$-330 \le L_{9R} \le 320$
$ep \longrightarrow \nu WX$	$-280 \le L_{9L} \le 260$
	$-530 \le L_{9R} \le 260$

One can see that, with the two-parameter fit, the bounds coming from the last two processes are narrower than those from $ep \longrightarrow \nu\gamma X$. It is important that the bounds resulting from the $ep \longrightarrow \nu WX$ data, in spite of the small cross section for the process, are quite stringent and turn out to be complementary to those

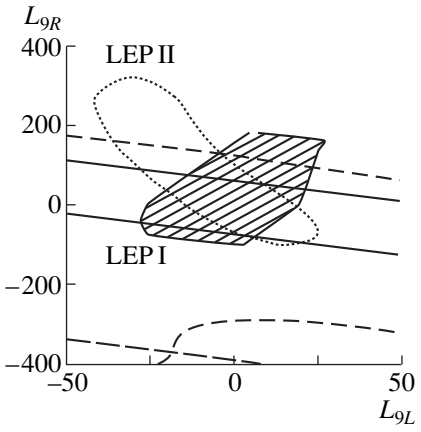

Fig. 21. Allowed regions (at a 95% C.L.) for couplings L_{9L} and L_{9R} from LEP I (shaded domain) [12], LEP II (domain within the dotted contour) [15], and HERA processes (the notation for curves is identical to that in Fig. 20).

from the process $ep \longrightarrow eWX$. In the case of a one-parameter fit, i.e., when only one coupling is varied at a time, the individual bounds from the last two processes become narrower:

Process	Bounds
$ep \longrightarrow eWX$	$-75 \le L_{9L} \le 55$
	$-80 \le L_{9R} \le 60$
$ep \longrightarrow \nu WX$	$-250 \le L_{9L} \le 100$
	$-290 \le L_{9R} \le 120$

Of course, it is interesting to compare these bounds with those coming from the processes at LEP I and LEP II. It was shown [12] that accurate measurements of Z partial widths imply

$$-28 \le L_{9L} \le 27,$$
$$-100 \le L_{9R} \le 190.$$

The expected bounds [15] from LEP II coming from data on the process $e^+e^- \longrightarrow W^+W^-$ at $\sqrt{s}$ = 190 GeV and an integrated luminosity of 500 pb^{-1} are

$$-41 \le L_{9L} \le 26,$$
$$-100 \le L_{9R} \le 330.$$

In Fig. 21, we present the 95% C.L. bounds on the couplings L_{9L} and L_{9R} that follow from the analysis of Z partial widths (shaded domain), data on the process $e^+e^- \longrightarrow W^+W^-$ at LEP II (dotted contour), and data on HERA processes (the notation for bounding contours is identical to that in Fig. 20).

One can see that the bounds from $ep \longrightarrow \nu\gamma X$ are more flexible than LEP I or LEP II results. However, both the process $ep \longrightarrow eWX$ and the process $ep \longrightarrow \nu WX$ provide bounds that can be considered as complementary to the LEP I and LEP II results. It turns out that the data on the HERA processes are unable to improve the bounds on the coupling L_{9L}, but they reduce significantly the allowed region for L_{9R}. A combined analysis of the data from LEP I, LEP II, and HERA could exclude a large portion of the allowed domain for the couplings in the region of large positive L_{9R} values and slightly improve the LEP I + LEP II bounds for negative L_{9R} values.

5. CONCLUSION

We have presented a comparative analysis of the $ep \longrightarrow \nu\gamma X$ (eWX, νWX) process sensitivity to anomalous couplings that parametrize the $WW\gamma(Z)$ vertices. For anomalous couplings, we used the approach of the effective Lagrangian and considered the model where the electroweak-symmetry sector is strongly coupled and there is no light Higgs particles. We found that the processes $ep \longrightarrow \nu\gamma X$ (eWX, νWX) reveal a high sensitivity to anomalous contributions. In spite of the small cross section, the processes $ep \longrightarrow eWX$ (νWX) provide the most severe bounds on the anomalous parameters.

At the HERA collider with an integrated luminosity of 1000 pb^{-1}, one can confine the anomalous couplings with a 95% C.L. at the level of

$$-390\left(\frac{\Lambda}{2\ \text{TeV}}\right)^2 \le L_{9L} + L_{9R} \le 600\left(\frac{\Lambda}{2\ \text{TeV}}\right)^2$$

from the data on the process $ep \longrightarrow \nu\gamma X$;

$$-75\left(\frac{\Lambda}{2\ \text{TeV}}\right)^2 \le L_{9L} \le 55\left(\frac{\Lambda}{2\ \text{TeV}}\right)^2,$$

$$-80\left(\frac{\Lambda}{2\ \text{TeV}}\right)^2 \le L_{9R} \le 60\left(\frac{\Lambda}{2\ \text{TeV}}\right)^2$$

from the $ep \longrightarrow eWX$ data; and

$$-250\left(\frac{\Lambda}{2\ \text{TeV}}\right)^2 \le L_{9L} \le 100\left(\frac{\Lambda}{2\ \text{TeV}}\right)^2,$$

$$-290\left(\frac{\Lambda}{2\ \text{TeV}}\right)^2 \le L_{9R} \le 120\left(\frac{\Lambda}{2\ \text{TeV}}\right)^2$$

from the $ep \longrightarrow \nu WX$ data. The bounds from the last two processes turn out to be complementary.

We conclude that, from the data on HERA processes, one is unable to improve the bounds on the coupling L_{9L} coming from LEP I and LEP II, but these data could result in significantly narrowing the allowed region for L_{9R}.

ACKNOWLEDGMENTS

The authors would like to express their gratitude to Prof. A. Wagner and members of the DESY Theory Group for kind hospitality during the visit to DESY,

where a part of this work was done. The authors would like to thank Prof. F. Schrempp for reading this manuscript and making valuable remarks and Dr. L. Gladilin for useful discussions on the data analysis.

This work was supported in part by the Russian Foundation for Basic Research (project nos. 99-02-16558 and 96215-96575) and INTAS-RFBR (grant no. 95I1300).

REFERENCES

1. T. Hilbig and H.Spiesberger, in *Proceedings 1991 Workshop on Physics at HERA*, Ed. by W. Buchmuller and G. Ingelman (DESY, Hamburg, 1992), Vol. 2, p. 973; Nucl. Phys. B **373**, 73 (1992); U. Baur and M. A. Doncheski, Phys. Rev. D **46**, 1959 (1992).
2. U. Baur and D. Zeppenfeld, Nucl. Phys. B **325**, 253 (1989).
3. U. Baur, J. A. M. Vermaseren, and D. Zeppenfeld, Nucl. Phys. B **375**, 3 (1992).
4. M. Bohm and A. Rosado, Z. Phys. C **42**, 479 (1989).
5. C. S. Kim, J. Lee, and H. S. Song, Z. Phys. C **63**, 673 (1994).
6. V. A. Noyes, in *Proceedings of 1995/1996 Workshop on Future Physics at HERA*, Ed. by G. Ingelman *et al.* (DESY, Hamburg 1996), Vol. 1, p. 190.
7. T. Appelquist and C. Bernard, Phys. Rev. D **22**, 200 (1980); A. Lunghitano, Nucl. Phys. B **188**, 118 (1981).
8. B. Holdom, Phys. Lett. B **258**, 156 (1991); A. Falk, M. Luke, and E. Simmons, Nucl. Phys. B **365**, 523 (1991); J. Bagger, S. Dawson, and G. Valencia, Nucl. Phys. B **399**, 364 (1993); T. Appelquist and G.-H. Wu, Phys. Rev. D **48**, 3235 (1993).
9. A. A. Likhoded, T. Han, and G. Valencia, Phys. Rev. D **53**, 4811 (1996).
10. S. Dawson, A. A. Likhoded, and G. Valencia, in *Proceedings of 1996 DPF/DPB Summer Study on New Directions for High-Energy Physics (Snowmass 96)*; hep-ph/9610299.
11. K. Hagiwara *et al.*, Nucl. Phys. B **282**, 253 (1987).
12. S. Dawson and G. Valencia, Nucl. Phys. B **439**, 3 (1995); Phys. Lett. B **333**, 207 (1994).
13. CTEQ Collab. (H. L. Lai *et al.*), Phys. Rev. D **55**, 1280 (1997).
14. Particle Data Group, Eur. Phys. J. C **3**, 1 (1998).
15. F. Boudjema, in *Proceedings of Workshop on Physics and Experiments with Linear e^+e^- Colliders*, Ed. by F. A. Harris *et al.* (World Sci., Singapore, 1993), p. 713 and references therein.

Physics of Atomic Nuclei, Vol. 63, No. 5, 2000, pp. 870–881. Translated from Yadernaya Fizika, Vol. 63, No. 5, 2000, pp. 940–952.

ELEMENTARY PARTICLES AND FIELDS
Theory

Searches for Electroweak γ–*Z*–*Z*' Interference at the LEP2 e^+e^- Collider

A. A. Pankov*
P. Sukhoĭ State Technical University, Gomel, Belarus
Received February 23, 1999; in final form, June 26, 1999

Abstract—Indirect effects of the Z' boson in the process $e^+e^- \longrightarrow \mu^+\mu^-$ as implemented at the LEP2 electron–positron collider are investigated in terms of new integrated observables $\sigma_\pm$. It is demonstrated that these observables furnish more definitive information about Z'-boson effects than the canonical observables $\sigma_{\mu\mu}$ and A_{FB}. It is established that the deviations $\Delta\sigma_\pm$ induced by Z' bosons show a specific energy dependence, which is determined primarily by the parameters of the Standard Model. This permits making unambiguous model-independent predictions. In particular, two points, $\sqrt{s_+} \approx 78$ GeV and $\sqrt{s_-} \approx 113$ GeV, are determined at which, respectively, σ_+ and σ_- vanish both in the Standard Model and in presence of the extra Z' boson. These energy values can be of use in searches for phenomenological manifestations of alternative sources of new physics that are different from Z'. *© 2000 MAIK "Nauka/Interperiodica".*

1. INTRODUCTION

The Standard Model (SM) of strong and electroweak interactions of elementary particles, which is based on the gauge group $SU(3)_C \times SU(2)_L \times U(1)_Y$, has achieved impressive successes in describing experimental data over the entire range of currently available energies [1, 2]. The modern phenomenological status of the SM relies on a comprehensive analysis of processes, including leptonic, lepton–hadron, and hadron–hadron interactions. In particular, the results of the experiments that were performed at the LEP1 electron–positron collider and which were aimed at a precision determination of the constants of intermediate-vector-boson coupling to fermions are in excellent agreement with SM predictions to within 0.1%.

Nonetheless, the SM cannot be considered as the fundamental theory of everything for a number of reasons. First, it involves many free parameters. Second, it cannot provide answers to some fundamental questions, including those associated with the problem of particle-mass hierarchies, with the number of generations, and with the nature of *P* and *CP* violations. It would therefore be natural to assume that there exists a more fundamental theory whose low-energy limit coincides with the SM. A rather wide class of models involving an extended gauge sector (see, for example, [3]) stands out among candidate theories that cannot solve at least some of the problems arising within the SM. These include left–right symmetric models, alternative left–right symmetric models, and E_6 models. A feature peculiar to many of such models is that they predict the existence of new physical objects and the occurrence of new phenomena in the energy region above 1 TeV—in particular, phenomena associated with the existence of new neutral (Z') or charged ($W'^{\pm}$) vector bosons, fermions, and scalar particles.

Searches for new particles and interactions predicted by nonstandard new physics beyond the SM represent one of the main tasks for experiments at the existing and future accelerating facilities. The mass of extra gauge bosons may be sufficient for inducing direct or indirect (virtual) effects observable even at the operating colliders or at high-energy next-generation colliders. If the threshold for the production of new particles had been achieved, this would obviously have been direct evidence for the existence of new physics. Here, however, the interval of searches for the masses of new particles is restricted by the maximal collider energy. In particular, there are no prospects for a direct production of the new neutral gauge Z' boson at the LEP2 collider, whose energy $\sqrt{s}$ cannot be pushed above 200 GeV, since the experiments at the Tevatron hadronic collider constrained its mass $M_{Z'}$ to be below 600 GeV [4]. However, a much broader interval of masses $M_{Z'}$ can be explored by pursuing indirect effects of Z' bosons for $\sqrt{s} \ll M_{Z'}$ [5]. In this case, it is possible to trace deviations in the behavior of some observables from the corresponding SM predictions. If experimental data agree with the SM within the current level of accuracy—that is, if no deviations from SM predictions are observed—this experimental information can be used to set constraints on the parameters of the Z' boson, such as its coupling constants and mass $M_{Z'}$.

* e-mail:pankov@gpi.gomel.by

One of the most natural ways to seek Z'-boson effects is provided by the annihilation production of a fermion pair through the process

$$e^+ + e^- \longrightarrow \bar{f} + f \qquad (1)$$

($f = l, q$), where the Z' boson contributes to observables even in the Born approximation. Briefly listed immediately below are basic conceivable phenomenological manifestations of the Z' boson in e^+e^- annihilation at energies $\sqrt{s} \ll M_{Z'}$ and some possibilities for their experimental observation. First of all, these are electroweak interference effects due to Z' bosons. The energy regions above and below the resonance pole of the standard Z boson are highly favorable for the above searches. These are precisely the energy values that were achieved at the TRISTAN and LEP2 colliders. The interference contribution to observables is proportional to the Z'-boson-exchange amplitude; therefore, this contribution depends on the product of the constants of the Z'-boson coupling to fermions and the Z'-boson propagator. We note that the sensitivity of observables increases with increasing energy of e^+e^- beams, whence it follows that the high-energy LEP2 collider has an obvious advantage over the TRISTAN collider.

Apart from interference, the Z' boson can also manifest itself in Z–Z' mixing [3]. It is advisable to explore the effects of Z–Z' mixing in the vicinity of the resonance peak corresponding to the standard Z boson (this was done at the LEP1 and SLC colliders [6]). The point is that, at $\sqrt{s} = M_Z$, the leading contribution to the amplitude of process (1) comes from resonance Z-boson exchange, the electromagnetic and the Z'-boson contribution being much less. Possible deviations of resonance observables induced by Z–Z' mixing are due both to the corresponding modification of the fermionic coupling constants and to the change in the mass of the standard Z boson [7]. As was mentioned above, precision resonance measurements performed at LEP1 did not reveal any deviations of observables from SM predictions. This resulted in establishing a stringent constraint on the parameter of Z–Z' mixing: $|\phi| \leq O(10^{-3})$ [6].

As to nonresonance measurements, their accuracy is significantly poorer than that achieved at the Z-boson peak. At the PEP and PETRA e^+e^- colliders, a test of the SM in process (1) was nevertheless performed at energies below the Z-boson resonance peak ($\sqrt{s}$ = 12–46 GeV) [8, 9]. Similar data, but at higher energies of $\sqrt{s}$ = 50–64 GeV, was obtained at the TRISTAN collider [10]. In addition, the process $e^+e^- \longrightarrow \mu^+\mu^-\gamma_{ISR}$, where γ_{ISR} stands for a hard photon emitted by the initial e^+e^- state, was investigated at LEP1 [11, 12]). Following hard-photon emission, the invariant mass of the $\mu^+\mu^-$ pair is shifted to the region below the Z-boson resonance peak, predominantly occurring between the TRISTAN energy and M_Z. Once the LEP2 collider had been commissioned, there appeared new data concerning the measurements on process (1) at energies above the resonance peak [13]. Although no considerable deviations from SM predictions have been found in the experiments performed thus far, a more meticulous analysis of the experimental data makes it possible to reveal some trend toward inconsistencies with SM predictions. In particular, the experimental results that were obtained at the maximal energy of the PETRA collider show a systematic deficit (of a few percent) of the total leptonic cross section for $e^+e^- \longrightarrow \mu^+\mu^-$ in relation to the SM prediction [14]. At the same time, the forward–backward asymmetry is in satisfactory agreement with the SM predictions. This tendency in the leptonic channel was also observed at higher energies of $\sqrt{s}$ = 50–64 GeV in early experiments at TRISTAN [10] and in LEP1 experiments that studied the process $e^+e^- \longrightarrow \mu^+\mu^-\gamma_{ISR}$ [11, 12]. It should be noted, however, that the accuracy of these measurements was rather poor because of insufficient statistics of lepton events.

A theoretical explanation for a possible decrease in the total lepton scattering cross section was given in [15]. In particular, the heavy vector Z' boson, which has a nonzero leptonic vector coupling constant can cause a deficit of the leptonic cross section in relation to the SM predictions because of destructive γ–Z' interference. The destructive character of γ–Z' interference in the leptonic channel is a model-independent prediction. On the other hand, it was noted in [15] that the forward–backward asymmetry is not modified by the presence of the Z' boson if its leptonic coupling constant is rather small.

More precise data from measurements of the process $e^+e^- \longrightarrow \mu^+\mu^-$ at the TRISTAN collider at $\sqrt{s} \approx$ 58 GeV were presented in [16, 17]. These data were accumulated over a period from 1991 to 1995, the integrated luminosity achieving 290 pb^{-1} in each of the three experiments (VENUS, TOPAZ, AMY). A typical precision in measuring the total leptonic cross section was 2% there. As in earlier experiments at $\sqrt{s} < M_Z$, the leptonic scattering cross section persisted in showing a tendency to fall short of the SM predictions. However, the difference between the theoretical and the experimental values did not exceed two standard deviations; that is, the statistical significance of this difference is insufficient for considering it a confirmation of deviations from the SM. Bearing in mind that, at higher energies, which have already been achieved at LEP2, the sensitivity of process (1) to effects of nonstandard physics becomes much higher, we can expect that the current experimental situation will be clarified in the near future. Even in the "worst" case, however—that is, even if experimental data show perfect agreement with the SM predictions—it would be possible to set more stringent constraints on the parameters of nonstandard physics.

In this connection, it is of paramount importance to optimize strategies of searches for effects of nonstandard physics at the operating LEP2 collider. In the present study, this problem is solved by introducing the integrated observables σ_+ and σ_- that have a more specific predictive power than conventional (canonical) observables like scattering cross sections σ_{ff} and forward–backward asymmetries A_{FB}. In particular, the energy dependence of the Z'-boson-exchange-induced deviations of the new observables from the SM predictions is governed predominantly by the parameters of the SM. In some cases, this makes it possible to predict unambiguously the signs of the deviations and the positions of their extrema and zeros. Owing to this, it will become possible to identify reliably effects induced by Z' bosons and to separate them from possible effects due to different reasons.

The ensuing exposition is organized as follows. In Section 2, we discuss the canonical variables σ_{ff} and A_{FB} and introduce the integrated variables $\sigma_\pm$. Section 3 is devoted to a comparative analysis of phenomenological implications of the possible existence of the extra Z' boson for the canonical and the new observables in the process $e^+e^- \longrightarrow \mu^+\mu^-$. In Section 4, we obtain model-independent constraints on the parameters of the Z' boson both on the basis of the existing experimental data and under the assumption that future experiments at LEP2 will show no signals from nonstandard physics. The effects of radiative corrections on the resulting constraints are also discussed. The last section summarizes the results obtained in this study and contains concluding comments on them.

2. CANONICAL AND NEW OBSERVABLES

The general form of the Lagrangian L_{NC} for fermion-neutral-current interactions caused by γ, Z-boson, and Z'-boson exchanges can be represented as

$$-L_{NC} = eJ^\mu_\gamma A_\mu + g_Z J^\mu_Z Z_\mu + g_{Z'} J^\mu_{Z'} Z'_\mu, \tag{2}$$

where $e = \sqrt{4\pi\alpha_{e.m.}}$ and where the Z- and Z'-boson gauge coupling constants are defined as $g_Z = e/s_W c_W$ ($s^2_W = 1 - c^2_W \equiv \sin^2\theta_W$) and $g_{Z'}$, respectively. The expressions for the currents appearing in Lagrangian (2) are given by

$$\begin{aligned} J^\mu_i &= \sum_f \bar\psi_f \gamma^\mu (L^f_i P_L + R^f_i P_R)\psi_f \\ &= \sum_f \bar\psi_f \gamma^\mu (V^f_i - A^f_i \gamma_5)\psi_f, \end{aligned} \tag{3}$$

where $i = \gamma, Z, Z'$ and where the projection operators are defined as $P_{L,R} = (1 \mp \gamma_5)/2$. We also have $R^f_i = V^f_i - A^f_i$ and $L^f_i = V^f_i + A^f_i$. The fermion coupling constants in the SM can be written as

$$\begin{aligned} V^f_\gamma &= Q_f, \quad A^f_\gamma = 0, \\ V^f_Z &= \frac{I^f_{3L}}{2} - Q_f s^2_W, \quad A^f_Z = \frac{I^f_{3L}}{2}. \end{aligned} \tag{4}$$

In the Born approximation, the differential cross section for the reaction $e^+e^- \longrightarrow \bar f f$ with unpolarized primary beams can be represented in the form

$$\frac{d\sigma_{ff}}{d\cos\theta} = N_C \frac{\pi\alpha^2_{e.m.}}{2s}[(1 + \cos^2\theta)F_1 + 2\cos\theta F_2], \tag{5}$$

where $N_C \approx 3\left(1 + \dfrac{\alpha_s}{\pi}\right)$ for quarks and $N_C = 1$ for leptons, while θ is the scattering angle for the fermion f with respect to the incident-electron momentum. In addition, the functions F_1 and F_2 have the form

$$F_1 = F^{SM}_1 + \Delta F_1, \quad F_2 = F^{SM}_2 + \Delta F_2, \tag{6}$$

where

$$\begin{aligned} F^{SM}_1 &= Q^2_e Q^2_f + 2Q_e v_e Q_f v_f \mathrm{Re}\chi_Z \\ &\quad + (v^2_e + a^2_e)(v^2_f + a^2_f)|\chi_Z|^2, \\ F^{SM}_2 &= 2Q_e a_e Q_f a_f \mathrm{Re}\chi_Z + 4 v_e a_e v_f a_f |\chi_Z|^2. \end{aligned} \tag{7}$$

Their deviations caused by the Z' boson can be represented as

$$\begin{aligned} \Delta F_1 &= 2Q_e v'_e Q_f v'_f \mathrm{Re}\chi_{Z'} \\ &\quad + (v'^2_e + a'^2_e)(v'^2_f + a'^2_f)|\chi_{Z'}|^2 \\ &\quad + 2(v_e v'_e + a_e a'_e)(v_f v'_f + a_f a'_f)\mathrm{Re}(\chi_Z \chi^*_{Z'}), \\ \Delta F_2 &= 2Q_e a'_e Q_f a'_f \mathrm{Re}\chi_{Z'} + 4 v'_e a'_e v'_f a'_f |\chi_{Z'}|^2 + \\ &\quad + 2(v_e a'_e + v'_e a_e)(v_f a'_f + v'_f a_f)\mathrm{Re}(\chi_Z \chi^*_{Z'}), \end{aligned} \tag{8}$$

where $\chi_V = s/(s - M^2_V + iM_V\Gamma_V)$ is the vector-boson ($V = Z, Z'$) propagator. The fermionic coupling constant are normalized as

$$\begin{aligned} v_f &= \frac{g_Z}{e} V^f_Z, \quad a_f = \frac{g_Z}{e} A^f_Z, \\ v'_f &= \frac{g_{Z'}}{e} V^f_{Z'}, \quad a'_f = \frac{g_{Z'}}{e} A^f_{Z'}. \end{aligned} \tag{9}$$

The total decay width of the Z' boson, $\Gamma_{Z'}$, is equal to the sum of the partial widths with respect to decays into fermion pairs:

$$\begin{aligned} \Gamma^{ff}_{Z'} &= N_C \frac{\alpha_{e.m.} M_{Z'}}{3} \sqrt{1 - 4m^2_f/M^2_{Z'}} \\ &\quad \times [v'^2_f + a'^2_f + 2m^2_f/M^2_{Z'}(v'^2_f - 2a'^2_f)]. \end{aligned} \tag{10}$$

Owing to e–l universality, the leptonic channel of reaction (1) has an obvious advantage over the production of a $\bar{q}q$ pair, since the leptonic observables depend on a smaller number of free parameters. Indeed, the leptonic process $e^+e^- \longrightarrow \mu^+\mu^-$ depends on two leptonic coupling constant, v_l' and a_l', and on the mass $M_{Z'}$. In order to describe the reaction $e^+e^- \longrightarrow \bar{q}q$, we need additional information about the quark coupling constants. In this article, we study precisely the leptonic process (1) with $l = \mu$.

In LEP2 experiments, the leptonic channel is traditionally investigated in terms of the following pair of integrated observables: (i) the total scattering cross section $\sigma_{\mu\mu}$ and (ii) the forward–backward asymmetry A_{FB}. These observables can be represented as

$$\sigma_{\mu\mu} = \int_{-1}^{1} \frac{d\sigma_{\mu\mu}}{d\cos\theta} d\cos\theta = \sigma_{pt} F_1, \quad (11)$$

where $\sigma_{pt} \equiv \sigma(e^+e^- \longrightarrow \gamma^* \longrightarrow \mu^+\mu^-) = (4\pi\alpha^2_{e.m.})/(3s)$ is the electromagnetic scattering cross section, and as

$$A_{FB} = \frac{\sigma_{FB}}{\sigma_{\mu\mu}} \equiv \frac{\sigma^F_{\mu\mu} - \sigma^B_{\mu\mu}}{\sigma_{\mu\mu}} = 3F_2/4F_1. \quad (12)$$

Here, the cross sections for scattering into the forward and the backward hemisphere are written as $\sigma^F_{\mu\mu} = \int_0^1 (d\sigma_{\mu\mu}/d\cos\theta) d\cos\theta$ and as $\sigma^B_{\mu\mu} = \int_{-1}^0 (d\sigma_{\mu\mu}/d\cos\theta) d\cos\theta$, respectively.

In order to reveal effects peculiar precisely to the Z' boson, we introduce the more appropriate observables σ_+ and σ_- defined as the differences of the integrated cross sections in specific kinematical regions of the scattering angle θ; that is,

$$\sigma_+ \equiv \left(\int_{-z^*}^{1} - \int_{-1}^{-z^*} \right) \frac{d\sigma_{\mu\mu}}{d\cos\theta} d\cos\theta, \quad (13)$$

$$\sigma_- \equiv \left(\int_{-1}^{z^*} - \int_{z^*}^{1} \right) \frac{d\sigma_{\mu\mu}}{d\cos\theta} d\cos\theta, \quad (14)$$

where $z^* > 0$ is derived from the condition requiring that the kinematical coefficients of F_1 and F_2 in (5) be equal upon integration with respect to $\cos\theta$. This condition has the form

$$\int_{-z^*}^{z^*} (1 + \cos^2\theta) d\cos\theta = \left(\int_{z^*}^{1} - \int_{-1}^{-z^*} \right) 2\cos\theta d\cos\theta, \quad (15)$$

whence if follows that z^* satisfies the equation

$$\frac{1}{3} z^{*3} + z^{*2} + z^* - 1 = 0, \quad (16)$$

its solution being $z^* = 2^{2/3} - 1 = 0.5874$, which corresponds to $\theta^* = 54°$. If measurements are performed in an incomplete kinematical region of the scattering angle—that is for $|\cos\theta| < c$—we obtain $z^* = (1 + 3c)^{1/3} - 1$.

The observables σ_+ and σ_- can be related to the function F_1 and F_2 as

$$\sigma_\pm = \sigma^*_{pt}(F_1 \pm F_2), \quad (17)$$

where

$$\sigma^*_{pt} \equiv \frac{3}{4}(1 - z^{*2})\sigma_{pt} \simeq 0.5\sigma_{pt}. \quad (18)$$

It is convenient to express these new observables $\sigma_\pm$ in terms of the helicity scattering cross sections $\sigma_{\alpha\beta}$ (here, α, β = L, R are the helicities of the initial electron and the final fermion, respectively). Specifically, we have

$$\sigma_+ \simeq \frac{1}{4}(\sigma_{RR} + \sigma_{LL}), \quad (19)$$

$$\sigma_- \simeq \frac{1}{4}(\sigma_{RL} + \sigma_{LR}), \quad (20)$$

where $A_{\alpha\beta} = (Q_e)_\alpha (Q_f)_\beta + g^e_\alpha g^f_\beta \chi_Z + g'^e_\alpha g'^f_\beta \chi_{Z'}$ is a helicity amplitude and $\sigma_{\alpha\beta} = N_C \sigma_{pt} |A_{\alpha\beta}|^2$. In this way, the role of these observables in separating the helicity cross sections $\sigma_{\alpha\beta}$ is clarified. An alternative possibility of separating the helicity cross sections that is based on an analysis of the differential cross sections was considered in [18]. In should be noted that the observables $\sigma_\pm$ are integrated characteristics; being mathematically equivalent to differential variables, they have some advantages over the latter in the case of limited statistics.

It should be noted that the new independent observables $\sigma_\pm$ can be represented as combinations of the canonical observables $\sigma_{\mu\mu}$ and A_{FB}. Indeed, it follows from (11), (12), (17), and (18) that

$$\sigma_\pm = 0.5\sigma_{\mu\mu}\left(1 \pm \frac{4}{3}A_{FB}\right) = 0.5\left(\sigma_{\mu\mu} \pm \frac{4}{3}\sigma_{FB}\right). \quad (21)$$

This means that σ_+ and σ_- can be either measured directly as the difference of the integrated cross sections [see (13) and (14)] or determined indirectly in terms of $\sigma_{\mu\mu}$ and A_{FB}.

3. STRUCTURE OF Z' INTERFERENCE

A clearer representation of the above results can be obtained in an approximation based on some simplifying assumptions:

(i) In estimating Z'-boson-induced contributions to observables, it is sufficient to take into account only Z'-boson interference effects, since the characteristic lower bound on the Z'-boson mass significantly exceeds the maximal energy of the LEP2 collider.

(ii) In the expressions for the deviations of the observables from their values predicted by the SM, we can neglect the vector leptonic constant v_l against the axial-vector constant a_l, because $|v_l| \ll |a_l| < 1$ in the SM. In addition, we can also disregard the contribution of the imaginary part of the Z'-boson propagator against its real part.[1)]

3.1. Z' Interference in the Cross Section and Forward–Backward Asymmetry

In the approximation specified by items (i) and (ii), the deviation of the total scattering cross section from the SM prediction is given by

$$\Delta\sigma_{\mu\mu} \equiv \sigma_{\mu\mu} - \sigma_{\mu\mu}^{\mathrm{SM}} \approx 2\sigma_{\mathrm{pt}}(v_l'^2 + a_l'^2 a_l^2 \mathrm{Re}\chi_Z)\chi_{Z'}, \quad (22)$$

where the first (second) term in the parenthetical expression on the right-hand side of (22) corresponds to γ–Z (Z–Z') interference, while v_l' and a_l' are constants of, respectively, the vector and the axial-vector Z'-boson coupling to charged leptons [see (9)].

If the constants v_l' and a_l' are on the same order of magnitude, then the destructive γ–Z' interference dominates over the constructive Z–Z' interference at energies of the TRISTAN collider. Therefore, the deviation (22) of the cross section must be negative in this energy region. At higher energies (but at the same time, those that are less than M_Z), the relative contribution of the Z–Z' interference ever increases, and the two types of interferences cancel each other completely at

$$\sqrt{s_0} = \frac{M_Z}{\sqrt{1 + (a_l a_l'/v_l')^2}}; \quad (23)$$

that is, $\Delta\sigma_{\mu\mu} = 0$. It should be noted here that $\sqrt{s_0}$ is independent of $M_{Z'}$. Finally, we have $\Delta\sigma_{\mu\mu} > 0$ for $\sqrt{s_0} < \sqrt{s} < M_Z$.

At energies $\sqrt{s} > M_Z$, either type of the interferences, γ–Z' and Z–Z', is destructive; hence, they add up. Indeed, the right-hand side of (22) involves only the squares of the leptonic coupling constants, whence it follows that, at LEP2 energies, the sign of the Z'-boson-induced deviation of the cross section from the behavior predicted by the SM is determined by the sign of the propagator $\chi_{Z'}$, $\Delta\sigma_{\mu\mu} < 0$. It should be emphasized that this property is model-independent; that is, it takes place for any heavy vector states with arbitrary vector or axial-vector (or both) leptonic coupling constants for $M_Z < \sqrt{s} \ll M_{Z'}$. Moreover, it follows from (8) that this property is unaffected by the simplifying assumption (ii). Only for the leptonic process (1) is the deviation $\Delta\sigma_{\mu\mu}$ of fixed sign if leptonic e–μ universality holds. As to the cross section for the process $e^+e^- \longrightarrow \bar{q}q$, it does not possess this property in general.

In order to obtain a quantitative representation of the interference pattern, we consider three cases that differ from one another by the choice of the leptonic coupling constants v_l' and a_l', but which feature the same value of the mass $M_{Z'}$. These are the cases of (a) the vector Z_V' boson ($v_l' = 1$, $a_l' = 0$), (b) the axial-vector Z_A' boson ($v_l' = 0$, $a_l' = 1$), and (c) the Z_{VA}' boson ($v_l' = 1$, $a_l' = 1$). In all cases, the mass $M_{Z'}$ was set to 500 GeV. It should be recalled that, in the SM, the coupling constants are $a_l = -0.6$ and $v_l = 0.08a_l$ at $\sin^2\theta_W = 0.23$. We can easily trace the role of electroweak interference in the cross section for the leptonic process (1) in Fig. 1*a* and its role in the relative deviation of the cross section, $\Delta\sigma_{\mu\mu}/\sigma_{\mu\mu}^{\mathrm{SM}}$ in Fig. 1*b*.

The statistical significance defined as

$$S[\sigma] = \frac{|\sigma_{\mu\mu} - \sigma_{\mu\mu}^{\mathrm{SM}}|}{\delta\sigma_{\mu\mu}} = \frac{|\Delta\sigma_{\mu\mu}|}{\sqrt{\sigma_{\mu\mu}^{\mathrm{SM}}}}\sqrt{\mathscr{L}_{\mathrm{integr}}}, \quad (24)$$

where $\delta\sigma_{\mu\mu}$ is the statistical uncertainty in measuring the scattering cross section and $\mathscr{L}_{\mathrm{integr}}$ is the integrated luminosity ($\mathscr{L}_{\mathrm{integr}} = \int dt\mathscr{L}$), is yet another important characteristic in an analysis of the cross section for process (1). Thus, the statistical significance determines the deviation of the observable in standard-deviation units. Figure 1*c* shows the energy dependence of $S[\sigma]$ as a function of energy at $\mathscr{L}_{\mathrm{integr}} = 300$ pb^{-1} for $M_{Z'} = 500$ and 800 GeV. From this figure, we can see that the scattering cross section appears to be quite sensitive to Z'-boson effects at the maximal energy of the LEP2 collider.

By analogy with (22), the deviation of the absolute forward–backward asymmetry σ_{FB} in (12) from the SM prediction, $\Delta\sigma_{\mathrm{FB}} = \sigma_{\mathrm{FB}} - \sigma_{\mathrm{FB}}^{\mathrm{SM}}$, can be represented in the form

$$\Delta\sigma_{\mathrm{FB}} \approx \frac{3}{2}\sigma_{\mathrm{pt}}(a_l'^2 + v_l'^2 a_l^2 \mathrm{Re}\chi_Z)\chi_{Z'}. \quad (25)$$

From (22) and (25), we can see that, apart from the interchange of the coupling constants v_l' and a_l', $v_l' \rightleftharpoons a_l'$, the expressions for the deviations of the cross section and of the absolute forward–backward asymmetry are similar in structure. Thus, the two observables have the same properties upon the above interchange of the coupling constants. Hence, all the conclusions drawn above for the scattering cross section can be extended to the absolute forward–backward

[1)]It should be noted here that all quantitative results presented below were derived on the basis of the exact expressions.

asymmetry. By way of example, we indicate that, at LEP2 energies, the deviation $\Delta\sigma_{FB}$ is negative at arbitrary constants of Z' coupling to leptons. In seeking signals from new physics at LEP2 as deviations of observables from SM predictions, these general properties of $\Delta\sigma_{\mu\mu}$ and $\Delta\sigma_{FB}$ for Z' bosons to be of a constant sign can be used to separate, in a model-independent way, the above interference effects from other effects, those that are induced by nonstandard physics of alternative nature.

As to the forward–backward asymmetry (12), its deviation ΔA_{FB} from the SM-predicted value A_{FB}^{SM},

$$\Delta A_{FB} = A_{FB} - A_{FB}^{SM} \propto \left[\left(a_l'^2 - \frac{4}{3}A_{FB}^{SM}v_l'^2\right) + \left(v_l'^2 - \frac{4}{3}A_{FB}^{SM}a_l'^2\right)a_l^2\mathrm{Re}\chi_Z\right]\chi_{Z'}, \quad (26)$$

does not exhibit the aforementioned property, which is characteristic of $\sigma_{\mu\mu}$ and σ_{FB}; that is, the quantity in (12) can take both negative and positive values at LEP2 energies, depending on actual values of the leptonic coupling constants.

3.2 Z' Interference in $\sigma_\pm$

Let us now consider the observables σ_+ and σ_-. In the approximation specified by (i) and (ii), it is convenient to represent them as

$$\sigma_\pm/\sigma_{pt}^* \approx \left|1 \pm a_l^2\chi_Z\right|^2 + 2(v_l'^2 \pm a_l'^2)\chi_{Z'}(1 \pm a_l^2\mathrm{Re}\chi_Z). \quad (27)$$

First, we will study the behavior of σ_+. The first term in the expression on the right-hand side of (27) determines the SM contribution approaching its minimal (almost vanishingly small) value at $\sqrt{s} = \sqrt{s_+}$:

$$\sqrt{s_+} = \frac{M_Z}{\sqrt{1 + a_l^2}} \simeq 78\ \mathrm{GeV}. \quad (28)$$

Figure 2*a* illustrates the energy dependence of σ_+ in the SM.

The Z'-boson-induced deviation of σ_+ from this behavior can be represented in the form

$$\Delta\sigma_+ = \sigma_+ - \sigma_+^{SM} \approx \sigma_{pt}(1 + a_l^2\mathrm{Re}\chi_Z)(v_l'^2 + a_l'^2)\chi_{Z'}. \quad (29)$$

The first and the second term in parentheses on the right-hand side of (29) are due to γ–Z' and Z–Z' interferences, respectively. It should be emphasized that, in contrast to what was found for the canonical variables $\sigma_{\mu\mu}$ and σ_{FB}, there is no cancellation of the γ–Z' and Z–Z' interference contributions in the expression for σ_+ in the entire energy region $\sqrt{s} \ll M_{Z'}$. This leads to noticeable enhancement of the Z'-boson interference effects.

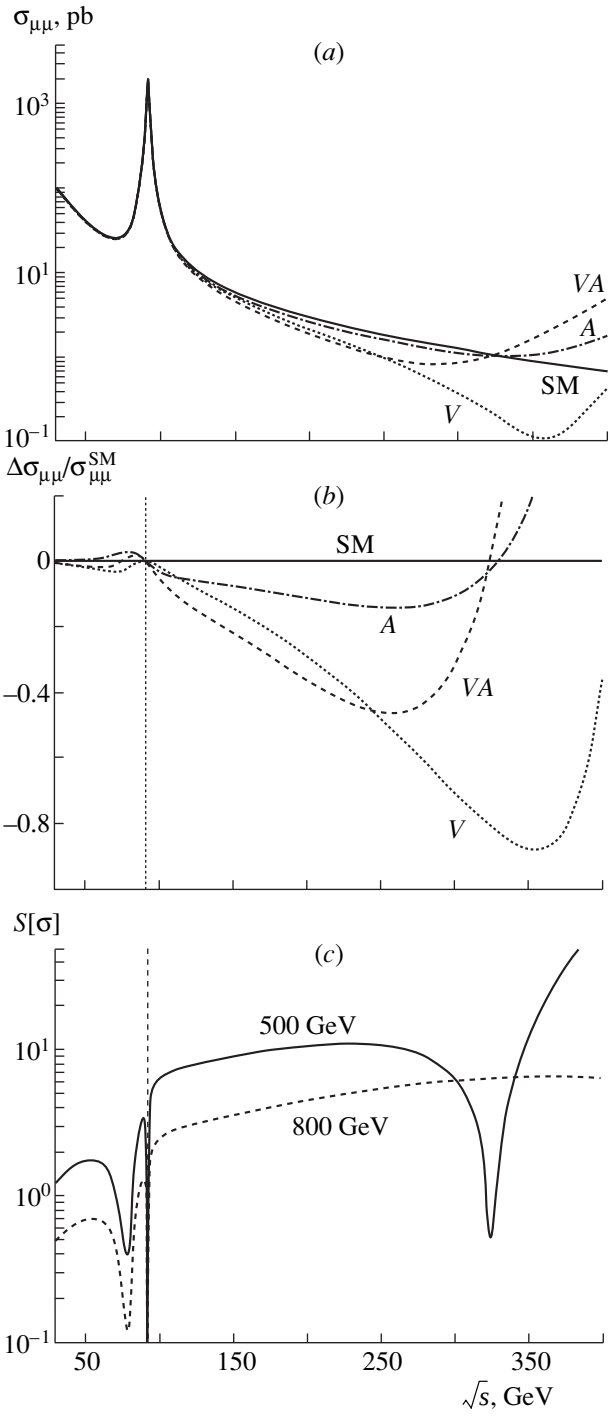

Fig. 1. (*a*) Total cross section $\sigma_{\mu\mu}$ as a function of energy within the SM (SM curve) and in the presence of the Z' boson with mass $M_{Z'} = 500$ GeV for the cases of Z'_V ($v_l' = 1$, $a_l' = 0$), Z'_A ($v_l' = 0$, $a_l' = 1$), and Z'_{VA} ($v_l' = 1$, $a_l' = 1$). (*b*) As in Fig. 1*a*, but for the relative cross-section deviation $\Delta\sigma_{\mu\mu}/\sigma_{\mu\mu}^{SM}$. (*c*) As in Fig. 1*a*, but for the statistical significance $S[\sigma]$ at $M_{Z'} = 500$ and 800 GeV and an integrated luminosity of $\mathscr{L}_{integr} = 300\ \mathrm{pb}^{-1}$.

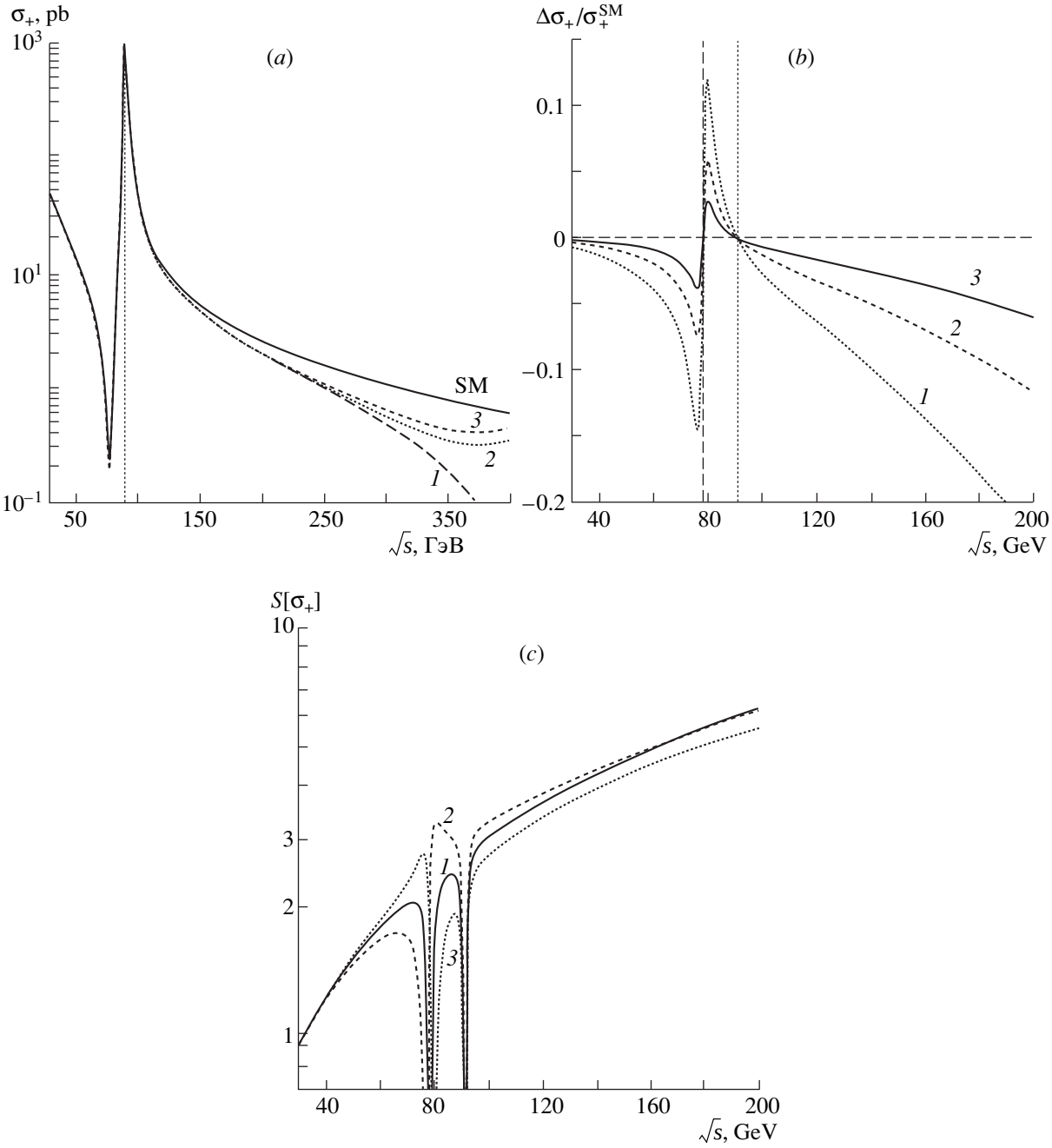

Fig. 2. Observable σ_+ as a function of energy within the SM (SM curve) and in the presence of the Z' boson with mass $M_{Z'} = 600$ GeV for coupling-constant values satisfying the condition $v_l'^2 + a_l'^2 = 1$. Curves *1*, *2*, and *3* correspond to the product of the coupling constants that takes values of $v_l'a_l' = 0, 1, -1$, respectively. (*b*) As in Fig. 2*a*, but for the relative deviation $\Delta\sigma_+/\sigma_+^{SM}$. Curves *1*, *2*, and *3* correspond to $v_l'^2 + a_l'^2 = 1$, 0.5, and 0.25. In all cases, it is assumed that $v_l'a_l' = 0$. (*c*) As in Fig. 2*a*, but for the statistical significance $S[\sigma_+]$ at an integrated luminosity of $\mathcal{L}_{integr} = 300$ pb^{-1}.

Apart from this, formula (29) shows that the dependence $\Delta\sigma_+$ on the parameters of the Z' boson is determined by the expression $(v_l'^2 + a_l'^2)\chi_{Z'}$, which, for $\sqrt{s} \ll M_{Z'}$, is negative definite for arbitrary constants of Z'-boson coupling to leptons. Herein lies the similarity of the observable σ_+, on one hand, and the variables $\sigma_{\mu\mu}$ and σ_{FB}, on the other hand, in what is concerned with the possible manifestations of the Z' boson. However, σ_+ has yet another extremely important property that is

of use for identifying effects associated with extra neutral vector bosons. Namely, the energy dependence of the deviation $\Delta\sigma_+$ is governed primarily by the function $(1 + a_l^2 \mathrm{Re}\chi_Z)$, which is dependent only on the well-known SM parameters. In other words, we can predict in advance the positions of the extrema and zeros of the deviation $\Delta\sigma_+$. Indeed, $\Delta\sigma_+$ attains extremal values at $|\sqrt{s_+} - \sqrt{s}| \approx \Gamma_Z/2$. In addition, it can easily be seen from (27) and (29) that, at $\sqrt{s} = \sqrt{s_+}$, we have not only the condition $\sigma_+^{\mathrm{SM}} \approx 0$ but also the condition $\Delta\sigma_+ = 0$. It follows that the energy point $\sqrt{s_+}$ is extremely suitable for seeking phenomenological manifestations of both nonstandard physics beyond the SM and models predicting the existence of Z' bosons. It should also be emphasized that the point in (28) is completely determined by the SM parameters M_Z and a_l. We recall that the localization of the similar point in the scattering cross section [see (23)] depends explicitly on the constants of Z'-boson coupling to leptons. All these facts obviously demonstrate the advantages of the new observable σ_+ over the canonical variables in searches for Z'-boson effects.

Figure 2*b* displays the relative deviation $\Delta\sigma_+/\sigma_+^{\mathrm{SM}}$ as a function of energy. Here, the Z' boson is taken in the so-called consistent model [19], where the leptonic coupling constants are defined in the same way as in the SM: $v_l' = v_l$ and $a_l' = a_l$. For the Z'-boson mass, we took the values of $M_{Z'} = 500$ and 700 GeV. In Fig. 2*b*, we can easily trace a characteristic correlation between the signs of the deviation $\Delta\sigma_+$ at different energy values. In particular, $\Delta\sigma_+/\sigma_+^{\mathrm{SM}}$ is negative for $\sqrt{s} < \sqrt{s_+}$ and positive for $\sqrt{s_+} < \sqrt{s} < M_Z$; for $\sqrt{s} > M_Z$, it again becomes negative.

That $\sqrt{s_+}$ is independent of v_l' and a_l' results from the approximation specified in (ii), where it is assumed that $v_l \approx 0$. Upon taking exactly into account a finite value of the vector coupling constant, there arises only a moderate energy shift that is determined by the factor $1 + \delta$, where $\delta = v_l a_l \cos\gamma/(1 + a_l^2)$ with $\cos\gamma = 2(v'/a')/[1 + (v'/a')^2]$. The maximal value of this shift is about 1.6 GeV at $|\cos\gamma| = 1$. In addition, a nonzero value of the constant v_l leads to the splitting of the curves plotted in Fig. 2*a* for the three different values of $v_l' a_l' = 0, \pm 1$.

Figure 2*c* illustrates the energy dependence of the statistical significance $S[\sigma_+]$ for the observables σ_+. In just the same way as the scattering cross section, the observable σ_+ shows the highest sensitivity to Z'-boson effects at the maximal energy of the LEP2 collider.

The observable σ_- has many features in common with σ_+. In particular, σ_-^{SM} vanishes at

$$\sqrt{s_-} = \frac{M_Z}{\sqrt{1 - a_l^2}} \simeq 113 \text{ GeV}. \tag{30}$$

The energy dependence of the deviation of the observable σ_- from the SM prediction,

$$\Delta\sigma_- = \sigma_- - \sigma_-^{\mathrm{SM}} \approx \sigma_{\mathrm{pt}}(1 - a_l^2 \mathrm{Re}\chi_Z)(v_l'^2 - a_l'^2)\chi_{Z'}, \tag{31}$$

is completely determined by the propagator χ_Z and by the SM parameters. In contrast to what was found for $\Delta\sigma_+$, the sign and the magnitude of $\Delta\sigma_-$ are determined by the expression $(v_l'^2 - a_l'^2)\chi_{Z'}$, which can be positive or negative, depending on the sign of the difference $v_l'^2 - a_l'^2$. From (31), it also follows that, at $\sqrt{s} = \sqrt{s_-}$, $\Delta\sigma_- = 0$ both in the SM and upon taking into account the Z' boson. Thus, the energy region around $\sqrt{s_-}$ is quite favorable for seeking effects of new physics other than Z'-boson effects with the aid of the observable σ_-. Figure 3*a* displays the energy dependence of σ_- in the SM and in the presence of the Z' boson characterized by the mass of $M_{Z'} = 600$ GeV and by coupling-constant values satisfying the condition $v_l'^2 - a_l'^2 = -1$ (curve *1*) or +1 (curve *2*). Figure 3*b* shows the relative deviation $\Delta\sigma_-/\sigma_-^{\mathrm{SM}}$ for the Z' boson having the same mass value and the coupling constants satisfying the conditions $v_l'^2 - a_l'^2 = -1$, –0.5, or –0.25. The curves corresponding to positive values of the combination $v_l'^2 - a_l'^2$ can be obtained by a mere reflection of the curves in Fig. 3*b* with respect to the abscissa. In just the same way as $\Delta\sigma_+$, the quantity $\Delta\sigma_-$ is characterized by a specific correlation of the signs of the deviation at different energy values (see Table 1). Figure 3*c* illustrates the energy dependence of $S[\sigma_-]$ for the Z' boson with mass $M_{Z'} =$ 600 GeV at $v_l'^2 - a_l'^2 = -1$ (curve *1*) and +1 (curve *2*).

Basic properties of the canonical and the new observables with respect to Z'-boson manifestations are listed in Table 2. As was emphasized above, these properties could prove to be convenient for identifying the Z' boson as the possible reason for deviations from the SM predictions, should such deviations be detected experimentally.

At the LEP1 collider, the DELPHI collaboration [12] made an attempt at seeking effects of nonstandard physics (in particular, of Z' bosons) in the process $e^+e^- \longrightarrow \mu^+\mu^-$ at an energy of about 80 GeV by using the observables $\sigma_\pm$. Specifically, DELPHI measured the ratio σ_+/σ_-. The data obtained in this way are displayed in Fig. 4, along with the corresponding SM predictions.

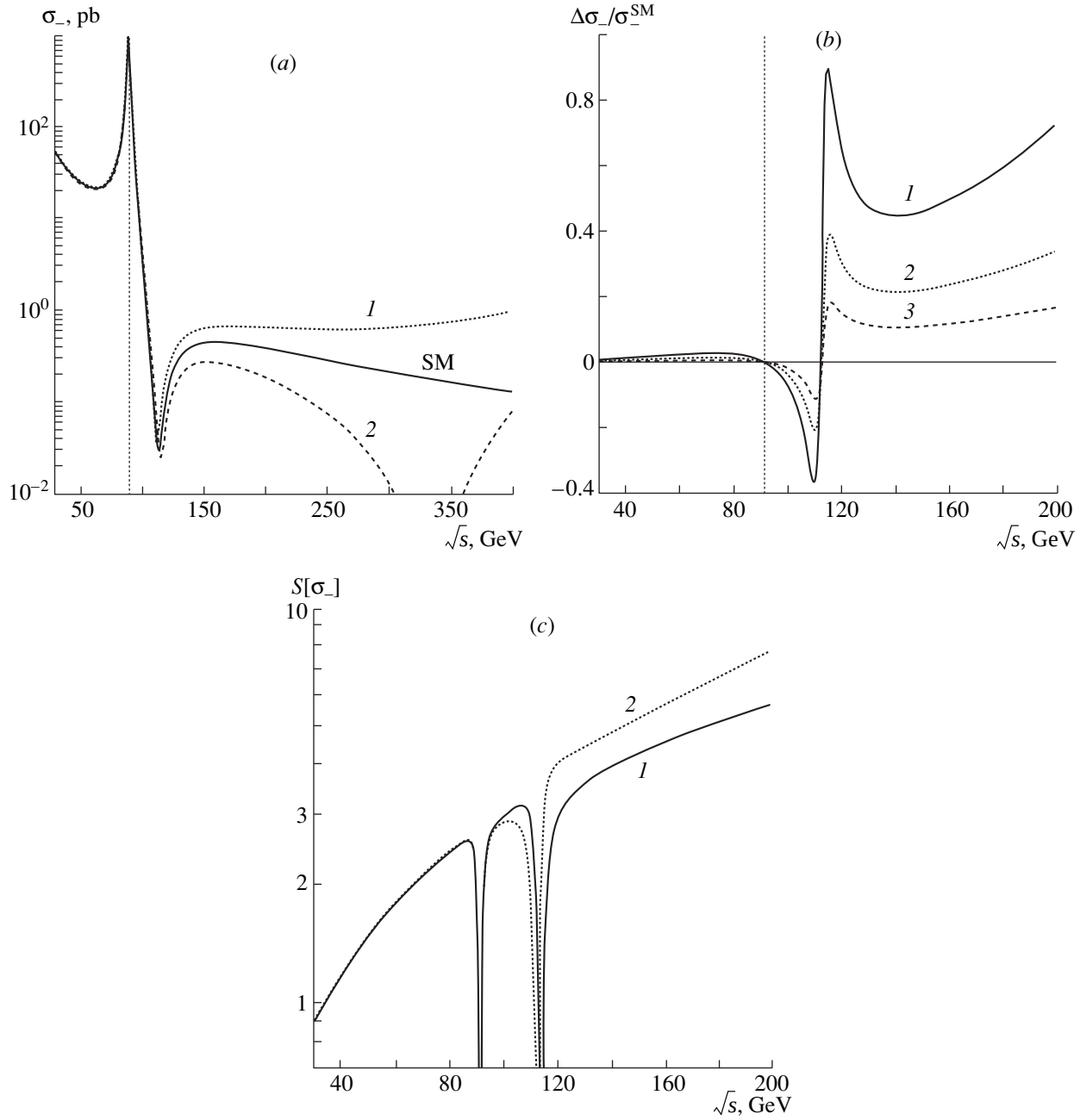

Fig. 3. (*a*) Observable σ_ as a function of energy within the SM (SM curve) and in the presence of the Z' boson with mass $M_{Z'}$ = 600 GeV. Curves *1* and *2* correspond to $v_l'^2 - a_l'^2 = \mp 1$. (*b*) As in Fig. 3*a*, but for the relative deviation $\Delta\sigma_-/\sigma_-^{SM}$. Curves *1*, *2*, and *3* correspond to $v_l'^2 - a_l'^2 = -1, -0.5$, and -0.25. (*c*) As in Fig. 3*a*, but for the statistical significance $S[\sigma_-]$ at an integrated luminosity of $\mathscr{L}_{integr} = 300\ pb^{-1}$.

The conclusion drawn in [12] was that no deviations from the SM were observed at the level of the experimental precision achieved there. In my opinion, however, the energy region chosen for the experiments reported in [12] was not the best one—from the above analysis, it follows that not only is it difficult to reveal Z'-boson effects in this region, but even an accurate verification of SM predictions is questionable there.

4. MODEL-INDEPENDENT CONSTRAINTS ON THE Z'-BOSON PARAMETERS

If experiments at LEP2 fail to discover deviations from SM predictions at a level of attained or planned accuracy, then we will be able to estimate the sensitivity of the observables to Z'-boson effects and to set constraints on the parameters of the Z'-boson. In particular,

we can perform a model-independent analysis on the basis of data currently available from LEP2 for various energy values [13] and take additionally into account statistics of events to be obtained in the near future [5]. Table 3 quotes the energy values and the corresponding integrated luminosities at which experimental data have already been obtained. Data for the last two energy values occurring in the region of maximal LEP2 energies have not yet been obtained, but they will have been accumulated by the end of 2000.

To facilitate our analysis, it is convenient to use the model-independent parametrization of the constants of Z'-boson coupling to leptons [20, 21]:

$$V_f = V_{Z'}^f \sqrt{\frac{g_{Z'}^2}{4\pi}\frac{M_Z^2}{M_{Z'}^2 - s}}, \qquad A_f = A_{Z'}^f \sqrt{\frac{g_{Z'}^2}{4\pi}\frac{M_Z^2}{M_{Z'}^2 - s}}. \tag{32}$$

The sensitivity of the observables $\sigma_\pm$ can be estimated by using the χ^2 functional defined as

$$\chi^2 = \sum_{k=1}^{n}\left[\left(\frac{\Delta\sigma_{+k}}{\delta\sigma_{+k}}\right)^2 + \left(\frac{\Delta\sigma_{-k}}{\delta\sigma_{-k}}\right)^2\right], \tag{33}$$

where summation is performed over $n(\leq 6)$ energy regions listed in Table 3 and where the experimental uncertainty $\delta\sigma_{\pm k}$ includes both statistical and systematic errors. The condition $\chi^2 < \chi^2_{\text{crit}}$ was used as the criterion for constraining the model-independent leptonic coupling constants V_l and A_l. The χ^2_{crit} value was determined by the required level of statistical significance. In deriving numerical estimates, we assumed the integrated luminosities that have already been achieved and used the systematic errors at LEP2 for the leptonic process $e^+e^- \longrightarrow \mu^+\mu^-$ [13]. In order to assess the future potential for improvement of the sensitivity at higher energies, we have considered a specific example where we have used the expected eventual luminosity of LEP2 at the systematic error of $\delta_{\text{syst}} = 0.5\%$.

From (11)–(14), it follows that the observables under investigation can be expressed in terms of the differential cross sections. It is well known that the shape and the numerical values of the cross sections are modified sizably by radiative corrections such as those that are associated with the emission of real photons by initial electrons and positrons. The inclusion of the radiative corrections was performed on the basis of the scheme proposed in [22]. In particular, the contribution of hard-photon emission in the second order in the electromagnetic coupling constant (α^2) was calculated within this scheme; also, the leading contributions of soft photons and virtual electromagnetic corrections were estimated on same basis. In this scheme, the radiative corrections for the differential cross sections are

Table 1. Energy correlation of the signs of the deviation $\Delta\sigma_-$ induced by the Z' boson

$\sqrt{s}$	$<M_Z$	M_Z–133 GeV	>113 GeV
Sign of the deviation $\Delta\sigma_-$	–	+	–
The same	+	–	+

Table 2. Model-independent properties of the observables related to Z'-boson effects

Observable	Energy dependence has been determined for $E_{\text{SM}} < 200$ GeV	Sign of the deviation has been determined at LEP2
ΔA_{FB}	No	No
$\Delta\sigma_{\mu\mu}$	No	Yes
$\Delta\sigma_{\text{FB}}$	No	Yes
$\Delta\sigma_-$	Yes, for $\lvert\Delta\sigma_-\rvert$	No
$\Delta\sigma_+$	Yes	Yes

calculated as the convolutions of the coefficients F_1 and F_2 with the radiator functions $R_T^e(k)$ and $R_{\text{FB}}^e(k)$, respectively, k being the energy fraction lost by radiation. The expression for the differential cross section with allowance for the radiative corrections takes the form

$$\frac{d\sigma}{d\cos\theta} = \frac{3}{8}[(1+\cos^2\theta)\sigma_s + 2\cos\theta\sigma_a], \tag{34}$$

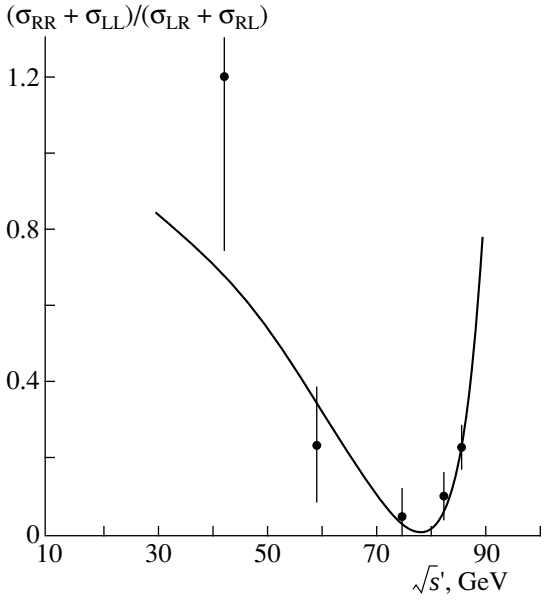

Fig. 4. Ratio σ_+/σ_- as a function of the energy of a $\mu^+\mu^-$ pair according to data obtained at the DELPHI facility [12]. The solid curve represents the corresponding dependence obtained within the SM.

Table 3. Energies and corresponding integrated luminosities for experiments that have been performed at LEP2 or which are planned at this collider

E_{SM}, GeV	133	161	172	183	190	200
$\mathcal{L}_{int}$, pb^{-1}	10	10	10	50	200	250

where θ is the angle between the direction of μ^- emission and the electron-beam direction in the c.m. frame of the $\mu^+\mu^-$ pair [23]. The symmetric and the antisymmetric part of the scattering cross section (σ_s and σ_a, respectively) are determined as the convolutions with the radiator functions; that is,

$$\sigma_s = \int_0^\Delta dk R_T^e(k)\sigma_{pt}(s')F_1(s'),$$
$$\sigma_a = \int_0^\Delta dk R_{FB}^e(k)\sigma_{pt}(s')F_2(s'), \quad (35)$$

where $s' = s(1 - k)$. Because of the so-called radiative return to the Z resonance at $\sqrt{s} > M_Z$, the energy spectrum of emitted photons has a maximum at $E_\gamma/E_{beam} \approx 1 - M_Z^2/s$ [22].

In order to enhance the Z'-boson signal, it is necessary to eliminate hard-photon-emission events by subjecting the photon energy to the cut $\Delta = E_\gamma/E_{beam} < 1 - M_Z^2/s$. The observables $\sigma_\pm$ involving radiative corrections can also be determined by means of formulas (13) and (14) with the same value of z^* since the form (34) of the cross section modified by radiative corrections does not differ from the cross-section form (5). However, the convolution of the coefficients F_1 and F_2 with the radiator functions $R_T^e(k)$ and $R_{FB}^e(k)$, respectively, leads to some shift in the position of the zeros $\sqrt{s_\pm}$ and extrema in the energy dependence of the deviations $\Delta\sigma_\pm$. These changes can be reliably taken into consideration with the aid of expression (34). The quantitative analysis reveals that the these energy shifts do not exceed 100 MeV. This means that radiative corrections do not lead to significant changes in the interference pattern shown in Figs. 1–3. The quantitative analysis illustrated graphically in Fig. 5 was performed on the basis of the ZEFIT code used in conjunction with the ZFITTER code [24]. Displayed in Fig. 5 are the admissible regions obtained for the constants of Z'-boson coupling to leptons from a global analysis of the observables $\sigma_\pm$ on the basis of the experimental data already collected at LEP2 in the energy range $\sqrt{s}$ = 133–183 GeV (see Table 3) and data expected from LEP2 in the future at $\sqrt{s}$ = 190 and 200 GeV. The level of statistical significance corresponds to two standard deviations ($\chi^2_{cr} = 4$).

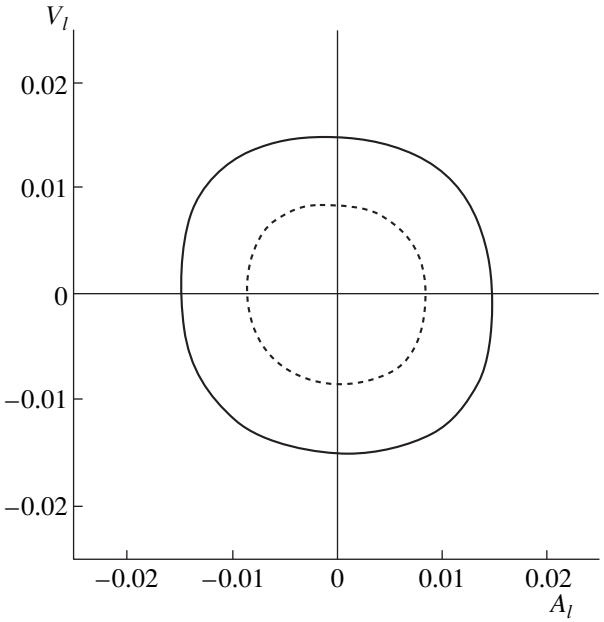

Fig. 5. 2σ upper bound on the Z'-boson coupling constants on the (A_l, V_l) plane from an analysis of the observables $\sigma_\pm$. The solid curve was obtained on the basis of data on the process $e^+e^- \longrightarrow \mu^+\mu^-$ by taking into account the first four points from Table 3. The dashed curve was plotted with allowance for all six points.

5. CONCLUSION

Let us summarize our results and list the most important features of the proposed approach to revealing and studying the indirect effects induced by the Z' boson at the LEP2 e^+e^- collider. This approach is based on the use of the new integrated observables $\sigma_\pm$ in investigating the process $e^+e^- \longrightarrow \mu^+\mu^-$ at energies $\sqrt{s} \le 200$ GeV. It has been shown that the observables σ_+ and σ_- can be represented in the form of the sum of independent pairs of the helicity cross sections. This opens the possibility to obtain, in the leptonic channel, more definitive information about Z'-boson effects in relation to information that can be deduced with the aid of the canonical observables $\sigma_{\mu\mu}$ and A_{FB}, which depend on the entire set of the helicity cross sections. The deviations $\Delta\sigma_\pm$ induced by the Z' boson have a specific energy dependence determined by the well-known SM parameters. In particular, we can make unambiguous model-independent predictions for the deviation $\Delta\sigma_+$. Specifically, the sign of this deviation over the entire energy region investigated here and the positions of its extrema and zeros have been determined to a high precision. On the other hand, information about $\Delta\sigma_-$ is less precise since the common factor in (31), which determines the Z'-boson contribution to this observable, is not of fixed sign. For this reason, we can predict only

the energy dependence of the absolute value of the deviation $|\Delta\sigma_-|$ and consider the correlation of the signs of this deviation at different energy values. It has also been shown that the sensitivity of the observables $\sigma_\pm$ to the extra Z' boson increases with energy, reaching the highest level (in the energy region under consideration) at the maximal energy of the LEP2 collider.

Apart from this, we have revealed two energy points, $\sqrt{s_+} \approx 78$ GeV and $\sqrt{s_-} \approx 113$ GeV, at which the new observables σ_+ and σ_- vanish in the leptonic channel both in the SM and in models featuring the extra Z' boson. For this reason, these points are extremely convenient for seeking phenomenological manifestations of alternative effects of new physics that are associated neither with the SM nor with theories involving the extra Z' boson. For example, these could be effects caused by scalar-particle exchanges in supersymmetric theories with broken R parity [25] and by leptoquark exchanges [26] or effects induced by anomalous gauge coupling constants [27].

In my opinion, the above arguments indicate unambiguously that the observables $\sigma_\pm$ are highly efficient for revealing Z'-boson effects in the lepton channel. In view of this, it seems reasonable to perform a global analysis of available leptonic data over a broad energy interval that come from the PEP, PETRA, TRISTAN, LEP1, SLC, and LEP2 colliders with the aim of deducing experimental information about $\sigma_\pm$ and comparing it with theoretical predictions. I am going to perform such an analysis in the near future and to present it as a separate publication.

ACKNOWLEDGMENTS

I am grateful to A.A. Babich for assistance in the preparation of the graphical data of this study and to I.S. Satsunkevich for stimulating discussions and enlightening comments.

REFERENCES

1. J. Erler and P. Langacker, in *Proceedings of the 5th International Wein Symposium: Conference on Physics beyond the Standard Model (WEIN-98), Santa Fe, 1998.*
2. M. Grünwald and D. Karlen, talk given at *The XXIX International Conference on High Energy Physics, Vancouver, 1998.*
3. L. Hewett and T. G. Rizzo, Phys. Rep. **183**, 193 (1989).
4. CDF and D0 Collab. (J. A. Valls) in *XXXII Rencontres de Moriond: QCD and High Energy Interactions, Les Arcs, 1997*; Preprint No. Conf-97/135-E, Fermilab (Batavia, 1997).
5. *Z' Physics, Physics at LEP2*, Ed. by G. Altarelli, T. Sjöstrand, and F. Zwirner (CERN, Geneva, 1996), No. 96-01, Vol. 1, p. 577.
6. G. Altarelli, Preprint No. TH.97-278, CERN (Geneva, 1997).
7. A. A. Pankov and N. Paver, Phys. Rev. D **48**, 63 (1993).
8. D. Bender *et al.*, Phys. Rev. D **30**, 515 (1984); M. Derrick *et al.*, Phys. Rev. D **31**, 2352 (1985); E. Fernández *et al.*, Phys. Rev. Lett. **50**, 1238 (1983); W. W. Ash *et al.*, Phys. Rev. Lett. **55**, 1831 (1985); M. E. Levi *et al.*, Phys. Rev. Lett. **51**, 1941 (1983).
9. H. J. Behrend *et al.*, Phys. Lett. B **191**, 209 (1987); W. Bartel *et al.*, Z. Phys. C **26**, 507 (1985); **30**, 371 (1986); S. Hegner *et al.*, Z. Phys. C **46**, 547 (1990); B. Adeva *et al.*, Phys. Rev. Lett. **55**, 665 (1985); Phys. Rev. D **38**, 2665 (1988); Ch. Berger *et al.*, Z. Phys. C **21**, 53 (1983); **27**, 341 (1985); W. Braunschweig *et al.*, Z. Phys. C **40**, 163 (1988).
10. K. Abe *et al.*, Z. Phys. C **48**, 13 (1990); Phys. Lett. B **246**, 297 (1990); A. Bacala *et al.*, Phys. Lett. B **218**, 112 (1989); C. Velissaris *et al.*, Phys. Lett. B **331**, 227 (1994); I. Adachi *et al.*, Phys. Lett. B **208**, 319 (1988); B. Howell *et al.*, Phys. Lett. B **291**, 206 (1992).
11. P. D. Acton *et al.*, Phys. Lett. B **273**, 338 (1991); F. Cao *et al.*, in *Proceedings of the 28th International Conference on High Energy Physics, Warsaw, 1996* (DELPHI 96-80 CONF-12, 1996); M. Acciari *et al.*, Phys. Lett. B **374**, 331 (1996).
12. P. Abreu *et al.*, Z. Phys. C **75**, 581 (1997).
13. ALEPH Collab., Preprint ALEPH No. 98-021 (1998); L3 Collab., Preprint No. EP/98-31, CERN (Geneva, 1998); OPAL Collab. (K. Ackerstaff *et al.*), Preprint No. PPE/97-101, CERN (Geneva, 1997); DELPHI Collab. (A. Behrmann *et al.*), Preprint DELPHI No. 97-132 CONF-110 (1997).
14. U. Amaldi *et al.*, Phys. Rev. D **36**, 1385 (1987).
15. A. A. Pankov and I. S. Satsunkevich, Yad. Fiz. **47**, 1064 (1988) [Sov. J. Nucl. Phys. **47**, 679 (1988)]; Nuovo Cimento A **103**, 1121 (1990); A. A. Pankov and C. Verzegnassi, Phys. Lett. B **233**, 259 (1989); S. S. Gershtein, A. A. Likhoded, A. A. Pankov, and O. P. Yushchenko, Phys. Lett. B **275**, 169 (1992); Z. Phys. C **56**, 279 (1992).
16. M. Sakuda, Nuovo Cimento A **107**, 2389 (1994); K. Miyabayashi, Recent Electroweak Results from Tristan, talk presented at Moriond-95.
17. M. Miura *et al.*, Preprint No. 97-210, KEK (1997).
18. J.-M. Frère, V. A. Novikov, and M. I. Vysotsky, Phys. Lett. B **386**, 437 (1996).
19. G. Altarelli, B. Mele, and M. Ruíz-Altaba, Z. Phys. C **45**, 109 (1989).
20. A. Leike, Preprint No. LMU-03-98 (1998).
21. P. Osland and A. A. Pankov, Phys. Lett. B **403**, 93 (1997); **406**, 328 (1997).
22. A. Djouadi *et al.*, Z. Phys. C **56**, 289 (1992).
23. Z. Was and S. Jadach, Phys. Rev. D **41**, 1425 (1990).
24. S. Riemann, FORTRAN program ZEFIT Version 4.2; D. Bardin *et al.*, Preprint No. TH.6443/92, CERN (Geneva, 1992).
25. T. G. Rizzo, Preprint No. PUB-7982, SLAC (Stanford, 1998).
26. J. Kalinowski, R. Rückl, H. Spiesberger, and P. Zerwas, Phys. Lett. B **406**, 314 (1997).
27. A. A. Babich, A. A. Pankov, and N. Paver, Phys. Lett. B **452**, 355 (1999).

Translated by A. Isaakyan

Physics of Atomic Nuclei, Vol. 63, No. 5, 2000, pp. 882–890. From Yadernaya Fizika, Vol. 63, No. 5, 2000, pp. 953–961.

ELEMENTARY PARTICLES AND FIELDS
Theory

On Some Rare Weak Decays of Vector Mesons*

L. M. Kurdadze and Z. K. Silagadze**

Budker Institute of Nuclear Physics, Siberian Division, Russian Academy of Sciences, pr. Akademika Lavrent'eva 11, Novosibirsk, 630090 Russia

Received May 12, 1999; in final form, July 7, 1999

Abstract—Some semileptonic weak decays of vector mesons are considered within the most popular quark models. Unfortunately, the predicted branching ratios are too small to make a study of these decays realistic at meson factories under construction. © *2000 MAIK "Nauka/Interperiodica".*

1. INTRODUCTION

Weak decays of hadrons play an important role in our understanding of both perturbative and nonperturbative aspects of the Standard Model. On one hand, they involve Kobayashi–Maskawa matrix elements and higher order corrections to weak currents. The latter are calculable perturbatively to a high precision within the Standard Model; the former, which are crucial parameters of the theory, are not determined by it, but they must be extracted from experiments. On the contrary, another ingredient of these weak decays, the hadronic matrix elements of weak currents, is not calculable at present from first principles and is the subject of nonperturbative QCD, the acronym that in reality means a paradise for various phenomenological models of hadron structure.

Semileptonic decays with $0^- \longrightarrow 0^-$ and $0^- \longrightarrow 1^-$ hadron transitions have attracted considerable attention, since they are promising experimental sources for extracting the Kobayashi–Maskawa matrix elements. The reviews of the theoretical models involved in such a type of exercise, along with relevant references, can be found in [1–4], and we do not repeat them here. Instead, we focus our efforts on giving a reliable estimate for semileptonic decays with $1^- \longrightarrow 0^-$ hadron transitions. Such weak decays have escaped consideration simply because very tiny rates are expected for them. Indeed, a rough estimate of the semileptonic-decays rate is given by the one-third of the free-quark decay width under the assumption that the spectator antiquark is irrelevant. It is straightforward to get this decay width [5]

$$\Gamma(Q \longrightarrow qe\bar{\nu}) = \frac{G_F^2 m_Q^5}{192\pi^3}|V_{qQ}|^2 F\left(\frac{m_q}{m_Q}\right), \qquad (1)$$

where V_{qQ} is the relevant Kobayashi–Maskawa matrix element and $F(x) = 1 - 8x^2 + 8x^6 - x^8 - 24x^4\ln x$ is a phase-space factor, lepton mass being neglected.

The branching ratio, which follows from (1), for example, for the decay $J/\psi \longrightarrow D_s^- e^+\nu$ is about 10^{-9}, and other branching ratios for weak semileptonic decays of vector mesons appear to be even smaller.

Below, we use two of the most popular models to give more elaborate estimates for the rates of semileptonic decays of vector mesons. These calculations were motivated by the fact that several high-luminosity meson factories are expected to come into operation in the near future.

2. GENERAL CONSIDERATIONS

Let us consider $V(Q\bar{Q}) \longrightarrow P(q\bar{Q})e^-\bar{\nu}$ semileptonic decays, where $V(Q\bar{Q})$ and $P(q\bar{Q})$ stand for vector 1^- and pseudoscalar 0^- mesons made up from $Q\bar{Q}$ and $q\bar{Q}$ quark–antiquark pairs, respectively. The corresponding amplitude has the form

$$A = \frac{G_F}{\sqrt{2}} V_{qQ}\bar{u}_e(\mathbf{k}_1)\gamma^\mu(1-\gamma_5)v_\nu(\mathbf{k}_2)\langle P|J_\mu(0)|V\rangle;$$

after averaging over the vector-meson polarization and summation over the lepton spins (the lepton mass is neglected, and the normalization condition $u^+u = 2E$ is used for lepton spinors), the squared amplitude takes the form

$$\overline{|A|^2} = \frac{1}{3}G_F^2|V_{qQ}|^2 \mathrm{tr}(1-\gamma_5)\hat{k}_1\gamma^\mu\hat{k}_2\gamma^\nu \times \sum_{s_V}\langle V|J_\nu^+(0)|P\rangle\langle P|J_\mu(0)|V\rangle. \qquad (2)$$

Let us decompose the sum in (2) (see [6]) as

$$\sum_{s_V}\langle V(P,\epsilon)|J_\nu^+(0)|P(P')\rangle\langle P(P')|J_\mu(0)|V(P,\epsilon)\rangle$$

* This article was submitted by the authors in English.

** e-mail: silagadze@inp.nsk.su

$$= -\alpha g_{\mu\nu} + \sum_{\sigma_1,\sigma_2=\pm} \beta_{\sigma_1\sigma_2}(P+\sigma_1 P')_\mu (P+\sigma_2 P')_\nu \quad (3)$$

$$+ i\gamma\epsilon_{\mu\nu\lambda\sigma}(P+P')^\lambda (P-P')^\sigma;$$

we note that the terms from (3) that contain $(P-P')_\mu$ or $(P-P')_\nu$ do not contribute to (2), because, for example,

$$(P-P')_\mu \mathrm{tr}(1-\gamma_5)\hat{k}_1\gamma^\mu\hat{k}_2\gamma^\nu$$
$$= \mathrm{tr}(1-\gamma_5)\hat{k}_1(\hat{k}_1+\hat{k}_2)\hat{k}_2\gamma^\nu = 0,$$

since the electron mass is assumed to be zero.

Thus, only α, β_{++}, and γ-invariant form factors contribute to $\overline{|A|^2}$, and it is straightforward to obtain the following expression for the differential width [6, 7] (in $\mathbf{P}=0$ vector-meson rest frame):

$$\frac{d^2\Gamma(V\longrightarrow Pe\bar{\nu})}{dxdy}$$
$$= \frac{1}{3}\frac{G_F^2 M_V^5}{32\pi^3}|V_{qQ}|^2\left\{\alpha\frac{y}{M_V^2} + 2\beta_{++}[4x(x_+-x) \right. \quad (4)$$
$$\left. -y(1-2x)] - 2\gamma y\left(x_+ - 2x + \frac{1}{2}y\right)\right\}.$$

Here, $x_+ = \frac{1}{2}\left(1-\frac{M_P^2}{M_V^2}\right)$, and we have introduced the dimensionless variables $x = E_e/M_V$ and $y = \frac{(P-P')^2}{M_V^2} \equiv \frac{t}{M_V^2}$, E_e being the electron energy.

Thus, the decay width is

$$\Gamma(V\longrightarrow Pe\bar{\nu}) = \int_{x_-}^{x_+}\int_{y_-}^{y_+}\frac{d^2\Gamma}{dxdy}, \quad (5)$$

where (x_+ was given above) [7]

$$x_- = 0, \quad y_- = 0, \quad y_+ = \frac{4x(x_+-x)}{1-2x}.$$

These integration limits are determined by decay kinematics.

Note that, for decays to $e^+\nu$, the sign of the term proportional to γ in (4) should be reversed. The simplest way to see this is the following. If the electron mass is neglected, then the quantity $\frac{d^2\Gamma(V\longrightarrow P^-e^+\nu)}{dxdy}$ can be obtained from $\frac{d^2\Gamma(V\longrightarrow P^+e^-\bar{\nu})}{dxdy}$ by means of the substitution $x\longrightarrow x^* = \frac{E_\nu}{M_V}$. It is easy to see that $x^* = x_+ - x + \frac{1}{2}y$; hence, $4x^*(x_+-x^*) - y(1-2x^*) = 4x(x_+-x) - y(1-2x)$, but $x_+ - 2x^* + \frac{1}{2}y = -\left(x_+ - 2x + \frac{1}{2}y\right)$.

It is convenient to introduce form factors that characterize the hadronic matrix element itself:

$$\langle P(P')|J_\mu(0)|V(P,\epsilon)\rangle$$
$$= ig\epsilon_{\mu\nu\lambda\sigma}\epsilon^\nu(P+P')^\lambda(P-P')^\sigma - f\epsilon_\mu \quad (6)$$
$$-(\epsilon\cdot P')a_+(P+P')_\mu - (\epsilon\cdot P')a_-(P-P')_\mu.$$

Comparing (6) and (3) and using the formula

$$\sum_{s_V}\epsilon_\mu\epsilon_\nu^* = -g_{\mu\nu} + \frac{P_\mu P_\nu}{M_V^2},$$

we can easily find that the coefficients in (4) are

$$\alpha = f^2 + 4M_V^2 g^2 \mathbf{P}'^2, \quad \gamma = 2gf,$$
$$\beta_{++} = \frac{f^2}{4M_V^2} - M_V^2 g^2 y + \frac{1}{2}\left[\frac{M_P^2}{M_V^2} - y - 1\right] f a_+ + a_+^2\mathbf{P}'^2, \quad (7)$$

where

$$\mathbf{P}'^2 = \frac{[M_V^2(1-y)+M_P^2]^2}{4M_V^2} - M_P^2.$$

Another well-known set of form factors is defined by [8]

$$\langle P(P')|J_\mu(0)|V(P,\epsilon)\rangle$$
$$= \frac{2i}{M_V+M_P}\epsilon_{\mu\nu\lambda\sigma}\epsilon^\nu P'^\lambda P^\sigma V(q^2) \quad (8)$$
$$-\epsilon_\mu(M_V+M_P)A_1(q^2) - \frac{\epsilon\cdot q}{M_V+M_P}(P+P')_\mu A_2(q^2) + \ldots,$$
$$q = P - P'.$$

Here, the ellipsis stands for terms proportional to $(P-P')_\mu$, which do not contribute to the decay width of massless leptons.

The obvious relations between these two sets of form factors are

$$g(q^2) = \frac{V(q^2)}{M_V+M_P}, \quad f(q^2) = (M_V+M_P)A_1(q^2), \quad (9)$$
$$a_+(q^2) = -\frac{A_2(q^2)}{M_V+M_P}.$$

Some model for the hadron structure is needed to render the form factors that we introduced more specific.

3. ISGUR–SCORA–GRINSTEIN–WISE MODEL

The Isgur–Scora–Grinstein–Wise (ISGW) model [9] uses nonrelativistic quark-model wave functions to predict weak hadronic form factors. Strictly speaking, this model becomes rigorous in the weak-coupling limit, where $M_V \approx 2m_Q$ and $M_P \approx m_Q + m_q$, and near the zero recoil point, where $t = q^2$ reaches its maximum value $t_m = (M_V - M_P)^2$. But it is assumed that the resulting form-factor formulas are valid even beyond the weak-coupling regime. A more serious problem is that the nonrelativistic-quark-model predictions for the $(t_m - t)$ dependence of form factors are not reliable when $t_m - t$ becomes too large in relation to typical hadronic scales. Nevertheless, this model proved to be successful and, up to now, remains one of the most popular ones, maybe because "it is better to have the right degrees of freedom moving at the wrong speed than the wrong degrees of freedom moving at right speed" [10]. An updated version of the ISGW model, which incorporates relativistic corrections, heavy-quark-symmetry constraints, and more realistic behavior of form factors at large $t_m - t$, is given in [10].

In the weak-coupling limit, the state vectors of the nonrelativistic $V(Q\bar{Q})$ vector or $P(q\bar{Q})$ pseudoscalar mesons can be represented as a superposition of the free quark–antiquark states [9, 11]:

$$\begin{aligned}|V(\mathbf{P},\epsilon)\rangle &= \sqrt{2M_V}\int\frac{d\mathbf{p}}{(2\pi)^3}\sum_{ms\bar{s}} C^{1m}_{s\bar{s}}\,\epsilon\cdot\epsilon^*_{(m)}\varphi_V(\mathbf{P})\\ &\times\left|Q\left[\frac{m_Q}{M_V}\mathbf{P}+\mathbf{p},s\right]\bar{Q}\left[\frac{m_Q}{M_V}\mathbf{P}-\mathbf{p},\bar{s}\right]\right\rangle,\\ |P(\mathbf{P})\rangle &= \sqrt{2M_P}\int\frac{d\mathbf{p}}{(2\pi)^3}\sum_{s\bar{s}} C^{00}_{s\bar{s}}\varphi_P(\mathbf{P})\\ &\times\left|q\left[\frac{m_q}{M_P}\mathbf{P}+\mathbf{p},s\right]\bar{Q}\left[\frac{m_Q}{M_P}\mathbf{P}-\mathbf{p},\bar{s}\right]\right\rangle.\end{aligned} \tag{10}$$

We use the normalization condition $\langle\mathbf{P}'|\mathbf{P}\rangle = (2\pi)^3 2E\delta(\mathbf{P}'-\mathbf{P})$ for the meson state vectors and the normalization condition $\langle\mathbf{p}'|\mathbf{p}\rangle = (2\pi)^3\frac{E}{m}\delta(\mathbf{p}'-\mathbf{p})$ for the state vectors of quarks (or antiquarks) with mass m. Here, $\epsilon_{(-)}$, $\epsilon_{(0)}$, and $\epsilon_{(+)}$ are three independent polarization 4-vectors for the vector mesons, while $C^{jj_z}_{s\bar{s}}$ are the usual Clebsch–Gordan coefficients that couple quark and antiquark spins s and $\bar{s}$ into the meson spin and polarization. At last, $|Q[\mathbf{p}_1, s]\bar{Q}[\mathbf{p}_2, s]\rangle = a^+_s(\mathbf{p}_1)b^+_{\bar{s}}(\mathbf{p}_2)|0\rangle$, a^+ and b^+ being the quark and antiquark creation operators. Note that our normalization convention indicates the anticommutation relations

$$\begin{aligned}\{a_s(\mathbf{p}), a^+_{s'}(\mathbf{p}')\} &= \{b_s(\mathbf{p}), b^+_{s'}(\mathbf{p}')\}\\ &= (2\pi)^3\frac{E}{m}\delta(\mathbf{p}'-\mathbf{p}).\end{aligned} \tag{11}$$

To obtain the quark-model weak-transition matrix element, one should replace the weak current $J_\mu(0)$ in $\langle P(P')|J_\mu(0)|V(P,\epsilon)\rangle$ by the quark weak current $j_\mu(0) = \bar{q}(0)\gamma_\mu(1-\gamma_5)Q(0)$ (the Kobayashi–Maskawa matrix element was already separated), decompose the quark-field operator (note the normalization $u^{+(\lambda)}(\mathbf{k})u^{(\lambda')}(\mathbf{k}) = v^{+(\lambda)}(\mathbf{k})v^{(\lambda')}(\mathbf{k}) = \frac{k_0}{m}\delta_{\lambda\lambda'}$ for Dirac spinors) as

$$\Psi(0) = \sum_\lambda\int\frac{d\mathbf{k}}{(2\pi)^3}\frac{m}{k_0}[a_\lambda(\mathbf{k})u^{(\lambda)}(\mathbf{k}) + b^+_\lambda(\mathbf{k})v^{(\lambda)}(\mathbf{k})],$$

and use the anticommutation relations (11) along with the nonrelativistic approximation $E = \sqrt{m^2+\mathbf{p}^2} \approx m$. As a result, we obtain (in the vector-meson rest frame $\mathbf{P} = 0$)

$$\begin{aligned}&\langle P(P')|J_\mu(0)|V(P,\epsilon)\rangle\\ &= \sqrt{4M_PM_V}\int\frac{d\mathbf{p}}{(2\pi)^3}\varphi^*_P\left(\frac{m_Q}{M_P}\mathbf{P}'+\mathbf{p}\right)\varphi_V(\mathbf{p})\\ &\times\sum_{mss'\bar{s}} C^{00}_{s'\bar{s}}C^{1m}_{s\bar{s}}\,\epsilon\cdot\epsilon^*_{(m)}\bar{u}^{(s')}_{(q)}(\mathbf{P}'+\mathbf{p})\gamma_\mu(1-\gamma_5)u^{(s)}_{(Q)}(\mathbf{p}).\end{aligned} \tag{12}$$

To simplify (12), we note that

$$u^{(s)}(\mathbf{p}) = \frac{(\hat{p}+m)}{\sqrt{2m(p_0+m)}}\chi^{(s)} \approx \frac{(\hat{p}+m)}{2m}\chi^{(s)},$$
$$p_0 \approx m,$$

where $\chi^{(s)}$ is the rest-frame spinor, and

$$\begin{aligned}\sum_{mss'\bar{s}} C^{00}_{s'\bar{s}}\epsilon\cdot\epsilon^*_{(m)}C^{1m}_{s\bar{s}}\chi^{(s)}\bar{\chi}^{(s')} &= \frac{1}{2}\{(\chi^{(+)}\bar{\chi}^{(+)}\\ -\chi^{(-)}\bar{\chi}^{(-)})\epsilon\cdot\epsilon^*_{(0)} &- \sqrt{2}\chi^{(+)}\bar{\chi}^{(-)}\epsilon\cdot\epsilon^*_{(+)}\\ +\sqrt{2}\chi^{(-)}\bar{\chi}^{(+)}\epsilon\cdot\epsilon^*_{(-)}\} &= \frac{1}{4}(1+\gamma_0)\\ \times\{\gamma_3\epsilon\cdot\epsilon^*_{(0)} + \gamma_+\epsilon\cdot\epsilon^*_{(+)} &+ \gamma_-\epsilon\cdot\epsilon^*_{(-)}\}\gamma_5\\ &= \frac{1}{4}(1+\gamma_0)\boldsymbol{\gamma}\cdot\boldsymbol{\epsilon}\gamma_5.\end{aligned}$$

Here, $\gamma_+ = -\frac{1}{\sqrt{2}}(\gamma_1 + i\gamma_2)$ and $\gamma_- = \frac{1}{\sqrt{2}}(\gamma_1 - i\gamma_2)$, and the property $\epsilon^*_\pm = -\epsilon_\mp$ was used at the latter step (note that $\boldsymbol{\gamma}\cdot\boldsymbol{\epsilon} = \sum_{s=0,\pm}(-1)^s\gamma_{-s}\epsilon_{(s)}$).

Thus, expression (12) transforms into

$$\begin{aligned}&\langle P(P')|J_\mu(0)|V(P,\epsilon)\rangle\\ &= \frac{\sqrt{M_PM_V}}{8m_qm_Q}\int\frac{d\mathbf{p}}{(2\pi)^3}\varphi^*_P\left(\frac{m_Q}{M_P}\mathbf{P}'+\mathbf{p}\right)\varphi_V(\mathbf{p})\end{aligned} \tag{13}$$

$$\times \mathrm{tr}\{(1+\gamma_0)\boldsymbol{\gamma}\cdot\boldsymbol{\epsilon}\gamma_5(\hat{p}'+m_q)\gamma_\mu(1-\gamma_5)(\hat{p}+m_Q)\},$$

where $p_0' = m_q$ and $\mathbf{p}' = \mathbf{P}' + \mathbf{p}$.

It is now straightforward to extract the Lorentz invariant form factors from (13) once the wave functions φ_P and φ_V have been specified. It is assumed in the ISGW approach that, for these wave functions, one should solve a Schrödinger problem for the usual Coulomb plus linear potential, which proved to be useful in quarkonium spectroscopy. But to facilitate the numerical calculations, the authors of the model used in fact the variational method for the Schrödinger problem based on Gaussian-type harmonic-oscillator wave functions. In our case, the relevant trial function is $\varphi(\mathbf{r}) = \frac{\beta^{3/2}}{\pi^{3/4}}\exp(-\beta^2 r^2/2)$, its momentum Fourier transform being

$$\varphi(\mathbf{p}) = \left(\frac{2\sqrt{\pi}}{\beta}\right)^{3/2}\exp(-\mathbf{p}^2/2\beta^2) \tag{14}$$

with β as a variational parameter.

Let us introduce the notation

$$\langle A_0\rangle = \frac{1}{4}\mathrm{tr}\{(1+\gamma_0)\boldsymbol{\gamma}\cdot\boldsymbol{\epsilon}\gamma_5(\hat{p}'+m_q)\gamma_0\gamma_5(\hat{p}+m_Q)\}$$

and a similar notation for $\langle\mathbf{A}\rangle$, $\langle V_0\rangle$, and $\langle\mathbf{V}\rangle$. In the nonrelativistic limit, we will then have [11]

$$\begin{aligned}
\langle A_0\rangle &= (m_Q+p_0)\mathbf{p}'\cdot\boldsymbol{\epsilon} + (m_q+p_0')\mathbf{p}\cdot\boldsymbol{\epsilon}\\
&\longrightarrow 2\{m_Q(\mathbf{P}'+\mathbf{p})\cdot\boldsymbol{\epsilon} + m_q\mathbf{p}\cdot\boldsymbol{\epsilon}\},\\
\langle\mathbf{A}\rangle &= (\boldsymbol{\epsilon}\cdot\mathbf{p}')\mathbf{p} + (\boldsymbol{\epsilon}\cdot\mathbf{p})\mathbf{p}' + (\mathbf{p}'\cdot\mathbf{p})\boldsymbol{\epsilon}\\
&\quad + m_q p_0\boldsymbol{\epsilon} + m_Q p_0'\boldsymbol{\epsilon} + m_q m_Q\boldsymbol{\epsilon}\\
&\longrightarrow 4m_q m_Q\boldsymbol{\epsilon} - \{\mathbf{p}\cdot(\mathbf{P}'+\mathbf{p})\}\boldsymbol{\epsilon} + (\mathbf{p}\cdot\boldsymbol{\epsilon})(\mathbf{P}'+\mathbf{p})\\
&\quad + (\mathbf{P}'\cdot\boldsymbol{\epsilon})\mathbf{p} + (\mathbf{p}\cdot\boldsymbol{\epsilon})\mathbf{p},\\
\langle\mathbf{V}\rangle &= i\{(m_Q+p_0)\boldsymbol{\epsilon}\times\mathbf{p}' - (m_q+p_0')\boldsymbol{\epsilon}\times\mathbf{p}\}\\
&\longrightarrow 2i\{m_Q\boldsymbol{\epsilon}\times(\mathbf{P}'+\mathbf{p}) - m_q\boldsymbol{\epsilon}\times\mathbf{p}\}.
\end{aligned} \tag{15}$$

Using the last expression in (15), along with the equalities

$$\begin{aligned}
&\int\frac{d\mathbf{p}}{(2\pi)^3}\varphi_P^*\left(\frac{m_Q}{M_P}\mathbf{P}'+\mathbf{p}\right)\varphi_V(\mathbf{p})\\
&= \left(\frac{\beta_P\beta_V}{\beta_{PV}^2}\right)^{3/2}\exp\left\{-\frac{m_Q^2}{4M_PM_V}\frac{t_m-t}{\beta_{PV}^2}\right\}\equiv F(t),
\end{aligned} \tag{16}$$

where $\beta_{PV}^2 = \frac{1}{2}(\beta_P^2+\beta_V^2)$, and

$$\int\frac{d\mathbf{p}}{(2\pi)^3}\varphi_P^*\left(\frac{m_Q}{M_P}\mathbf{P}'+\mathbf{p}\right)\mathbf{p}\varphi_V(\mathbf{p}) = -\frac{m_Q}{M_P}\frac{\beta_V^2}{2\beta_{PV}^2}F(t)\mathbf{P}', \tag{17}$$

we get from (13) (it is supposed that the vector weak current will be not mixed with a symbol V of the vector meson)

$$\begin{aligned}
&\langle P(P')|\mathbf{V}(0)|V(P,\boldsymbol{\epsilon})\rangle\\
&= i\boldsymbol{\epsilon}\times\mathbf{P}'\sqrt{M_PM_V}\left\{\frac{1}{m_q} - \frac{1}{2\mu_-}\frac{m_Q}{M_P}\frac{\beta_V^2}{2\beta_{PV}^2}\right\}F(t),
\end{aligned}$$

where

$$\mu_\pm = \left[\frac{1}{m_q}\pm\frac{1}{m_Q}\right]^{-1}. \tag{18}$$

On the other hand, it follows from (16) that, in the $\mathbf{P} = 0$ frame we have

$$\langle P|\mathbf{V}(0)|V\rangle = 2iM_Vg\boldsymbol{\epsilon}\times\mathbf{P}'.$$

Comparing these two expressions, we immediately obtain

$$g = \frac{1}{2}\sqrt{\frac{M_P}{M_V}}F(t)\left\{\frac{1}{m_q} - \frac{1}{2\mu_-}\frac{m_Q}{M_P}\frac{\beta_V^2}{\beta_{PV}^2}\right\}. \tag{19}$$

Similarly, the first equation in (15) leads to

$$\begin{aligned}
&a_+(M_P+M_V) + a_-(M_V-M_P)\\
&= -\sqrt{M_PM_V}\left\{\frac{1}{m_q} - \frac{1}{2\mu_+}\frac{m_Q}{M_P}\frac{\beta_V^2}{\beta_{PV}^2}\right\}F(t).
\end{aligned} \tag{20}$$

There is some subtlety in using the equation for $\langle\mathbf{A}\rangle$ from (15). For $\boldsymbol{\epsilon}\perp\mathbf{P}'$ polarization, it gives

$$f = 2\sqrt{M_PM_V}F(t), \tag{21}$$

while, for $\boldsymbol{\epsilon}\parallel\mathbf{P}'$ polarization, it involves $\mathbf{p}^2$ terms about which there is no guarantee in our nonrelativistic approach. Nevertheless, one can get the true answer by separating the D-wave partial amplitude, because there is nothing intrinsically relativistic in recoiling into a D wave [9]. Thus, we disregard $\boldsymbol{\epsilon}$ terms within $\langle\mathbf{A}\rangle$, which corresponds to the S wave, and also in

$$\int\frac{d\mathbf{p}}{(2\pi)^3}\varphi_P^*(\mathbf{p}+\mathbf{q})p_ip_j\varphi_V(\mathbf{p}) = A\mathbf{q}^2\delta_{ij} + Bq_iq_j, \tag{22}$$

and omit the first term, which leads to the S-wave amplitude too. Using the relations

$$\int\frac{d\mathbf{p}}{(2\pi)^3}\varphi_P^*(\mathbf{p}+\mathbf{q})\mathbf{p}^2\varphi_V(\mathbf{p}) = \left[\frac{3}{2}\frac{\beta_P^2\beta_V^2}{\beta_{PV}^2} + \frac{q^2}{4}\frac{\beta_V^4}{\beta_{PV}^4}\right]F(t)$$

and

$$\int \frac{d\mathbf{p}}{(2\pi)^3}\varphi_P^*(\mathbf{p}+\mathbf{q})(\mathbf{p}\cdot\mathbf{q})^2\varphi_V(\mathbf{p}) = \left[\frac{1}{2}\frac{\beta_P^2\beta_V^2}{\beta_{PV}^2}+\frac{q^2}{4}\frac{\beta_V^4}{\beta_{PV}^4}\right]\mathbf{q}^2F(t),$$

we easily obtain

$$B = \frac{1}{4}\frac{\beta_V^4}{\beta_{PV}^4}F(t). \quad (23)$$

Now, we have all necessary ingredients to get a relation that follows from the relevant D-wave terms of $\langle \mathbf{A}\rangle$:

$$a_+ - a_- = \frac{\sqrt{M_PM_V}}{m_qm_Q}F(t)\left[\frac{m_Q}{M_P}\frac{\beta_V^2}{2\beta_{PV}^2}-\frac{1}{4}\frac{m_Q^2}{M_P^2}\frac{\beta_V^4}{\beta_{PV}^4}\right]. \quad (24)$$

With the aid of (20) and (24), we can evaluate the form factor a_+. Noting that, in the weak-binding approximation, $\frac{M_V-M_P}{m_qm_Q}\approx\frac{m_Q-m_q}{m_qm_Q}=\frac{1}{\mu_-}$, we get

$$a_+ = \sqrt{\frac{M_P}{M_V}}F(t)\left\{\frac{1}{2m_q}\frac{m_Q}{M_P}\frac{\beta_V^2}{\beta_{PV}^2}-\frac{1}{8\mu_-}\frac{m_Q^2}{M_P^2}\frac{\beta_V^4}{\beta_{PV}^4}-\frac{1}{2m_q}\right\}.$$

Let us further transform

$$\frac{1}{m_q}\frac{m_Q}{M_P}\frac{\beta_V^2}{\beta_{PV}^2} = \frac{1}{m_q}\frac{m_Q}{M_P}\frac{(\beta_V^2-\beta_P^2)+(\beta_V^2+\beta_P^2)}{(\beta_V^2+\beta_P^2)}$$

$$= \frac{1}{m_q}\frac{m_Q}{M_P}\frac{\beta_V^2-\beta_P^2}{\beta_V^2+\beta_P^2}+\frac{1}{m_q}\frac{m_Q+m_q-m_q}{M_P}$$

$$\approx \frac{1}{m_q}-\frac{1}{M_P}+\frac{1}{M_P}\frac{m_Q}{m_q}\frac{\beta_V^2-\beta_P^2}{\beta_V^2+\beta_P^2}.$$

This procedure allows us to rewrite the form factor a_+ as

$$a_+ = \sqrt{\frac{M_P}{M_V}}\frac{F(t)}{2M_P}\left[-1+\frac{m_Q}{m_q}\frac{\beta_V^2-\beta_P^2}{\beta_V^2+\beta_P^2}-\frac{1}{4\mu_-}\frac{m_Q^2}{M_P}\frac{\beta_V^4}{\beta_{PV}^4}\right]. \quad (25)$$

By means of (19), (21), and (25), the expressions for the form factors g, f, and a_+ and the semileptonic-decay width can be evaluated by using formulas (4), (5), and (7).

4. BAUER–STECH–WIRBEL MODEL

The Bauer–Stech–Wirbel (BSW) model [8, 12] uses the quark model to deal only with one point $q^2 = 0$. In contrast to the zero recoil point, considered previously in the ISGW model, relativistic effects can be highly important for the point $q^2 = 0$. Thus, the relativistic treatment of quark dynamics becomes unavoidable, although this dynamics is greatly simplified in the infinite-momentum frame. For convenience, we represent the meson state vectors in this frame using a form slightly different from (10):

$$|V(P,\boldsymbol{\epsilon})\rangle = \sqrt{2}\sum_{s\bar{s}m}\int\frac{d\mathbf{p}_1d\mathbf{p}_2}{(2\pi)^{3/2}}\delta(\mathbf{P}-\mathbf{p}_1-\mathbf{p}_2) \times\sqrt{\frac{m_Qm_{\bar{Q}}}{p_{10}p_{20}}}C_{s\bar{s}}^{1m}\boldsymbol{\epsilon}\cdot\boldsymbol{\epsilon}_m^*\varphi_V(\mathbf{p}_1) \times|Q[\mathbf{p}_1,s]\bar{Q}[\mathbf{p}_2,\bar{s}]\rangle, \quad (26)$$

$$|P(P')\rangle = \sqrt{2}\sum_{s\bar{s}}\int\frac{d\mathbf{p}_1d\mathbf{p}_2}{(2\pi)^{3/2}}\delta(\mathbf{P}'-\mathbf{p}_1-\mathbf{p}_2) \times\sqrt{\frac{m_qm_{\bar{Q}}}{p_{10}p_{20}}}C_{s\bar{s}}^{00}\varphi_P(\mathbf{p}_1)|q[\mathbf{p}_1,s]\bar{Q}[\mathbf{p}_2,\bar{s}]\rangle.$$

In the infinite-momentum frame and for $\mathbf{q} = \mathbf{P}_V - \mathbf{P}_P = 0$, we have $(P_{V_\mu}) = (E_V, 0, 0, P)$, $(P_{P_\mu}) = (E_P, 0, 0, P)$, and $P\longrightarrow\infty$. At the same time, $E_V - E_P \approx \frac{M_V^2-M_P^2}{2P}\longrightarrow 0$; that is, $\mathbf{q} = 0$ just gives the point $q^2 = 0$.

Let us introduce the longitudinal momentum fraction carried by the active quark in the meson, $x = \frac{p_{1z}}{P}$, when the normalization condition for the wave function $\varphi(\mathbf{p}_1)$, which follows from (26), is

$$\int dx d\mathbf{p}_T|\varphi(x,\mathbf{p}_T)|^2 = 1. \quad (27)$$

In practice, a form of this wave function is inspired by the relativistic harmonic-oscillator model and reads [8] (for the meson of mass M made up from the active quark q and the spectator antiquark $\bar{Q}$)

$$\varphi(x,\mathbf{p}_T) = N\sqrt{x(1-x)}\exp\left(-\frac{\mathbf{p}_T^2}{2\omega^2}\right) \times\exp\left\{-\frac{M^2}{2\omega^2}\left(x-\frac{1}{2}-\frac{m_q^2-m_Q^2}{2M^2}\right)^2\right\}, \quad (28)$$

where N is determined from the normalization condition (27). The dimensional parameter ω provides transverse-momentum suppression, and its square is equal to the averaged square of the transverse momentum, $\omega^2 = \langle\mathbf{p}_T^2\rangle$. Instead of ω, we can use the parameter β from (14), since $\mathbf{p}_T$ is not changed by the boost along the z direction.

Manipulations that led to (12) now give, for $\mathbf{q} = \mathbf{P}_V - \mathbf{P}_P = 0$, the relation

$$\langle P(P)|J_\mu(0)|V(P,\epsilon)\rangle = 2\sum_{mss'\bar{s}}\int d\mathbf{p}\sqrt{\frac{m_q m_Q}{p_0 p_0'}}C^{00}_{s'\bar{s}}C^{1m}_{s\bar{s}}\epsilon\cdot\epsilon^*_{(m)}\varphi^*_P(\mathbf{p}) \times \varphi_V(\mathbf{p})\bar{u}^{(s')}_{(q)}(\mathbf{p})\gamma_\mu(1-\gamma_5)u^{(s)}_{(Q)}(\mathbf{p}). \quad (29)$$

In the infinite-momentum limit, we have

$$p_0 = \sqrt{m_Q^2 + \mathbf{p}^2} = \sqrt{m_Q^2 + x^2P^2 + \mathbf{p}_T^2} \longrightarrow xP,$$

$$p_0' = \sqrt{m_q^2 + \mathbf{p}^2} \longrightarrow xP,$$

$$u^s(\mathbf{p}) = \frac{\hat{p}+m}{\sqrt{2m(p_0+m)}}\chi^{(s)} \longrightarrow \frac{\hat{p}+m}{\sqrt{2mxP}}\chi^{(s)}.$$

Thus, equation (29) transforms into

$$\langle P|J_\mu(0)|V\rangle = \int dx d\mathbf{p}_T \frac{\varphi^*_p(\mathbf{p})\varphi_V(\mathbf{p})}{x^2P} \times \mathrm{tr}\left\{\frac{1}{4}(1+\gamma_0)\boldsymbol{\gamma}\cdot\boldsymbol{\epsilon}\gamma_5(\hat{p}'+m_q)\gamma_\mu(1-\gamma_5)(\hat{p}+m_Q)\right\}, \quad (30)$$

where $\mathbf{p}' = \mathbf{p}$ and $p_0' \longrightarrow xP$.

In the limit $P \longrightarrow \infty$, relations (15) yield

$$\langle \mathbf{V}\rangle \longrightarrow i(m_Q - m_q)\boldsymbol{\epsilon}\times\mathbf{p}.$$

On the other hand, according to (6)

$$\langle P|\mathbf{V}(0)|V\rangle = 2ig(E_V - E_P)\boldsymbol{\epsilon}\times\mathbf{P}_V \longrightarrow ig\frac{M_V^2 - M_P^2}{P}\boldsymbol{\epsilon}\times\mathbf{P}_V.$$

Comparing these expressions for $\langle P|\mathbf{V}(0)|V\rangle$ and using the relation

$$\int d\mathbf{p}\frac{1}{x^2P}\varphi^*_P(\mathbf{p})\boldsymbol{\epsilon}\times\mathbf{p}\varphi_V(\mathbf{p}) \longrightarrow \frac{1}{P}J\boldsymbol{\epsilon}\times\mathbf{P}_V,$$

where

$$J = \int d\mathbf{p}_T\int_0^1\frac{dx}{x}\varphi^*_P(x,\mathbf{p}_T)\varphi_V(x,\mathbf{p}_T), \quad (31)$$

we get

$$g(q^2=0) = \frac{m_Q - m_q}{M_V^2 - M_P^2}J. \quad (32)$$

We have found the form factor for the point $q^2 = 0$ alone. For q^2 values different from zero, the BSW model assumes the nearest pole dominance:

$$A_1(q^2) = \frac{h_{A_1}}{1-\frac{q^2}{M^2_{1^+}}}, \quad A_2(q^2) = \frac{h_{A_2}}{1-\frac{q^2}{M^2_{1^+}}}, \quad V_1(q^2) = \frac{h_V}{1-\frac{q^2}{M^2_{1^-}}}. \quad (33)$$

Thus, the q^2 dependence of form factors is determined once the masses of the appropriate 1^- and 1^+ vector mesons are known.

Then, relation (32) indicates that

$$h_V = \frac{m_Q - m_q}{M_V - M_P}J. \quad (34)$$

Using the relations $\langle\mathbf{A}\rangle \longrightarrow x(m_Q + m_q)P\boldsymbol{\epsilon} + 2(\boldsymbol{\epsilon}\cdot\mathbf{p})\mathbf{p}$, $\langle P|\mathbf{A}(0)|V\rangle = f\boldsymbol{\epsilon} + 2(\boldsymbol{\epsilon}\cdot\mathbf{P}_P)a_+\mathbf{P}_V$, and $\boldsymbol{\epsilon}\cdot\mathbf{P}_\mathbf{P} \longrightarrow \left(\frac{E_P}{E_V} - 1\right)\boldsymbol{\epsilon}\cdot\mathbf{P}_V$, we can similarly get $f = (M_Q + M_q)J$; therefore,

$$h_{A_1} = \frac{m_Q + m_q}{M_V + M_P}J. \quad (35)$$

Again, there is a subtlety in extracting a_+. Instead of giving a rigorous derivation, we prefer the following educated guess. Noting that, for $(P_V)_\mu = (E_V, 0, 0, P)$, the longitudinal polarization 4-vector $\epsilon_{\|\mu} = \frac{1}{M_V}(P, 0, 0, E_V) \longrightarrow \frac{P}{M_V}(1, 0, 0, 1)$, we obtain

$$\int d\mathbf{x}\langle P|A_0(x)|V\rangle = (2\pi)^3\delta(\mathbf{P}_V - \mathbf{P}_P)\langle P|A_0(0)|V\rangle \longrightarrow (2\pi)^3\delta(\mathbf{P}_V - \mathbf{P}_P) \times\left\{f\epsilon_0 + \left(\frac{E_P}{E_V} - 1\right)\epsilon_3 P(E_V + E_P)a_+\right\} \longrightarrow (2\pi)^3\delta(\mathbf{P}_V - \mathbf{P}_P)\{f - (M_V^2 - M_P^2)a_+\}\frac{P}{M_V}.$$

On the other hand, $Q_{50} = \int d\mathbf{x}A_0(x)$ is an appropriate weak charge, which, in the exact flavor-symmetry limit, transforms the initial state $|V\rangle$ into the final state $|P\rangle$ and so

$$\int d\mathbf{x}\langle P|A_0(x)|V\rangle = \langle P(P_P)|Q_{50}|V(P_V)\rangle = \langle P(P_P)|P(P_V)\rangle \longrightarrow 2P(2\pi)^3\delta(\mathbf{P}_V - \mathbf{P}_P).$$

In the opposite case of broken flavor symmetry, one should instead expect $\langle P(P_P)|Q_{50}|V(P_V)\rangle = 2PI(2\pi)^3\delta(\mathbf{P}_V - \mathbf{P}_P)$, where I is the overlap integral of the wave functions:

$$I = \int d\mathbf{p}_T \int_0^1 dx \varphi_P^*(x, \mathbf{p}_T)\varphi_V(x, \mathbf{p}_T). \quad (36)$$

Thus, we obtain

$$a_+ = \frac{1}{M_V^2 - M_P^2}[f - 2M_V I];$$

therefore,

$$h_{A_2} = \frac{2M_V}{M_V - M_P} I - \frac{M_V + M_P}{M_V - M_P} h_{A_1}. \quad (37)$$

Thus, formulas (34), (35), and (36) and the hypothesis of nearest pole dominance completely determine the weak form factors in the BSW model.

5. HEAVY-QUARK LIMIT

In the limit where the quarks that are active in a weak transition are too heavy, all form factors for this transition can be expressed in terms of a single function $\xi(\zeta)$ called the Isgur–Wise function [13]. In the case of $1^- \longrightarrow 0^-$ transitions, these relations are given by

$$A_1 = \frac{\sqrt{M_P M_V}}{M_P + M_V}(1 + \zeta)\xi(\zeta),$$
$$A_2 = V = \frac{1}{2}\sqrt{\frac{M_P}{M_V}}\left(1 + \frac{M_V}{M_P}\right)\xi(\zeta), \quad (38)$$

where

$$\zeta = v_P v_V = \frac{M_P^2 + M_V^2 - q^2}{2M_V M_P}.$$

Again, some dynamical model of mesons is needed to calculate the Isgur-Wise function $\xi(\zeta)$ (as an example of such calculations, see [14, 15]); instead, one can use some phenomenologically successful parametrization. In particular, the following parametrizations were shown [16] to fit experimental data reasonably well:

$$\xi(\zeta) = 1 - \rho^2(\zeta - 1), \quad \rho \approx 1.08,$$
$$\xi(\zeta) = \frac{2}{1 + \zeta}\exp\left\{-(2\rho^2 - 1)\frac{\zeta - 1}{\zeta + 1}\right\}, \quad \rho \approx 1.52,$$
$$\xi(\zeta) = \left(\frac{2}{\zeta + 1}\right)^{2\rho^2}, \quad \rho \approx 1.45, \quad (39)$$
$$\xi(\zeta) = \exp\{-\rho^2(\zeta - 1)\}, \quad \rho \approx 1.37.$$

In our case, the heavy-quark limit can be applied to the decay $\Upsilon \longrightarrow B_c^+ e^- \bar{\nu}_e$. Despite different analytic forms of the Isgur–Wise function, all four parametrizations from (39) lead to very close values for $\mathrm{Br}(\Upsilon \longrightarrow B_c^+ e^- \bar{\nu}_e)$: 4.1×10^{-10}, 3.7×10^{-10}, 3.8×10^{-10}, and 3.8×10^{-10}.

For heavy–light transitions—for example, in the decay $J/\psi \longrightarrow D_d^- e^+ \nu_e$—the Isgur–Wise scaling (38) is not applicable. Recently, Stech proposed [17] a phenomenological model with enlarged Isgur–Wise scaling for semileptonic form factors. It is supposed that, instead of (38), the following relations hold:

$$A_1 = \frac{\sqrt{M_P M_V}}{M_P + M_V}(1 + \zeta)h_{A_1}(\zeta)\xi_{PV}(\zeta),$$
$$A_2 = \frac{1}{2}\sqrt{\frac{M_P}{M_V}}\left(1 + \frac{M_V}{M_P}\right)h_{A_2}(\zeta)\xi_{PV}(\zeta), \quad (40)$$
$$V = \frac{1}{2}\sqrt{\frac{M_P}{M_V}}\left(1 + \frac{M_V}{M_P}\right)h_V(\zeta)\xi_{PV}(\zeta).$$

The function $\xi_{PV}(\zeta)$ is the same for all form factors for given initial and final states. It approximates the Isgur–Wise function in the heavy-quark limit. On the contrary, the functions h are different for each form factor and are equal to unity in the heavy-quark limit. The special expressions for the functions $\xi_{PV}(\zeta)$ and h can be found in the original paper [17].

6. NUMERICAL RESULTS

To perform numerical calculations within the ISGW model, we use the following values (in GeV) for the quark masses [10] and the variational parameters β:

$$m_u = m_d = 0.33 \text{ GeV}, \quad m_s = 0.55 \text{ GeV},$$
$$m_c = 1.82 \text{ GeV}, \quad m_b = 5.12 \text{ GeV},$$
$$\beta_K = 0.44, \beta_{D_d} = 0.45, \beta_{D_s} = 0.56, \beta_{B_u} = 0.43,$$
$$\beta_{B_c} = 0.92, \beta_\varphi = 0.37, \beta_{J/\psi} = 0.62, \beta_\Upsilon = 1.1. \quad (41)$$

All but the last values in (41) are from Table A2 of [10]. The result for Υ was obtained by minimizing $\left\langle \frac{\mathbf{p}^2}{m_b} + V \right\rangle$, with (14) as a trial function and $V(r) = -\frac{4\alpha_s}{3r} + C + br$, where $\alpha_s \approx 0.3$, $b = 0.18$ GeV^2, and $C = -0.84$ GeV [10]. This minimization problem leads to the cubic equation

$$\beta^3 - \frac{8\alpha_s m_b}{9\sqrt{\pi}}\beta^2 - \frac{2bm_b}{3\sqrt{\pi}} = 0$$

with $\beta \approx 1.1$ as a solution.

Table 1

Decay	$\varphi \longrightarrow K^+e^-\bar{\nu}$	$J/\psi \longrightarrow D_d^-e^+\nu$	$J/\psi \longrightarrow D_s^-e^+\nu$	$\Upsilon \longrightarrow B_u^+e^-\bar{\nu}$	$\Upsilon \longrightarrow B_c^+e^-\bar{\nu}$
M_{1^+}, GeV	1.273 (K_1)	2.422 (D_1)	2.535 (D_{s1})	5.745	6.717
M_{1^-}, GeV	0.892 (K^*)	2.010 (D^*)	2.112 (D_s^*)	5.325 (B^*)	6.317

Table 2

Decay	$\varphi \longrightarrow K^+e^-\bar{\nu}$	$J/\psi \longrightarrow D_d^-e^+\nu$	$J/\psi \longrightarrow D_s^-e^+\nu$	$\Upsilon \longrightarrow B_u^+e^-\bar{\nu}$	$\Upsilon \longrightarrow B_c^+e^-\bar{\nu}$
ISGW [9]	7.9×10^{-15}	2.3×10^{-11}	4.8×10^{-10}	2.9×10^{-13}	1.6×10^{-10}
BSW [8]	3.1×10^{-14}	3.9×10^{-11}	8.9×10^{-10}	3.5×10^{-13}	2.0×10^{-10}
Stech [17]	–	3.1×10^{-11}	5.2×10^{-10}	3.0×10^{-12}	3.1×10^{-10}

Note that this variational procedure leads to the Υ-meson mass $M_\Upsilon = 2m_b + \left\langle \frac{\mathbf{p}^2}{m_b} + V \right\rangle \approx 9.44$ GeV, which should be compared with the experimental value of 9.46 GeV [18].

As was mentioned above, the ISGW model predictions about the high-$(t_m - t)$ behavior of the form factors are not reliable. In numerical calculations, we use more realistic behavior proposed in [10] (although we do not use other refinements of the model given in [10]); that is,

$$F(t) \longrightarrow \left(\frac{\beta_P\beta_V}{\beta_{PV}^2}\right)^{3/2}\left[1 + \frac{1}{12}r^2(t_m - t)\right]^{-2}, \qquad (42)$$

where

$$r^2 = \frac{3}{4m_qm_Q} + \frac{3m_Q^2}{2M_PM_V\beta_{PV}^2} + \frac{\Delta r^2}{M_PM_V}. \qquad (43)$$

The last term in (43) is nonzero only for $b \longrightarrow c$ transitions, where it is equal to $\Delta r^2 \approx 0.39$ [10].

For the BSW model, it is necessary, in addition to 1^- and 1^+ pole masses, to introduce a q^2 dependence for the form factors. We use the values given in Table 1.

Beauty–charm mesons have not yet been discovered experimentally. Predictions for their masses were taken from [19] (in particular, $M_{B_c} = 6.25$ GeV). The value of $M_{1^+} = 5.745$ GeV for the $(b\bar{u})$ meson is also a potential model prediction taken from [20].

As was mentioned earlier, we consider the parameter ω of the BSW model in (28) to be identical to the corresponding parameter β of the ISGW model from (14). For the decay $\Upsilon \longrightarrow B_c^-e^-\bar{\nu}$, this choice gives only 1/5 of the branching ratio in relation to what is expected from the heavy-quark limit. The branching ratio $\mathrm{Br}(\Upsilon \longrightarrow B_u^-e^-\bar{\nu})$, which is, in fact, determined by the overlap of the wave-function tails, is especially sensitive to this parameter, and it is hard to expect that these tails are correctly given by the simple parametrization used in the BSW model. Thus, we conclude that it is better to take the value of ω_Υ such that the heavy-quark-limit prediction is reproduced for $\mathrm{Br}(\Upsilon \longrightarrow B_c^-e^-\bar{\nu})$ to the greatest possible extent. This choice provides $\omega_\Upsilon \approx 2.2$ GeV versus $\beta_\Upsilon \approx 1.1$ GeV of the ISGW model. For other quarkonia, the $\omega = \beta$ prescription was used.

The numerical results for various semileptonic branching ratios are summarized in Table 2.

7. CONCLUSION

We have considered some semileptonic weak decays of vector mesons, using the most popular ISGW and BSW quark models. The predictions of these models agree with each other reasonably well (within a factor of two) for all cases considered here, with the exception of the decay $\varphi \longrightarrow K^+e^-\bar{\nu}$, where the predicted branching ratios differ by a factor of four.

The corresponding branching ratios were also calculated on the basis of Stech's phenomenological model [17]. The results agree again with the ISGW and BSW model predictions, for the majority of cases, but not for the decays $\varphi \longrightarrow K^+e^-\bar{\nu}$ and $\Upsilon \longrightarrow B_u^+e^-\bar{\nu}$. As for the decay $\varphi \longrightarrow K^+e^-\bar{\nu}$, where the result is $\mathrm{Br}(\varphi \longrightarrow K^+e^-\bar{\nu}) = 2.7\times10^{-12}$, we do not expect Stech's model to be valid for it. But it is interesting to note that we can assume that the pole position for $\xi_{PV}(\zeta)$ depends on the form factor where it appears, as in the BSW model (that is, the 1^- pole for the V form factor and the 1^+ pole for the A_1 and A_2 form factors). Stech's model modified in this way then predicts $\mathrm{Br}(\varphi \longrightarrow K^+e^-\bar{\nu}) = 9.0\times10^{-15}$, again close to the ISGW and BSW results. The residual decay modes are not affected significantly by this mod-

ification. In particular, an order of magnitude difference between Stech's model and the ISGW or BSW model for the decay $\Upsilon \longrightarrow B_u^+ e^- \bar{\nu}$ still persists. It seems that Stech's model has difficulties in handling this decay mode.

Unfortunately, the predicted branching ratios are too small; therefore, an experimental study of the decays considered is questionable in the near future.

ACKNOWLEDGMENTS

We are grateful to V. Chernyak for stimulating discussions.

REFERENCES

1. A. Le Yaouanc, Nucl. Instrum. Methods Phys. Res. A **351**, 15 (1994).
2. N. Isgur, in *Proceedings of the International Conference on Heavy Quark Physics, Cornell*, Toronto University, Preprint No. UTPT-89-25 (1989).
3. M. Wirbel, Dortmund University, Preprint No. DO-TH-89/4 (1989).
4. D. Melikhov, Phys. Rev. D **53**, 2460 (1996).
5. G. Altarelli *et al.*, Nucl. Phys. **208**, 365 (1982); N. Cabibbo, G. Corbo, and L. Maiani, Nucl. Phys. B **155**, 93 (1979).
6. B. Grinstein, M. B. Wise, and N. Isgur, Phys. Rev. Lett. **56**, 298 (1986).
7. D. Scora and N. Isgur, Phys. Rev. D **40**, 1491 (1989).
8. M. Wirbel, B. Stech, and M. Bauer, Z. Phys. C **29**, 637 (1985); M. Bauer and M. Wirbel, Z. Phys. C **42**, 671 (1989).
9. N. Isgur, D. Scora, B. Grinstein, and M. B. Wise, Phys. Rev. D **39**, 799 (1989).
10. D. Scora and N. Isgur, Phys. Rev. D **52**, 2783 (1995).
11. T. Altomari and L. Wolfenstein, Phys. Rev. D **37**, 681 (1988).
12. B. Konig, J. G. Korner, M. Kramer, and P. Kroll, Phys. Rev. D **56**, 4282 (1997).
13. N. Isgur and M. B. Wise, Phys. Lett. B **232**, 113 (1989); **237**, 527 (1990); M. Neubert and V. Rieckert, Nucl. Phys. B **382**, 97 (1992).
14. A. Le Yaouanc, L. Oliver, O. Péne, and J.-C. Raynal, Phys. Lett. B **365**, 319 (1996).
15. D. Melikhov, Phys. Rev. D **56**, 7089 (1997).
16. ARGUS Collab. (H. Albrecht *et al.*), Z. Phys. C **57**, 533 (1993).
17. B. Stech, Z. Phys. C **75**, 245 (1997); Nucl. Phys. B (Proc. Suppl.) **50**, 45 (1996).
18. Particle Data Group, Phys. Rev. D **54**, 43 (1996).
19. S. S. Gershtein, V. V. Kiselev, A. K. Likhoded, and A. V. Tkabladze, Usp. Fiz. Nauk **165**, 3 (1995).
20. S. N. Gupta and J. M. Johnson, Phys. Rev. D **51**, 168 (1995).

Physics of Atomic Nuclei, Vol. 63, No. 5, 2000, pp. 891–896. From Yadernaya Fizika, Vol. 63, No. 5, 2000, pp. 962–967.

ELEMENTARY PARTICLES AND FIELDS
Theory

Unitarity, (Anti)Shadowing, and Black-Disk Limit*

P. Desgrolard[1), **], L. Jenkovszky[***], and B. V. Struminsky[****]

Bogolyubov Institute for Theoretical Physics, National Academy of Sciences of Ukraine, Metrologicheskaya ul. 14b, Kiev, 252143 Ukraine

Received February 2, 1999

Abstract—By using realistic models for elastic hadron scattering, we demonstrate that, at current accelerator energies, the *s*-channel unitarity bound is safe and is not to be reached until 10^5 GeV, while the black-disk limit is saturated around 6 TeV. It will be followed by a larger transparency of the scattered particles near the center.

1. INTRODUCTION

Our decision to write this article was motivated partly by recent claims that, in high-energy hadron scattering, the black-disk limit has been reached and that the violation of the *s*-channel unitarity in some models is just around the corner. While the first statement is true and has interesting physical consequences, the second one is wrong for any realistic model fitting the existing data on proton and antiproton scattering up to highest accelerator energies.

To start with, we recall the general definitions and notation. Unitarity in the impact-parameter (b) representation reads

$$\mathrm{Im}h(s, b) = |h(s, b)|^2 + G_{\mathrm{in}}(s, b), \quad (1)$$

where $h(s, b)$ is the elastic-scattering amplitude at the center-of-mass energy $\sqrt{s}$ [with $\mathrm{Im}h(s, b)$ usually called a profile function representing hadron opacity] and $G_{\mathrm{in}}(s, b)$, called the inelastic overlap function, is the sum over all inelastic-channel contributions. Integrated with respect to b, equation (1) reduces to a simple relation between the total, elastic, and inelastic cross sections: $\sigma_{\mathrm{tot}}(s) = \sigma_{\mathrm{el}}(s) + \sigma_{\mathrm{in}}(s)$.

Equation (1) imposes the absolute limit

$$0 \le |h(s, b)|^2 \le \mathrm{Im}h(s, b) \le 1, \quad (2)$$

while the so-called black-disk limit $\sigma_{\mathrm{el}}(s) = \sigma_{\mathrm{in}}(s) + \frac{1}{2}\sigma_{\mathrm{tot}}(s)$ or

$$\mathrm{Im}h(s, b) = 1/2 \quad (3)$$

is a particular realization of the optical model—namely, it corresponds to the maximum absorption within the eikonal unitarization when the scattering amplitude is approximated as

$$h(s, b) = \frac{i}{2}(1 - \exp[i\omega(s, b)]), \quad (4)$$

with a purely imaginary eikonal $\omega(s, b) = i\Omega(s, b)$.

Eikonal unitarization corresponds to a particular solution to the unitarity equation,

$$h(s, b) = \frac{1}{2}[1 \pm \sqrt{1 - 4G_{\mathrm{in}}(s, b)}], \quad (5)$$

the one with a minus sign.

The alternative solution, that with a plus sign, is known [1, 2] and is realized within the so-called U-matrix[2)] approach [3, 4] with the unitarized amplitude

$$h(s, b) = \frac{U(s, b)}{1 - iU(s, b)}, \quad (6)$$

where U is now the input "Born term," the analog of the eikonal ω in (4).

In the U-matrix approach, the scattering amplitude $h(s, b)$ may exceed the black-disk limit as the energy increases. A transition from a (central) black disk to a (peripheral) black ring, surrounding a gray disk, for the inelastic overlap function in the impact-parameter space corresponds to the transition from shadowing to antishadowing [1]. We will present a particular realization of this regime.

The impact-parameter amplitude can be calculated either directly from data, as this was done, for example, in [5, 6] (where, however, the real part of the amplitude was neglected), or by using a particular model that fits data sufficiently well. There are several models appropriate for this purpose. In a classical article [7] on the subject, from the behavior of $G_{\mathrm{in}}(s, b)$, the proton is characterized as getting "BEL" (Blacker, Edgier, and Larger). As is anticipated in the title of our article, the

* This article was submitted by the authors in English.

1) Institut de Physique Nucléare de Lyon, IN2P3-CNRS et Université Claude Bernard Lyon-1, 43 Bd. du 11 Novembre 1918, F-69622 Villeurbanne CEDEX, France.
** e-mail: desgrolard@ipnl.in2p3.fr
*** e-mail: jenk@bitp.kiev.ua
**** e-mail: eppaitp@bitp.kiev.ua

2) We follow traditional terminology, although the word "matrix" in this context is misleading, since U, similar to the eikonal, is a single function rather than a matrix.

proton, after having reached its maximal darkness around the Tevatron energy region, may get less opaque beyond.

Actually, the construction of any scattering amplitude rests on two premises: the choice of the input, or Born term, and the relevant unitarization procedure (eikonal or U matrix in our case). Within the current accelerator energy region, there are several models that fit data reasonably well. Compatible within the region of the present-day experiments, they differ significantly when extrapolated to higher energies. We will consider two representative examples—namely, the Donnachie–Landshoff (DL) model [8, 9] and the dipole-Pomeron (DP) model [4, 10].

This article is organized as follows. In Section 2, we present necessary details on two realistic models (DL and DP); then, focusing on the DP model, we investigate, in Section 3, the unitarity properties at the Born level. In Section 4, we study the optical properties (transparency) after unitarization; a comparison with the DL model is given in the Appendix.

2. BORN TERM

The DL model [8] is popular for its simplicity. Essentially, it means the following four-parameter empirical fit to all total hadronic cross sections:

$$\sigma_{\text{tot}} = Xs^{\delta} + Ys^{\delta_r}. \tag{7}$$

Here, two of the parameters—namely, $\delta = \alpha_{\mathbf{P}}(0) - 1 \approx 0.08$ and $\delta_r (< 0)$—are universal. While the violation of the Froissart–Martin (FM) bound,

$$\sigma_{\text{tot}}(s) < C(\ln s)^2, \quad C = 60 \text{ mb}, \tag{8}$$

inherent in that model, is rather an aesthetic than a practical defect (because of the remoteness of the energy where it eventually will overshoot the FM limit), other deficiencies of the DL model (or any other model based on a supercritical Pomeron) are sometimes criticized in the literature, but, so far, nobody has been able to suggest anything significantly better instead. A particularly attractive feature of the DL Pomeron, made from a single term, is its factorability, although this may be too crude an approximation to reality.

The t dependence in the DL model is usually chosen [9] in the form close to the dipole form factor. For the present purposes, a simple exponential residue in the Pomeron amplitude will do as well, with the signature included,

$$A(s, t) = -N\left(-i\frac{s}{s_{\text{DL}}}\right)^{\alpha(t)} e^{Bt}, \tag{9}$$

where $\alpha(t) = \alpha(0) + \alpha' t$ is the Pomeron trajectory and N is a dimensionless normalization factor related to the total cross section at $s = s_{\text{DL}}$ by the optical theorem

$$N = \frac{s_{\text{DL}}}{4\pi \sin \pi\alpha(0)/2} \sigma_{\text{tot}}(s = s_{\text{DL}}). \tag{10}$$

According to the original fits [8, 9], we have $s_{\text{DL}} = 1 \text{ GeV}^2$, $\alpha(0) = 1.08$, $\alpha' = 0.25 \text{ GeV}^{-2}$, and $X = 21.70$ mb [see equation (7)] resulting in $N = \dfrac{X}{4\pi \sin \pi\alpha(0)/2} = 4.44$.

By identifying

$$\frac{d\sigma(s, t)}{dt} = \frac{d\sigma(s, t = 0)}{dt} e^{B_{\text{exp}}(s)t} \tag{11}$$

and choosing the CDF or E410 result for the slope B_{exp} at the Tevatron energy, we obtain

$$B = \frac{1}{2} B_{\text{exp}}(s) - \alpha' \ln \frac{s}{s_{\text{DL}}} = 4.75 \text{ GeV}^{-2}.$$

In the DP model [4], factorable at asymptotically high energies, logarithmically rising cross sections are produced only at the Pomeron intercept equal to unity; therefore, the DP is not in conflict with the FM bound. While data on the total cross sections are compatible with a logarithmic rise (DP with the intercept equal to unity), the ratio $\sigma_{\text{el}}/\sigma_{\text{tot}}$ is found (see [11] for details) for $\delta = 0$ to be a monotonically decreasing function of the energy for any physical values of the parameters. The experimentally observed rise of this ratio can be achieved only for $\delta > 0$ and thus requires the introduction of a supercritical Pomeron, $\alpha(0) > 1$. As a result, the rise of the total cross sections is driven and shared by the dipole and the supercritical intercept. The parameter $\delta = \alpha(0) - 1$ in the DP model is nearly one-half as great as that of the DL model, making it safer from the point of view of the unitarity bounds. Generally speaking, the closer the input to the unitarized output, the better the convergence of the unitarization procedure.

Let us recall that, apart from the "conservative" FM bound, any model should also satisfy s-channel unitarity. We demonstrate below that both the DL and the DP model are well below this limit and will remain so within the foreseeable future. (Let us recall that the DL and the DP model are close numerically, although they are different conceptually and, consequently, their extrapolations to superhigh energies will differ as well.)

The elastic-scattering amplitude corresponding to the exchange of a dipole Pomeron reads

$$\begin{aligned} A(s, t) &= \frac{d}{d\alpha}[e^{-i\pi\alpha/2} G(\alpha)(s/s_0)^{\alpha}] \\ &= e^{-i\pi\alpha/2}(s/s_0)^{\alpha}[G'(\alpha) + (L - i\pi/2)G(\alpha)], \end{aligned} \tag{12}$$

where $L \equiv \ln \dfrac{s}{s_0}$, and $\alpha \equiv \alpha(t)$ is the Pomeron trajectory; in this paper, we use a linear trajectory $\alpha(t) = \alpha(0) + \alpha' t$ for the sake of simplicity.

By identifying $G'(\alpha) = -ae^{b_{\mathbf{P}}(\alpha-1)}$, we can recast equation (12) into the geometric form

$$A(s,t) = i\frac{as}{b_{\mathbf{P}}s_0}[r_1^2(s)e^{r_1^2(s)[\alpha(t)-1]} - \epsilon r_2^2(s)e^{r_2^2(s)[\alpha(t)-1]}], \quad (13)$$

where

$$r_1^2(s) = b_{\mathbf{P}} + L - i\frac{\pi}{2}, \quad r_2^2(s) = L - i\frac{\pi}{2}. \quad (14)$$

The model contains the following adjustable parameters: a, $b_{\mathbf{P}}$, $\alpha(0)$, α', ϵ, and s_0.

In Table 1, we quote the numerical values of the parameters of the dipole Pomeron fitted in [10] to data on proton–proton and proton–antiproton elastic scattering:

$$\sigma_{\text{tot}}(s) = \frac{4\pi}{s}\text{Im}A(s,0), \quad \rho(s) = \frac{\text{Re}A(s,0)}{\text{Im}A(s,0)}; \quad 4 \le \sqrt{s}(\text{GeV}) \le 1800, \quad (15)$$

as well as the differential cross section

$$\frac{d\sigma(s,t)}{dt} = \frac{\pi}{s^2}|A(s,t)|^2, \quad 23.5 \le \sqrt{s}(\text{GeV}) \le 630, \quad 0 \le |t|(\text{GeV}^2) \le 6. \quad (16)$$

In that fit, apart from the Pomeron, the odderon and two subleading trajectories ω and f were also included. For the sake of simplicity and clarity, we consider here only the dominant term at high energy due to Pomeron exchange with the parameters fitted in [10]. The extent to which this Pomeron is a good approximation in the TeV region is discussed in detail in [12]. The quality of this fit is illustrated and discussed in [10]. With such a simple model and small number of parameters, better fits are hardly to be expected.

We use the above set of parameters to calculate the impact-parameter amplitude and to scrutinize, in Section 3, the unitarity properties of this Born level amplitude. In Section 4, we introduce a unitarization procedure necessary at higher energies and discuss the relevant physical consequences.

To summarize, the DP model with the intercept equal to unity is self-consistent in the sense that its functional (logarithmic) form is stable with respect to unitarization. Moreover, the presence of the second term (proportional to ϵ) in (13) has the meaning of absorptions, and it is crucial for the dip mechanism. It can be viewed also as one more unitarity feature of the model.

In the limit of very high energies, when $L \gg b_{\mathbf{P}}$, the two (squared) radii $R_i^2 = \alpha' r_i^2$ become equal and real, and the model obeys exact geometric scaling as well as factorization (see next section). Alternatively, this corresponds to the case of no absorptions ($\epsilon = 0$).

Table 1. Parameters of the dipole Pomeron found in [10]

a	$b_{\mathbf{P}}$	$\alpha(0)$	α', GeV^{-2}	ϵ	s_0, GeV^2
355.6	10.76	1.0356	0.377	0.0109	100.0

Table 2. Central opacity of the nucleon, Im$h(s,0)$, calculated at ISR, SPS, and Tevatron energies along with experimental data

$\sqrt{s}$	53 GeV	546 GeV	1800 GeV
Experiment	0.36 [6]	0.420 ± 0.004 [13]	0.492 ± 0.008 [14]
Theory	0.36	0.424	0.461

However attractive, the case of the intercept equal to unity ($\delta = 0$) is only an approximation to the more realistic model requiring $\delta > 0$ to meet the observed rise of the ratio $\sigma_{\text{el}}/\sigma_{\text{tot}}$. For such a "supercritical" Pomeron, unitarization becomes inevitable.

3. IMPACT-PARAMETER REPRESENTATION, UNITARITY, AND BLACK-DISK LIMIT

In the impact-parameter representation, the elastic amplitude in our normalization is

$$h(s,b) = \frac{1}{2s}\int_0^\infty dqqJ_0(bq)A(s,-q^2), \quad q = \sqrt{-t}. \quad (17)$$

The impact-parameter representation for linear trajectories [3] is calculable explicitly for the model specified by (13). The result is

$$h(s,b) = ig_0[e^{r_1^2\delta}e^{-b^2/4R_1^2} - \epsilon e^{r_2^2\delta}e^{-b^2/4R_2^2}], \quad (18)$$

where

$$R_i^2 = \alpha' r_i^2 (i = 1,2), \quad g_0 = \frac{a}{4b_{\mathbf{P}}\alpha' s_0}. \quad (19)$$

Asymptotically (i.e., when $L \gg b_{\mathbf{P}}$, which corresponds to $\sqrt{s} \gg 2.0$ TeV, with the parameters of Table 1),

$$h(s,b) \xrightarrow[s\to\infty]{} ig(s)(1-\epsilon)e^{-\frac{b^2}{4R^2}}, \quad (20)$$

where

$$R^2 = \alpha' L, \quad g(s) = g_0\left(\frac{s}{s_0}\right)^\delta, \quad (21)$$

and $b_{\mathbf{P}}$ is the constant part of the slope parameter.

To illustrate the s-channel unitarity, we display, in Fig. 1*a*, a family of curves showing the imaginary part of the amplitude in the impact-parameter representation at various energies; also shown is the calculated [from (1)] inelastic overlap function.

[3] Other cases were treated e.g., in [4].

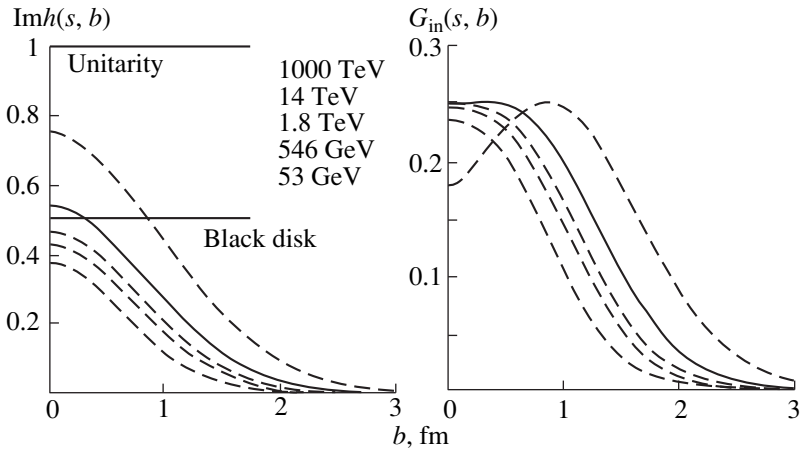

Fig. 1. Calculated dimensionless Born level Im$h(s, b)$ (left panel) and $G_{in}(s, b)$ (right panel) plotted versus the modulus of the impact parameter b for some characteristic energies as indicated (solid curve is for the LHC energy). The top of the scale on the left is the unitary limit, and the value of 1/2 corresponds to the black-disk limit (both are indicated by horizontal lines). The calculations were performed for the dipole Pomeron model; similar results were obtained for the DL model (see main body of the text). The sequence of the calculated curves follows that of the relevant energies indicated.

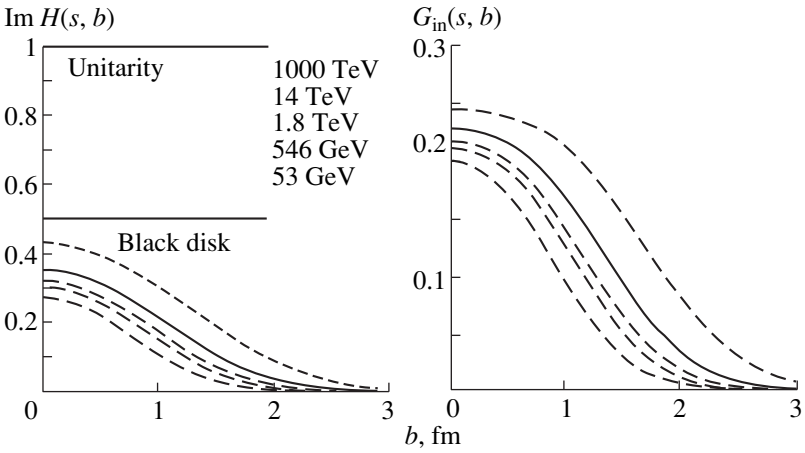

Fig. 2. As in Fig. 1, but for the unitarized amplitude $H(s, b)$ and the overlap function calculated without refitting the parameters used at the Born level.

Our confidence in the extrapolation of Im$h(s, b)$ to the highest energies rests partly on the good agreement of our (not fitted) results with the experimental analysis of the central opacity of the nucleon (see Table 2).

It is important to note that the unitarity bound, 1, for Im$h(s, b)$ will not be reached at the LHC energy, while the black-disk limit, 1/2, will be slightly exceeded, the central opacity of the nucleon being Im$h(s, 0) = 0.54$.

The black-disk limit is reached at $\sqrt{s} \sim 6$ TeV, where the overlap function reaches its maximum of 1/4. This energy corresponds to the appearance of the antishadowing mode in agreement with the general considerations in [1]. Notice that, while Im$h(s, b)$ remains central all the way, $G_{in}(s, b)$ gets more peripheral as the energy increases starting from the Tevatron energy. By the way of example, we indicate that, at $\sqrt{s} = 14$ TeV, the central region of the antishadowing mode below $b \sim 0.4$ fm is discernible from the peripheral region of shadowing scattering below $b \sim 0.4$ fm, where $G_{in}(s, b) = 1/4$. In terms of [7], the proton will tend to become more transparent at the center ("gray," in the sense of becoming a gray object surrounded by a black ring); i.e., it is expected to become "GEL" instead of "BEL."

The s-channel unitarity limit will not be endangered until extremely high energies (10^5 for the DL model and 10^6 GeV for the DP), safe for any credible experiment. It is interesting to compare these limits with the limitations imposed by the FM bound: actually, the Pomeron amplitude saturates the FM bound at 10^{27} GeV. As might have been expected, the FM bound is even more conservative than that following from s-channel unitarity.

The DP and DL models are confronted in the Appendix.

4. UNITARIZATION AND TRANSITION FROM A BLACK TO A GRAY DISK

Now, we consider the unitarized amplitude according to the "U-matrix" prescription [3, 4]

$$H(s, b) = \frac{h(s, b)}{1 - ih(s, b)}, \quad (22)$$

with the Born term $h(s, b)$ defined in the previous section in (13) and (14).

Figure 2 shows the behavior of the unitarized impact-parameter amplitude $H(s, b)$ and the corresponding inelastic overlap function at various energies. By comparing it with similar curves (Fig. 1) obtained at the Born level, we see that unitarization lowers significantly both the elastic and the inelastic impact-parameter amplitudes.

An inevitable consequence of the unitarization is that, when calculating the observables, one should also replace the Born amplitude $A(s, t)$ by a unitarized amplitude $\tilde{A}(s, t)$ defined as the inverse Fourier–Bessel transform of $H(s, b)$,

$$\tilde{A}(s, t) = 2s\int_0^\infty dbbJ_0(b\sqrt{-t})H(s, b). \quad (23)$$

Thus, the above picture may change since the parameters of the model should in principle be refitted under the unitarization procedure (this effect of changing the parameters was clearly demonstrated, e.g., in [15]).

Actually, searches for a new fit of the parameters by using a unitarization procedure is time-consuming and unnecessary for the present discussion because the behavior of the amplitude and of the overlap function in the impact-parameter representation obtained at the Born level will be almost restored after unitarization. We checked that the parameters of the complete model (with the secondary Reggeons and odderon added in the fit) after unitarization may be rearranged so as to reproduce well the data and give roughly the same extrapolated properties as at the Born level.

While the unitarity limit is now secured automatically [recall that $\mathrm{Im}h(s, 0)$ is well below that limit even at the Born level in the TeV region], the behavior of the elastic impact-parameter amplitude after it has reached the black-disk limit corresponds (see [1]) to the transition from shadowing to antishadowing. In other words, the proton (antiproton), upon reaching its maximal blackness around 6 TeV, will become gradually more transparent with increasing energies at its center.

Table 3. Maximum values of the amplitude and overlap function at the Born level and after U-matrix unitarization calculated at 14 TeV for the DP and DL models without refitting the parameters

	$\mathrm{Im}h(s, 0)$	$G_{\mathrm{in}}(s, 0)$	$\mathrm{Im}H(s, 0)$	$G_{\mathrm{in}}(s, 0)$
DP	0.535	0.247	0.349	0.227
DL	0.539	0.246	0.351	0.227

5. CONCLUSION

While the results of our analysis in the impact-parameter representation are in agreement with the earlier observations that $\mathrm{Im}h(s, b)$ remains central and $G_{\mathrm{in}}(s, b)$ becomes peripheral as the energy exceeds 6 TeV (see Fig. 1), there is a substantial difference from the known "BEL-picture" [7], according to which the proton becomes Blacker, Edgier, and Larger with increasing energy.

We confirm that, getting edgier and larger, the proton, after reaching its maximal blackness, will tend to be more transparent or "GEL"—a gray disk surrounded by a black ring—when the energy exceeds that of the Tevatron. This transition from shadowing to a new antishadowing scattering mode is expected to occur at the LHC energy.

To conclude, we stress once again that the data and relevant models at present energies are well below the s-channel unitarity limit. In our opinion, deviations due to the diversity of realistic models may result in discrepancies concerning $\mathrm{Im}h(s, 0)$ of at most 10%, while its value at 6 TeV is still half that of the unitarity limit, so that there is no reason to worry about it! Opposite statements may result from confusion with normalization. Therefore, model amplitudes at the Born level may still be quite interesting and efficient in analyzing the data at present accelerator energies and giving some predictions beyond. The question of which model is closer to reality and meets better the requirements of the "fundamental theory" remains of course topical.

Extrapolations to and predictions for the energies of the future accelerators (see, e.g., [12]) are both useful and exciting since they will be checked in the not-so-far future at LHC and other machines. The fate of the "black-disk limit" is one among these.

ACKNOWLEDGMENTS

We thank S.M. Troshin for a useful correspondence.

APPENDIX

Comparison of the DP and DL Models

The DL amplitude in the impact-parameter representation at the Born level, as calculated from (9) and

(17), is

$$h(s,b) = -\frac{N}{2s}\left(-\frac{s}{s_{\mathrm{DL}}}\right)^{\alpha(0)}\frac{e^{\frac{-b^2}{4B'(s)}}}{2B'(s)},$$

$$B'(s) = B + \alpha'\left(\ln\frac{s}{s_{\mathrm{DL}}} - i\frac{\pi}{2}\right).$$

As has already been noted, the *s*-channel unitarity limit both for the DP and the DL model will not be endangered until extremely high energies (10^5 GeV for the DL and 10^6 GeV for the DP model, the order-of-magnitude differences coming from the smaller intercept in the DP model), while the FM bound is saturated at 10^{27} GeV (for more details, see [16]).

Table 3 presents a selection of results concerning the DP and DL models for the Pomeron in the impact-parameter representation of the elastic amplitude and inelastic overlap function calculated at $b = 0$ at the LHC energy.

We conclude that the two models give similar results; all conclusions on unitarity and black-disk limits for the DP model hold for the DL model as well (the curves in Figs. 1 and 2 would be indistinguishable by eye).

Note that both models are supercritical, with asymptotic s^{δ}-type behavior of the total cross sections. They are known to give fits that cannot be discriminated by present data from an asymptotic behavior of the $\ln^2 s$ type. This is another argument to neglect unitarization effects.

REFERENCES

1. S. M. Troshin and N. E. Tyurin, hep-ph/9810495 and references therein.
2. A. Basetto and F. Paccanoni, Nuovo Cimento **61**, 486 (1969).
3. V. Savrin, N. Tyurin, and O. Khrustalev, Fiz. Élem. Chastits At. Yadra **7**, 21 (1976) [Sov. J. Part. Nucl. **7**, 9 (1976)].
4. A. N. Vall, L. L. Jenkovszky, and B. V. Struminsky, Fiz. Élem. Chastits At. Yadra **19**, 180 (1988) [Sov. J. Part. Nucl. **19**, 77 (1988)] and references therein.
5. U. Amaldi and K. R. Schubert, Nucl. Phys. B **166**, 301 (1980).
6. R. Castaldi and G. Sanguinetti, Annu. Rev. Nucl. Part. Sci. **5**, 351 (1985).
7. R. Henzi and P. Valin, Phys. Lett. B **132**, 443 (1983).
8. A. Donnachie and P. V. Landshoff, Phys. Lett. B **296**, 227 (1992).
9. A. Donnachie and P. V. Landshoff, Z. Phys. C **2**, 55 (1979); Phys. Lett. B **123**, 345 (1983); Nucl. Phys. B **231**, 189 (1984); **244**, 322 (1984).
10. P. Desgrolard, M. Giffon, and L. Jenkovszky, Z. Phys. C **55**, 637 (1992).
11. L. L. Jenkovszky, B. V. Struminsky, and A. N. Vall, Yad. Fiz. **46**, 1519 (1987) [Sov. J. Nucl. Phys. **46**, 901 (1987)].
12. S. Chatrchian *et al.* (in preparation).
13. CDF Collab. (S. Abe *et al.*), Phys. Rev. D **50**, 5550 (1994).
14. CDF Collab. (P. Giromini), in *Proceedings of the International Conference (5th Blois Workshop) on Elastic and Diffractive Scattering*, Ed. by H. M. Fried, K. Kang, and C.-I. Tan (World Sci., Singapore, 1993), p. 30.
15. R. J. M. Covolan, J. Monthanha, and K. Goulianos, Phys. Lett. B **389**, 176 (1996).
16. M. Bertini, P. Desgrolard, and Yu. Ilyin, Int. J. Phys. **1**, 45 (1995).

Physics of Atomic Nuclei, Vol. 63, No. 5, 2000, pp. 897–902. Translated from Yadernaya Fizika, Vol. 63, No. 5, 2000, pp. 968–974.

ELEMENTARY PARTICLES AND FIELDS
Theory

Structure of the Exact Effective Action and Quark Confinement in MSSM QCD

K. V. Stepanyantz*

Moscow State University, Vorob'evy gory, Moscow, 119899 Russia

Received March 19, 1999; in final form, June 1,1999

Abstract—An expression for the exact (beyond perturbation theory) effective action in $N = 1$ supersymmetric gauge theories where all particles, with the exception of gauge bosons, are massive is proposed. By analyzing the form of this expression, it is shown that, in supersymmetric theories, instanton effects can lead to quark confinement. On the basis of first principles, the characteristic scale of confinement is calculated within MSSM QCD, and the result is found to be consistent with experimental data. The proposed explanation differs drastically with the dual Higgs mechanism. *© 2000 MAIK "Nauka/Interperiodica".*

1. INTRODUCTION

Quark confinement presents one of the most important unresolved problems in modern theoretical physics [1]. It is commonly believed that there are fundamental connections between confinement and the nonperturbative dynamics of field theory. Considerable advances in these realms were made by Seiberg and Witten [2], who were able to obtain an expression for the sum of all instanton corrections in the simplest case of $N = 2$ supersymmetric Yang–Mills theory. It should be emphasized, however, that the model considered by those authors is not physical—an investigation of $N = 1$ supersymmetric theories is of much greater interest since indirect experimental data [3, 4] indicate that there is $N = 1$ supersymmetry in the Standard Model. This is the reason why we address here precisely this case.

On the other hand, the presence of supersymmetry is of paramount importance for the proposed explanation of confinement. This explanation, which differs drastically from the dual Higgs mechanism [5], usually used to obtained qualitative insights into the phenomenon, actually invokes an assumption on the structure of the effective potential beyond perturbation theory and relies heavily on the presence of an auxiliary field D in supersymmetric theories.

That confinement is induced by instanton effects is indirectly suggested by a formidable difference between QCD and Grand Unification scales, a circumstance referred to in the literature as the gauge-hierarchy problem. Recall that the two fundamentally different scales arise in instanton calculations [6], their ratio being proportional to $\exp(-8\pi/e^2)$. However, expressions proposed thus far in the literature for the effective action of $N = 1$ supersymmetric gauge theories beyond perturbation theory [7–9] do not lead to confinement.

A new (hypothetical) expression for the effective action in the case where all particles of the theory, with the exception of gauge bosons, are massive has been inferred in the present study from an analysis of instanton effects. This expression leads to the emergence of confinement—in particular, in the $SU(3)$ sector of the minimal supersymmetric Standard Model (MSSM QCD). The characteristic scale of confinement can be calculated here from first principles.

The ensuing exposition is organized as follows. In Section 2, we discuss the structure of instanton contributions to the effective action and make an attempt at constructing an expression for their sum (that is, a low-energy effective action for $N = 1$ supersymmetric Yang–Mills theory with matter in the case where all particles, with the exception of gauge bosons, have nonzero masses) on the basis of some general arguments. As a result, it is established that the superpotential depends on gauge and auxiliary fields in quite a peculiar way. It is shown in Section 3 that a dependence of this type leads to quark confinement in the sense that there are no asymptotic color states in this case. An investigation reveals that, in this model, there exist two "phases": a confined phase at distances exceeding some critical size and a conventional phase at small distances. In the same section, we also obtain an expression for the potential of quark interaction. The confinement scale is calculated and contrasted against experimental data in Section 4. In the Conclusion, we briefly discuss the results obtained in the present study.

2. LOW-ENERGY EFFECTIVE ACTION FOR MSSM QCD

MSSM QCD represents an $N = 1$ supersymmetric Yang–Mills theory that is based on the $SU(3)$ gauge group and which involves six matter supermultiplets. In this theory, all particles, with the exception of gauge bosons, are massive. In the present study, we will con-

* e-mail: stepan@theor.phys.msu.su

1063-7788/00/6305-0897$20.00

sider a similar theory that is based on the $SU(N_c)$ gauge group and which features N_f matter supermultiplets. This theory is described by the action functional

$$S = \frac{1}{16\pi}\mathrm{tr}\,\mathrm{Im}(\tau\int d^4x d^2\theta W^2) + \frac{1}{4}\int d^4x d^4\theta \sum_{A=1}^{N_f}(\phi_A^+ e^{-2V}\phi^A + \tilde{\phi}^{+A} e^{2V}\tilde{\phi}_A) + S_m, \quad (1)$$

where the matter superfields ϕ and $\tilde{\phi}$ belong to, respectively, the fundamental and the antifundamental representation of the $SU(N_c)$ gauge group, while S_m stands for the sum of the massive terms for all fields.

Here, we have also used the notation

$$\phi(y,\theta) = \varphi(y) + \sqrt{2}\bar{\theta}(1+\gamma_5)\psi(y) + \frac{1}{2}\bar{\theta}(1+\gamma_5)\theta f(y),$$

$$\tilde{\phi}(y,\theta) = \tilde{\varphi}(y) + \sqrt{2}\bar{\theta}(1+\gamma_5)\tilde{\psi}(y) + \frac{1}{2}\bar{\theta}(1+\gamma_5)\theta \tilde{f}(y),$$

$$V(x,\theta) = -\frac{i}{2}\bar{\theta}\gamma^\mu\gamma_5\theta A_\mu(x) + i\sqrt{2}(\bar{\theta}\theta)(\bar{\theta}\gamma_5\lambda(x)) + \frac{i}{4}(\bar{\theta}\theta)^2 D(x), \quad (2)$$

$$W(y,\theta) = \frac{1}{2}(1+\gamma_5)(i\sqrt{2}\lambda(y) + i\theta D(y) + \frac{1}{2}\Sigma_{\mu\nu}\theta F_{\mu\nu}(y) + \frac{1}{\sqrt{2}}\bar{\theta}(1+\gamma_5)\theta\gamma^\mu D_\mu\lambda(y)),$$

$$\tau = \frac{\theta}{2\pi} + \frac{4\pi i}{e^2}, \quad y^\mu = x^\mu + \frac{i}{2}\bar{\theta}\gamma^\mu\gamma_5\theta,$$

$$\Sigma_{\mu\nu} = \frac{1}{2}(\gamma_\mu\gamma_\nu - \gamma_\nu\gamma_\mu), \quad D_\mu = \partial_\mu + i[A_\mu, \ ],$$

where A_μ is a gauge (gluon) field, λ is its spinor superpartner (gluino), and D is an auxiliary field.

The quarks are constructed from the fields ψ and $\tilde{\psi}$ as

$$\Psi = \frac{1}{\sqrt{2}}((1+\gamma_5)\psi + (1-\gamma_5)\tilde{\psi}). \quad (3)$$

The scalars φ and $\tilde{\varphi}$ appear to be their superpartners (squarks). The fields f and $\tilde{f}$ are auxiliary.

In the following, we assume that supersymmetry is broken softly by introducing a mass term for the gluino.

Since quark confinement is a low-energy phenomenon, we will try to construct the exact effective action for this theory below the threshold for the production of all massive particles.[1)] This effective action must satisfy the following requirements:

(i) It must depend on the original fields of the theory (not on composite ones).

(ii) It must be in accord with dynamical (both perturbative and instanton) calculations (this requirement is stronger than that which demands conformity with the law of transformation of the instanton measure and which was used in [9]).

Of course, the exact expression for the effective action can be obtained only upon performing dynamical calculations and summing a series of instanton corrections. In this study, we present, however, some arguments leading to a specific assumption about its form.

First of all, we will try to establish the general structure of the effective action. We assume that it can be represented as the sum of an expression that is invariant under supersymmetry transformations and (mass) terms that may break supersymmetry. We will be interested only in the holomorphic part of terms that are invariant under supersymmetry transformations. In order to find it, we note that there is a close relation between the perturbative contribution and the instanton corrections [6, 10, 11]. In particular, the requirement that the instanton contributions be perturbatively invariant under renormalization-group transformations makes it possible to construct exact beta functions of supersymmetric theories.

Let us now try to formulate this relation rigorously. For this, we introduce some scale M and denote by e the coupling-constant value at this scale. The one-loop result will then be proportional to $-1/4e^2$, while the instanton contributions will be proportional to $\exp(-8\pi n/e^2)$, where n is the modulus of the topological number. (The one-loop contribution and the instanton corrections are perturbatively invariant under renormalization-group transformations individually.)

Let us represent the holomorphic part of the perturbative effective Lagrangian as

$$L_a = \frac{1}{16\pi}\mathrm{Im}\,\mathrm{tr}\int d^2\theta W^2\left(\frac{4\pi i}{e_{\mathrm{eff}}^2} + \frac{\vartheta_{\mathrm{eff}}}{2\pi}\right), \quad (4)$$

where e_{eff} and ϑ_{eff} are some quantities that appear to be functions of the fields involved and which are invariant under renormalization-group transformations; specifically, these are, respectively, the effective coupling constant and the coefficient of the topological term within perturbation theory. Introducing the notation

$$z \equiv \exp\left[2\pi i\left(\frac{4\pi i}{e_{\mathrm{eff}}^2} + \frac{\vartheta_{\mathrm{eff}}}{2\pi}\right)\right], \quad (5)$$

[1)] We will see in the following that this condition does not hold for the u and d quarks, but this is not very important, since the mass dependence of the effective action does not change upon traversing the threshold.

we can represent the exact effective Lagrangian (the instanton contributions being included) in the form

$$L_a = \frac{1}{32\pi^2}\mathrm{Im}\,\mathrm{tr}\int d^2\theta W^2 g(z) = \frac{1}{32\pi^2}\mathrm{Im}\,\mathrm{tr}\int d^2\theta W^2\left(-i\ln z + \sum_{n=1}^{\infty} c_n z^n\right). \quad (6)$$

(So far, we have nowhere invoked the constant-field approximation, which is usually used to obtain exact results.)

In order to find the function $g(z)$, we will make use of the statement that the conditions

$$g(z) = -i\ln z + \sum_{k=0}^{\infty} c_n z^n, \quad \mathrm{Im}\,g(z) > 0, \quad c_n \in \mathrm{Im} \quad (7)$$

determine unambiguously its form, apart from some constant. [The inequality $\mathrm{Im}\,g(z) > 0$ represents the requirement that the Euclidean effective action be positive definite, while the condition $c_n \in \mathrm{Im}$ follows from the structure of the instanton contributions.] The constant is chosen on the basis of the condition that the effective charge can take arbitrary real values; hence, there exists a point z where $g(z) = 0$. In [12], it was shown that these conditions lead unambiguously to a z dependence of the form

$$g(z) = 2\pi\tau(z^{-1/4}), \quad (8)$$

where the function $\tau(a)$ is the Seiberg–Witten solution

$$\tau(a) = \left.\frac{da_D(u)}{da}\right|_{u=u(a)}, \quad (9)$$

the functions a and a_D in turn being given by

$$a(u) = \frac{\sqrt{2}}{\pi}\int_{-1}^{1} dx\frac{\sqrt{x-u}}{\sqrt{x^2-1}}; \qquad a_D(u) = \frac{\sqrt{2}}{\pi}\int_{1}^{u} dx\frac{\sqrt{x-u}}{\sqrt{x^2-1}}. \quad (10)$$

Therefore, we eventually obtain

$$L_a = \frac{1}{16\pi}\mathrm{Im}\int d^2\theta W^2\tau(z^{-1/4}), \quad (11)$$

where the parameter z can be determined in the one-loop approximation or exactly by studying the instanton measures by using the same method as in [10, 11].

Since the one-loop expression for the beta function has the form

$$\beta^{(1)}(e) = -\frac{e^3}{16\pi^2}(3N_c - N_f), \quad (12)$$

the parameter z must be proportional to $M^{3N_c-N_f}$, where M is the ultraviolet-cutoff momentum. The same result is obtained from the expression for the instanton measure [13] (this is in perfect conformity with the above arguments).

Our objective here is to construct the effective action in the low-energy region—that is, below the threshold for the production of all massive particles. For massive particles, the values of the running coupling constants are stabilized at the mass value; therefore, their contribution will be proportional to the ratio M/m raised to the power that is determined by the corresponding coefficient in the beta function. The situation with massless gauge fields is somewhat more intricate. In the presence of massless fields, the coupling constant is not stabilized at any value. Therefore, the behavior of the theory in the infrared region must be analyzed in detail. We note that we are interested primarily not in the renormalization-group functions but in the effective action, which can be calculated, for example, in the constant-field approximation. Therefore, the contributions from massless gauge fields to the parameter z will involve some functions of these fields rather than their masses.

Since z is a scalar, we must find, in the constant-field approximation, a chiral scalar superfield that does not involve derivatives of $F_{\mu\nu}$ and which does not have anticommuting quantities in the lower component (otherwise, all powers of z from some power that is sufficiently large will be equal to zero or infinity). The only superfield B that satisfies these requirements is given by

$$B = -\frac{1}{8}\bar{D}(1-\gamma_5)D(W_a^*)^2 = (D^a)^2 - \frac{1}{2}(F_{\mu\nu}^a)^2 - \frac{i}{2}F_{\mu\nu}^a\tilde{F}_{\mu\nu}^a + O(\theta), \quad (13)$$

where the index a numbers the generators of the gauge group. (In the perturbative approach, a similar expression was proposed in [14].)

From a dimensional analysis, we therefore find that the contribution of massless gauge fields to the parameter z is proportional to the quantity $M/B^{1/4}$ raised to the power that is determined by the corresponding coefficient in the beta function.

The one-loop beta function can be represented in the form

$$\beta^{(1)}(e) = -\frac{e^3}{16\pi^2}(c_G + c_\lambda + c_q + c_{sq}), \quad (14)$$

where

$$c_G = \frac{11}{3}N_c, \quad c_\lambda = -\frac{2}{3}N_c, \quad c_q = -\frac{2}{3}N_f, \quad c_{sq} = -\frac{1}{3}N_f \quad (15)$$

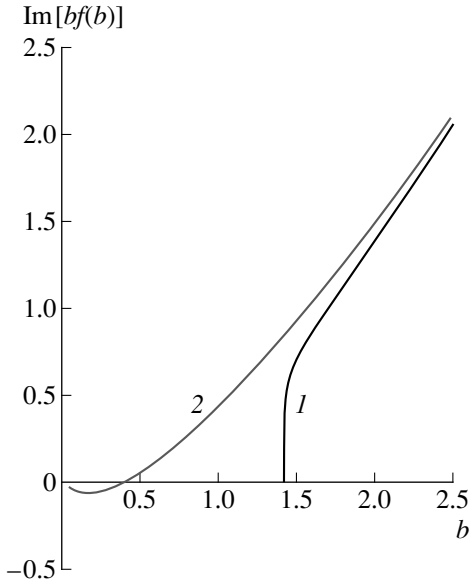

Fig. 1. Graph of the function Im[$bf(b)$] (curve *1*). Presented for the sake of comparison is also the graph of the corresponding perturbative expression (curve *2*).

for the contributions of, respectively, Yang–Mills fields (with ghosts), their spinor superpartners, quarks, and squarks. Taking into account the above arguments, we then obtain

$$z = e^{-8\pi^2/e^2} M^{3N_c - N_f} \left(\frac{m_\lambda^{2/3}}{B^{11/12}}\right)^{N_c} (m_q^{2/3} m_{sq}^{1/3})^{N_f}, \qquad (16)$$

where m_λ is the gluino mass, while $(m_q)_i^j$ and $(m_{sq})_i^j$ are the quark and squark mass matrices.

It should be noted that expression (16) was obtained in the one-loop approximation. Multiloop effects can be taken into account [10, 11] by considering that, in the expression for the instanton measure [13], there appears the factor $(1/e^2)^{N_c}$, which will of course generate the corresponding contribution in the expression for z, while the gluino mass changes in such a way that $\tilde{m}_\lambda \equiv \dfrac{e m_\lambda}{\beta(e)} = \text{const}$. Eventually, the parameter z (apart from some constant C) will therefore become

$$z = C\left(\frac{1}{e^2}\right)^{N_c} e^{-8\pi^2/e^2} M^{3N_c - N_f} \left(\frac{\tilde{m}_\lambda^{2/3}}{B^{11/12}}\right)^{N_c} \times [\det(m_q)_i^j]^{2/3} [\det(m_{sq})_i^j]^{1/3}, \qquad (17)$$

where we have also taken into consideration $SU(N_f)$ symmetry with respect to rotations in flavor space and recovered the generation indices.

We denote

$$\Lambda_c = \left(\frac{1}{e^2}\right)^{3/11} \tilde{m}_\lambda^{2/11} (C e^{-8\pi^2/e^2} M^{3N_c - N_f} \times [\det(m_q)_i^j]^{2/3} [\det(m_{sq})_i^j]^{1/3})^{3/(11N_c)}. \qquad (18)$$

The expression for z can then be recast into the form

$$z = \left(\frac{\Lambda_c}{B^{1/4}}\right)^{11N_c/3}. \qquad (19)$$

We will see below that the quantity Λ_c represents the characteristic confinement scale.

3. CONFINEMENT MECHANISM

We now note that the field D, though being auxiliary, appears to be one of the quantum fields of the theory. This field must be eliminated with the aid of the equations of motion. In the low-energy limit considered here, all wave functions of the squarks must of course be set to the corresponding vacuum expectation values, which are equal to zero since the $SU(3)$ group is not broken. Therefore, the equation of motion for the field D can be derived by varying the action functional

$$\Gamma = \frac{1}{16\pi} \mathrm{Im}\,\mathrm{tr} \int d^4x d^2\theta W^2 \tau(z^{-1/4}). \qquad (20)$$

We further note that, owing to the presence of supersymmetry and by virtue of (13), the field D appears in Γ only in the combination

$$b = (D^a)^2 - \frac{1}{2}(F_{\mu\nu}^a)^2 - \frac{i}{2} F_{\mu\nu}^a \tilde{F}_{\mu\nu}^a. \qquad (21)$$

It is straightforward to see that, by calculating the integral with respect to the anticommuting coordinate, we can therefore represent the bosonic component of the Lagrangian in the form

$$L_{\mathrm{Bose}} = \frac{1}{8\pi} \mathrm{Im}[b^* f(b)], \qquad (22)$$

where $f(b) \equiv \tau[z^{-1/4}(b)]$.

In the vacuum state, the field D takes a value such that the functional L_{Bose} is minimized. Since the relation $\tilde{F}_{\mu\nu} F_{\mu\nu} = 0$ holds in the absence of a magnetic field, the parameter b can be taken to be real-valued.

The graph of the function Im[$bf(b)$] is shown in Fig. 1. (For the sake of simplicity, we set $\Lambda_c = 1$ in all the graphs.)

By using the expressions for $a(u)$ and $a_D(u)$ in terms of elliptic functions [15], we can easily show that the function Im[$bf(b)$] has the only extremum, that which occurs at the point b_0 and which satisfies the condition

$$a(b_0) = z^{-1/4}(b_0) = 4/\pi. \qquad (23)$$

At the point of minimum, we have $\tau[z^{-1/4}(b_0)] = 0$; owing to this, there is no kinetic term for the gauge field in the vacuum state. Hence, the field A^a_μ appears to be a Lagrange multiplier, the corresponding constraint being

$$J^a_\mu = 0. \tag{24}$$

The constraint in (24) means the absence of asymptotic color states—that is, confinement of color charges.

At first glance, the above seems to lead to the erroneous conclusion that color states cannot in principle occur at different points of space. Indeed, the kinetic term for Yang–Mills theory can be written in the standard form

$$-\frac{1}{4e^2}\mathrm{tr}F^2_{\mu\nu}, \tag{25}$$

where $F_{\mu\nu} = \partial_\mu A_\nu - \partial_\nu A_\mu + i[A_\mu, A_\nu]$. As a matter of fact, the absence of the corresponding term means that the effective charge becomes infinitely large, which in turn leads to infinitely strong interaction.

In studying the interaction between the quarks, it is necessary to take into account, however, the chromomagnetic field created by the quarks. In the simplest case, we have

$$A^a_\mu = \frac{q^a}{r}\delta_{\mu 0}. \tag{26}$$

In the absence of a magnetic field, relation (21) becomes real, taking the form

$$b = (D^a)^2 + (\mathbf{E}^a)^2. \tag{27}$$

It follows that, at sufficiently small values of r, the second term comes to be greater than b_0, in which case it is impossible to minimize the function $\mathrm{Im}[bf(b)]$ at real values of the field D^a. Since $\mathrm{Im}(bf(b))$ is a monotonically increasing function (see the graph in Fig. 1), it attains a minimum when b assumes the minimum possible value, which obviously corresponds to $D = 0$. In this case, b is not of course equal to b_0, so that $\tau(b)$ is different from zero; therefore, there arises a kinetic term for a gauge field, and the theory reduces to conventional QCD.

Thus, there are two basically different regions in the model being considered. In the first region, which corresponds to $b_0 > (\mathbf{E}_a)^2$, the auxiliary field D is nonzero [more precisely, $(D_a)^2 + (\mathbf{E}_a)^2 = b_0$], the gauge field does not develop a kinetic term, and color charges are confined. In the second region, we have $b_0 < (\mathbf{E}_a)^2$ and $D = 0$, in which case conventional methods can be used to describe the theory. The "phase-transition" point r_c corresponds to

$$b_0 = (\mathbf{E}^a)^2 \approx \frac{1}{r^4}. \tag{28}$$

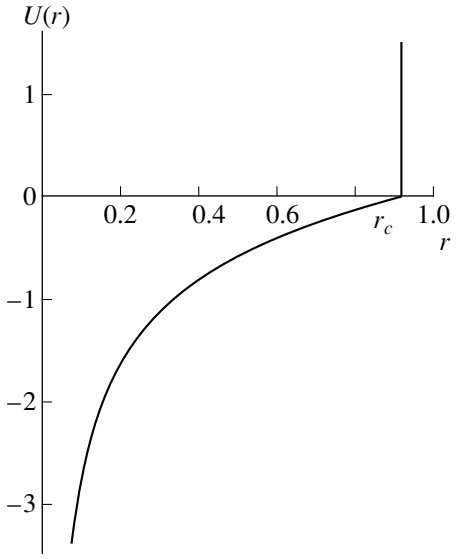

Fig. 2. Graph of the potential $U(r)$ of the interquark interaction within MSSM QCD.

Since it follows from (19) and (23) that

$$(b_0)^{1/4} = \Lambda_c\left(\frac{4}{\pi}\right)^{12/(11N_c)}, \tag{29}$$

Λ_c does indeed appears to be the characteristic scale of confinement.

However, the pattern exposed here does not predict a linear growth of the interquark potential. Instead, we arrive at an infinitely large potential for r values greater than the critical dimension r_c. By virtue of the equations of motion, which can be recast into the form

$$\nabla(\mathrm{Im}\, f_1(1/r^4)\nabla U) = \mathrm{const}\,\delta(\mathbf{r}), \tag{30}$$

where $f_1(b) = f(b) + bf'(b)$, the expression for the potential at smaller values of r takes the form

$$U(r) \sim \int \frac{dr}{r^2(\mathrm{Im}\, f_1(1/r^4))}, \tag{31}$$

which represents the Coulomb potential modified by quantum corrections.

The graph of the potential (31) is displayed in Fig. 2. [As before, we set $\Lambda_c = 1$; in addition, we disregard the quark charges, which are on the order of unity. Owing to this, we have $r_c = (b_0)^{-1/4}$.] The normalization constant is chosen in such a way that $U(r_c) = 0$.

4. CONFINEMENT SCALE

In this section, we will study only MSSM QCD, which represents a particular case of the above model at $N_c = 3$ and $N_f = 6$.

By virtue of invariance under renormalization-group transformations, the quantity Λ_c can in principle be calculated at an arbitrary scale—for example, at the

Grand Unification scale. In this case, the coupling constant in MSSM QCD must be set to $e^2 \approx 1/2$, and it follows from (18) that the confinement scale becomes

$$\Lambda_c = Me^{-16\pi^2/11}\left(\frac{m_q^4 m_\lambda^2 m_{sq}^2}{M^8}\right)^{1/11}. \quad (32)$$

Unfortunately, the masses of the superpartners are unknown. Moreover, a constant factor, which can be sufficiently larger and which can therefore affect somewhat the result, was discarded in (32). (Since, on the other hand, a root of eleventh degree is extracted from this factor, the corresponding contribution is expected to be on the order of unity.)

Nonetheless, a rough estimate of Λ_c can be obtained. Assuming that all masses lie within the range 10–100 GeV ($M = 2 \times 10^{16}$ GeV), we obtain

$$\Lambda_c \approx 0.09\text{–}0.46 \text{ GeV}, \quad (33)$$

which agrees well with experimental data.

5. CONCLUSION

A confinement mechanism has been proposed that differs drastically from the dual Higgs mechanism [5], which is usually used to obtain insights into this phenomenon. This mechanism, however, is a natural corollary of the structure of the exact effective action (11) involving the parameter z that is determined by relation (17).

It should be noted, however, that the form in (11) only reflects some hypothesis that can be confirmed (disproved or modified) only on the basis of perturbative and instanton calculations similar to those performed, for example, in [16]. This hypothesis is supported by some circumstances mentioned in the present study—for example, agreement with the exact beta function of Novikov, Shifman, Vainstein, and Zakharov [10] (this can easily be verified) and a positive definite value obtained for the effective charge. Nonetheless, fulfillment of these necessary conditions cannot be considered as a rigorous proof.

Two basic factors are of paramount importance in the confinement mechanism proposed in the present study. These are, first, the presence of an auxiliary field D in gauge supersymmetric theories and, second, the fact that, for the bosonic part of the effective action, use is made of a nontrivial form that is obtained upon summing a series of instanton corrections.

In the potential of interquark interaction, however, there proved to be no linear growth at large distances. Instead, there arise two different regions ("phases"). In one of these (at distances in excess of some critical dimension), the gauge field develops no kinetic term, and the potential becomes infinitely large. In the other region, the behavior of the theory is described in the standard way, while the potential is close to the Coulomb potential. (Similar potentials are used in bag models [17].)

Of course, the proposed confinement mechanism does not reduce to the presence of this potential—first of all, it is predicted that there are no color states at large distances, in agreement with what is actually observed in nature. In addition, we automatically arrive at the confinement of electric (rather than magnetic) charges, so that there arises no need for invoking the idea of duality.

The confinement scale is calculated from first principles, and the result agrees well with experimental data, especially if we take into consideration the absence of experimental information about the masses of the superpartners.

ACKNOWLEDGMENTS

I am grateful to P.I. Pronin, O. Pavlovskiĭ, and K. Kazakov and to my colleagues from the Institute of Theoretical and Experimental Physics (ITEP, Moscow) for stimulating discussions and enlightening comments.

It is a pleasure to thank V.V. Asadov for financial support of the present investigation.

REFERENCES

1. Yu. A. Simonov, Usp. Fiz. Nauk **166**, 337 (1996) [Phys. Usp. **39**, 313 (1996)].
2. N. Seiberg and E. Witten, Nucl. Phys. B **426**, 19 (1994).
3. Particle Data Group, Phys. Rev. D **50**, 1173 (1994).
4. K. Dienes, hep-th/9602045.
5. S. Mandelstam, Phys. Lett. B **53**, 476 (1975); G. 't Hooft, Nucl. Phys. B **190**, 455 (1981).
6. G. 't Hooft, Phys. Rev. Lett. **37**, 8 (1976); Phys. Rev. D **14**, 3432 (1976).
7. I. Affleck, M. Dine, and N. Seiberg, Nucl. Phys. B **241**, 493 (1984).
8. N. Seiberg, Phys. Rev. D **49**, 6857 (1994).
9. P. Pronin and K. Stepanyantz, Teor. Mat. Fiz. **120**, 82 (1999).
10. V. Novikov, M. Shifman, A. Vainstein, and V. Zakharov, Nucl. Phys. B **229**, 381 (1983).
11. M. Shifman and A. Vainstein, hep-th/9902018.
12. G. Bonelli, M. Matone, and M. Tonin, Phys. Rev. D **55**, 6466 (1997); R. Flume, M. Magro, L. O'Raifeartaigh, *et al.*, Nucl. Phys. B **494**, 331 (1997).
13. S. Cordes, Nucl. Phys. B **273**, 629 (1986).
14. V. Novikov, M. Shifman, A. Vainshtein, and V. Zakharov, Phys. Lett. B **166**, 329 (1986).
15. L. Álvarez-Gaume and S. Hassan, Fortschr. Phys. **45**, 159 (1997).
16. A. Yung, Nucl. Phys. B **485**, 38 (1997).
17. F. Close, *An Introduction to Quarks and Partons* (Academic, New York, 1979; Moscow, Mir, 1982).

Translated by A. Isaakyan

Physics of Atomic Nuclei, Vol. 63, No. 5, 2000, pp. 903–907. Translated from Yadernaya Fizika, Vol. 63, No. 5, 2000, pp. 975–979.

ELEMENTARY PARTICLES AND FIELDS
Theory

Phonon-like Excitations of Instanton Liquid

G. M. Zinovjev[1)], S. V. Molodtsov, and A. M. Snigirev[2)]

Institute of Theoretical and Experimental Physics, Bol'shaya Cheremushkinskaya ul. 25, Moscow, 117259 Russia

Received February 25, 1999; in final form, May 31, 1999

Abstract—Phonon-like excitations of an anti-instanton–instanton liquid that are due to adiabatic variations in the instanton dimension are considered on the basis of an approximate calculation of the relevant path integral, which is saturated by quasizero modes. The kinetic term and the effective Lagrangian are found for such excitations. The properties of their spectrum, which has a mass gap determined by Λ_{QCD}, are discussed. © *2000 MAIK "Nauka/Interperiodica".*

The model of an (anti)instanton liquid (gas) underlies one of the seminal phenomenological approaches to the QCD vacuum. This model provides a correct qualitative description of some important quantities, such as the gluon condensate and the topological susceptibility, and explains chiral-symmetry breaking [1, 2]. It is assumed that the path integral of the model is saturated by semiclassical configurations that are generally close to exact solutions of the Yang–Mills equations [in particular, to Euclidean solutions represented by (anti)instantons] and that the wave function of the vacuum is homogeneous in metric space, its properties being reproduced by averaging the relevant solution over its collective coordinates. In the theory of an anti-instanton–instanton liquid, the form

$$A_\mu(x) = \sum_{i=1}^{N} A_\mu(x;\gamma_i) \tag{1}$$

representing a superposition of pseudoparticle fields is taken for one of the simplest admissible approximations to the true vacuum configuration A_μ. In equation (1), $A_\mu(x;\gamma_i)$ stands for the field of an individual (anti)instanton in the singular gauge; this fields depends on $4N_c$ [for the $SU(N_c)$ group] coordinates γ [$\gamma = (\rho, z, \Omega)$, ρ, z, and Ω being, respectively, the size of the (anti)instanton, the position of its center, and its color orientation] that characterize an exact (anti)instanton Euclidean solution to the Yang–Mills equations. Specifically, we have

$$A^a_\mu(x;\gamma) = \frac{2}{g}\Omega^{ab}\bar{\eta}_{b\mu\nu}\frac{y_\nu}{y^2}\frac{\rho^2}{y^2+\rho^2}, \quad y = x - z, \tag{2}$$

where η ($\bar{\eta} \longrightarrow \eta$) is the 't Hooft symbol [3] for an instanton (anti-instanton). That we have chosen the singular gauge makes it possible to sum solutions without distorting their asymptotic behavior. In order to simplify the notation, we will not introduce specific symbols for an instanton or for an anti-instanton; by N in the superposition given by (1), we then mean the total number of pseudoparticles in the volume V occupied by the system under study, their density being naturally $n = N/V$. The action functional of an instanton liquid is given by

$$\langle S\rangle = \int d^4z \int d\rho\, n(\rho) s(\rho). \tag{3}$$

Integration is performed over the volume occupied by the liquid and is accompanied by averaging the action functional per instanton, $s(\rho)$, over the size distribution $n(\rho)$ of instantons. The action functional per instanton has the well-known form

$$\begin{aligned} s_1(\rho) &= \beta(\rho) + 5\ln(\Lambda\rho) - \ln\tilde{\beta}^{2N_c} \\ &\quad + \beta\xi^2\rho^2\int d\rho_1 n(\rho_1)\rho_1^2, \end{aligned} \tag{4}$$

where $\beta(\rho) = -\ln C_{N_c} - b\ln(\Lambda\rho)$, with $b = \frac{11}{3}N_c$ and $\Lambda = \Lambda_{\overline{MS}} = 0.92\Lambda_{PV}$ and with the constant C_{N_c} dependent on the renormalization scheme (in particular, $C_{N_c} \approx \frac{4.66\exp(-1.68N_c)}{\pi^2(N_c-1)!(N_c-2)!}$), is the Gell-Mann–Low beta function; $\beta = \beta(\bar{\rho})$ is the value of the beta function at a fixed value of ρ (mean instanton size $\bar{\rho}$); and $\tilde{\beta} = \beta + \ln C_{N_c}$.

Some terms (part of functional dependence) in expression (4) can be deduced by supplementing an outcome of classical field theory with loop (quantum) corrections that lead to variations in the coupling constant g with distance. Indeed, the first term represents the one-instanton action functional $8\pi^2/g^2$ corrected by taking into account the instanton-size dependence of g. The last term describes the pair interaction in the

[1)] Bogolyubov Institute for Theoretical Physics, National Academy of Sciences of Ukraine, Metrologicheskaya ul. 14b, Kiev, 252143 Ukraine.

[2)] Institute of Nuclear Physics, Moscow State University, Vorob'evy gory, Moscow, 119899 Russia.

pseudoparticle ensemble, ξ being a constant that characterizes the strength of this interaction ($\xi^2 = \frac{27}{4}\frac{N_c}{N_c^2-1}\pi^2$). The dependence on the instanton size is disregarded in the beta function by virtue of the smallness of the packing-fraction parameter $n\rho^4$ peculiar to an instanton liquid. The logarithmic terms, which are of a purely quantum origin, describe the preexponential factor in the path integral. Taken together with the reciprocal of the factor ρ^5 from the second term, the integration measure in the path integral with respect to the instanton size and the instanton position in metric space (the corresponding contributions to this measure are $d\rho$ and d^4z, respectively) yields a dimensionless quantity. The argument of the logarithm in the third term is the quantity obtained by raising the square root of the one-instanton action functional, $\tilde{\beta}$, to the power $4N_c$, which is equal to the number of zero modes of the one-instanton solution, the ρ dependence being again disregarded here because of the smallness of the logarithm.

Let us take the size distribution of instantons in the form of an exponential of the action functional, $n(\rho) = e^{-s_1(\rho)}$, and specify averaging according to the natural prescription $\overline{\rho^2} = \int d\rho\,\rho^2 n(\rho)/n$ with $n = \int d\rho\, n(\rho)$. From (4), we then immediately obtain a closed description of the equilibrium state of an instanton liquid with the well-known vacuum distribution[3)]

$$\mu(\rho) = \rho^{-5}\tilde{\beta}^{2N_c} e^{-\beta(\rho) - \nu\rho^2/\overline{\rho^2}},$$

$$\nu = \frac{1}{2}(b-4), \quad \left(\overline{\rho^2}\right)^2 = \frac{\nu}{\beta\xi^2 n}.$$

The physical meaning of the distribution $\mu(\rho)$ is that the quantity $d^4z d\rho\mu(\rho)$ is proportional to the probability of finding an instanton of dimension ρ at some point occurring in the volume element d^4z. At small ρ, the behavior of the distribution function is governed predominantly by the quantum-mechanical result that forbids the solution to shrink to a point (radiative corrections). At large ρ, there is a constraint associated with the repulsive interaction of pseudoparticles, which becomes stronger with increasing (anti)instanton size.

In deriving expression (3), we must perform averaging over instanton positions in metric space. Obviously, it is necessary that the characteristic linear dimension L of the region to be taken into consideration in doing this be greater than the mean instanton size $\bar{\rho}$. At the same time, it is not required to be indefinitely large, since there are no causal links between widely spaced fragments of an instanton liquid. At this scale $L \geq \bar{R}$ ($\bar{R}$ is the mean spacing between pseudoparticles), it is assumed that the vacuum wave function is homogeneous (each pseudoparticle appears in the path integral with a weight proportional to $1/V$, where $V = L^4$). A typical configuration saturating the path integral in question is taken in the form of the superposition given by (1), with N being equal to the number of pseudoparticles in the volume V. This number must be so great that the pseudoparticles can be sorted according to their dimensions. We denote by $\Delta N(\rho_i)$ the number of pseudoparticles with dimensions ρ lying in the interval between ρ_i and $\rho_i + \Delta\rho$. The superposition in (1) can then be recast into the form of a double sum over the number (from 1 to K) of intervals covering the range (ρ_{in}, ρ_{fin}) and over the number of pseudoparticles of a given sort; that is,

$$A_\mu(x) = \sum_{j=1}^{K}\sum_{i=1}^{\Delta N(\rho_j)} A_\mu(x; \rho_j; z_i, \Omega_i), \qquad (5)$$

where $A_\mu(x; \rho_j; z_i, \Omega_i)$ is an (anti)instanton solution for a pseudoparticle of a gauged dimension $\rho \in (\rho_i, \rho_i + \Delta\rho)$. By definition, we have $\sum_{i=1}^{K}\Delta N(\rho_i) = N$. We further introduce the distribution function $n(\rho) = \frac{\Delta N(\rho)}{\Delta\rho}\frac{1}{V}$ such that $\sum_{i=1}^{K} n(\rho_i)\Delta\rho V = N$ (in the continuum limit $\Delta\rho \longrightarrow 0$, this condition reduces to $V\int d\rho\, n(\rho) = N$) and evaluate the classical action functional $S_c = \frac{1}{4}\int d^4x G_{\mu\nu}^2$ for this configuration by taking an average over the positions of the instantons in metric and color spaces. As a result, we find that, for the superposition ansatz (1), there remain only single-particle and pair contributions in the averaged action functional

$$\langle S_c\rangle = \prod_{i=1}^{N}\int_V \frac{d^4z_i}{V} d\Omega_i S_c$$
$$= \int_V d^4z \int d\rho\, n(\rho)\left\{\frac{8\pi^2}{g^2} + \frac{8\pi^2}{g^2}\xi^2\rho^2\int d\rho_1 n(\rho_1)\rho_1^2\right\}. \qquad (6)$$

As was mentioned above, the quantity $\langle S_c\rangle$ appears in the path integral with the one-loop correction.

It can be seen that expression (3) describes correctly even nonequilibrium states of the instanton liquid, in which case the distribution function $n(\rho)$ does not coin-

[3)] These arguments correspond to the principle of maximum from [2a]. In order to clarify this point in some detail, it is advisable to note that, if we approximate the functional in (3) by the local expression $\langle S_1\rangle = \int d\rho\, s_1(\rho) n(\rho)/n$, where $s_1(\rho) = \beta(\rho) + 5\ln(\Lambda\rho) - \ln\tilde{\beta}^{2N_c} + \beta\xi^2\rho^2 n\overline{\rho^2}$, and take the distribution function in the form $n(\rho) = Ce^{-s(\rho)}$, where C is a constant (this renders the problem self-consistent), a variation of the difference $\langle S\rangle - \langle S_1\rangle = \int d\rho\,\{s(\rho) - s_1(\rho)\}e^{-s(\rho)}/n$ yields $s(\rho) = s_1(\rho) + \text{const}$, where it has been considered that the normalization can be chosen arbitrarily.

cide with the vacuum distribution function; moreover, this expression admits a generalization to the case of a inhomogeneous liquid, provided that the characteristic size of inhomogeneity satisfies the obvious requirement $\lambda \geq L > \bar{\rho}$.

We will now try to describe the excited states of the instanton liquid by choosing, for configurations saturating the path integral, those that are formed by quasizero modes rather than the instanton solution (in the relevant functional space, the former represent the deformed configurations that are the closest ones to the latter). By way of example, we will consider a configuration where the size of the instanton changes with time rather slowly. Here, we proceed from the simple considerations that of physical significance are deformations measured in the action-functional units $\frac{dqdp}{2\pi\hbar}$ (here, q and p are the generalized coordinate and momentum). As to the instanton, it is characterized only by the static coordinates γ; therefore, it is necessary to define momenta conjugate to them. For ρ, the most appropriate momentum is that which is associated with the derivative $\dot{\rho} = d\rho/dx_4$.

Let us first calculate corrections to the one-instanton action functional. Within the assumption of the superposition ansatz (1), we must take into account an additional contribution to the chromoelectric field:

$$G'^{a}_{\mu\nu} = G^{a}_{\mu\nu} + g^{a}_{\mu\nu}, \tag{7}$$

Here, the first term describes the strength tensor that is generated by the instanton profile and which can be represented as

$$G^{a}_{\mu\nu} = -\frac{8}{g}\frac{\rho^2}{(y^2+\rho^2)^2}\left(\frac{1}{2}\bar{\eta}_{a\mu\nu} + \bar{\eta}_{a\nu\rho}\frac{y_\mu y_\rho}{y^2} - \bar{\eta}_{a\mu\rho}\frac{y_\nu y_\rho}{y^2}\right),$$

while $g^{a}_{\mu\nu}$ stands for corrections to this tensor. In the adiabatic approximation, these corrections are given by

$$g^{a}_{4i} = \frac{\partial A^{a}_{i}}{\partial\rho}\dot{\rho} = \frac{4}{g}\bar{\eta}_{ai\nu}\frac{y_\nu\rho}{(y^2+\rho^2)^2}\dot{\rho},$$

$$g^{a}_{ij} = 0, \quad g^{a}_{i4} = -g^{a}_{4i}, \quad i, j = 1, 2, 3,$$

where $O(\ddot{\rho})$, $O(\dot{\rho}^2)$, … terms have been neglected. For variations in the instanton size to be smooth (adiabatic), it is necessary that the corrections be much less than the field generated by the instanton proper—that is, $g^{a}_{\mu\nu} \ll G^{a}_{\mu\nu}$—whence it follows that the rate of deformation must satisfy the condition $\dot{\rho} \ll O(1)$. If this condition is satisfied, integration that must be performed over the four-dimensional volume in evaluating corrections to the action functional can be simplified by factoring $\dot{\rho}$ out of the integral sign. For the one-instanton action functional, we then obtain

$$s_c = \frac{1}{4}\int d^4x G'^{2}_{\mu\nu} \simeq \frac{8\pi^2}{g^2} + C\dot{\rho} + \frac{\kappa_{\text{s.t.}}}{2}\dot{\rho}^2. \tag{8}$$

Here, $\dot{\rho}$ is the mean rate of a slow deformation of the solution over the characteristic instanton lifetime [this quantity, which is proportional to ρ, is taken, for the sake of definiteness, at the instanton center—$\dot{\rho}(x, z)|_{x=z}$]; the constant C, which is determined by the interference term, is equal to zero, because the first variation of the action functional, $\delta S/\delta A$, vanishes on the manifold specified by the true solution; and, for the kinetic term, we obtain

$$\kappa_{\text{s.t.}} = 12\pi^2/g^2. \tag{9}$$

By virtue of scale invariance, $\kappa_{\text{s.t.}}$ does not depend explicitly on ρ; such a dependence arises only owing to coupling-constant renormalization (in the regular gauge, we arrive at the same value).

Without going beyond the ansatz specified by equation (1), we took into account only those corrections that are associated with variations in the strength tensor (s.t.) and disregarded possible variations in the potentials (2). Considering that the expressions for the potential in the regular (r.g.) and in the singular (s.g.) gauge are given by

$$A^{a}_{\mu} = \frac{1}{g}\eta_{a\mu\nu}\partial_\nu \ln(y^2+\rho^2) \quad \text{(r.g.)},$$
$$A^{a}_{\mu} = -\frac{1}{g}\bar{\eta}_{a\mu\nu}\partial_\nu \ln\left(1+\frac{\rho^2}{y^2}\right) \quad \text{(s.g.)}, \tag{10}$$

we determine the adiabatic corrections to the potential in the form

$$a^{a}_{\mu} = \frac{2}{g}\eta_{a\mu4}\frac{\rho}{y^2+\rho^2}\dot{\rho} \quad \text{(r.g.)}. \tag{11}$$

In order to go over to the singular gauge, we must make the substitution $\eta \longrightarrow -\bar{\eta}$. For configurations that saturate the path integral, we will now make use of the representation in (7), where $g^{a}_{\mu\nu}$ stands for additional chromomagnetic and chromoelectric fields generated by a^{a}_{μ} [as before, we take into account only $O(\dot{\rho})$ terms]. For the kinetic term κ, we then have

$$\kappa = 32\pi^2/g^2 \quad \text{(r.g.)} \tag{12}$$

(for the singular gauge, the result is $\kappa = \frac{3}{2}\frac{32\pi^2}{g^2}$). Since variations in the instanton size are assumed to be adiabatic, we can disregard the ρ dependence in the kinetic term. Having fixed the kinetic term at the scale of the mean instanton size, $\kappa = \kappa(\bar{\rho})$, we will try to find out how the path integral calculated over the quasizero mode is modified in this case. It can be seen easily that, because of the smallness of the kinetic energy, its effect

on the preexponential factor can be disregarded, since the contribution of the preexponential factor is small as such. Moreover, we can also ignore the effect of the preexponential factor on the kinetic term itself. By applying the same operations as those performed in deriving expression (3), we find that, to the required degree of precision, the sought expression for an excited liquid can be reduced to the form[4)]

$$\langle S\rangle = \int d^4z \int d\rho n(\rho)\left\{\frac{1}{2}\kappa\dot{\rho}^2 + s(\rho)\right\}. \qquad (13)$$

It should be borne in mind that, for the interaction of each pair of pseudoparticles, the relevant integral averaged over color orientations [2a],

$$\langle S(12)\rangle = \int\frac{d^4z_1}{V}\int\frac{d^4z_2}{V}\bar{U}_{\rm int}(12), \qquad (14)$$

where

$$\bar{U}_{\rm int}(12) = \frac{8\pi^2}{g^2}\frac{N_c}{N_c^2-1}$$
$$\times\int d^4x\frac{[7y_1^2y_2^2-(y_1y_2)^2]\rho_1^4\rho_2^4}{y_1^4(y_1^2+\rho_1^2)^2y_2^4(y_2^2+\rho_2^2)^2},$$
$$y_i = x - z_i, \quad \rho_i = \rho_i(x, z_i)\big|_{x=z_i} = \rho_i(z_i),$$

with $i = 1, 2$, is somewhat modified because of adiabatic changes in the instanton dimensions. The effect of the instanton of dimension ρ_1 on the instanton of dimension ρ_2 can be estimated in terms of the integral

$$\int\frac{d^4z_1}{V}\bar{U}_{\rm int}(12) \simeq \frac{8\pi^2}{g^2}\frac{\xi^2}{V}\rho_1^2(z_2)\rho_2^2(z_2).$$

Indeed, the condition that these sizes vary adiabatically makes it possible to change the scale of the integration variable as follows: $\frac{dz}{\rho} = d\left(\frac{z}{\rho}\right) + \frac{z}{\rho^2}d\rho \approx d\left(\frac{z}{\rho}\right)$. In addition, the slowly varying function $\rho_1(z_1)$ can be fixed at the point where the integrand attains a maximum. An analysis reveals that, in this case, the mean spacing between the instantons proves to be on the order of their dimensions, $|z_1 - z_2| \sim \max\{\rho_1, \rho_2\}$; for an acceptable approximation, we can then take a contact interaction, replacing $\rho_1(z_1)$ by $\rho_1(z_2)$. In the particular case of pseudoparticles having fixed dimensions, we then arrive at the well-known expression $\langle S_{\rm int}\rangle = \frac{8\pi^2}{g^2}\frac{\xi^2}{V}\rho_1^2\rho_2^2$. In the adopted approximation, the integral $\int d\rho\,\rho^2 n(\rho)/n$ reduces to $\bar{\rho}^2$, whereby there arises pseudoparticle self-interaction.

In Minkowski space, the braced expression in the integrand on the right-hand of (13) can be interpreted as a mechanical system governed by the Lagrangian $\mathcal{L} = \frac{1}{2}\kappa\dot{\rho}^2 - U_{\rm eff}(\rho)$, provided that, for the characteristic velocity $\left.\frac{\partial\rho(x,z)}{\partial x_4}\right|_{x=z}$, we take the field deformation $\rho(x, z)|_{x=z} = \rho(z)$: $\frac{\partial\rho}{\partial x_4} \sim \frac{\partial\rho}{\partial z_4}$; the action functional per instanton then plays the role of the potential energy $U_{\rm eff}(\rho) = \beta(\rho) + 5\ln(\Lambda\rho) - \ln\tilde{\beta}^{2N_c} + \nu\frac{\rho^2}{\bar{\rho}^2}$. In the vicinity of the minimum of the potential at $\rho_c^2 = \frac{b-5}{2\nu}\bar{\rho}^2$ $\left(\frac{dU_{\rm eff}(\rho)}{d\rho} = 0\right)$, the motion being considered is of an oscillatory character. By using the configuration corresponding to (12) and evaluating the second derivative $\left.\frac{d^2U_{\rm eff}(\rho)}{d\rho^2}\right|_{\rho_c} = \frac{4\nu}{\bar{\rho}^2}$, we find that the frequency can be represented as[5)]

$$m^2 = \frac{4\nu}{\kappa\bar{\rho}^2} = \frac{\nu}{\beta\bar{\rho}^2}. \qquad (15)$$

So far, we have analyzed deformations only in the time direction. Deformations along each spatial axis can be taken into account quite similarly. By virtue of the symmetry of the problem in four-dimensional space, the expression for the kinetic term remains unchanged. It is only necessary to supplement the velocities with the corresponding gradients of the function $\rho(x, z)$; that is, $\dot{\rho}$ must be replaced by $\frac{\partial\rho}{\partial x}$ $\left(\left.\frac{\partial\rho(x,z)}{\partial x}\right|_{x=z} \sim \frac{\partial\rho}{\partial z}\right)$ for the instanton deformed in this way. In this form, the frequency of natural vibrations is interpreted as a mass-type term, while excitations are of a phonon character and are governed by the Lagrangian density

$$\mathcal{L} = \frac{1}{2}\kappa[\dot{\rho}^2 - \nabla\rho\nabla\rho] - U_{\rm eff}(\rho), \qquad (16)$$

where crossed terms of the $\dot{\rho}\,\rho'$ type vanish identically.[6)]

The parameters $\bar{\rho}$ and β determined self-consistently by minimizing the generating functional for the instanton–anti-instanton liquid take the following val-

[4)] In principle, the path integral over quasizero modes can be calculated exactly.

[5)] In other words, we minimize the effective action at the end of the calculations, thereby demonstrating how quasizero modes can manifest themselves in a minimal way.

[6)] It is interesting to note that, in contrast to what we have for the dilatation mode, the center of the instanton solution cannot be shifted because the corresponding deformation leads to singular κ. As to a variation with respect to the color coordinate Ω, it leads to the trivial case of $\kappa = 0$.

ues for the $SU(3)$ group with $n(\rho) = \mu(\rho)$: $\bar{\rho}\Lambda \approx 0.37$, $\beta \approx 17.5$, and $n\Lambda^{-4} \approx 0.44$. For the mass gap, this yields $m \approx 1.21\Lambda$. The wavelength in the x_4 direction is $\lambda_4\Lambda \approx 0.83 \sim \bar{R}\Lambda > \bar{\rho}\Lambda$ (in spatial directions, the radius of phonon localization can be arbitrary; in particular, it can exceed considerably λ_4, in which case the number of particles, N, that take part in forming the excitation may be quite large). The above numerical values are of a qualitative (rather than quantitative) character, illustrating the very possibility of obtaining particle-like excitations on the basis of quasizero modes. It is obvious that, in a consistent theory, we must go beyond the superposition ansatz, taking into account in-medium variations in the instanton profile; some other refinements, including a more realistic description of instanton interaction (in our treatment, it seems overestimated considerably), will also be necessary in that case.

In summary, we have considered excitations of an instanton liquid that are associated with adiabatic dilatation deformations of instantons. In principle, the assumption that the variations in question are adiabatic leads to a consistent pattern and shows that the instanton-liquid model itself dictates the most favorable regime of such deformations, which prove to be of a phonon-like character, having a mass gap that is given by (15) and which is determined by the parameter Λ_{QCD}. If a quark condensate is included in the consideration,[7)] it is quite natural to associate the phonon-like excitations that we obtained with some sort of light hadrons whose nature is different from that of (pseudo)Goldstone mesons that arise owing to a spontaneous breakdown of chiral invariance. An investigation of these issues is now under way, and their discussion is beyond the scope of the present article. The problem of quark confinement is explained within the present framework as a consequence of the fact that phonons cannot be decomposed.

[7)]Since we analyze the adiabatic regime, standard perturbation theory is applicable here. A preliminary analysis performed within the $N_c \longrightarrow \infty$ approximation [5] reveals that, in the adiabatic regime, the quark-condensate-induced contribution to the kinetic term is small (about 0.2) for the instanton-liquid parameters used here. This is in accord with the generally accepted viewpoint that, although the effect of the quark component of the theory on the gluon component is insignificant, this effect is crucial for the formation of excitations. At the same time, it is clear that the contribution of the pion cloud to phonon-like excitations and, vice versa, the effect of these excitations on the pions must also be taken into account in a full theory.

ACKNOWLEDGMENTS

This work was supported in part by the Russian Foundation for Basic Research (project nos. 96-02-16303, 96-02-00088G, and 97-02-17491) and by the International Association for the Promotion of Cooperation with Scientists from the Independent States of the Former Soviet Union (grant nos. INTAS-93-0283 and INTAS-96-0678).

S.V. Molodtsov and A.M. Snigirev are also indebted to Professor M. Namiki for stimulating discussions and the to the HUJUKAI Fund for financial support.

REFERENCES

1. G. G. Gallan, R. Dashen, and D. J. Gross, Phys. Rev. D **17**, 2717 (1978); Phys. Lett. B **66**, 375 (1977); E.-M. Ilgenfritz and M. Müller-Preussker, Nucl. Phys. B **184**, 433 (1981); E. V. Shuryak, Nucl. Phys. B **203**, 93, 116, 140 (1982); **328**, 85, 102 (1989); T. Schäfer and E. V. Shuryak, Rev. Mod. Phys. **70**, 323 (1998).
2. D. I. Diakonov and V. Yu. Petrov, Nucl. Phys. B **245**, 259 (1984); in *Hadronic Matter under Extreme Conditions*, Ed. by V. Shelest and G. Zinovjev (Kiev, 1986), p. 192; D. I. Diakonov, V. Yu. Petrov, and P. V. Pobylitsa, Phys. Lett. B **226**, 471 (1989).
3. G. 't Hooft, Phys. Rev. D **14**, 3432 (1976).
4. I. I. Balitsky and A. V. Yung, Phys. Lett. B **168**, 113 (1986).
5. P. V. Pobylitsa, Phys. Lett. B **226**, 387 (1989).

Translated by A. Isaakyan

Physics of Atomic Nuclei, Vol. 63, No. 5, 2000, pp. 908–911. Translated from Yadernaya Fizika, Vol. 63, No. 5, 2000, pp. 980–984.

ELEMENTARY PARTICLES AND FIELDS
Theory

Impact-Parameter Dependences of the Number of Interacting Nucleons and Mean Multiplicities in Heavy-Ion Collisions

C. Pajares[1), *] and Yu. M. Shabelski**

Petersburg Nuclear Physics Institute, Russian Academy of Sciences, Gatchina, 188350 Russia

Received April 6, 1999; in final form, September 20, 1999

Abstract—The impact-parameter dependence of the mean number of interacting nucleons in high-energy heavy-ion collisions is considered in the case of identical atomic weights of colliding nuclei and in the case where one nucleus is much heavier than the other. It is shown that the use of a rare event—for example, an event of J/ψ or Υ production—as a trigger may change significantly quantities representing the averages of the multiplicities for accompanying secondaries over impact-parameter values. The multiplicities of accompanying particles in central collisions can have but a slight dependence on the trigger. The observed multiplicity ratios for various secondaries in central and minimum-bias events can be used as a test in searches for quark–gluon plasma. © *2000 MAIK "Nauka/Interperiodica".*

1. INTRODUCTION

Analysis of experiments in heavy-ion physics often requires taking into account the possible dependence of the mean multiplicity of secondaries on the trigger. For example, the observed suppression of J/ψ production can be explained, at least partly, by their interaction with other nascent hadrons [1, 2]. In order to obtain numerical estimates, it is necessary, however, to know the multiplicity of accompanying particles in events leading to J/ψ production.

In the present study, we discuss the impact-parameter dependences of the mean number of interacting nucleons and the mean multiplicities of secondaries in high-energy heavy-ion collisions. Our results are based almost completely on event geometry—in particular, they do not depend on the details of the interaction model. In the case of interactions averaged over impact-parameter values, the variance of the distributions with respect to the number of interacting nucleons (such distributions are similar to those with respect to transverse energy or multiplicity of secondaries) is very large. In view of this, some features of the interactions—for example, mean multiplicities—may depend greatly on the trigger used. In contrast to what occurs in this case, similar variances in central collisions are very small, which guarantees a weak dependence on any trigger.

We will consider a heavy-ion collision as a superposition of independent nucleon–nucleon (NN) interactions. Therefore, the results obtained in this way can be considered as yet another test in searches for quark–gluon plasma (QGP): in the case of processes that feature collective interactions, including QGP production, there is no reason to expect fulfillment of relations presented below. Moreover, we can indicate particle species for which QGP production will violate our predictions and specify the character of such violations.

2. DISTRIBUTIONS WITH RESPECT TO THE NUMBER OF INTERACTING NUCLEONS FOR VARIOUS IMPACT-PARAMETER VALUES

Let us consider the production of secondary particles in minimum-bias collisions (that is, collisions integrated with respect to the impact-parameter values) of nuclei A and B. In this case, the mean number $\langle N_A \rangle_{\text{m.b.}}$ of inelastically interacting nucleons of nucleus A is [3]

$$\langle N_A \rangle_{\text{m.b.}} = \frac{A\sigma_{NB}^{\text{prod}}}{\sigma_{AB}^{\text{prod}}}. \quad (1)$$

If either nucleus, A or B, is sufficiently heavy, the cross sections in (1) are given by

$$\sigma_{NB}^{\text{prod}} = \pi R_B^2, \quad (2)$$

$$\sigma_{AB}^{\text{prod}} = \pi(R_A + R_B)^2. \quad (3)$$

When colliding nuclei are identical ($A = B$), we obviously have

$$\langle N_A \rangle_{\text{m.b.}} = A/4. \quad (4)$$

Thus, the mean number of interacting nucleons in collisions integrated with respect to impact-parameter values must be one-fourth as great as that in the case of central collisions, where we have $\langle N_A \rangle_c \approx A$ by definition.

[1)] Departamento de Física de Particulas, Universidad de Santiago de Compostela, 15706 Santiago de Compostela, Spain.

* e-mail: pajares@gaes.usc.es

** e-mail: shabelsk@thd.pnpi.spb.ru

The distributions with respect to inelastically interacting nucleons of nucleus A will be calculated within the so-called rigid-target approximation [4–6]. According to this approximation, the probability that N_A nucleons participate in the interaction is given by [7, 8]

$$V(N_A) = \frac{1}{\sigma_{AB}^{\text{prod}}}\frac{A!}{(A-N_A)!N_A!} \times \int d^2b[I(b)]^{A-N_A}[1-I(b)]^{N_A}, \quad (5)$$

where

$$I(b) = \frac{1}{A}\int d^2b_1 T_A(b_1-b)\exp[-\sigma_{NN}^{\text{inel}}T_B(b_1)], \quad (6)$$

$$T_A(b) = A\int dz\rho(b,z). \quad (7)$$

Expression (5) corresponds to events integrated with respect to the impact parameter. If interactions occurs in some interval of impact-parameter values, integration in (5) must be performed between $b_{\min}$ and $b_{\max}$. In particular, the condition $b \le b_0$, $b_0 \ll R_A$, corresponds to central collisions.

The calculated mean numbers of inelastically interacting nucleons of the projectile nucleus, $\langle N_{\text{in}}\rangle$, as a function of the impact parameter b are displayed in Fig. 1 for Pb–Pb collisions at three different energies (the value of $\sqrt{s} = \sqrt{s_{NN}}$ determines the c.m. energy per nucleon–nucleon pair) and for S–U collisions at $\sqrt{s_{NN}} = 20$ GeV. The energy dependence of these distributions is rather weak—in the approximation adopted here, it emerges only owing to the energy dependence of the cross section $\sigma_{NN}^{\text{inel}}$.

In a collision of two heavy ions with identical atomic weights (in our case, Pb–Pb collision), nearly 6% of the nucleons of either nucleus do not participate in inelastic interactions at $\sqrt{s_{NN}} = 18$ GeV even at zero impact parameter. More precisely, 11.8 nucleons, on average, do not interact, which is in agreement with the value of 13 ± 2 nucleons [9] obtained in the VENUS 4.12 model [10]. At $A = B$ and $b = 0$, the peripheral nucleons of one of the nuclei traverse the low-density peripheral region of the other nucleus. Therefore, the probability that they undergo no inelastic interactions is sufficiently large. At $\sqrt{s_{NN}} = 5.5$ TeV, the number of noninteracting nucleons decreases to approximately 3% owing to an increase in $\sigma_{NN}^{\text{inel}}$. With increasing b, $\langle N_{\text{in}}\rangle$ decreases because, even at small $b \neq 0$, there are nonoverlapping regions of identical colliding nuclei.

In collisions of nuclei with different atomic weights (for example, S and U nuclei) at small impact parameters, all nucleons of the light nucleus traverse regions in the heavy nucleus that are characterized by a sufficiently high density of nuclear matter. Therefore, almost all of these nucleons undergo inelastic interactions. In the specific case of S–U collisions at $\sqrt{s_{NN}} = 20$ GeV, this is possible for $b < 2$–3 fm.

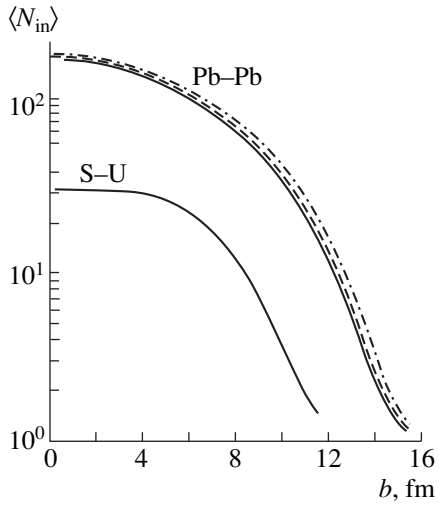

Fig. 1. Mean numbers of inelastically interacting nucleons in Pb–Pb collisions at $\sqrt{s}$ = (solid curve) 18, (dashed curve) 200, and (dash-dotted curve) 5.5 GeV and in S–U collisions at $\sqrt{s} = 20$ GeV.

It is interesting to consider the distributions with respect to the number of inelastically interacting nucleons for various values of the impact parameter. By using expression (5), we have calculated the probabilities of finding a given number of such nucleons in Pb–Pb interactions. The results integrated with respect to the impact parameter are displayed in Fig. 2*a*. A sharp peak at small values of $\langle N_{\text{in}}\rangle$ corresponds to the contribution of extremely peripheral interactions, where, at a relatively large cross section, the total interaction probability is distributed among a few values of $N_{\text{in}} = 1, 2, \ldots$ (see Fig. 1). The resulting mean value of $\langle N_{\text{in}}\rangle = 50.4$ is in reasonable agreement with (4): a 3% discrepancy may be due to the different values of the effective radii of nuclei in (2) and (3). We emphasize that, in this case, the variance of the distribution with respect to N_{in} is very large.

The results of similar calculations for various regions of the impact parameter are presented in Fig. 2*b*, which illustrates the cases of central ($b < 1$ fm), peripheral (12 fm $< b <$ 13 fm), and intermediate (6 fm $< b <$ 7 fm) Pb–Pb interactions. The variances of all these distributions are significantly lower than those of the distributions integrated with respect to the impact parameter and shown in Fig. 2*a*. It is worth noting that the curve in Fig. 2*a* represents the envelope of all peaks of the type in Fig. 2*b* with allowance for their "weights"—that is, the cross sections in the specified intervals of the impact-parameter values.

The distributions with respect to N_{in} in central and peripheral interactions are substantially narrower than

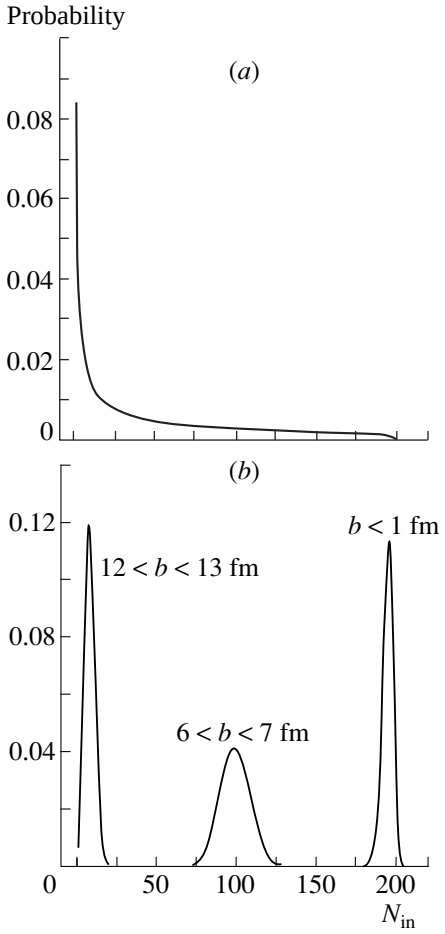

Fig. 2. Distributions with respect to the number of inelastically interacting nucleons in Pb–Pb collisions at $\sqrt{s_{NN}}$ = 18 GeV (*a*) for interactions averaged over impact-parameter values and (*b*) for various intervals of impact-parameter values.

those in the intermediate case. The reason is that, in one of the nuclei, the number of peripheral nucleons that can either undergo a collision or escape it is relatively small in a central collision. In extremely peripheral processes, the total number of nucleons that can participate in the interaction is small. In the intermediate cases, a relatively large number of nucleons of one of the nuclei traverse the peripheral region of the other nucleus, where the density of nuclear matter is relatively low and where each such nucleon can either undergo a collision or escape it.

3. RATIO OF THE MEAN MULTIPLICITIES OF SECONDARIES IN CENTRAL AND MINIMUM-BIAS INTERACTIONS

Let us estimate the multiplicity of secondaries in the central section of the spectrum. This quantity must be proportional to the number of interacting nucleons of the projectile nucleus. It must also depend on the mean number $\langle \nu_{NB} \rangle$ of inelastic interactions suffered by a projectile nucleon in the target nucleus. At asymptotically high energies, the mean multiplicity of secondaries in nucleon–nucleus interactions must be proportional to $\langle \nu \rangle$ [11, 12]. It was shown in [13] that the mean number of interactions in a central nucleon–nucleus interaction, $\langle \nu \rangle_c$, is approximately 1.5 times as great as that in the minimum-bias nucleon–nucleus interaction, $\langle \nu \rangle_{\text{m.b.}}$. Therefore, the mean multiplicity of secondaries in a central nucleus–nucleus collision at $A = B$, $\langle n \rangle_c$, must be approximately six times as great as that in the case of integration with respect to the impact parameter: $\langle n \rangle_c \approx 6\langle n \rangle_{\text{m.b.}}$.

It is necessary to take into account some corrections to our result. At available energies, the multiplicity of secondaries in nucleon–nucleus collisions is proportional to $(1 + \langle \nu \rangle)/2$ rather than to $\langle \nu \rangle$ [12, 14]. For heavy nuclei, $\langle \nu \rangle_{\text{m.b.}}$ values fall within the interval from 3 to 4. Therefore, the ratio of $\langle \nu_{NB} \rangle_c / \langle \nu_{NB} \rangle_{\text{m.b.}} \sim 1.5$ must lead to an increase in the multiplicity of secondaries by a factor of about 1.4. A more significant correction is caused by the fact that, in central collisions of nuclei with identical atomic weights, only some of the projectile nucleons interact with the central region of the target nucleus. This reduces the effective enhancement factor to a value about 1.2. Finally, a few percent of the nucleons undergo no interactions with the target even in central collisions of heavy nuclei, because they move in the low-density region (see above).

As a result, our prediction assumes the form

$$\langle n \rangle_c \sim 4.5 \langle n \rangle_{\text{m.b.}}. \tag{8}$$

This estimate determines the multiplicity of secondaries in the central section of the spectrum.

In the case where QGP is produced or where some other collective phenomena occur, there are no reasons for fulfillment of the relation in (8). By way of example, we indicate that, when $\langle n \rangle_c$ and $\langle n \rangle_{\text{m.b.}}$ are calculated within the model from [15] with allowance for the fusion of quark–gluon strings—this is a possible version of taking into account collective multinucleon interactions—the relation in (8) is violated in Au–Au collisions at RHIC energies by approximately 40%.

In standard multiple-scattering theory considered here, relation (8) must be valid for any kinds of secondaries, including pions, kaons, J/ψ, Drell–Yan l^+l^- pairs, and prompt photons. For the sake of simplicity, we assume that QGP is produced only in central interactions (this implies that the probability of QGP production at moderately small impact-parameter values is not high). In this case, the relation in (8) can be strongly violated for prompt photons and, possibly, for low-mass Drell–Yan pairs owing to an additional thermal-emission-induced contribution to their multiplicity in central collisions. At the same time, the relation in (8) can be valid for pions if the main part of these particles are produced at a later stage of the interaction process following QGP decay. Thus, the violation of relation

(8) for particles that can be emitted by the plasma state would be a signal of QGP production. It is of course necessary to take here into account the possible contribution from final-state interactions.

In [16], it was shown that, in heavy-ion collisions, the main contribution to the variance of the multiplicity distributions comes from the variance of the distributions with respect to the number of *NN* interactions, but the latter were found to depend strongly on the impact parameter.

According to [16], the normalized variance $D/\langle n\rangle$, where $D^2 = \langle n^2\rangle - \langle n\rangle^2$, is

$$\frac{D^2}{\langle n\rangle^2} = \frac{\nu_{AB}^2 - \langle \nu_{AB}\rangle^2}{\langle \nu_{AB}\rangle^2} + \frac{1}{\langle \nu_{AB}\rangle}\frac{d^2}{\bar{n}^2}, \qquad (9)$$

where $\langle \nu_{AB}\rangle = \langle N_A\rangle\langle \nu_{NB}\rangle$ is the mean number of *NN* interactions in the *AB* nucleus–nucleus collision, while $\bar{n}$ and d are, respectively, the mean multiplicity and the variance per *NN* interaction.

In the case of heavy-ion collisions, the mean number $\langle \nu_{AB}\rangle$ is about 10^2–10^3; therefore, we can neglect the second term on the right-hand side of (9) [16]—the first term, which represents the normalized variance of the distribution with respect to the number of *NN* interactions, is dominant. From Fig. 2*a*, it can be seen that, in the case of *AB* collisions averaged over impact-parameter values, the second term in (9) is relatively large. If some trigger (for example, J/ψ production) is used without fixing the impact parameter, the multiplicity of secondaries may differ significantly in this case from the mean multiplicity in events without any trigger. It can be seen from Fig. 2*b* that the variance of the N_A distribution for a specific narrow interval of impact-parameter values is much lower, especially in central collisions. The variance of the distribution with respect to the number of interactions suffered by an individual projectile nucleon in the target nucleus, ν_{NB}, must be either identical to or lower than that in minimum-bias interactions. Thus, the variance of the multiplicity distribution of secondaries cannot be large. Therefore, any trigger can lead only to small variations in the multiplicity of secondaries in central heavy-ion collisions, even if this trigger changes significantly the multiplicity in *NN* interactions.

4. CONCLUSION

We have calculated the distributions with respect to the number of interacting nucleons in heavy-ion collisions at various values of the impact parameter. The variances of these distributions are very small for central and extremely peripheral collisions, but they are much greater at intermediate values of the impact parameter.

We have also estimated the ratios of the mean multiplicities of secondaries in events integrated with respect to the impact parameter and in central collisions. The resulting predictions can be used in searches for QGP.

It has been shown that, in central collisions, any trigger can change only slightly (at a level of 10–15%) the multiplicity of secondaries.

ACKNOWLEDGMENTS

We are grateful to A. Capella and A. B. Kaidalov for stimulating discussions.

Special thanks are due to the Dirección General de Política Científica and CICYT of Spain for financial support. The work was also supported in part by grant no. OUTR.LG 971390 from NATO.

REFERENCES

1. A. Capella, A. Kaidalov, A. Kouider Akil, and C. Gershel, Phys. Lett. B **393**, 431 (1997).
2. N. Armesto, A. Capella, and E. G. Ferreiro, hep-ph/9807258.
3. A. Bialas, M. Bleszynski, and W. Czyz, Nucl. Phys. B **111**, 461 (1976).
4. G. D. Alkhazov *et al.*, Nucl. Phys. A **280**, 365 (1977).
5. R. D. Viollier and E. Turtschi, Ann. Phys. (N.Y.) **124**, 290 (1980).
6. C. Pajares and A. V. Ramallo, Phys. Rev. D **31**, 2800 (1985).
7. A. P. Gasparyan, A. P. Cheplakov, and Yu. M. Shabelski, Yad. Fiz. **34**, 1328 (1981) [Sov. J. Nucl. Phys. **34**, 739 (1981)].
8. V. M. Braun and Yu. M. Shabelski, Int. J. Mod. Phys. A **3**, 2417 (1988).
9. T. Alber *et al.*, Phys. Rev. Lett. **75**, 3814 (1995).
10. K. Werner, Phys. Lett. B **208**, 520 (1988).
11. Yu. M. Shabelski, Nucl. Phys. B **132**, 491 (1978).
12. A. Capella, U. Sukhatme, C. I. Tan, and J. Tran Thanh Van, Phys. Rep. **236**, 225 (1994).
13. Yu. M. Shabelski, Yad. Fiz. **50**, 239 (1989) [Sov. J. Nucl. Phys. **50**, 149 (1989)].
14. W. Q. Chao, C. B. Chiu, Z. He, and D. M. Tow, Phys. Rev. Lett. **44**, 518 (1980).
15. N. S. Amelin, M. A. Braun, and C. Pajares, Phys. Lett. B **306**, 312 (1993).
16. J. Díaz de Deus, C. Pajares, and C. A. Salgado, Phys. Lett. B **407**, 335 (1997).

Translated by M. Kobrinsky

Physics of Atomic Nuclei, Vol. 63, No. 5, 2000, pp. 912–914. Translated from Yadernaya Fizika, Vol. 63, No. 5, 2000, pp. 985–987.

ELEMENTARY PARTICLES AND FIELDS
Theory

Supersymmetry Constraints on the Neutrino Mass

P. A. Dalakishvili and G. G. Devidze*

High-Energy Physics Institute, Tbilisi State University, Universitetskaya ul. 9, GE-380086 Tbilisi, Republic of Georgia

Received July 1, 1998; in final form, July 13, 1999

Abstract—Within the minimal supersymmetric extension of the Standard Model, the one-photon decay of the neutrino is studied on the basis of astrophysical, cosmological, and experimental data. Limits on the neutrino masses are obtained. © *2000 MAIK "Nauka/Interperiodica".*

There are no theoretical grounds for the vanishing of the neutrino mass. It is highly plausible that each massless particle corresponds to some exact local gauge symmetry. Since no such symmetry associated with the neutrino is known, it is not necessary to assume that the neutrino is a massless particle.

The pioneering experiment to measure the neutrino mass was performed in 1980 [1]. All experiments yield only upper limits on the neutrino masses: $m(\nu_e) < 4$ eV, $m(\nu_\mu) < 170$ keV, and $m(\nu_\tau) < 18.2$ MeV [2–5]. At the same time, astrophysical and cosmological observations may result in more stringent constraints on the fundamental characteristics of elementary particles—in particular, on the neutrino mass and lifetime [6–13]. The point is that massive neutrinos contribute to the energy density in the Universe. Requiring that their contribution not exceed the observed upper bound on this energy density, we can set limits on the mass of stable neutrinos and on the masses and lifetimes of unstable neutrinos [6–12]. Stable neutrinos must be lighter than 40 eV or heavier than 8 GeV. Unstable neutrinos may have a mass in the forbidden region (40 eV–8 GeV), provided that their mass and lifetime satisfy the conditions [6–12]

$$\begin{aligned} &m^2(\nu)\tau(\nu)/t_0 \le 4\times 10^3\ \text{eV}^2, \quad m(\nu) \le O(\text{MeV}),\\ &m^{-4}(\nu)\tau(\nu)/t_0 > 4\times 10^{-39}\ \text{eV}^{-4}, \quad m(\nu) > O(\text{MeV}), \end{aligned} \tag{1}$$

where t_0 is the age of the Universe ($t_0 = 1.3\times 10^{10}$ yr). If photons or charged particles appear among the products of neutrino decays, there arise additional constraints stemming from the following requirements: Big Bang nucleosynthesis and background radiation must not change, the γ-ray flux from $e\bar{e}$ annihilation must not exceed the observed flux, and deuteron photodisintegration must be forbidden. Each of these effects corresponds to a specific range of neutrino lifetimes. The overall constraint on the neutrino lifetime is [11–13]

$$\tau(\nu) \le 5\times 10^3\ \text{s}. \tag{2}$$

In the extended versions of the Standard Model, massive neutrinos are generally unstable. The one-photon decay of the neutrino, $\nu_a \longrightarrow \nu_b\gamma$, provides a good example for exploring the neutrino-mass range consistent with cosmological data [13, 14].

In the minimal supersymmetric extension of the Standard Model (MSSM), the leading contribution to the one-photon decay of the neutrino comes from one-loop diagrams. The one-loop MSSM diagrams contributing to the amplitude of the reaction $\nu_a \longrightarrow \nu_b\gamma$ (see Fig. 1) are classified according to particles propagating in the loop: (i) charged gauge fermions ($\tilde{\chi}^*$) and charged scalar leptons ($\tilde{l}$) and (ii) charged Higgs particles and charged leptons.

Owing to electromagnetic-current conservation, the amplitude of the decay $\nu_a \longrightarrow \nu_b\gamma$ has the form

$$\begin{aligned} &A(\nu_a \longrightarrow \nu_b\gamma)\\ &= \epsilon^\mu \bar{\nu}_a(q)\sigma_{\mu\nu}(q-p)^\nu(F^V + F^A\gamma_5)\nu_b(p). \end{aligned} \tag{3}$$

With the aid of (3), we find that the corresponding decay width is

$$\begin{aligned} &\Gamma(\nu_a \longrightarrow \nu_b\gamma)\\ &= \frac{|F^V|^2 + |F^A|^2}{8\pi}\left(\frac{m^2(\nu_a) + m^2(\nu_b)}{m(\nu_a)}\right)^3. \end{aligned} \tag{4}$$

The Lagrangian describing neutrino interactions with the aforementioned supersymmetric particles has the form [15, 16]

$$\begin{aligned} L_{\nu\tilde{\chi}^*\tilde{l}} &= -\frac{1}{2}ig\bar{\nu}_a O_{ab}\\ &\times\left[U_{j1}(1+\gamma_5) - \frac{m(\nu_a)V_{j2}}{\sqrt{2}m_W\cos\beta}(1-\gamma_5)\right]\tilde{\chi}^*\tilde{l}_{Lb}\\ &+ \frac{igm(l_b)}{2\sqrt{2}m_W\cos\beta}U_{j2}\bar{\nu}_a O'_{ab}(1-\gamma_5)\tilde{\chi}^*\tilde{l}_{Rb}, \end{aligned} \tag{5}$$

$$L_{\nu Hl} = \frac{ig}{2\sqrt{2}m_W}\bar{\nu}_a$$

* e-mail: devidze@hepi.edu.ge

$$\times S_{ab}[m(l_a)\tan\beta(1+\gamma_5) + m(\nu_b)\cot\beta(1-\gamma_5)]Hl_b,$$

where $g = e\sin\theta_W$ (θ_W is the Weinberg angle); the matrices U and V, O and O', and S describe the mixing of, respectively, charged gauge fermions, charged scalar leptons, and leptons; and $\tan\beta = v_1/v_2$, v_1 and v_2 being the vacuum expectation values of the Higgs fields [15, 16]. We now present some relations between supersymmetric parameters. For the charged gauge fermions, the masses and mixing matrices are given by

$$m(\tilde{\chi}^*_{1,2}) = \frac{1}{2}\{M^2 + \mu^2 \pm [(M^2-\mu^2)^2 + 4m_W^4\cos^2 2\beta + 4m_W^2(M^2+\mu^2+2M\mu\sin 2\beta)]\}^{1/2},$$

$$U = O_-, \quad V = \begin{cases} O_+, & \det X \geq 0 \\ \sigma_3 O_+, & \det X < 0, \end{cases} \tag{6}$$

$$O_\pm = \begin{pmatrix} \cos\phi_\pm & \sin\phi_\pm \\ -\sin\phi_\pm & \cos\phi_\pm \end{pmatrix},$$

where σ_3 is a Pauli matrix; M and μ are supersymmetry-breaking parameters; and the angles $\phi_\pm$ are defined as

$$\tan 2\phi_- = \frac{2\sqrt{2}m_W(\mu\cos\beta + M\sin\beta)}{m^2 - \mu^2 + 2m_W^2\cos 2\beta},$$
$$\tan 2\phi_+ = \frac{2\sqrt{2}m_W(\mu\sin\beta + M\cos\beta)}{M^2 - \mu^2 - 2M_W^2\cos 2\beta}. \tag{7}$$

For charged gauge fermions, the mass matrix has the form [15, 16]

$$\begin{pmatrix} M & m_W\sqrt{2}\cos\beta \\ m_W\sqrt{2}\sin\beta & \mu \end{pmatrix}. \tag{8}$$

For the form factors F^V, straightforward calculations yield

$$F^V_{\rm L} = \frac{1}{(4\pi)^2}eg^2\sum_{i,j}\lambda_1^i\left\{\frac{m(\tilde{\chi}^*_j)}{\sqrt{2}m_W\cos\beta}\frac{1}{m^2(\tilde{\chi}^*_j)}\right.$$
$$\times[m(\nu_a)U_{j1}V_{j2} + m(\nu_b)U^*_{j1}V^*_{j2}]f_1(x^{\rm L}_{ij})$$
$$\left.+\left[U^2_{j1} + \frac{m(\nu_a)m(\nu_b)V^2_{j2}}{2m_W^2\cos^2\beta}\right]\frac{m(\nu_a)+m(\nu_b)}{m^2(\tilde{\chi}^*_j)}f_2(x^{\rm L}_{ij})\right\},$$

$$F^V_{\rm R} = \frac{1}{(4\pi)^2}eg^2\sum_{i,j}\lambda_2^i U^2_{j2}\frac{m(\nu_a)+m(\nu_b)}{m_W^2\cos^2\beta}x^{\rm R}_{ij}f_2(x^{\rm R}_{ij}), \tag{9}$$

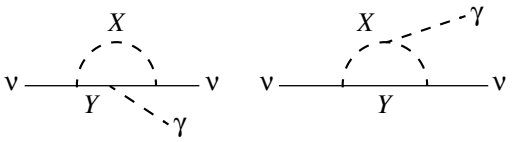

Fig. 1. One-photon decay of the neutrino in the MSSM ($X = \tilde{l}, H$, $Y = \tilde{\chi}^*, l$).

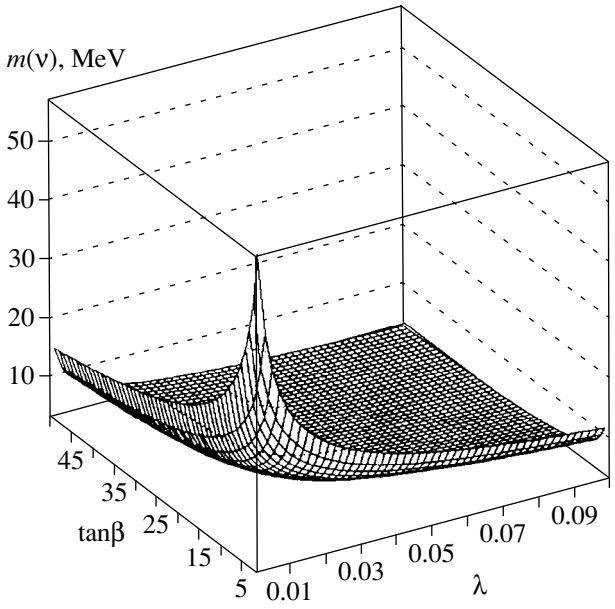

Fig. 2. Lower bound on the neutrino mass.

$$F^V_H = \frac{1}{(4\pi)^2}eg^2\sum_{i,j}\lambda_3^i\left\{\frac{m(\nu_a)+m(\nu_b)}{m_W^2}y_i f_3(y_i)\right.$$
$$-\frac{1}{2}f_2(y_i)\left[y_i\tan^2\beta + \frac{m(\nu_a)m(\nu_b)}{m_H^2}\cot^2\beta\right]$$
$$\left.\times\frac{m(\nu_a)+m(\nu_b)}{m_W^2}\right\},$$

where $F^V_{\rm L}$ and $F^V_{\rm R}$ are the contributions of the left- and right-handed scalar charged leptons to the vector form factor for the decay $\nu_a \longrightarrow \nu_b\gamma$, F^V_H is the contribution of the Higgs particle, $\lambda_1^i = O_{ai}O^*_{bi}$, $\lambda_2^i = O'_{ai}O'^*_{bi}$, and $\lambda_3^i = S_{ai}S^*_{bi}$; we have also introduced the following notation:

$$f_1(x) = \frac{1-x+x\ln x}{2(1-x)^2}, \quad f_2(x) = \frac{x^2-1-2x\ln x}{8(1-x)^3},$$
$$f_3(x) = \frac{x-1-\ln x}{4(1-x)^2}, \tag{10}$$

$$x_{ij}^{\mathrm{L}} = \frac{m^2(\tilde{l}_{\mathrm{L}i})}{m^2(\tilde{\chi}_j^*)}, \quad x_{ij}^{\mathrm{R}} = \frac{m^2(\tilde{l}_{\mathrm{R}i})}{m^2(\tilde{\chi}_j^*)}, \quad y_i = \frac{m^2(l_i)}{m_H^2}.$$

The form factors F^A are obtained from (9) by means of the relation

$$F^A(m(\nu_a), m(\nu_b)) = F^V(m(\nu_a), -m(\nu_b)). \qquad (11)$$

The tanβ and λ dependences of the lower bound on the neutrino mass can now be derived by using the astrophysical and cosmological constraints on the neutrino mass and lifetime [formulas (1) and (2)] in expressions (4) and (6)–(11). The results are illustrated in Fig. 2. In our numerical estimates, we assumed that the masses of the supersymmetric particles are on the order of 100 GeV and that the difference between the masses of the supersymmetric particles (charged scalar leptons) is not less than 10 GeV. The contribution of the charged Higgs particles to the form factors F^V and F^A is less than the contribution of the charged gauge fermions by a factor of $m^2(l)/m_H^2$. The leading contribution comes from the left-handed charged scalar leptons $\tilde{l}_L$. The parameter λ in Fig. 2 corresponds to the left-handed charged scalar leptons ($\lambda \equiv \lambda_1^i$). It should be noted that the lower bound on the neutrino mass depends only slightly on the mixing angles ϕ_+ and ϕ_- for the charged gauge fermions (Fig. 2 corresponds to ideal mixing). A global analysis that involves the astrophysical and cosmological constraints yields the following results: the electron and muon neutrinos must be light, $m(\nu_e) < 4$ eV and $m(\nu_\mu) < 40$ eV; the tau neutrino may be relatively heavy—its mass may lie above a few MeV. At large values of the parameters tanβ and λ ($\tan\beta \simeq 50$, $\lambda \simeq 10^{-1}$), the lower bound on the tau-neutrino mass may be as low as 3 MeV [Fig. 2].

ACKNOWLEDGMENTS

We are grateful to N. Amaglobeli, N. Lomidze, M. Kopadze, and T. Sakhelashvili for stimulating discussions and support.

REFERENCES

1. V. A. Lyubimov *et al.*, Phys. Lett. B **94**, 266 (1980).
2. Particle Data Group, Phys. Rev. D **54**, 1 (1996).
3. ALEPH Collab. (D. Buskalic *et al.*), Phys. Lett. B **349**, 585 (1995); ALEPH Collab. (R. Barate *et al.*), Report No. PPE-97-138, CERN (Geneva, 1997); Eur. Phys. J. C **2**, 395 (1998).
4. K. Assamagan *et al.*, Phys. Rev. D **53**, 6065 (1996).
5. A. I. Beleser *et al.*, Phys. Lett. B **350**, 263 (1995).
6. A. D. Dolgov and Ya. B. Zeldovich, Rev. Mod. Phys. **53**, 1 (1981).
7. H. Harari and Y. Nir, Nucl. Phys. B **292**, 251 (1987).
8. E. W. Kolb, in *Proceedings of the 1986 Santa Crue JASJ* (World Sci., Singapore, 1987), Vol. 2, p. 67.
9. B. W. Lee and S. Weinberg, Phys. Rev. Lett. **39**, 165 (1977).
10. J. Bernstein *et al.*, Phys. Rev. D **32**, 3261 (1985).
11. M. Kawasaki *et al.*, Phys. Lett. B **178**, 347 (1986).
12. S. Sarkar and A. M. Cooper, Phys. Lett. B **148**, 347 (1984).
13. G. Degrasi and A. Masiero, Phys. Lett. B **202**, 117 (1988).
14. G. G. Volkov *et al.*, Yad. Fiz. **52**, 283 (1990) [Sov. J. Nucl. Phys. **52**, 179 (1990)].
15. H. E. Haber and G. L. Kane, Phys. Rep. **117**, 75 (1985).
16. G. G. Volkov *et al.*, Fiz. Élem. Chastits At. Yadra **19**, 1026 (1988) [Sov. J. Part. Nucl. **19**, 442 (1988)].

Translated by R. Rogalyov

Physics of Atomic Nuclei, Vol. 63, No. 5, 2000, pp. 915–917. From Yadernaya Fizika, Vol. 63, No. 5, 2000, pp. 988–990.

ELEMENTARY PARTICLES AND FIELDS
Theory

Degenerate Odd Poisson Bracket on Grassmann Variables*

V. A. Soroka**

National Research Center, Kharkov Institute for Physics and Technology, Akademicheskaya ul. 1, Kharkov, 310108 Ukraine

Received March 18, 1999

Abstract—A linear degenerate odd Poisson bracket (antibracket) realized solely on Grassmann variables is proposed. It is revealed that this bracket has at once three Grassmann-odd nilpotent Δ-like differential operators of the first, second and third orders with respect to the Grassmann derivatives. It is shown that these Δ-like operators, together with the Grassmann-odd nilpotent Casimir function of this bracket, form a finite-dimensional Lie superalgebra. © *2000 MAIK "Nauka/Interperiodica".*

1. Predominantly, nondegenerate odd Poisson brackets have hitherto been studied and applied in the Batalin–Vilkovisky formalism [1–6] for the quantization of gauge theories and in the description of the Hamiltonian dynamics by means of an odd bracket [7–18]. However, as is well known from the example of usual even Poisson brackets, degenerate brackets also play a very important role in mathematics and in physical applications (see, for example, [19] and references therein).

In this paper, we propose a linear degenerate odd Poisson bracket realized solely on the Grassmann variables. We found that this bracket, in contrast to a nondegenerate odd bracket having only one Grassmann-odd nilpotent differential Δ operator of the second order, has at once three Grassmann-odd nilpotent Δ-like differential operators of the first, second, and third orders with respect to the Grassmann derivatives. We show that these Δ-like operators, together with the Grassmann-odd nilpotent Casimir function of this degenerate odd bracket, form a finite-dimensional Lie superalgebra.

2. There is a well-known linear degenerate even Poisson bracket given in terms of the commuting (Grassmann-even) variables X_α,

$$\{X_\alpha, X_\beta\}_0 = \varepsilon_{\alpha\beta\gamma}X_\gamma \quad (\alpha, \beta, \gamma = 1, 2, 3), \tag{1}$$

where $\varepsilon_{\alpha\beta\gamma}$ is the Levi-Civita tensor. The linear even Poisson brackets like (1) play a very important role in the theory of Lie algebras, Lie groups, and their representations (see, for example, [19, 20]). In general, the degenerate Poisson bracket has Casimir functions $C_k(X)$ whose brackets with any function $f(X)$ vanish:

$$\{C_k(X), f(X)\}_0 = 0.$$

As a rule, the level surfaces $C_k(X)$ = const of all independent Casimir functions define symplectic leaves on which the bracket becomes nondegenerate, and a closed 2-form (symplectic form) can be defined. The bracket specified by (1) has only one Casimir function,

$$C = \sum_{\alpha=1}^{3} (X_\alpha)^2,$$

and symplectic leaves in the form of S^2 spheres of a definite radius.

Let us now replace in (1) the commuting variables X_α by Grassmann variables θ_α. Then, we obtain the binary composition

$$\{\theta_\alpha, \theta_\beta\}_1 = \varepsilon_{\alpha\beta\gamma}\theta_\gamma \quad (\alpha, \beta, \gamma = 1, 2, 3), \tag{2}$$

which meets all the properties of the odd Poisson bracket:

$$\{A, B + C\}_1 = \{A, B\}_1 + \{A, C\}_1, \tag{3}$$

$$g(\{A, B\}_1) = g(A) + g(B) + 1 \pmod 2, \tag{4}$$

$$\{A, B\}_1 = -(-1)^{(g(A)+1)(g(B)+1)}\{B, A\}_1, \tag{5}$$

$$\sum_{(ABC)} (-1)^{(g(A)+1)(g(C)+1)}\{A, \{B, C\}_1\}_1 = 0, \tag{6}$$

$$\{A, BC\}_1 = \{A, B\}_1 C + (-1)^{(g(A)+1)g(B)}B\{A, C\}_1. \tag{7}$$

Here, A, B, and C are functions of the phase variables θ_α; $g(A)$ is the Grassmann parity of the quantity A; and the sum with the symbol (ABC) in (6) denotes a summation over cyclic permutations of the quantities A, B, and C. In order to establish the validity of the Jacobi identities (6) for the bracket in (2), we need to use the following relation for the completely antisymmetric tensor $\varepsilon_{\alpha\beta\gamma}$:

$$\varepsilon_{\alpha\beta\lambda}\varepsilon_{\gamma\delta\lambda} = \delta_{\alpha\gamma}\delta_{\beta\delta} - \delta_{\alpha\delta}\delta_{\beta\gamma}. \tag{8}$$

It is surprising enough that the odd bracket can be realized solely on the Grassmann variables as well as an even Martin bracket [21].

* This article was submitted by the author in English.

** e-mail: vsoroka@kipt.kharkov.ua

Using relation (8), we can verify that the degenerate odd bracket (2) has the following Grassmann-odd nilpotent Casimir function:

$$\Delta_{+3} = \frac{1}{\sqrt{3!}}\varepsilon_{\alpha\beta\gamma}\theta_\alpha\theta_\beta\theta_\gamma, \quad \{\Delta_{+3}, \ldots\}_1 = 0, \qquad (\Delta_{+3})^2 = 0. \tag{9}$$

This notation for the Casimir function in question will be clarified below.

By the way, let us note that, with the use of the completely antisymmetric five-tensor $\varepsilon_{\alpha\beta\gamma\delta\lambda}$ ($\alpha, \ldots, \lambda = 1, \ldots, 5$), we can also build, only in terms of Grassmann variables, a nonlinear degenerate odd Poisson bracket of the form

$$\{\theta_\alpha, \theta_\beta\}_1 = \varepsilon_{\alpha\beta\gamma\delta\lambda}\theta_\gamma\theta_\delta\theta_\lambda. \tag{10}$$

Indeed, with the use of the relations for the five-tensor $\varepsilon_{\alpha\beta\gamma\delta\lambda}$ that are similar to (8) we can establish, for the bracket (10), the relation

$$\{\theta_\alpha, \{\theta_\beta, \theta_\gamma\}_1\}_1 = 0$$

and, therefore, the validity of the Jacobi identities (6). The rest of the odd-bracket properties (3)–(5) and (7) are evidently fulfilled for the bracket in (10). The odd bracket (10) has several nilpotent Casimir functions,

$$C = \varepsilon_{\alpha\beta\gamma\delta\lambda}\theta_\alpha\theta_\beta\theta_\gamma\theta_\delta\theta_\lambda, \quad \{C, \ldots\}_1 = 0, \quad C^2 = 0;$$

$$C_\alpha = \varepsilon_{\alpha\beta\gamma\delta\lambda}\theta_\beta\theta_\gamma\theta_\delta\theta_\lambda, \quad \{C_\alpha, \ldots\}_1 = 0, \quad (C_\alpha)^2 = 0;$$

$$C_{\alpha\beta} = \varepsilon_{\alpha\beta\gamma\delta\lambda}\theta_\gamma\theta_\delta\theta_\lambda, \quad \{C_{\alpha\beta}, \ldots\}_1 = 0, \quad (C_{\alpha\beta})^2 = 0,$$

where no summations in the indices is assumed in the nilpotency conditions.

3. It is well known that, in contrast to the even Poisson bracket, in the case of the odd Poisson bracket, a Grassmann-odd nilpotent differential Δ operator of the second order can be built, which has naturally appeared in the Batalin–Vilkovisky scheme [1–6] for the quantization of gauge theories in the Lagrangian approach. This operator also plays a very important role in the formulation of Hamiltonian dynamics by means of the odd Poisson bracket with the help of the Grassmann-odd Hamiltonian $\overline{H}$ ($g(\overline{H}) = 1$) [7–11, 15],

$$\frac{dx^A}{dt} = \{x^A, \overline{H}\}_1, \tag{11}$$

where t is the time and $x^A = (x^i, \theta_i)$ ($i = 1, \ldots, n$) are the canonical phase coordinates. In Hamiltonian dynamics expressed in terms of the odd Poisson bracket, the Δ operator can be used to distinguish between nondissipative and dissipative dynamical systems. In fact, for a conventional nondegenerate odd Poisson bracket in the canonical form,

$$\{A, B\}_1 = A\sum_{i=1}^{n}(\overleftarrow{\partial}_{x^i}\overrightarrow{\partial}_{\theta_i} - \overleftarrow{\partial}_{\theta_i}\overrightarrow{\partial}_{x^i})B,$$

where $\overleftarrow{\partial}$ and $\overrightarrow{\partial}$ are, respectively, the right- and the left-hand derivative, the notation $\partial_{x^A} \equiv \partial/\partial x^A$ is introduced,

$$\Delta = 2\sum_{i=1}^{n}\partial_{x^i}\partial_{\theta_i},$$

and the infinitesimal form of the Liouville theorem is

$$\mathrm{str}(\partial_{x^A}\{x^B, \overline{H}\}_1) \equiv (-1)^{g(x^A)}\partial_{x^A}(\{x^A, \overline{H}\}_1) = \Delta\overline{H} = 0.$$

If $\Delta\overline{H} \neq 0$, the Liouville theorem does not hold, and a dynamical system described by means of Hamilton's equation in terms of the odd Poisson bracket (11) with such a Hamiltonian is dissipative.

Let us now try to build the Δ operator for the linear degenerate odd bracket (2). It is amusing that we are able to build at once three Δ-like Grassmann-odd nilpotent operators, which are the differential operators of the first, second, and third orders, respectively:

$$\Delta_{+1} = \frac{1}{\sqrt{2}}\theta_\alpha\theta_\beta\varepsilon_{\alpha\beta\gamma}\partial_{\theta_\gamma}, \quad (\Delta_{+1})^2 = 0, \tag{12}$$

$$\Delta_{-1} = \frac{1}{\sqrt{2}}\theta_\alpha\varepsilon_{\alpha\beta\gamma}\partial_{\theta_\beta}\partial_{\theta_\gamma}, \quad (\Delta_{-1})^2 = 0, \tag{13}$$

$$\Delta_{-3} = \frac{1}{\sqrt{3!}}\varepsilon_{\alpha\beta\gamma}\partial_{\theta_\alpha}\partial_{\theta_\beta}\partial_{\theta_\gamma}, \quad (\Delta_{-3})^2 = 0. \tag{14}$$

It is also surprising to reveal that these Δ-like operators, together with the Casimir function Δ_{+3} (9), are closed into a finite-dimensional Lie superalgebra in which the anticommuting relations between the quantities Δ_λ ($\lambda = -3, -1, +1, +3$) with a nonzero right-hand side are[1)]

$$\{\Delta_{-1}, \Delta_{+1}\} = Z, \tag{15}$$

$$\{\Delta_{-3}, \Delta_{+3}\} = -6 - 3Z, \tag{16}$$

where

$$Z = D^2 - 3D \tag{17}$$

is the central element of this superalgebra,

$$[Z, \Delta_\lambda] = 0 \quad (\lambda = -3, -1, +1, +3), \tag{18}$$

and

$$D = \theta_\alpha\partial_{\theta_\alpha} \tag{19}$$

[1)]In order to avoid confusion, let us note that $[A, B] = AB - BA$ and $\{A, B\} = AB + BA$.

is the "dilatation" operator for the Grassmann variables θ_α, which distinguishes the Δ_λ operators with respect to their uniformity degrees in θ,

$$[D, \Delta_\lambda] = \lambda\Delta_\lambda \quad (\lambda = -3, -1, +1, +3). \tag{20}$$

We can supplement this superalgebra with the generators S_α of rotations in the θ space,

$$S_\alpha = \theta_\gamma \varepsilon_{\alpha\beta\gamma}\partial_{\theta_\beta}, \tag{21}$$

with the commutation relations

$$[S_\alpha, S_\beta] = \varepsilon_{\alpha\beta\gamma}S_\gamma, \quad [S_\alpha, \Delta_\lambda] = 0, \tag{22a, b}$$

$$[S_\alpha, Z] = 0, \quad [S_\alpha, D] = 0. \tag{22c, d}$$

In order to prove the nilpotency of the operators Δ_{+1} and Δ_{-1} and to establish the majority of the permutation relations for the Lie superalgebra (15)–(22), we have to use relations (8) for the Levi-Civita tensor $\varepsilon_{\alpha\beta\gamma}$. Note that the central element Z (17) coincides with the expression for the quadratic Casimir operator of the Lie algebra (22a) for the generators S_α given in the representation (21):

$$S_\alpha S_\alpha = Z. \tag{23}$$

4. Thus, both the even and the odd linear degenerate Poisson brackets [equations (1) and (2), respectively] are internally inherent in the Lie group with the structure constants $\varepsilon_{\alpha\beta\gamma}$. However, only for the linear degenerate odd Poisson bracket (2) realized in terms of Grassmann variables does there exist the Lie superalgebra (15)–(22) for the Δ-like operators of this bracket.

The Lie superalgebra (15)–(22) can be used to develop further the Batalin–Vilkovisky formalism for the quantization of gauge theories. In particular, very similar to (2), odd Poisson brackets on the Grassmann algebra are used in [22][2)] on a generalization of the triplectic formalism [23], which is a covariant version of the $Sp(2)$-symmetric Lagrangian quantization [3] of general gauge theories. We should therefore expect that the Lie superalgebra (15)–(22), closely related to the linear degenerate odd bracket (2), will also be applied to a further development of the above-mentioned generalization of the triplectic formalism.

ACKNOWLEDGMENTS

I am sincerely grateful to V.D. Gershun for stimulating discussions.

This work was supported in part by the Ukrainian State Foundation for Basic Research, grant no. 2.5.1/54, and by INTAS, grant no. 93-127 (Extension) and 93-633 (Extension).

[2)]This paper appeared after the present work had been performed.

REFERENCES

1. I. A. Batalin and G. A. Vilkovisky, Phys. Lett. B **102**, 27 (1981).
2. I. A. Batalin and G. A. Vilkovisky, Phys. Rev. D **28**, 2567 (1983).
3. I. A. Batalin, P. M. Lavrov, and I. V. Tyutin, J. Math. Phys. **31**, 1487 (1990).
4. I. A. Batalin and I. V. Tyutin, Int. J. Mod. Phys. A **8**, 2333 (1993).
5. A. S. Schwarz, Commun. Math. Phys. **155**, 249 (1993).
6. O. M. Khudaverdian and A. P. Nersessian, Mod. Phys. Lett. A **8**, 2377 (1993).
7. D. A. Leites, Dokl. Akad. Nauk SSSR **236**, 804 (1977).
8. D. V. Volkov, A. I. Pashnev, V. A. Soroka, and V. I. Tkach, Pis'ma Zh. Éksp. Teor. Fiz. **44**, 55 (1986) [JETP Lett. **44**, 70 (1986)]; Teor. Mat. Fiz. **89**, 117 (1989).
9. V. A. Soroka, Lett. Math. Phys. **17**, 201 (1989).
10. O. M. Khudaverdian, J. Math. Phys. **32**, 1934 (1991).
11. O. M. Khudaverdian and A. P. Nersessian, J. Math. Phys. **32**, 1938 (1991).
12. D. V. Volkov, V. A. Soroka, and V. I. Tkach, Yad. Fiz. **44**, 810 (1986) [Sov. J. Nucl. Phys. **44**, 522 (1986)].
13. D. V. Volkov and V. A. Soroka, Yad. Fiz. **46**, 110 (1987) [Sov. J. Nucl. Phys. **46**, 69 (1987)].
14. V. A. Soroka, Pis'ma Zh. Éksp. Teor. Fiz. **59**, 205 (1994) [JETP Lett. **59**, 219 (1994)].
15. V. A. Soroka, in *Proceedings of the Workshop on Variational and Local Methods in the Study of Hamiltonian Systems, ICTP, Trieste, Italy, 1994*, Ed. by A. Ambrosetti and G. F. Dell'Antonio (World Sci., Singapore, 1995), p. 192; hep-th/9503214.
16. A. P. Nersessian, Pis'ma Zh. Éksp. Teor. Fiz. **58**, 64 (1993) [JETP Lett. **58**, 66 (1993)].
17. D. V. Volkov, A. V. Tur, and V. V. Yanovsky, Phys. Lett. A **203**, 357 (1995).
18. V. A. Soroka, Yad. Fiz. **59**, 1327 (1996) [Phys. At. Nucl. **59**, 1270 (1996)]; hep-th/9507030.
19. M. V. Karasev and V. P. Maslov, *Nonlinear Poisson Brackets: Geometry and Quantization* (Nauka, Moscow, 1991).
20. F. A. Berezin, *Introduction to Algebra and Analysis with Anticommuting Variables* (Mosk. Gos. Univ., Moscow, 1983).
21. J. L. Martin, Proc. R. Soc. London A **251**, 536 (1959).
22. M. A. Grigoriev, Phys. Lett. B **458**, 499 (1999).
23. I. A. Batalin, R. Marnelius, and A. M. Semikhatov, Nucl. Phys. B **446**, 249 (1995).

Physics of Atomic Nuclei, Vol. 63, No. 5, 2000, pp. 918–919. Translated from Yadernaya Fizika, Vol. 63, No. 5, 2000, pp. 991–992.

NEWS ITEMS

Anatoliĭ Filippovich Tulinov is 75

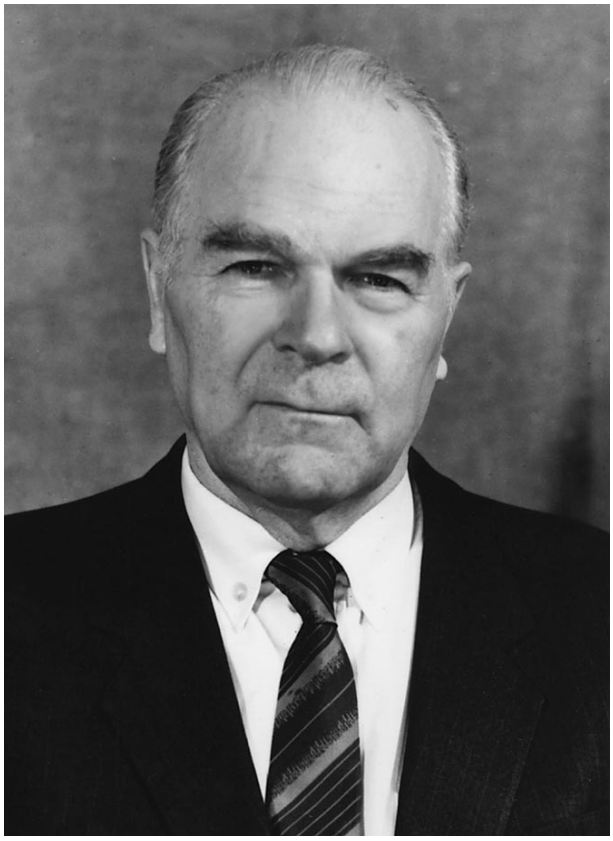

Anatoliĭ Filippovich Tulinov, a distinguished physicist and teacher, celebrated his 75th birthday on September 24, 1999. He is a professor of physics at Moscow State University and a leading researcher at the Institute of Nuclear Physics, Moscow State University (INP MSU).

Like many of his peers, Tulinov had to fight in World War II and could take up science only in the postwar years. Joining the Faculty of Physics at Moscow State University in 1946 proved to be decisive for his whole career in science: it was at the university that he gradually advanced from a student to an eminent professor and head of the department of nuclear physics and of the largest department of INP MSU. At Moscow State University, Professor Tulinov has delivered major lecture courses on nuclear physics for over 40 years and may therefore count thousands of nuclear physicists among his students.

Beginning in his student years, Tulinov took interest in nuclear reactions. As a student of the accelerator department headed by V.I. Veksler, he started his investigations of nuclear reactions at the cyclotron that was commissioned at INP MSU in 1949. These early studies even then revealed his unique gift of an experimentalist, which fully matured in his subsequent investigations. His fertile and inventive mind perpetually conceived delicate and elegant experiments, posed nonstandard problems, and sought original solutions thereof.

As a postgraduate (in 1955), Tulinov proposed a novel technique for probing the excited states of light nuclei on the basis of the emission angle of recoil nuclei. In 1957 and 1958, he conceived and implemented an original method for measuring the lifetimes of excited nuclei by their radiative transitions in the range between 10^{-12} and 10^{-14} s. Ever since, Tulinov has maintained keen interest in evolution of nuclear reactions in real time. Around 1960, he again invoked "nuclear times" in order to understand how the structure of light nuclei affects the mechanisms of nuclear reactions. He realized that the underlying mechanism of a reaction might be identified by its duration in time, but measuring the latter seemed utterly unrealistic: only times between some 10^{-10} and 10^{-14}, which are typical of radiative transitions, could be measured directly. The lower boundary of this interval had to be pushed down by several orders of magnitude in order to measure the duration of a nuclear reaction. An innovative solution, masterminded by Tulinov in 1964, was to use a single-crystal target. The idea was to analyze the emission angles of reaction products with respect to the linear chain of nuclei in the crystal lattice: Tulinov argued that the angular distribution of the products should show local minima (shadows). The displacement of a compound nucleus from the chain, which is determined by its lifetime, should manifest itself in the shapes of the shadows.

The predicted effect of shadows had to be proven experimentally, and they were indeed detected and investigated by Tulinov and his colleagues in proton scattering on various single crystals. The observation of the novel phenomenon of shadows in nuclear reactions on single crystals was later recognized officially as a scientific discovery.

Using single crystals as targets, Tulinov was able to measure time intervals as small as 10^{-15}–10^{-20} s. This method won worldwide recognition and, apart from nuclear physics proper, now finds applications in high-energy collisions involving the formation of new particles. It made it possible to probe directly the time evolution of a nuclear reaction and, thereby, initiated a new and promising direction in nuclear physics. Relying on

1063-7788/00/6305-0918$20.00 © 2000 MAIK "Nauka/Interperiodica"

the new method, Tulinov and his collaborators were able to derive the temporal characteristics of some reactions and, in particular, of the fission of heavy nuclei. For a number of fissile nuclei, the method helped elucidate the structure of the fission barrier, the level density in the second potential well, the symmetries of the spatial shape of fissile nuclei, and the viscosity of nuclear matter in the fission process. These investigations are being actively pursued at Tulinov's laboratory and elsewhere.

The idea to irradiate a single-crystal target with a beam of accelerated particles, which we owe to Tulinov, gave rise to yet another direction of research dubbed protonography. Combining the methods of nuclear and solid-state physics, protonography allows one to investigate the structure of a crystal by the shape and pattern of the aforementioned shadows. Protonography is a proven and incisive tool for probing a thin layer near the surface of a crystal without rupturing the sample. Thereby, the structure is scanned layer-by-layer, imperfections of the lattice are revealed, and alien atoms are precisely located in the lattice. Unlike the traditional approaches to studying the structure of a crystal that are largely based on the phenomenon of diffraction, protonography relies on the purely corpuscular aspect of the probe.

Tulinov is the founding father and undisputed leader of a robust scientific school in experimental physics that deals with interactions between elementary particles and crystals. That Moscow University has become a regular venue of the International Conference on Particle–Crystal Interactions, convened for the twenty-ninth time last year, may be credited to Tulinov. He may boast over 40 candidates of physics and six doctors of physics among his immediate students. Tulinov's works on particle interactions with crystals won him a Lomonosov Prize of First Degree and a State Prize.

Apart from research and teaching, Prof. Tulinov devotes much of his time to social and science-policy work. For many years, he was deputy chair of the Committee for Applied Nuclear Physics, chaired by Academician G.N. Flerov, and chair of the Commission on Discoveries in Physics at the State Committee for Discoveries and Inventions. At his home university, Tulinov is a Professor Emeritus and head of the Physical Society.

At an advanced age of 75, Tulinov is still teaching and doing research work at the INP MSU. At the university, he delivers annual lecture courses on nuclear and solid-state physics to the students. At INP, he continues to guide a large physics community of his students and collaborators.

On behalf on the many colleagues, friends, and pupils of Professor Tulinov, we congratulate him on this anniversary and wish him good health and new achievements in science.

V. V. Balashov, G. A. Iferov, Yu. V. Melikov,
M. I. Panasyuk, V. I. Trukhin,
N. G. Chechenin, and O. A. Yuminov